Controlled pore glasses and alginate hydrogels as form-giving matrices for nanoporous organosilicas

Dissertation

zur Erlangung des Grades Doktor der Naturwissenschaften (Dr. rer. nat.)

an der Fakultät für Mathematik, Informatik und Naturwissenschaften

im Fachbereich Chemie der Universität Hamburg

vorgelegt von

Malina Bilo

aus Essen

Hamburg 2019

Die vorliegende Arbeit wurde in der Zeit von April 2014 bis März 2019 unter wissenschaftlicher Betreuung von Prof. Dr. Michael Fröba am Institut für Anorganische und Angewandte Chemie der Universität Hamburg angefertigt.

1. Gutachter: Prof. Dr. Michael Fröba
2. Gutachter: JProf. Dr. Simone Mascotto

Datum der Disputation: 03.05.2019

Datum der Druckfreigabe: 03.05.2019

Hiermit versichere ich an Eides statt, die vorliegende Dissertation selbst verfasst und keine anderen als die angegebenen Hilfsmittel benutzt zu haben. Die eingereichte schriftliche Fassung entspricht der auf dem elektronischen Speichermedium.
Ich versichere, dass diese Dissertation nicht in einem früheren Promotionsverfahren eingereicht wurde.

Hamburg, den 13.03.2019
Malina Bilo

Danke!

An dieser Stelle möchte ich mich bei Herrn Prof. Dr. Michael Fröba für die Aufnahme in den Arbeitskreis, für das mir entgegengebrachte Vertrauen und die Freiheiten bei der Bearbeitung dieser verschiedenen Themenfelder bedanken.

Herrn JProf. Dr. Simone Mascotto danke ich für die Übernahme des Zweitgutachtens. Herrn Prof. Dr. Dr. h.c. mult. Wittko Francke und Herrn Prof. Dr. Michael Steiger danke ich für die Bereitschaft zur Teilnahme in der Prüfungskommission meiner Disputation.

Für eine sehr gute Zusammenarbeit danke ich unseren Kooperationspartnern im DFG Projekt. Dabei danke ich besonders Herrn Prof. Dr. Dirk Enke und den Mitarbeitern Andrei Barascu, Dr. Christian Küster, und Maximilian Münzner für die Bereitstellung verschiedener CPGs und den Erfahrungsaustausch. Herrn Prof. Dr. Dieter Bathen und den Mitarbeitern Dirk Bucher und Dr. Roman Orthmann danke ich für die Adsorptionsmessungen an meinen Materialien.

Herrn Prof. Dr. Jochen Schlüter und dem Mineralogischen Museum der Universität Hamburg danke ich, mir anschauliche Beispiele für die pseudomorphe Transformation zur Verfügung gestellt zu haben und Dr. Frank Hoffmann für die wertigen Fotografien.

Für die Analytik meiner zahlreichen Proben danke ich Sandra König, Isabelle Nevoigt, Renate Walter, Andreas Kornowski, Claudia Wontorra und Uta Sazama sowie Dawid Bednarski, Dr. Michael Dreifke, Eva Gjuzi, Dr. Anika Juhl, Dr. Paul Kallenberger und Tamás Simon. Besonders danke ich Dr. Young Joo Lee für viele Festkörper-NMR Messungen, ihre geduldigen Erklärungen und Unterstützung bei der Auswertung.

Für zwei offene Ohren hinter einer stets geöffneten Türe und diverses Korrekturlesen möchte ich mich bei Dr. Felix Brieler bedanken.

Dr. Dorothee Fried danke ich für ihre tatkräftige Unterstützung beim Herantasten an das Konzept der pseudomorphen Transformation und für ihre hilfreichen Ratschläge in der Anfangsphase der Promotion.

Außerdem danke ich Norman Freudenreich, Hiba Nasser, Dustin Peters und Natascha Speil, die als Praktikanten und Praktikantinnen, sowie Philip Lenz und Marlen Müller die in ihren Bachelorarbeiten und als HiWis diese Arbeit mit ihrer Unterstützung im Labor bereichert haben.

Dr. Michael Sartor und Timo Stein danke ich besonders für die kritischen und hilfreichen Korrekturen dieser Arbeit.

Für tolle Bürozeiten mit wissenschaftlichem und gänzlich unwissenschaftlichem Austausch danke ich Tamás Simon, Matthias Rogaczewski und Julia Ziegler.

Für das Überbrücken von Hunger- und Stimmungstiefs, für offene Ohren und vor allem für geteilte (kulinarische) Freude danke ich dem Küchensquad – auch denen die dazugehörten als es noch die Küchenfraktion war. Danke an alle AK-Mitglieder, die mich während meiner Zeit in der Arbeitsgruppe mit viel Hilfsbereitschaft und einer angemessenen Portion Unfug begleitet haben.

Besonders dankbar bin ich meinen Eltern für ihre bedingungslose Unterstützung mit Rat und Tat, nicht nur in den Jahren der Promotion. Fürs Mitfiebern, wertvolle Ablenkung und dafür, dass ihr mir so viel Freude macht danke ich außerdem Nicolas, Karina, Luka und Maximilian Bilo.

Über alles hinaus danke ich Peer, der es geschafft hat, trotz Entfernung immer für mich da zu sein und mir den Rücken zu stärken.

Table of Contents

List of Abbreviations

APTES	3-aminopropyltriethoxysilane
B-	benzene-bridged
BET	Brunauer, Emmett and Teller
BJH	Barrett, Joyner and Halenda
BP-	biphenyl-bridged
BTEB	1,4-bis(triethoxysilyl)benzene
BTEE	1,2-bis(triethoxysilyl)ethane
BTEV2FB	1,4-((*E*)-2'-bis(triethoxysilyl)vinyl)-2,5-difluorobenzene
BTEVA	2,5-((*E*)-2'-bis(triethoxysilyl)vinyl)aniline
BTEVB	2,5-((*E*)-2'-bis(triethoxysilyl)vinyl)benzene
BTEVClB	2-chloro-1,4-((*E*)-2'-bis(triethoxysilyl)vinyl)benzene
BTEVFB	1,4-((*E*)-2'-bis(triethoxysilyl)vinyl)-2-fluorobenzene
CMR	Carcinogenic, mutagenic, reprotoxic
C_{10}TAB	decyltrimethylammonium bromide
C_{16}TAB/ C_{16}TAC	cetyltrimethylammonium bromide / chloride
C_{16}TAOH	cetyltrimethylammonium hydroxide
C_{18}TAB / C_{18}TAC	octadecyltrimethylammonium bromide / chloride
CP	cross polarization
CPG	controlled pore glasses
COSY	correlation spectroscopy
DEPT	distortionless enhancement by polarization transfer
DMF	*N*, *N*-dimethylformamide
DTA	differential thermal analytic
DVA-	divinylaniline-bridged
DVB-	divinylbenzene-bridged
e.g.	*exempli gratia* (lat.) for example
et al.	*et alii* (lat.) and others
FSLG	frequency-switched Lee–Goldburg
HCl	hydrochloric acid
HETCOR	heteronuclear correlation
HMBC	heteronuclear multiple bond correlation
HPLC	High performance liquid chromatography
HSQC	heteronuclear single quantum correlation

HTT	hydrothermal treatment
i.e.	*id est* (lat.) that is to say
IR	infrared
IUPAC	International Unit of Pure and Applied Science
MAS	magic angle spinning
MCM-41	Mobil Composition of Matter no. 41
MOF	metal-organic framework
MOS	mesoporous organosilicas
MIP	mercury intrusion porosimetry
MS	mass spectrometry
MTS	micelle-templated silica
NaOH	sodium hydroxide
NLDFT	nonlinear density functional theory
NMR	nuclear magnetic resonance
O/W	oil-in-water
PFG NMR	pulsed field gradient nuclear magnetic resonance
PMO	periodic mesoporous organosilica
SBA	University of California Santa Barbara
SEM	Scanning electron microscopy
ss	solid state (NMR)
TEM	transmission electron microscopy
TEOS	tetraethyl orthosilicate
TG	thermogravimetry
TLC	thin layer chromatography
TMB	1,3,5-trimethylbenzene
TMOS	tetramethyl orthosilicate
vol%	volume percent
w/	with
w/o	without
W/O	water-in-oil
wt%	weight percent
XRD	X-ray diffraction

1 Introduction

1.1 Hierarchically porous silicas

With bones, wood and sponges, nature provides good examples of nanoporous materials.[1] Their unique properties, which include a high surface area and low density, allow us to mimic materials with similar porosity.

In their recommendations from 1985, the International Union of Pure and Applied Chemistry (IUPAC) defines a pore as a crack in a material which is deeper than it is wide. Nanopores are classified according to their diameter in nanometers as micropores (< 2 nm), ultramicropores (< 0.7 nm), supermicropores (0.7–2.0 nm), mesopores (2–50 nm) and macropores (50–100 nm). Materials within these different groups of pore sizes show different physisorption behaviors that is decisive in the classification and is described in detail in section 3.1.[2,3]

With respect to porous silica-based materials, different synthesis paths that result in different pore systems are possible. To start, zeolites must be named among the silica-based nanoporous materials as these naturally occurring sediments have been used unconsciously since ancient times. Their discovery goes back to 1756 when the Swedish mineralogist, Axel F. Cronstedt, classified the first samples and coined the term zeolite.[4] These mainly microporous alumino-silicates are interesting catalysts and can be used for size-dependent separations, for which the synthesis of new zeolites is still a relevant topic of research.[5,6] The sol-gel route usually gives meso/microporous silica materials. A way to generate homogeneous mesopores larger than those of zeolites is given by micelle templating during sol-gel processes of silica, which is described in section 1.2 below. The addition of polymers to a silica sol-gel reaction can cause phase separation where narrow pore size distributions in the meso- to macropore range can be obtained, as established by Nakanishi and Soga.[7] Likewise, the phase separation of glasses leads to meso/macroporous silicate glasses that play a role in this thesis and are described in section 1.3. These glasses are well established as starting materials for hierarchical porous systems.

Hierarchy, a term derived from the Greek (*hieros* =sacred and *arkhein* = to lead/rule), originally meant a ranking in power and importance. Nowadays, it is used more generally for graded classifications in different contexts. Hierarchical systems are requisite for mass transport, as in the branched and far-reaching roots of trees to provide essential nutrition to the treetop.

Further, the blood-stream in our bodies is hierarchically structured to bring oxygen-rich blood to the whole body. It is based on a main artery, the aorta, and other arteries from where arterioles branch off and in turn subdivide into capillaries. Another example of hierarchical transport is a

freeway that has exits leading to streets in different cities. In all these cases it is of particular relevance that the branches, veins and streets are connected rather than existing side by side. Although this seems obvious in all the examples, when one examines porous systems this is not always the case. The above examples reveal the advantages of hierarchically porous materials for mass-flow systems. Small pores significantly increase the surface area which simultaneously decreases the density of the material. In turn, larger pores prevent pore blocking and delayed diffusion. Maximized accessibility and diffusion of the whole surface area is possible by connecting pore systems with different diameters, i.e. a hierarchical system. The wide field of applicability for different kinds of hierarchical materials was recently reviewed in different contexts, from energy storage or catalysis up to separation processes.[8]

Schwieger *et al*. defined two types of hierarchy according to the interconnection of pore systems.[9] Hierarchy type I are "pore systems in which each level (larger/wider pores) subdivides into several species of a next level (smaller/narrower pores)", as is the case in the given examples of roots or arterioles and capillaries. This is depicted in Figure 1-1 on the left. Hierarchy type II are "interconnected pore systems of different pore size, where the larger (wider) pores intersect the smaller pore system, i.e. small pores branch off from a continuous large pore" an in main streets and side streets. This is depicted in the central scheme in Figure 1-1. A key aspect of hierarchical pore systems is that the inlet flow, e.g. of gases, is disturbed so that it also has to pass through the smaller pores. On the other hand, asymmetric pores and unconnected pore systems of different size cannot be named hierarchical as shown in Figure 1-1 on the right.

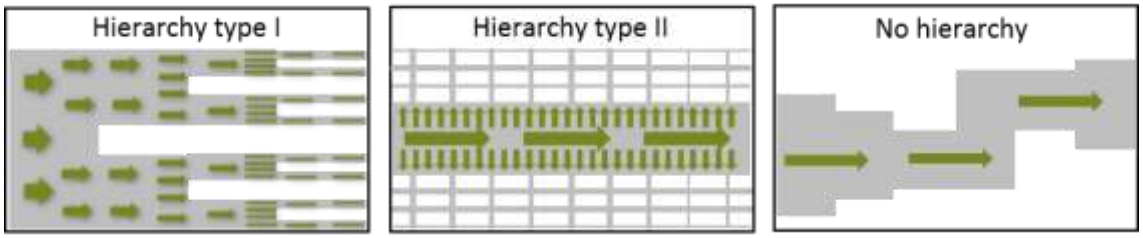

Figure 1-1: Different types of hierarchy defined according to Schwieger *et al.* Hierarchy type I has pores that are subdivided stepwise into smaller pores. Hierarchy type II implies a main pore that intersects a smaller pore system. No hierarchy exists as long as the inlet flow is not disturbed. Reproduced from [9].

Whether pores of different diameters are interconnected or not is a key question in the characterization of porous materials. The physisorption behavior of the materials may provide evidence for this. In the case of hierarchical mesoporous networks, hysteresis phenomena can occur due to pore blocking or cavitation effects. By extensive inspection of the hysteresis at different temperatures and with different adsorptives one might distinguish between the different mechanisms that promote hysteresis in ink bottle models with different neck widths. A new approach is given by scanning measurements that interrupt the adsorption or desorption process

in the respective pressure range where the hysteresis occurs, so that the pores partially fill and empty. The behavior of the curves determines whether the different pores are interconnected or not.[10] General information on the characterization of porous materials by physisorption is given in section 3.1.

1.2 Ordered mesoporous silicas

In 1992, the Mobil Oil Company became a trendsetter by describing the development of the M41S family as a possibility to generate well-structured mesoporous silica materials with a narrow pore size distribution.[11,12] The synthesis principle is based on the common sol-gel approach, whereby strongly alkaline or acidic conditions lead to the hydrolysis of a silica species, followed by its condensation, the general mechanism will be described here first with the help of Figure 1-2.

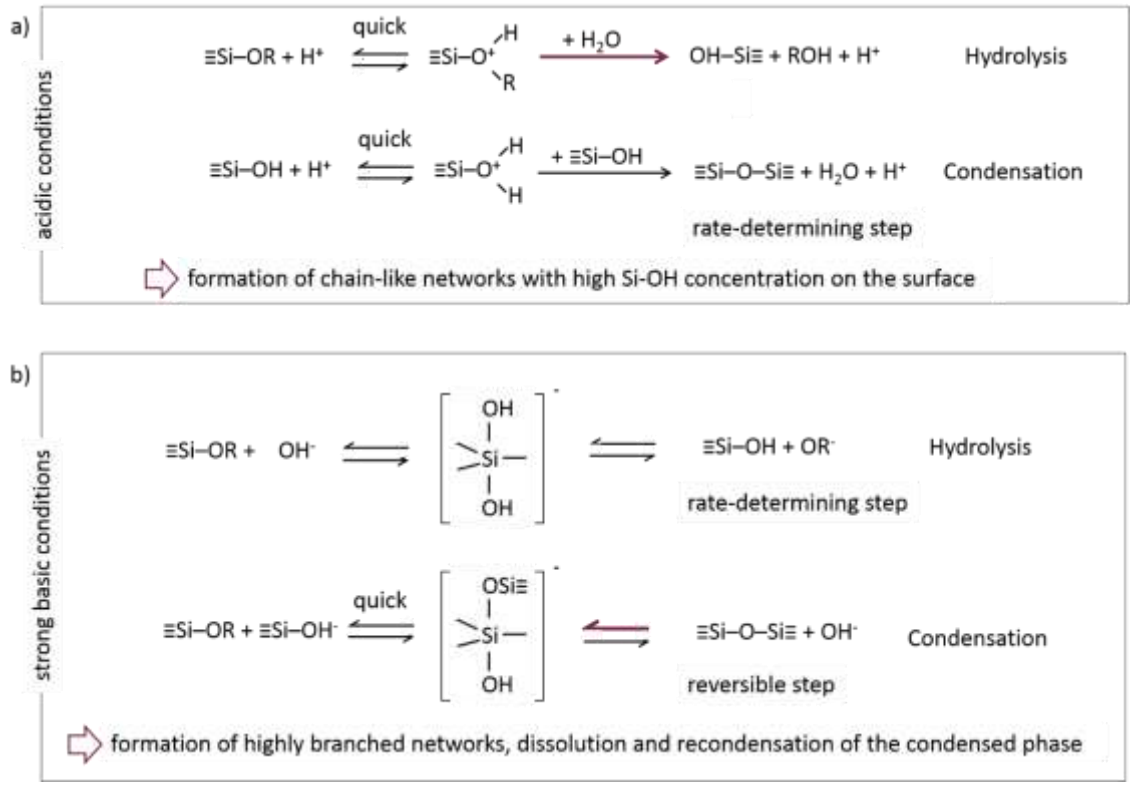

Figure 1-2: Overview of the mechanism of hydrolysis and condensation under (a) acidic and (b) strong basic conditions. Reproduced from [13].

Figure 1-2 a) shows the mechanism under acidic conditions at pH values below the point of zero charge of silica (between pH 1.5-4.5).[14] The first step, the rapid protonation of the oxygen atom of the alkoxy or hydroxyl group, leads to water or an alcohol as a good leaving group and decreases the electron density of the silicon atom. Under acidic conditions, the hydrolysis is favored and the condensation is the rate-determining step, which causes the formation of chain-like networks and a large number of monomers with a higher concentration of reactive Si–OH

groups on the surface. Under basic conditions, shown in Figure 1-2 b), a nucleophilic attack on the silicon atom by a hydroxide ion(OH^-), which is the hydrolysis reaction, or of a silanol ion (Si-O^-), which is the condensation reaction, occurs. An intermediate state with a five-binding central silicon atom is formed and subsequently an alkoxy ion (OR^-) or a hydroxide ion (OH^-) is eliminated. The hydrolysis is the rate-determining step under basic conditions, so that highly branched networks are formed. The reversibly of the last step of the condensation under strong basic conditions, which means that dissolution and recondensation of the condensed phase occurs, plays a particular role in Section 1.4.

The electron density at the silicon atom depends on the attached substituents due to inductive effects, following the order

$$\equiv Si–R > \equiv Si–OR > \equiv Si–OH > \equiv Si–O–Si$$

Hence, organically substituted alkoxysilanes are more reactive under acidic conditions and less reactive under basic conditions, compared to pure silica species, since the increased electron density effects the transitions states of hydrolysis and condensation, respectively.[14]

For the synthesis of M41S materials, quaternary ammonium surfactants are added to the alkaline solution to form a template. Silica sources including fumed silica, sodium silicate and often esters of silicic acid such as tetraethyl orthosilicate (TEOS) are used. Micelles of the surfactant arrange themselves into cylindrical, rod-shaped micelles which, in turn, form a hexagonal phase as depicted in Figure 1-3. When the silica source is added it undergoes hydrolysis and condensation as described before and occupies the vacancies in the template. A composite of inorganic solid and surfactant is formed. Next to the true liquid crystal approach, path (a) in Figure 1-3, a cooperative mechanism, path (b) in Figure 1-3, allows the self-assembly of surfactant and the silica species, resulting, in turn, in the same composite with an even lower surfactant concentration. The organic surfactant can be removed by extraction with an appropriate solvent or by calcination.[13] The resulting material in this example has a 2D hexagonal pore system and is known as MCM-41. Silica materials which are synthesized according to this synthesis path are often referred to as micellar-templated silicas (MTS). This term is widely used in the literature and will be used in the following as well, but it has to be pointed out that the templating process does not only imply micelles but an assembly of micelles as in a lyotropic crystal.

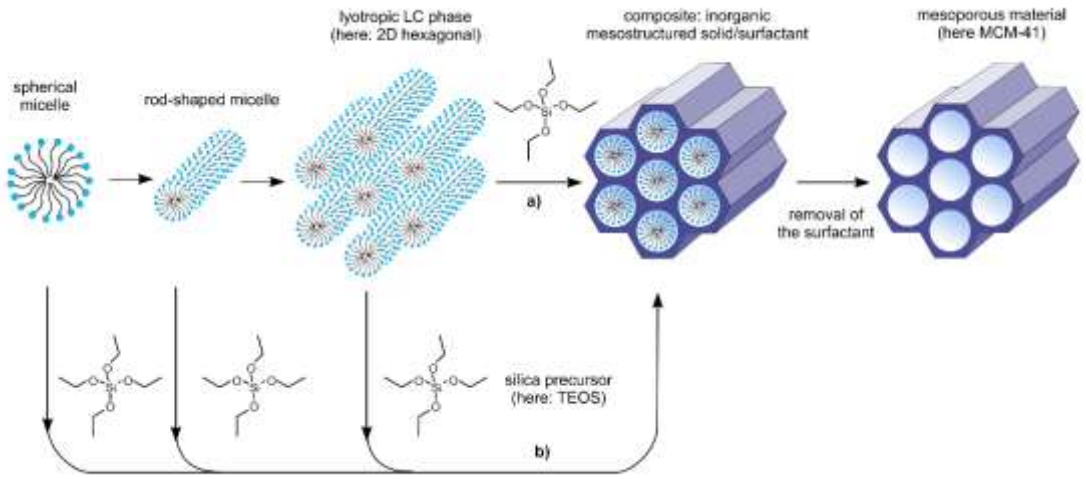

Figure 1-3: Synthesis mechanism of MCM-41 as an example of micelle-templated silica materials with TEOS as a silica source. Following path (a), the true liquid crystal mechanism is shown. Path (b) illustrates a cooperative mechanism, where the hydrolyzed silica source condenses and meanwhile encloses the template appropriately despite the micelle concentration being insufficient to form a liquid-crystalline phase. Reprinted from [16] with permission from Wiley.

Next to the 2D hexagonal phase, the micelles of the surfactant can also arrange themselves in cubic or lamellar phases. Representative materials are known as MCM-48 and MCM-50, respectively. The resulting pore structures are shown in Figure 1-4. The small-angle range of powder X-ray diffraction (P-XRD) patterns can be used to distinguish between the different phases, as can be seen in Figure 1-4 below the structures.

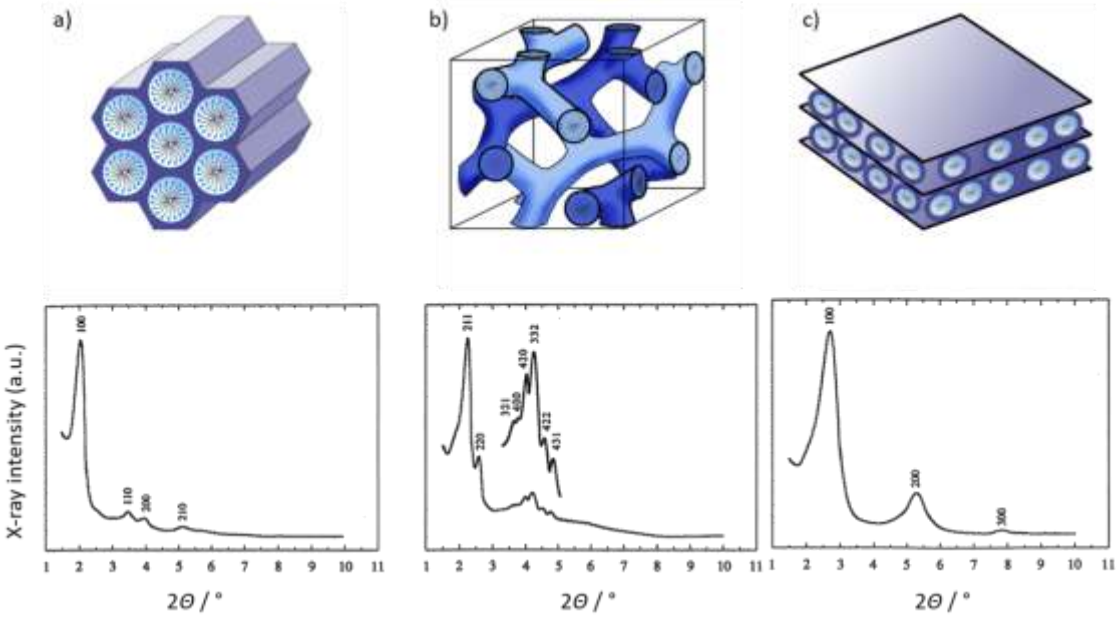

Figure 1-4: Different phases of the rod-shaped micelles with examples of the materials resulting from them: (a) 2D hexagonal phase p6m (e.g.MCM-41), (b) cubic phase Ia$\bar{3}$d (e.g. MCM-48) and (c) lamellar phase (e.g. MCM-50). Reprinted from [16] with permission from Wiley. The P-XRD patterns are adapted with permission from [17]. Copyright 2000 American Chemical Society.

The specific phase resulting from a synthesis depends mainly on the surfactant used, the micelle concentration and the pH value.[18] The packing parameter *g* has a large influence on the resulting mesophase. It is calculated with equation (1) and depends on the volume *V* of the surfactant chain, its length *l* as well as on a_0, the effective head group area.

$$g = V/l \cdot a_0 \quad (1)$$

where

V volume of the surfactant chain

L length of the surfactant chain

a_0 effective head group area

The specific mesophase resulting from different packing parameters is summarized in Table 1-1.[19]

Table 1-1: Correlation between packing parameter *g* and the respective mesophase and its space group.

g	**mesophase**	**space group**
⅓	cubic	$Pm\bar{3}n$
½	hexagonal	P6m
½-⅔	cubic	$Ia\bar{3}d$
1	lamellar	-

It should be mentioned that different surfactants are also possible for this synthesis path. The use of hexadecyltrimethylammonium bromide or chloride is prevalent, but among the named quaternary ammonium surfactants of the formula $C_nH_{2n+1}(CH_3)_3NX$, with X = Cl or Br both shorter or longer (C8-C18) alkyl chains are possible, leading to different pore diameters from 2 nm to 4 nm.[12]

The formation of ordered mesoporous silica is only possible due to attractive interactions between the head group of the surfactant and the silica phase. When a cationic surfactant is used, the Si-OH species needs to be negatively charged, which is the case under alkaline conditions. The interactions between the cationic surfactant S^+ and the inorganic moiety I^- is shown in Figure 1-5 (a). Under acidic conditions, below the isoelectric point of Si-OH (pH ≈ 2), a mediator ion X^-, e.g. a halide, is necessary (Figure 1-5 (b)) for successful interaction with a cationic surfactant. Bacille *et al*. investigated the differences between the surfactant-silica interface under alkaline and acid media with solid-state nuclear magnetic resonance (NMR) spectroscopy. They found that the network is slightly more condensed under alkaline conditions and proved the presence of water in the surfactant-silica interface (not shown in Figure 1-5).[20] The mechanism is reversed in the case of anionic surfactants where a mediator cation (M^+) is

needed under alkaline conditions (see Figure 1-5 (c)) but not under acidic conditions (see Figure 1-5 (d)). Besides, other classes of surfactants, such as block copolymers, have also already been established in similar syntheses. Using these surfactants, larger mesopore diameters up to 30 nm can be generated as in the 2D hexagonal representative SBA-15.[21] As the head groups of these polymers are not charged, no electrostatic interactions with the silica network are given. Instead, attractive interactions through hydrogen bonds to uncharged surfactants S^0 (e.g. polyethylene oxide or a long-chained amine N^0) exist in two cases: either with uncharged inorganic species (at the point of zero charge), as shown in Figure 1-5 (e), or with a positively charged inorganic species that forms an ion pair $(XI)^0$ with a mediator ion (X^-) under acidic conditions (see Figure 1-5 (f)).[16]

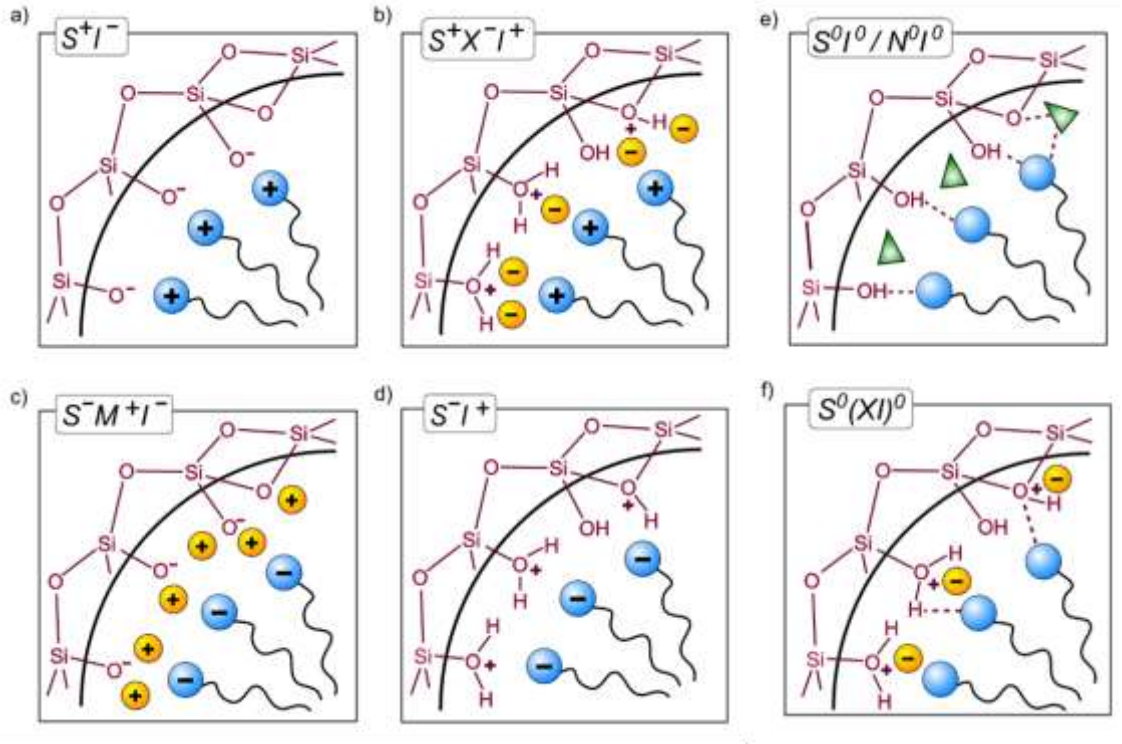

Figure 1-5: Overview of interactions between different surfactants (S) and the inorganic backbone (I) of the silica network. A distinction should be made between electrostatic interactions, on the one hand, with cationic surfactants under alkaline (a) or acidic (b) conditions, and anionic conditions (c) and (d), respectively. M^+ is a mediator ion. On the other hand, hydrogen bonds in the case of uncharged surfactants S^0, e.g. polyethylene oxide or a long-chained amine N^0 with the inorganic species, as well uncharged (I^0) or under acidic conditions as an ion pair with a mediator anion (XI). Reprinted from [16] with permission from Wiley.

1.3 Controlled pore glasses (CPG)

In 1938, Hook and Nordberg from the Corning Glass Company patented the synthesis of quartz glass-like silica glasses [22] using comparably low temperatures of about 1200 °C instead of the typically required 2000 °C.[23,24] The glasses are obtained from a ternary mixture of 5–10 wt% R_2O (sodium, potassium or lithium oxide), 25–30 wt% B_2O_3 (boronic acid) and of 55–70 wt% SiO_2 (silica).[25] The secret behind the successful decrease in the synthesis temperature is the thermally induced phase separation of alkali borosilicate glasses into a silica-rich, acid-insoluble and alkali and boron oxide-rich, acid-soluble phase at a certain temperature, depending on the system composition. Although the mechanism for the phase separation was controversially discussed in the literature, an explanation by spinodal decomposition is common today.[26] After leaching with acid, the remaining silica phase can be sintered to a 96 % SiO_2 glass, the so-called VYCOR® glass. The intermediate of the VYCOR® process before sintering is hard, mechanically sturdy, chemically inert and has a sponge-like, porous structure.[25] In the 1960s, Haller paved the path for using this process and this intermediate for the synthesis of controlled pore glasses (CPG) with very narrow pore size distributions.[27,28] The resulting pore size and pore volume depend on the composition of the initial glass composition, time and temperature of the heat treatment and the leaching conditions. As can be seen in Figure 1-6, after a short treatment up to temperatures of 580 °C, two phases, the silica–rich, stable phase and the acid– soluble, alkali-rich borate phase, are generated. After leaching, microporous glasses remain. In contrast to this, with a longer heat treatment at temperatures exceeding 580 °C silica is dissolved in the borate phase, which leads to finely dispersed silica after completion of the process. This silica phase, in turn, can be removed by a second alkaline leaching step. From this, a meso- to macroporous structure is obtained.[24] Today, porous glasses with pore volumes of 0.3–2 $cm^3 \cdot g^{-1}$ and pores from < 2 nm up to 1 mm can be adjusted this way.[29] This approach allows the synthesis of isoporous batches i.e. those with the same pore diameter at different pore volumes and different pore wall thickness.[25]

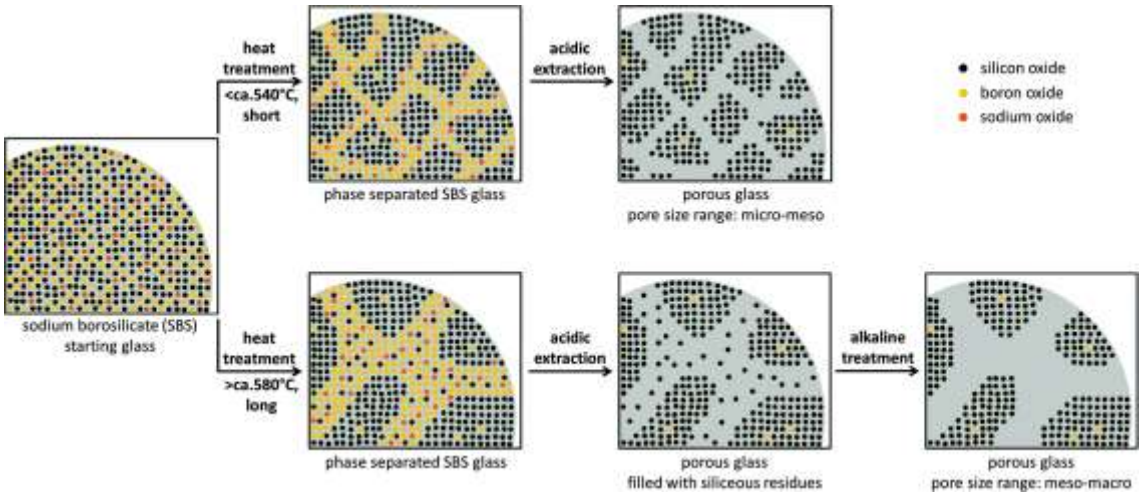

Figure 1-6: Overview of the leaching process in the VYCOR® process. Depending on time and temperature of the treatment of sodium borosilicate (SBS), the phase separation leads to smaller or larger boron oxide/sodium oxide domains. This phase can be removed by acidic extraction. In the case of small domains, micro-mesopores are obtained. In case of larger domains, a second alkaline leaching step is necessary to remove siliceous residues which exposes meso- or even macropores. Reprinted from [30] with permission from the Royal society of chemistry.

CPG can be synthesized in different geometric shapes, such as plates, tubes or rods, simply by pressing the initial glass mixture into the respective form for different applications.[31] Further development of this approach allows the synthesis of hierarchically porous glasses (the advantages of hierarchically porous systems have already been mentioned in section 1.1).

In order to produce hierarchically porous CPG, salts, e.g. potassium sulfate and sodium chloride, are added to the glass mixture and act as pore-forming agents. Pores in the size range of the salt crystals are also produced in the glass body after sintering and extraction.[32] Another interesting example underlining the flexible usability of porous glasses is hierarchically porous glass fibers[24] obtained by the so-called drawdown process of glass bundles. These may be interesting for optical devices. While the previously mentioned pioneer, Haller, used grains for chromatography,[28] Enke *et al*. recently presented the advantages of the use of monoliths for this.[29] Monoliths, generally speaking, provide a higher external surface area and thus a larger contact area between flowing and stagnant fluids exists which improves mass transport. As macroporosity, macropore size and skeleton thickness are controllable and independently adjustable in CPG-based monoliths, they are promising candidates for high performance liquid chromatography (HPLC) or high throughput catalysis.

For this work, the research group of Professor Enke from the University of Leipzig provided CPG granulate and micro beads in the size range of 40-100 µm. The synthesis of the glass beads involves an additional step to shape the beads from granulate using a riser reactor with a cyclone. Such glass beads were recently presented for the use as the solid phase in the separation of chiral anesthetics from a gas flow.[33] Figure 1-7 shows a schematic representation and a picture of the construction. Prior to the shaping process, granulate sodium borosilicate glass is size-

dependently fractionated by sieving. The granulate material is preheated before it enters the methane flame at the feeding point, from where it is transported in the flying chamber by the strong gas flow. At this point, it is partially softened at 950 °C and becomes spherical following the principle of minimized outer surface. The resulting spheres cool down and fall down into the collection vessel. Afterwards, phase separation is thermally initiated, and the beads obtain their porous structure after leaching according to the mechanism depicted in Figure 1-6.

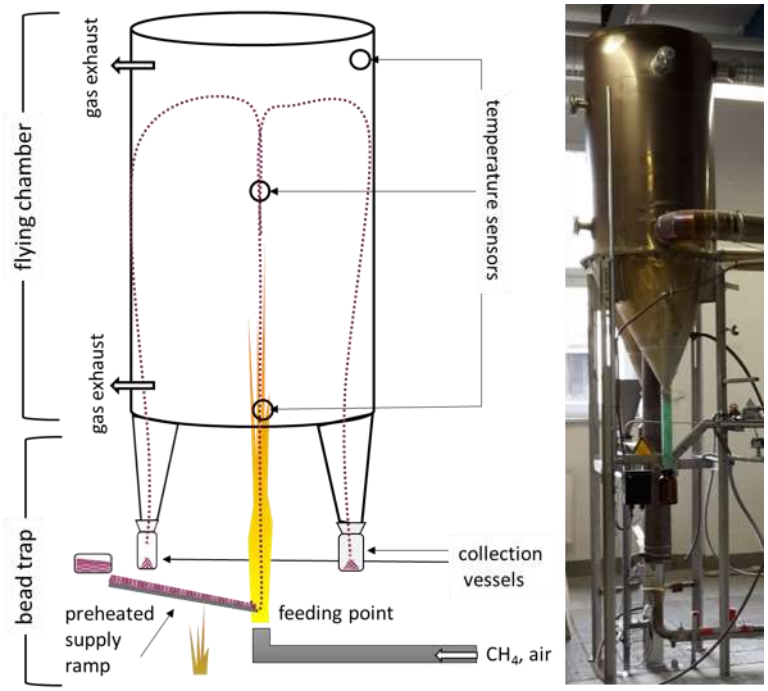

Figure 1-7: Schematic representation of the synthesis of glass beads from granulate in a riser reactor with a cyclone on the left, a photograph of the reactor on the right. Granulate sodium borosilicate glass (magenta) is added to a methane flame at the feeding point. The flame transports the glass inside the cyclone where it takes on a spherical shape and subsequently falls down to be collected in appropriate vessels. Adapted with permission from Wiley.[33]

One possibility for producing hierarchically porous CPG from these glass beads is given by pseudomorphic transformation that is explained in the following chapter.

1.4 Pseudomorphic transformation

The term pseudomorphism (gr. *pseudos* = false, *morphe* = form) originates in mineralogy and is defined as ”the crystallization of a mineral with a crystal shape foreign to that”.[34] In nature, changes in environmental conditions can cause changes in the chemical composition of a crystal: it can be coated or partially replaced by another mineral that thereby appears in an unusual external form, namely that of the initial mineral. Conservation of the shape and volume of the initial crystal are the conditions for a pseudomorphic process. Figure 1-8 shows the pseudomorph of limonite, which is an amorphous mixture of hydrated iron(III) oxide-hydroxides

(Fe(III)O(OH)·nH$_2$O), after marcasite an iron sulfide (Fe(II)S$_2$) which appears in orthorhombic crystal structure. The minerals were found in Farafra an oasis in the Western Desert in Egypt.

Figure 1-8. Natural examples of pseudomorphism in photographs of limonite (Fe(III)O(OH)·nH$_2$O) (right) after marcasite (Fe(II)S$_2$) in orthorhombic crystal structure (left) from the Farafra oasis in Egypt. Photo credit: Frank Hoffmann.

The phenomenon of pseudomorphism inspired material science researchers to change the chemical composition of particularly shaped materials. In 2002 Di Renzo with Galarneau and coworkers adopted the term pseudomorphic transformation for a synthesis approach that implies the transformation of amorphous silica monoliths into micelle-templated silica (MTS) under preservation of the morphology and size of the initial silica particle.[35] Thus, a strategy that allows the independent optimization of the morphology and porosity features of silica-based materials was given.

In general, the concept takes advantage of the kinetic dependence of silica dissolution in alkaline media and recondensation in the presence of a surfactant. The silica/surfactant composite is structured in a cooperative mechanism analogous to the previously presented synthesis path of MTS (see Figure 1-3 in section 1.2). According to the authors, pseudomorphic transformation requires the same rate of dissolution and recondensation of silica.[35]

The underlying mechanism of pseudomorphic transformation of silica into MCM-41 was investigated in subsequent years by different groups. First, Galarneau *et al.* [36] as well as Einicke *et al.*[37] focused on different commercially available silica gels, which were are synthesized in a sol-gel process, before Uhlig *et al.*[38] and Guillot *et al.*[39–41] extended the possible silica sources by using porous glasses (see section 1.3). These two types of silica materials differ in terms of the microstructure, e.g. their condensation degree, and thus show different behavior in the pseudomorphic synthesis.

On the understanding that amorphous silica gel particles are nanoporous as they consist of aggregated silica nanoparticles, it is assumed that as the treatment with an alkaline surfactant solution progresses over time, these nanoparticles grow to larger templated domains until the

complete particle is gradually rearranged.[36] After complete transformation, the whole particle shows homogeneous hexagonal pore ordering of MCM-41. During this transformation process the volume of the material increases, so that the interparticle space of the aggregated nanoparticles inside the monolith is subsequently filled. Thus, a certain pore volume in the initial silica phase is required for successful pseudomorphic transformation of amorphous silica.[36] A diagram representing the proposed mechanism is given in Figure 1-9.

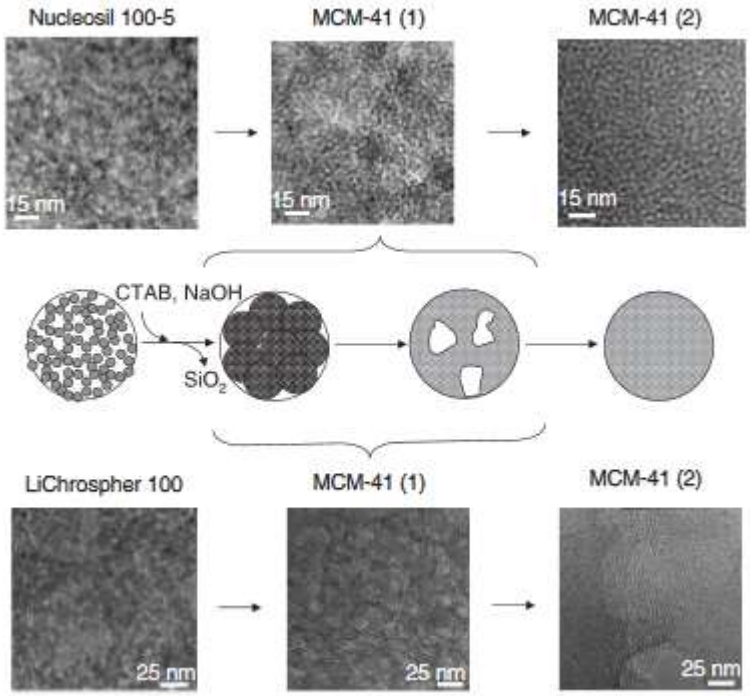

Figure 1-9: Diagram showing the pseudomorphic transformation mechanism. The particles of the nanoparticle aggregate dissolve and recondense into small domains that grow together with time and gradually fill the complete volume of the particle. A homogenous pore system emerges. Reproduced with the permission from Wiley. [36]

The indicator for the presumed mechanism involving domain formation was the physisorption behavior of partially and completely transformed silica. After four days of treatment with alkaline surfactant solution, the initial pore size vanished completely while the product gave a type IVb isotherm and a new pore size of about 3.8 nm. Pore ordering was proven by XRD. By contrast, after only one hour of the pseudomorphic process, an additional hysteresis effect of the nitrogen physisorption isotherm indicated cavitation processes that were explained by the interparticle porosity of enlarged particles. Further, the domains can be seen in TEM images in Figure 1-9.[36] In 2013, Einicke *et al.* affirmed the formation of MCM-41 domains using pulsed field gradient nuclear magnetic resonance (PFG NMR).[37] They investigated the diffusivity of *n*-heptane in silica gel monoliths of about 10 µm particle size with different transformation degrees. Three different spatial arrangements of the silica gel and MCM-41 phase were discussed, and are shown in Figure 1-10.

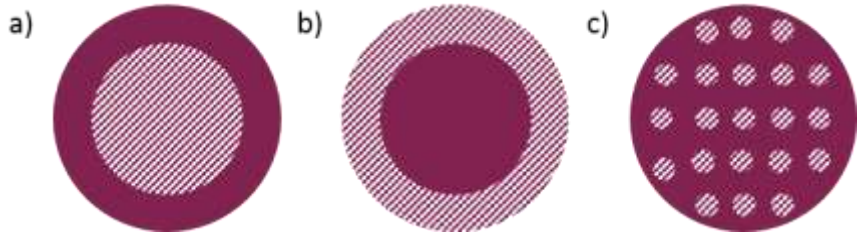

Figure 1-10: Proposed spatial arrangements of MCM-41 phases in the silica gel monolith after partial pseudomorphic transformation of silica monoliths. The MCM-41 phase (shown as striped pattern) could form either (a) a core, (b) a shell of the particle or (c) homogeneously distributed domains. Adapted from [37].

In the case of two phases, a growing MCM-41-type and an amorphous one, as is the case in a core/shell model (see (a) and (b) in Figure 1-10), a linear course of the diffusivity over the different transformation degrees can be expected. But another behavior is observed in the experiments. The diffusivity in the parent silica gel decreases with the transformation despite the decrease in tortuosity and even passes through a minimum at a certain transformation degree. This happens as the domains for the diffusion become smaller. Thereafter the diffusivity increases again due to growing MCM-41 domains. This behavior substantiates the thesis of independent domain formation during the pseudomorphic transformation, as in diagram (c) in Figure 1-10.[37] Additionally, the authors observed a decrease in the Brunauer-Emmett-Teller (BET) surface area and a disappearance of the initial pore system at a low transformation degree and concluded that, in contrast to the first model given by Galarneau *et al.*, dissolution of the parent silica takes place before the MCM-41-type silica is formed. Further, mass loss of the parent silica material is mentioned, which is in contrast to the assumption that the same rate of silica dissolves and precipitates. The progress of the pseudomorphic transformation depends on the initial particle size as was also demonstrated with PFG-NMR.[42] Comparing particles of 5 µm, 10 µm and 50 µm, it was found that large particles became hollow after a longer time treatment with alkaline surfactant solution. This was explained by retarded diffusion of the surfactant inside the particle and thus less stabilized silica species that remain dissolved.[42]

Uhlig *et al.*[38] and Guillot *et al.*[39,40] worked independently, but at approximately the same time, on the transformation of CPG (see section 1.3) into MCM-41 to generate hierarchical pore systems.

Uhlig *et al.* investigated the results of the transformation of CPG starting materials with different pore sizes and pore volumes into MTS by comparing it to a MCM-41 reference material that was obtained by transformation from silica-gel.[38] The transformation of CPG with pore volumes of 0.4–0.5 $cm^3 \cdot g^{-1}$ and different pore diameters (50–150 nm) led to materials with smaller pore volumes and surface areas compared to the reference material. Using CPG with larger pore volumes around 1.00–1.44 $cm^3 \cdot g^{-1}$ and pores from 34–274 nm, the transformation led to

porosity parameters that were similar to the reference material. The respective physisorption isotherms of the materials as well as SEM images are given in Figure 1-11.

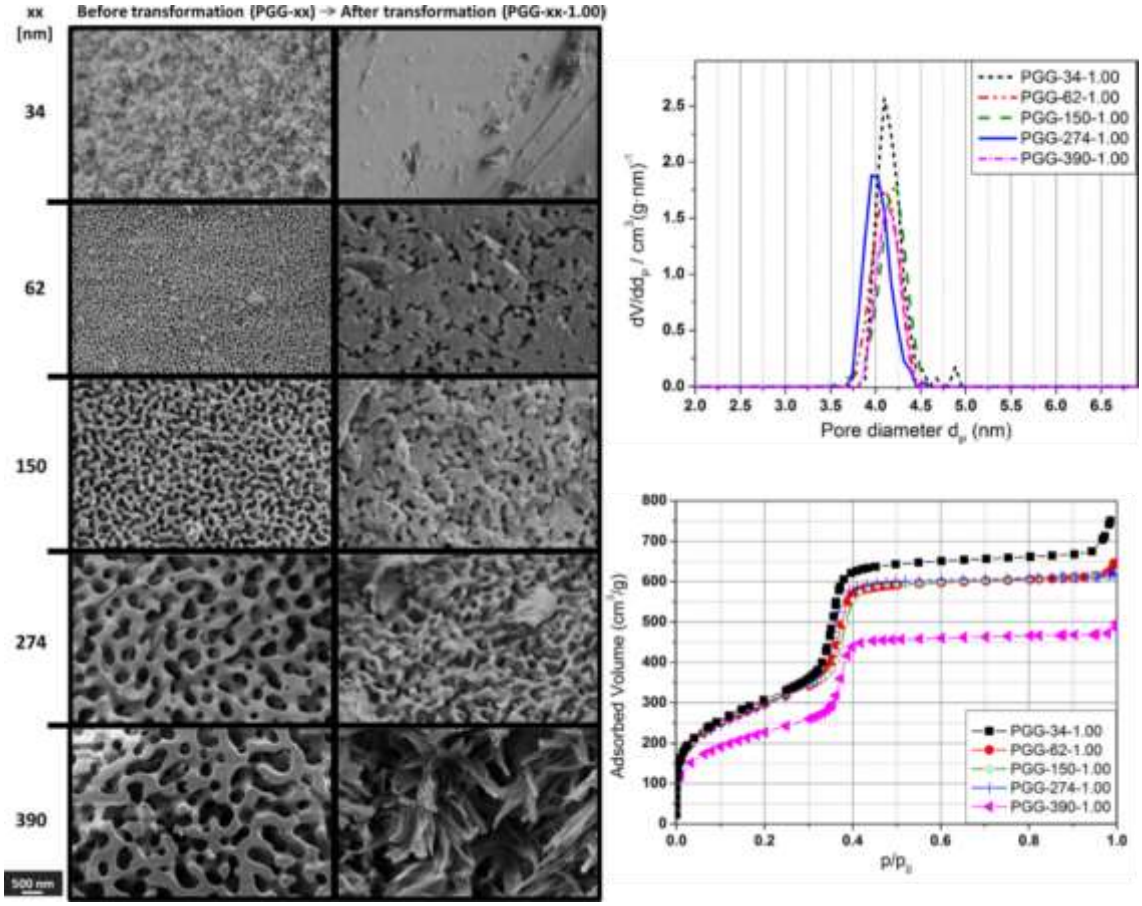

Figure 1-11: SEM images of the porous glasses before and after the transformation approach on the left. On the right the respective physisorption isotherms (lower plot) and pore size distribution (upper plot) are given.[1] Reprinted with the permission from Elsevier [38]

After complete transformation, the initial pore structure was completely overgrown in the case of small pores (34 nm), but remained visible in CPG with 150 nm and 274 nm pore size. Starting with pores of 340 nm and a pore volume of 0.89 $cm^3 \cdot g^{-1}$, the transformation degree was lower and the sponge-like structure of the pores was destroyed. The authors explained this by the lower pore volume and surface area accompanied by thicker pore walls. Thus, the initial pore size seems to be of minor importance for the resulting transformation degree, but it depends on the initial pore volume and wall thickness of the CPG. In this example the wall thickness in these examples can only be estimated in SEM images.

[1] The authors calculated the pore size distribution curves from the adsorption branch of the isotherm on the basis of the NLDFT method. Only for the samples assigned to the starting glass with 34 nm pore diameter the BJH method (adsorption branch) was used for pore size determination. Irregularities of the NLDFT fit will be discussed in section 4.2 with a similar case.

The differences in the transformation mechanism of meso- and macroporous glasses are summarized in Figure 1-12 assuming a material with 1.0 $cm^3 \cdot g^{-1}$ pore volume.[43] In the case of pores smaller than 50 nm, an MTS phase is formed between the pristine pore walls (b) in pores around 34 nm. MTS domains that block the initial pore are generated, so that the initial intra-particle porosity is still detectable after transformation (a). In larger pores, the transformation proceeds in the form of layers on the pore wall that do not grow together in the middle of the pore (c). In the case of even larger pores over 390 nm with the same pore volume, the pore walls become too thick so a complete transformation is no longer possible. An MCM-41 layer is growing on a dense silica wall (d). The results are in agreement with Guillot *et al.*[39]

It should be mentioned that, due to the volume increase during the transformation process, the allegory with pseudomorphism does not perfectly fit in this context. Further, the term originates from mineralogy and conveys the impression of dealing with crystalline materials which is explicitly not the case with silica.

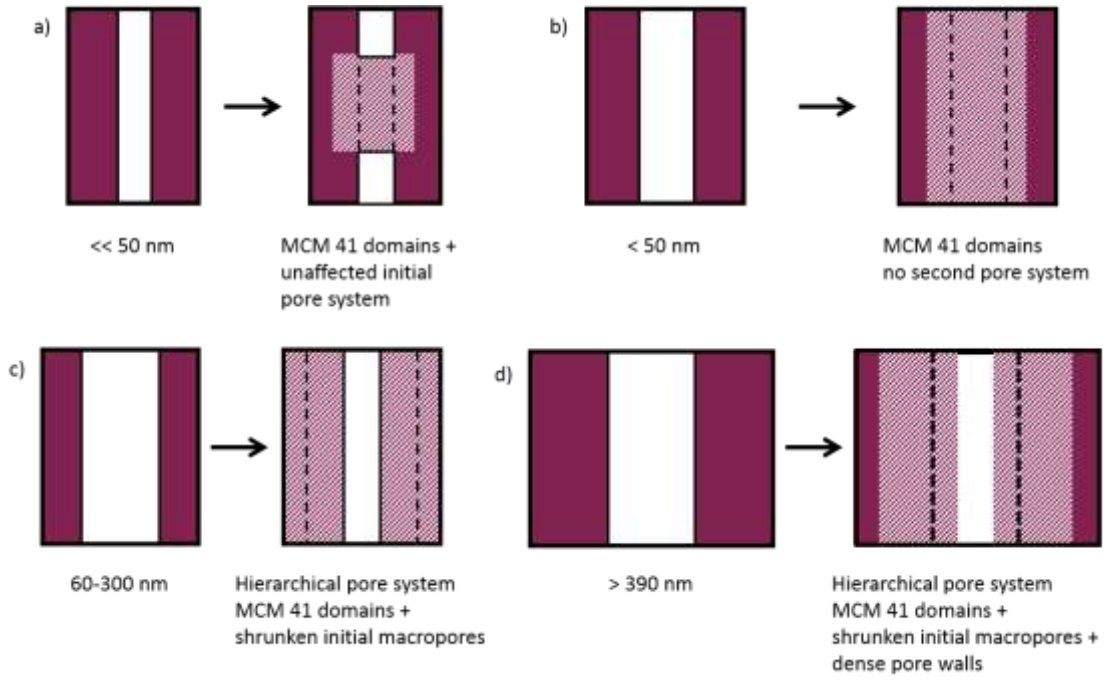

Figure 1-12: Diagram of the transformation mechanism of meso- and macroporous glasses with 1.0 $cm^3 \cdot g^{-1}$ of pore volume. Based on [43].

For further investigation of the pseudomorphic transformation pathway, the transformation degree was varied for the materials with 34 nm, 150 nm and 274 nm pore size.[38]

In the case of the materials with 150 nm and 274 nm initial pore diameter this pore size was reduced stepwise to smaller pores while the pore volume of mesopores increased and swelling was observed in the SEM images. In contrast, for the CPG with 34 nm, the pore volume of the larger mesopores decreased with increasing transformation degree, but no shift to smaller pores could be observed.

In previous work, different approaches were used to receive partial transformation of the silica species in order to investigate the transformation process. Initially, the premature termination of the transformation synthesis in solutions of sodium hydroxide and hexadecyltrimethylammonium bromide (NaOH/C_{16}TAB) was pursued.[35,44] In contrast to this, Einicke *et al.* and Uhlig *et al.* used a solution of hexadecyltrimethylammonium hydroxide (C_{16}TAOH) with a defined concentration prepared by ion exchange of an aqueous C_{16}TAB solution. An improved hydrothermal stability was demonstrated for MCM-41 type silica materials from sodium free synthesis.[45] It is assumed that additional ions hinder the interactions between the surfactant head group and the silica surface in the MCM-41 formation.[30]

Einicke *et al.* varied the solution volume, thus the respective ratios of hydroxide ions and surfactant to silica at constant pH value.[37] The authors claim the transformation degree is well defined and less error-prone than time-dependent transformation adjustment due to consistent cooling rates. Uhlig *et al.,* however, varied the transformation degree by the ratio of C_{16}TAOH/(C_{16}TAOH+C_{16}TAB) in the solution.[38] This lead to variable pH values as well as the silica/hydroxide ion ratio at constant silica/surfactant ratio and surfactant concentration.

With regard to a possible application, namely the use of pseudomorphic transformed glasses as a confinement matrix for radioactive contaminant e.g. Cs^{137}, Gulliot *et al.* intended to decrease the softening point of the glass by incorporating of sodium during the transformation process in a NaOH/C_{16}TAB solution.[39] Hence, they could seal the mesopores of the material by thermal treatment at a comparatively low temperature of 700 °C and successfully enclose cesium inside a CPG that was functionalized with Prussian blue analogues in multiple steps.

Corresponding to the MCM-41 synthesis from different silica sources, in a pseudomorphic synthesis the pore size could be varied by the chain length of the surfactant,[37] and larger pores were obtained using 1,3,5-trimethylbenzene (TMB) as swelling agents.[46] Even the complex phase transformation MCM-41/48 could be archived in a morphology-retaining way by careful changes of the alkalinity and temperature of the synthesis.[46,47] The synthesis of MCM-48, with a 3D cubic pore structure is described as very challenging as it is in transition between the kinetically favored hexagonal (MCM-41) structure and the thermodynamically favored lamellar structure. Synthesis conditions for this phase transition were also found for CPG with macropores of 150 nm as the starting material, even though the initial macropore system was not retained and inaccessible inclusions were formed during the restructuring of the material.[48]

The research group of Brühwiler used not only amorphous silica as the starting material for the pseudomorphic transformation into MCM-41, but also a micro- and mesoporous SBA-15 material with a mesopore diameter of 7.3 nm.[49] By partial transformation of the initial phase, they derived a bimodal mesoporous silica with bottleneck pores. The pore interconnectivity is of

particular interest here and was investigated by argon physisorption. For the structure and interconnectivity of the SBA-15 and MCM-41, a core/shell structure with an MCM-41 shell on the outer surface of an SBA-15 core after partial transformation was proposed, notwithstanding the previous results from Einicke *et al.* for the transformation of amorphous silica.[50,51] The same group followed an approach to functionalize the silica surface with 3-aminopropyltriethoxysilane (APTES) by simultaneous inclusion of the organosilica source in the pseudomorphic transformation process. They managed to incorporate up to 0.96 mmol of the amino groups into 1 g of material and proved a homogeneous distribution of the amino groups in the silica network by fluorescent labeling.[52] The pseudomorphic transformation of silica particles with a very broad particle size distribution is usually accompanied with a significant amount of fractured silica. Liu *et al.* intended to facilitate this by adding an organosilica source as well, namely 3-(2-aminoethyl aminopropyl) trimethoxysilane, during the transformation process. The organosilica affects the transformation process as an additional silica source shifts the equilibrium between dissolving and recondensation. It was observed that a certain amount of the organosilica source can indeed preserve the morphology of the silica particles, but at the same time the mesoscopic structure is negatively affected.[53]

Next to the pseudomorphic transformation of silica phases, the incorporation of alumina having Al-MCM-41 within an analogue process was discussed in 2002[35] and was further investigated in the research group of Professor Fröba.[43] Further interesting approaches, e.g. the pseudomorphic transformation of silica into zeolites[54–56] and the transformation of silica into titania,[57,58] will not be discussed here.

1.5 Organosilicas

1.5.1 Functionalization of mesoporous silicas

The incorporation of organic functions opens new fields of application for silica-based materials. In general, there are three methods to covalently bind mono-, bis- or multi-silylated organic substances, the so-called silsesquioxanes, to a porous silica network: 1. grafting onto the surface of mesoporous silica materials, 2. co-condensation during the micelle templating process together with a pure silica source (e.g. TEOS) and 3. formation of a network using only bridged silsesquioxanes.[59]

The diagrams in Figure 1-13 and Figure 1-14 show the grafting and the co-condensation process.

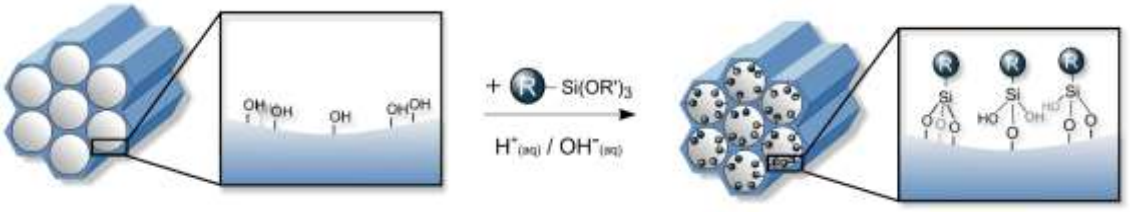

Figure 1-13: The post-synthetic grafting of mesoporous silica with an organotrialkoxysilane. Reproduced from [59] with permission from Wiley.

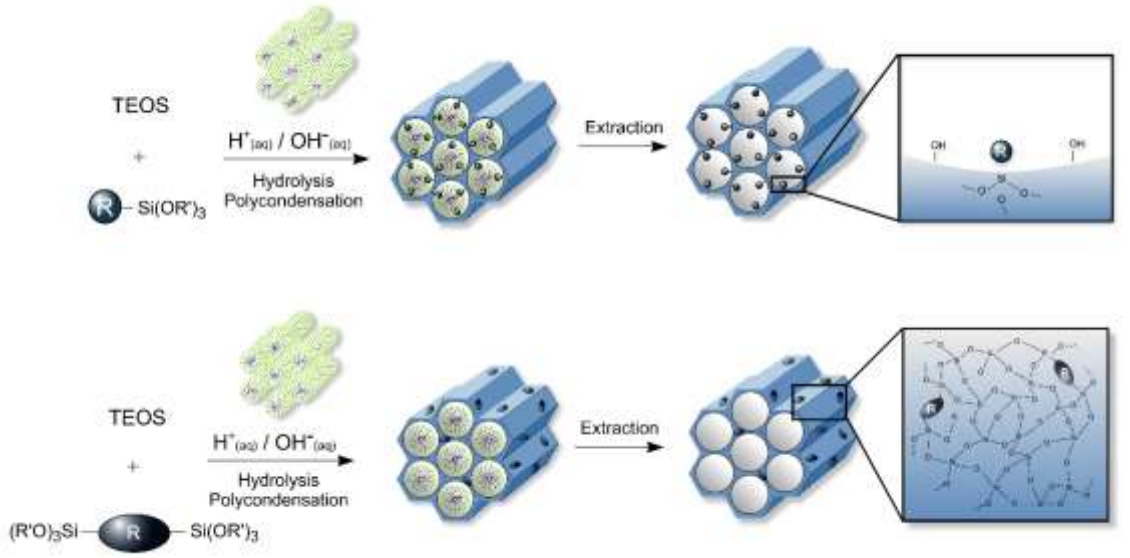

Figure 1-14: Co-condensation during the micelle templating process of TEOS with a mono-silylated organic compound (upper diagram) allows homogeneous distribution of the organic moiety in the material. A bis-silylated organic bridge is incorporated in the wall of the mesoporous material with TEOS (lower diagram). Reproduced from [59] with permission from Wiley.

By co-condensation of silsesquioxanes together with a pure silica source, a more homogeneous distribution of the organosilica source is possible and the organic moiety is directly incorporated into the pore wall. This is shown for mono-silylated silsesquioxanes[60] in the upper diagram in

Figure 1-14 and for the case of bis-or multi-silylated precursors (lower diagram in Figure 1-14). Following this approach, the loading of the organosilica species is usually about 5–15 mol%, whereby the molar proportion of organosilica in the starting mixture mostly exceeds the ratio of incorporated organosilica in the resulting hybrid material.[61]

With a higher organosilica content the ordering of the obtained material is disturbed, which can be explained by the differences in hydrolysis and condensation rate for the different silica sources.[62] The organosilica/silica ratio can be determined by thermogravimetric analysis, elemental analysis or ^{29}Si solid-state magic angle spinning (MAS)-NMR spectroscopy. ^{29}Si{1H} 2D heteronuclear correlation (HETCOR) NMR experiments were used to investigate the distribution of the organic bridge in the network obtained from co-condensed TEOS and 1,4-bis(triethoxysilyl)benzene (BTEB).[63] Thus, the correlation between spatially adjacent species as a function of contact time was monitored. A correlation between the protons of the benzene ring and the ^{29}Si corresponding to the inorganic moiety affirmed the spacial proximity which indicates random distribution of the organosilica species rather than a formation of two phases. There are many different examples for grafting and co-condensation approaches that are nicely reviewed by Sayari *et al.* in 2001[64] and Hoffmann *et al.* in 2006.[13]

1.5.2 Periodic mesoporous organosilicas (PMOs)

The highest functionalization density is achievable by synthesizing the organosilica hybrid material only from bridged silsesquioxanes of the form [R'$_3$O-Si-R-Si-OR'$_3$.]. In this way, the organic content can be increased by up to 80 wt%, depending on the size of the organic moiety. Xerogels from a sol-gel process with bridged silsesquioxanes are usually microporous or mesoporous but disordered. This class of materials was intensively studied in the past decades by the research groups of Corriu[65–67] and Shea[68–71]. Nowadays, there are a lot of examples for bridged silsesquioxanes, even from very elaborate or large precursors, as was reviewed in 2016 by Croissant *et al.,* who showed their variable applicability from nanomedicine through photoluminescence to pollutant removal.[72] Contemporary studies concerning the influence of different organic groups on the microporosity in organosilica materials show how every bridged silsesquioxanes increases the disparity in micropore entrance sizes in the micropore range. This was explained by lower monomer mobility due to changes in size and shape compared to inorganic silica monomers.[73]

The combination of silsesquioxanes and micelle templating was done in 1999 by chance by three research groups at the same time: Inagaki, Ozin and Stein. All three still have a great impact in the progress of the new class of materials they founded – periodic mesoporous organosilicas (PMOs).

The general synthesis path for PMOs, as depicted in Figure 1-15, is similar to the mechanism described for MTS in section 1.2. Bridged silsesquioxanes undergo hydrolysis and condensation under acid or alkaline media. In the presence of a surfactant, a composite material is obtained following a true liquid crystal mechanism or a cooperative mechanism. After being extracted, the surfactant leaves ordered pores behind. In the synthesis of PMOs, calcination of the surfactant is not recommended as the organic bridge might be affected by the heat treatment.

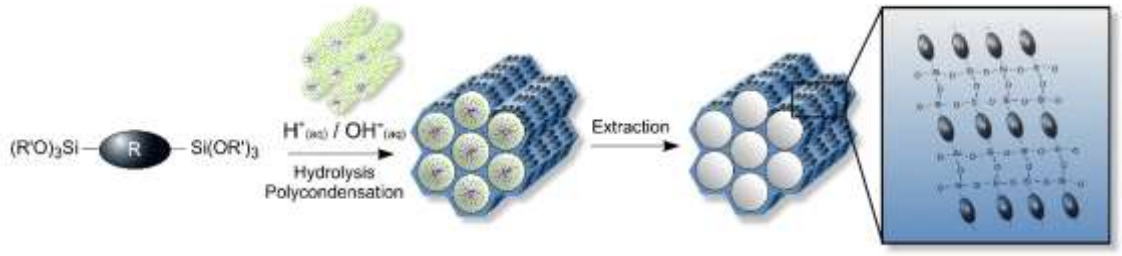

Figure 1-15: Diagram of the synthesis path for PMOs. The silica source is a bis-silylated organic compound that undergoes hydrolysis under acid or alkaline media. In the presence of a surfactant templating takes place following a true liquid crystal or cooperative mechanism. The surfactant is removed from the composite by extraction. Reproduced from [59] with permission from Wiley.

In the following paragraphs, different groups of precursors are discussed which have already been used in PMO syntheses. The precursors are consecutively numbered over this section in different subchapters. The bridging groups of the two first-used precursors are given in Figure 1-16.

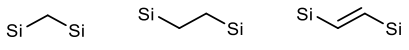

1 **2** **3**

Figure 1-16: The smallest organic bridge leads to methane PMOs (**1**), the bridging unit of the first PMOs are ethane (**2**) and ethene (**3**). Si = $Si(OR)_3$ with R = CH_3, CH_2CH_3.

PMOs with the smallest possible methane bridge (**1** in Figure 1-16) were first published in 2000.[74] This bridging unit is still relevant e.g. in the form of hierarchically structured mesoporous silica core/shell nanoparticles for adsorption and controlled release of the fungicide propiconazole,[75] but less frequently mentioned as ethane- and ethene-bridged precursors (bridging units **2** and **3** in Figure 1-16).

Inagaki *et al.* presented the synthesis of PMOs using 1,2-bis(trimethoxysilyl)ethane (**2**) as a precursor, with octadecyltrimethylammonium chloride (C_{18}TAC) as surfactant. Under different synthesis conditions they obtained materials with 2D and 3D hexagonal pore structures having specific BET surface areas of 750 and 1170 $m^2 \cdot g^{-1}$ with pores of 3.1 nm and 2.7 nm, respectively, determined according to the Barrett-Joyner-Halenda (BJH) method.[76]

The research groups of Ozin and Stein presented PMO synthesis using bis(triethoxysilyl)ethane (BTEE), bridging unit **3** in Figure 1-16. Ozin's research group synthesized a series with decreasing

TEOS to BTEE content from 100 % to 0 %, under alkaline conditions with C_{16}TAB, whereby the pure ethylene-bridged material showed comparably poor ordering of the pores according to the X-ray diffraction (XRD) pattern. The BET surface area was 637 $m^2 \cdot g^{-1}$ with pores of 3.9 nm according to BJH.[77] The research group of Stein presented PMOs with an ethane (**2**), as well as those with an ethene (**3**) bridge. They also used C_{16}TAB as the surfactant but chose different molar compositions in the synthesis mixture. It is worth mentioning that the synthesis protocol separates the hydrolysis under acidic conditions from the condensation step under alkaline conditions. Additionally, it does not include hydrothermal treatment.[78] With this approach PMOs with 1234 $m^2 \cdot g^{-1}$ (ethane **2**) and 1225 $m^2 \cdot g^{-1}$ (ethene **3**) were obtained with pore diameters of 2.2 nm and 2.4 nm according to BJH.

In 2008, the differences in hydrolysis and condensation behavior of ethylene- and ethane-bridged precursors were investigated in detail in order to combine them in bifunctional PMOs. The formation of domains or a homogeneous structure of both organic bridges was controllable by either joined or separated pre-hydrolysis as examined by ^{1}H-^{29}Si HETCOR MAS NMR.[79]

As the first, the Fröba research group used the triblock copolymer P123 in PMO synthesis with the bridging unit **3** to generated significantly larger pores of 6.5 nm (according to BJH) with a specific BET surface area of 913 $m^2 \cdot g^{-1}$.[80]

Even though more complex bridges have been incorporated in PMOs since then, the simple bridges are still of interest today. To demonstrate this, some selected examples are presented here. Recently, new synthesis pathways were presented[81,82] for ethane-bridged PMOs, and they were found to be promising candidates in catalysis or as heterogeneous lyophobic systems used in adsorption or storage applications after hydrophobization with bis(trimethylsiliy)amine.[83]

Ethene-bridged PMOs offer the possibility of surface modification based on olefin chemistry. Sanchez *et al.* took advantage of this and modified an ethylene-bridged PMO by epoxidation followed by sulfonating or hydrolysis. [84] The respective materials were evaluated as adsorbent materials for dehumidification.

Aromatic PMOs

Figure 1-17 gives examples of thus far established aromatic PMO precursors. Figure 1-18 shows further (aromatic) precursors which contain heteroatoms. Selected examples will be discussed below with emphasis on those used in this work which are highlighted in color. For more detailed information concerning the up-to-date applications of different organic bridges, a general PMO review from 2013,[85] as well as an overview from 2015 dealing with PMO nanoparticles,[86] is recommended.

Well-established in 1999 are benzene-bridged and thiophene-bridged PMOs (**4** and **20** in Figure 1-17 and Figure 1-18).[87] Morell *et al.* combined these two precursors in bifunctional aromatic periodic mesoporous organosilicas and prepared a series of highly ordered PMOs with 4.8nm–5.4 nm or 3.3 nm pore diameter. The amount of incorporated thiophene precursor changes with the different ratio of the two precursors changing in 25 % steps. The obtained materials can serve as adsorbents or hosts for the immobilization of thiophilic compounds like Au_{55}-clusters.[88]

Rebbin *et al*. investigated the formation of PMOs with both precursors under acidic conditions with the surfactant Brij 76 (polyethylene (10) stearylether) by in-situ with small-angle X-ray diffraction. An intermediate 3D hexagonal phase was an intermediate structure during the formation of both, the benzene-bridged and of the thiophene-bridged 2D hexagonally ordered PMOs.[89] Benzene-bridged PMOs still enjoy a lot of attention, one potential reason being that the BTEB precursor is commercially available and its synthesis in one step is comparably easy.

In addition the post-synthetic modification of the benzene bridge e.g. by amination or sulfonation,[90–93] as well as grafting of the material in order to receive a catalytically active material, is well-established.[94] Recently, a benzene-bridged PMO was post-synthetically modified by nitration and subsequent hydrogenation to receive an aniline-bridged PMO, which in turn was coupled with the amino acid L-serine.[95] The respective organosilica material was used as a catalyst in aldol condensation reactions.

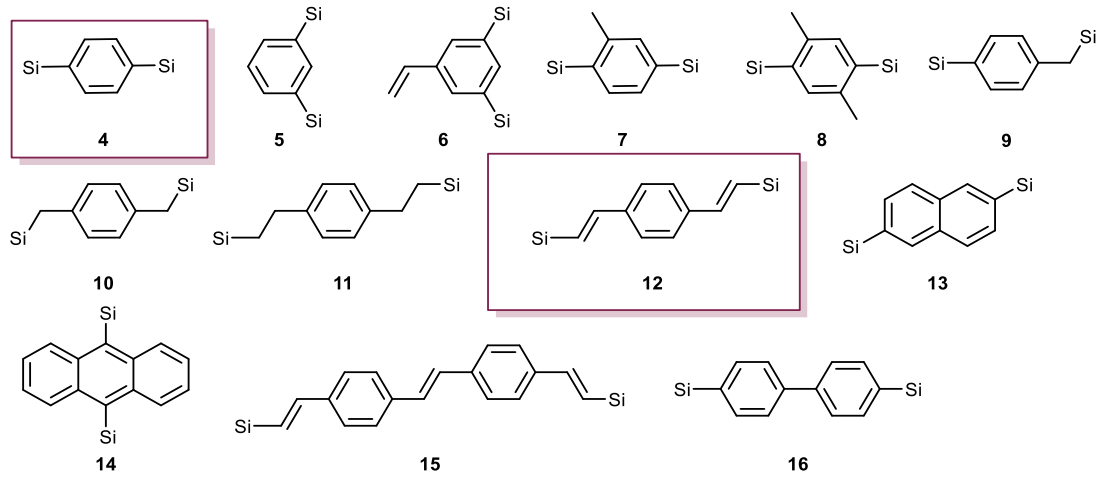

Figure 1-17: Examples of aromatic PMO bridges. The structures that are of interest for this work are framed in magenta. Si = $Si(OR)_3$ with R = CH_3, CH_2CH_3.

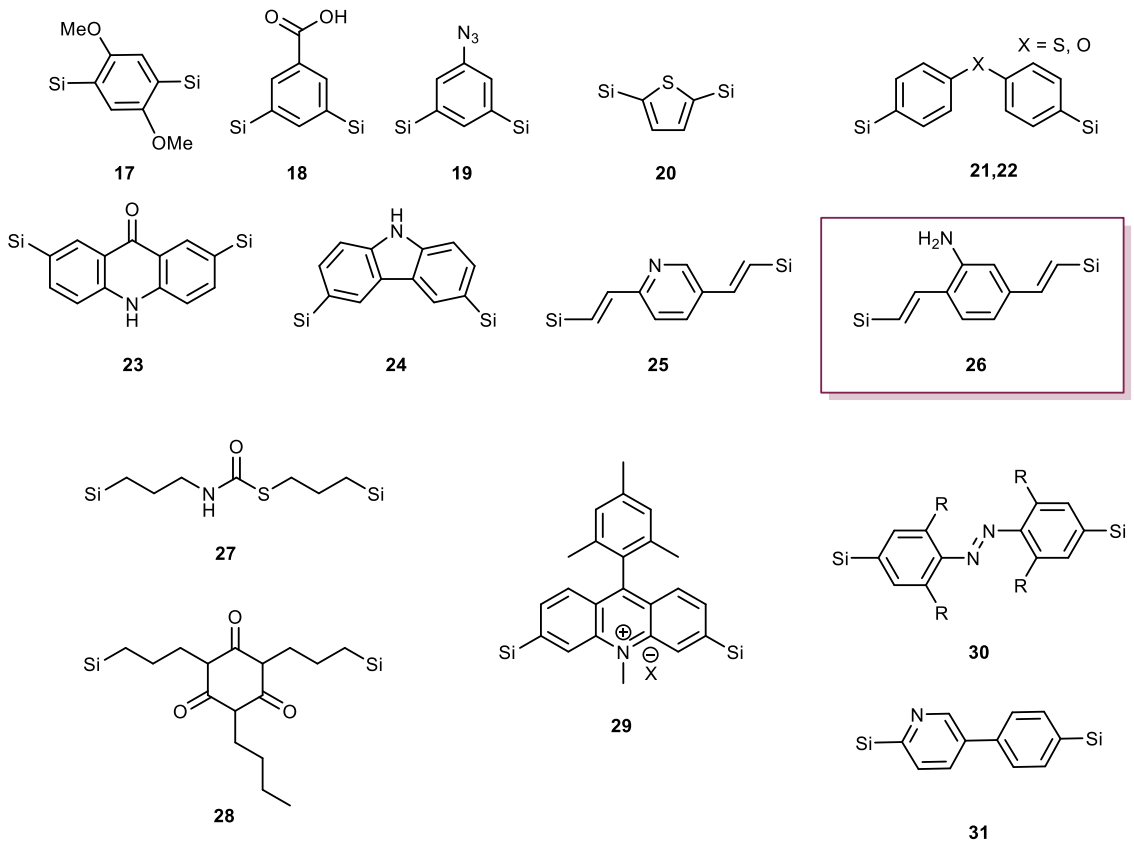

Figure 1-18: Examples of organic PMO bridges containing heteroatoms. The structures that are of importance in this work are framed in magenta. Si = $Si(OR)_3$ with R = CH_3, CH_2CH_3.[85,96,97]

In 2002, Inagaki *et al.* were the first to show periodic stacking of the benzene bridge, a so-called crystal-like wall structure.[90] Under suitable conditions, the precursor probably arranges due to *π*-*π* interactions. A diagram of the arrangement of the bridges is shown on the left hand side in Figure 1-19, next to structural models for crystal-like arrangements of the benzene bridges (structure **4**, Figure 1-17). Additional reflections appear in the XRD pattern and the corresponding *d*-values could be assigned to the size of the repeated entities of the benzene bridge with a length of *d* = 7.6 Å. The mechanisms of the arrangement were unclear for several years until *in-situ* synchrotron small angle X-ray scattering measurements showed the simultaneous formation of reflections corresponding to the periodic mesophase and the periodic order within the walls.[98] Such a crystal-like arrangement was also shown for PMOs synthesized from other precursors [99–101] all having a rigid bridge with sp^2-hybridized carbon bonded to silicon and no bulky substituents in common.[102]

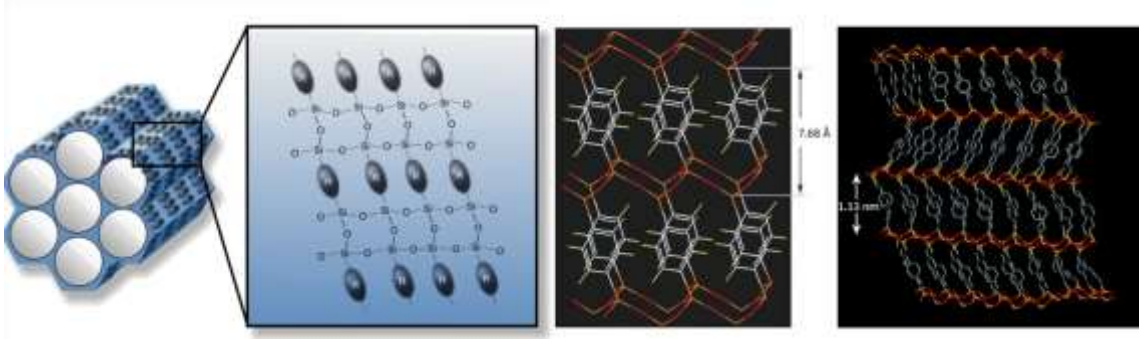

Figure 1-19: Diagram of the crystal-like arrangement of precursors in the pore walls of PMOs. Reprinted from[59] with permission from Wiley. Structural models of PMOs consisting of the benzene-bridged precursor (**4**) in the middle (reused with the permission from Nature Springer [90] Copyright 2002) and divinylbenzene-bridged precursor (**10**) on the right. (Reprinted with permission from [103]. Copyright 2005 American Chemical Society).

The *para*-divinylbenzene-bridged (DVB)-PMO from the precursor 1,4-(*E*)-(bis(triethoxysilyl)-vinyl)benzene (BTEVB) (structure **12**, Figure 1-17) was independently established in 2005 by both Sayari *et. al.*[104] and Cornelius *et. al.*[103] It shows crystal-like structuring with a spacing of 11.9 Å, as shown on the right in Figure 1-19. This precursor was part of a series of organosilica materials with tuned optical properties by a systematically extended length of the π-system.[105] The deuterium-enriched pendant *p*-DVB-d_4-PMO was used to investigate the rotation dynamics of *p*-phenylene moieties confined in a 2D nanolayer.[106] Structurally similar is the 2,5-((*E*)-2-bis(triethoxysilyl)vinyl)aniline (BTEVA) precursor, the bridging unit **26** in Figure 1-18, which can likewise arrange in a crystal-like manner. The amino-function of a respective (DVA)-PMO has been used for peptide coupling with the amino acid L-alanine, which emphasizes the accessibility of the organic function.[107]

Further, the adsorption performance of DVB-PMO and DVA-PMO for aldehydes, which belong to the typical toxic traces in many industrial production processes, was compared, and chemisorption using a Schiff base reaction at the amino function could be proven.[108]

Mietner *et al.* compared the properties of water confined in pure silica MCM-41, B-PMO, biphenyl-bridged (BP)-PMO and DVA-PMO (bridging structures **4**, **16**, **26** in Figure 1-17 and Figure 1-18) with regard to different surface polarity.[109] For materials with the same pore diameter, the pore condensation step in water vapor adsorption measurements shifts with BP-PMO >> B-PMO > MCM-41 > DVA-PMO. This behavior proves that the hydrophilic character of DVA-PMO is comparable to pure silica, maybe due to the capability of forming hydrogen bonds between the amino group and water.[109,110] The normalized water vapor sorption isotherms are shown in Figure 1-20. Interactions between the inorganic moiety and confined water was seen in 2D ^{29}Si{^{1}H}-HETCOR MAS NMR experiments for all materials. Hydrogen bonds between the amino function of DVA-PMO and water could be confirmed by 2D ^{1}H-^{13}C-HETCOR MAS NMR spectroscopy. In contrast to this, no interaction between the organic bridge and confined water was detected in the case of B-PMO and BP-PMO with neither smaller pore diameter, nor higher

water filling degree. Thus, a modulated pore filling was concluded for alternating hydrophobic/hydrophilic pore surfaces as in BP-PMO and B-PMO, where uniform water filling is expected for hydrophilic pore surfaces as in a DVA-PMO. This is shown in Figure 1-20.

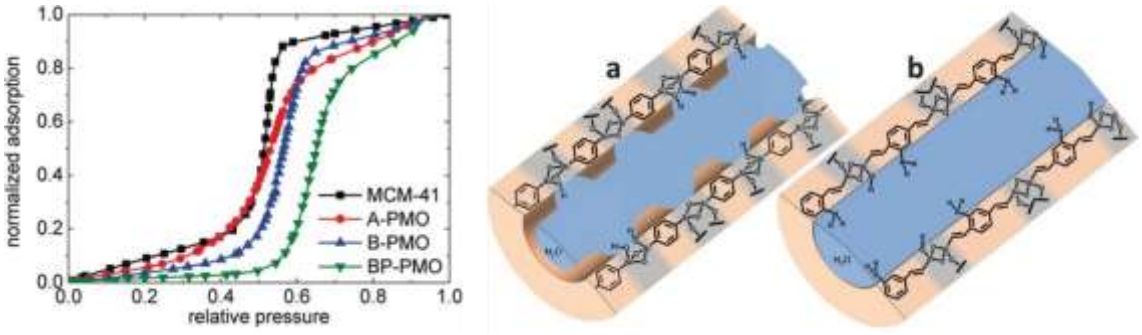

Figure 1-20: Left: Normalized water vapor sorption isotherms at 298 K of pure silica and different PMOs with the same pore diameter of 3.2 nm. A shift in the condensation step shows the differences in hydrophilic character due to different bridging units. Right: Diagrams of the water filling in pores of PMOs: (a) modulated filling at alternating hydrophobic-hydrophilic pore surfaces as in BP-PMO and B-PMO or (b) uniform filling in hydrophilic-hydrophilic pore surfaces as in A-PMOs. Reprinted from [109] with permission from Wiley.

Simon *et al.* were able to cast PMOs with an inverse opal structure with benzene (**4**), divinylbenzene (**10**), and divinylaniline (**26**) precursors using sedimented PMMA particles (400 nm in diameter).[111] Further inspired by the pseudomorphic transformation of amorphous silica into MCM-41, they were able to generate postsynthetic mesoporosity in these pure organosilica materials. Figure 1-21 shows the structures before and after the pseudomorphic transformation. Despite the treatment with an alkaline surfactant solution, the morphology of all materials remains intact.

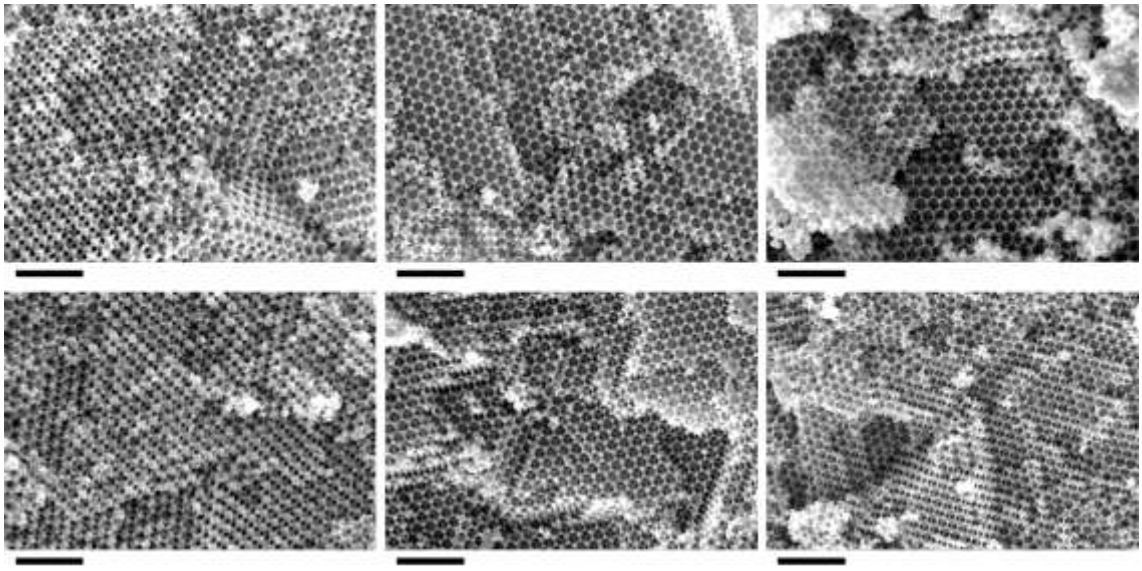

Figure 1-21: SEM images of the inverse opal structures of benzene-, divinylbenzene- and divinylaniline-bridged organosilica materials in sequence from left to right. The upper images show the materials before, while the lower images are after alkaline treatment for pseudomorphic transformation. Scale bar is 2 µm in all images. Reproduced from [111] with permission of the Royal Society of Chemistry.

Only the benzene-bridged material showed porosity before the transformation step. After the transformation, the BET surface was increased from 682 $m^2 \cdot g^{-1}$ to 948 $m^2 \cdot g^{-1}$. In the case of DVB- and DVA-organosilica it increased from a non-porous material to 775 $m^2 \cdot g^{-1}$ and 592 $m^2 \cdot g^{-1}$ respectively. It has to be mentioned that only the benzene-bridged material showed an ordered pore structure and crystal-like molecular periodicity in the pore walls according to the powder XRD pattern. By contrast, the pore size distribution in the other materials was rather broad.

Chiral Organosilicas

Chiral (meso)porous organosilica materials have high potential in chiral separation or chromatography. Due to their interesting features, chiral structures and multi-silylated PMO precursors will be mentioned briefly here, although they are not part of this work.

Many promising materials were obtained from grafting on a silica surface or from co-condensation with a pure silica source like TEOS.[112,113] Others were obtained by co-condensation with other bis-silylated precursors, also called bulk monomers.[114–116]

Enantiopure microporous organosilicas with an *apparent* specific BET surface areas up to 480 $m^2 \cdot g^{-1}$ were obtained with the two enantiomers of the precursors in Figure 1-22 which were synthesized in a multi-step synthesis route from L-valine or D-valine, respectively.[117] The two materials showed opposing signals in circular dichroism spectroscopy.

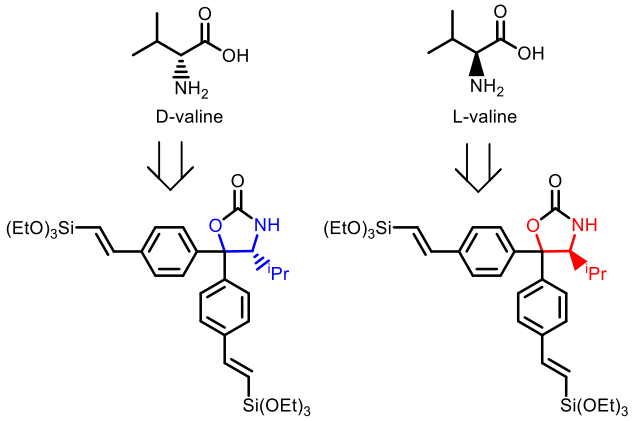

Figure 1-22: Both enantiomers of the precursors which were synthesized from D-valine and L-valine led to enantiopure microporous organosilica materials. [117]

Figure 1-23 summarizes chiral silsesquioxanes that were integrated in pure organosilicas, most of them are PMOs by definition, meaning that periodicity is given in a mesoporous structure.

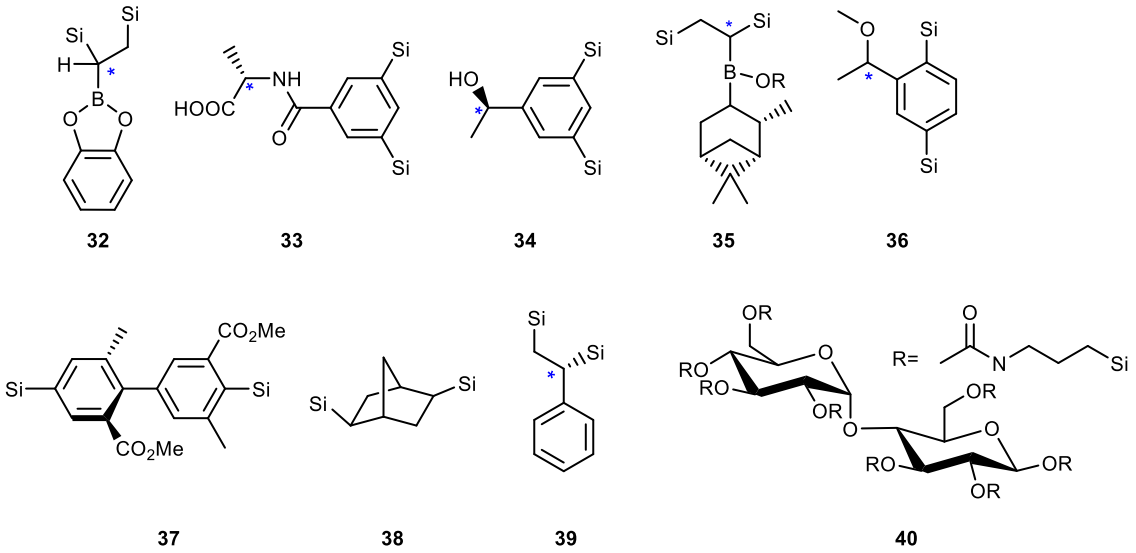

Figure 1-23: Chiral bridges that were successfully integrated into PMOs. Si = $Si(OR)_3$ with R = CH_2CH_3, $C(CH_3)_2$.[85,118]

In 2006 Polarz and Kuschel showed a PMO from the chiral bridging unit **32**, although they did not prove the chirality of the received PMO.[119] In the following years they presented further PMOs from bridging unit **33**, whereby the chiral information was incorporated with the amino acid L-alanine and **34** which was obtained from enantioselective hydroboration of a carbonyl function where they proved the chirality with circular dichroism spectroscopy.[120,121] Also bridging unit **35** was synthesized from enantioselective hydroboration from an ethene-bridged precursor by Ide *et al.* Mesoporous materials with variable porosity were obtained from self-organization of the precursor and a periodic mesoporous organosilica material was synthesized in co-condensation with TEOS in the presence of the block-copolymer F127.[122] In 2008 Morell *et al.* presented a PMO with a specific BET surface area of 820 $m^2 \cdot g^{-1}$ from bridging unit **36** in Figure 1-23 which was synthesized in a multi-step synthesis involving an asymmetric hydrogenation in the presence of a chiral ruthenium catalyst. The chirality of the organic bridging unit with 88 % enantiomeric excess was proven by the optical activity of the PMO.[123] Also in 2008, the Crudden research group presented a mesoporous single source organosilica material from bridging unit **37** and chiral PMOs from co-condensation with **16.**[115] These systems were still investigated intensively until recently.[124] The microporous organosilica from bridging unit **39** with 1180 $m^2 \cdot g^{-1}$ was presented by Inagaki *et al.* in the same year,[125] the PMO with bridging unit **38** which shows a specific BET surface area of 900 $m^2 \cdot g^{-1}$ and pores around 4.8 nm (BJH) was presented two years later.[126] The largest and newest precursor is a multi-silylated structure of a modified D-mannose disaccharide, bridging unit **40** in Figure 1-23.[118] With P123 as surfactant, it was successfully incorporated in a single source PMO with pores of 5.0 nm according to BJH and a rather small surface area of 419 $m^2 \cdot g^{-1}$. Another way to incorporate chirality in PMOs, the post synthetic modification with different amino acids in peptide coupling reactions has already been

mentioned. It is also worth mentioning, that chiral organosilica precursors are not the only way to incorporate chiral information into a silica species. Chiral transfer, e.g. from a chiral surfactant, has been frequently demonstrated in the literature.[127–131]

Multi-silylated precursors

As the last group, multi-silylated compounds, which were mainly processed between 2002 and 2005 by the Ozin research group, should not be left out as they had a high impact at the time of publication. Figure 1-24 shows the representatives. Distinct interactions between the building blocks and the template during the self-assembly were expected for precursor **41** and **42,** but this is, thus far, not proven.[132,133] The research group of Van der Voort modified the cyclic precursor with an ethene function (precursor **43)** and showed on the one hand its pH and temperature stability as a chromatographic packing material,[134] while on the other hand it was further functionalized by click chemistry to synthesize a stable support for a Ru(III) catalyst.[135] Periodic mesoporous dendrisilicas were obtained in 2003 from precursors **46**–**48**. While precursor **46** was templated with C_{18}TAB leading to a material with a BET surface area of 1102 $m^2 \cdot g^{-1}$ and 2.5 nm pore diameter (BJH), the larger precursors were templated with non-ionic surfactant P123, which explains the larger pore diameters of 8–9 nm as well as the smaller BET surface areas of around 770 $m^2 \cdot g^{-1}$.[136] Two years later, with the help of P123 as a surfactant, PMOs from **44** with 967 $m^2 \cdot g^{-1}$ and pores with a diameter of 7 nm, and from **45** with 714 $m^2 \cdot g^{-1}$ and a pore diameter of 11 nm could be presented. [137,138]

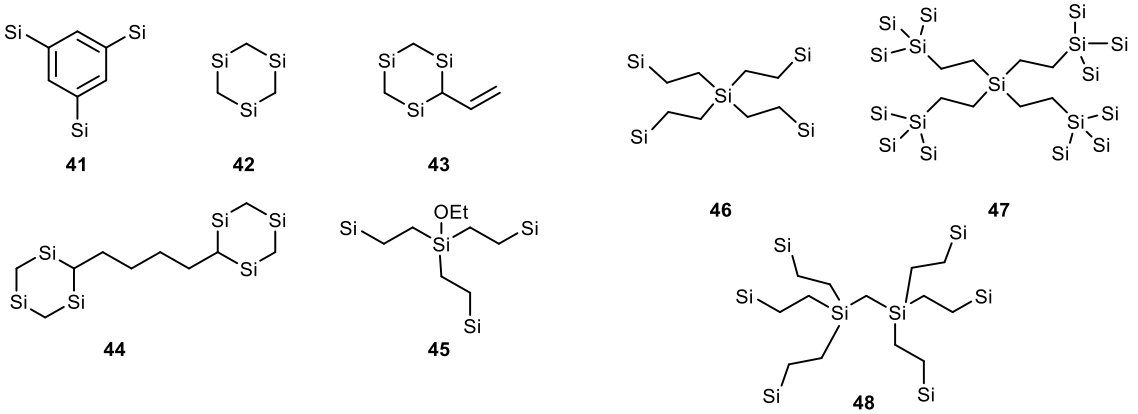

Figure 1-24: Overview of multi-silylated PMO precursors. Si = $Si(OR)_3$ with R = CH_3, CH_2CH_3.

Halogen-containing PMOs

Different ways have been established to incorporate halogens into PMOs. Postsynthetic bromination of an ethene-bridged PMO was already carried out in the introductory pioneer work by the research groups of Stein and Ozin, as mentioned above.[77,78] In contrast to this, the

postsynthetic bromination of benzene-bridged PMOs is more complex and was intensively investigated by the Cool research group who tested different brominating reagents before they found a suitable synthesis route four years later.[139,140] The retro synthesis path is shown in Figure 1-25. Similar to their work which was previously mentioned in context of the aromatic PMOs, an aniline-bridged PMO was synthesized first.[95] The amino function was subsequently converted to bromine via a nitroaniline intermediate.

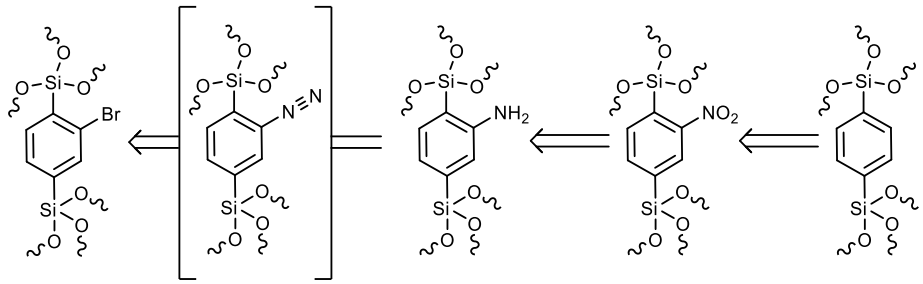

Figure 1-25: Retro synthesis of the postsynthetic bromination of a benzene-bridged PMO according to Huybrechts *et al.*[140] . Waved lines indicate the interconnection in the PMO network in distinction to a free precursor.

The first single source PMO from a brominated precursor was shown by Kuschel *et al.* a decade ago (precursor **49**).[141] They established its diverse modifiability as a flexible starting material for chemical reactions. Figure 1-26 gives an overview of all halogen-containing PMO precursors.

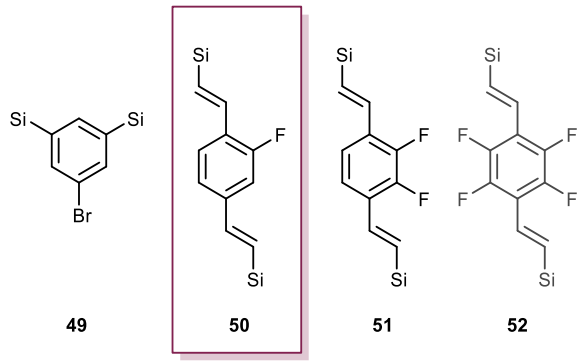

Figure 1-26: Halogen-containing bis-silylated precursors for organosilica materials. Precursor **52** is drawn in gray as no PMO can yet be synthesized from it. Si = $Si(OR)_3$ with R = CH_3, CH_2CH_3.

In the last years, much attention was spent on fluorinated precursors. Bracco *et al.* synthesized a 2-fluoro-1,4-divinylbenzene-bridged PMO and a 2,3-difluoro-1,4-divinylbenzene-bridged PMO from the respective fluorinated precursors (**50** and **51**), analogs to the long-known divinylbenzene-bridged equivalent.[142] Due to the strong polarity of the carbon-fluorine bond, both fluorine PMOs could be used as molecular dipolar rotors. Besides, fluorinated materials are known for good CO_2 adsorption capacity – hence, the materials were characterized regarding their temperature-dependent CO_2 adsorption.

Recently, Ge and Liu presented a polysilsesquioxane that incorporates tetrafluorobenzene bridges (precursor **52**).[143] In this case no PMO, but instead a microporous hybrid material that showed an *apparent* BET surface area of 600 $m^2 \cdot g^{-1}$and enhanced CO_2 adsorption was obtained.

Organosilica monoliths

While most nanomaterials are well-suited for the previously-named applications, in other cases monoliths are required to exploit the advantages of organosilicas. An improved separation efficiency of monoliths as the stationary phase is discussed in liquid chromatography.[144] Up to now, microspheres with a very narrow size distribution are preferred for this application, whereby the resulting pressure during the separation process in high pressure liquid chromatography depends directly on the size of the particles.[145]

As strong carcinogens are trapped in micrometer-sized particles that are suspended in tobacco smoke, the adsorption required larger particles as adsorbents as well.[146] For continuous -flow catalytic microreactors, monoliths of about 0.5–10 mm are needed to perform nano- and microsynthesis.[147] To meet these demands, silica monoliths are established, but just as in the presented cases of powders, further functionalization with the well-known concepts of grafting and co-condensation expands the spectrum. As mentioned at the beginning of section 1.1, hierarchy in the pore system of the monoliths allows improved throughflow and accessibility of the internal surface.

For cylindrical silica monoliths, aerogels are usually generated inside a formative vessel, e.g. a capillary, whereas porous microspheres can be generated by spray drying [148] or by oil-in-water (O/W) or alternatively by reverse water-in-oil (W/O) approaches. In an ethyl ether in water emulsion, mesoporous, hollow silica nanoparticles with diameters around 150 nm and shell thickness of 20 nm were synthesized that assemble to form centimeter sized spheres. The stirring rate is crucial for the macroscopic particle size.[149] Further, the particles were grafted with APTES and the adsorption of phenylalanine of the large spheres was compared to powder MCM-41-type silica whereby an improvement could be demonstrated. A photo of the centimeter-sized beads and SEM and TEM images that show the hollow nanoparticles are shown in Figure 1-27.

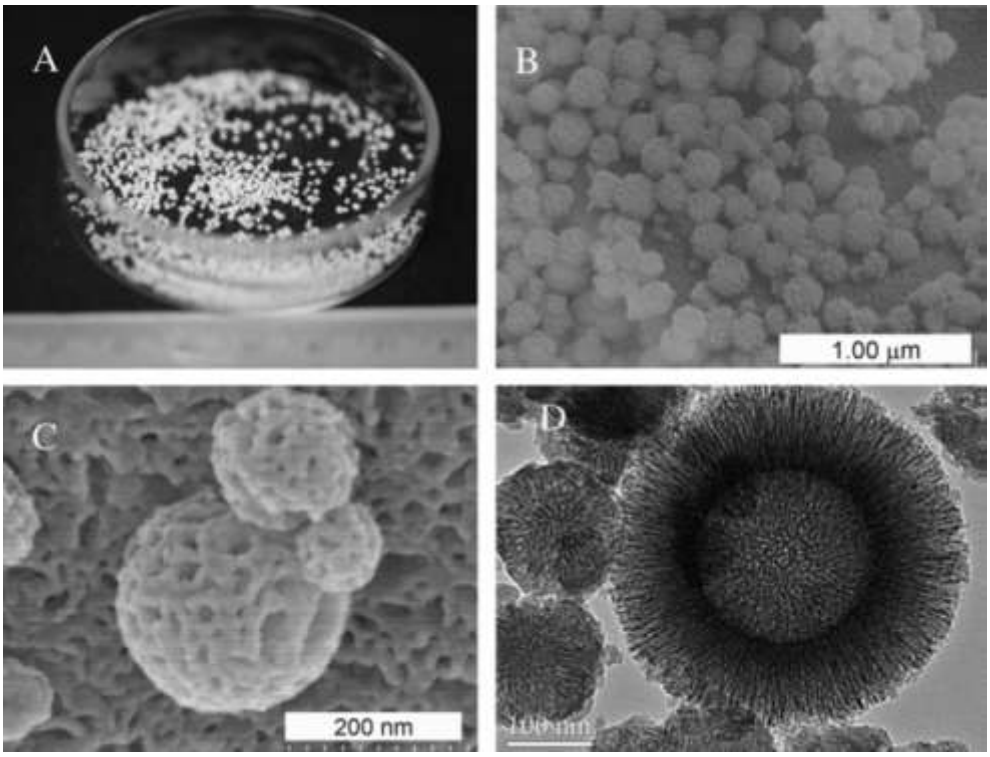

Figure 1-27: A photograph (A) of the centimeter-sized silica beads from ethyl ether/water emulsion and SEM images (B), (C) as well as a TEM image (D) of the hollow particles they are built from. Reprinted from [149] with permission from Elsevier.

Scholz and Lercher were able to control the morphology of hierarchically structured spheres with particle diameters between 0.3 mm and 2.5 mm by co-condensation of a pure silica species with [3-(2-aminoethylamino)propyl]trimethoxysilane and phenyltrimethoxysilane. A photograph of this is shown in Figure 1-28. They investigated intensively the impact of the synthesis composition, especially the influence of the surfactant concentration on the macroporosity and synthesized pure silica particles, but improved the solvent extraction instead of calcination in order to retain the organic functions.[150,151]

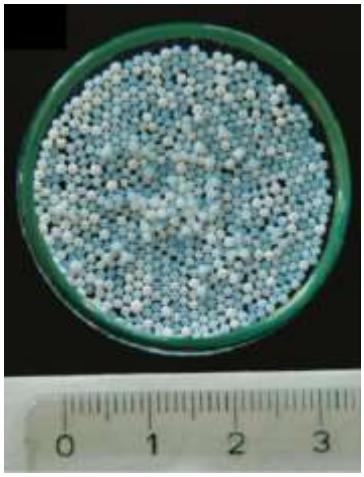

Figure 1-28: Photograph of the macroporous silica particles that were synthesized via an emulsion-based sol-gel synthesis. Reprinted from [150]. Copyright 2011 American Chemical Society.

Von der Lehr *et al.* studied the formation of macroporous monoliths by a Nakanishi phase-separation with polyethylene glycol from the co-condensation of a pure silica precursor, tetramethyl orthosilicate (TMOS) with 5–10 % ortho-, meta- or para-substituted bis(trimethoxysilyl)benzene or bis((trimethoxysilyl)phenyl)dimethoxysilane.[152–154] The monoliths obtained showed surface areas of 470–590 $m^2 \cdot g^{-1}$ and pore diameter maxima between 7.5–10.4 nm.[154] To demonstrate the applicability of the monoliths in proton conduction, their performance was measured after postsynthetic sulfonation of the bridged precursor.[153] Figure 1-29 gives an overview of their work.

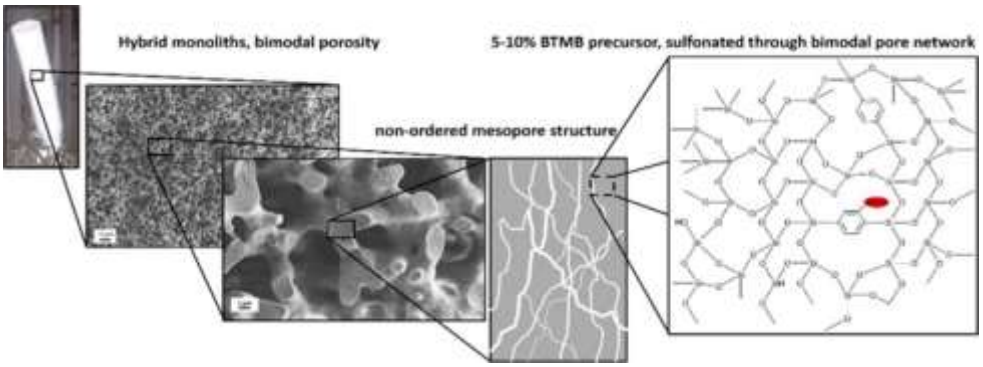

Figure 1-29: Photograph of the bis(trimethoxysilyl)arene containing monoliths. Their macropores can be seen in the SEM images, the mesopores are shown in the diagram. The organic function can be functionalized postsynthetically by sulfonation as shown on the right. Reprinted from [153]. Copyright 2011 American Chemical Society.

Only a few examples for monoliths purely from silsesquioxanes are known. Similar to the synthesis procedure for macroporous silica monoliths, Nakanishi *et al.* presented the synthesis of a hierarchical macro-mesoporous monolith using 1,2-bis(trimethoxysilyl)ethane (precursor **2** in Figure 1-16).[155] By optimizing the reaction composition with the block copolymer P123 as surfactant, 1,3,5-trimehtylbenzene (TMB) as swelling agent and nitric acid as catalyst, 2D hexagonal alignment of mesopores with a sharp pore diameter distribution could be obtained. The additional co-continuous macropore system generates a sponge-like pore structure. Later, also differently shaped ethane-bridged organosilica monoliths, such as disks and long and short columns, were also synthesized by the same group.[156]

The research group of Hüsing also used a phase separation process with P123 for the synthesis of hierarchically structured organosilica monoliths. In order to have water-soluble precursors, in 2006 they modified BTEB, and in 2009, BTEE with ethylene glycol in a transesterification.[157–159] The template and the pore fluid were removed by supercritical fluid extraction to avoid cracking and shrinking of the monoliths. The benzene-bridged monolith showed a surface area of 500 $m^2 \cdot g^{-1}$, mesopores of 6.5 nm and macropores of 260 nm in diameter. The meso- and macropore volumes were 0.55 $cm^3 \cdot g^{-1}$ and 0.85 $cm^3 \cdot g^{-1}$ respectively. A photograph, an SEM image and TEM images of the material shown the hierarchical pore structure in Figure 1-30.

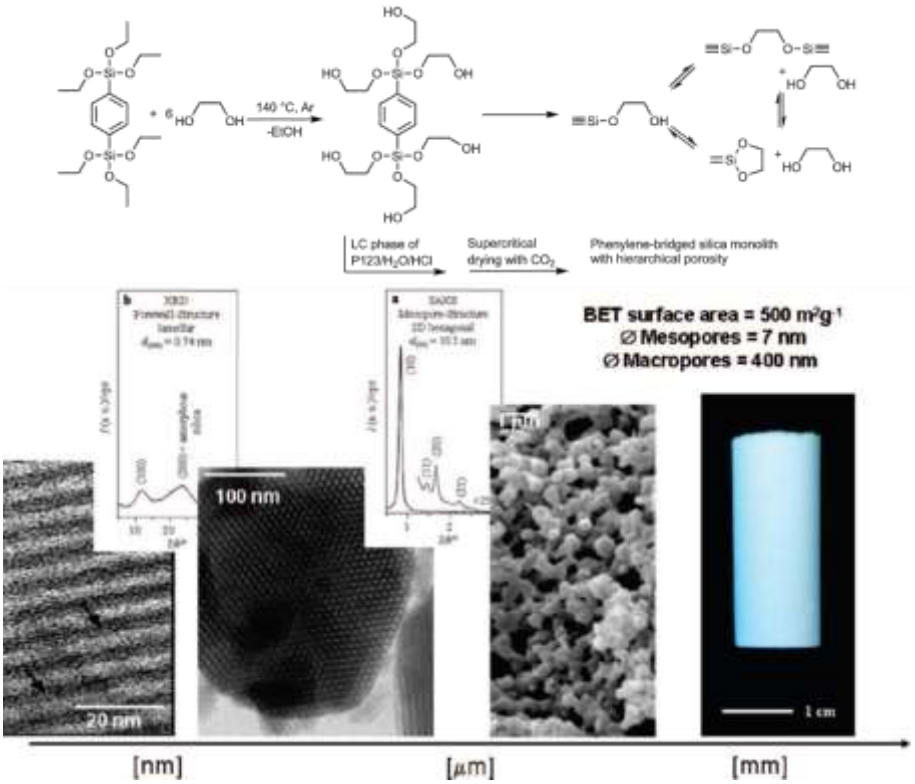

Figure 1-30: The hierarchical pore structure of the benzene-bridged silica monolith synthesized with a glycol-modified precursor is shown with a scale bar, and from left to right: TEM image, SEM image and photograph. Reprinted from [160]. Copyright 2007 American Chemical Society.

Similar results were obtained using the ethane-bridged precursor having BET surface areas up to 611 $m^2 \cdot g^{-1}$ and pores of 5.5 nm. The size of the macropores increases with decreasing P123 content (from 100 to 500 nm). An overview of the respective monolith is given in Figure 1-31.

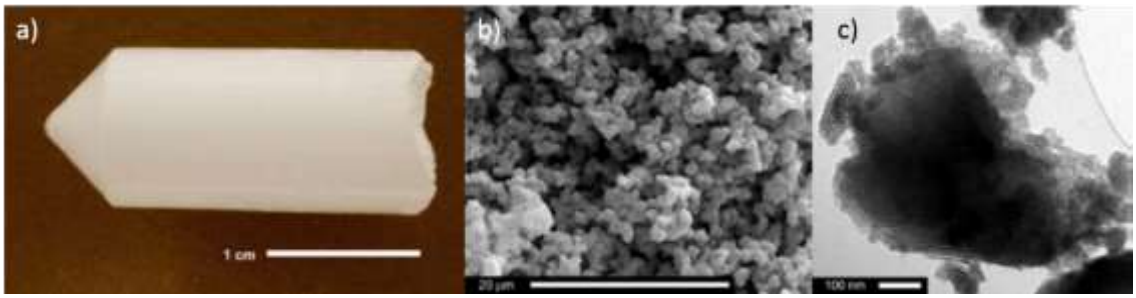

Figure 1-31: Photograph, SEM image and TEM image of the hierarchical porous ethane-bridged organosilica monolith. Reprinted with permission from Springer Nature [159] Copyright 2009.

With the synthesis of silicon oxycarbide (SiOC) monoliths by pyrolysis of an organosilica material in mind, the same research group realized the synthesis of a monolith from 1,3,5-tris-[dimethoxysila]cyclohexane (precursor **42** in Figure 1-24) in 2010, in a similar approach using P123. In this case, neither the structuring of the mesophase, nor the phase separation was successful, but the material showed a very high surface area of 1071 $m^2 \cdot g^{-1}$.[161]

In 2009 and 2010, it was again the Nakanishi group, who achieved the phase separation of benzene-bridged and biphenyl-bridged precursors in the presence of another block-copolymer,

namely F127, using N,N-dimethylformamide (DMF) and N,N-dimethylacetamide, respectively, as solvents.[162,163] The monoliths obtained with a sponge-like macropore system were further transformed into SiC/C by pyrolysis. In these cases less importance was attributed to ordered mesopores as these would collapse during the heat treatment.

More recently, in 2016, Wu *et al.* synthesized ethene-bridged organosilica monoliths, one with expansions of 4.6 mm x 5 cm and one in a capillary having a diameter of 100 µm. The bulk monolith provides a very high BET surface area of 1707 $m^2 \cdot g^{-1}$ from micro- and mesopores and a pore volume of 2.3 $cm^3 \cdot g^{-1}$. Unfortunately, no information concerning the periodicity of the pores is given.[164] The size of the macropores was not mentioned but their presence can be seen in the SEM images in Figure 1-32 and they allow a good permeability for throughflow. Due to the ethylene function, the organic bridge postsynthetical functionalization via thiol-ene click chemistry was possible with octadecanethiol (C_{18}-SH). The organosilica capillary was used for the nano-reversed phase liquid chromatography-based separation of alkylbenzenes.

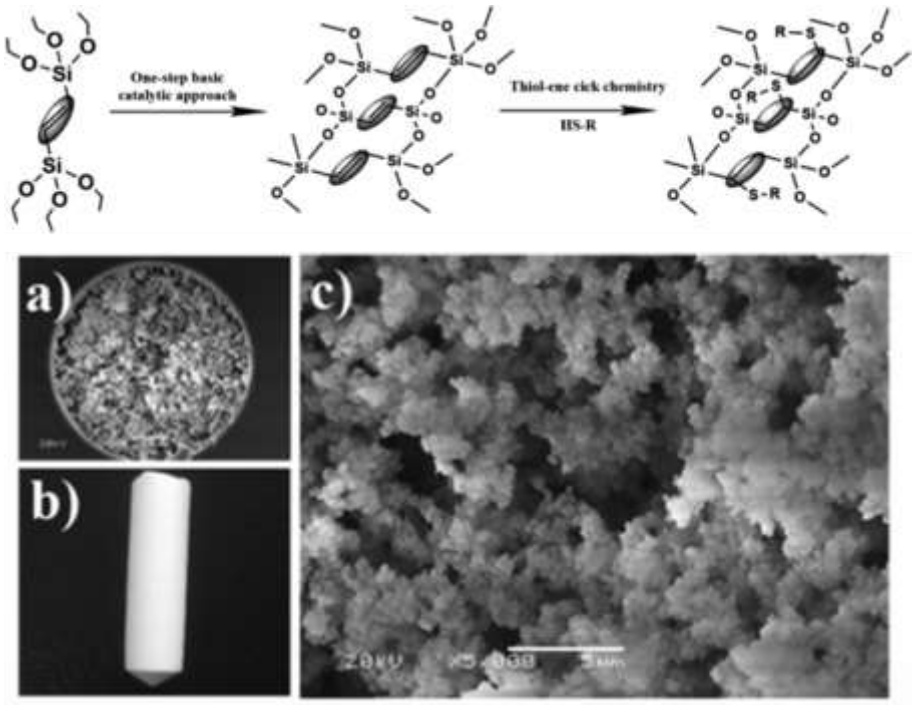

Figure 1-32: Overview of the synthesis procedure of the ethylene-bridged organosilica monolith and its functionalization by thiol-ene click chemistry. A photograph of the larger monolith is shown in (b) and SEM images of the capillary with different magnifications are shown in (a) x900 and (c) x5000. Reprinted with permission [164]. Copyright 2016 American Chemical Society.

Schachtschneider *et al.* were able to synthesize the precursor molecule 1,5-bis-tri(isopropoxysilyl)-benzene-3-azide (**19** in Figure 1-18) and used it successfully both in a PMO and for the synthesis of a mesoporous aerogel organosilica monolith.[96] The aerogel was synthesized without any surfactant and no ordering of the pores could be detected, hence it cannot be called a PMO. However, the specific surface area of the material of 662 $m^2 \cdot g^{-1}$ is

noteworthy. The azide function in the monoliths allowed for the performance of click chemistry, whereby gradual functionalization and a gradient in pore size was achieved. In addition, by using two different alkyne compounds, two opposed gradients are imaginable. Figure 1-33 shows a diagram of the gradually functionalized material as well as a photograph of the monolith.

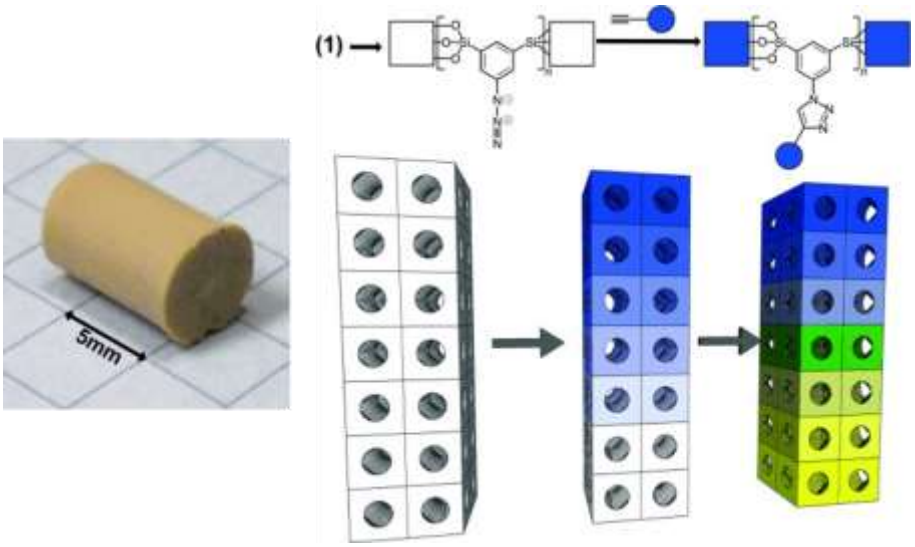

Figure 1-33: Photograph of the dry monolith of the nanoporous phenylazide organosilica material (left), next to a diagram (right) that visualizes how the monolith can be functionalized gradually by click chemistry with one alkyne compound (blue) or even multiple compounds indicated in blue and yellow, where mixed phases of both compounds are indicated in green. 1,5-bis-tri(isopropoxysilyl)-benzene-3-azide is denoted as (**1**) in this diagram. Reprinted from [96] with permission from Wiley.

1.6 Alginate for spherical morphology

Compared to powders, millimeter-sized spherical particles that contain porous materials simplify handling, especially at an industrial level. Therefore, they are of interest for applications like adsorption or heterogenic catalysis. Different approaches are used to create inorganic materials as well as organic/inorganic composite materials in this requested shape. Porous zirconium titanium oxide beads of 0.59 mm were obtained by phase separation of polyacrylnitrile as a matrix for uranium adsorption.[165] A zeolitic imidazole framework ZIF-8 was embedded in polysulfone or polyethersulfone polymers to form composites of beads with 2.5 mm diameter that were used for CO_2 adsorption and the selective removal of the dye methyl blue, respectively.[166,167] The oil in water (O/W) emulsion templating allowed the synthesis of silica beads of 1.15 mm or 0.3 mm, where the smaller beads show promising results for the adsorption of organic liquids and oils.[168,169] In addition to these approaches, the use of polysaccharides as an encapsulation matrix for spherical beads is of interest as these compounds are non-toxic and of natural origin. Alginate is a polysaccharide, a biopolymer that can be dissolved in water and forms millimeter-sized hydrogel beads in contact with metal cations by ionotropic gelation.[170,171] Alginate can be isolated from different algae. It is a block copolymer of 1,4-linked β-D-mannuronate (M) and α-L-guluronate (G) that are composed differently to MM-, MG- and GG-blocks.[172] The hydrogel formation is made possible as the guluronic acid (G) blocks bind to metal cations in a so called egg-box model as depicted in Figure 1-34. Calcium(II) ions are the most commonly used cations, but depending on the alginate composition and sequence, other cations, e.g. strontium(II) or barium(II) are also used.[172] Moreover, at low pH values the formation of alginate acid gels is possible by intermolecular hydrogen bonding. On the other hand, hydrolytic degradation of alginate is possible under strong alkaline or acid conditions. [173]

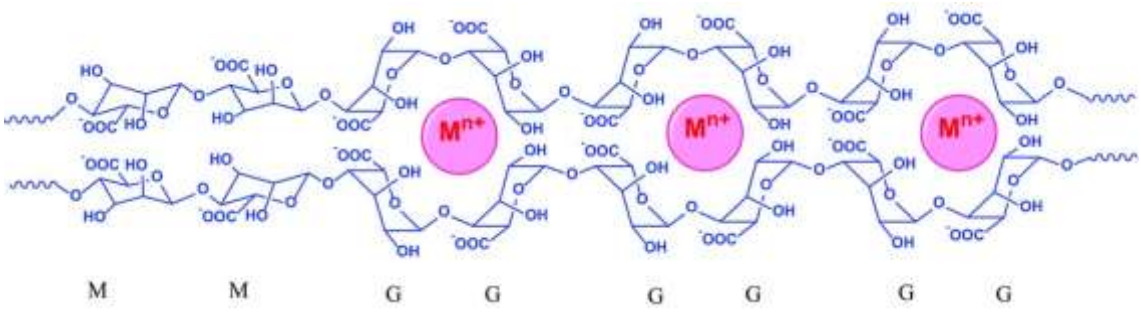

Figure 1-34: Alginate is composed of different sequences of β-D-mannuronate (M) and α-L-guluronate (G). GG blocks can be cross-linked by metal cations (here M^{n+} can be Ca^{2+}, Sr^{2+} or Ba^{2+}). The resulting structure is similar to an egg box, hence the name "egg-box model". Reprinted from [174] with the permission from Wiley.

Because it fits in the green chemistry trend and is relevantly affordable, alginate has already been used as form-giving matrix for various systems. Yolk/shell microcapsules of the above-

mentioned standard adsorptive ZIF-8 were achieved with a 210 µm diameter and used for controlled dye release.[175] Zhu *et al.* did not incorporate preformed particles of solid composite materials inside a spherical alginate matrix, but realized the formation of different metal-organic frameworks (MOF) within. For this purpose, they induced cross-linking of the hydrogel with different metal ions, as these are needed for the MOFs.[176] In a second step they added the gels to a solution of the respective bridging organic unit whereby under suitable conditions the MOF is formed.

Kallenberger *et al*. discussed the use of composite materials of alginate and different salts for thermochemical heat storage applications.[177] They presented two different bottom-up synthesis paths, on the one hand, the incorporation of gelation salts $CaCl_2$ or $SrCl_2$, on the other hand the incorporation of pre-shaped $Mg_5(CO_3)_4(OH)_2{\cdot}4H_2O$ particles of 10 µm in diameter which were converted to $MgSO_4$ inside the alginate matrix with the help of sulfuric acid or to $MgCl_2$ with the help of hydrochloric acid. The composites from both syntheses show very high salt loadings around 86 wt% resulting in promising heat storage densities. The formation of beads with adjustable diameter between 0.5 mm and 5.0 mm improves the permeability of the materials significantly and allows the packing in beds or columns. The composite of alginate and $CaCl_2$ was further investigated for the use of water harvesting. It shows high water uptake capacities at ambient temperatures of 26 °C and 30 % relative humidity, conditions as in regions were the production of fresh water is difficult.[178]

Silica gels play an important role in biomedical applications like cell or enzyme immobilization and can be complemented by silica/alginate composites where the cells are able to grow and even divide.[179,180] Conversely, aminopropyl-grafted silica particles can improve the mechanical and biological properties of alginate hydrogels for tissue engineering as well as wound-dressing applications.[181–183] Ulker and Erkey showed how a layer of alginate aerogel on a silica aerogel prevent its collapse in a buffer solution. In addition, the material obtained is a promising drug delivery vehicle as drug release is delayed in the composite material in comparison to pure silica.[184] Equipped with γ-Fe_2O_3, particles silica/alginate composites can be used for DNA isolation.[185]

There are also examples for beads of inorganic materials, e.g. an outstandingly active photo catalyst of titania in an alginate matrix.[186] For the synthesis of pure titania/zirconia beads that were used for uranyl-sorption,[187] alginate was used for the shaping process but was subsequently removed by calcination. In contrast, in the synthesis pathway of γ-Fe_2O_3 /silica beads, the calcium alginate was removed with the help of citric acid which coordinately binds calcium ions.[188]

The combination of the ionotropic gelation and sodium borosilicate glass was done by Inayat *et al.* The granulate sodium borosilicate glass was added to alginate and incorporated in the hydrogel. Removal of the alginate matrix and sintering of the glass were thermally induced. Afterwards, phase separation was induced in the glass beads with diameters of 2-4 mm. The macroporous structure is generated by leaching as described in section 1.3. Due to interparticle voids between the sintered particles a bimodal pore system is obtained of pure CPG beads with narrow pore size distributions.[30]

These diverse examples demonstrate that the alginate hydrogel formation is a promising method to synthesize porous silica-based materials as millimeter-sized spherical particles.

2 Motivation

The diversity of nanoporous organosilicas has fascinated researchers for many decades, and PMOs have of special focus over the last twenty years. Their field of application has been constantly expanded and their properties have been investigated from different perspectives. Tailor-made organic bridges were designed for special applications and well-known representatives of the bis-silylated precursors were rediscovered for modern challenges in the last years. While the synthesis of organosilica nanoparticles received a lot of attention and has already been applied successfully, e.g. in medical applications, the synthesis of monolithic organosilicas was discussed less often. Since the transferability of established synthesis concepts from silica monoliths to organosilica monoliths is limited to some extent, particularly for structurally ambitious precursors, new strategies need to be developed.

In this work, different paths have been taken to fit nanoporous organosilicas to additional applications. Within the context of a project from the Deutsche Forschungsgemeinschaft (DFG) the targeted field of application was the adsorption of inhalation anesthetics and toxic traces in a gas flow. This led to three different projects:

1. The first project did not focus on the morphology of the organosilicas but on the optimization of organosilica materials as adsorbents for inhalation anesthetics. As microporous materials were promising candidates for the adsorption of halogenated ethers in the past, a flexible synthesis strategy for microporous organosilicas from different well-established precursor molecules was proposed. In addition, the synthesis of halogen-containing bis-silylated compounds and their conversion in the synthesis of microporous organosilicas and PMOs was also planned. The adsorption capacity of these materials for isoflurane at low concentration in a gas flow should be measured in cooperation with the research group of Professor Bathen in Duisburg.

2. In the second project, a general concept for the applicability of nanoporous organosilicas in gas chromatographic purification, or for the enrichment of substances from a gas flow for recycled use was proposed. For this, spherical particles in the size range of 100 µm are needed for a consistent pressure profile in a column. For the synthesis of organosilica-containing particles that meet these requirements, porous glass bodies are used as a basis for the formation of organosilica/silica hybrid materials. CPG of the favored size and porosity were supplied by the research group of Professor Enke who are leading experts in this field.

   Structural similarities and differences in silica and organosilica were to be used in order to incorporate organosilica into the porous system of the glass matrix. Different

approaches were used for the homogeneous incorporation of a significant percentage of organosilica in the resulting hybrid material.

In an additional step, a hierarchically porous organosilica/silica hybrid material with increased specific BET surface area was required to ensure good accessibility of the organic moiety. This was to be achieved by adapting the concept of pseudomorphic transformation which is well established for the postsynthetic generation of mesoporous structures in silica materials of particular morphology. Prior to the transformation of the hybrid material, the pseudomorphic transformation of silica beads with different porosity features needs to be extensively studied.

The main challenge of this project was the characterization of the product of the pseudomorphic transformation of the hybrid materials. Advanced solid-state NMR studies should help to prove the integrity of the organic bridging unit in the mesoporous hybrid material as well as quantify it. Further, this method should be used to estimate whether the organosilica phase participates in the pseudomorphic transformation.

In addition to the glass beads in the micrometer size range, the concept should be transferred to porous glass membranes of 2.5 cm^2 with low pore volume. Due to the geometry, these glass bodies have further requirements and their characterization is even more challenging.

3. The last project dealt with silica and organosilica monoliths that are in the millimeter size range, e.g. for breathing masks or for industrial applications, where dusty materials cannot be used.

   The synthesis of these beads was achieved with the help of calcium alginate hydrogels. By dropping an alginate solution into a calcium ion-containing solution, spherical beads in the respective size range are obtained. The aim was to enclose a silica or an organosilica species inside these beads and to again take advantage of the pseudomorphic transformation to generate a spherical PMO monolith from this. In order to generate a hierarchical pore system and to allow the characterization of pure organosilica monoliths, the enclosure matrix needed to be removable which necessarily means that the PMO beads have to be stable.

3 Methods

3.1 Gas Physisorption

Physisorption of gases can be used to determine the specific surface area, pore size and pore volume of micro- and mesoporous materials. This involves the physical adsorption of a fluid, the adsorptive, onto the solid surface of the adsorbent and the respective desorption. The adsorbed matter is called adsorbate as shown in Figure 3-1. Adsorption (either physisorption or chemisorption) is not to be confused with the process of absorption which occurs when the gas penetrates the surface of the solid.

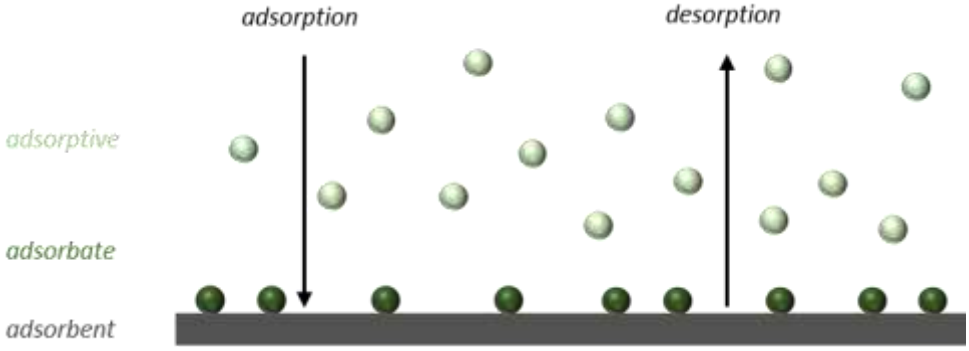

Figure 3-1: The adsorption of an adsorptive on the solid surface of the adsorbent, known as the adsorbate in the adsorbed state.

The IUPAC recommendation from 1985 concerning gas physisorption has already been mentioned as it classifies porous systems into micro-, meso- and macropores according to their physisorption behavior.[2] This recommendation was updated in 2015.[3] Below the critical temperature of a gas the adsorbate forms a liquid film on the pore walls. Usually the volumetric or molar gas uptake in $cm^3 \cdot g^{-1}$ and $mol \cdot g^{-1}$, respectively is plotted against the relative pressure p/p^0 wherein p^0 is the temperature-dependent saturation pressure. The actual classification of the different isotherms is shown in Figure 3-2.

Isotherms of type I(a) are obtained from microporous solids where strong adsorbent-adsorptive interactions dominate and is characterized by a steep uptake at very low relative pressures, followed by a plateau. As soon as the pore size distribution is broader or larger pores up to ca. 2.5 nm are present, the isotherm shape changes to type I(b) where reaching the plateau is delayed and a transition pressure range is given. Point B in isotherm type II indicates the completed formation of a monolayer and a multilayer is formed afterwards. This behavior is often seen in non-porous or macroporous solids. Stepwise formation of multilayers can be observed in type VI isotherms. Type III and V isotherms indicate low adsorbate-adsorptive interactions. Type V plays a special role in water vapor adsorption, which uses an extraordinary

adsorptive as in addition to the porosity feature of the solid the surface chemistry is of importance.

In mesoporous materials fluid/fluid interactions are of relevance as a phase transfer from gas into a liquid-like phase, namely capillary or pore condensation, takes place. Mesopores smaller than 4 nm give isotherms of type IV(b), whereas hysteresis phenomena occur in the presence of larger pores giving isotherms of type IV(a). The shifted condensation is caused by the formation of a metastable adsorption film compared to the desorption process which is in the equilibrium state. In both cases IV(a) and IV(b), a final plateau is reached at high relative pressures.

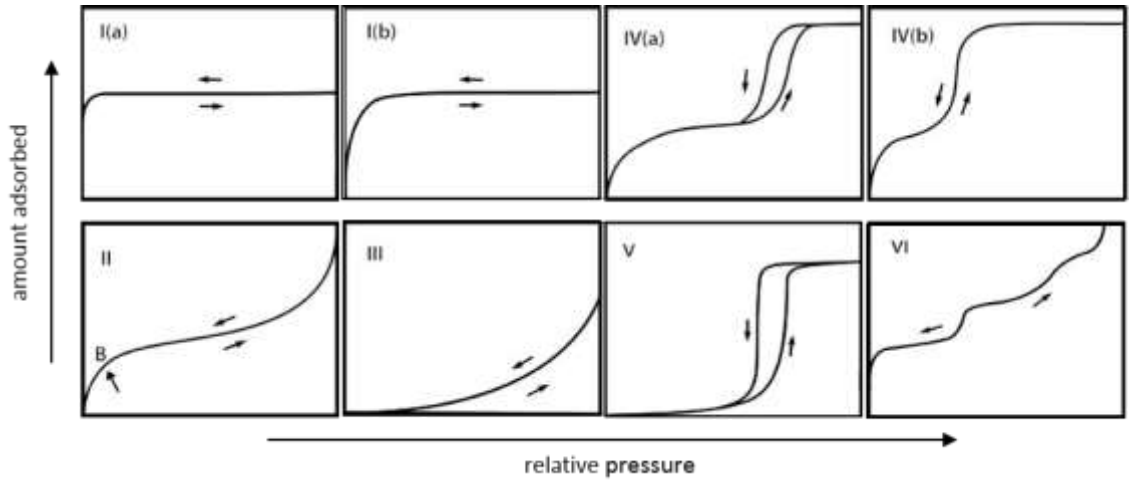

Figure 3-2: Overview of the IUPAC classification of physisorption isotherms from 2015, reproduced with the permission of the Royal Society of Chemistry.[189]

Different types of hysteresis were also classified by IUPAC, as shown in Figure 3-3.

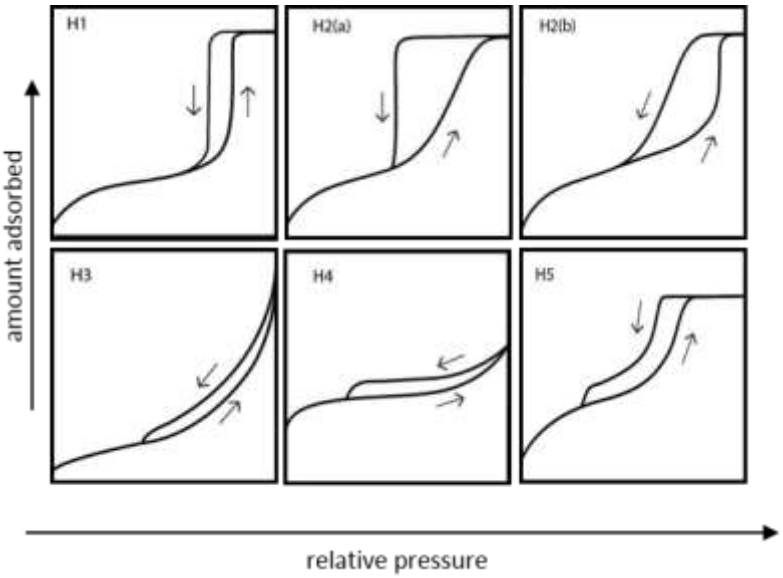

Figure 3-3. Classification of hysteresis loops according to IUPAC, reproduced with the permission of the Royal Society of Chemistry.[189]

If the hysteresis is caused by delayed pore condensation in monomodal cylindrical mesopores larger than a critical value (4 nm in case of nitrogen at 77 K), hysteresis type H1 is observed in single pores as well as in networks of pores with the same pore size. Figure 3-4 (a) is a schematic representation of this process. In the case of interconnected pores of different pore diameter, disordered pore systems or pores with irregular pore size, hysteresis effects can also occur, the explanation of which can be complex at times.

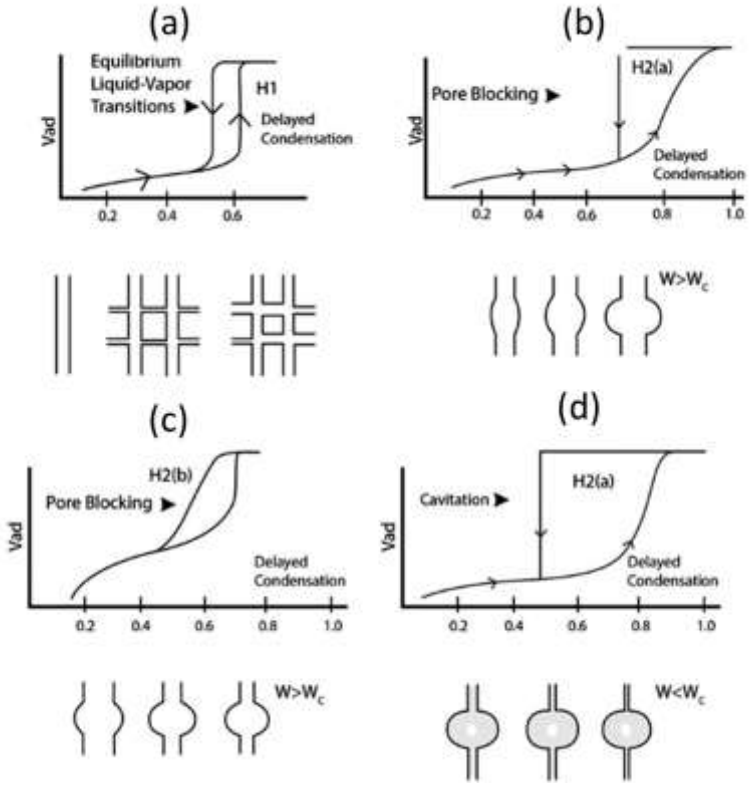

Figure 3-4: Different hysteresis types and the underlying mechanism. (a) Hysteresis type 1, (b) hysteresis type 2(a) as a result of pore blocking in materials with a wide distribution of pore body size, (c) hysteresis type 2(b) as a result of pore blocking in materials with a wide distribution of pore neck size and (d) hysteresis type 2(a) as a result of cavitation in a pore system with very narrow neck size. Reprinted with permission from Springer [190] Copyright 2014.

In ink-bottle pore systems, with pore necks over a critical size, pore blocking occurs. The hysteresis behavior depends mainly on the size and the size distribution of the bottle neck as well as on the pore body size distribution.

For pores with narrow pore neck diameter distribution, hysteresis type 2(a) occurs, whereby the pore size distribution can be broad. This hysteresis type is characterized by abrupt desorption. The relative pressure of desorption depends on the pore neck size, which implies that the step in the desorption branch can be used to analyse the pore neck size. In pore networks evaporation occurs through the largest accessible pore neck, which is called percolation, see Figure 3-4 (b).

In contrast, hysteresis type 2(b) is observed in ink-bottle pores when the pore body is of narrow pore size distribution but the pore neck diameter distribution is broad. Here, the desorption branch is not abrupt and is less steep than the adsorption (see Figure 3-4 (c)).

This is valid unless the pore neck diameter falls below a critical size, where desorption follows the mechanism of cavitation, as depicted in Figure 3-4 (d). Cavitation is the spontaneous formation of a gas bubble in the metastable condensed fluid, so that the pore body empties while the pore neck remains filled. For nitrogen at 77 K the critical pore neck diameter for cavitation is smaller than 6 nm and the relative pressure where desorption occurs, is usually around 0.41–0.49. In the case of cavitation, no information concerning the pore neck size can be obtained.

Hysteresis type H3, H4 and H5 occur in other disordered pore systems. Type II isotherms show hysteresis type H3 in the case of incompletely filled macropores or non-rigid aggregates as well as plate-like particles. H4 occurs in materials that contain micropores together with mesopores or macropores. Hysteresis type H5 shows two steps in the desorption branch, it occurs in the presence of both blocked and open pores in the adsorbents.

The specific surface area of the adsorbents is one of the most important pieces of information obtained by physisorption measurements. For this, the method by Brunauer, Emmett and Teller (BET method) is used consistently. In contrast to the Langmuir method, it takes the formation of multilayers into account. From the isotherm, a BET plot is generated in linear form using equation (2) where an expression of the molar amount of the adsorbate at a specific relative pressure p/p^0 is equal to a term with the molar capacity n_m and the BET constant C, which is exponentially related to the energy of monolayer adsorption.

$$\frac{p/p^0}{n(1-p/p^0)} = \frac{1}{n_m \cdot C} + \frac{C-1}{n_m \cdot C} \cdot (p/p^0) \qquad (2)$$

where

p/p^0	relative pressure
n_m	monolayer capacity
N	molar amount of the adsorbate
C	BET constant

From this equation, the monolayer capacity n_m is calculated and further used in equation (3) to determine the specific surface area S_{BET} per mass of the adsorbate m having the Avogadro constant N_A and a molar cross-sectional area σ_m of the adsorptive.

$$S_{BET} = \frac{n_m \cdot N_A \cdot \sigma_m}{m} \quad (3)$$

where

S_{BET} specific BET surface area

n_m monolayer capacity

N_A Avogadro constant

σ_m molar cross-sectional area

m mass of adsorbate

For the specific surface area S_{BET}, the relative pressure range of 0.05–0.3 is usually considered, but in some cases, especially in the presence of micropores and small mesopores, this range has to be reconsidered. There are three criteria that must be satisfied for a reasonable result: first, the value of the BET constant C must be positive and preferably not too high (less than 300); second, the term $n(1-p/p^0)$ must be continuously increasing; third, the selected range should include the relative pressure corresponding to the monolayer capacity n_m. Whenever a type I isotherm is given, only an *apparent* specific surface area can be determined.

The most widely used adsorptive is nitrogen at 77 K as it is commonly available. However, it brings with it another source of error for the determination of S_{BET}. As nitrogen is a quadrupole, there might be specific interactions that have an influence on its orientation on the surface. Thus, the assumed molar cross-sectional area of 0.162 $nm^2 \cdot mol^{-1}$ might distort the specific surface area by up to 20 %, and the accuracy of the used cross section has been questioned. [191] Therefore, argon at 87 K, with a slightly smaller molar cross-sectional area of 0.142 $nm^2 \cdot mol^{-1}$, is often the better choice to determine the specific surface area, especially for microporous materials. The absence of specific interactions causes faster diffusion and equilibration and results in a shift of the micropore filling of 1–1.5 orders of magnitude to higher relative pressures. This allows more exact measurements, but as liquid argon is less common, a costly cryostat is often needed to adjust the temperature. The apparatus setup makes the measurements more time-consuming than nitrogen physisorption measurements.

Pore size determination based on the Kelvin equation, e.g. the often-used method by Barrett, Joyner and Halenda (BJH), is not suitable for pores smaller than ca. 10 nm as an underestimation of 20–30 % occurs. This can be averted by density functional theory (DFT)-based methods. An assortment of kernels is available assuming different pore geometries and interconnectivity for different adsorptives on different adsorbent surfaces. Unfortunately, there are no kernels available for hybrid materials so that kernels for carbons or silicas are used in the first instance. Appropriate assumptions regarding the pore geometry are crucial for an adequate pore size

determination. In contrast to classical methods, the literature provides good agreement for calculations of the pore size distributions from the adsorption and the desorption branch for NLDFT, so that the adsorption branch is preferred whenever hysteresis effects occur.[189]

For microporous materials, argon measurements are essential for the determination of the pore size especially for organosilica materials, as the surface interactions of nitrogen are undefined. Carbon dioxide has a very high saturation pressure at 273 K and a smaller kinetic diameter than N_2 and Ar which allows micropore analysis in a comparably high pressure range without kinetic restrictions. This makes CO_2 an affordable and attractive adsorptive despite its quadrupole momentum and larger cross-sectional area of 0.210 $nm^2 \cdot mol^{-1}$. Unfortunately, only DFT kernels based on carbons with slit pores are available for CO_2, so this method is unsuitable for micropore volume and pore size determination of organosilica materials. As the kinetic diameter of water is even smaller (0.27 nm), it seems attractive for the determination of micropore volumes at first glance, but it is unsuitable due to its strong dipole momentum and distinct interaction with different surfaces.[189] Table 3-1 summarizes the kinetic diameter and cross sections for the above-mentioned adsorptives.

Table 3-1: Overview of the physical parameters of the relevant adsorptives for this work

adsorptive (temperature)	**cross-sectional area / $nm^2 \cdot mol^{-1}$**	**kinetic diameter / nm**
argon (87 K)	0.142	0.34
nitrogen (77 K)	0.162	0.36
carbon dioxide (273 K)	0.210	0.33
water (298 K)	0.125	0.27

3.2 Mercury porosimetry

Mercury porosimetry allows the determination of pore volume, pore size and density of porous materials and it can give further information about pore networks and even particle size distributions. The technique covers the characterization of pores of five decades between 360 µm to 3 nm by taking advantage of non-wetting liquid mercury. Mercury has to be forced to penetrate pores, and a comparably easy correlation between the applied pressure *P* and the pore diameter *D* is given in the Washburn equation (4), a modified Young-Laplace equation.

$$D = \frac{-4\gamma \cos\theta}{P} \qquad (4)$$

where

γ surface tension

θ contact angle

D pore diameter

P applied pressure

Figure 3-5 shows the relationship between pore diameter *D* and applied pressure *P*.

In the literature, slightly different assumptions are made for the surface tension *γ,* of 480 dyne·cm^{-1} or 485 dyne·cm^{-1}, as well as for the contact angle of mercury θ of 130° and 140°. In comparison to this, water as a wetting liquid has a contact angle of between 20° to 30°.

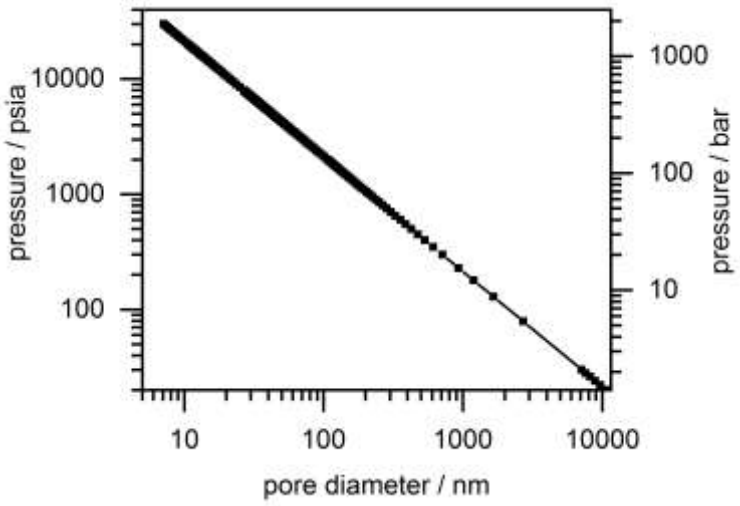

Figure 3-5: Plot of the measured pore diameter in nm against the applied pressure in psia and bar according to the Washburn equation.

The measured parameter is the intruded volume depending on the applied pressure. Presumption for mercury intrusion is a cylindrical geometry of the pores and it is further

restricted as only the pore entrance is considered. For evacuation and filling of the system, a vertical assembly is preferred in order to minimize head pressure effects, whereas the high-pressure assembly requires a horizontal assembly. In contrast to gas adsorption, mercury intrusion porosimetry includes the filling of the pore system at low pressure and the penetration at high pressure in the intrusion, whereas the extrusion is measured only to ambient pressure. Figure 3-6 shows exemplarily a mercury porosimetry curve which is subdivided in different sections.

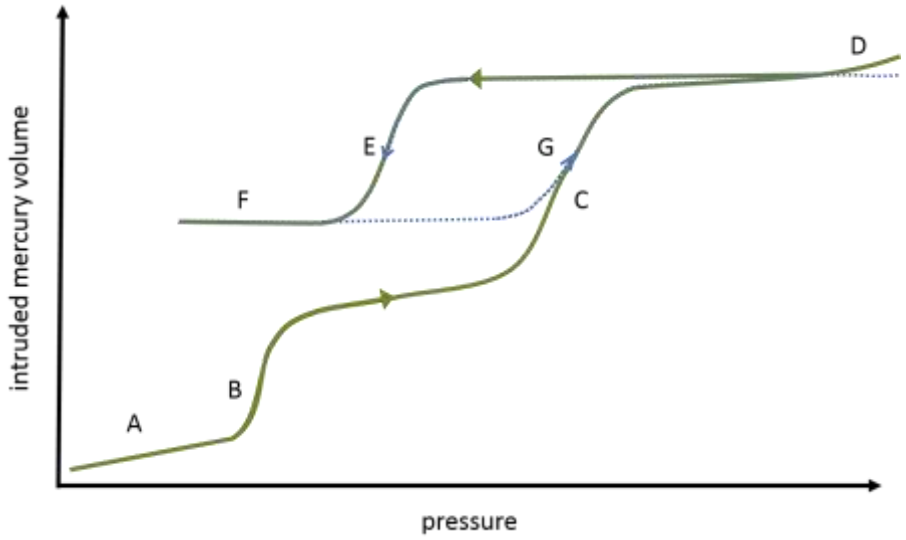

Figure 3-6: Schematic plot of a mercury porosimetry curve (green). The intrusion is subdivided in sections: powder rearrangement (A), interparticle filling (B), pore filling intrusion (C), and compression (D). The extrusion (E) follows with hysteresis, and some mercury remains in the materials (F). Hence, a second intrusion cycle, shown as dotted blue line, (G) starts at higher intrusion volume. In most samples, the second intrusion follows the same extrusion as the first. Adapted by permission from Springer. [192]

In case of powers, a first intrusion occurs due to rearrangement or densification of the particles (A). It is followed by interparticle filling (B) where the pressure corresponds to the interparticle size and can give evidence on the particle size of the powder. Mercury intrusion in the pores within the material occurs at higher pressures (C) depending on the pore size as described before. The last section of the intrusion curve (D) occurs in susceptible materials and may be reversible. The extrusion cure follows (E), where some mercury always remains in the material (F). Mercury that is trapped behind a smaller pore window stays inside the material during extrusion as it is not forced through the narrowing, so that in some particular cases no extrusion occurs. The extruded mercury portion and the hysteresis between intrusion and extrusion can provide network information in this way. A second cycle (G) starts at the higher intrusion volume level and follows the same extrusion as the first cycle in most samples.[192]

3.3 Nuclear magnetic resonance spectroscopy

Nuclear magnetic resonance (NMR) spectroscopy can be operated in the liquid state to identify the chemical structure of dissolved organic compounds, or in solid states to get information about spatial assembly and the molecular structure. Although the methods differ in many aspects and provide different information, the physical background of both methods is the same. It is outlined here very briefly. Refer to the literature for more detailed information.[193,194]

NMR active nuclei with a nuclear spin $I = ½$ have two possible orientations ($2I+1$), that split into two different energetic states, the Zeeman states, when a static magnetic field B_0 is applied. The energetic difference ΔE is given according to equation (5)

$$\Delta E = \gamma \cdot \hbar \cdot B_0 \tag{5}$$

where

γ gyromagnetic ratio

$\hbar$ reduced Planck constant

B_0 applied magnetic field

The gyromagnetic ratio γ is a characteristic parameter for every isotope and is decisive for the energy difference of the Zeeman states and for the NMR sensitivity of nuclei. Table 3-2 summarizes the NMR active nuclei which were used in this thesis with their natural abundance and the gyromagnetic ratio γ.

Table 3-2: NMR-active nuclei used in this work, their natural abundance and the gyromagnetic ratio that has an impact on the NMR sensitivity of the nucleus.

½ spin nuclei	natural abundance / %	gyromagnetic ratio / 10^7 rad/Ts
^{1}H	99.9	26.75
^{13}C	1.10	6.728
^{15}N	0.37	-2.712
^{19}F	100	25.18
^{29}Si	4.67	-5.319

The distribution of nuclei in the two energetic states follows the Boltzmann distribution and only a few more nuclei are in low-energy state. This is shown in Figure 3-7.

NMR Spectroscopy measures the transition between the two energetic states with the resonance frequency of the respective nucleus. To give an example for an applied magnetic field of 7 Tesla, the resonance frequency for ^{1}H is 300 MHz, and for ^{13}C it is 75.43 MHz.

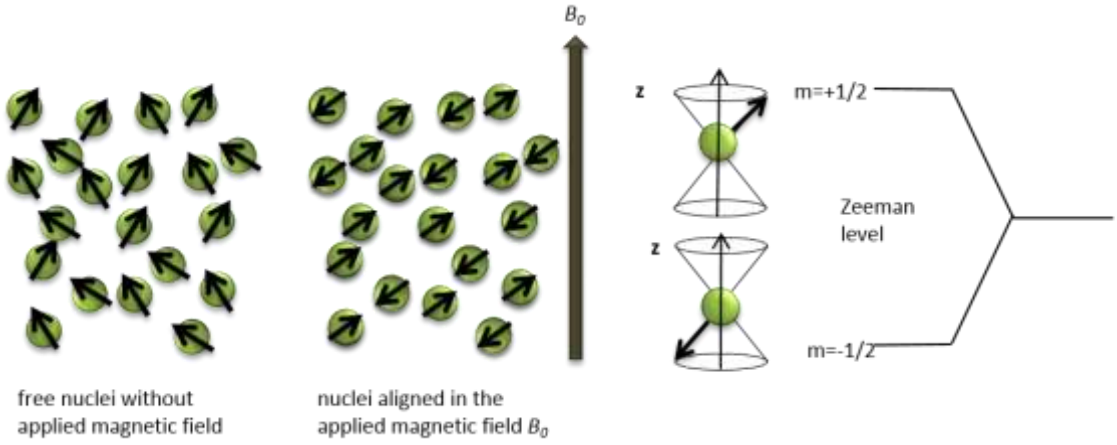

Figure 3-7: Principle of NMR spectroscopy. The energy states of nuclei with a spin *I* = ½ splits into two with nuclear spin quantum number +½ and -½, the so-called Zeeman level. The distribution of nuclei in the upper and those in the lower energy state follows the Boltzmann distribution. Adapted from [193,195].

Depending on the chemical environment, the resonance frequency of nuclei shifts with respect to a reference sample so that the chemical shift can be used as basis to ascribe NMR signals to structural elements of a compound. In liquid–state ^{1}H NMR spectroscopy, the integral of a peak area is proportional to the number of equal nuclei. The splitting pattern of a signal resulting from *J*-coupling, depends on NMR active coupling partners of the nucleus which are neighboring nuclei, usually two-bond coupling, three-bond coupling, and up to four-bond coupling. Taking chemical shift, integral of the peak area and splitting pattern together, the signal can be assigned to a proton species in an organic compound.

In NMR spectra of fluorine-containing organic molecules, couplings between ^{1}H and ^{19}F that stand out with coupling constants up to 85 Hz are noticeable in ^{1}H- as well as in ^{19}F-NMR spectra. One-bond coupling constants between ^{13}C and ^{19}F can even exceed 400 Hz.[193]

For more complex structures, 2D experiments are helpful tools for the interpretation of the NMR spectra. H,H-COSY (correlation spectroscopy) experiments provide information on the correlation between protons. Experiments for heteronuclear correlation are HMBC (heteronuclear multiple-bond correlation), which allows among others the assignment of quaternary carbons, and HSQC (Heteronuclear Single-Quantum Correlation) or HMQC (Heteronuclear Multiple-Quantum Correlation), both of which show correlation of directly bonded nuclei.

Solid-state NMR spectroscopy

Via solid-state NMR spectroscopy, information on internuclear distances, torsions angles, atomic orientations or exchange processes can be obtained. However, aspects like heteronuclear and homonuclear dipolar couplings and chemical shift anisotropy broaden the signals and impose particular challenges for this method.[196] These interactions exist in the liquid state as well but are rarely observed as they are averaged by fast molecular motion in solution.

Heteronuclear dipolar coupling is the interaction between different nuclear spin pairs which causes line broadening in ^{13}C and ^{15}N of organic compounds, due to the interactions with spins of higher abundance such as ^{1}H. It is a through-space interaction that is effective to spin pairs that are closer to each other than 10 Å. The strength of this effect can be expressed by the Hamiltonian in equation (6) where *I* is the spin of higher abundance and *S* is the rare spin.[196]

$$H_{IS} = -d(3\cdot\cos^2\theta - 1)\cdot I_z \cdot S_z \qquad (6)$$

where

- H_{IS} Hamiltonian for heteronuclear dipolar coupling
- d dipolar coupling constant
- Θ angle between B_0 and internuclear vector
- I_z *z* components of the nuclear spin momentum operator *I*, the abundant spin
- S_z *z* components of the nuclear spin momentum operator *S,* the rare spin

The dipolar coupling constant *d* depends on the internuclear distance and the gyromagnetic ratios of both nuclei. The angle θ corresponds to the orientation of the internuclear vector to the applied magnetic field B_0. For an angle of 54.74°, the term $(3\cdot\cos^2\theta - 1)$ becomes zero. This is the so-called magic angle. By spinning of the sample at this angle, so-called "magic angle spinning" (MAS), the term of heteronuclear dipolar coupling disappears, enabling high resolution spectra to be acquired. This is schematically shown in Figure 3-8.

The last aspect that needs to be mentioned is the chemical shift anisotropy which is associated with the electronic environment of nuclei. This phenomenon affects mostly nuclei that are not surrounded by a spherical electron distribution but a more ellipsoid one, as is the case for a carbonyl carbon. The surrounding electrons are also affected by the external magnetic field and cause different chemical shifts in solid-state NMR according to the orientation of the electron cloud with respect to the magnetic field B_0. By spinning around the magic angle at a high spinning speed, the chemical shielding is averaged out, leaving only isotropic values. At lower spinning speed, residual effects of dipolar coupling and chemical shielding interactions appear as spinning

side bands at equal distance in frequency domain that can be identified by comparing measurements of the same compound under the same conditions but with different spinning speeds.

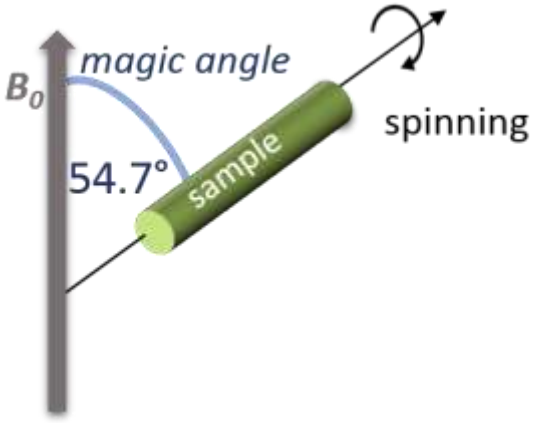

Figure 3-8: Effects that broaden the signals in solid-state NMR can be reduced by spinning the sample at a magic angle with respect to the magnetic field (MAS). Adapted from [196].

To acquire NMR spectra of rare nuclei such as ^{13}C and ^{29}Si, cross polarization (CP) technique is often used since it takes advantage of the high polarization and short relaxation time of high abundant nuclei, e.g. ^{1}H, allowing for signal enhancement and short measurement time. For this, the polarization is transferred to the rare nucleus, and can be compared to DEPT (distortionless enhancement by polarization transfer) ^{13}C-NMR experiments.

For organosilica hybrid materials, ^{13}C CP-MAS NMR experiments are very important to prove the integrity of the organic bridge, and further ^{29}Si-CP-MAS-NMR experiments are essential as they provide information on the condensation degree and the integrity of the Si-C bond. Silicon species are classified according to the number of siloxane bridges into mono (M)-, di (D)-, tri (T)- and tetra (Q)-substituted building units.[59] In the case of silsesquioxanes, T species are expected, whereas the presence of Q species indicates cleavage of the Si-C bond in this context. M and D species do not play a role in this work. The condensation degree of the respective silicon species is stated as an exponential number, e.g. T^n and Q^n. [197,198] These species differ in their chemical, Q^n signals are usually between -120 ppm and -85 ppm, whereas the literature gives a chemical shift between -70 and -45 ppm for T^n species.[199] The chemical shift of the T^n group vary widely, depending in organosilicas on the chemical shift of the bridging unit, but for each type of organosilica, the chemical shift increases with decreasing cross-linking.[199] Figure 3-9 gives an overview of the general chemical shift ranges of the different silica species collected from the literature.

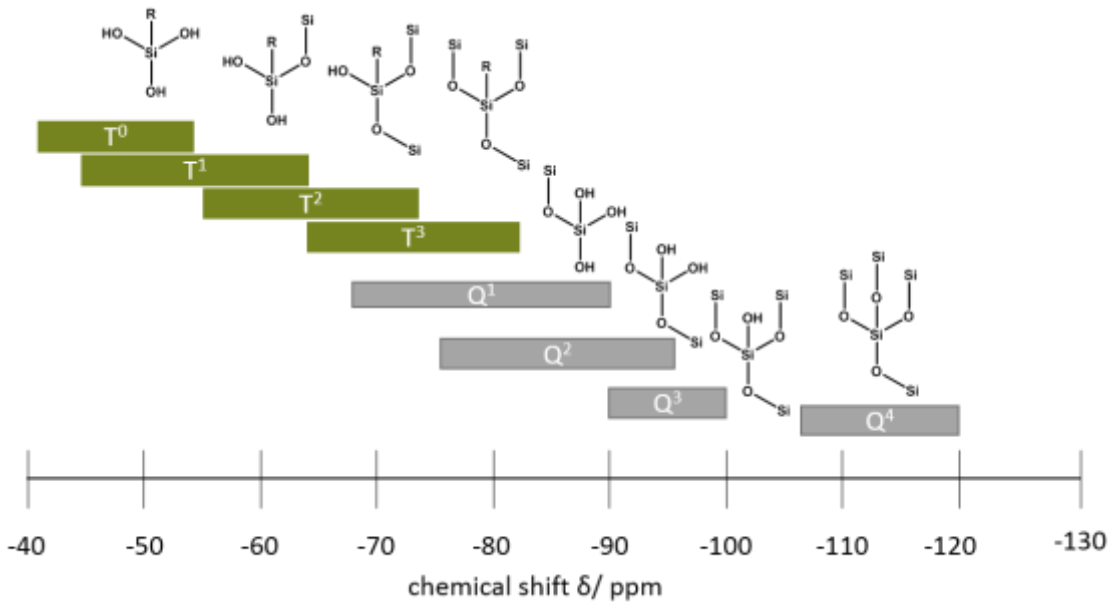

Figure 3-9: Overview of chemical shift in ^{29}Si NMR spectra for tri-(T) and tetra-(Q) substituted siloxane bridges with the condensations degree given as exponential number.[68,79,108,109,198]

Due to the high abundance and the large gyromagnetic ratio of protons, the homonuclear dipolar interactions have a particular impact on ^{1}H NMR spectroscopy. Unfortunately, spinning around the magic angle reduces the effect less effectively than the other interferences so that solid-state ^{1}H-NMR spectra are usually much broader than spectra from the liquid state. Hence, very fast spinning frequency is often necessary for ^{1}H-MAS NMR.

As for the liquid state, 2D experiments are also available in solid-state NMR spectroscopy. In heteronuclear correlation (HETCOR) experiments, the magnetization of an abundant nucleus, mainly ^{1}H, is transferred to a nuclei with low abundance, e.g. ^{13}C or ^{29}Si, which is written as ^{13}C{^{1}H} or ^{29}Si{^{1}H} respectively, and the correlation of the two nuclei is detected. In contrast to the correlation in the liquid state, solid-state HETCOR experiments rely on dipolar interaction. Depending on the chosen experimental parameter, either directly bound spin pairs or short-range through-space correlation between nearby species with a distance below around 1 nm are observed in HETCOR spectra. [200] To achieve high resolution in ^{1}H dimension, frequency switched Lee-Goldburg (FSLG) homonuclear decoupling can be applied during the proton spin evolution time (FSLG-HETCOR).[196]

Within the scope of this work, also Si{H} FSLG HETCOR experiments with spin diffusion were carried out, which allows the detection of weak dipole–dipole interactions or interactions over higher distances. Therefore, the pulse sequence of the experiment is slightly changed by adding a mixing time, where proton spin diffusion occurs. The homonuclear coupling allows mixing of magnetization before it is transferred to the other nucleus. This extends the applicability to larger distances.[201]

4 Results and discussion

4.1 Syntheses of organosilicas

One aspect of this thesis was the synthesis of suitable adsorbents for halogenated organic compounds like isoflurane, sevoflurane and desflurane which are commonly used in modern medicine as inhalation anesthetics.[202] These compounds have a high impact on the global climate they are greenhouse gases and may result in injuries to the clinical personnel.[203–205]

The research group of Bathen systematically investigated the adsorption capacity of various adsorbents like zeolites and activated carbons that differ in pore structure and surface chemistry at trace levels for isoflurane[206] as well as desflurane, sevoflurane and further ethers.[207] A central statement of their work was the positive impact of microporosity on adsorption capacity. Hence, one taget of this work was the synthesis of microporous organosilicas. In order to evaluate the performance of different adsorbents, the adsorption capacity was considered relative to the specific BET surface area, but it is application-oriented to consider the gravimetric adsorption capacity of the adsorbents. Since the adsorption capacity of all materials increases with the specific BET surface area in the mentioned studies, another target was the synthesis of PMOs and microporous and mesoporous organosilicas with high specific surface areas. Theoretical studies considering the adsorption of hydrogen on a set of so-called isoreticular MOFs (different pore size, but same basic framework topology) showed that there are three pressure-dependent adsorption regimes. It was shown that the hydrogen uptake correlates with the surface area at medium pressure, 30 bar, but with the head of adsorption (adsorbent/guest interaction) at low pressure, 0.1 bar, and with the free volume at high pressure (120 bar).[208] The general trend of these results could be transferable to other systems as well, but it needs to be discussed whether the impact of the surface area or of the adsorption head has higher impact on the adsorption of the ethers on the adsorbents in the studies by Bathen *et al.*

Unfavorably, halogenated ethers do not provide an attractive target for chemical reactions but their fluorophilic character might be exploitable. Up to now, this area of research has mainly been investigated in the field of MOFs,[209–212] and a highly porous molecular crystal from a highly fluorinated trispyrazole compound was intensively investigated.[213–216]

Having this application in mind, different halogen-organic bis-silylated precursors, which were further used for the syntheses of PMOs and microporous organosilicas were synthesized within this work. In the following chapter, the precursor's syntheses are briefly presented, before the organosilica materials are characterized.

4.1.1 Precursor synthesis

Within the scope of this thesis, different bis-silylated organosilica precursors were used. These are shown in Figure 4-1.

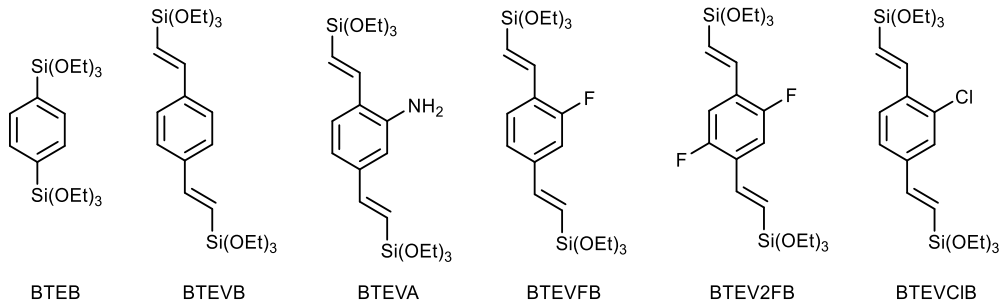

Figure 4-1: Set of the bis-silylated precursors and their abbreviation used in this thesis.

The synthesis path for some of the precursors is already published in the literature. Whereas the 1,4-bis(triethoxysilyl)benzene (BTEB) precursor was synthesized according to the literature in a Grignard reaction from 1,4-dibromobenzene and TEOS,[68] the other precursors were obtained in double Heck cross-coupling reactions with triethoxyvinylsilane and the respectively substituted derivate of 1,4-dibromobenzene. In previous publications the synthesis of 2,5-((*E*)-2'-bis(triethoxysilyl)vinyl)aniline (BTEVA), 1,4-((*E*)-2'-bis(triethoxysilyl)vinyl)benzene (BTEVB) and 1,4-((*E*)-2'-bis(triethoxysilyl)vinyl)-2-fluorobenzene (BTEVFB) was carried out in double Heck cross-coupling reactions using the palladium catalyst tetrakis(triphenylphosphine)-palladium(0) with DMF as a solvent over four days.[103,106,107,142] Using a more suitable catalyst, namely bis(tri-tert-butylphosphine)palladium(0), the syntheses of BTEVB and BTEVFB could be optimized and the same synthesis path could be established for the syntheses of 1,4-((*E*)-bis(triethoxysilyl)-vinyl)2,5-difluorobenzene (BTEV2FB) and 2-chloro-1,4-((*E*)-2'-bis(triethoxysilyl)vinyl)benzene (BTEVClB).[217] Thus complete consumption of the starting material was possible within twenty hours. An additional benefit is the avoidance of the carcinogenic, mutagenic, or toxic for reproduction (CMR) substance *N*,*N*-dimethylformamide by substitution with 1,4-dioxane. The synthesis procedure in Scheme 1 is generalized for all precursors.

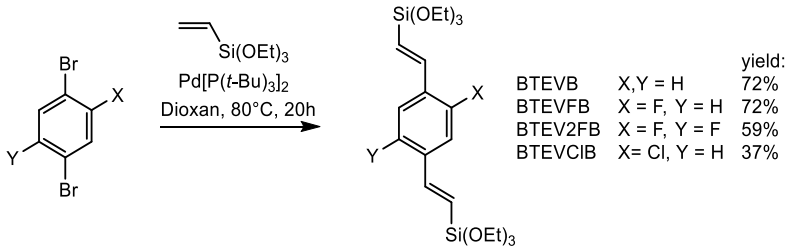

Scheme 1: Generalized synthesis pathway for the precursors BTEVB, BTEVF1B, BTEV2FB, BTEVClB.

Scale-up synthesis of the precursors BTEVB and BTEVFB was possible up to 62 mmol and 39 mmol of the starting material, respectively, without any problems. However, losses in yield or

incomplete cross-couplings were registered for the synthesis of the precursors BTEV2FB and BTEVClB as soon as more than 18 mmol of the respective starting material was used.

Complete consumption of the starting materials in the double Heck cross-coupling was detected by thin layer chromatography (TLC). The complete synthesis procedure is described in the Experimental Section. The work-up process includes a washing step of the organic phase with hydrochloride acid and brine in order to completely remove the by-product salts and the high-boiling solvent 1,4-dioxane. This step is very delicate as the bis-silylated compounds tend to undergo condensation in contact with the aqueous phase. It was noted that BTEVA condenses most easily, which might be due to the influence of its amino function on the resulting pH value in the solution. Due to this, the synthesis of BTEVA was maintained according to the literature without this washing step.[107]

The precursor molecules could be obtained in good purity and yields. Further, the crude products of the precursors BTEVB, BTEVFB and BTV2FB could be purified by distillation. In contrast to this, distillation of BTEVA was not successful because the molecule decomposes or condenses at higher temperatures. A similar behavior was observed for the BTEVClB precursor which explains the low yield of only 39 % despite complete conversion of the starting material in the Heck cross-coupling.

Overall, the synthesis of BTEVB and BTEVFB could by optimized, whereas the successful synthesis of BTEV2FB and BTEVClB were described here for the first time. Full characterization of the precursors are given in the Experimental Section.

4.1.2 PMOs with halogen substituents

Fluorine-containing PMOs

As described in the Introduction, the synthesis of PMOs from the precursors BTEB, BTEVB and BTEVA are well established in the literature. PMOs with BTEVFB and another divinylbenzene-bridged derivate which is fluorinated at position 2 and 3 in the aromatic ring (precursor **51** in Figure 1-26) were published in 2015 by Bracco *et al.*[142] Starting with the precursor BTEVFB, a 2D hexagonally well-ordered material that shows a specific BET surface area of 860 $m^2 \cdot g^{-1}$ was obtained. The pore diameter was evaluated by the BJH method and found to be 33.4 Å. As described in section 3.1, the BJH method leads to an underestimation of the pore diameter of 20–30 %, and for this reason the NLDFT method is preferred in the following chapters. This has to be considered when the materials are compared to the following samples.

The results from the literature could not be reproduced with good quality (materials synthesized from BTEVFB are denoted as F-PMO). As a parameter for the quality of the products, the specific BET surface area, the pore size distribution, as well as the ordering of the mesophase, which was indicated by the reflections in the P-XRD pattern, were chosen.

Since the literature only gives the molar ratio of all components but not the batch size, a batch size of 0.6 mmol of the precursor was chosen randomly for the initial approaches. It was seen that the quality of the product could be improved by simply scaling it up to 2.1 mmol. Therefore, the reproducibility of the synthesis path is not given when only the molecular composition is noted. In the following, only materials from up-scaled syntheses are shown.

In order to improve the results, in a first attempt, the composition of the reaction mixture was slightly adjusted by increasing the concentration of sodium hydroxide and the surfactant. The pH value of 13.75 from the literature was slightly increased to pH 13.8. A comparison of the molar ratios is summarized in Table 4-1.

Table 4-1: Comparison of the molar composition of the synthesis mixture from the literature and for F-PMO 1-5.

	BTEVFB	**C_{18}TAB**	**NaOH**	**H_2O**	**pH value**
literature	1	1.4	6.7	660	13.75
F-PMO 1–5	1	1.5	7.1	656	13.8

In the original synthesis, C_{18}TAB was used as the surfactant. It was found that replacement with C_{18}TAC or surfactants with shorter aliphatic chains did not yield highly ordered products so that the results from these experiments are not shown here.

For further improvement of the product quality, the composition of the reaction mixture as well as the synthesis procedure was investigated in detail.

In the literature, the PMO materials were obtained from a common PMO synthesis protocol, where the precursor was stirred in an alkaline, surfactant-containing solution at room temperature before hydrothermal treatment (HTT) was carried out at 95 °C under static conditions for 24 hours. F-PMO 1–3 were also synthesized with HTT, the influence of the changed parameter on the quality of the product can be best comprehended by comparing the results from nitrogen physisorption measurements. The isotherms are given in Figure 4-2 (left). The pore diameter distributions (Figure 4-2, right) were calculated for all materials with NLDFT from the adsorption branch for silica with cylindrical pores.

F-PMO 1 was synthesized under analogous conditions (at 100 °C) as the material from the literature. In his thesis, M. Cornelius describes the synthesis optimization of PMOs from the BTEVB precursor by reducing the time of the hydrothermal treatment.[218] Based on these experiences the hydrothermal treatment time was shortened to 6.5 hours here as well, but the quality of the product F-PMO 2 obtained could not be improved as the pore diameter distribution is rather broad and shifted to higher pore diameters. In contrast, decreasing the reaction temperature from 100 °C to 80 °C improves the quality of the product (F-PMO 3) with a narrower pore diameter distribution.

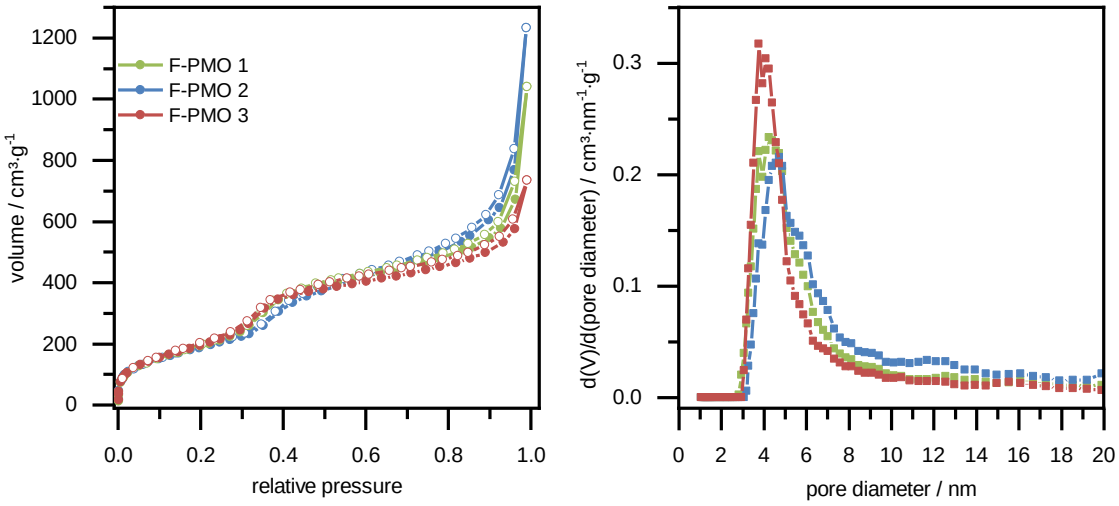

Figure 4-2: Physisorption isotherms (N_2, 77 K) of F-PMO 1-3 on the left. The synthesis of these materials includes hydrothermal treatment. The pore diameter distributions (calculated from the adsorption branch with NLDFT kernel for silica, cylindrical pores) are given on the right.

In all cases, a sharp increase due to capillary condensation is given in the relative pressure range between 0.3 and 0.45. This is the shape of a type IVb isotherm as no noteworthy hysteresis phenomenon occurs that indicates the presence of mesopores smaller than 4 nm. However, another steep step can be seen at high relative pressure of over 0.9. This is evidence for

macropores or a high external surface area as in nonporous materials. Here it is most likely interparticle porosity.

In contrast to the named materials, the synthesis of F-PMO 4 and F-PMO 5 was carried out in a round bottom flask under reflux conditions and continuous stirring instead of HTT in order to improve the homogeneity of the product. The nitrogen physisorption isotherms of the materials that were synthesized under reflux conditions are shown in Figure 4-3. Comparing the plots of the isotherms with those in the previous figure, the changed scale bar should be considered. All isotherms are of type IVb as well. However, the isotherm of the material that was treated at 100 °C (F-PMO 4) shows further volume uptake over a wide pressure range, indicating mesopores of larger diameter. This is reflected in the pore diameter distribution by tailing towards larger pore diameters. The presence of mesopores larger than 4 nm can also explain the small hysteresis in the isotherm. The different types of hysteresis and their formation mechanism are shown in Methods, section 3.1. Since the hysteresis is not distinctly developed in this case, its origin cannot be easily assigned.

Additionally, the isotherm shows a steep step at high relative pressure of 0.9 where it is not as distinctive as in the previously presented HTT materials. Description of the isotherm from F-PMO 5 is easier, as it is a classical type IVb-shaped isotherm with a very narrow pore diameter distribution. These results show that syntheses under reflux conditions and under reduced temperature have a positive effect on the porosity features. Improved homogeneity in the reaction solution on the one hand, and higher temperatures on the other, might promote hydrolysis of the silica material which leads to degradation of the pore walls as M. Cornelius described for DVB-PMOs in his thesis.[218]

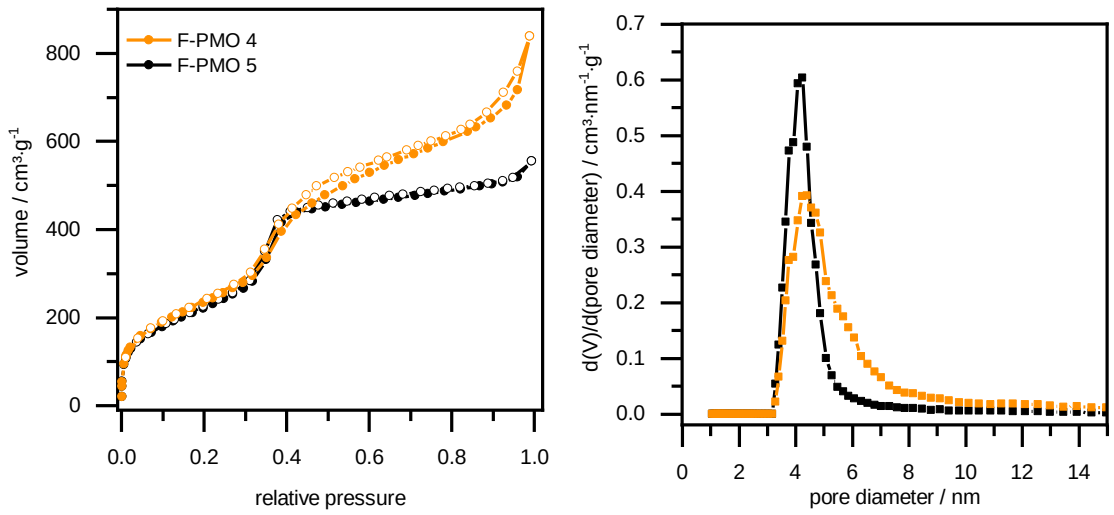

Figure 4-3: Physisorption isotherms (N_2, 77 K) of F-PMOs that were synthesized under reflux conditions at 100 °C(F-PMO 4) and 80 °C (F-PMO 5) on the left. The pore diameter distributions (calculated from the adsorption branch with NLDFT kernel for silica, cylindrical pores) are shown on the right.

The different synthesis approaches of all five syntheses are summarized in Table 4-2 with the respective textural data of the products. The specific BET surface area varied only slightly over all F-PMOs between 750–900 $m^2 \cdot g^{-1}$ and is therewith close to the specific surface area given in the literature. The cumulative pore volume is determined using the NLDFT kernel for silica with cylindrical pores. Here and in the following, pores smaller 20 nm were considered for the cumulative pore volume, as larger pores are expected to be interparticle spaces. The sample with the highest specific BET surface area, F-PMO 4, shows also a significantly higher pore volume as the other samples.

Table 4-2: Overview of the F-PMOs that were synthesized under different synthesis conditions with hydrothermal treatment (HTT) or under reflux conditions and the respective specific BET surface areas as well as the pore diameter and the pore volume *V* (both calculated from NLDFT kernel, adsorption branch for silica with cylindrical pores, adsorption branch).

Sample	Synthesis conditions	S_{BET} / $m^2 \cdot g^{-1}$	pore diameter /nm	$V_{NLDFT,\ ads}$ / $cm^3 \cdot g^{-1}$
F-PMO 1	HTT 100°C 24 hours	758	4.3	0.78
F-PMO 2	HTT 100 °C 6.5 hours	720	4.6	0.81
F-PMO 3	HTT 80 °C 24 hours	773	4.2	0.75
F-PMO 4	Reflux 100 °C 24 hours	901	4.6	0.98
F-PMO 5	Reflux 80 °C 24 hours	853	4.2	0.75

The P-XRD patterns in Figure 4-4 prove the formation of a highly ordered 2D hexagonal mesophase in all F-PMOs 1–5 with reflections at 2θ = 1.8°, 3.3° 3.7°, which correspond to *d*-spacing = 48.0 Å, 27.0 Å, 23.4 Å. In addition, distinct crystal-like ordering in the pore walls can be registered for all F-PMOs by reflections at 2θ = 7.4°, 14.8°, 22.2°, 29.7° (*d*-spacing = 12.0 Å, 6.0 Å, 4.0 Å, 3.0 Å). This is in accordance with the literature[142] and congruent with the reflections of PMOs from BTEVB.[103]

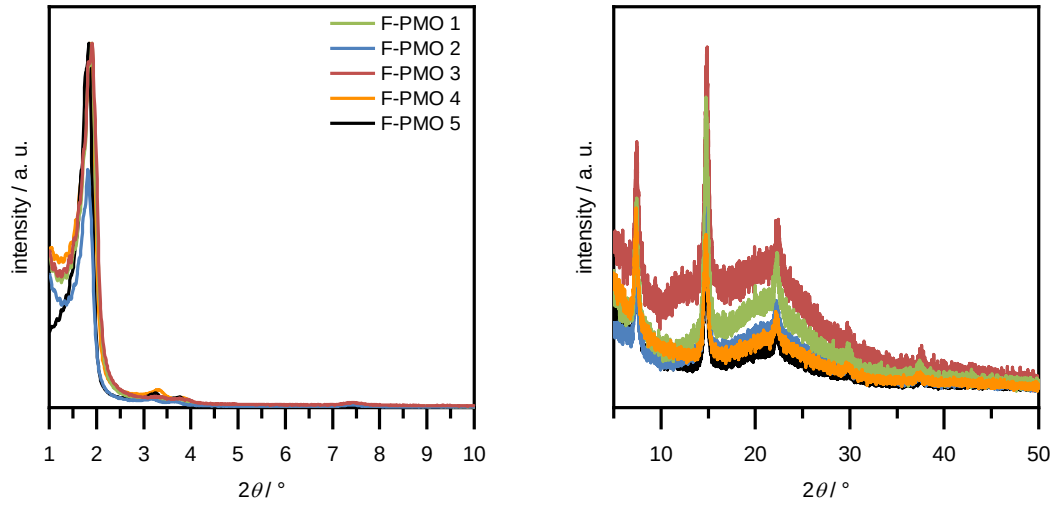

Figure 4-4: P-XRD patterns of the F-PMOs 1–5. Small angle region on the left, 7–50 ° 2θ on the right.

Therefore, the chosen changes to the synthesis procedure affect only the uniformity of the pores, whereas the ordering of the pore system is similar in all syntheses.

PMOs were also successfully generated from the BTEVF2B precursors (denoted to as 2F-PMOs) at the same pH value and surfactant concentration as the F-PMOs. In contrast to the other precursors used here, this precursor is not liquid under ambient conditions but in the solid state, which makes homogeneous distribution in the reaction solution especially challenging.
Hence, the synthesis was only carried out under reflux conditions and stirring at the common PMO synthesis temperature of 100 °C instead of the classical static HTT.
P-XRD pattern are shown in Figure 4-5. Since only one first reflection of the small angle region at 2θ = 1.7° (d-spacing = 50.3 Å) is distinctive, the ordering is not sufficient to be assigned to a 2D hexagonal mesophase. Crystal-like ordering on molecular scale in the pore walls can be tracked in the wide-angle region, the reflections having the same values as for the F-PMOs which is reasonable since the organic bridging unit is expected to be of the same length.

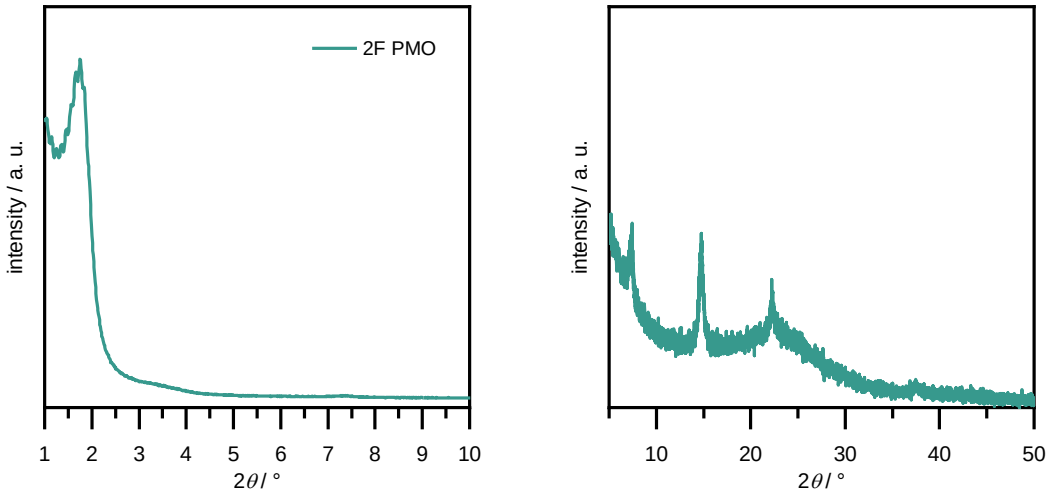

Figure 4-5: P-XRD of 2F-PMO. Small angle region on the left, 7–50 ° 2θ on the right.

The nitrogen physisorption isotherm and pore diameter distribution of the respectively obtained material from BTEV2FB is shown in Figure 4-6. It is a type IVb isotherm with the previously mentioned additional step in the relative pressure range > 0.85 that is caused by interparticle porosity. For the obtained material 2F-PMO, a specific BET surface area of 807 $m^2 \cdot g^{-1}$ was determined. The maximum pore diameter was 3.9 nm, the cumulative pore volume is 0.84 $cm^3 \cdot g^{-1}$, both are calculated from the adsorption branch with NLDFT, kernel for silica with cylindrical pores, pores smaller 20 nm were considered for the cumulative pore volume to avoid interference with interparticle voids. However, a slight tailing of the pore diameter distribution is visible in Figure 4-6 on the right.

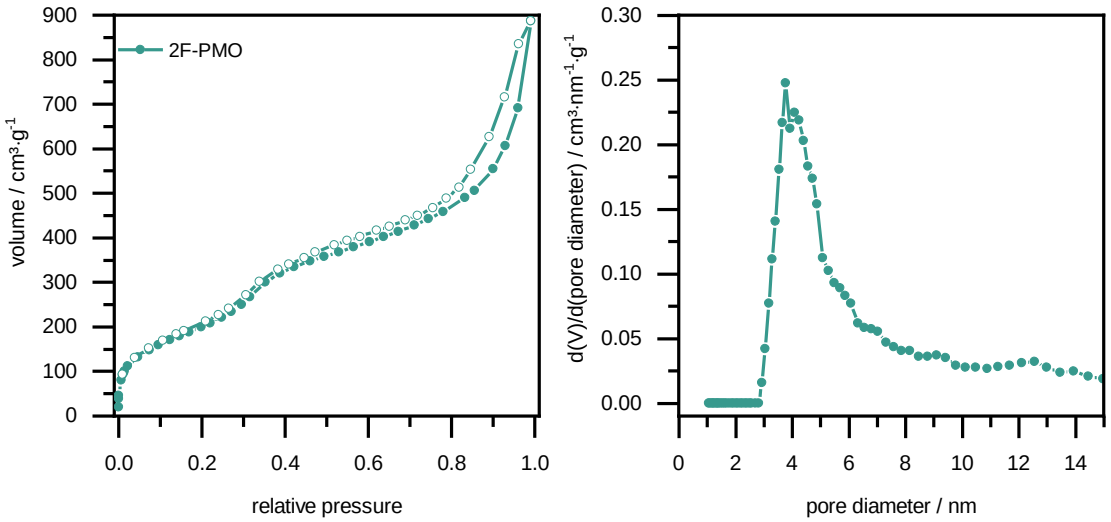

Figure 4-6: Physisorption isotherms (N_2, 77 K) of 2F-PMO that was synthesized under reflux conditions at 100 °C on the left, with the pore diameter distribution (calculated from the adsorption branch with NLDFT kernel for silica with cylindrical pores) on the right.

Advanced characterization of fluorine-containing PMOs

Due to the dipole of C-F bonds,[219] interactions between the surface of the fluorinated PMOs and the quadrupole of nitrogen were expected. In order to minimize erroneous interpretations of the nitrogen physisorption measures, e.g. the specific BET surface area and the pore size, the materials F-PMO 5 and 2F-PMO were additionally characterized by argon physisorption. Isotherms are shown in Figure 4-7 (left). For calculation of the pore diameter distribution and the pore volumes from the adsorption branch of argon physisorption measurements, NLDFT kernel for silica or zeolites with cylindrical pores were used.

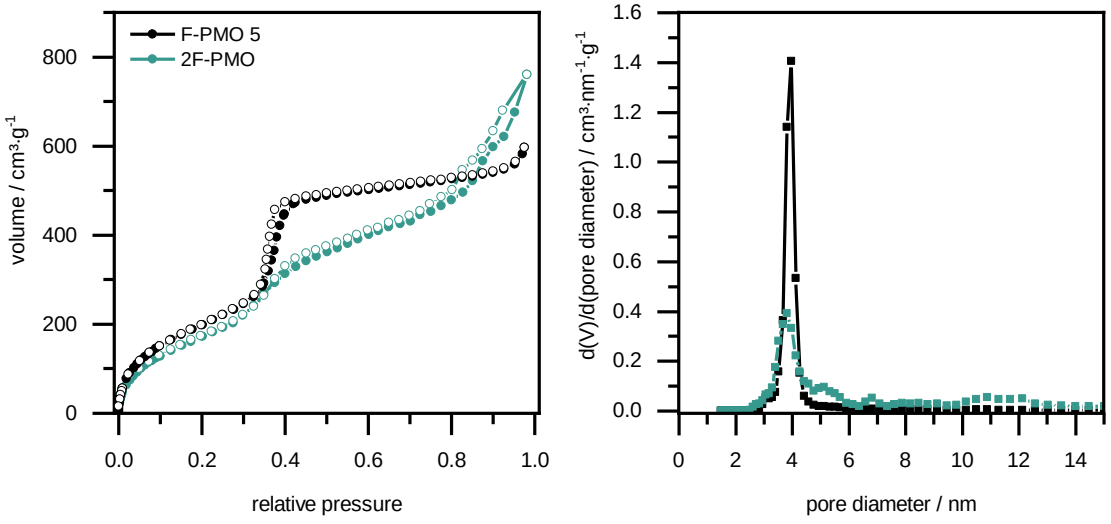

Figure 4-7: Physisorption isotherms (Ar, 87 K) of F-PMO 5 and 2F-PMO on the left. Pore diameter distribution (calculated from the adsorption branch with NLDFT kernel for silica/zeolites with cylindrical pores) on the right.

The shape of the argon isotherms can be described as type IV for both materials, the isotherm of 2F-PMO do not show any hysteresis in the capillary condensation step in the relative pressure

of 0.35-0.40, thus it is type IVb, but the isotherm of F-PMO 5 show slight hysteresis and is thus a type IVa isotherm. In case of F-PMO 5 the condensation step is very steep and the pore diameter distribution is very narrow. In the isotherm of 2F-PMO an additional step occurs in the relative pressure range of 0.85–0.9. This is reflected in the pore diameter distribution of pores between 10 to 12 nm. The origin of these pores cannot be explained here, however larger pores that lead to gas uptake at relative pressures over 0.9 are detected with argon in the same way as with nitrogen. The specific BET surface area calculated from the argon measurements is significantly lower (see Table 4-3) than it was for nitrogen physisorption measurements. This trend is reasonable due to the differences between the two gases as was explained in section 3.1. In case of 2F-PMO the specific BET surface area is 618 $m^2 \cdot g^{-1}$ measured with argon, but 807 $m^2 \cdot g^{-1}$ measured with nitrogen. In case of F-PMO-5 it is 853 $m^2 \cdot g^{-1}$ with nitrogen but 711 $m^2 \cdot g^{-1}$ measuring with argon. Additionally, it needs to be mentioned that the argon measurement of F-PMO 5 was carried out one and a half year later than the measurement wit nitrogen. A reference measurement with nitrogen showed that the specific BET surface area decreased to 788 $m^2 \cdot g^{-1}$ during that time for this materials. This decreasing trend of the surface area over time was noted for different PMOs and is no specific phenomenon.

Table 4-3: Specific BET surface area and pore diameter distribution and pore volume calculated from NLDFT compared with N_2 and argon physisorption of F-PMO 5 and 2F-PMO.

Sample	**Nitrogen physisorption**			**Argon physisorption**		
	S_{BET} / $m^2 \cdot g^{-1}$	pore diameter / nm	$V_{N_2, NLDFT}$ / $cm^3 \cdot g^{-1}$	S_{BET} / $m^2 \cdot g^{-1}$	pore diameter / nm	$V_{Ar, NLDFT}$ / $cm^3 \cdot g^{-1}$
F-PMO 5	853	4.2	0.75	711	4.0	0.67
2F-PMO	807	3.9	0.84	618	3.8	0.91

Hence, the comparison of the measurements with these two gases give no evidence of interactions with the surface of the materials. However, argon physisorption is the favored method in general since it is monatomic, spherical and nonpolar and hence, the determination of the cross section area is more precise than in the case of nitrogen.

Fluorinated organic molecules are known to be rather hydrophobic. In order to get an insight into the hydrophobic character of these PMOs, water vapor sorption experiments were carried out with F-PMO 5 and 2F-PMO. In contrast to nitrogen physisorption, the relative pressure at which pore condensation takes place does not only depend on the pore size of the respective material, but also on the polarity of the surface. The surface polarity of PMOs, in turn, depends significantly on the amount of silanol groups, and thus on the conditioning of the sample. In order to leave this aspect out of the consideration, water sorption was measured in two cycles.

The plot in Figure 4-8 considers the molar water uptake of both cycles. In the first measurement cycle for F-PMO 5 the water adsorption is very low, which is surprising since the materials are not calcined and the presence of silanol groups on the surface is assumed. In the literature, extremely low adsorption has been described for silicate which was synthesized in a fluorine-mediated synthesis route,[220] however the results seem inconsistent but cannot be explained at this point. By contrast, the second cycle shows significant higher water adsorption. The both cycles of 2F–PMO differ less significant and are comparable to the measurements from PMOs by Mietner.[110] The second cycle of F-PMO 5 shows even higher adsorption than the respective cycle from 2F-PMO. The isotherms of the second cycles of both materials follow a type V shape, as is expected for water vapor sorption.

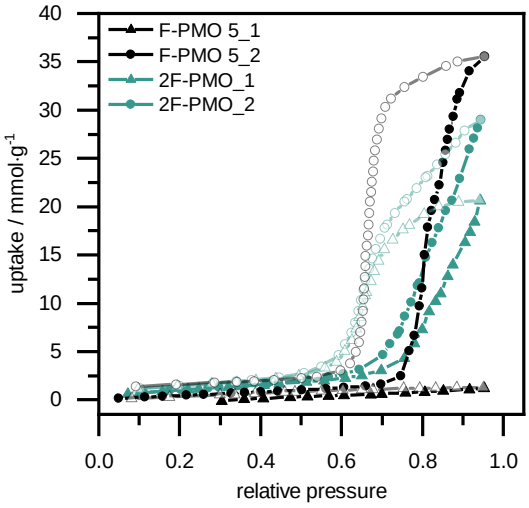

Figure 4-8: Water vapor sorption isotherms (H_2O, 25 °C) of F-PMO 5 and 2F-PMO from two cycles. The first is symbolized in triangles, the second in circles. Desorption is symbolized in transparent symbols.

Water adsorption measurements can be used to evaluate the hydrophilicity of a material and different approaches for the generation of a hydrophilicity index have been discussed. Thommes *et al*. presented a hydrophilicity index for microporous and mesoporous materials, using the example of hierarchically porous zeolites.[221] The key assumption of their work is, that the wetting of the surface with water depends on the surface, whereas nitrogen and argon at their boiling temperature wet the surface completely, so that the determined parameter is also called the wettability index. Assuming complete filling of the mesopore volume at a relative pressure of 0.92 for nitrogen or argon in accordance with the Gurvich rule,[3] the pore volume filling of water at the same relative pressure correlates directly with the wetting behavior of water, hence the ratio of the filled pore volumes is the hydrophilicity index of the surface. For microporous materials the filling at a relative pressure of 0.15 is determined for the comparison. Precondition for the use of this index is the complete filling of the pore volume, which is indicated by a plateau in the isotherm. In case of the materials discussed here, this is not given so that erroneousness

of the calculated hydrophilicity index needs to be considered. Also mesoporous siliceous cellular foams show water vapor sorption isotherms without complete filling of the mesopores. Hence, Fried *et al.* developed another hydrophilicity index that is the ratio of the monolayer capacity n_m from water to the maximal theoretical monolayer capacity, calculated from the from argon physisorption measurement using the BET equation.[222] The calculation of the hydrophilicity index according to Fried *et al.* is given in equation (7).

$$\chi_{n_m} = \frac{n_m(H_2O)}{n_m(Ar)} = \frac{\frac{S_{BET}(H_2O)\cdot \mathrm{M}(H_2O)}{\mathrm{N_A}\cdot\sigma_\mathrm{m}}}{\frac{S_{BET}(Ar)\cdot \mathrm{M}(Ar)}{\mathrm{N_A}\cdot\sigma_\mathrm{m}}} \quad (7)$$

where

S_{BET} specific BET surface area

n_m monolayer capacity

N_A Avogadro constant

σ_m molar cross-sectional area

M Molecular weight (18.0 g·mol^{-1} for water, 28.0 g·mol^{-1} for nitrogen),

The hydrophilicity indices according to Thommes *et al*. χ_{vol} and according to Fried *et al*. χ_{n_m} for the materials F-PMO 5 and 2F-PMO are given in Table 4-4.

Table 4-4: Summary of the onset, the point of inflection (p.o.i.) and hydrophilicity indices χ_{vol} and χ_{n_m} together with the parameters which are needed for the calculation, respectively.

sample	$S_{BET\ (Ar)}$ / m²·g^{-1}	$V_{(Ar)}$ / cm³·g^{-1}	$S_{BET\ (H_2O)}$ / m²·g^{-1}	$V_{(H_2O)}$ / cm³·g^{-1}	$\chi_{vol.}$	χ_{n_m}	*onset*	*p.o.i*
F-PMO 5	711	0.71 (p/p^0 = 0.95)	41	0.64 (p/p^0 = 0.95)	0.91	0.03	0.75	0.82
2FPMO	618	0.86 (p/p^0 = 0.95) 0.61 (p/p^0 = 0.80)	74	0.52 (p/p^0 = 0.95) 0.26 (p/p^0 = 0.80)	0.61 0.43	0.11	0.69	0.84

The first index correlates χ_{vol} the pore volumes at which the pores are completely filled with argon with the respective pore volume filled with water at the same relative pressure. Here, the pore volumes are determined according to the Gurvich rule at a relative pressure of 0.95, but not using the NLDFT method for comparability with data from the literature. Also there is no NLDFT kernel for water adsorption available, yet. The second slope in isotherms from 2F PMO indicates the presence of interparticle voids, so that pore filling at a relative pressure of 0.80 is compared additionally for this sample. However, the index is significantly higher for F-PMO 5

than for 2F-PMO which indicates that the F-PMO-5 shows higher hydrophilicity since the pore volume is nearly completely filled with water. Since 2F-PMO is higher fluorinated, the results do meet the expectation. The specific BET surface area determined from water vapor adsorption is significantly lower for F-PMO 5 (41 $m^2 \cdot g^{-1}$) than for 2F-PMO (74 $m^2 \cdot g^{-1}$) having a closer look on the isotherms, the second cycle of water vapor sorption from 2F-PMO shows slightly more uptake in the low pressure range whereas nearly no water uptake occurs in the second cycle of F-PMO 5 below a relative pressure of 0.6. By contrast, the BET specific surface area from argon measurements shows a higher value for F-PMO 5 than for 2F-PMO. Since the hydrophilicity index χ_{n_m} is based on this parameter, the value for F-PMO 5 is significantly lower than for 2F-PMO. For the difference in the χ_{n_m} values the BET specific surface area from water sorption has the most significant impact and the same trend would be given if the specific BET surface area was calculated from the nitrogen measurements instead of argon. Hence, the hydrophilicity index χ_{n_m} shows an opposite trend compared to χ_{vol} since the two values are based on different parameters. In order to compare different materials with similar pore diameter, the onset of the pore condensation and its point of inflection (p.o.i.) are well suited parameters, both are also given in Table 4-4. In Figure 4-9 the isotherms are plotted with normalized uptake to focus on this aspect. Contrary to expectations, the onset of pore condensation is almost identical at a relative pressure of 0.75 for F-PMO-5 and 0.69 for 2F-PMO, although it is difficult to determine for 2F-PMO as the uptake already increases at lower relative pressures and the condensation step is less steep. Also the points of inflections are very similar 0.82 and 0.84, for F-PMO 5 and 2F-PMO, respectively.

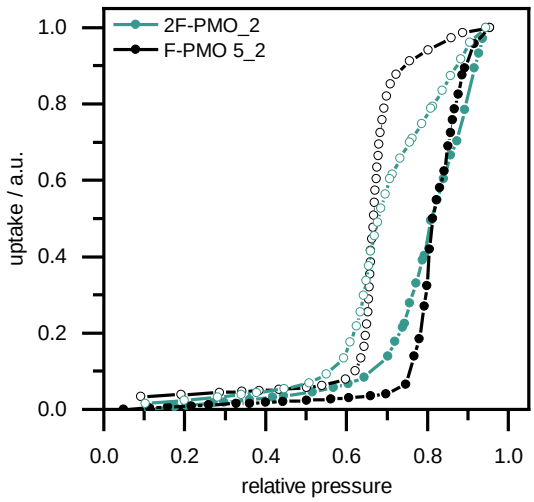

Figure 4-9: Normalized water vapor sorption isotherms (H_2O, 25 °C) of F-PMO 5 and 2F-PMO from the second cycles.

Comparison of the water vapor uptake at 298 K with sorption isotherms from the literature is difficult as this method is not yet that common for PMOs. The best investigation of MCM-41

silica and other PMOs is given by Mietner *et al.*,[109] who considers materials with pore diameters around 3.2 nm, which is 1 nm smaller than is the case in here. The water uptake of the F-PMO 5 and the 2F-PMO is higher than for these materials, but as both, the molar water uptake and the onset of the pore condensation are affected by the mesopore size and the pore volume, the comparison is difficult to evaluate. The evaluation of the results from the hydrophilicity index that appear contradictive is difficult at this point. In follow-on research, additional measurements with similar materials that show very narrow pore diameter distributions are necessary to find a distinct trend of hydrophilicity.

The exact degree of condensation could be determined by the relative ratio of the T^n signal intensities obtained from direct excitation ^{29}Si-MAS NMR spectroscopy which is a quantitative but extremely time consuming method.[68] Thus we use ^{29}Si-CP-MAS NMR spectroscopy to get semi-quantitative information of the condensation degree. The respective spectra of both PMOs can be seen in Figure 4-10. Both materials show dominant T^3 and weaker T^2 signals, 2F-PMO shows only slightly higher intensity of the T^2 signal and T^1 signals with very low intensity. This indicates that both materials are highly condensed and the condensation degree of F-PMO 5 is only slightly higher as for 2F-PMO. Further, the absence of Q signals confirms the integrity of the Si-C bonds in both materials.

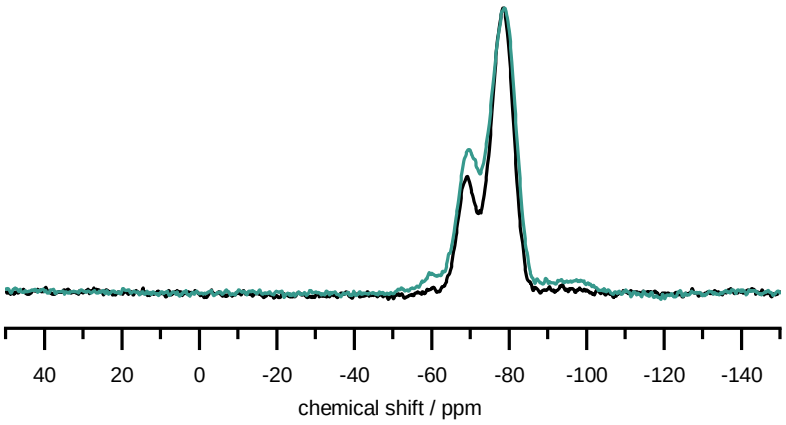

Figure 4-10: ^{29}Si CP-MAS NMR (spinning speed = 5 kHz) of the F-PMO 5 (black) and 2F-PMO (green) with normalized intensity.

The chemical structure and the integrity of the organic bridges can be characterized by ^{13}C-CP MAS NMR as shown in Figure 4-11 and Figure 4-12. Liquid state spectra of the respective precursors are also given in the figures for comparison. Since NMR frequencies are sensitive to the surrounding environments, caution needs to be taken when comparing liquid state NMR to solid state NMR spectra. Nonetheless, ^{13}C-NMR spectra of both PMO materials are in good agreement with those of corresponding precursors, suggesting the integrity of the organic bridges.

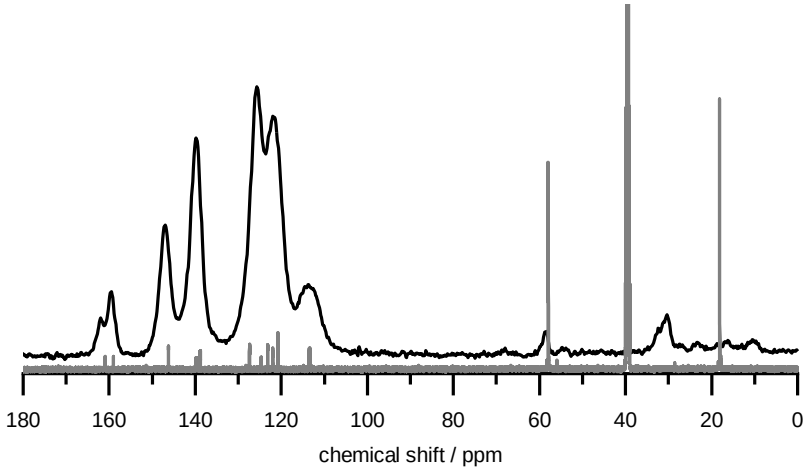

Figure 4-11: ^{13}C-CP MAS NMR spectrum, (spinning speed = 13 kHz) of F-PMO 5 (black) in comparison with the liquid-state NMR spectrum of BTEVFB in DMSO-d_6 (gray).

Compared to the ^{13}C-NMR spectrum of BTEVB, in the ^{13}C-NMR spectrum of BTEVFB and BTEVF2B appear signals of aromatic carbons in a wider chemical shift range. In particular, the signal of the aromatic carbon which is directly bonded to fluorine shows a particularly high chemical shift of 160 ppm for BTEVFB and 156 ppm for BTEV2FB, resulting from significant deshielding effect of electronegative fluorine. Doublet splitting arises from single bond *J*-coupling between C-F with a splitting value of approximately 250 Hz for both compounds. The spectrum of BTEV2FB is simpler than the spectrum of BTEVFB, due to the symmetric nature of the bridging molecule. For a detailed interpretation of the ^{13}C-NMR spectra of the precursors see the Experimental Section. Additional signals at 20–70 ppm that result from residues of the surfactant and ethoxy groups occur in the ^{13}C-CP MAS NMR spectrum of 2F-PMO. Thus, the extraction of the surfactant was not sufficient in this sample.

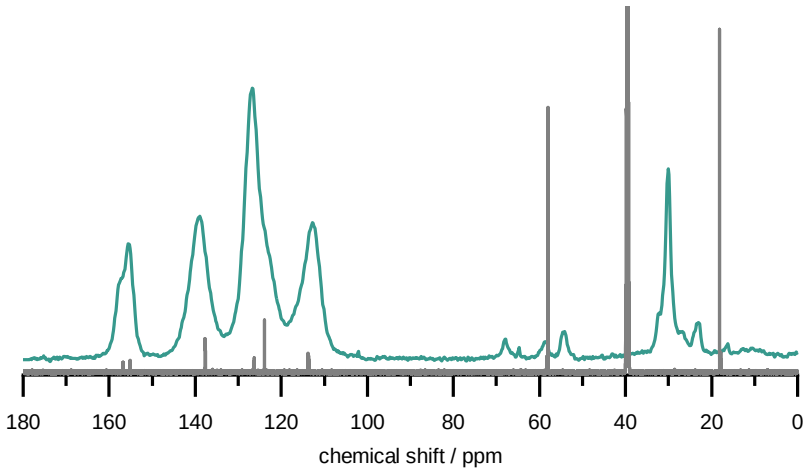

Figure 4-12: ^{13}C-CP MAS NMR spectrum (spinning speed = 13 kHz) of 2F-PMO (green) in comparison with the liquid-state NMR spectrum of BTEV2FB in DMSO-d_6 (gray).

TG/DTA/MS measurements are necessary for the complete characterization of F-PMO and 2F-PMO, see the plots in Figure 4-13. This technique gives information about the thermal stability of the PMOs and allows conclusions on the weight ratio of the organic moiety in the material. Further, it can give the first hints on the hydrophobic character of a material. Focus on the mass spectra was on the ion currents m/z = 18 and m/z = 44 that are assumed to be H_2O and CO_2 and m/z = 58 that was assigned to C_3H_8N, the main ion current of the surfactant in ESI-MS.[193] The mass loss in different temperature intervals is given in Table 4-5. Different temperature intervals were chosen to discuss the mass loss of the two materials.

Table 4-5: Mass loss in given temperature intervals of TG analysis (Ar/O_2 80/20) of F-PMO and 2F-PMO. Entries marked with an asterisk (*) denote corrected values.

temperature interval	F-PMO	2F-PMO
25–150 °C	1.1 %	2.7 %
320–450 °C	–	25 %*
380–450 °C	15 %*	–
450–800 °C	35 %*	33 %*
320–800 °C	–	61 %*
380–800 °C	50 %*	–

Mass loss at temperatures below 150 °C are usually due to surface-adsorbed water. For the 2F-PMO it is 2.7 % whereas the F-PMO loses only 1.1 %. It is unexpected that the PMO with higher fluorine content adsorbs more water on the surface, but the discrepancy is in accordance with the unexpected behavior in the water vapor adsorption. The values of the mass loss are corrected, since the mass loss due to surface-adsorbed water, in the temperature range 25–150 °C differ. The decomposition of the F-PMO starts at 380 °C with a total mass loss of 50 % up to 800 °C which is in good agreement with the literature. By contrast, the 2F-PMO already decomposes from 320 °C onwards, and the overall mass loss is 61 %, which is slightly higher than the theoretical value where the organic content was 57 % (assuming complete condensation). This can be explained by residues of the surfactant in this sample which were found in solid-state ^{13}C CP-MAS NMR spectroscopy, despite the low intensity of the ion current m/z = 58, which seems to be less sensitive. The presence of surfactant would also explain the premature decomposition and the higher water uptake in the 2F-PMO. It has to be considered that all materials were treated the same way for extraction of the surfactant. In addition, this behavior was reproducible. Thus, it seems as though the extraction of the surfactant from 2F-PMO is hindered. This could be due to steric hindrance inside the pore system or due to interactions of the organic moiety with the surfactant.

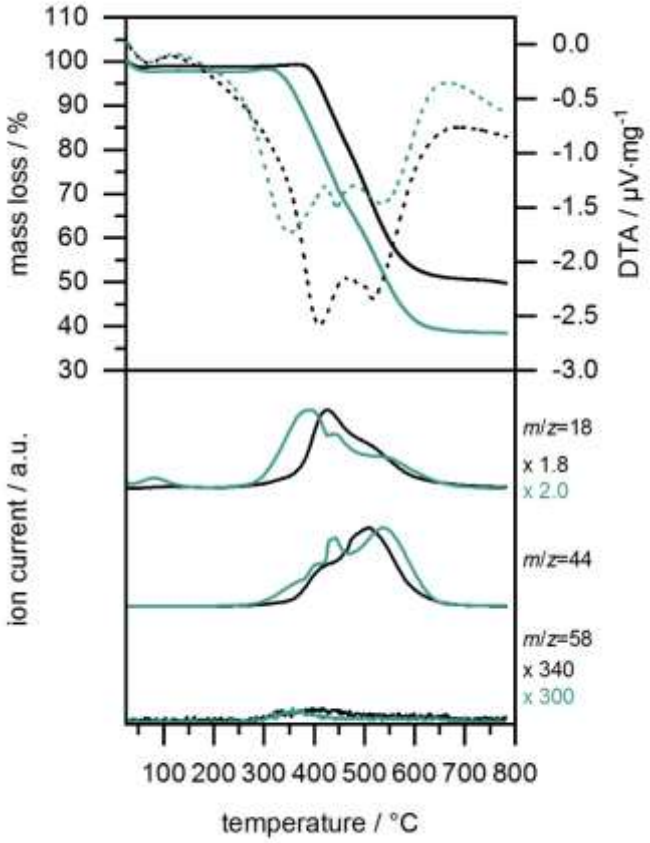

Figure 4-13: TG/DTA/MS analysis in Ar/O_2 80/20 of F-PMO (black) in comparison with 2F-PMO (green). Mass loss, as well as the DTA signal, is plotted over temperature in the upper part. Normalized selected ion currents are given in the lower plot.

Chlorine-containing Organosilica

Next to fluorine-containing organosilica materials, the chlorine-containing equivalent from BTEVClB was synthesized under the same conditions as 2F-PMO.

The material shows only one very broad reflection (see P-XRD pattern in Figure 4-14) in the small angle region, so that it cannot be named as a PMO but rather a mesoporous organosilica (MOS). The absence of other reflections indicates no crystal-like ordering of the precursor molecules.

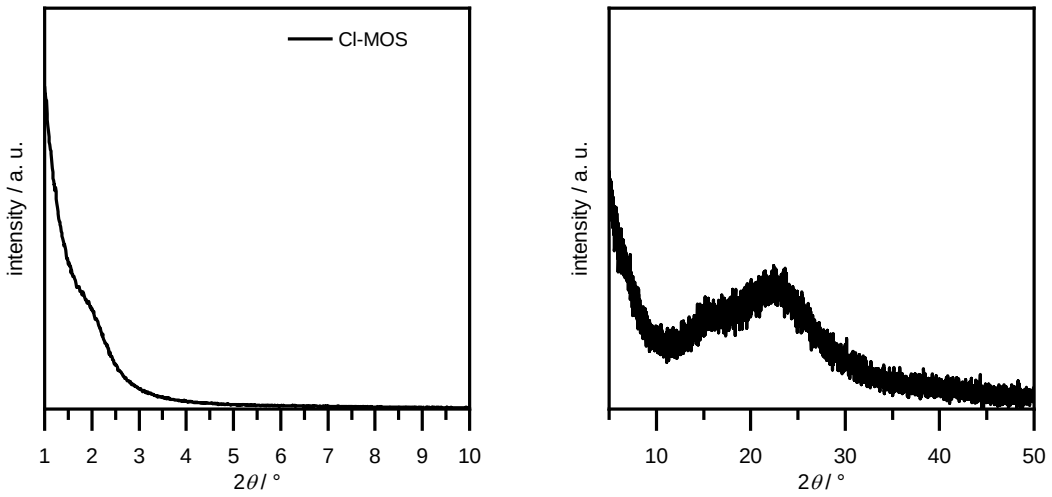

Figure 4-14: P-XRD of Cl-MOS. Small angle region on the left, 7–50° 2θ on the right.

The physisorption isotherm is shown in Figure 4-15. The specific BET surface area of the obtained mesoporous organosilica Cl-MOS is 595 $m^2 \cdot g^{-1}$. The maximum pore diameter distribution is very broad, between 2–8 nm, so that a maximum pore diameter is not meaningful. The isotherm shows a continuous slope over the entire pressure range without any distinct capillary condensation step. This is in accordance with the broad pore size distribution. Hysteresis occurs, which indicates connectivity of pores of different size.

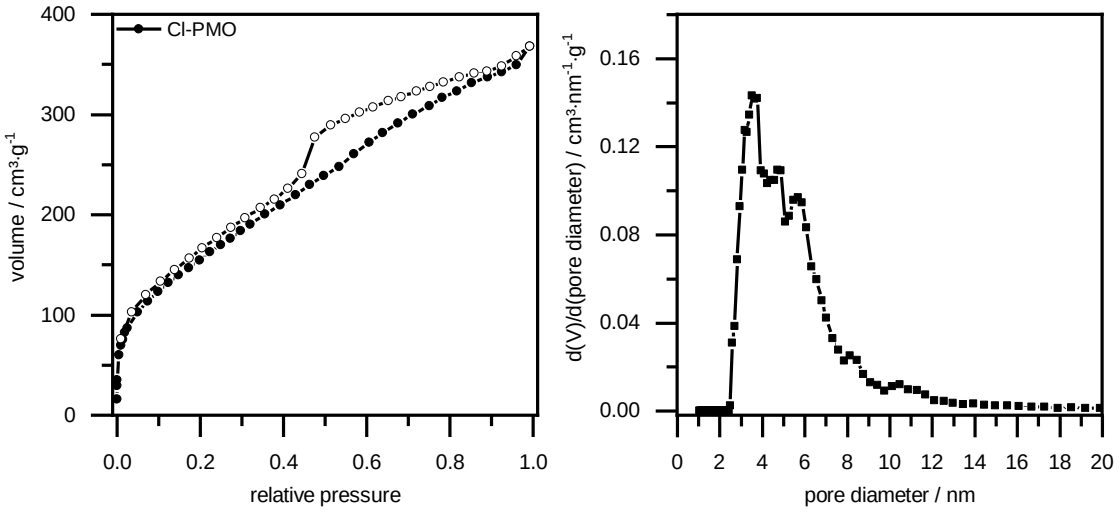

Figure 4-15: Physisorption isotherm (N_2, 77 K) of Cl-MOS that was synthesized under reflux conditions at 100 °C on the left, with the pore diameter distribution (calculated from the adsorption branch with NLDFT kernel for silica with cylindrical pores) on the right.

Unfortunately, no suitable conditions for the synthesis of a Cl-PMO with ordered pores were found in this work. The synthesis could potentially be optimized by changing the pH-value and the batch size. Also, the synthesis under acidic conditions with nonionic surfactants is often promising.

4.1.3 High specific surface area PMOs synthesized under acidic conditions

With particular applications like the adsorption of gases in mind, an improved performance of the PMOs is assumed with high specific BET surface areas. In the following, different approaches to increase the surface area will be discussed.

The lasting relevance of benzene-bridged (B-) PMOs was highlighted in the Introduction, and the synthesis procedure has already been variously modified since the first mention. Whereas most B-PMOs synthesized under basic conditions with C_{16}TAB as surfactants show a 2D hexagonal pore structure and a specific BET surface area around 800 $m^2 \cdot g^{-1}$, a B-PMO with a 3D cage pore structure was developed under acidic conditions which increases the specific BET surface area to 1002 $m^2 \cdot g^{-1}$. [223] As described in context of the formation of ordered mesoporous silicas (section 1.2), the mechanism of hydrolysis and condensation of (organo)silica under acidic and strong basic conditions follow different mechanisms and lead to materials of different condensation degrees and charge densities. Beyond, the interactions of cationic surfactants (S^+) and the inorganic moiety differ under basic and acidic conditions, since it is negatively charged under basic conditions (I^-) but positively charged under acidic conditions (I^+) so that a mediator ion X^- is necessary in the latter case (see Figure 1-5). It has been discussed in the context of mesoporous silica that the mediator ion (e.g. SO_4^{2-}, Cl^-, Br^- or NO_3^-) effects the packing parameter *g* (see Table 1-1) and in consequence the formed mesophase due to different hydrated radii and binding strength.[224,225] It has to be mentioned that the impact of the counter ion on the mesophase has been discussed for ethane PMO synthesis under basic conditions as well, where the 2D hexagonal mesostructure was transformed to a cubic $Pm\bar{3}n$ structure in presence of Cl^- instead of Br^- as counter anion of the surfactant.[226]

B-PMO synthesis with the surfactant C_{16}TAB

As mentioned above, a B-PMO with high specific BET surface area was developed under acidic conditions (0.06 $mol \cdot L^{-1}$ hydrochloric acid) with C_{16}TAB as surfactant.[223] In the following section, a similar synthesis approach under acidic conditions, likewise with C_{16}TAB was optimized. Here, the concentration of hydrochloric acid was varied between 0.1 $mol \cdot L^{-1}$ in B-PMO 1 and 1.0 $mol \cdot L^{-1}$ in B-PMO 2. Since the higher concentration of the acid gave the best material, the synthesis was scaled up in B-PMO 3 with only a slight change of the molar composition. In Table 4-6 the molar ratios of the synthesis mixtures are summarized.

Table 4-6: Summary of the molar composition of the B-PMOs 1-3 and the respective *apparent* specific BET surface areas as well as the pore diameter and the pore volume *V* according to NLDFT (adsorption branch, kernel for silica with cylindrical pores).

Sample	molar composition				S_{BET} / $m^2 \cdot g^{-1}$	pore diameter / nm	$V_{NLDFT, ads}$ / $cm^3 \cdot g^{-1}$
	BTEB	C_{16}TAB	HCl	H_2O			
B-PMO 1	1	1.1	1.2	750	1116	2.9	0.63
B-PMO 2	1	1.1	11.7	727	1626	3.3	1.02
B-PMO 3	1	0.82	10	544	1539	3.5	1.04

The P-XRD patterns of the materials are given in Figure 4-16.

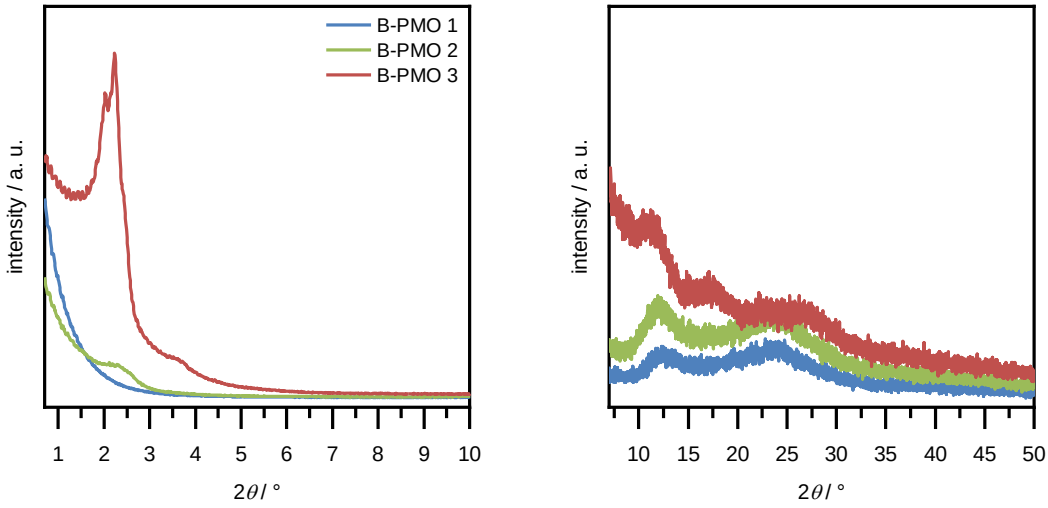

Figure 4-16: P-XRD pattern of the B-PMOs 1–4 in the low angle region (left) and the middle angle region (right).

In accordance with the examples from the literature, reflections at 2θ = 2.0°, 2.2° and 2.4° which correspond to *d*-spacing of 4.3 nm, 3.9 nm and 3.6 nm were obtained and assigned to (200), (210) and (211) reflections of cubic symmetry in the space group $Pm\bar{3}n$. This cage-like structure is known from SBA-1.[227] The respective mesophase of spherical surfactant micelles is usually given for small packing parameters of ⅓ (see equation (1) in section 1.2) which is preferential, e.g. for large head groups. On the one hand, the presence of mediate counter ions Cl^- in the surrounding of the surfactant head group decreases their repulsive interactions and causes closer packing of the surfactant molecules. This increases the packing parameter and makes another mesophase more likely. On the other hand, the requirement of charge density match for the organic and inorganic species explains why synthesis with C_{16}TAB leads to hexagonal phases under alkaline conditions (S^+I^- mechanism, as it is commonly known for MCM-41 and B-PMOs), but to a cubic mesophase under acidic conditions ($S^+X^-I^+$ mechanism).[19,228] The charge density of the silica surface is high under alkaline conditions but under strongly acidic conditions

it is lower due to the low pK_a of silica. Thus, charge density match is given with spherical micelles of similar low charge density.

The P-XRD patterns of B-PMO 1–3 all have very broad reflections at 2 θ = 12 ° which corresponds with the lengths of the benzene precursor of 7.6 Å and indicates low periodicity of the precursors in the pore wall. The physisorption isotherms and pore diameter distributions are shown in Figure 4-17.

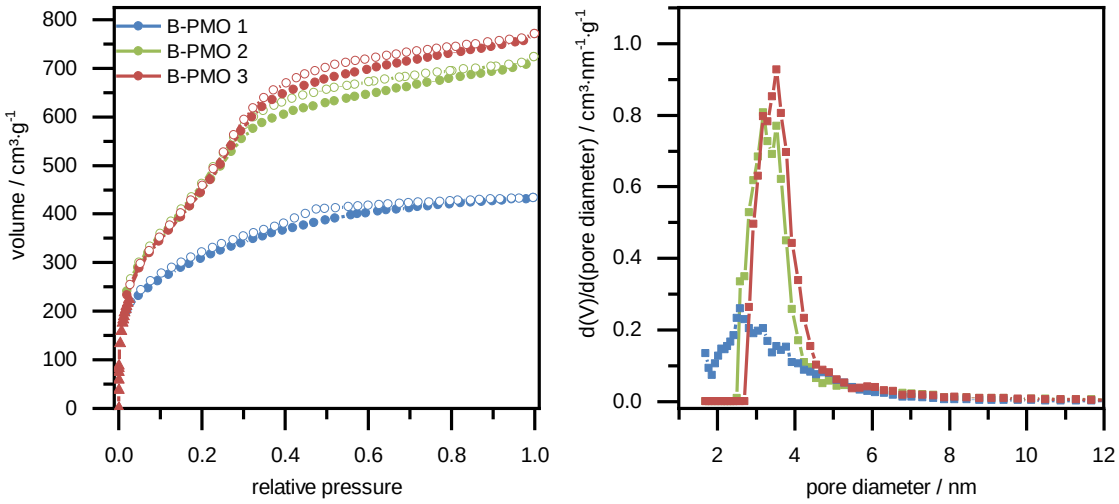

Figure 4-17: Physisorption isotherms of the B-PMOs synthesized under acidic conditions with different concentrations of hydrochloric acid and the respective pore diameter distributions (calculated from the adsorption branch with NLDFT kernel for silica with cylindrical pores) on the right.

The physisorption isotherm of B-PMO 1 is of type Ib, as it is typical for materials with micro- or small mesopores. This is in accordance with the respective pore diameter distribution, which is broader with a maximum at 2.9 nm. For this sample an *apparent*[2] specific BET surface area of 1116 $m^2 \cdot g^{-1}$ was determined. Physisorption isotherms of the samples that were synthesized with hydrochloric acid of higher concentration (1.0 $mol \cdot L^{-1}$), B-PMO 2 and B-PMO 3, are of type IVb. In these physisorption isotherms, a steep increase due to capillary condensation starts at a relative pressure p/p^0 of 0.15. This is in the middle of the classical range for the determination of the specific BET surface area. Therefore, the classical BET range cannot be used to determine the *apparent* specific surface area, so it was decided to adjust the BET range following the recommendations of the IUPAC specifically for microporous materials.[3] By taking the whole BET range into account the *apparent* specific surface area of B-PMO 3 would be 1900 $m^2 \cdot g^{-1}$ which is

[2]The common pressure range used for the determination of the specific BET surface area is 0.05–0.3. Here and in the following the pressure range was reconsidered to avoid overlapping with the pore condensation step in small mesopores. Hence, the criteria for reasonable results as mentioned in 3.1 are not met in the commonly used pressure range. According to the IUPAC recommendation the specific BET surface area is denoted as the *apparent* specific BET surface area to indicate the use of a divergent pressure range. [3]

an overestimation of the specific surface area. The adjusted values are 1626 $m^2 \cdot g^{-1}$ for B-PMO 2 and 1529 $m^2 \cdot g^{-1}$ for B PMO-3, respectively.

Generally speaking, the BET method is an estimation that does not fit unconditionally in these cases, and can only be used for comparison of equally treated samples. This problem will appear in the following section with other samples as well.

Benzene-bridged mesoporous organosilica synthesis with the surfactant C_{10}TAB

By using surfactants with shorter alkyl chains smaller pores are generated and the *apparent* specific BET surface area could be increased. In the literature, a highly ordered material with a 2D hexagonal pore structure that shows a specific BET surface area of 1354 $m^2 \cdot g^{-1}$ was successfully synthesized with the use of C_{14}TAB instead of C_{18}TAB.[109]

Therefore, the synthesis of B-PMO 3 was carried out with 2.1 equivalents of C_{10}TAB, a surfactant with even shorter alkyl chain length. In this case, the *apparent* specific surface area is still high at 1583 $m^2 \cdot g^{-1}$ calculated according to BET from the nitrogen physisorption, the cumulative pore volume calculated from NLDFT kernel for silica with cylindrical pores for pores smaller 20 nm is 0.83 $cm^3 \cdot g^{-1}$. For the corresponding nitrogen physisorption isotherm (type Ib) see Figure 9-1 in the Appendix. The shape of the isotherm and pore size distribution indicates the presence of micropores so that argon physisorption measurements were necessary for the characterization. The argon physisorption isotherm can be seen in Figure 4-18.

The *apparent* specific surface area calculated from the argon physisorption isotherm is lower at 1342 $m^2 \cdot g^{-1}$. The differences in the *apparent* specific BET surface area calculated from isotherms that were measured with different gases can be explained by the incorrect assumption concerning the orientation of the N_2 molecule to the surface and therefore the incorrect assumption on the molar cross section which substantially affects the calculation of the specific surface area. The consequential error was already discussed in section 3.1. The specific BET surface area from argon measurement is, in general, more reliable. However, values from nitrogen physisorption are comparable to the literature, as argon measurements at 87 K are less common.

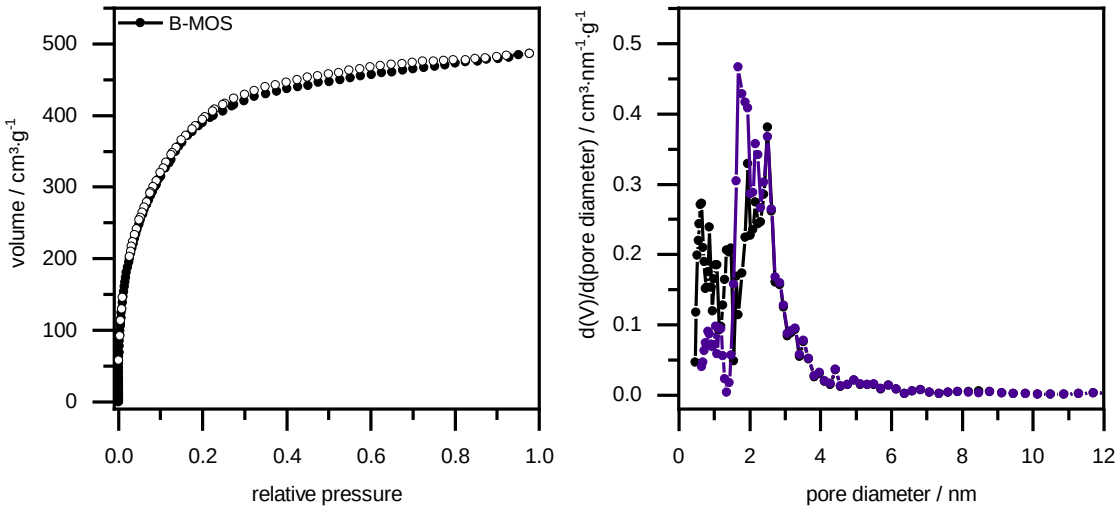

Figure 4-18: Argon physisorption isotherm (Ar, 87 K) of B-MOS that was synthesized under acidic conditions (left) and the respective pore diameter distribution on the right: NLDFT kernels for silica and zeolites with cylindrical pores in black and for cylindrical and spherical pores in purple.

The pore diameter distribution was calculated from the adsorption branch with two different NLDFT kernels, both of which are plotted together on the right in Figure 4-18. On the one hand, using a kernel for Ar, 87 K zeolites and silica with cylindrical pores (shown in black), and on the other hand, a kernel for Ar, 87 K zeolites and silica with cylindrical and spherical pores, whereby spherical pores with pore diameter < 2nm and cylindrical pores with pore diameter > 2 nm are considered (shown in purple). Here, a broad pore size distribution from 0.6–4 nm is given in the plot of the NLDFT kernel that considers only cylindrical pores, but it seems to narrow in the plot of the NLDFT kernel that also considers spherical pores. Using a Gaussian fit, the maximum pore diameter is 2.2 nm in both cases, whereas the micropore ratio is lower when spherical pores are considered. The presence of spherical pores is reasonable with the background of the materials that were obtained from C_{16}TAB with cubic pore symmetry, although the material discussed here is amorphous to X-ray diffraction (see Figure 9-2 in the Appendix) so that it can be referred to as PMO but only a microporous and mesoporous organosilica (MOS). The cumulative pore volume for pores smaller 20 nm is 0.6 $cm^3 \cdot g^{-1}$ calculated with both NLDFT kernels.

In summary, two B-(P)MOs with different pore size and very high specific BET surface areas were synthesized here under acidic conditions. The cubic symmetry in the space group $Pm\bar{3}n$ is assumed to have easily accessible pores that would increase the applicability of the B-PMOs for gas adsorption.

Approaches for DVB-, F-, 2F-PMO synthesis under acidic conditions

A lot of effort was invested to transfer the synthesis of B-PMO-3 to BTEVB and the fluorine containing precursor BTEVFB and BTEV2FB.

With BTEVB different acids, namely hydrochloric acid, sulfuric acid and phosphoric acid were used in different concentrations with the surfactant C_{16}TAC. Phosphoric acid was chosen as it gave promising results in context of ethane bridged PMOs synthesized with the help of a triblock copolymer (P123).[229] The best results were obtained with a concentration of 1.0 mol·L^{-1} for all acids, despite the fact that the resulting pH value differed significantly as sulfuric acid is a diprotic acid and phosphoric acid a weaker acid. The pH value for hydrochloric acid is 0, while for sulfuric acid it is lower (-0.3 calculated) and for phosphoric acid it is higher (1.1). The isotherms of the DVB materials are shown in Figure 4-19.

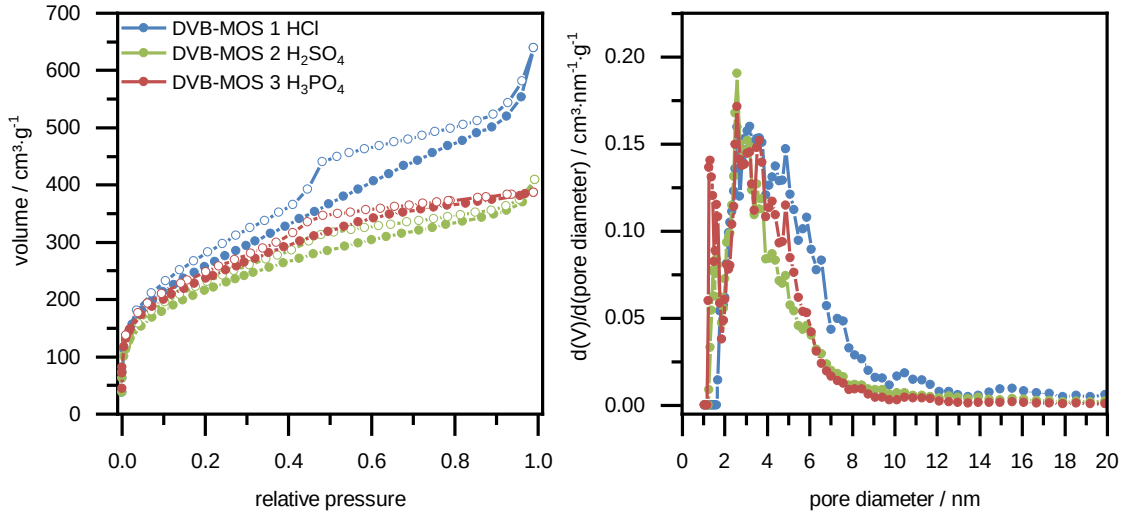

Figure 4-19: Physisorption isotherms (N_2, 77 K) of DVB-bridged materials, synthesized with different acids of 1.0 mol·L^{-1}. The respective pore diameter distributions are given on the right.

All isotherms show the same hysteresis behavior with a distinct step in the desorption branch at a relative pressure of 0.4 due to pore blocking phenomena, for which the mechanism is not clear. The specific *apparent* BET surface areas are summarized in Table 4-7. All materials are micro- and mesoporous as can be seen in the pore diameter distribution, the cumulative pore volume according to NLDFT (kernel for silica cylindrical pores, adsorption branch) of all samples is similar between 0.62–0.62 cm²·g^{-1}. The broad pore diameter distribution cannot be represented by an average pore diameter. The materials are called micro-and mesoporous organosilicas (MOS). The materials are X-ray amorphous.

Table 4-7: Summary of the specific *apparent* BET surface areas and the cumulative pore volume *V* (determined for pores smaller 20 nm using NLDFT kernel using the adsorption branch for silica with cylindrical pores) of DVB-bridged materials synthesized under acidic conditions.

sample	*apparent* S_{BET} / $m^2 \cdot g^{-1}$	$V_{N_2, NLDFT}$ / $cm^3 \cdot g^{-1}$
DVB-MOS 1 HCl	930	0.62
DVB- MOS 2 H_2SO_4	764	0.52
DVB-MOS 3 H_3PO_4	830	0.56

For analogous synthesis with the precursors BTEVFB and BTEV2FB; only hydrochloric acid was used since it gave the highest specific BET surface area for the DVB-MOS. The respective materials were highly microporous and for that reason argon physisorption measurements were carried out, which are shown in Figure 4-20 (For N_2, 77 K isotherms see the Appendix Figure 9-3).

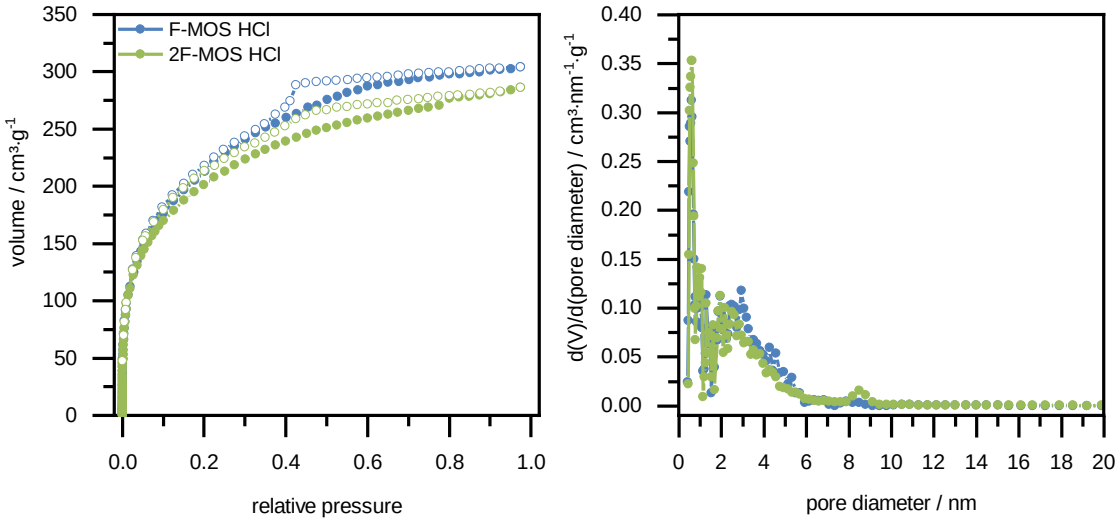

Figure 4-20: Physisorption isotherms (Ar, 87 K) of F-MOS and 2F-MOS synthesized with HCl (1.0 $mol \cdot L^{-1}$). The respective pore diameter distributions are given on the right (NLDFT kernel, for silica, cylindrical pores, adsorption branch).

The *apparent* specific BET surface areas calculated from nitrogen and argon isotherms are given in Table 4-8. Here, the same phenomenon of lower specific surface area by calculation with argon that was discussed earlier concerning B-PMO-4 occurs. The isotherms show hysteresis with sudden desorption at a relative pressure of 0.4 due to undefined pore blocking phenomena. Prominent micropores with pore diameter of 0.6 nm are shown in the pore diameter distribution from both precursors next to broadly distributed mesopores from 2–4 nm. The cumulative pore volume of both samples are similar about 0.40 $cm^3 \cdot g^{-1}$ it was calculated with NLDFT kernel for silica and zeolites with cylindrical pores.

Table 4-8: Summary of the *apparent* specific BET surface areas calculated from physisorption experiments of F-MOS and 2F-MOS with N_2 and Ar and the respective pore volumes calculated using NLDFT kernel from the adsorption branch for silica with cylindrical pores (N_2) and silica/zeolites with cylindrical pores (Ar).

sample	*apparent* S_{BET} (N_2) / $m^2 \cdot g^{-1}$	$V_{N_2,\ NLDFT}$ / $cm^3 \cdot g^{-1}$	*apparent* S_{BET} (Ar) / $m^2 \cdot g^{-1}$	$V_{Ar,\ NLDFT}$ / $cm^3 \cdot g^{-1}$
F-MOS HCl	848	0.43	691	0.40
2F-MOS HCl	764	0.44	649	0.38

In summary, it can be said that no conditions were found that lead to cubic mesostructures in DVB-PMOs, F-PMOs or 2F-PMOs. One hypothesis could be that the length of the rigid organic bridge hinders interaction with surfactant micelles with strong curvature. However, materials with comparably high *apparent* specific BET surface areas were obtained, although the integrity of the organic bridge was not investigated with solid state NMR spectroscopy.

4.1.4 Microporous organosilica

For the adsorption of inhalation anesthetics microporous materials showed the best performance in studies by the Bathen research group, so that the synthesis of microporous organosilica materials was of interest. Two different approaches were used. In the first approach, microporous organosilicas were obtained in the presence of the surfactant C_{10}TAB at a comparably low pH value of 12.0 using three different precursors: BTEB (B-), BTEVB (DVB-) and BTEVA (DVA-). By contrast in absence of any surfactant, no condensation of the organosilica precursor BTEB occurs within 24 hours at this pH value. In comparison to this, common PMO synthesis with the precursors used was successful at pH 13.5—14.0. However, different examples from the literature describe similar microporous silica and organosilica materials that were synthesized in the presence of a surfactant with the same alkyl chain length (C_{10}TAB or C_{10}TAC).[230,231]

In the second approach the divinylbenzene-based precursors were treated with ethanol and sodium hydroxide without any surfactant in a very low total volume which result in a high concentration of the precursor. There were no comparable approaches found in the literature.

Microporous organosilica materials synthesized at pH 12.0

The results from the first synthesis approach will be discussed in the following section. As previously mentioned materials from three precursors were synthesized which are referred to as B-micro, DVB-micro and DVA-micro. For the characterization of porosity features in microporous materials, argon physisorption suits best. As previously explained, it is commonly known that the *apparent* specific BET surface area obtained from the measurements with nitrogen is larger than with argon. However, the measurements with argon are more reliable for microporous materials.

The physisorption isotherms from argon measurements are shown in Figure 4-21 together with the respective plots of the pore diameter distribution.

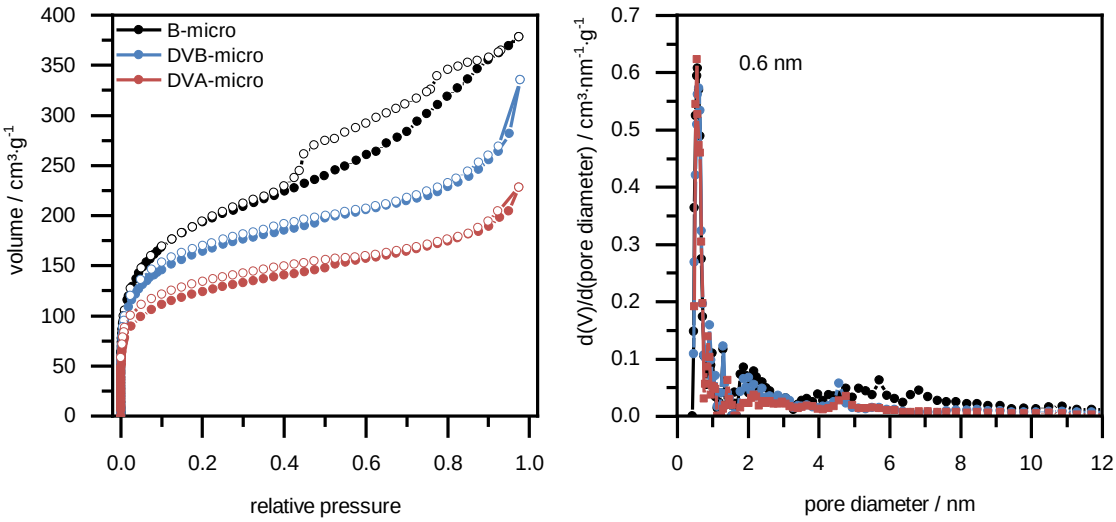

Figure 4-21: Physisorption isotherms (Ar, 87 K) of microporous organosilica synthesized at pH 12.0. Pore diameter distributions (calculated from the adsorption branch with NLDFT kernel for silica/zeolites with cylindrical pores) are shown on the right.

Regarding the adsorption branch, all isotherms can be assigned to type Ib isotherms that occur for materials with micropores and narrow mesopores. The isotherm of the benzene-bridged material also shows further gas uptake at higher relative pressure as well as hysteresis with two steps in the desorption branch. This indicates pore blocking in larger blocked or ink-bottle shaped mesopores. Since it is a microporous material, it is likely that the pore diameter of the neck is smaller than the critical size so that cavitation effects can be assumed. According to the pore diameter distribution from NLDFT for silica/zeolites with cylindrical pores all samples prominently show the same pore diameter of 0.6 nm. By contrast, the prominent pore diameter in the distribution from NLDFT for silica with cylindrical pores from nitrogen measurements is 1.2 nm (see Figure 9-4 in the Appendix for the pore size distribution). This might be an artefact due to the NLDFT kernel for silica, so that the pore diameter size has to be considered with caution. In comparison of the pore volumes the micropore volume is in general smaller and the mesopore volume is higher in the nitrogen measurements than the argon measurements which meets the expectations since argon is in general suited better to determine the microporosity.
In the pore diameter distribution, pores around 6 nm are also determined. The textural data is summarized in Table 4-9, while also considering the results from nitrogen physisorption (see Figure 9-4 in the Appendix for the isotherms).

Table 4-9: Summary of the *apparent* specific surface areas, as well as micropore volume (NLDFT pores < 2 nm) and mesopore volume (pores between 2 nm and 20 nm) from N_2 77 K and Ar 87 K measurements of organosilicas synthesized at pH 12.0.

	nitrogen			***argon***		
sample	***apparent*** S_{BET} / $m^2 \cdot g^{-1}$	$V_{NLDFT,\ micro}$ / $cm^3 \cdot g^{-1}$	$V_{NLDFT,\ meso}$ / $cm^3 \cdot g^{-1}$	***apparent*** S_{BET} / $m^2 \cdot g^{-1}$	$V_{NLDFT,\ micro}$ / $cm^3 \cdot g^{-1}$	$V_{NLDFT,\ meso}$ / $cm^3 \cdot g^{-1}$
B-micro	822	0.13	0.48	620	0.19	0.29
DVB-micro	630	0.10	0.35	524	0.18	0.17
DVA-micro	469	0.12	0.15	397	0.15	0.12

For determination of the *apparent* specific BET surface areas, the relative pressure range had to be adjusted (see Table 8-4 in the Experimental Section) following the recommendations by IUPAC for microporous materials. The *apparent* specific BET surface area of the benzene-bridged material is significantly higher than the divinylaniline-bridged material. It is likely that the amino function of the divinylaniline-bridged precursor affects the synthesis pH value so that the chosen synthesis conditions are not a good fit for this precursor. Common synthesis conditions for DVA-PMOs and DVB-PMOs differ as well, main difference is the concentration of the base which is significantly higher in DVA-PMO syntheses.[103,107,108] Although, simple change of the sodium hydroxide solution did not improve the microporosity features of DVA-micro.

Comparing the textural data from measurements with nitrogen and with argon of B-micro and DVB-micro, respectively, it should be noted that the micropore volume of the benzene-bridged material is smaller but the *apparent* specific BET surface area is higher. This is due to the presence of additional mesopores in this sample.

The mechanism of micropore formation cannot be explained here. The presence of C_{10}TAB is necessary in the synthesis procedure, but it cannot be assumed that it acts as a mesophase template as the generated pores are too small. All materials are X-ray amorphous.

In summary, a first approach for the synthesis of microporous materials was described, and can be applied for different precursors. The transfer of this approach to syntheses with halogen-containing precursors is possible, but is not discussed here as no argon physisorption measurements are available for the respective materials, so that no adequate characterization of the pore system is possible.

Microporous organosilica materials synthesized in an EtOH/NaOH solution

Secondly, microporous organosilica materials were obtained by treatment of the respective precursors in high concentrations with a solution of ethanol and sodium hydroxide (c = 0.31 $mol \cdot L^{-1}$ pH 13.5) at 80 °C. This solution will be used in another context in 4.3.2 and was

found to generate microporous materials high specific BET surface areas. The precursors BTEVB, BTEVA, BTEVFB and BTEV2FB were treated this way and materials with very high *apparent* specific BET surface areas were obtained. For differentiation with the other microporous organosilicas, the materials are denoted with (EtOH).

Figure 4-22 shows the argon physisorption isotherms of these materials (for nitrogen physisorption isotherms see Figure 9-5 in the Appendix).

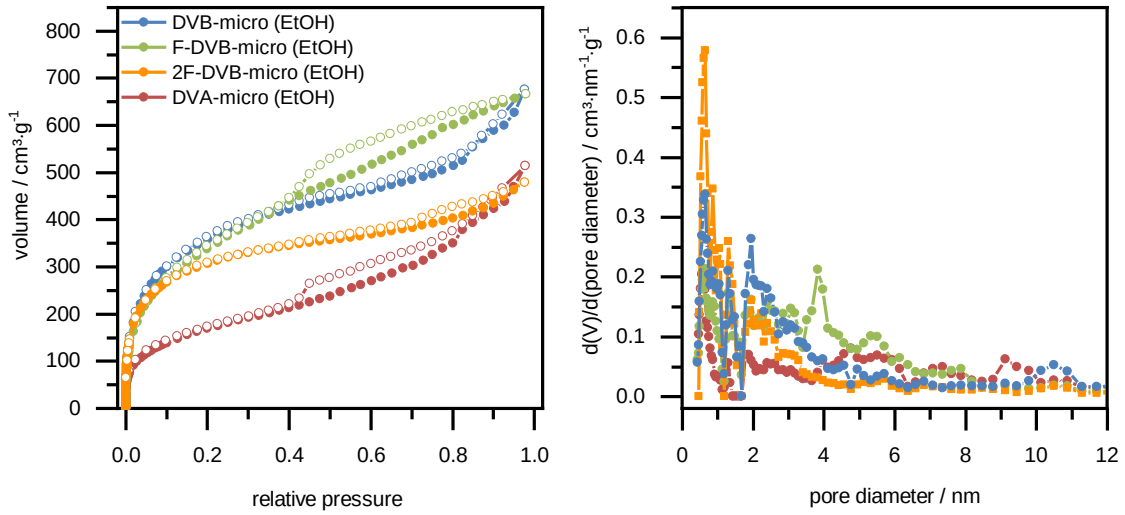

Figure 4-22: Physisorption isotherms (Ar, 87 K) for materials from given precursors that were obtained after treatment with an EtOH/NaOH solution (pH 13.75) at 80 °C. Right: pore diameter distributions from adsorption branch calculated with NLDFT kernel for silica/zeolites with cylindrical pores.

The BET specific surface areas from argon and nitrogen physisorption measurements, as well as the micropore volume from argon measurements, are shown in Table 4-10. The physisorption isotherms of the respective materials are all of type Ib. The isotherms of DVA–micro (EtOH) and DVB–micro (EtOH) show a small second step at a relative pressure around 0.8 which indicates the presence of larger pores. Besides, hysteresis phenomena are prominent in the isotherms of F-DVB–micro (EtOH) and DVA–micro (EtOH) which is caused by the interconnection of pores with different diameters.

The differences between the BET specific surface areas obtained from measurements with argon and those with nitrogen are similar to the previously mentioned samples. DVB-micro (EtOH) has an *apparent* specific BET surface area of 1401 $m^2 \cdot g^{-1}$ according to the measurement with nitrogen, but 1158 $m^2 \cdot g^{-1}$ according to the measurement with argon. The *apparent* specific BET surface areas from argon measurements of F-DVB-micro (EtOH) and 2F-DVB-micro (EtOH) are similar, at 1110 $m^2 \cdot g^{-1}$ and 1000 $m^2 \cdot g^{-1}$, respectively. Although it has a lower BET specific surface area, 2F-DVB-micro (EtOH) has the highest micropore volume of about 0.3 $cm^3 \cdot g^{-1}$. Again, the material from BTEVA (DVA-micro-(EtOH)) stands out, with a comparably low *apparent* specific BET surface area of 553 $m^2 \cdot g^{-1}$. Also, the influence of the amino function on the pH value might

result in the synthesis conditions of the other materials not being transferable. For determination of the *apparent* specific BET surface area, the relative pressure range had to be adjusted as documented in Table 9-3 in the Appendix.

The pore diameter distribution on the right in the figure is obtained from the adsorption branch with a NLDFT kernel for silica/zeolites with cylindrical pores. All samples show micropores of 0.6 nm and mesopores with broad distributions up to 6 nm, whereas the most dominant pore diameter from nitrogen measurements was just 1.2 nm. The same values were established in the syntheses mentioned previously. This seems to be an artefact that occurs in all measurements. The named sample DVA-micro-(EtOH) shows less dominant microporosity.

Table 4-10: Summary of the *apparent* specific surface areas from N_2, 77 K and Ar, 87 K measurements, as well as the cumulative pore volume for pores smaller 20 nm from N_2 measurement (NLDFT kernel adsorption branch, silica cylindrical pores) and the micropore volume from argon measurements (NLDFT kernel, adsorption branch, silica/zeolites, cylindrical pores, pores < 2 nm) and the cumulative mesopore volume (same NLDFT kernel, pores 2 nm–20 nm) of organosilicas synthesized with ethanol and sodium hydroxide (pH 13.75).

	nitrogen		***argon***		
sample	S_{BET} / $m^2 \cdot g^{-1}$	V_{NLDFT} / $cm^3 \cdot g^{-1}$	S_{BET} / $m^2 \cdot g^{-1}$	$V_{<2\ nm,\ NLDFT}$ / $cm^3 \cdot g^{-1}$	$V_{2–20\ nm,\ NLDFT}$ / $cm^3 \cdot g^{-1}$
DVB-micro (EtOH)	1401	0.92	1158	0.27	0.49
DVA-micro (EtOH)	759	0.73	553	0.10	0.44
F-DVB-micro (EtOH)	1326	1.02	1110	0.20	0.62
2F-DVB-micro (EtOH)	1210	0.79	1000	0.31	0.28

To the best of the author's knowledge, no comparable synthesis of organosilica gels with such high specific surface areas are known in the literature. In the following chapter, advantage was taken of the behavior of the precursor to condense with especially high specific surface areas under the given conditions.

The microporous organosilicas that were synthesized as described here, were used for measurements of the adsorption capacity of inhalation anesthetics by the group of Professor Bathen from the University of Duisburg Essen as part of the cooperation.

4.2 Pseudomorphic transformation of CPG beads and granules

As preparatory work for the synthesis of micrometer-sized organosilica beads, the pseudomorphic transformation of pure CPG was first investigated. Everything that has been learned about the mechanism of the pseudomorphic transformation from these approaches formed the basis for the following (partial) pseudomorphic transformation approaches of organosilica/silica hybrid materials.

As described in the Introduction 1.4, the pseudomorphic transformation of pure silica CPG has been investigated intensively by different research groups in the last years. In general, the synthesis takes place in an alkaline surfactant solution, where C_{16}TAOH solutions are often chosen in order to avoid the presence of additional ions, e.g. Na^+, which might decrease the softening point of the glass. Different approaches were explored to pursue partial transformation of the silica phase in order to adjust the resulting macropore size in hierarchically porous CPG. Three approaches have been discussed in detail up to now: First, the premature interruption of the process, which changes the parameter of time but keeps all other parameters constant;[39,48] second, the variation of the volume of C_{16}TAOH solution used, which changes the ratios of silica to surfactant, hydroxide ions and solvent, respectively, but keeps time, temperature and pH value constant;[37,232] third, the variation of C_{16}TAOH/(C_{16}TAOH+C_{16}TAB) in solution which changes the pH value, but keeps the time as well as the ratio of silica to surfactant and solvent constant.[38]

In order to understand the influence of the different parameters during the pseudomorphic transformation, the approaches discussed in the literature were first reproduced. Further, other parameters, like the transformation temperature, were varied and microwave-assisted syntheses were investigated. CPG were provided by the research group of Professor Enke in Leipzig.

Pseudomorphic transformation of a CPG batch with pore volume of 1.5 $cm^3 \cdot g^{-1}$ and 168 nm pore size

A CPG batch with a pore volume of 1.5 $cm^3 \cdot g^{-1}$ and 168 nm macropore size was used as starting material. Figure 4-23 shows the SEM image of the sponge like pore system at different magnifications.

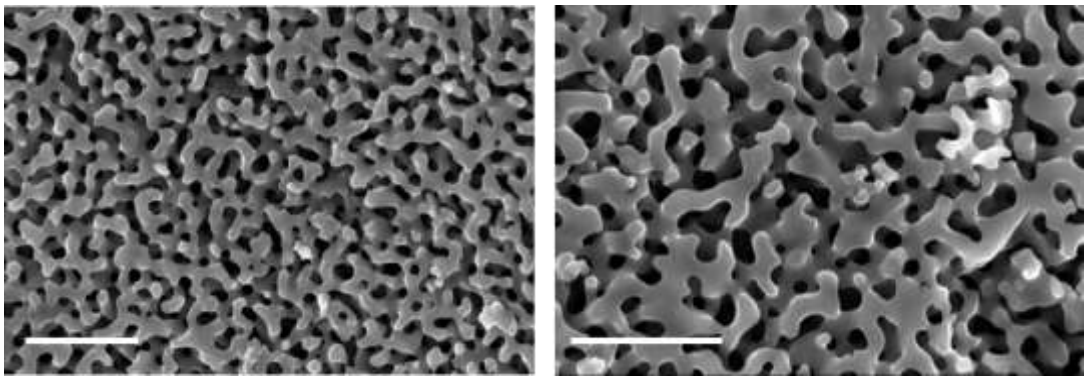

Figure 4-23: SEM images of the CPG starting material with 1.5 $cm^3 \cdot g^{-1}$ pore volume and 168 nm macropore size with 50000x and 70000x magnification, scale bar of 1.0 µm.

At first, the C_{16}TAOH solution volume was changed. For 1.0 g of silica, 40 mL of an aqueous C_{16}TAOH solution with a concentration of 0.08 $mol \cdot L^{-1}$ was set as 100 % volume, similar to the synthesis prescription in the literature where 42 mL were used.[37,38]

The C_{16}TAOH solution was obtained by anion exchange of C_{16}TAB over Ambersep® 900 resin. The measured pH value was reproducible at 12.7, and the calculated pH was 12.9. Deviation from the measured pH value to the calculated value can be caused by incomplete ion exchange, but also the error in measurements of the pH meter increases with higher pH values as the range of effective measurements is reached.

Figure 4-24 shows the nitrogen physisorption isotherms of samples that were transformed for four days at 100 °C with 48 %, 75 %, 100 % and 200 % volume of the respective C_{16}TAOH solution. In all cases, isotherms type IVb were obtained as expected for mesoporous samples with pores around 4 nm.

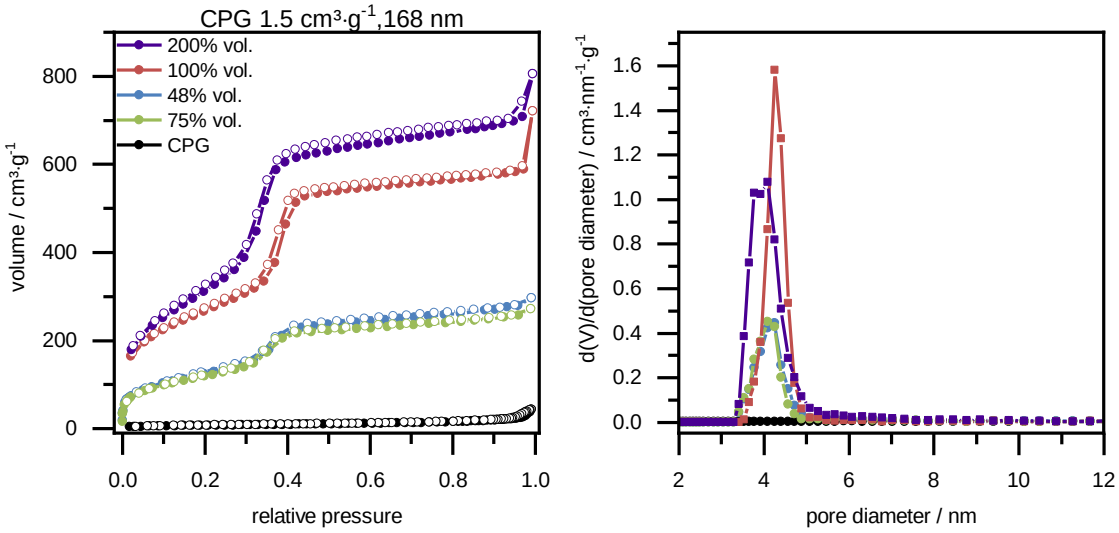

Figure 4-24: Physisorption isotherm (N_2, 77 K) of CPG after pseudomorph transformation under variation of the volume of C_{16}TAOH solution (left). The respective pore diameter distributions (calculated from the adsorption branch using NLDFT kernel for silica with cylindrical pores) are shown on the right.

As expected, lower volumes of C_{16}TAOH solution led to smaller specific BET surface areas and broadening of the pore size distribution. In this particular case, a further increase of the volume beyond the 40 mL per 1.0 g silica resulted in a further specific surface area increase of up to 1237 $m^2 \cdot g^{-1}$. This is in good accordance with the completed transformation for similar CPG in the literature.[38] As discussed earlier, the macropore size and the thickness of the silica wall of the starting material are crucial for the transformation degree as these parameters determine whether the pore volume is sufficient for the increasing silica volume during the transformation process.

Comparing the materials which were treated with 48 % of the C_{16}TAOH solution volume with the solution with 75 %, it should be noted that the specific BET surface areas of 464 $m^2 \cdot g^{-1}$ and 444 $m^2 \cdot g^{-1}$ do not increase with increasing solution volume and do not differ significantly. Thus, no reliable trend of the transformation degree can be given by changing the volume of the surfactant solution in this sample series. The pore size distribution is shown on the right in Figure 4-24. Table 4-11 gives an overview of the specific BET surface area and maximum pore diameter of the samples. The given transformation degree is the quotient of the specific BET surface area of the respective sample and the 100 % volume sample. The specific BET surface area was used as the basis for the calculation of the transformation degree as this is the common procedure in the literature although it gives no information concerning the ordering of the pore system.[37] Here, the transformation degree shows a nonlinear behavior.

Table 4-11: Summary of the textural data of pseudomorphic transformations for four days with different volumes of C_{16}TAOH solution.

Sample	C_{16}TAOH / Si ratio	S_{BET} / $m^2 \cdot g^{-1}$	$d_{N_2, NLDFT}$ / nm	V_{NLDFT, N_2} / $cm^3 \cdot g^{-1}$	Transformation degree
CPG 1.5$cm^3 \cdot g^{-1}$ 168 nm	-	26	-	0.03	-
48 % volume	0.09	467	4.2	0.40	0.48
75 % volume	0.14	444	4.1	0.37	0.46
100 % volume	0.19	966	4.3	0.85	1
200 % volume	0.38	1237	4.0	1.02	1.3

The P-XRD patterns are given in Figure 4-25. The samples prepared with 48 %, 75 % and 100 % C_{16}TAOH solution volume show a reflection at 2θ = 1.9 °, which corresponds to a *d*-spacing of 4.5 nm, whereas it is shifted to 2θ = 2.3 °, *d*-spacing of 3.8 nm, for the sample with 200 % volume of the C_{16}TAOH solution. This indicates a mesophase for all samples. Further small reflections between 2θ = 3–5 ° are very broad so that classification of the mesophase is not possible. However, 2D hexagonal ordering of the mesophase is likely due to experiences from the literature. As

an MCM-48 type pore system was obtained using a C_{16}TAOH solution with higher concentration[233] as well as after a longer time,[36] this cannot be ruled out here for the sample synthesized with 200 % volume of the C_{16}TAOH.

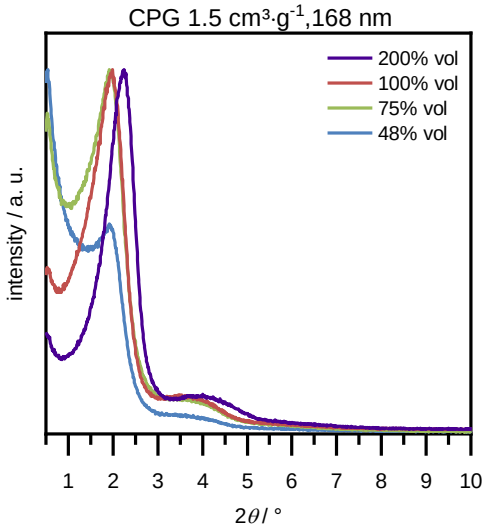

Figure 4-25: P-XRD patterns of the pseudomorphically transformed samples with different volumes of C_{16}TAOH solution.

After the variation of the synthesis composition the time of the transformation was also varied for the same CPG batch between one hour and seven days. The nitrogen physisorption isotherms as well as the pore diameter distribution according to NLDFT kernel from the adsorption branch for silica with cylindrical pores are given in Figure 4-26. As in the previously presented samples isotherms of type IVb are obtained from all materials with only very slight hysteresis indicating pores slightly larger than 4 nm. Here, an increasing specific BET surface area and thus increasing transformation degree, can be observed with increasing time up to four days. With a longer transformation time the specific BET surface area decreases again. As all of these synthesis series are not statistically collected but once-off experiments, deviations can occur randomly. On the other hand, this effect was previously observed in the literature, although no explanation was given.[39] It is possible that the surfactant itself starts to decompose after excessively long transformation in C_{16}TAOH solution at high temperatures.

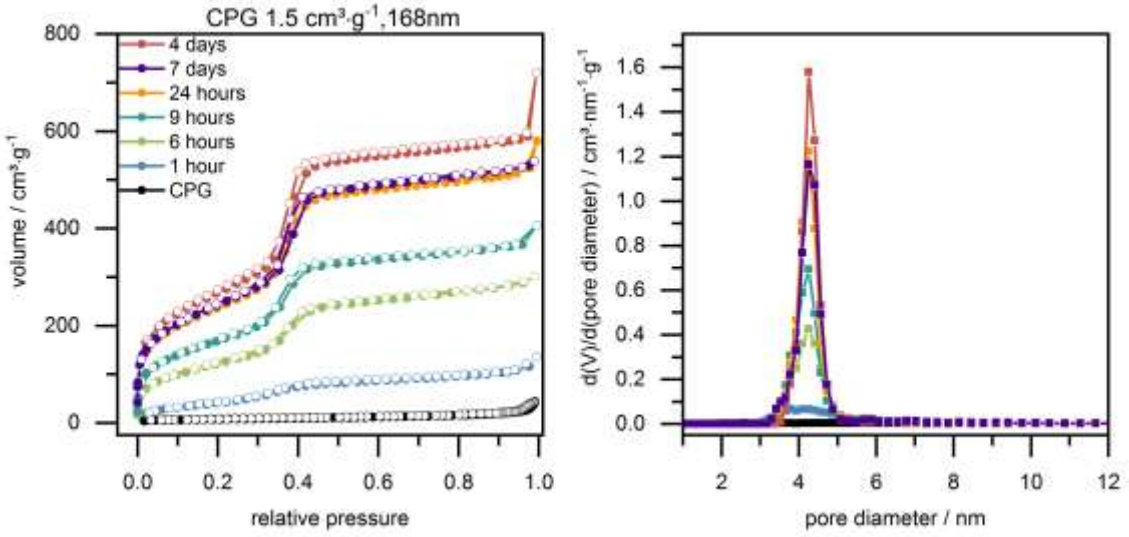

Figure 4-26: Physisorption isotherms (N_2, 77 K) of CPG after different treatment durations with a consistent volume of C_{16}TAOH solution. The respective pore diameter distributions (calculated from the adsorption branch with NLDFT kernel for silica, cylindrical pores) are shown on the right.

Table 4-12 summarizes the textural data of the materials that were treated with 100 % volume C_{16}TAOH solution at 100 °C for different times. It has to be considered that the sample which was transformed for four days is the same as the 100 % volume in the previous examples. For the calculation of the transformation degree this sample was again used as the basis.

Table 4-12: Summary of the specific BET surface areas and pore diameters of samples that were treated with C_{16}TAOH solution (0.08 mol·L^{-1}) at 100 °C between one hour and seven days.

Sample	S_{BET}/ m²·g^{-1}	d_{NLDFT, N_2} / nm	V_{NLDFT, N_2} / cm³·g^{-1}	Transformation degree
CPG 1.5cm³·g^{-1} 168 nm	26	-	0.03	-
1 hour	173	-	0.15	0.18
6 hours	459	4.3	0.42	0.47
9 hours	625	4.3	0.53	0.65
24 hours	857	4.3	0.75	0.89
4 days	966	4.3	0.85	1.0
7 days	879	4.3	0.77	0.91

P-XRD patterns of all samples that were treated for different time spans are shown in Figure 4-27.

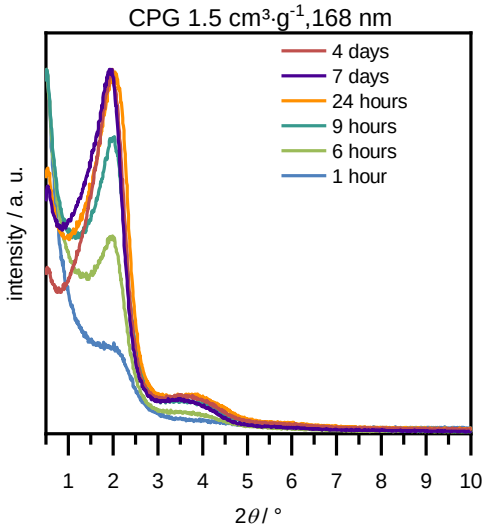

Figure 4-27: P-XRD patterns of samples after pseudomorphic transformation starting with CPG (1.5 $cm^3 \cdot g^{-1}$ pore volume and 168 nm pore size) with increasing transformation time.

Here the reflection at $2\theta = 1.9$ ° (*d*-spacing of 4.5 nm) is apparent even after one hour of treatment and the intensity increases for samples up to four days. Further broad reflections in the area of $2\theta = 3–5$ ° are noted from 24 hours onwards, without further change. In addition, classification of the mesophase is not possible here, but as the first reflection does not change, it stands to reason that the mesophase does not change with increasing time.

The material swells during the transformation which leads to shrinking of the initial macropore system. In the case of 168 nm initial pores diameter the shrinking could be observed via SEM images shown in Figure 4-28. Swelling of the pore walls is obvious after four days of pseudomorphic transformation in the case of 100% and a doubled volume of C_{16}TAOH solution. It is also visible after 24 hours whereas the effect cannot be seen in the material that was treated for only one hour. It should be mentioned that carbon sputtering of the sample surface was necessary for images with a high magnification. Hence, the pore size or the pore wall thickness cannot be estimated from the SEM images.

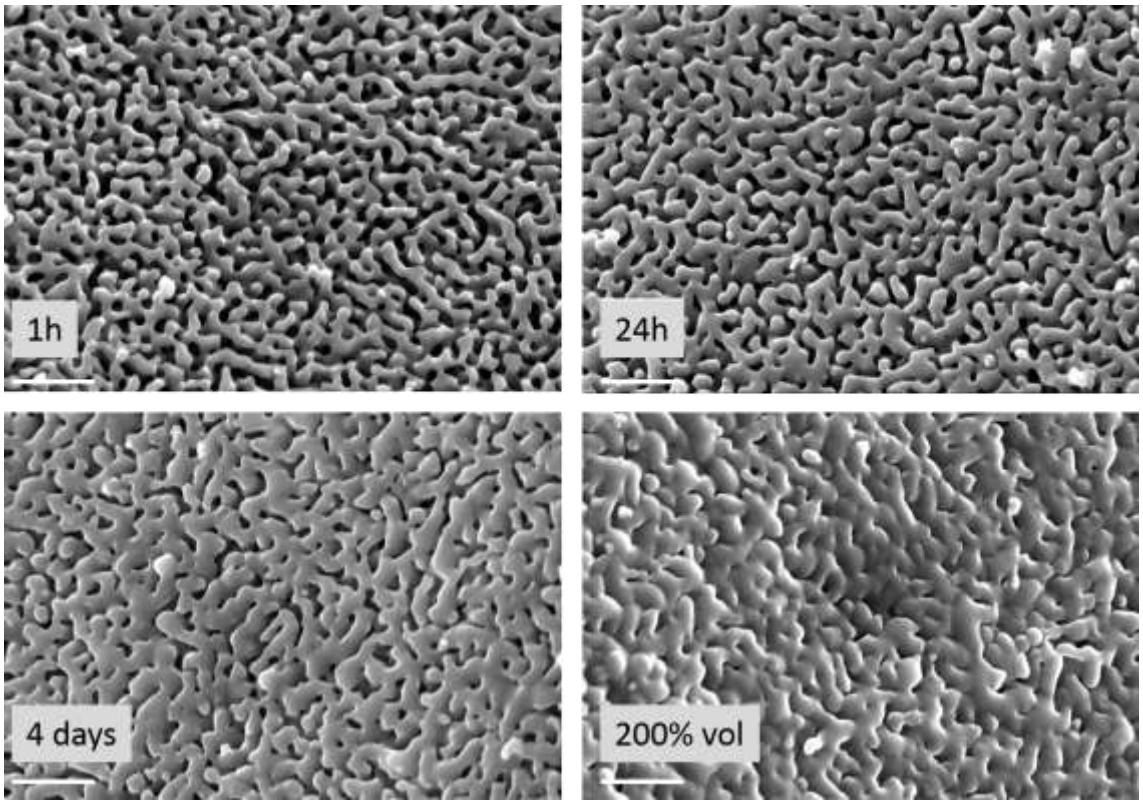

Figure 4-28: SEM images of CPG after pseudomorphic transformation with 40 mL per 1.0 g of silica for one hour, 24 hours and four days, as well as with 80 mL per 1.0 g silica for four days. Magnification is x40000, the scale bar is 1 µm in all images.

Quantitative information is obtained by comparison of the macropore diameter measured with MIP. Figure 4-29 shows the mercury intrusion curves and the pore diameter distributions that was calculated from MIP for the samples that were treated for one hour, 24 hours and four days all with 100 % volume of the C_{16}TAOH solution and also the sample that was treated for four days with 200 % volume of the C_{16}TAOH solution. The intrusion curve shows a first slope below the pressure of 1500 psi, which is due to filling of interparticle spaces. Very steep intrusion, hence filling of the pore system, follows for the CPG starting material and samples treated with 100 % volume of the C_{16}TAOH solution, which indicates comparably narrow pore diameter distributions. The intrusion volume of the samples shrinks with increasing transformation time, which indicates a decreasing pore volume. By contrast, for the sample which was treated with higher C_{16}TAOH solution volume, intrusion occurs over a broad pressure range, indicating a broad pore size distribution. Also the intrusion volume is very low for this sample. The intrusion for all samples was measured up to the maximum of 33000 psi, the mesopore system cannot be investigated using this method. As expected for monomodal macropore systems, nearly complete extrusion of mercury occurs. The pore diameter distributions are shown on the right in the same Figure. As can be seen the initial macropore of 168 nm has already shrunk slightly after one hour to 151 nm, after 24 hours to 108 nm and to 101 nm after 4 days. Using the doubled amount of C_{16}TAOH solution not only increases the specific BET surface area further,

but destroys the macropore system up to a very low pore volume of 0.4 $cm^3 \cdot g^{-1}$. The pore size distribution is too broad to give a maximum diameter.

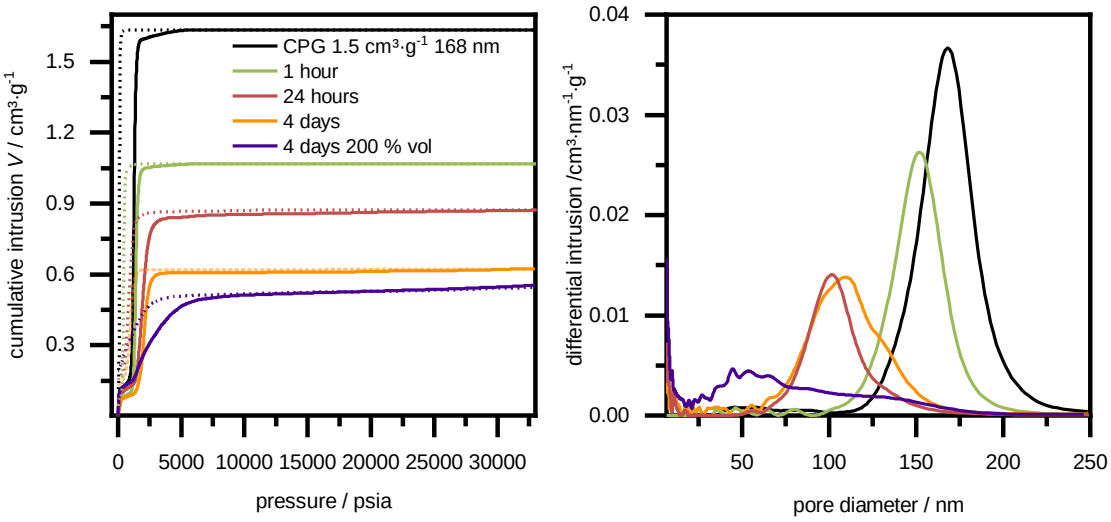

Figure 4-29: Left: mercury intrusion curve (extrusion in dotted line) of CPG after pseudomorphic transformation for different times and with doubled C_{16}TAOH volume. Right: pore diameter distribution calculated from MIP.

The macropore volumes and pore diameters are summarized in Table 4-13 together with the textural data from the physisorption measurements that have already been discussed.

Table 4-13: Summary of macropore diameters and pore volumes according to MIP together with the respective specific BET surface areas.

Sample	S_{BET} / $m^2 \cdot g^{-1}$	d_{NDLFT, N_2} / nm	Transformation degree	V_{Hg} / $cm^3 \cdot g^{-1}$	d_{Hg} /nm
CPG 1.5$cm^3 \cdot g^{-1}$ 168 nm	26	-	-	1.5	168
1 hour, 100 % volume	173	-	0.18	0.96	151
24 hours, 100 % volume	857	4.3	0.89	0.74	108
4 days, 100 % volume	966	4.3	1.0	0.52	101
4 days, 200 % volume	1237	4.0	1.3	0.40	58

In most examples from the literature the transformation was carried out at 100 °C,[39] 110 °C[37] or 120 °C.[38] It was tested whether decreasing the temperature to 80 °C or 60 °C is an option to slow down the process and provoke only partial pseudomorphic transformation. The transformations at different temperatures were carried out with 100 % of the C_{16}TAOH solution for four days. In view of the transformation of organosilica, which will be discussed later in this work, the lower temperature might also protect the organic bridging group from temperature induced degradation.

As can be seen in Figure 4-30, mesopores are generated at all temperatures as isotherms of type IVb are obtained in all cases. With higher temperatures, the specific BET surface areas increase for samples that were treated between 60 °C and 100 °C and the pore size distribution narrows.

However, at 120 °C the specific BET surface area decreases again, it is possible that the surfactant starts to decompose after four days at this high temperature. Although the isotherm looks normal, only measurement points up to 0.85 could be considered for a good fit of the condensation step with the NLDFT kernel. It could be that residues of the surfactant, which occur, e.g. due to decomposition at the high temperature, change the chemical environment of the surface in the pores which makes the kernel unsuitable. This would also explain the low specific BET surface area of the sample.

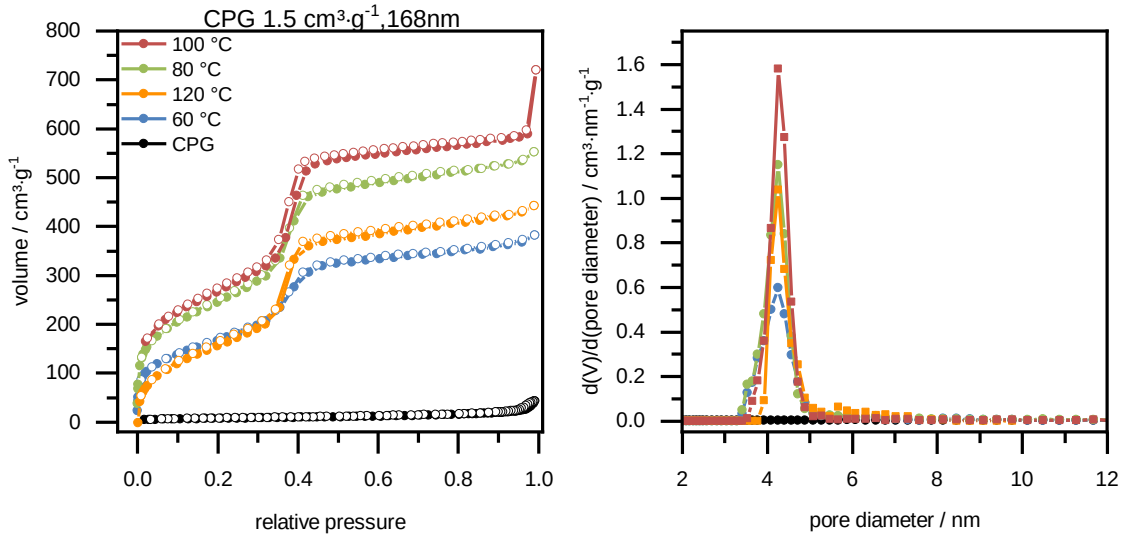

Figure 4-30: Physisorption isotherms (N_2, 77 K) of CPG after pseudomorphic transformation for four days at different temperatures. The respective pore diameter distributions (calculated from the adsorption branch with NLDFT kernel for silica, cylindrical pores) are shown on the right.

Table 4-14 summarizes the textural data for the materials treated at 60 °C to 120 °C. The transformation degree was calculated as previously described using the sample with 100 °C as a basis.

Table 4-14: specific BET surface areas, pore diameters and pore volume (both calculated from the adsorption branch with NLDFT kernel for silica, cylindrical pores) of CPG after pseudomorphic transformation at 60 °C to 120 °C.

Sample	S_{BET} / $m^2 \cdot g^{-1}$	$d_{N_2, NLDFT}$ / nm	$V_{meso, NLDFT}$ / $cm^3 \cdot g^{-1}$	Transformation degree
CPG 1.50 $cm^3 \cdot g^{-1}$ 168 nm	26	-	0.03	-
60 °C	621	4.2	0.54	0.64
80 °C	906	4.2	0.77	0.94
100 °C	966	4.3	0.85	1.0
120 °C	632	4.4	0.62	0.65

The P-XRD patterns are in good agreement with the results of the previously mentioned pseudomorphic transformations, having one reflection $2\theta = 1.9\,°$ (d-spacing of 4.5 nm) and broad reflections in the area of $2\theta = 3–5\,°$, shown in Figure 4-31.

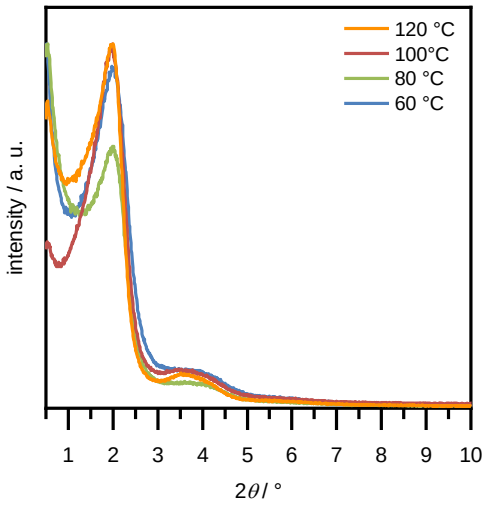

Figure 4-31: P-XRD patterns of samples after pseudomorphic transformation starting with CPG (1.5 $cm^3 \cdot g^{-1}$ pore volume and 168 nm pore size) with increasing transformation temperature.

To summarize the results obtained from the different approaches for partial pseudomorphic transformation of a CPG batch with 168 nm pore diameter, it can be said that the formation of the mesophase that is indicated in the P-XRD patterns seems to be either a question of time or of the ratio of surfactant to silica, rather than of the temperature, as 60 °C seems to be sufficient. Using the specific BET surface area as the parameter to name the transformation degree, it can be similarly adjusted by time and volume of the C_{16}TAOH solution, whereas the time variation allows a finer adjustment. Figure 4-32 summarizes how the variation of one of the three parameters affect the transformation degree.

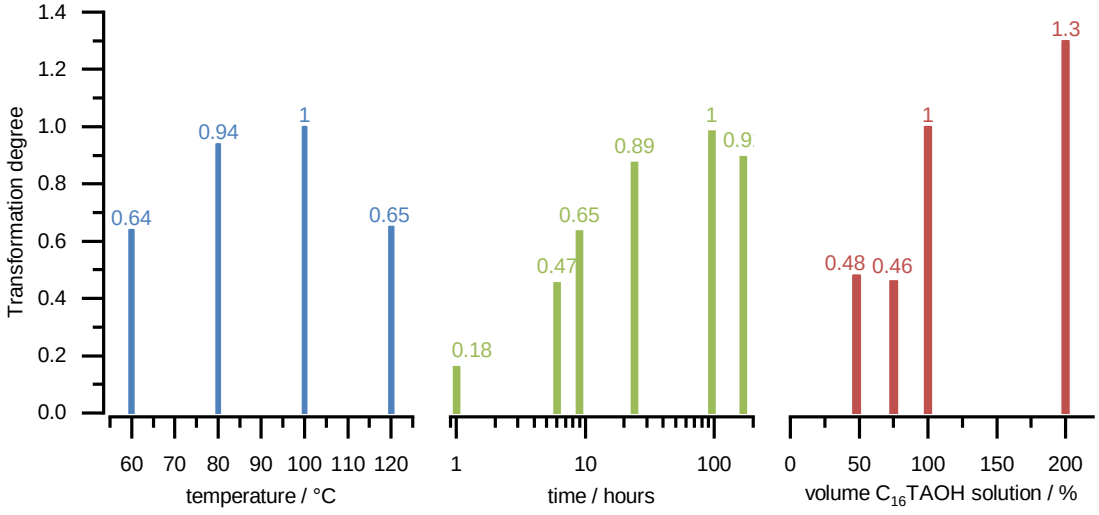

Figure 4-32: Summary of the transformation degrees that result from pseudomorphic transformation of CPGs with 1.5 $cm^3 \cdot g^{-1}$ pore volume and 168 nm pore diameter, under variation of one out of three parameters, the temperature (blue, left), the time (green, center), the volume of C_{16}TAOH solution (red, right).

Pseudomorphic transformation of a CPG batch with pore volume 1.5 $cm^3 \cdot g^{-1}$, 52 nm pore size

As mentioned in the Introduction the transformation mechanism in CPG depends on the pore size of the initial pore system since the pore diameter shrinks in the case large macropores but vanishes in case of smaller macropores due to swelling of the material (see Figure 1-12). Hence, after the investigation of the transformation process in large macropores, a sample with pores at the boundary between meso- to macropores, 52 nm and the same pore volume of 1.5 $cm^3 \cdot g^{-1}$ was additionally investigated. Therefore, partial transformations with different volumes of C_{16}TAOH solution and time were also carried out as presented below. In this case, the CPG are beads of 40–100 µm diameter, as can be seen in SEM images on the left in Figure 4-33. The pores are too small for monitoring the swelling of the material during the pseudomorphic transformation with SEM images as the structure in Figure 4-33 on the right shows.

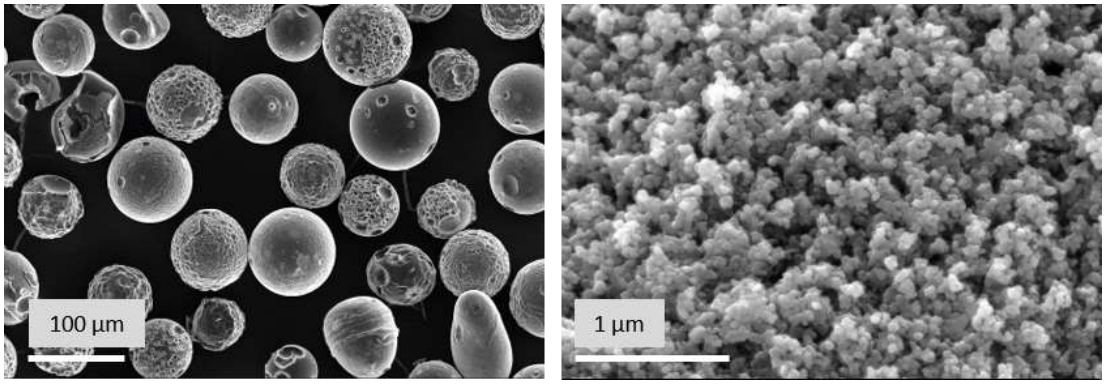

Figure 4-33: SEM images of the CPG beads with pore sizes of 52 nm and pore volume of 1.5 $cm^3 \cdot g^{-1}$ with different magnifications: x500 (left), x80000 (right).

Nitrogen physisorption isotherms of the transformation products using 35 %, 48 % and 100 % of the C_{16}TAOH solution at 100 °C for four days are shown in Figure 4-34.

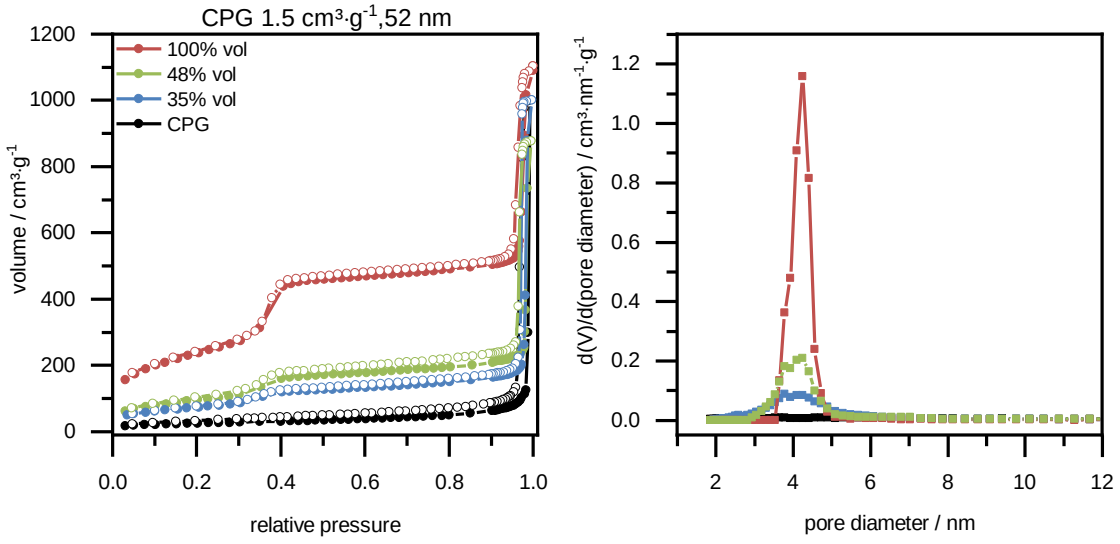

Figure 4-34: Physisorption isotherms (N_2, 77 K) after pseudomorphic transformation of CPG with 1.5 $cm^3 \cdot g^{-1}$ and 52 nm pore diameter with variation of the volume of C_{16}TAOH solution. The respective pore diameter distributions, shown on the right, are calculated with NLDFT kernel for silica with cylindrical pores from the adsorption branch.

A first step in the relative pressure range of 0.35–0.4, as in the type IVb isotherms, indicates mesopores smaller than 4 nm. A second step at higher relative pressures gives evidence of larger mesopores around 52 nm, as in the case of the starting material. With the highest volume of C_{16}TAOH solution a specific BET surface area of 857 $m^2 \cdot g^{-1}$ is generated whereas the specific surface areas of the other materials are 267 $m^2 \cdot g^{-1}$ and 356 $m^2 \cdot g^{-1}$, respectively. These values are significantly lower than in previously mentioned samples with 168 nm initial macropore size, where a specific BET surface area of 966 $m^2 \cdot g^{-1}$ was generated with 100 % of the C_{16}TAOH solution (for a detailed comparison see Table 4-11).

From the results of partial pseudomorphic transformation of the macroporous sample, stepwise shrinking of the initial pore system is expected, but this is not observed in this case. Apparently, the partial transformation follows the mechanism that is visualized in Figure 1-12. In the case of small macropores, the initial macropore collapses during the transformation process and does not shrink stepwise, as is the case for larger initial macropores. The collapse of the pore causes inclusions of the initial mesopore system, so that even 100 % of the C_{16}TAOH solution is not sufficient for a complete transformation of the whole CPG body, and residues of the initial macropore system are still accessible to physisorption.

Table 4-15 gives an overview of the specific BET surface area and maximum pore diameter of the samples. The transformation degree is calculated analogously to the previously mentioned materials, using the sample with 100 % of C_{16}TAOH volume as the basis. Additionally the pore volume was calculated with the help of NLDFT kernel for silica with cylindrical pores. In order to distinguish between the pore volume of the newly formed mesopores and the initial pore system, the pore volume is determined for pores smaller and larger 20 nm, respectively.

Table 4-15: Summary of the textural data of pseudomorphic transformations with different volumes of C_{16}TAOH solution.

Sample	**C_{16}TAOH / Si ratio**	**S_{BET} / $m^2 \cdot g^{-1}$**	**$d_{N_2, NLDFT}$ / nm**	**V_{NLDFT, N_2} / $cm^3 \cdot g^{-1}$**		**Transformation degree**
				<20 nm	>20 nm	
CPG 1.5 $cm^3 \cdot g^{-1}$ 52 nm	–	87	–	0.08	022	–
35 % volume	0.07	267	4.1	0.20	0.80	0.31
48 % volume	0.09	356	4.1	0.28	0.56	0.42
100 % volume	0.19	857	4.2	0.67	0.88	1.0

The transformation time was also varied for this CPG batch between 1 hour and four days, using 100 % of the C_{16}TAOH solution at 100 °C. The nitrogen physisorption isotherms are shown in Figure 4-35 next to the respective pore diameter distributions.

The shape of the isotherms is similar to the examples mentioned previously and has already been discussed here. However, the variation of time allows a stepwise increase of the transformation degree. This confirms the results from the other CPG batch with larger macropores.

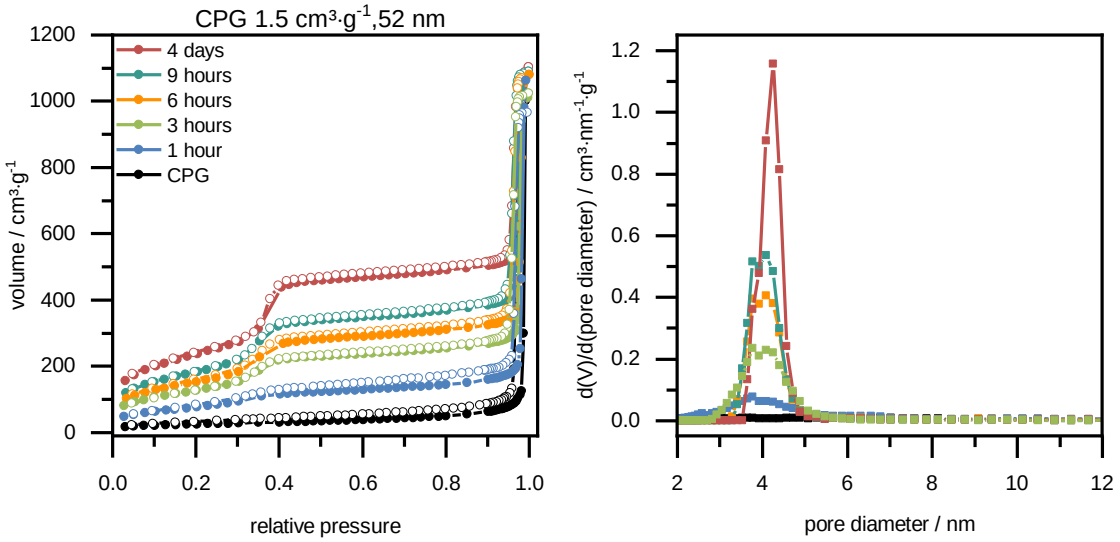

Figure 4-35: Physisorption isotherms (N_2, 77 K) after pseudomorphic transformation of CPG with 1.5 $cm^3 \cdot g^{-1}$ and 52 nm pore diameter with variation in transformation time. The respective pore diameter distributions, shown on the right, are calculated with NLDFT kernel for silica with cylindrical pores from adsorption branch.

Table 4-16 gives an overview of the specific surface areas, the pore diameter and the transformation degree of the pseudomorphically transformed samples starting with CPG beads with 52 nm pore diameter.

Table 4-16: Summary of specific BET surface area and pore diameter of materials after pseudomorphic transformations for different times starting with a material with 52 nm macropores.

Sample	S_{BET} / $m^2 \cdot g^{-1}$	$d_{N_2, NLDFT}$ / nm	$V_{N_2, NLDFT}$ / $cm^3 \cdot g^{-1}$		Transformation degree
			<20 nm	>20 nm	
CPG 1.5 $cm^3 \cdot g^{-1}$ 52 nm	87	-	0.08	0.22	–
1 hour	296	3.9 nm	0.18	0.67	0.35
3 hours	479	4.0 nm	0.32	1.14	0.56
6 hours	569	4.0 nm	0.41	1.01	0.66
9 hours	677	4.0 nm	0.48	1.10	0.79
4 days	857	4.1 nm	0.67	0.88	1.0

The P-XRD patterns (Figure 4-36)of all materials that were obtained by pseudomorphic transformation, starting with CPG beads with 52 nm macropore size, show reflection at 2θ = 1.9° which corresponds to a *d*-spacing of 4.5 nm, just as the previously mentioned CPG samples which were pseudomorphically transformed using C_{16}TAOH as the templating surfactant. Additional broad reflections between 2θ = 3–5 ° are only visible for the sample which was treated for four days with 100 vol% of C_{16}TAOH solution.

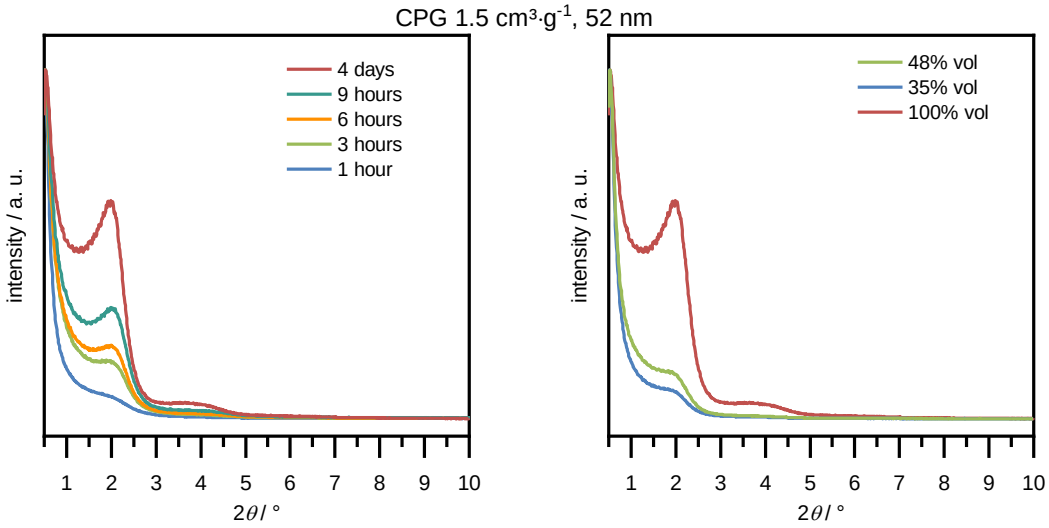

Figure 4-36: P-XRD patterns of CPG (1.5 $cm^3 \cdot g^{-1}$ pore volume, 52 nm initial pore size) after pseudomorphic transformation for different time with 100 % of the volume of C_{16}TAOH solution (left) and after treatment for four days with different volumes of C_{16}TAOH solution (right).

Figure 4-37 summarizes how the variation of one of the three parameters affect the transformation degree.

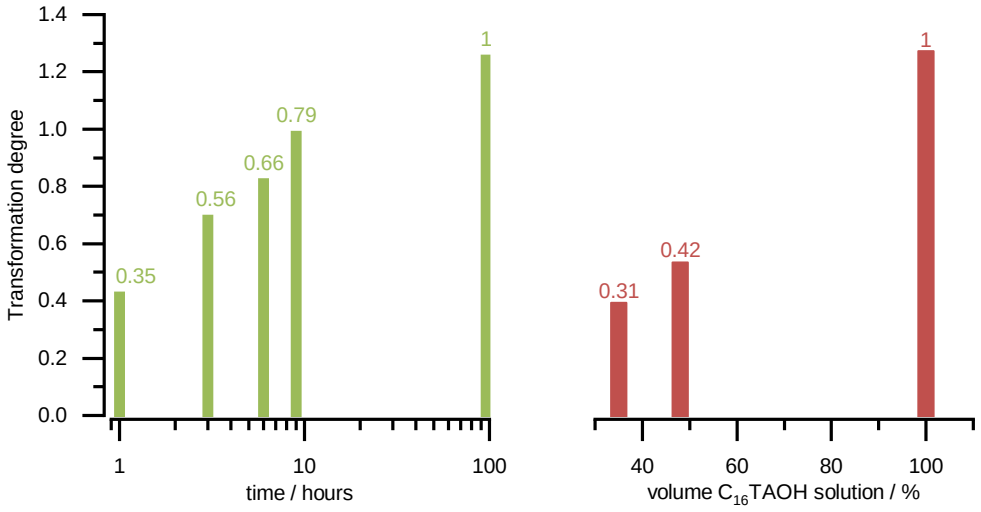

Figure 4-37: Summary of the transformation degrees that result from pseudomorphic transformation of CPGs with 1.5 $cm^3 \cdot g^{-1}$ pore volume and 52 nm pore diameter, under variation of either the time (green, left) or the volume of C_{16}TAOH solution (red, right).

Changeability of the mesopore size – proof of principle

It is worth noting that the size of the generated mesopores during pseudomorphic transformation of CPG beads can be changed just as is the case in common MCM-41 synthesis. By using C_{10}TAB, a surfactant with a shorter alkyl chain, smaller pores were generated than in the previously mentioned samples with C_{16}TAB. The CPG beads that were used as the starting material for this approach also showed pores around 50 nm. Under conditions similar to the transformation using C_{16}TAB, a material with pore diameter of 2.8 nm is obtained. This is in good accordance with the literature where the pore size was reduced to 3.2 nm with C_{12}TAOH.[37] The pore size distribution and the physisorption isotherm are given in Figure 4-38. The isotherm is of type IVb. The determination of the *apparent* specific BET surface area is difficult for materials with pores in this size range as pore condensation takes place in the pressure range where the specific BET surface area is usually determined(for explanation see footnote 2 on page 75). Due to this, the relative pressure range before the pore condensation is considered (here p/p^0 = 0.021–0.098) which might lead to an underestimation of the *apparent* specific BET surface area. The determined *apparent* specific BET surface area is 632 $m^2 \cdot g^{-1}$.

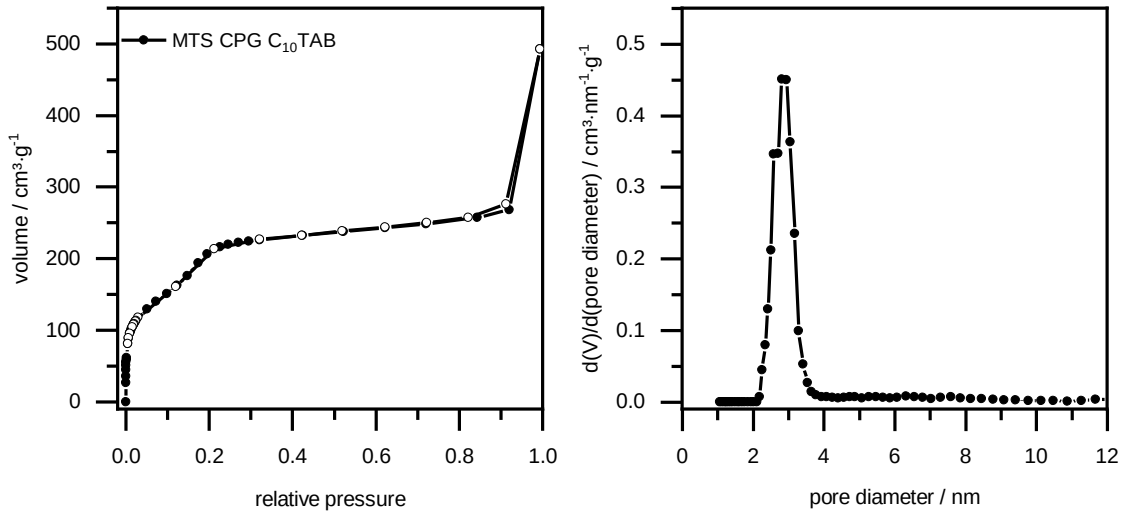

Figure 4-38: Physisorption isotherm (N_2, 77 K) of CPG after pseudomorphic transformation with C_{10}TAB and the respective pore diameter distribution (calculated from the adsorption branch using the NLDFT kernel for silica with cylindrical pores) on the right.

The respective P-XRD pattern is given in Figure 4-39. In comparison to the materials that were transformed with C_{16}TAOH the main reflection is shifted to 2θ = 2.8° (*d*-spacing = 30.7 Å).

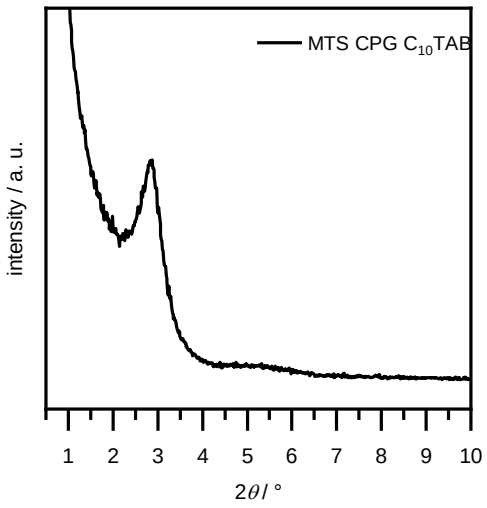

Figure 4-39: P-XRD pattern of the small angle scattering range of CPG treated with C_{10}TAB.

Therefore, the adjustability of the mesopore size down to pores of 2.8 nm from pseudomorphic transformation is proven.

Microwave-assisted pseudomorphic transformation

There are different examples of microwave-assisted ordered mesoporous silica and PMO syntheses in the literature.[234–236] Here, pseudomorphic transformation approaches were carried out in the microwave in order to take advantage of the reduced synthesis time. Another batch of CPG was used in this synthesis with 1.7 $cm^3 \cdot g^{-1}$ pore volume and 173 nm macropore size. The pseudomorphic transformation was carried out under slightly different conditions as mentioned previously using C_{16}TAB and sodium hydroxide solution with a concentration of 0.1 $mol \cdot L^{-1}$ instead of 0.08 $mol \cdot L^{-1}$, which causes a pH value of 13.0 with 40 mL per 1.0 g of silica at 100 °C. The conditions were changed because the C_{16}TAOH solutions, which were prepared in high volumes due to the ion exchange procedure, show aging phenomena, by contrast no negative impact due to the presence of sodium could be observed in these synthesis series. Additionally, the mixture of C_{16}TAB and sodium hydroxide solution allows the variation of the surfactant and the pH value independently.

The CPG were first transformed under classical conditions as reference materials. The physisorption isotherms and pore diameter distributions of these samples are given in Figure 4-40. The shape of the isotherms is of type IVb as expected for all samples.

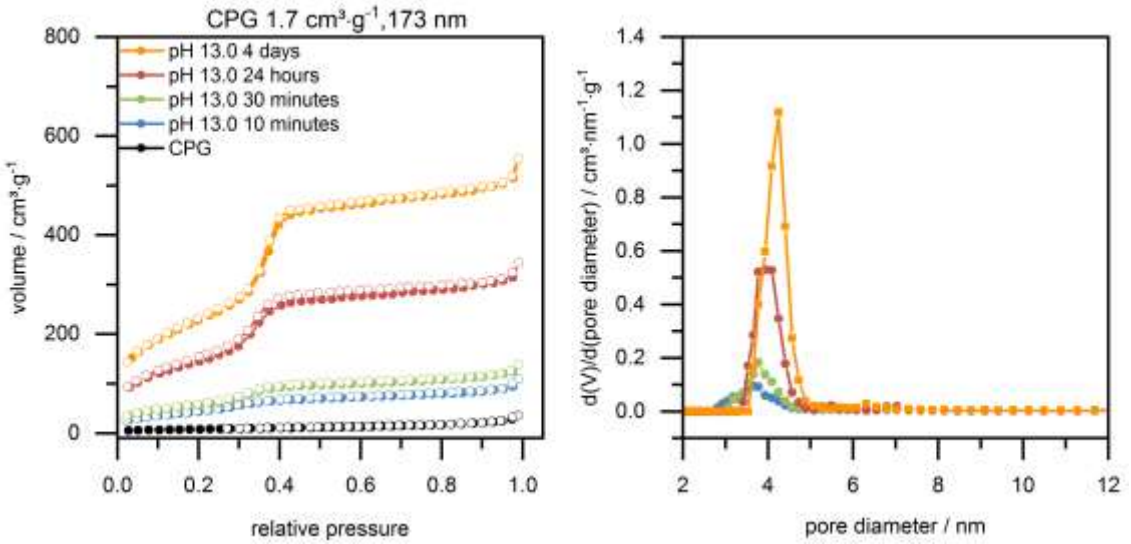

Figure 4-40: Physisorption isotherms (N_2, 77 K) of CPG after transformation in CTAB/NaOH solution (pH 13.0) for different times on the left, the respective pore size distributions (calculated with NLDFT kernel for silica with cylindrical pores from the adsorption branch) are shown on the right.

As expected from the previous results, no significant increase of the specific BET surface area was generated by 10 or 30 minutes of treatment (175 $m^2 \cdot g^{-1}$ and 222 $m^2 \cdot g^{-1}$, respectively), but a stepwise increase of the specific surface area was obtained with increasing transformation time. The transformation of 4 days lead to a specific BET surface area of 847 $m^2 \cdot g^{-1}$ and was set as the basis to calculate the transformation degree for the other samples. The values of the transformation degree are listed in Table 4-17 as well as the specific BET surface areas and pore diameter maxima of both samples that were treated under classical conditions and the microwave-assisted samples.

Figure 4-41 visualizes the temperature program for pseudomorphic transformation in the microwave. Due to the short synthesis time, the phase of heating up and cooling down are of particular importance for the synthesis. For this reason, the synthesis time was set to zero minutes in one sample and all samples were immediately filtered at 70 °C and were not cooled down to room temperature.

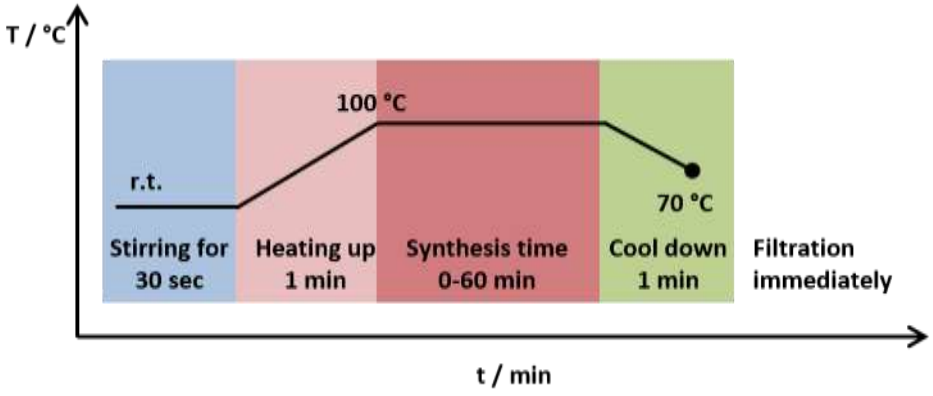

Figure 4-41: Temperature program of the pseudomorphic transformation in the microwave.

Figure 4-42 shows the physisorption isotherms (only the adsorption branches for better clarity) and the pore diameter distributions of the materials that were treated in the microwave in comparison to the material that was treated under classic conditions for four days.

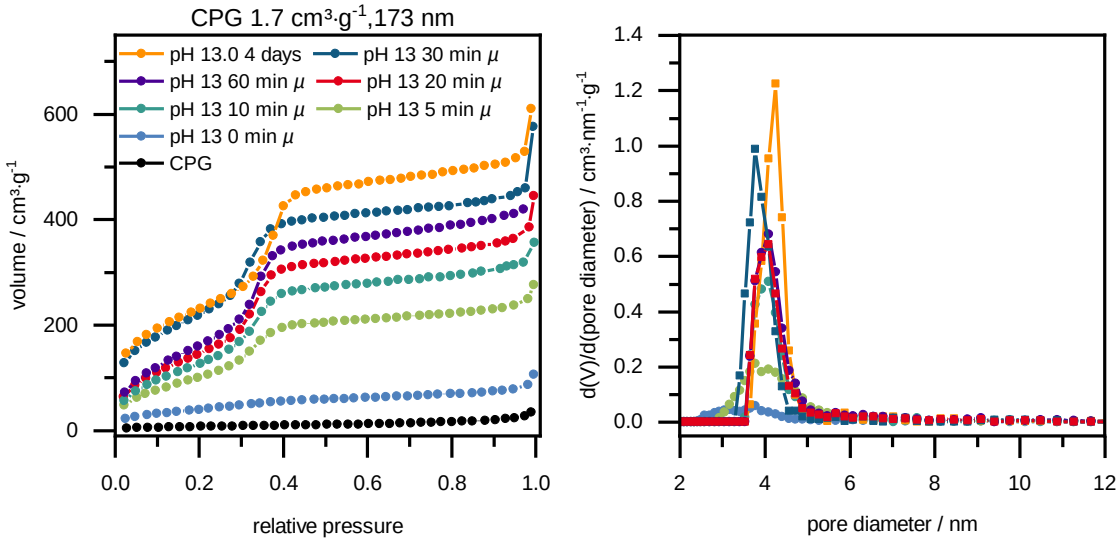

Figure 4-42: Physisorption isotherms (N_2, 77 K, only the adsorption branches for better clarity) after pseudomorph transformation in the microwave in comparison to the sample that was transformed for four days under classical conditions. The respective pore diameter distributions (calculated with NLDFT kernel for silica with cylindrical pores from the adsorption branch) are shown on the right.

By heating up to 100 °C and cooling down to 70 °C and 0 minutes of transformation time, the specific BET surface area was already increased to 155 $m^2 \cdot g^{-1}$. After 30 minutes it is 877 $m^2 \cdot g^{-1}$ and after 60 minutes it decreases again to 706 $m^2 \cdot g^{-1}$, so that maximum transformation is assumed after 30 minutes. A similar phenomenon of decreasing specific BET surface area has already been discussed concerning the samples that were treated with C_{16}TAOH solution for four and seven days starting with a CPG batch with 1.5 $cm^3 \cdot g^{-1}$ pore volume and 168 nm pore diameter (compare Table 4-12). Therefore, this effect is not random. There seems to be a limitation of the transformation degree that cannot be exceeded with a longer synthesis time on the one hand, while on the other hand, the decomposition of the material over time seems to be reproducible. However, the mechanism for the decomposition is not explained at this point. After 30 minutes pores with a maximum diameter of 3.9 nm are generated which is smaller than for all the other samples. The textural data is summarized in Table 4-17.

Table 4-17: Summary of the specific BET surface areas, mesopore volume (pores smaller 20 nm) and pore diameters (calculated with NLDFT kernel for silica with cylindrical pores from the adsorption branch) as well as of the transformation degrees of samples that were treated with a solution of pH 13.0 under classical conditions and in the microwave (μ-wave)

Sample	S_{BET} / $m^2 \cdot g^{-1}$	d_{NLDFT, N_2} / nm	V_{NLDFT, N_2} / $cm^3 \cdot g^{-1}$	Transformation degree
CPG 1.7 $cm^3 \cdot g^{-1}$ 173 nm	27	–	0.03	–
10 minutes	175	3.8	0.13	0.21
30 minutes	222	3.7	0.17	0.26
24 hours	547	4.0	0.45	0.65
4 days	841	4.2	0.74	1.00
0 minutes, μ-wave	155	4.0	0.11	0.18
5 minutes, μ-wave	441	4.2	0.34	0.52
10 minutes, μ-wave	561	4.2	0.44	0.66
20 minutes, μ-wave	626	4.2	0.53	0.74
30 minutes, μ-wave	877	3.9	0.64	1.03
60 minutes, μ-wave	706	4.2	0.60	0.83

All isotherms are of type IVb as expected, but isotherms of samples which were treated in the microwave for between 10 and 30 minutes show a second steep step in the adsorption branch in a relative pressure range of over 0.95, which is caused by interparticle voids. Since this abrupt volume uptake significantly distort the NLDFT data fit over the whole pressure range, only the measurement points in the relative pressure range up to 0.9 were considered for the determination of the pore diameter in these cases. This led to a better fit of the condensation step in the isotherm by the NLDFT kernel and to reasonable results for the pore diameter distribution. Uhlig *et al*. might have faced similar challenges since they decided to use the BJH method for the determination of the pore diameter distribution from an isotherm which showed a similar second steep step at high relative pressure due to the presence of large mesopores (compare with Figure 1-11).[38] Here, the use of another method was avoided in order to ensure the comparability of the results of all approaches. For the same reason the pore volume was calculated with the help of NLDFT kernel for silica with cylindrical pores only for pores smaller 20 nm. The P-XRD patterns of the materials that were treated at pH 13.0 under classical conditions and in the microwave are in accordance with the other materials, see Figure 4-43, with one reflection at 2θ = 1.9° (*d*-spacing of 4.5 nm) and additional broad reflections between 2θ = 3–5 °, so that classification of the mesophase is not possible here neither.

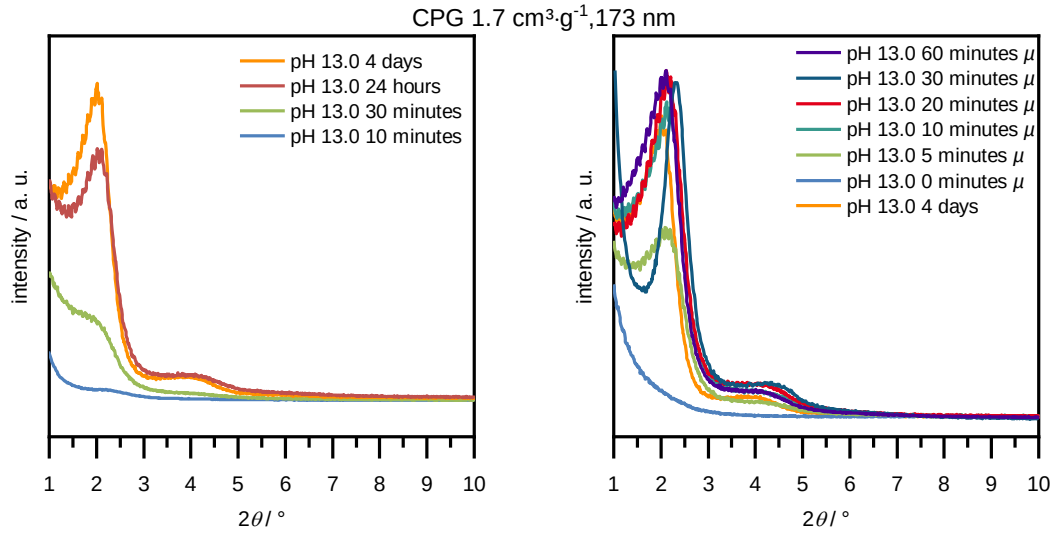

Figure 4-43: P-XRD patterns of the materials that were treated for different times at pH 13.0 under classical conditions (left) and those that were treated in the microwave for different times (right).

Figure 4-37 compares the transformation degree of the samples that were treated conventionally and those treated under microwave irritation.

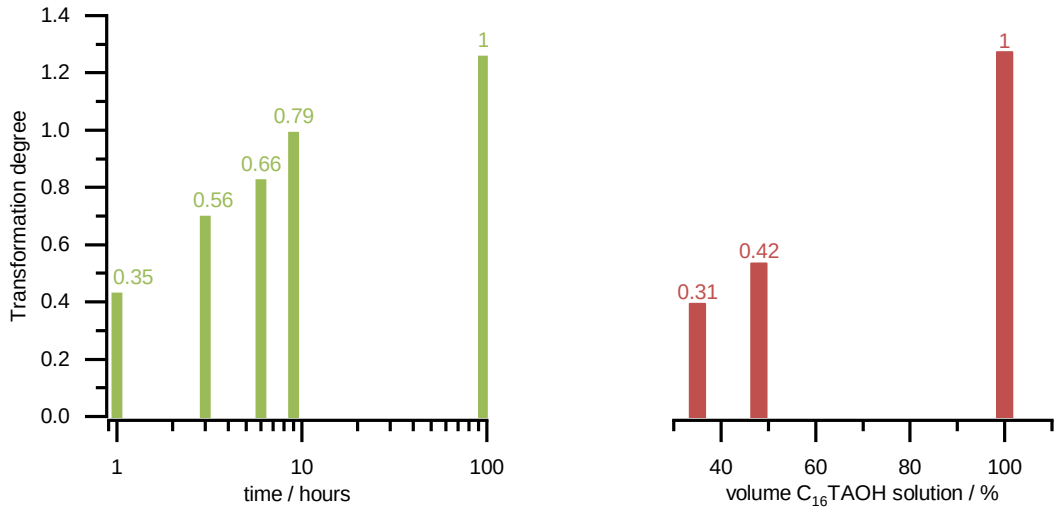

Figure 4-44: Summary of the transformation degrees that result from pseudomorphic transformation of CPGs with 1.7 $cm^3 \cdot g^{-1}$ pore volume and 173 nm pore diameter, under conventional treatment (green, left) and treatment under microwave irritation (red, right).

In summary, the microwave-assisted syntheses decrease the transformation time significantly so that a similar transformation degree is obtained after 24 hours under classical conditions and 20 minutes in the microwave, and maximum transformation is given after 4 days under classical conditions or 30 minutes in the microwave.

4.3 Organosilica/silica hybrid materials

4.3.1 Trial for the exchange of silica versus organosilica during pseudomorphic transformation

In order to combine the advantages of nanoporous organosilica materials with those of CPG, the intention was to incorporate bis-silylated organosilica into the silica network during pseudomorphic transformation. As explained in detail in section 1.4, the pseudomorphic transformation of silica involves two processes: the dissolution of silica in alkaline media and its re-precipitation in the presence of a surfactant. Here, the precipitation of organosilica is intended instead. A diagram showing this approach is shown in Figure 4-45.

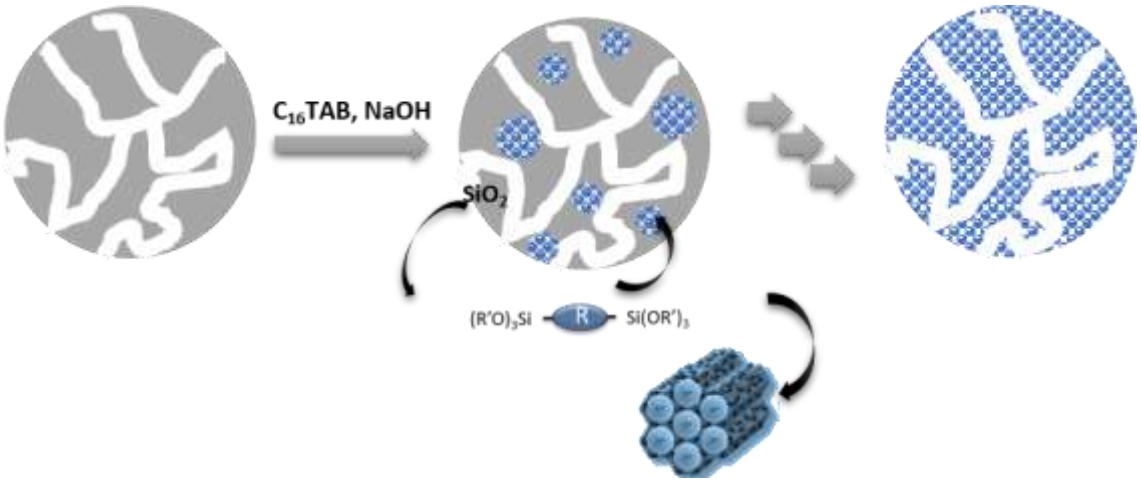

Figure 4-45: First approach for the incorporation of organosilica into a silica matrix by pseudomorphic transformation. Silica is dissolved in an alkaline solution and subsequently replaced by the composite of a bis-silylated organosilica and the surfactant. After a while the whole CPG bead is exchanged into an organosilica bead.

The approach is based on the observation that PMO syntheses require much higher pH values than the pseudomorphic transformation of silica. Therefore, it was attempted to find suitable conditions under which silica remains dissolved whereas organosilica, e.g. BTEB, condenses. The condensation of BTEB has to be delayed in order to prevent the formation of a separate phases of organosilica next to the silica.

For a better understanding of these processes, the condensation behavior of organosilica and the etching behavior of silica from CPG were first studied.

The following synthesis series was based on a standard B-PMO synthesis from Bion *et al.*[237]

The typical synthesis mixture had a molar composition of BTEB/C_{16}TAB/NaOH/H_2O of 1.00/0.96/4.86/531 which corresponds to pH 13.7. The mixture was stirred at room temperature before the hydrothermal treatment at 100 °C. In a first synthesis series, the concentration of sodium hydroxide was varied between 0.01 mol·L^{-1} and 0.4 mol·L^{-1}, corresponding to pH values

from 12.0 to 13.8. At pH 13.8 the yield was insufficient for further characterization, whereas the yield increased further with decreasing pH values. Figure 4-46 shows the respective isotherms of the materials.

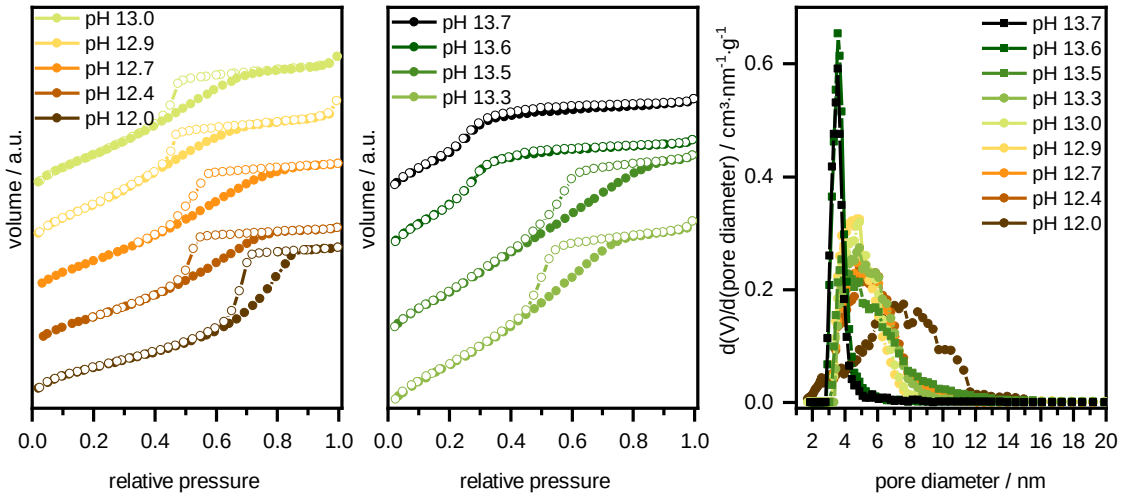

Figure 4-46: Physisorption isotherms (N_2, 77 K) of B-PMOs synthesized at different pH values. The respective pore diameter distributions (calculated with NLDFT, kernel for silica with cylindrical pores from the adsorption branch) are plotted on the right.

The specific BET surface areas exceed 700 $m^2 \cdot g^{-1}$ for all materials. The isotherms of the samples that were synthesized at pH 12 to 13.5 show hystereses which are characterized by steep desorption in all cases indicating a desorption process of interconnected pores where large pore bodies empty through smaller pores with narrower pore diameter, as in type H2(a) hysteresis. The pore diameter distribution, calculated with NLDFT kernel from the adsorption branch for silica with cylindrical pores, is shown on the right in Figure 4-46. In accordance with the course of the isotherms, the pore size distribution of the samples obtained at pH 13.5 or lower is broad. This indicates that additional pores are formed which do not result from the templating process or the condensation of the organosilica phase is insufficient to cast the template.

In contrast to this, the isotherms of the materials which were synthesized at pH 13.6 and pH 13.7 are of type IV(b) and do not show any hysteresis. The pore size distribution is narrow with pores of 3.6 nm. The porosity which includes the pore size distribution was chosen for the evaluation of the synthesis conditions. Hence, only the highest pH values are suitable for B-PMO synthesis. The pore volume decreases by half with increasing pH value from 12 to 13.7 which reinforces the theory of additional pores in the materials which were synthesized at lower pH value. The exact values for the specific BET surface area, the pore volume and the pore size (both calculated with NDFT from the adsorption branch for silica with cylindrical pores), as well as the precipitate mass is given in Table 4-18.

Table 4-18: Overview of the precipitate weight, the specific BET surface areas, the pore diameter and the pore volume (both calculated from the adsorption branch using NLDFT kernel for silica with cylindrical pores) from B-PMO synthesis at different pH values, with surfactant.

Sample	c_{NaOH} / mmol·L^{-1}	amount / mg	*apparent* S_{BET} / m²·g^{-1}	d_{NLDFT, N_2} / nm	$V_{DFT, ads}$ / cm³·g^{-1}
pH 13.8 C_{16}TAB	600	9	–	–	–
pH 13.7 C_{16}TAB	500	25	768	3.5	0.49
pH 13.6 C_{16}TAB	400	62	859	3.5	0.58
pH 13.5 C_{16}TAB	300	126	880	3–15	0.87
pH 13.3 C_{16}TAB	200	148	850	3–10	0.87
pH 13.0 C_{16}TAB	100	161	915	3–10	0.85
pH 12.9 C_{16}TAB	75	154	958	3–10	0.85
pH 12.7 C_{16}TAB	50	158	845	3–12	0.88
pH 12.4 C_{16}TAB	25	138	769	3–10	0.80
pH 12.0 C_{16}TAB	10	200	738	2–15	1.00

The synthesis of B-PMO was repeated under the same conditions without a surfactant. Precipitates were only obtained in the pH range of 13.3 to 13.6. The respective isotherms are shown in Figure 4-47. All products show microporosity and the *apparent* specific BET surface area decreased with the increasing pH of the reaction mixture. The textural data are given in Table 4-19.

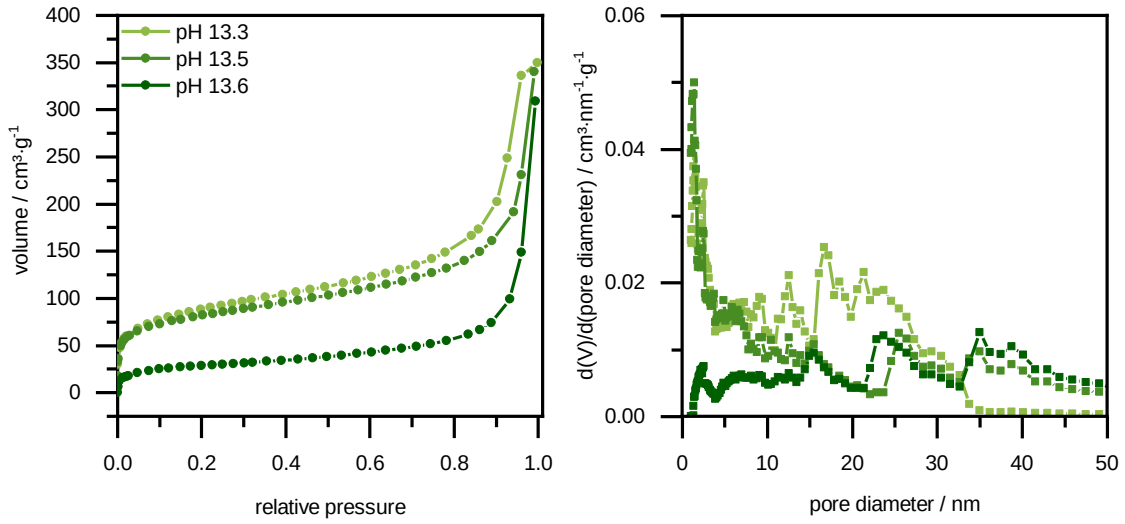

Figure 4-47: Physisorption isotherms (N_2, 77 K) of B-PMOs synthesized at different pH values without surfactant. The respective pore diameter distributions (calculated with NLDFT, kernel for silica with cylindrical pores from the adsorption branch) are plotted on the right.

It has to be considered that the sample amount was not sufficient for reliable measurements in the case of the samples which were synthesized at pH 13.3 and pH 13.5. The respective entries are marked with an asterisk in Table 4-19.

Table 4-19: Overview of the precipitate weight, the specific BET surface areas, the pore diameter and the pore volume (both calculated from the adsorption branch using NLDFT kernel for silica with cylindrical pores) from B-PMO synthesis at different pH values without surfactant. Entries marked with an asterisk (*) denote values from isotherms which were measured with insufficient sample amount.

Sample	amount / mg	*apparent* S_{BET} / $m^2 \cdot g^{-1}$	$V_{NLDFT, ads}$ / $cm^3 \cdot g^{-1}$
pH 13.8	0	–	–
pH 13.7	0	–	–
pH 13.6	57	104*	0.40*
pH 13.5	40	290*	0.48*
pH 13.3	90	312	0.52
pH 13.0	0	–	–
pH 12.9	0	–	–
pH 12.7	0	–	–
pH 12.4	0	–	–
pH 12.0	1	–	–

To study the etching behavior of CPG, beads of 40–100 µm in diameter with a pore volume of 1.1 $cm^3 \cdot g^{-1}$ and a pore size of 52 nm in diameter were used. The morphology of the beads is shown in Figure 4-48.

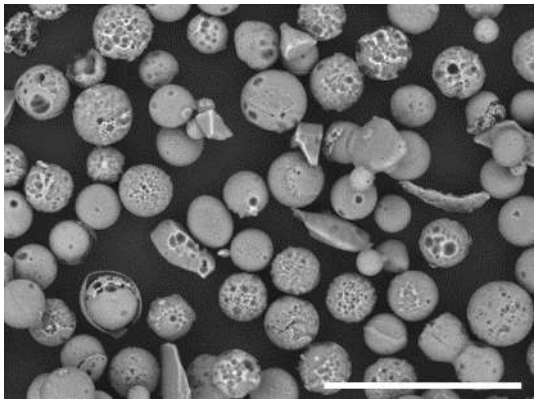

Figure 4-48: SEM image of the CPG batch which was used for the study of etching behavior (without carbon sputtering).

Etching of the CPG beads was carried out using the same C_{16}TAB concentration as in the B-PMO syntheses at pH 12.0 to 14.0 for 24 hours and for four days. Table 4-20 gives an overview of the sample amount, the specific BET surface area as well as the pore diameter distribution and the pore volumes, both calculated from the adsorption branch using NLDFT kernel for silica with cylindrical pores.

Table 4-20: Overview of the specific BET surface areas, the pore volume and the pore diameter (both calculated form the adsorption branch with NLDFT kernel for silica with cylindrical pores) for CPG etching at different pH values with C_{16}TAB for one or four days. Entries marked with an asterisk (*) denote values from isotherms which were measured with insufficient sample amount.

Samples w/ CTAB	c_{NaOH}/ mol·L^{-1}	amount / mg	*apparent* S_{BET} / m²·g^{-1}	$d_{NLDFT, ads}$ / nm	$V_{(<20\ nm)NLDFT, ads}$ / cm³·g^{-1}	$V_{(>20\ nm)NLDFT, ads}$ / cm³·g^{-1}
1 day						
pH 14.0	1.0	0	–	–	–	–
pH 13.5	0.3	17	–	–	–	–
pH 13.0	0.1	109	514	3.6	0.34	0.21
pH 12.5	0.12	95	234	4.2	0.21	0.40
pH 12.0	0.01	95	89*	–	0.07*	0.45*
4 days						
pH 14.0	1.0	0	–	–	–	–
pH 13.5	0.3	0	–	–	–	–
pH 13.0	0.1	5	–	–	–	–
pH 12.5	0.12	85	109	4.2	0.08	0.19
pH 12.0	0.01	81	36*	–	0.03*	0.20*

After one day of treatment at pH 14.0, the CPG were completely dissolved, whereas a small residue with undefined morphology was obtained at pH 13.5. At pH 13.0 and 12.5 CPG beads with a mesopore system were obtained so that successful pseudomorphic transformation can be assumed. However, after four days of treatment at pH 13.0, the beads were completely dissolved. This corresponds well with results in section 4.2, where the common pH value for pseudomorphic transformation of CPG is 12.8. The specific BET surface area increase with increasing pH value which is in accordance to the literature where the pH value was varied by the variation of C_{16}TAOH/(C_{16}TAOH+C_{16}TAB) in solution as has been mentioned earlier.[38] By contrast, it was unexpected that the specific BET surface area is smaller after treatment with the surfactant for four days. There is no reasonable explanation for this trend, but it has to be kept in mind that the treatment was not repeated so that these samples might be not representative. The morphology of the samples which are not completely dissolved, did not change after treatment for four days, see the SEM images in the Appendix Figure 9-7.

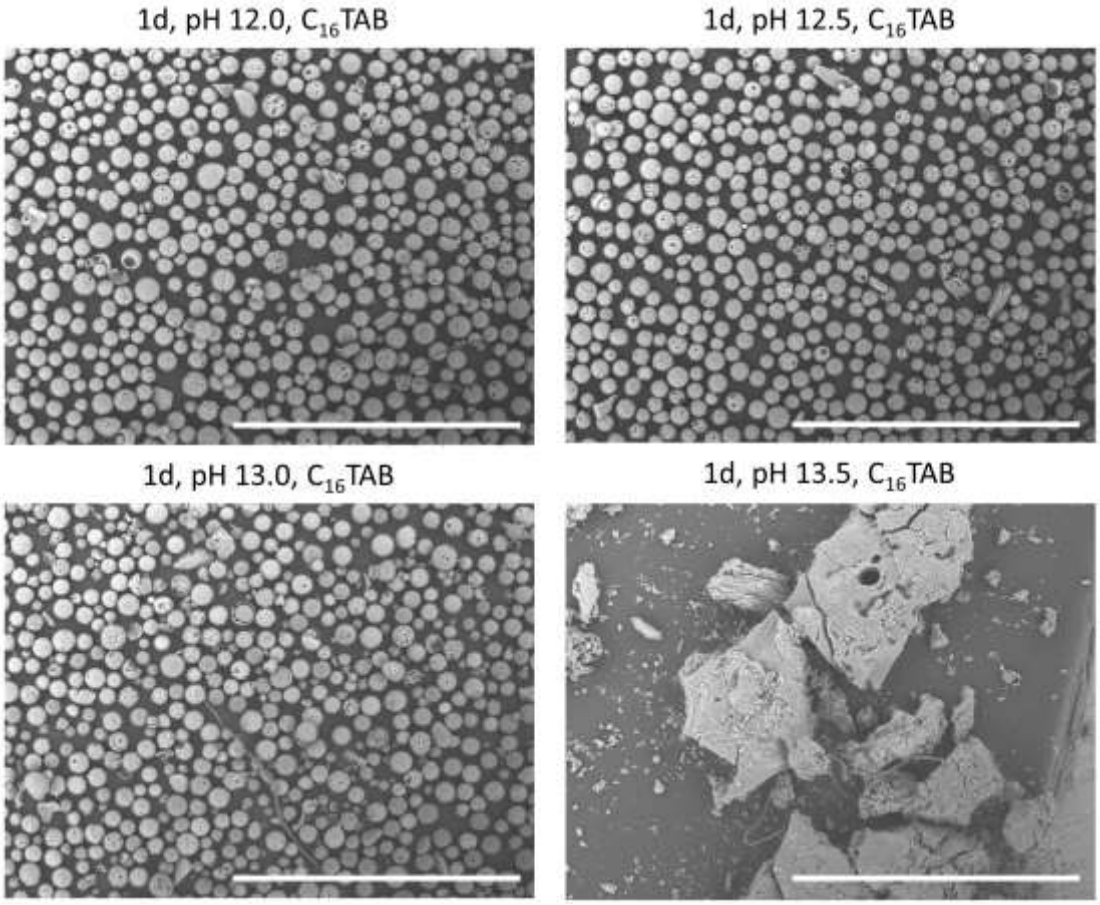

Figure 4-49: SEM images of products from CPG beads etching at different pH values with C_{16}TAB (magnification x100, scale bar of 1.0 mm). Samples without carbon sputtering.

The isotherms of the samples are given in Figure 4-50 as well as the pore diameter distribution according to NLDFT kernel for silica with cylindrical pores calculated from the adsorption branch.

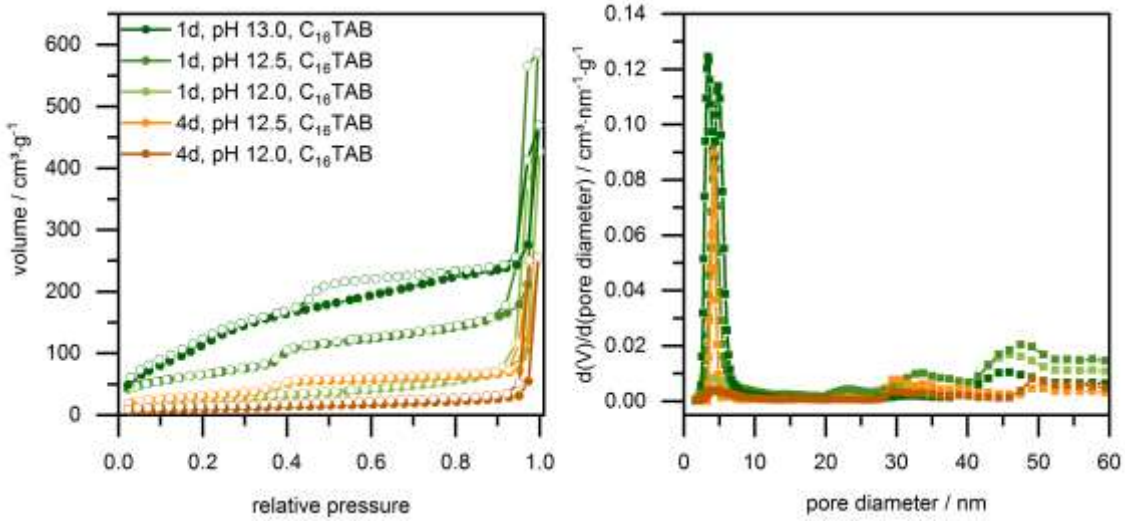

Figure 4-50: Physisorption isotherms (N_2, 77 K) of CPG etching at different pH values with C_{16}TAB. The respective pore diameter distributions (calculated with NLDFT, kernel for silica with cylindrical pores from the adsorption branch) are plotted on the right.

Just as the syntheses of B-PMO, CPG etching was repeated under the same conditions without a surfactant. The treatment did not affect the morphology of the beads, SEM images are given in

the Appendix Figure 9-6. With respect to the yield, the CPG etching showed the same trend as in the syntheses with surfactant, but the products were not porous, since the amount of the samples was insufficient for the measurement of reliable isotherms, those are not shown here. However, Table 4-21 summarizes the textural data of the respective samples.

Table 4-21: Overview of synthesis conditions and specific BET surface areas for etching of CPG at different pH values without surfactant for one or four days. Entries marked with an asterisk (*) denote values from isotherms which were measured with insufficient sample amount.

Samples w/o CTAB	amount / mg	*apparent* S_{BET} / $m^2 \cdot g^{-1}$	Samples w/o CTAB	amount / mg	*apparent* S_{BET} / $m^2 \cdot g^{-1}$
1 day			**4 days**		
pH 14.0	0	-	**pH 14.0**	0	-
pH 13.5	0	-	**pH 13.5**	0	-
pH 13.0	68	22*	**pH 13.0**	5	-
pH 12.5	81	21*	**pH 12.5**	65	-
pH 12.0	88	22*	**pH 12.0**	0	-

The observed trends of CPG etching and organosilica synthesis at different pH values with and without surfactant, are presented in Figure 4-51. The yield and the porosity were taken into account, where the porosity considers the specific BET surface area as well as the pore diameter distribution as a parameter of the quality of the mesoporous system.

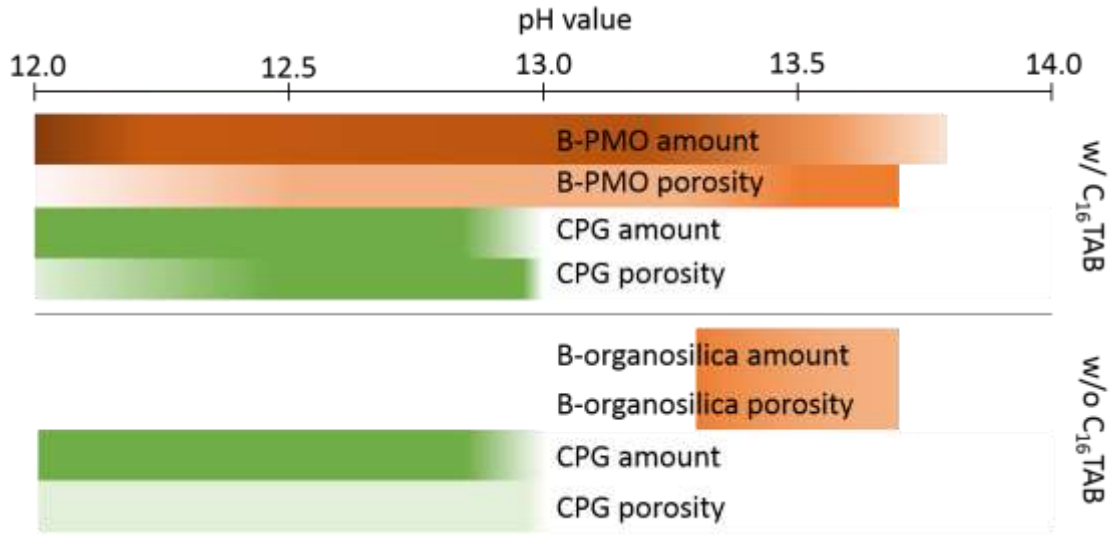

Figure 4-51: Trends in B-PMO syntheses and pseudomorphic transformation of CPG with or without surfactant C_{16}TAB. The parameters yield and porosity are shown.

It is worth noting that the pH range for successful B-PMO synthesis with narrow pore size distribution is pH 13.6-13.7 where the yield is very low. A compromise between these two parameters can be found around pH 13.0. In contrast, the pseudomorphic transformation of CPG is only successful in the pH range 12.5 to 13.0, hence the two processes overlap slightly.

In a first approach, different amounts of BTEB were added to the synthesis mixtures at the typical conditions of pseudomorphic transformation of CPG in C_{16}TAOH solutions at pH 12.8. These syntheses lead to the formation of precipitates with undefined morphology as can be seen in the SEM images in Figure 4-52.

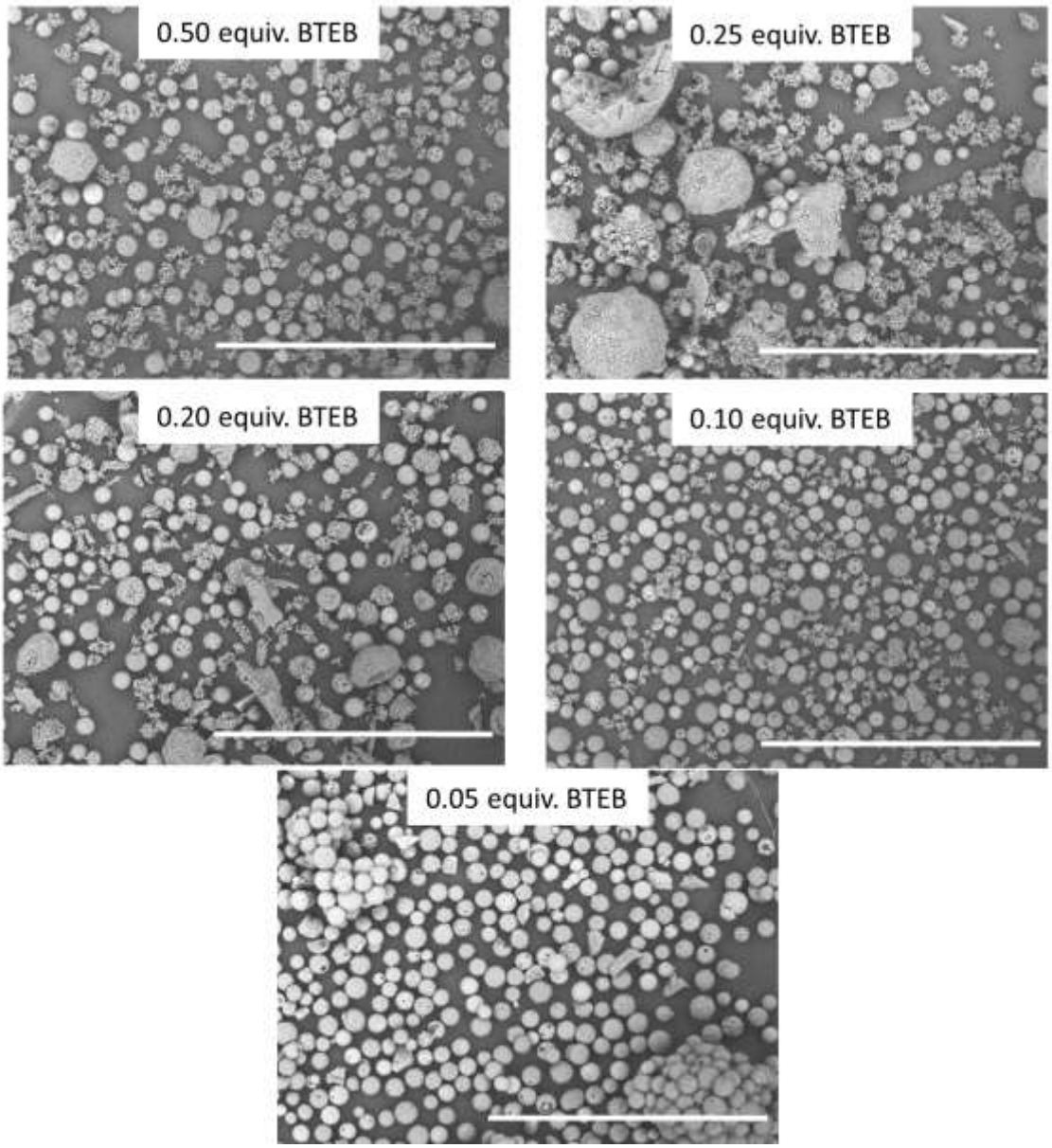

Figure 4-52: SEM images of products from pseudomorphic transformation at pH 12.8 of CPG beads with different amounts of BTEB (magnification x100, scale bar of 1.0 mm). Samples without carbon sputtering.

The initial CPG beads were present in all samples. Additionally, large spherical beads are visible in the images from batches with 0.50 to 0.20 equivalents of BTEB to CPG. The damaged hemisphere in the image from the sample prepared from 0.25 equivalents BTEB suggests that the organosilica phase encases the CPG beads. In the samples that contain only 0.10 equivalent BTEB, only smaller agglomerates are formed next to the CPG. With 0.05 equivalents of BTEB, the beads seem to be glued together, but no second phase precipitate is visible. This confirms the

interpretation that the second phase is mainly the organosilica phase, whereas the CPG beads remain undamaged in the reaction mixture.

Further approaches were carried out in which either the volume of the solvent was changed or C_{16}TAOH was replaced by C_{16}TAB and sodium hydroxide. Neither parameters changed the results significantly. The second approaches to combine these two processes were done at a sodium hydroxide concentration of 0.5 mol·L^{-1} (pH 13.7), with or without C_{16}TAB under hydrothermal conditions, where B-PMO syntheses were successful and dissolution of CPGs occurs. Figure 4-53 shows the SEM image of the product from hydrothermal treatment at pH 13.7 in the presence of C_{16}TAB. A second phase of undefined morphology with embedded CPG beads is formed. Without the surfactant, no precipitate was obtained.

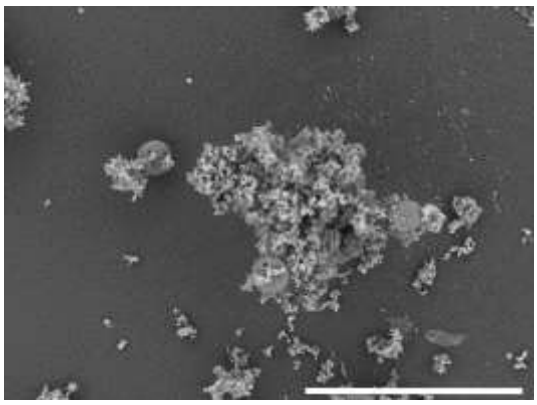

Figure 4-53: SEM image of the product from hydrothermal treatment of CPG together with BTEB at pH 13.7 in the presence of the surfactant C_{16}TAB (magnification x400, scale bar of 200 µm, no carbon sputtering).

In all syntheses it was observed that the reaction mixture turned opaque after the addition of BTEB. This allows for the interpretation that the condensation of the precursor starts immediately in the synthesis mixture, which causes the formation of an unintended second phase. Hence, no exchange of silica for organosilica is possible during the transformation process.

In the following paragraphs, different attempts have been made to delay the condensation process. The behavior of the precursor in solution without surfactant was studied at pH 13.5, pH 13.0 and pH 12.5. Solutions of water with variable volume percentages of 100 vol%, 75 vol%, 50 vol%, 25 vol% and 10 vol%, respectively, of each of methanol, ethanol (99.8 %), isopropyl alcohol and *tert*-butyl alcohol were prepared. BTEB was treated in these solutions under stirring at room temperature, 40 °C and 60 °C and visible turbidity was interpreted as the starting point of the condensation.

The precursor did not dissolve in all solutions which contained 20 vol% or 10 vol% of the alcohol. Therefore, these syntheses were not taken into consideration. Nor were those with *tert*-butyl alcohol, since sodium hydroxide does not dissolve in this case. The synthesis in isopropyl alcohol gave no precipitate at pH 13.5, whereas the solutions at pH 13.0 and pH 12.5 turned opaque

immediately. Consequently, isopropyl alcohol is not a suitable solvent for controlled delay of the condensation of BTEB. In contrast, when focusing on the synthesis in methanol, some differences were noticeable for different temperatures and pH values. Visible turbidity was reached after one hour in solutions with 75 vol% methanol at pH 13.0 and pH 13.5 at room temperature whereas it occurred immediately after addition of BTEB at pH 13.0 at 40 °C. It was not observed in the synthesis at pH 13.5. In contrast to these results, an opaque solution was noticed at 60 °C after 16 hours with 75 vol% methanol at pH 12.5 and pH 13.0, just as in pure methanol at pH 13.0. The other syntheses in pure methanol become opaque quicker. This was the case at pH 13.0 where it occurred after six hours at 40 °C. At pH 12.5 it occurred after one hour at all temperatures in pure methanol. At higher temperatures, the samples at pH 13.5 tend to gel in pure methanol and 75 vol% methanol. In solutions with 50 vol% methanol, no precipitate was obtained at any temperature or pH value. The results from the synthesis in methanol at different temperatures are shown graphically in Figure 4-54.

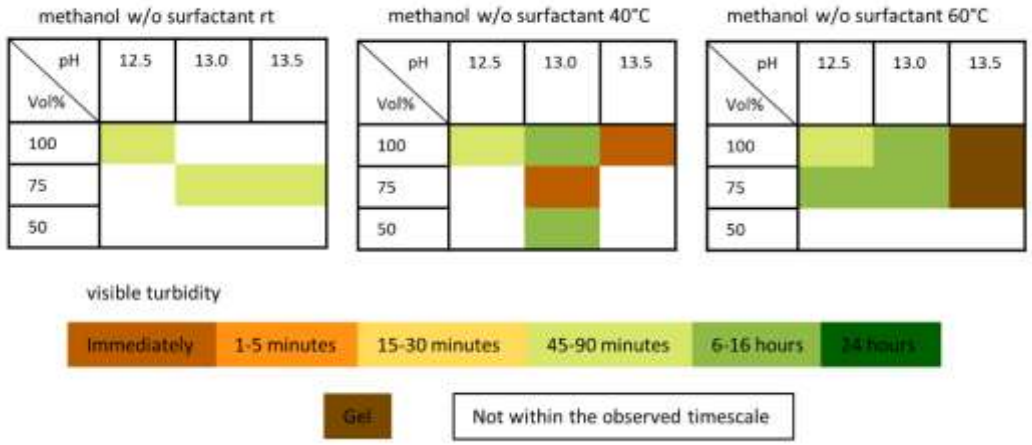

Figure 4-54: Observation of the turbidity of BTEB in methanol solutions without surfactant. The methanol content was varied between 100–50 vol% at pH values between 12.5–13.5. Syntheses were carried out at room temperature (rt), 40 °C and 60 °C. The color code for the time to visible turbidity is given underneath.

The most interesting trends were obtained using ethanol as a solvent. The synthesis with 75 vol% of ethanol showed turbidity as soon as the precursor was added, whereas the solution with 50 vol% of ethanol became clear before turbidity occurred after 20-45 minutes at room temperature or 40 °C. At 60 °C no clear solution was observed as visible turbidity was reached immediately.

In contrast, in pure ethanol (99.8 %), visible turbidity could be delayed to 24 hours in solutions with a pH value of 12.5. At higher pH values, condensation starts after 30–45 minutes. The results concerning the visible turbidity in synthesis in ethanol are shown graphically in Figure 4-55.

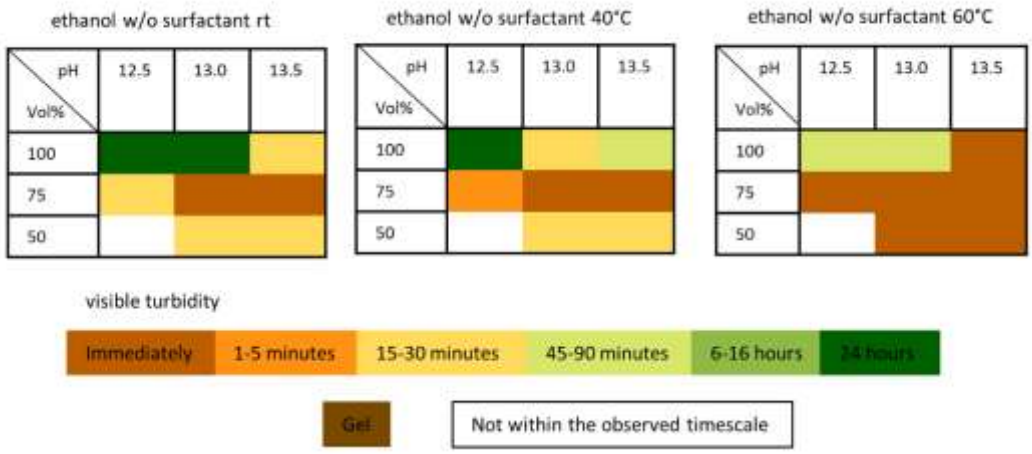

Figure 4-55: Observation of the turbidity of BTEB in ethanol solutions without surfactant. The ethanol content was varied between 100-50 vol% at pH values between 12.5–13.5, syntheses were carried out at room temperature (rt), 40 °C and 60 °C. The color code for the time to visible turbidity is given underneath.

As a result, synthesis conditions were found under which the condensation delay could be controlled. In order to adjust the conditions, the ethanol percentage was varied between 100 vol% and 80 vol% in steps of 5 vol% at room temperature and at 40 °C in another synthesis series. The syntheses were repeated with 0.23 and 2.3 equivalents of C_{16}TAB.

The results of all syntheses are summarized in Figure 4-56. In general, synthesis at pH 12.5 tend to the formation of gels. The visible turbidity was delayed in syntheses with 0.23 equivalents of C_{16}TAB at pH 12.5 and pH 13.5 at room temperature, plus in all syntheses at pH 13.0 in 100 % ethanol.

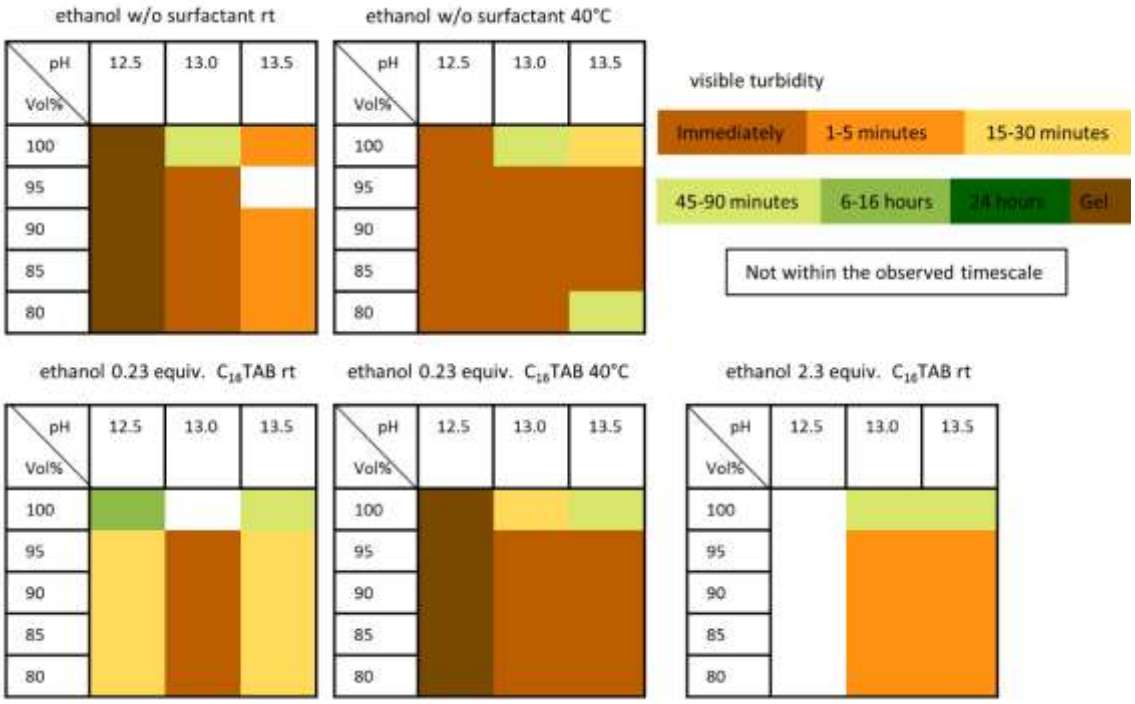

Figure 4-56: Graphical summary of the observation series of the turbidity of BTEB in volumetric mixtures of ethanol in water with and without surfactant at room temperature (rt) and at 40 °C. The color code of the visible turbidity is given on the side.

The insights into the condensation behavior of BTEB in ethanol without additional water were used for further attempts of pseudomorphic transformation of CPG. As the condensation can be delayed at 40 °C and at room temperature the synthesis was carried out at these temperatures. In order to keep the CPG beads intact, pH 13.0 was chosen. In the first synthesis series it was observed that the CPG beads were ground by the stirring bar. Hence, in the following syntheses, a KPG® stirrer with a stirrer shaft that fits exactly inside the synthesis vessel was used instead. Figure 4-57 shows SEM images of the respective products that were synthesized with 0, 0.17, 0.55 and 1.7 equivalents of C_{16}TAB with respect to BTEB. The exact synthesis conditions are given in the Experimental Section. Whereas the initial morphology of the beads was totally destroyed after alkaline treatment without surfactant, it was maintained in all the other syntheses. However, a precipitate with undefined morphology was formed in these syntheses next to the CPG beads. Thus, the products had no homogeneous morphologies.

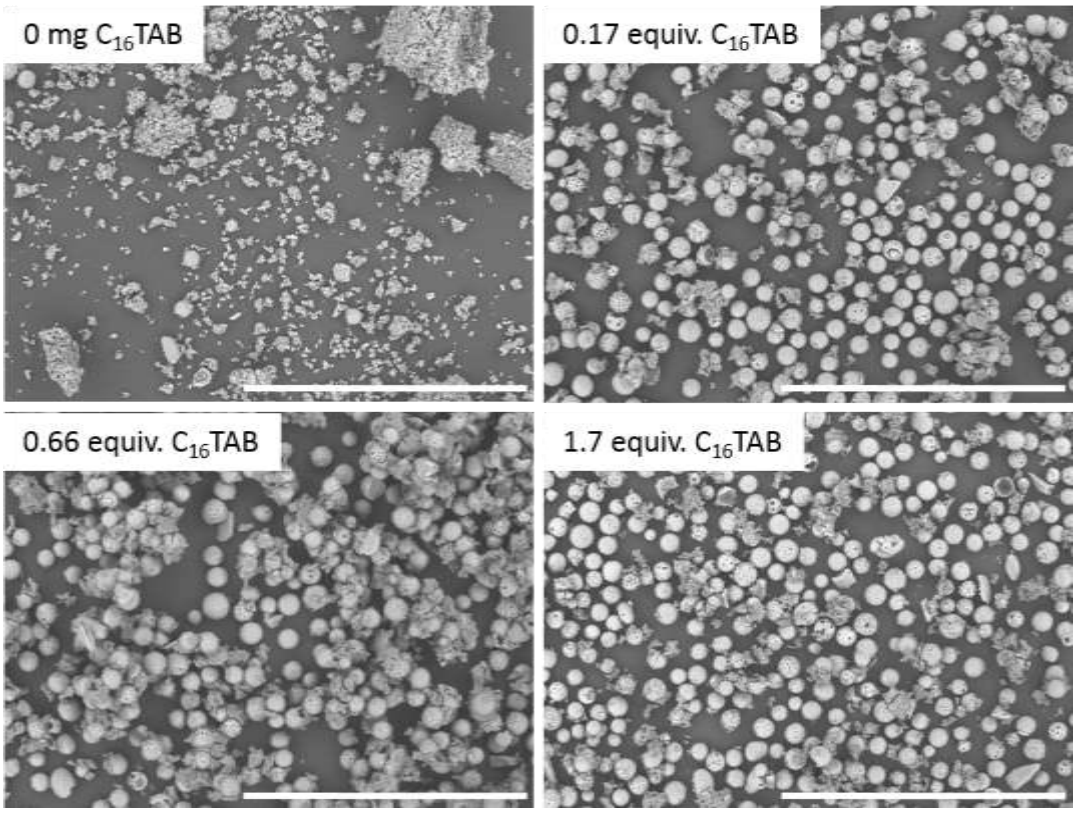

Figure 4-57: SEM images of CPG that were treated in ethanol with BTEB under stirring at 40 °C at pH 13.0 with varying amount of C_{16}TAB stirred with a KPG® stirrer. (Magnification x100, scale bar of 1.0 mm, samples without carbon sputtering.)

Ultimately, no way was found to exchange silica with organosilica in a pseudomorphic transformation without the formation of a second phase that interferes with any further characterization.

Hence, a completely different approach was found to incorporate an organosilica phase in a CPG matrix. The impregnation of the CPG pore system with organosilica precursors is presented in the following chapter.

4.3.2 Incipient wetness impregnation of CPG

Development of the impregnation process

For the combination of PMOs with CPG, it was intended to generate a layer of PMO on the pore surface inside the CPG whereby a hierarchical pore system is generated. The resulting hybrid material has the morphology and stability of CPG on the one hand, while on the other hand it has, the organic functionality together with the unique properties of PMOs, such as a tunable hydrophobic character and chemical modifiability.

To obtain this, the procedure was divided into two steps. First, the CPG was impregnated with the precursor, then micelle templating was carried out postsynthetically in a pseudomorphic transformation process. Here, a suitable strategy for the impregnation of the CPG with the organosilica precursor is discussed. As starting materials CPG beads with 40-100 µm diameter were used that provide pore volumes of 0.9–1.1 $cm^3 \cdot g^{-1}$ and pores of about 50 nm in diameter.

The impregnation followed a so-called incipient wetness approach which means that the volume of the impregnation solution is only as much as is necessary to fill the complete pore volume. This is in contrast to the wet impregnation approach, where the material to be impregnated is placed in an excess volume of the impregnation solution. The incipient wetness approach should prevent condensation of the precursor on the outer surface of the CPG beads.

The precursor BTEVA (see the chemical structure in Figure 4-1) was chosen for the optimization of the impregnation process. Having further applications in mind, such as the chemisorption of aldehydes, the amino function of BTEVA is an adjuvant. Further, BTEVA produces a deep yellow solution, thus its distribution within the CPG can be optically followed.

Impregnation with the organosilica precursor without any solvent are possible since most precursors which are used in this work are liquids at ambient temperature. The first impregnation attempts at room temperature showed that the precursor did not penetrate the pore system but formed a second phase on the outer surface of the particles.

In order to bind the organosilica covalently inside the pore system, an additional condensation step was established. It was assumed that the organosilica is leached out and causes the second phase on the outside of the pore system at less-than-ideal condensation conditions. Hence, this step was first optimized by investigation of different condensation solutions which were added to the impregnated CPGs. Treatments of the impregnated CPGs with different solutions of hydrochloric acid, sodium hydroxide, water and ethanol were compared. As already mentioned, BTEVA is intense in color so that the leaching behavior of BTEVA could be detected visually when the samples were washed with water and ethanol. As it turned out, no leaching of BTEVA

occurred after treatment with a solution of 75 vol% ethanol and 25 vol% sodium hydroxide solution (c = 0.31 mol·L^{-1}) at 80 °C. This same solution was used under the same conditions for the synthesis of microporous organosilica materials previously (see section 4.1.4 Microporous organosilica). Thus, the condensation step was conclusively optimized.

The impregnation should be improved with higher mobility of the precursor. Therefore, different parameter were adjusted: temperature, impregnation time, and volume and concentration of the precursor.

The SEM image in Figure 4-58 shows that the distribution of the organosilica could not be significantly improved at an increased temperature of 80 °C, as a second phase was still visible on the outside of the CPG beads.

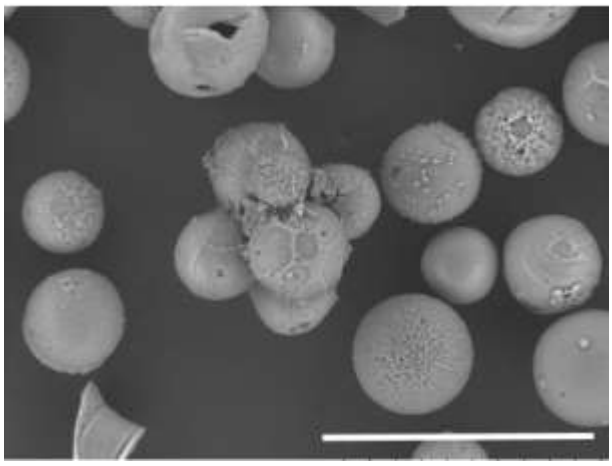

Figure 4-58: SEM images of the CPG incipient wetness half volume impregnation with BTEVA for 24 hours at 80 °C, x400 magnification, scale bar of 200 µm, no carbon sputtering.

Increasing the impregnation time to four days, where the samples were agitated manually every 24 hours did not improve the result.

Thus, the volume of the precursor was reduced in order to investigate whether the second phase was a result of excessive precursor volume. After impregnation with 5 vol%, 13 vol% and 25 vol% of BTEVA and condensation, no second phase was visible in the SEM images (see upper part in Figure 4-59). The presence and distribution of the precursor inside the CPG beads can be detected by the yellow color in the microscopic images (see lower part of Figure 4-59). In contrast to this, the precursor cannot be detected via IR spectroscopy which might be due to the low molar percentage in the CPG/organosilica hybrid material which is between 0.1 mol%–0.3 mol% of BTEVA although the weight percentage is nearly equivalent to the volume percentage (for IR spectra see Figure 9-9 in the Appendix).

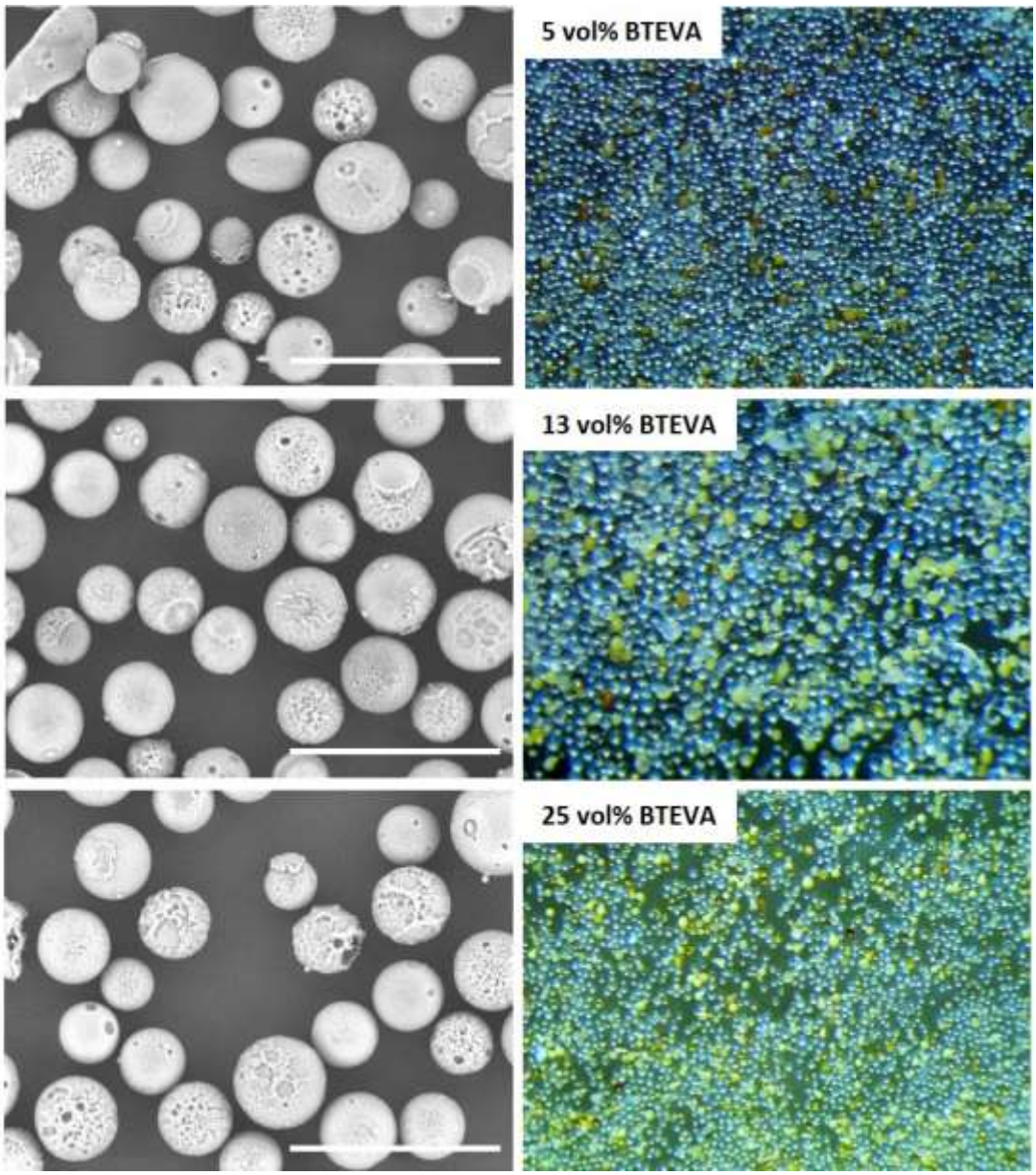

Figure 4-59: Upper part: SEM images (magnification x400, scale bar of 200 µm, samples without carbon sputtering), of CPG that were impregnated with 5 vol%, 13 vol% and 25 vol% of the pore volume for 24 hours at 80 °C. Microscopic images with undefined magnification of the same samples are shown in the lower part.

The results show that the incipient wetness impregnation was successful, since the solution penetrates the pore system. But the microscopic images show an inhomogeneous impregnation. Only a small percentage of the beads are colored yellow, whereas most are unaffected by the BTEVA treatment.

To improve the homogeneity of the impregnation, the organosilica precursor was dissolved in an organic solvents and the volume of the impregnation solution was increased so that it is equivalent to 100% of the macropore volume. Further, the distinctly decreased viscosity of these solutions, compared to the pure precursor should improve the impregnation. Key finding in the development of the impregnation protocol was the use of nonpolar solvents in order to avoid premature condensation of the precursor. Toluene turned out to be best suited for this.

In Figure 4-60, microscopic images of two differently impregnated samples are compared to study the improvement resulting from the above changes in the process. The sample on the left is impregnated with 25 vol% of the macropore volume of the precursor BTEVA. The sample on the right is impregnated with 100 vol% of the macropore volume using a solution that contains 25 wt% of the precursor in toluene. Hence, the amount of BTEVA in impregnations is the same (assuming a density of 1.0 $cm^3 \cdot g^{-1}$ for the precursor). Significant improvement of the distribution is initially visible as more CPG beads are yellow due to the presence of BTEVA in the impregnation with toluene.

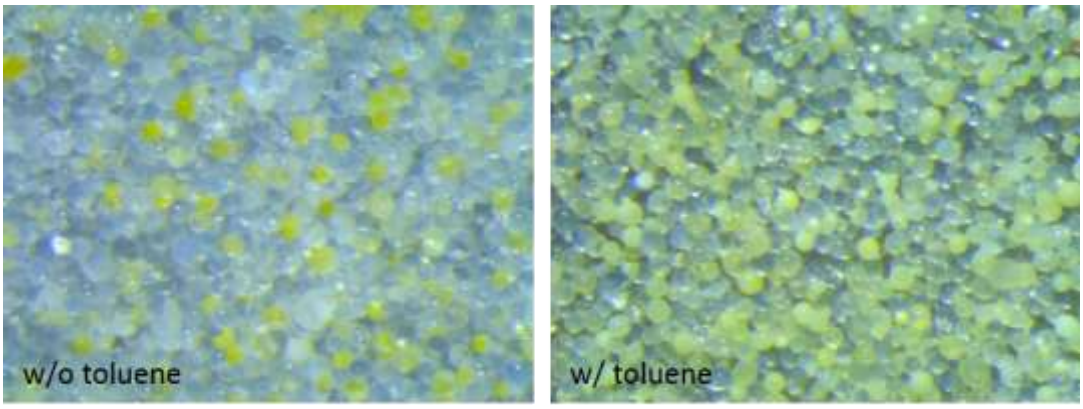

Figure 4-60: Microscopic images of CPG that were impregnated with a volume of BTEVA that is 25 vol% of the macropore volume (left), and those that were impregnated with 100 vol% of the macropore system with a solution that contains 25 wt% of BTEVA in toluene (right).

Further improvement was possible by impregnation under reduced pressure and temperatures up to 50 °C. In Figure 4-61 microscopic images of samples that were impregnated by incipient wetness under reduced pressure with a toluene-based solution containing 25 wt% and 50 wt% of BTEVA are presented.

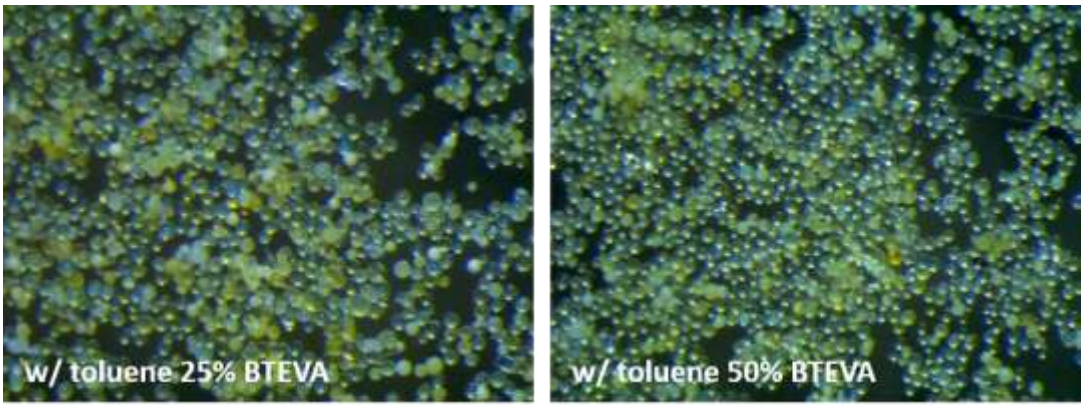

Figure 4-61: Microscopic images with undefined magnifications of CPG that were impregnated under reduced pressure with 100 vol% of the macropore volume using a toluene-based solution that contains 25 wt% of BTEVA on the left and 50 wt% of BTEVA on the right.

The pore systems were characterized by physisorption measurements. The isotherms of these two samples are given in Figure 4-62 and compared with the isotherm from the CPG starting material. The isotherms of all materials are very similar with a steep step at high relative pressure > 0.9. However, the isotherms differ in volume uptake in the relative pressure range of 0.8–1.0. The pore volume of the samples was determined with the help of NLDFT kernel for silica with cylindrical pores from the adsorption branch. The pore volume is 0.8 $cm^3 \cdot g^{-1}$ for the pure CPG (1.2 $cm^3 \cdot g^{-1}$ is the intrusion volume from mercury intrusion of the CPG batch see Figure 9-8 in the Appendix), it decreases to 0.7 $cm^3 \cdot g^{-1}$ for the sample with 25 wt% of BTEVA and 0.6 $cm^3 \cdot g^{-1}$ for the sample with 50 wt% of BTEVA. The decreased pore volume is caused by the impregnated organosilica inside the pores.

It is worth noting, that the specific BET surface area increases after impregnation from 72 $m^2 \cdot g^{-1}$ of the pure CPG to 219 $m^2 \cdot g^{-1}$ (25 wt% BTEVA) and 244 $cm^3 \cdot g^{-1}$ (50 wt% BTEVA), respectively. Since the condensation solution is the same as was used for the formation of microporous organosilicas, the formation of micro- to mesopores, and thus the increased specific BET surface area is explained. It should be mentioned, that pure CPG which were treated with the same solution were not affected (see physisorption isotherms in Figure 9-10 in the Appendix). Hence, the pores are generated only in the organosilica phase.

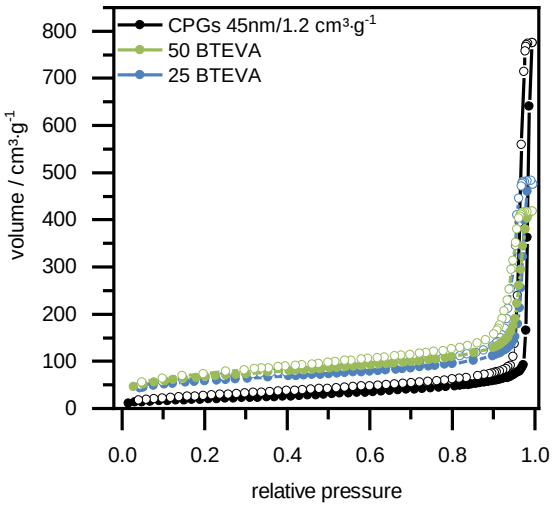

Figure 4-62: Isotherms (N_2, 77 K) of the CPG that were impregnated under reduced pressure with a toluene-based solution that contains 25 wt% of BTEVA and 50 wt% of BTEVA.

The pore size distribution was calculated by NLDFT for silica materials with cylindrical pores (adsorption branch). Due to the presence of large meso- to macropores the pore diameter was additionally calculated using the BJH method. Figure 4-63 shows the pore diameter distributions for both methods.

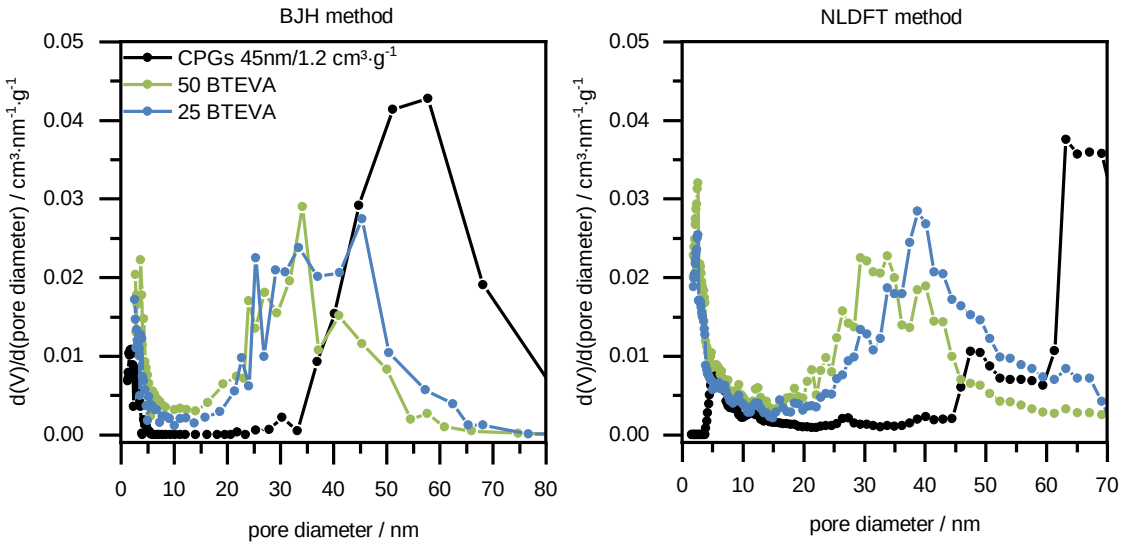

Figure 4-63: Pore size distribution from the BJH method using the desorption branch (left) and from NLDFT for silica with cylindrical pores using the adsorption branch (right).

It is obvious that the pore size distributions are rather broad. However, a slight shift of the pore size towards smaller pores after impregnation with increasing amount of the precursor can be seen in both methods. For the characterization of pores in the large pore size range, the BJH method is also reliable. In contrast, it is less suitable for smaller pores, as discussed in chapter 3.1. Nevertheless, pores larger than 50 nm are best characterized by MIP, which was additionally performed on the following samples. Beyond, it can be seen that micropores are formed during the treatment with ethanol and sodium hydroxide solution. The chosen solution was also used to synthesize microporous organosilicas from different organosilica precursors in Section 4.1.4. This will be discussed in details in the following section as well.

In summary, a protocol for incipient wetness impregnation and subsequent condensation of the precursor inside the pores was developed. This is applied for systematic impregnation with the precursors BTEVA and BTEVB of CPG batches that differ in pore size and pore volume and will be discussed below.

Systematic impregnation of different CPG batches with BTEVA and BTEVB

For a systematic approach different CPG batches were impregnated with toluene-based solutions with 10 wt%, 25 wt%, 50 wt% and 75 wt% of BTEVA and BTEVB, respectively. All samples were treated with a solution of 25 vol% ethanol and 75 vol% sodium hydroxide solution (c = 0.31 mol·L^{-1} pH 13.5) at 80 °C for condensation after the impregnation. These samples described below are named as 10BTEVA/10BTEVB, 25 BTEVA/25BTEVB, 50BTEVA/ 50BTEVB and 75BTEVA/75BTEVB.

Table 4-22 gives an overview of the five different CPG batches which were used with their specific BET surface area, the pore volumes from nitrogen physisorption, calculated with NLDFT kernel from the adsorption branch for silica with cylindrical pores, the pore volumes and pore diameter from MIP. CPG batches I–III were impregnated with both precursors, whereas batch IV and V were only impregnated with BTEVB. The CPG batches differ in pore size and pore volume. CPG batch I has a small pore size of 42 nm and a low pore volume of 0.9 $cm^3 \cdot g^{-1}$. In the case of batch IV, the pore volume is also low (1.15 $cm^3 \cdot g^{-1}$), but it is macroporous with 120 nm pore diameter. CPG batch II and III have already been used for the investigation of the pseudomorphic transformation process in Section 4.2. They show the same pore volume of 1.5 $cm^3 \cdot g^{-1}$ but differ in terms of pore size: batch II with 52 nm and batch III with 168 nm pore diameter. CPG batch V has the highest pore volume of 2.1 $cm^3 \cdot g^{-1}$ and is also macroporous with 148 nm pore diameter.

Table 4-22: Overview of the used CPG batches I–V for the impregnation with BTEVB and BTEVA

Batch No.	appearance	S_{BET} / $m^2 \cdot g^{-1}$	V_{NLDFT, N_2} / $cm^3 \cdot g^{-1}$	$V_{intr. Hg}$ / $cm^3 \cdot g^{-1}$	d_{Hg} / nm
CPG batch I	Beads	73	0.61	0.90	42
CPG batch II	Beads	87	0.30	1.50	52
CPG batch III	Granules	26	0.03	1.50	168
CPG batch IV	Beads	26	0.05	1.15	120
CPG batch V	Beads and Granules	50	0.09	2.10	148

The SEM images in Figure 4-64 show the morphology of the CPG batches I and II which are shaped to beads with a size of 40–100 µm together with the pore system that is visible at higher magnification. The pore system of batch II has already been shown in Section 4.2, see Figure 4-33. Unless otherwise specified, the samples are carbon-sputtered, thus the images are not reliable for estimation of pore size and no further SEM images of the mesoporous samples will be shown here.

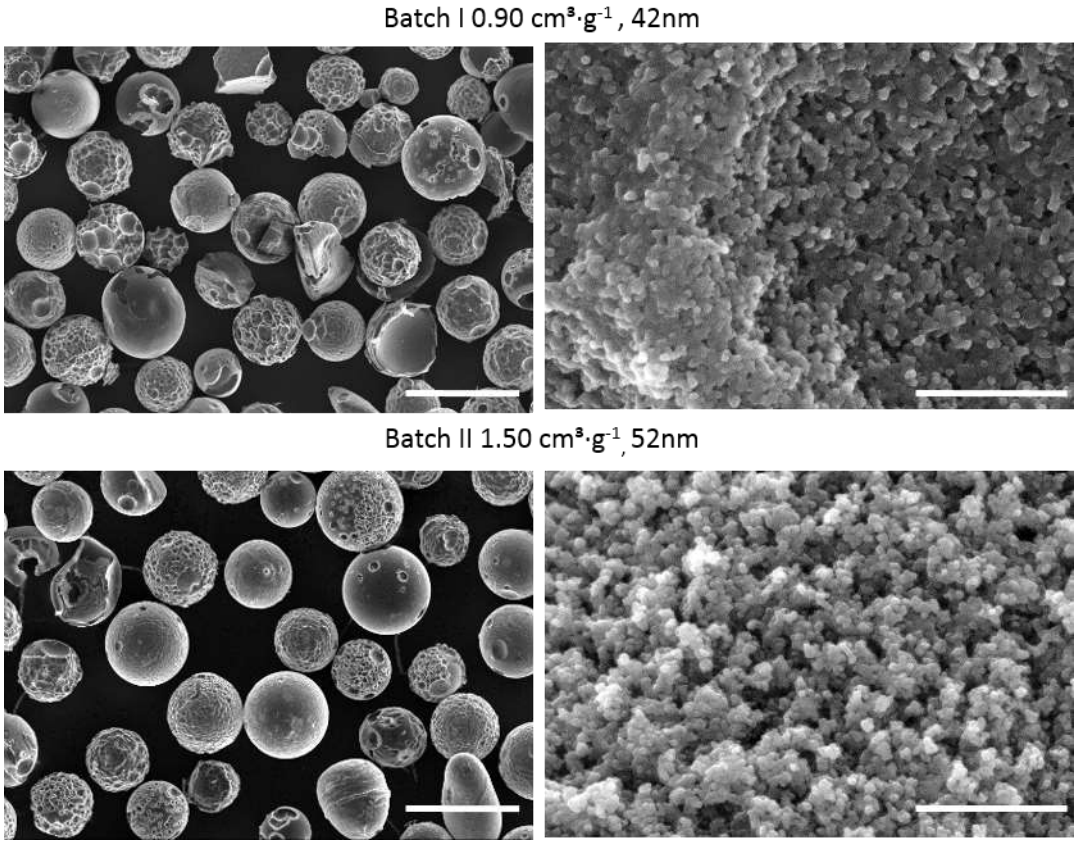

Figure 4-64: SEM images of the bead-shaped CPG batches I and II The morphology of the beads is shown with magnification of x500 the scale bar is 100 µm in these images on the left, on the right SEM images of the pore system with magnification x80000, scale bar of 1.0 µm.

The form-giving process of the CPG in a riser reactor with a cyclone (see Figure 1-7) is often accompanied by the formation of a sealing layer of silica on the outer surface of the beads due to the evaporation of boron oxide.[33] Removal of the sealing layer is possible under strong basic conditions, but is not always completely accomplished and accompanied by loss of the beads. For the samples used here, complete removal of the sealing layer is presumed. This problem is avoided by using granules. Hence, CPG batch III and V consists of granules which are not shown here while batch VI consists of beads and granules, as shown in Figure 4-65. The pore systems of these macroporous systems is shown in Figure 4-65 as well.

The influence of pore size and pore volume on the impregnation behavior and organosilica phase is investigated below.

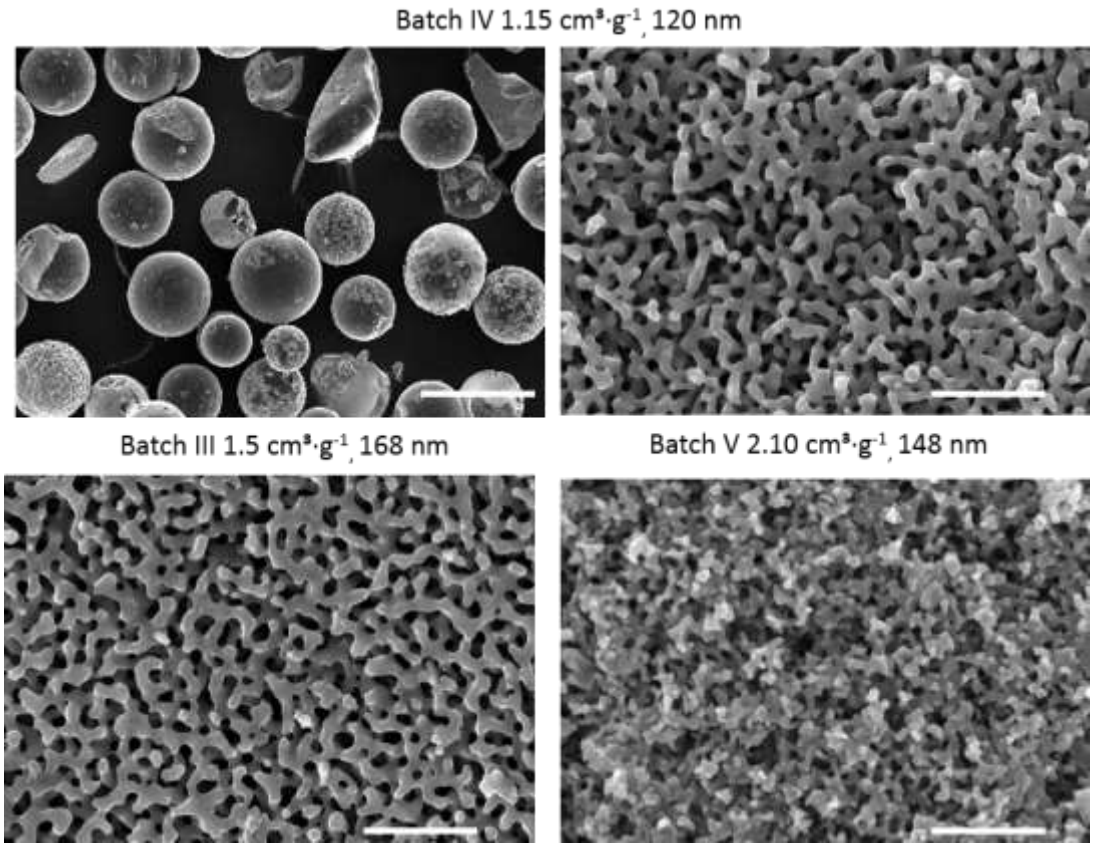

Figure 4-65: SEM images of the pore system of the CPG batches IV in the upper part with magnification x300, scale bar 100 µm, and the pore systems of the macroporous CPG batches III–V with magnifications x50000, scale bar of 200 nm.

Morphology and appearance of the pore systems of the impregnated CPG beads

One aspect of the impregnation quality is the preservation of the morphology of the CPG beads after the treatment. SEM images in Figure 4-66 show 10–75BTEVB and in Figure 4-67 10–75BTEVA of batch II, respectively. In all cases the beads remain intact. For SEM images of impregnated CPG batch I see Figure 9-11 (10-75BTEVB) and Figure 9-12 (10–75BTEVA) in the Appendix. In order to improve the organosilica uptake, CPG batch II was impregnated four times with the same solution containing 10 wt% BTEVB. Each step was also accompanied by condensation. It was expected, that multiple impregnation with solutions of lower organosilica content would improve the access of the pore system, since the solutions are of lower viscosity. The samples are named 1x10BTEVB, 2x10BTEVB, 3x10BTEVB and 4x10BTEVB. SEM images of the samples do not show any characteristics and are therefore found in the Appendix (see Figure 9-13).

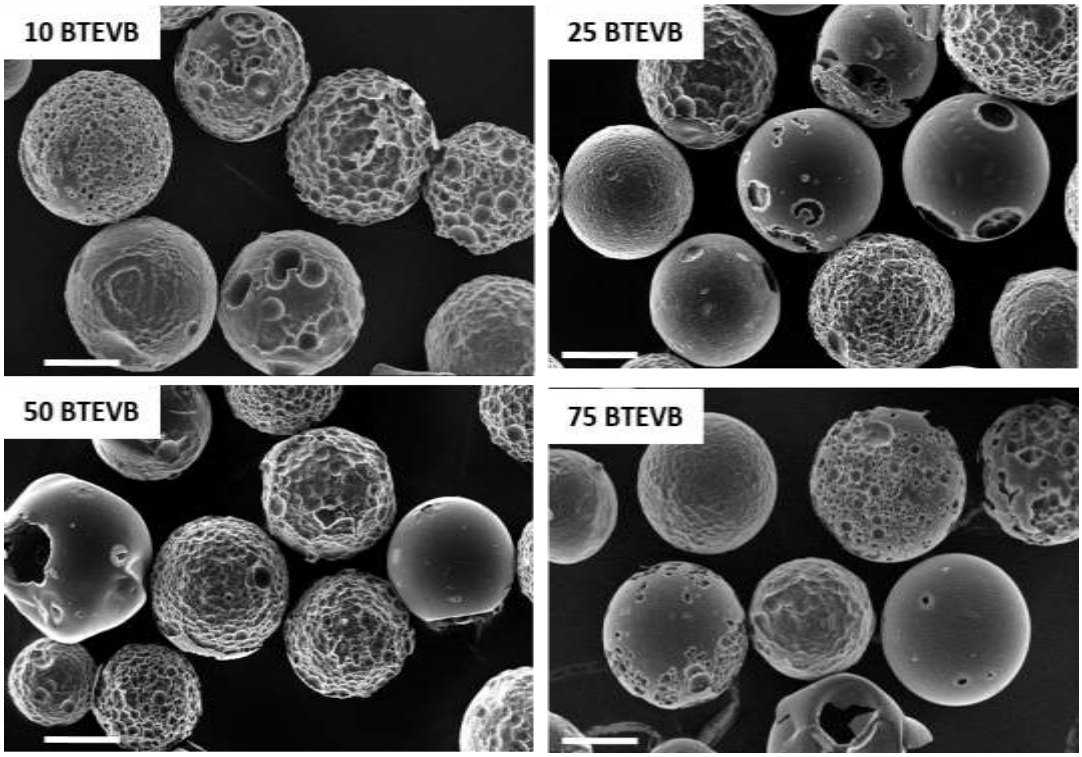

Figure 4-66: SEM images of the CPG beads batch II with varying organosilica content of 10–75BTEVB. Scale bar of 400 µm, x1000 magnification.

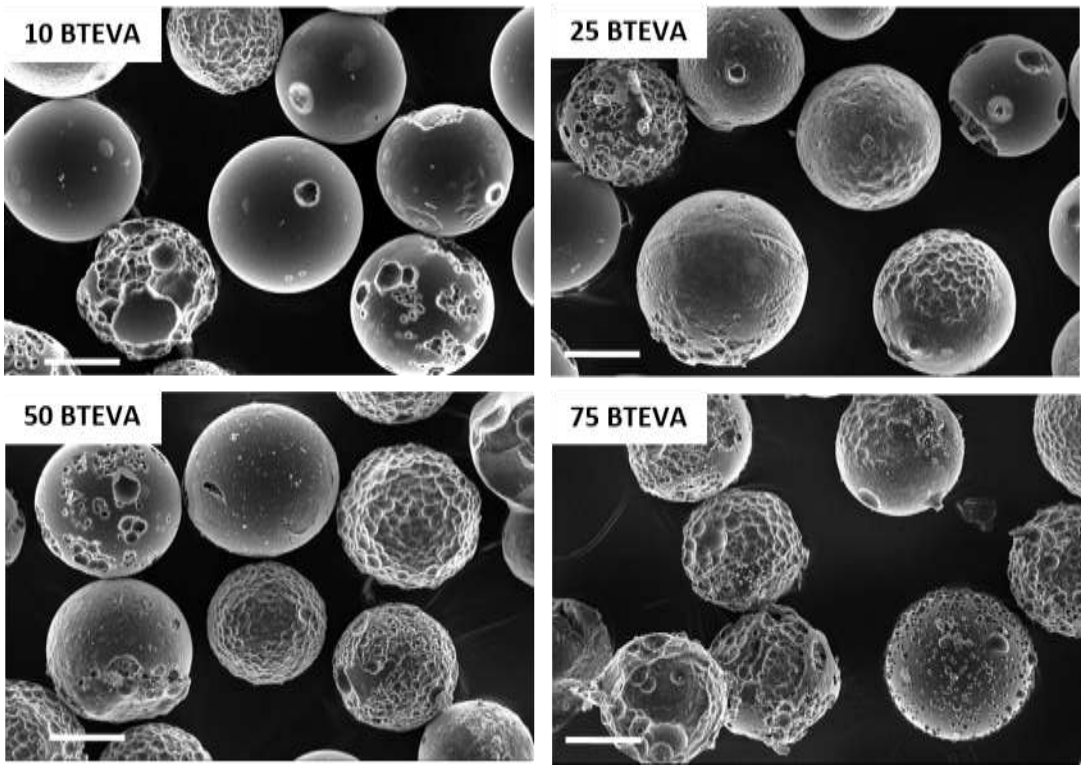

Figure 4-67: SEM images of the CPG beads batch II with varying organosilica content of 10–75BTEVA. Scale bar of 400 µm, x1000 magnification.

SEM images of the pore system in mesoporous materials are not meaningful due to limited magnifications, so that there will be no further images of these systems. By contrast, in the case

of macroporous starting materials, a visual impression of the effect of the impregnation on the pore system is given in SEM images. Figure 4-68 shows the samples 10–75BTEVB from batch III.

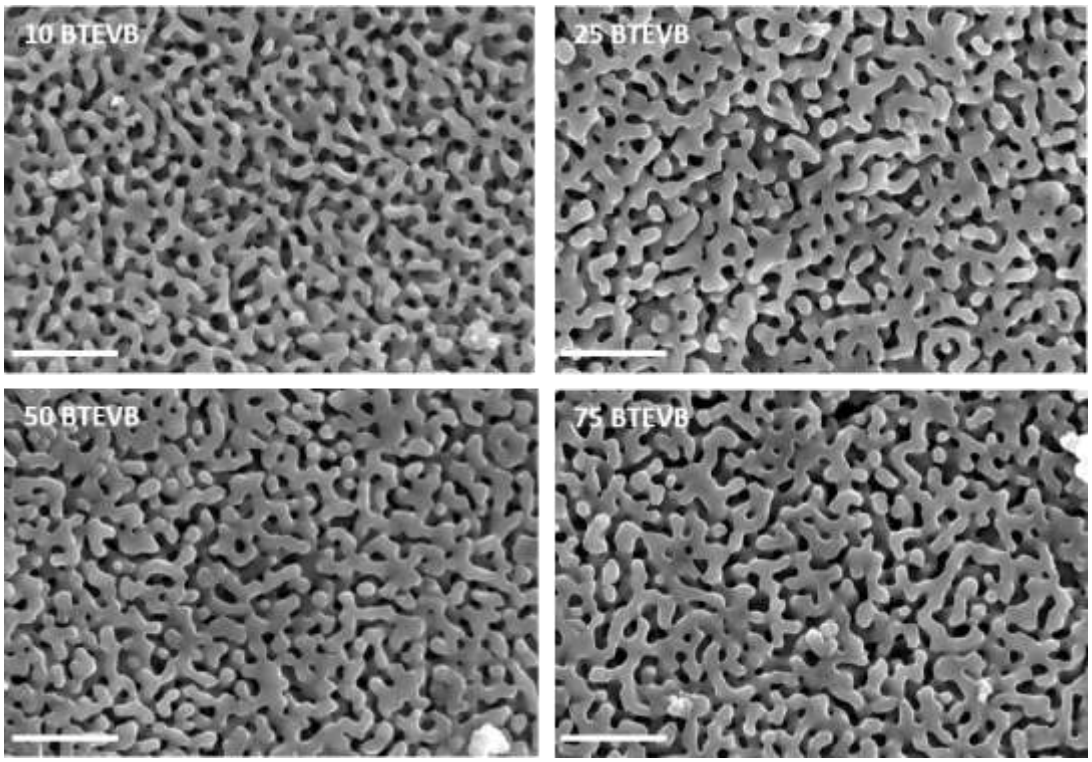

Figure 4-68: SEM images of CPG batch III with 10–75BTEVB. Scale bar of 1 µm, x50000 magnification.

Successive growth of the pore wall is visible due to the formation of an organosilica layer. Similar results were found for the impregnation of the same batch with 10–75BTEVA (Appendix, Figure 9-14), 10–75BTEVB of batch IV (Appendix, Figure 9-15) and batch V (Appendix, Figure 9-16).

In the case of 75BTEVA from batch II (Figure 4-67 lower part), a second phase of spherical particles was noticed sporadically on the surface of the beads. The same phenomenon was also found in case of 50BTEVA from CPG batch III (SEM images in the Appendix Figure 9-19). This phenomenon occurred with higher BTEVA content but is still a side effect that does not dominate the sample. In samples which were impregnated with BTEVB, no second phase was found, so this might depend on the precursor. It should be considered that the SEM images show only small sections of the samples and are not fully representative especially at high magnifications.

For further investigation of the pore structure after impregnation the sample 50BTEVB from batch III was characterized by transmission electron microscopy (TEM), with the samples needing to be ground in advance so that the initial morphology is no longer visible. Figure 4-69 compares the TEM images of the pure CPG batch III with the impregnated sample.

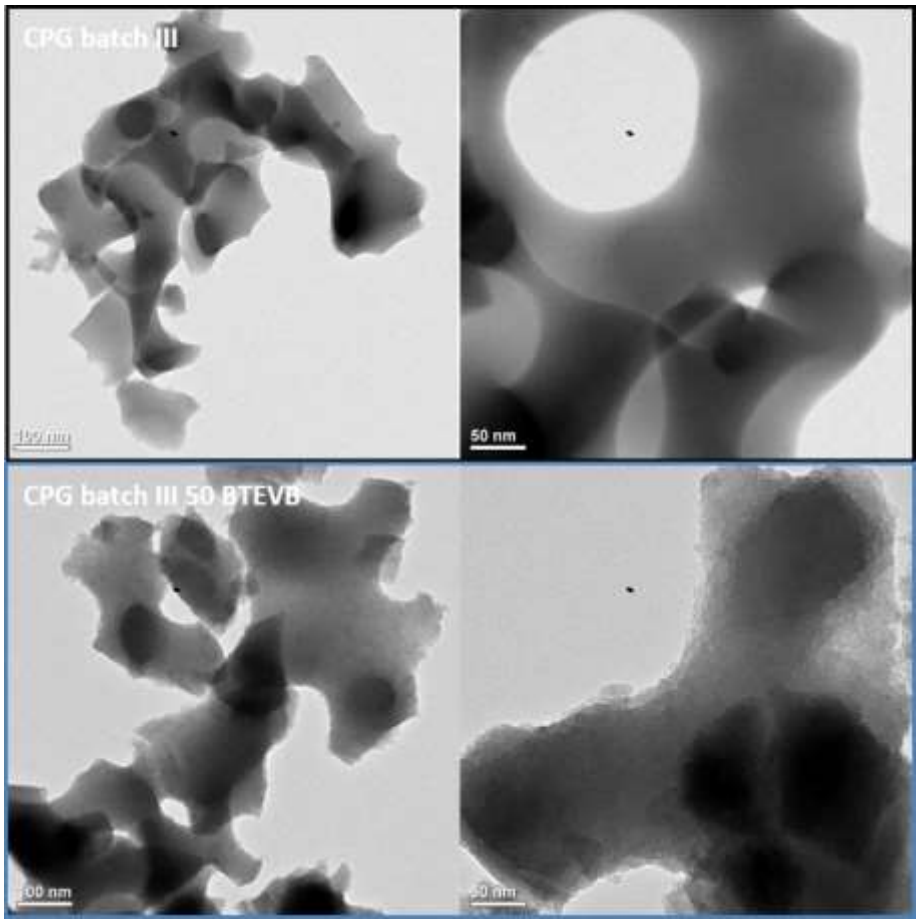

Figure 4-69: TEM images of CPG batch III (upper images) and impregnated sample 50BTEVB (lower images) both with two different magnifications.

Before impregnation the pore walls appear smooth, whereas they become rough after the impregnation and seem to consist of small domains. In the course of the TEM measurements, SEM images of the ground samples without carbon sputtering were also taken. The measurements are affected by charge effects which diminish the quality at high magnifications. Images are shown in Figure 9-17 and in Figure 9-18 in the Appendix.

Nanoporosity features of impregnated CPG – nitrogen physisorption

For all CPG batches it was found that the specific BET surface area of the organosilica/silica hybrid materials is significantly higher than for the CPG. Figure 4-70 shows the physisorption isotherms and the pore diameter distributions of batch I, impregnated either with BTEVB or BTEVA.

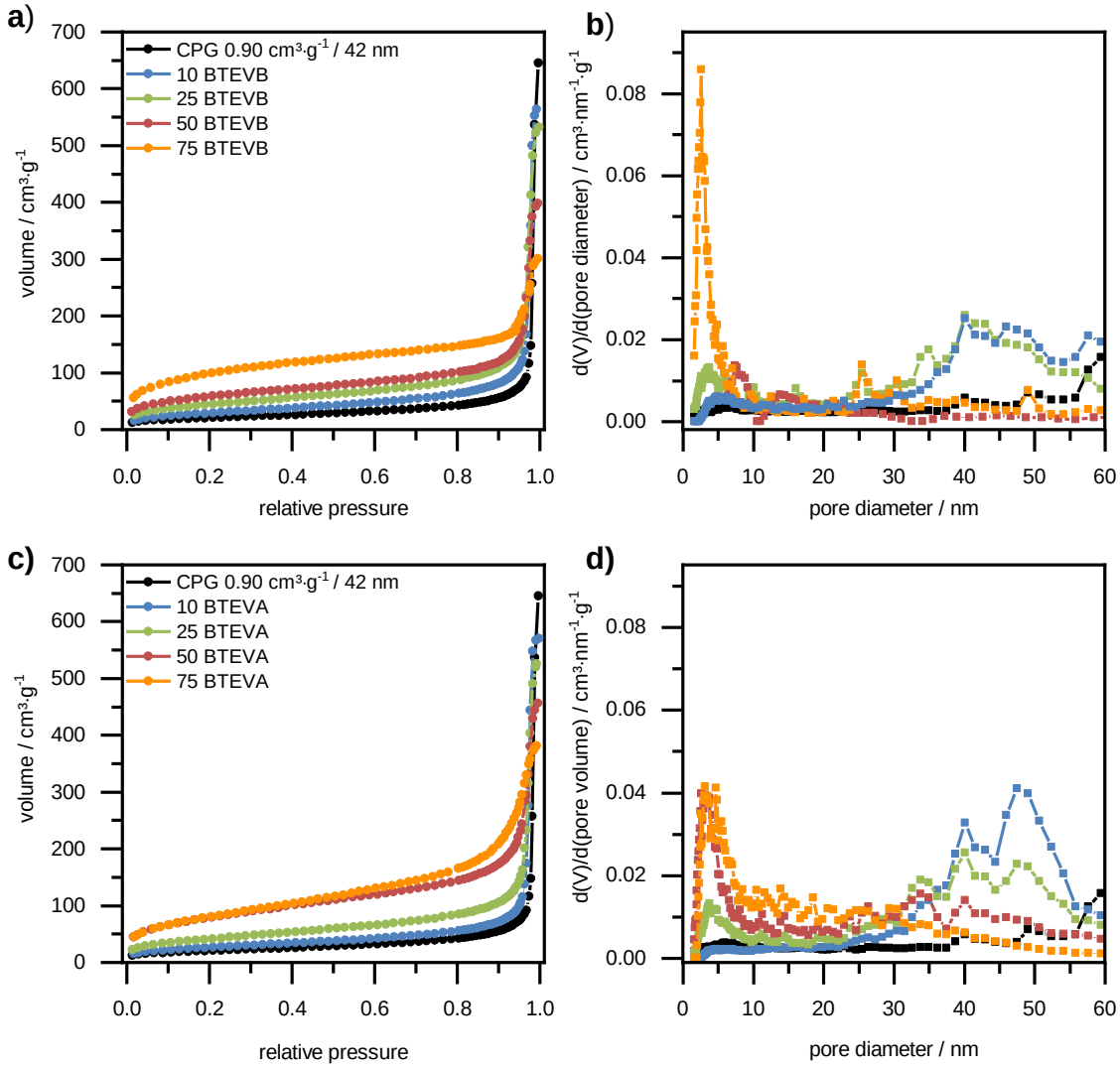

Figure 4-70: Physisorption isotherms (N_2, 77 K, only adsorption branches for better clarity) of CPG batch I and the impregnated samples a) 10–75BTEVB and c) 10–75BTEVA. The respective pore diameter distributions (calculated from the adsorption branch with NLDFT kernel for silica with cylindrical pores) are shown on the right b) for 10–75BTEVB and d) for 10–75BTEVA.

Due to the presence of large mesopores, the arrangement of the measurement points of the isotherms in this series is focused on the high relative pressure range. Within one measurement the coverable relative pressure range is limited, so that these measurements start at comparably high relative pressure but are still suitable to characterize the small mesopore range and the specific BET surface area reliably.

The isotherm of the initial CPG batch I is of type II, with high volume uptake at high relative pressure of over 0.90. In the adsorption branches of the impregnated samples a plateau is shown in the last measurement points at high relative pressure so that these isotherms could be assigned to type IV isotherms. The pore volumes were determined with NLDFT kernel for silica with cylindrical pores from the adsorption branch, just as the pore diameter distribution. Two pore diameter ranges were chosen to distinguish between new, under the conditions of the condensation formed pores, which are assumed to be smaller 20 nm, and the initial pore system with pore diameters over 20 nm. For the impregnations 10–75BTEVB and 10–75BTEVA the pore volume of pores smaller 20 nm increases with increasing organosilica content in the impregnation solution. This is caused by the presence of micro- and mesopores which are formed in the condensation process as it is also visible in the pore diameter distributions. Whereas the samples 10–50BTEVB show a broad distribution of micro- and mesopores, a comparably narrow pore diameter distribution in the range of 2.4 nm occurs in 75BTEVB. This occurs for 50BTEVA and 75BTEVA as well, although, in general, the total volume uptake is lower for the BTEVA samples than for the BTEVB samples. The height of the condensation step decreases with increasing organosilica content in the impregnation solution and the pore volume of pores larger than 20 nm (according to NLDFT) shrinks. This indicates filling of the pore system with the organosilica species for 25–75BTEVB and 25–75BTEVA. By contrast, for 10BTEVB and 10BTEVA, the pore volumes of pores larger 20 nm increases in comparison to the initial CPG and large mesopores are detected in the pore diameter distribution of these samples. This indicates that a part of the initial pores of the pure CPG are too large to be determined with nitrogen physisorption, and that this changes after impregnation with low organosilica content. The absence of a plateau in the isotherms of the pure CPG needs to be considered here, as it causes an error-prone determination of the initial pore volume. It might also come to mind, that etching of the CPG beads during the impregnation and subsequent washing steps could explain this trend. This has already been overruled before, since pure CPG was not affected by this treatment (see also Appendix Figure 9-10).

Due to the presence of micropores, the pressure range which is considered for determination of the *apparent* specific BET surface area had to be adjusted as mentioned before in accordance with the IUPAC recommendation (see also foot note 2 on page 75).[3] The respective relative pressure ranges are given in Table 9-4 in the Appendix. Whereas the initial CPG batch has a specific BET surface area of 73 $m^2 \cdot g^{-1}$, the *apparent* BET specific surface area increases with increasing organosilica content up to 291 $m^2 \cdot g^{-1}$ for 75BTEVA and to 358 $m^2 \cdot g^{-1}$ for 75BTEVB. Also in the results for the syntheses of microporous organosilica (section 4.1.4) with the same solution that was used for condensation after impregnation here, BTEVB-based materials

showed a significantly higher *apparent* specific BET surface area than the BTEVA-based analogs. This might explain the slight differences of the results found here. Hence, the impregnation conditions seem better suited for the formation of porous divinylbenzene-bridged organosilica than for porous divinylaniline-bridged materials.

Table 4-23 gives an overview of the specific BET surface areas and pore volumes for all samples from batch I.

Table 4-23: Overview of the *apparent* specific BET surface areas and the pore volumes from pores smaller or larger than 20 nm (calculated from the adsorption branch with NLDFT kernel for silica with cylindrical pores) of CPG batch I impregnated with 10–75BTEVB or 10–75BTEVA.

Sample	S_{BET} / $m^2 \cdot g^{-1}$	$V_{<20\ nm,\ NLDFT\ ads.}$ / $cm^3 \cdot g^{-1}$	$V_{>20\ nm,\ NLDFT\ ads.}$ / $cm^3 \cdot g^{-1}$	Sample	S_{BET} / $m^2 \cdot g^{-1}$	$V_{<20\ nm,\ NLDFT\ ads.}$ / $cm^3 \cdot g^{-1}$	$V_{>20\ nm,\ NLDFT\ ads.}$ / $cm^3 \cdot g^{-1}$
CPG batch I	73	0.03	0.58				
10BTEVB	105	0.06	0.75	**10BTEVA**	94	0.03	0.81
25BTEVB	158	0.12	0.63	**25BTEVA**	148	0.10	0.66
50BTEVB	203	0.15	0.44	**50BTEVA**	282	0.23	0.43
75BTEVB	358	0.22	0.21	**75BTEVA**	291	0.32	0.25

The isotherms as well as the pore diameter distributions of 10–75BTEVB and 10–75BTEVA from CPG batch II are shown in Figure 4-71. The respective plots for the multiple impregnation of 10BTEVB are given in the Appendix, Figure 9-20. The assignment of the isotherms is analogous to batch I. The initial CPG batch II shows a type II isotherm, whereas the last measurement points of the adsorption branch might form a plateau in the cases of the impregnated samples which is the precondition for a type IV isotherm. Just as in batch I, for 10–50BTEVB and 10-50BTEVA the *apparent* BET surface areas increases with increasing organosilica content in the impregnation solution. The sample 50BTEVB shows the highest *apparent* specific BET surface area of 447 $m^2 \cdot g^{-1}$, and the highest pore volume of 0.26 $cm^3 \cdot g^{-1}$, whereas with further increasing organosilica content (75BTEVB), it decreases to 276 $m^2 g^{-1}$. It is possible, that the higher BTEVB content hinders the spontaneous formation of pores inside the organosilica phase due to spatial limitation. In the case of the BTEVA-impregnated samples from batch II, the specific BET surface area increases up to 301 $m^2 \cdot g^{-1}$ in sample 50BTEVA and then it decreases, but only slightly to 251 $m^2 \cdot g^{-1}$ for 75BTEVA. Different to batch I, the initial pore system of the CPGs is not well visible in the pore diameter distribution because the pores are larger.

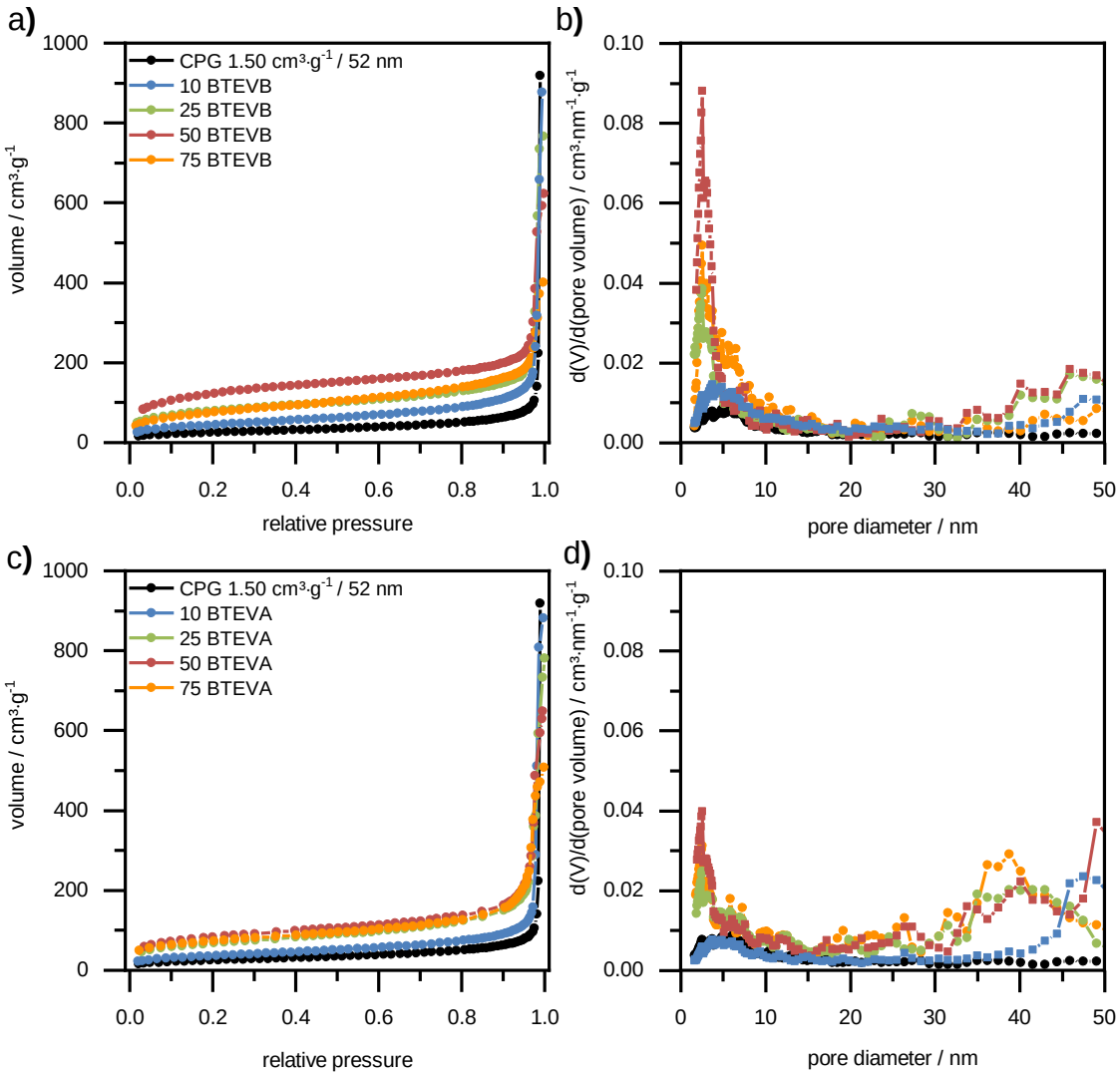

Figure 4-71: Physisorption isotherms (N_2, 77 K, adsorption branches only for better clarity) of CPG batch I and the impregnated samples a) 10–75BTEVB and c) 10–75BTEVA. The respective pore diameter distributions (calculated from the adsorption branch with NLDFT kernel for silica with cylindrical pores) are shown on the right b) for 10–75BTEVB and d)10–75BTEVA.

The pore volumes of pores smaller or larger 20 nm follow the same trend as in CPG batch I: The pore volume of the large pores increases after the impregnation in case of 10BTEVB and 10BTEVA and decreases successively with increasing organosilica filling of the initial pore filling. Also here the absence of a plateau in the isotherm of the initial CPG and thus error-prone determination of the pore volume might be a reasonable explanation for this phenomenon. The pore volume of the smaller pores increases with the organosilica content in the impregnation solution. As mentioned before, CPG batch II was impregnated four times with the same solution containing 10 wt% BTEVB, which was an approach to improve the formation of an organosilica layer. In comparison to the impregnation with higher organosilica content in the solution no significant higher *apparent* specific BET surface areas were determined, so that this parameter is not improved by this approach. The influence on the organosilica content will be discussed in

the following Sections. The *apparent* specific BET surface areas and the pore volumes of the impregnated samples from CPG batch II are shown in Table 4-24.

Table 4-24: Overview of the *apparent* specific BET surface areas and the pore volumes from pores smaller or larger than 20 nm (calculated from the adsorption branch with NLDFT kernel for silica with cylindrical pores) of the CPG batch II impregnated with 10–75BTEVB and 10–75BTEVA and multiple impregnation with 10BTEVB.

Sample	S_{BET} / $m^2 \cdot g^{-1}$	$V_{<20\ nm,\ NLDFT\ ads.}$ / $cm^3 \cdot g^{-1}$	$V_{>20\ nm,\ NLDFT\ ads.}$ / $cm^3 \cdot g^{-1}$	Sample	S_{BET} / $m^2 \cdot g^{-1}$	$V_{<20\ nm,\ NLDFT\ ads.}$ / $cm^3 \cdot g^{-1}$	$V_{>20\ nm,\ NLDFT\ ads.}$ / $cm^3 \cdot g^{-1}$
CPG batch II	87	0.08	0.25				
10BTEVB	161	0.13	0.62	**10BTEVA**	128	0.08	0.94
25BTEVB	289	0.17	0.83	**25BTEVA**	247	0.18	0.74
50BTEVB	447	0.26	0.57	**50BTEVA**	301	0.19	0.65
75BTEVB	276	0.23	0.30	**75BTEVA**	263	0.19	0.51
2x10BTEVB	254	0.22	0.62				
3x10BTEVB	285	0.22	0.72				
4x10BTEVB	309	0.23	0.75				

The third CPG batch was analogously impregnated with different BTEVB- or BTEVA-containing solutions. The physisorption isotherms and pore diameter distributions of 10–75BTEVB are shown in Figure 4-72 as representatives of the macroporous materials. The physisorption isotherms and pore diameter distributions of the BTEVA impregnation of batch III (Figure 9-21) and BTEVB impregnations of batch IV (Figure 9-22) and V (Figure 9-23) show similar trends in general and are hence shown in the Appendix.

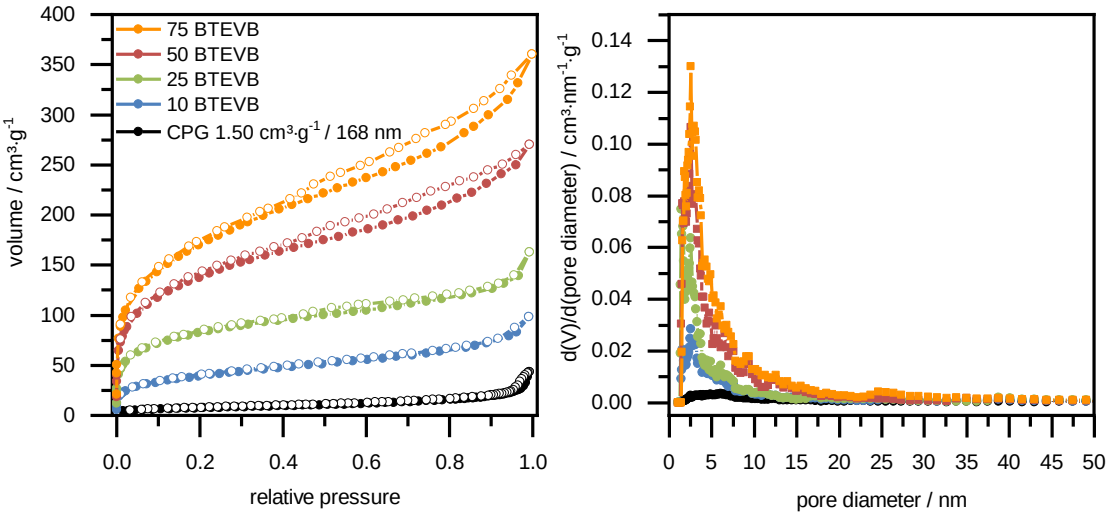

Figure 4-72: Physisorption isotherms (N_2, 77 K) of CPG batch III impregnated with 10–75BTEVB on the left. Pore diameter distributions (calculated from the adsorption branch with NLDFT kernel for silica with cylindrical pores) are shown on the right.

In contrast to the previously shown isotherms from batch I and II, the focus of the measurement points is not on the high relative pressure range since no large mesopores are characterized. This allows additional measurement points in the low pressure range to improve the characterization of small mesopores.

As the initial macropores are significantly larger than in the previously presented examples, no steep step occurs at high relative pressures. Hence, the isotherm of the CPG batch III is type II with low gas volume uptake in the high pressure range. With an increasing ratio of the precursor in the impregnation solution, additional gas volume uptake can be noticed over the whole relative pressure range, thus the isotherms are a combination of type II and type Ib isotherms. This is due to micropores and smaller mesopores that are formed in the organosilica layer, as in the previously presented samples. Further, the isotherms of 50BTEVB and 75BTEVB show hysteresis type H4 which might be due to the presence of small and larger mesopores. The *apparent* specific BET surface area increases with higher organosilica contents up to 596 $m^2 \cdot g^{-1}$ for 75BTEVB and 536 $m^2 \cdot g^{-1}$ for 75BTEVA. As can be seen in the pore size distribution for batch III, mesoporosity with narrow distribution occurs especially in the case of 75BTEVB.

High *apparent* specific BET surface areas are also observed for 10–75BTEVB from the CPG batches IV and V. The highest *apparent* specific BET surface area is obtained for 75BTEVB from batch V with 767 $m^2 \cdot g^{-1}$. Table 4-28 gives an overview of the *apparent* specific BET surface areas and the pore volume of the newly formed small mesopores of all samples from batch III–IV.

Table 4-25: Overview of the *apparent* specific BET surface areas and the pore volumes from pores smaller 20 nm (calculated from the adsorption branch with NLDFT kernel for silica with cylindrical pores) of CPG batch III, impregnated with 10–75BTEVA and 10–75BTEVB, and batch IV and V impregnated with 10–75BTEVB.

Sample	S_{BET} / $m^2 \cdot g^{-1}$	$V_{<20\ nm,\ N_2,\ NLDFT\ ads}$	Sample	S_{BET} / $m^2 \cdot g^{-1}$	$V_{<20\ nm,\ N_2,\ NLDFT,\ ads}$
CPG batch III	26	0.03	**CPG batch IV**	26	0.03
10BTEVB	137	0.11	**10BTEVB**	98	0.08
25BTEVB	299	0.19	**25BTEVB**	248	0.17
50BTEVB	476	0.35	**50BTEVB**	443	0.26
75BTEVB	596	0.45	**75BTEVB**	629	0.34
			CPG batch V	50	0.06
10BTEVA	78	0.08	**10BTEVB**	180	0.18
25BTEVA	203	0.17	**25BTEVB**	388	0.27
50BTEVA	278	0.25	**50BTEVB**	633	0.37
75BTEVA	536	0.44	**75BTEVB**	767	0.43

Although the initial CPGs are macroporous and hence, no distinction between pores smaller or larger 20 nm is necessary, only the pore volume for pores smaller 20 nm is considered for better comparability between the batches. In comparison to the previously discussed samples from batch I and II, the pore volume follows the same increasing trend as before.

Figure 4-73 summarizes the results of the (*apparent*) specific BET surface area for all samples which are impregnated with BTEVB on the left, samples which are impregnated with BTEVA on the right.

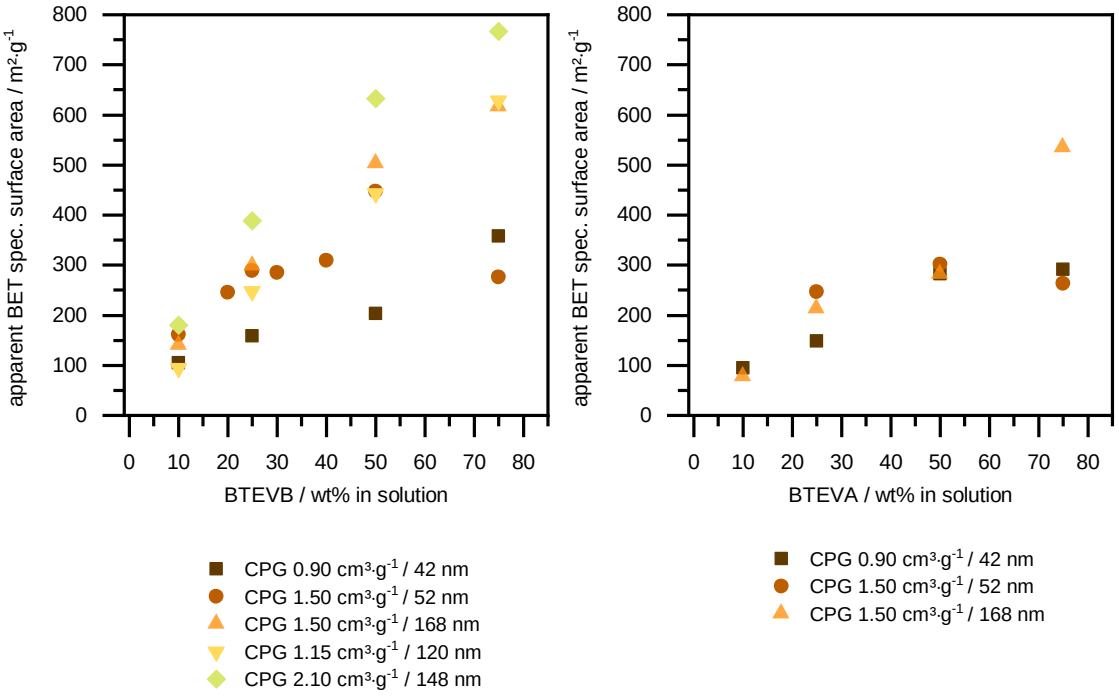

Figure 4-73: Plot of the *apparent* specific BET surface areas vs. the organosilica content in solution. On the left batch I–V impregnated with BTEVB, on the right batch I-III impregnated with BTEVA.

It was found, that treatment with the condensation solution introduces porosity only in the organosilica content which results in an increase of the *apparent* specific BET surface area. A trend towards higher *apparent* specific BET surface areas with increasing organosilica content in the impregnation solution was found for all CPG batches. 75 BTEVB and 75BTEVA from batch II are the exceptions from this trend. Further, it increases with the initial pore volume of the CPG batch, in general. The most significant differences are observed when comparing the samples 10–75BTEVB from batch I and V which differ the most in pore size and pore volume. In the case of 75BTEVB SBET differ between 358 $m^2 \cdot g^{-1}$ (batch I) and 767 $m^2 \cdot g^{-1}$ (batch V). Since it is assumed that the absolute organosilica content increases with the pore volume, because the volume of the impregnation solution is equal to it, this is in accordance with expectations. Comparing the results from batch II and III with the same pore volume and the difference being the

mesoporosity of batch II, the *apparent* specific BET surface area is slightly higher for 25 BTEVB and 50BTEVB as well as for 25 BTEVA and 50BTEVA of the macroporous batch III. The *apparent* specific BET surface areas of the impregnated samples from batches II and III with 1.5 $cm^3 \cdot g^{-1}$ and those of batch IV with 1.15 $cm^3 \cdot g^{-1}$ are very similar despite the difference in the pore volume. 75BTEVB of batch IV even shows a slightly higher *apparent* specific BET surface area of 629 $m^2 \cdot g^{-1}$ than the respective samples from batch III with 596 $m^2 \cdot g^{-1}$.

Key questions of this Sections is, which parameter limits the resulting *apparent* specific BET surface area and to which extend. The presented results might indicate that the size of the pristine pores in the CPG is the main aspect that limits the resulting *apparent* specific BET surface area and thus the formation of nanoporous organosilica phases. In order to verify this assumption, the organosilica content in the hybrid materials needs to be determined. In this context, it will be discussed whether the porosity might be limited by spatial limitations in small pores. Before this, the impact of the impregnation on the pristine CPG pore system is discussed based on MIP measurements.

Impact of the impregnation on large mesopore or macropore systems of CPG – mercury porosimetry intrusion

The effect of the impregnation on CPG batches with different initial pore systems is a key aspect in evaluating the impregnation process. Characterization of the macro- or large mesopore system which remain from the CPG is possible with MIP.

Figure 4-73 a) and c) show the high pressure mercury intrusion curves of 10–75BTEVB from the mesoporous batches I and II, respectively. For all samples a steep intrusion occurs and the intruded pore volume decreases with increasing organosilica content in the impregnation solution. In case of the samples 75BTEVB intrusion occurs over a broader pressure range, which indicates broad pore diameter distribution.[3] As usual, some mercury remains after complete extrusion in all samples, but no indication for ink-bottle pores or connected pores of different diameter is given, hence the extrusion curve does not provide additional information on the pore system. The respective pore diameter distributions are shown in the same Figure b) for batch I and d) for batch II. A decreasing trend of the pore size maxima is expected with increasing organosilica content in the impregnation solution since the formation of thicker organosilica layers is assumed. In contrast to the expectations, no significant trend of decreasing pore size maxima accompanies the increasing organosilica ratio in the case of batch I. This indicates that for the low initial pore volume and small pores in batch I, no homogeneous layer formation inside the initial CPG pores is possible. For batch II 10 –50BTEVB a trend is visible between 49 nm and 38 nm, hence, the formation of organosilica layers inside the initial pore system can be assumed for these samples. The higher pore volume of batch II compared to batch I might have positive impact on the impregnation process, although the initial pore size is comparable small. In contrast, the sample 75BTEVB from batch II shows an exceptionally high pore size of 45 nm. This indicates less homogeneous impregnation and blocking of the initial pore system in the sample which was impregnated with a solutions of higher concentration. This might be due to the decreased viscosity of the solution or premature condensation of the precursor at lower dilution. This result was reproduced with a second measurement device (*micromeritics AUTOPORE V SERIES* instead of *Quantachrome Poremaster®*) so that measuring errors can be excluded. The intruded pore volumes and pore diameter are given in Table 4-26 together with the results from impregnation with BTEVA.

[3] Focusing on the extrusion curve of 10BTEVB from batch I in Figure a), the extrusion is monitored only to 3500 psi which is due to a different measurement protocol. This sample was measured with another device, *micromeritics AUTOPORE V SERIES* instead of *Quantachrome Poremaster®* but the results are comparable, nonetheless.

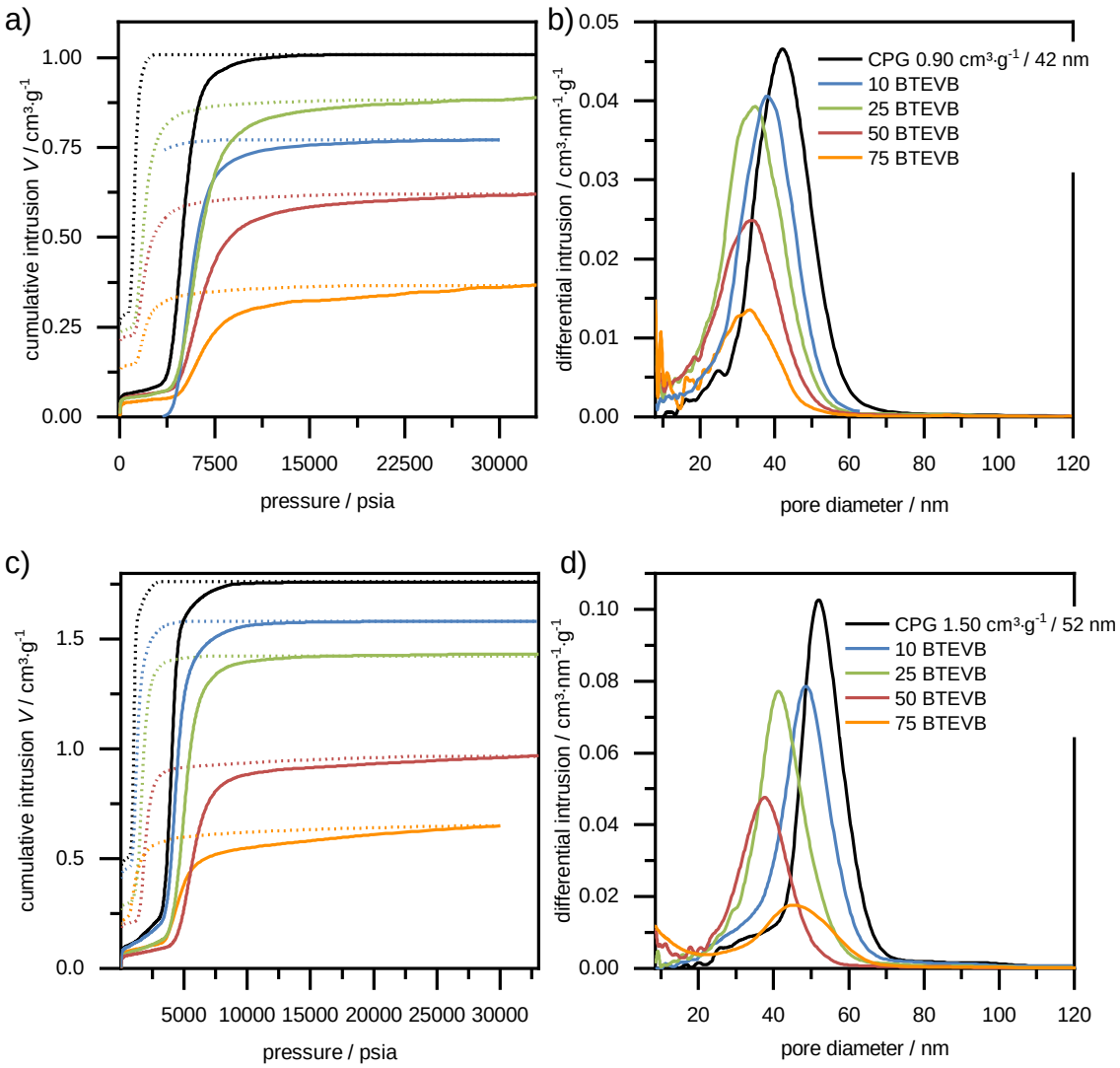

Figure 4-74: Mercury intrusion curves of CPGs impregnated with 10–75BTEVB batch I (a), batch II (c) and the respective pore diameter distributions from MIP of CPG batch I (b) and II (d).

The mercury intrusion curves of 10–75BTEVA from batch I are given in Figure 4-75 a), from batch II in Figure 4-75 c). The general trends of decreasing intrusion volume with increasing organosilica content in the impregnation solution is given for these samples as well with the exception of 75BTEVA from batch I which shows nearly the same intrusion volumes as 50BTEVA from the same batch. Also the pressure ranges of the intrusion of 75BTEVA are very broad for both batches, although the intrusions start at lower pressures. The pore diameter distributions are shown in Figure 4-75 b) for batch I 10–75BTEVA and d) batch II 10–75BTEVA, respectively. The intruded pore volumes and pore diameter are also summarized in Table 4-26.

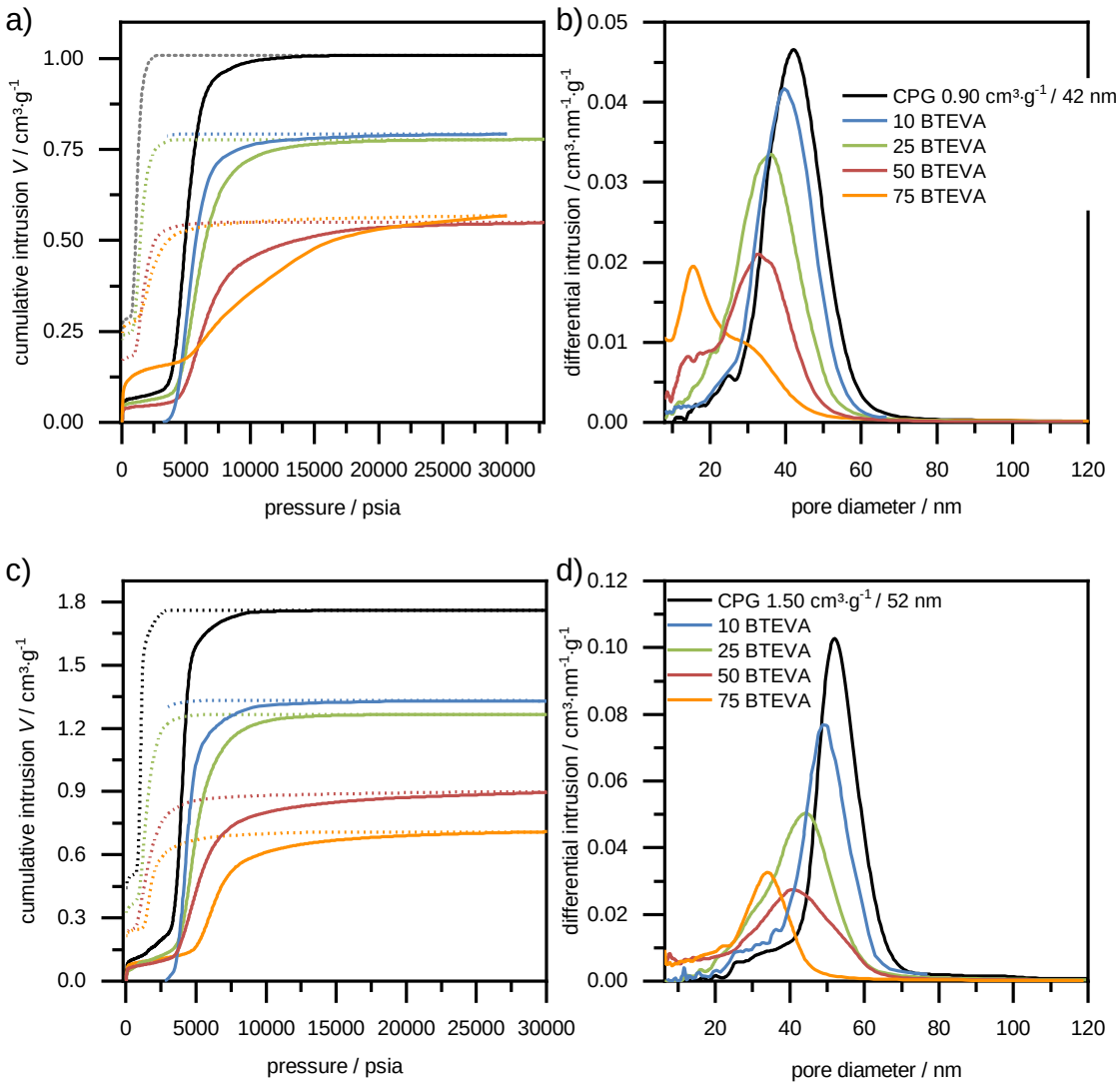

Figure 4-75: Mercury intrusion curves of CPGs impregnated with 10–75BTEVA batch I (a), batch II (c) and the respective pore diameter distributions from MIP of CPG batch I (b) and II (d).

After the pore diameter distribution and the measured pore volume, the filling degree is calculated from the intruded pore volume. It should be kept in mind, that the organosilica phases causes additional mass which is assumed to be impenetrable to mercury. The masses of the hybrid material are listed in Table 9-4 in the Appendix. The resulting pore volume has to be multiplied with a correction factor as shown in equation (8).

$$V_{\text{intr. Hg}} \cdot m_{\text{CPG+Organosilica}} = V_{\text{filled CPG}} \cdot m_{\text{CPG}} \tag{8}$$

$$V_{\text{filled CPG}} = \frac{m_{\text{CPG+Organosilica}}}{m_{\text{CPG}}} \cdot V_{\text{intr. Hg}}$$

where

$V_{\text{intr,Hg}}$ measured mercury intruded volume of the impregnated sample

$m_{CPG+Organosilica}$	mass of the hybrid material that was measured
m_{CPG}	initial mass of CPG
$V_{filled\ CPG}$	real pore volume of the impregnated CPG

With this, the pore volume of filled CPG ($V_{filled\ CPG}$) and the volume of the filling ($V_{filling}$) can be calculated (see equation (9)). The quotient of the filled volume and the initial volume of the CPG batch is the filling degree *F* as shown in equation (10).

$$V_{filling}=V_{CPG}-V_{filled\ CPG} \quad (9)$$

$$F=\frac{V_{filling}}{V_{CPG}} \quad (10)$$

where

$V_{filling}$	volume of the filling
V_{CPG}	pore volume of initial CPG batch
F	filling degree

Table 4-26 gives an overview of the intruded pore volume, the pore diameter and the filling degree of batches I and II impregnated with 10–75BTEVB and 10–75BTEVA.

Table 4-26: Overview of the mercury intruded volume, the pore diameter maxima and the filling degree *F* of CPG batch I and II impregnated with 10–75BTEVB and 10–75BTEVA respectively.

Sample	$V_{intr.\ Hg}$ / $cm^3 \cdot g^{-1}$	d_{Hg} / nm	Filling degree *F* / %	Sample	$V_{intr.\ Hg}$ / $cm^3 \cdot g^{-1}$	d_{Hg} / nm	Filling degree *F* / %
CPG batch I	0.9	42	-				
10BTEVB	0.77	40	14	**10BTEVA**	0.8	39	11
25BTEVB	0.80	34	11	**25BTEVA**	0.7	35	13
50BTEVB	0.55	33	26	**50BTEVA**	0.5	32	30
75BTEVB	0.31	32	52	**75BTEVA**	0.4	17	41
CPG batch II	1.50	52					
10BTEVB	1.36	49	9.3	**10BTEVA**	1.30	49	8.1
25BTEVB	1.28	41	2.7	**25BTEVA**	1.10	45	13
50BTEVB	0.86	38	23	**50BTEVA**	0.80	41	20
75BTEVB	0.47	45	48	**75BTEVA**	0.57	34	34

In the cases of batch I and II the mercury intruded pore volumes follow a decreasing trend with increasing organosilica content. Surprisingly, the pore volume of the sample 10BTEVB is nearly

the same as for the sample 25BTEVB. These differences might be within the error of the measurements. Also, the trend of the filling degree is similar for both batches. It increases with increasing organosilica content in a non-linear way, where the differences between the two precursors are more significant with a higher organosilica content. 25 BTEVA in both batches has a filling degree of 13 %, whereas 75BTEVA of batch I has a filling degree of 41 % and only 34 % in batch II. The filling degree is higher for the respective samples with BTEVB, e.g. 52 % for 75BTEVB of batch I and 48 % for 75BTEVB of batch II. An explanation for this behavior might be the second phase of spherical particles which was sporadically found in the SEM images on the outer surface of the BTEVA-impregnated CPG beads. Possible differences in the organosilica content of samples with BTEVA and with BTEVB will be discussed in the next chapters. The filling degree of 25BTEVB of batch I is 11 %, which is even lower than for 10BTEVB (14 %) from this batch. In batch II the filling degree of 25BTEVB is only 2.7 %. This value is an aberration and might be caused by insufficient drying of the sample which distorts the weight increase of the sample.

As already mentioned in context of the morphology of the impregnated CPG beads, multiple impregnation was carried out to improve the homogeneity of the impregnation. It would be of particular interest to evaluate if multiple impregnation has a positive impact on the impregnation process in terms of the pore diameter distributions from MIP. In context of the *apparent* specific BET surface area, no improvement was found with this approach. The respective intrusion curves and the pore size distributions are shown in Figure 4-76. The general shape of the intrusion curves follows the expectations and is hence not further discussed. For comparison, other samples that were impregnated with different BTEVB-containing solutions are included in pale colors in the same plot.

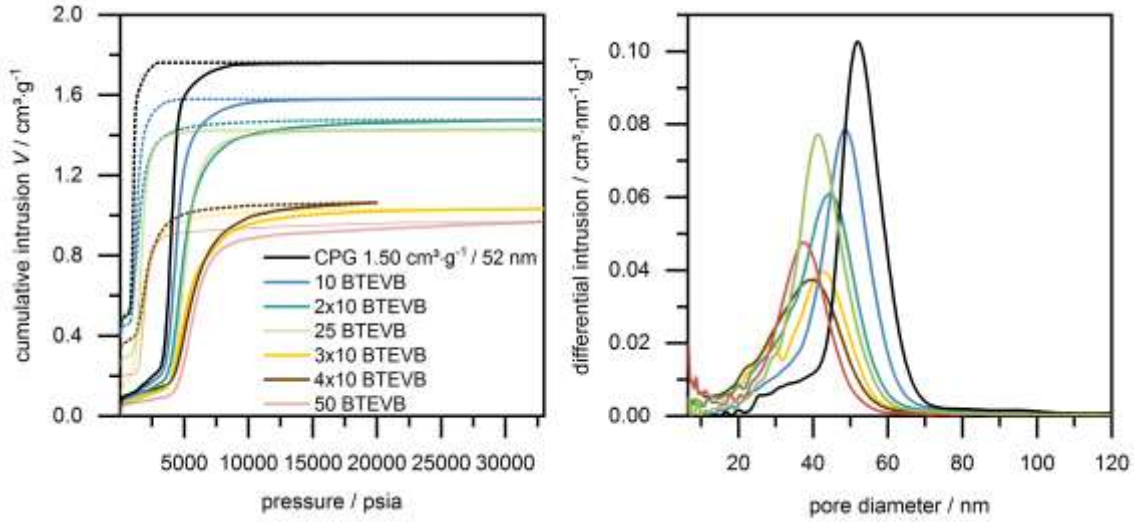

Figure 4-76: Left: Mercury intrusion curves of CPG batch II that was impregnated up to four times (1-4x10BTEVB), right: pore size distributions. Curves of 25BTEVB and 50BTEVB (in pale colors) are also shown for comparison purposes.

The intruded pore volumes and the pore diameter maxima are given in Table 4-27. The filling degree of these samples could not be determined since mass loss occurs in every impregnation step after condensation. This might be due to leaching of the organosilica content or to further condensation of the already existing organosilica layers. Thus, the calculations from equations 8–10 are not valid.

Table 4-27:Pore diameter and pore volume from MIP for CPG batch II that was impregnated up to four times with a solution containing 10 wt% BTEVB.

Sample	$V_{intr.\ Hg}$ / $cm^3 \cdot g^{-1}$	d_{Hg}/ nm
CPG batch II	1.5	52
1x10BTEVB	1.36	49
2x10BTEVB	1.28	44
3x10BTEVB	0.88	43
4x10BTEVB	0.90	40

The pore size of the multiple impregnated samples changes stepwise with each impregnation cycle without any irregularities. The pore diameter maxima of the samples that were impregnated two and three times (2x10BTEVB and 3x10BTEVB) and 25BTEVB are all similar between 44 nm and 41 nm. However, the pore diameter distribution of the multiple impregnated samples are broader. 3x10BTEVB shows a bimodal pore size distribution which is not explainable here. In contrast, the change of the intruded pore volume is disproportional for the multiple impregnated samples. The sample that was impregnated twice, 2x10BTEVB, and the sample 25BTEVB have the same intruded pore volume of 1.25 $cm^3 \cdot g^{-1}$. The intruded pore volumes of 3x10BTEVB and 50BTEVB are also very similar with 0.88 $cm^3 \cdot g^{-1}$ and 0.86 $cm^3 \cdot g^{-1}$. Surprisingly, the pore volume of the sample that was impregnated four times does not change any further, it is 0.90 $cm^3 \cdot g^{-1}$, which could be due to leaching of the organosilica content. Hence, from these results no positive impact can be assumed from multiple impregnation.

CPG batch III, which is macroporous, but has the same pore volume as batch II, was also impregnated with both precursors BTEVA and BTEVB. Here, different trends are expected due to the large initial pores. The mercury intrusion curves and pore diameter distributions are show in Figure 4-77.

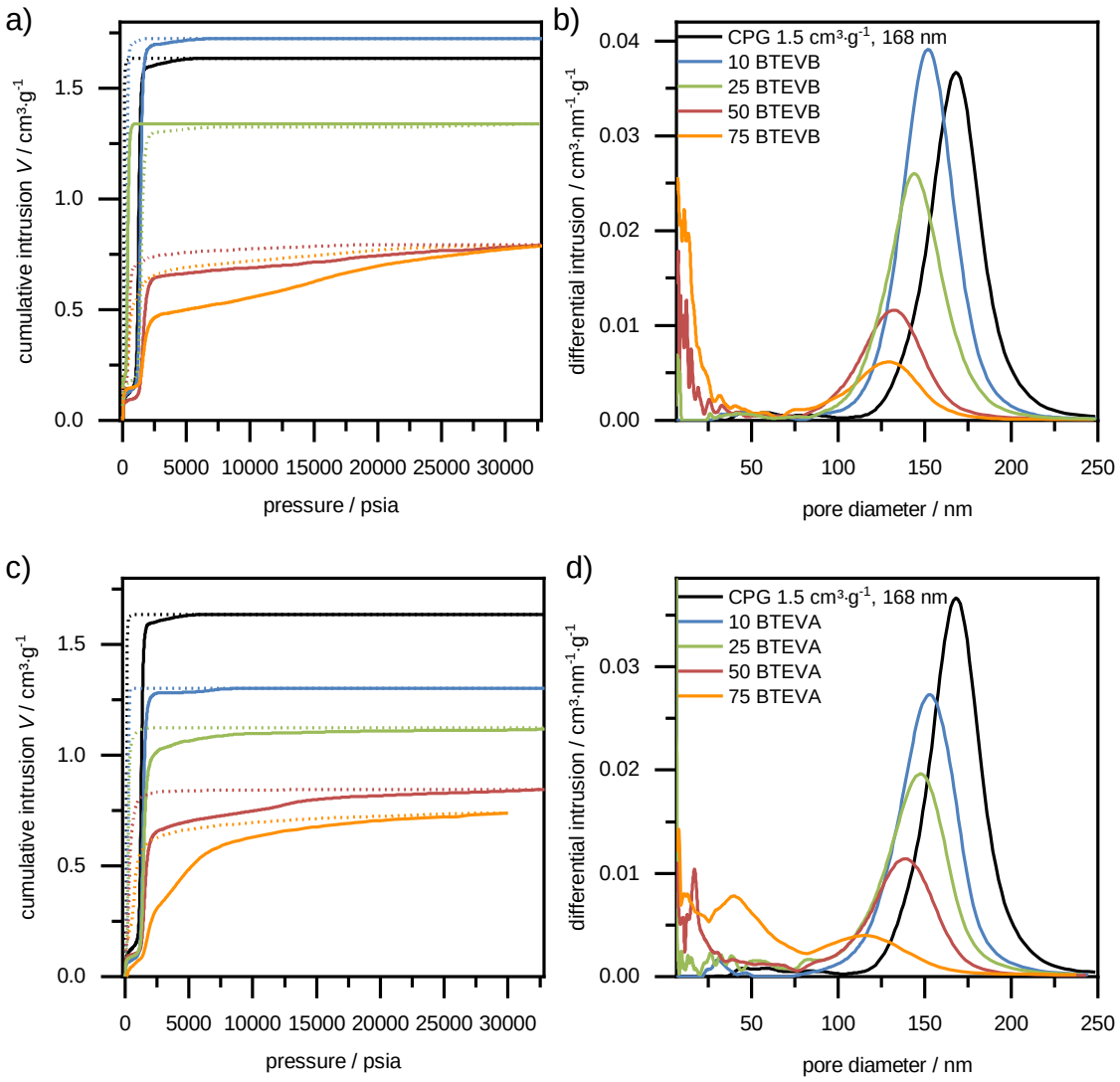

Figure 4-77: Mercury intrusion curves of CPG batch III impregnated with 10–75BTEVA a), and 10–75 BTEVA c), respective pore diameter distributions of b) 10–75BTEVB and d) 10–75BTEVA.

In general, the pore size as well as the intruded pore volume shifts for 10-50BTEVB and 10–50BTEVA. It is noticeable that the mercury intrusion volume of 10BTEVB is higher than for the pure CPG. This would cause a negative filling degree, and is thus not calculated here. The higher pore volume might be an artefact of the MIP measurement or due to inhomogeneity in the CPG batch. Another reason could be leaching of finely dispersed silica residues inside the pores, by washing and treatment with the ethanol/sodium hydroxide solution. The intrusion volumes of 50BTEVB and 75BTEVB seem to be very similar, although it is prominent in the curve of 75BTEVB that the intrusion curve shows a steep increase up to 2400 psi and a less steep increase over the whole following pressure range. In the pore diameter distribution this is represented in additional pores below 20 nm which are not reliably determined by MIP. Here, no shift of the pore diameters, but rather of the pore volume and the filling degree is noticed. This is similar to the results from 75BTEVB of batch II. This inhomogeneous filling is interpreted as pore blocking. It occurs for the same impregnations for both batches which have the same initial pore volume,

despite the differences in pore size. The intrusion curves of 10–75BTEVA follow the expected trend of decreasing intrusion volume. The intrusion of the samples 50BTEVA and 75BTEVA both show two steep regions, which indicates the presence of a second pore size. Indeed, the pore diameter distribution is bimodal and hints at an inhomogeneous impregnation. Also 50BTEVA shows a second pore size below 20 nm. The intruded pore volumes, filling degrees and pore diameter maxima are summarized in Table 4-28.

Table 4-28: Pore volumes and pore diameters as well as filling degree *F* according to MIP of CPG batch III and the samples that were impregnated with 10–75BTEVA or 10–75BTEVB, respectively.

Sample	$V_{intr.\ Hg}$ / $cm^3 \cdot g^{-1}$	d_{Hg} / nm	*F* / %	Sample	$V_{intr.\ Hg}$ / $cm^3 \cdot g^{-1}$	d_{Hg} / nm	*F* / %
CPG batch III	1.5	168	-				
10BTEVB	1.57	153	-	**10BTEVA**	1.2	153	17
25BTEVB	1.14	144	21	**25BTEVA**	1.0	147	23
50BTEVB	0.69	132	22	**50BTEVA**	0.70	138	33
75BTEVB	0.64	130	33	**75BTEVA**	0.65	122	26

BTEVA and BTEVB show different hydrophilicity and the amino function in BTEVA enables the formation of hydrogen bonds. This is assumed to cause differences in the impregnation and the condensation behavior of the two precursors. Indeed, the experiences from common PMO syntheses show that BTEVA condensates, in general, more easily and unintended due to water from. One possible result would have been a more inhomogeneous impregnation with BTEVA than with BTEVB. Although differences occur between the precursors, no distinct impact of the different functionality of the precursors can be found so far.

The macroporous batches IV and V were both only impregnated with 10–75BTEVB. The mercury intrusion curves and pore diameter distributions from both batches are shown in Figure 4-78. The intrusion curves show no mentionable specifics. A shift of the pore size maxima is visible for batch IV up to only 25BTEVB, while for batch V it visible is up to 50BTEVB. It is nearly indistinguishable for the samples with higher organosilica content. It should be mentioned that the initial pore system of batch V is bimodal. Here, only the larger macropores are discussed for better clarity.

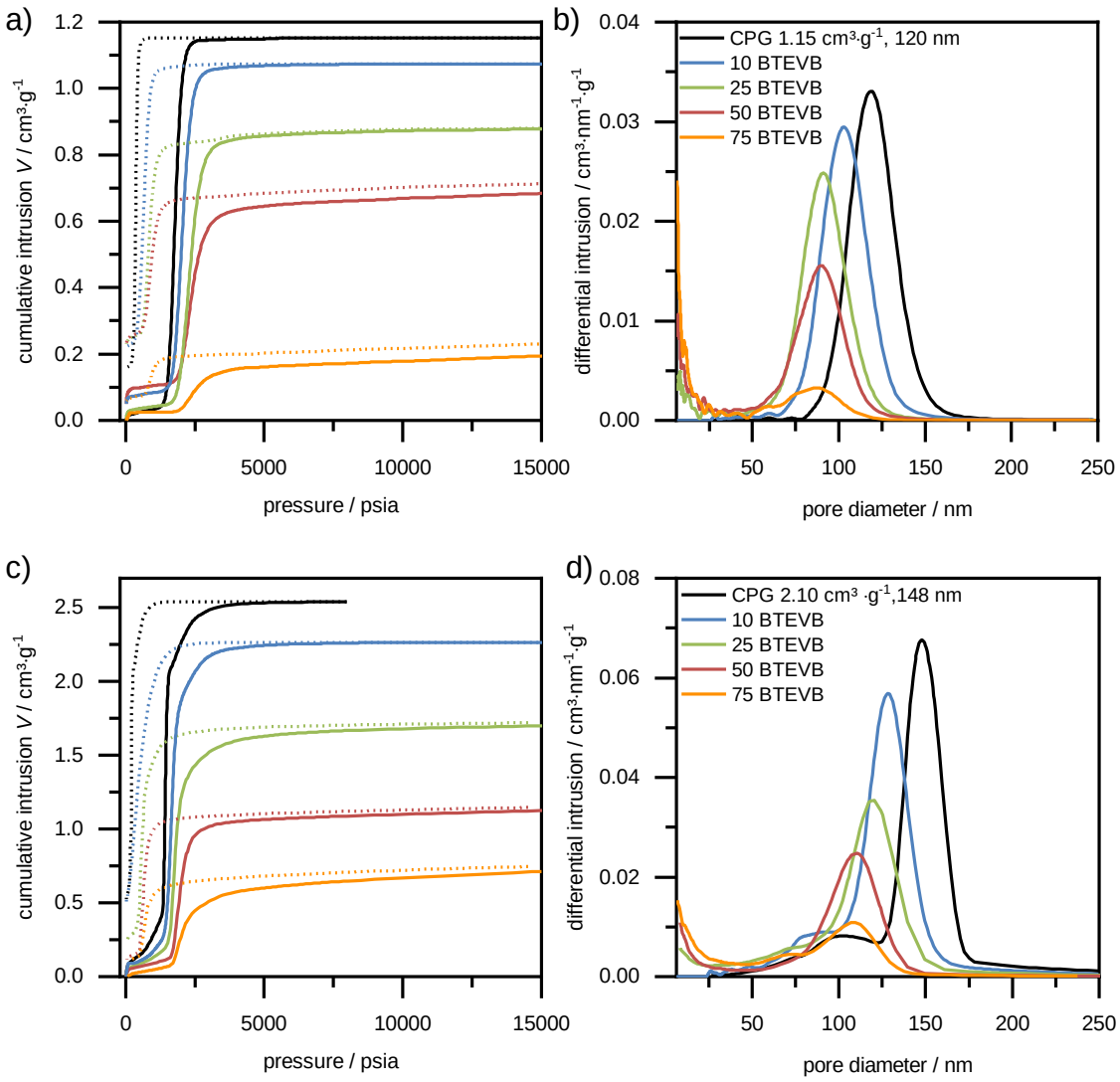

Figure 4-78: Mercury intrusion curves of CPG batch III impregnated with 10–75BTEVA a), and 10–75 BTEVA c), respective pore diameter distributions of b) 10–75BTEVB and d) 10–75BTEVA.

The pore volumes, filling degrees and pore diameter maxima of the impregnated samples from batches IV and V are summarized in Table 4-29.

Table 4-29: Pore volumes and pore diameters as well as filling degree *F* according to MIP of CPG batch IV and batch V impregnated with 10–75BTEVB.

Sample	$V_{intr.\ Hg}$ / cm³·g⁻¹	d_{Hg} / nm	*F* / %	Sample	$V_{intr.\ Hg}$ / cm³·g⁻¹	d_{Hg} / nm	*F* / %
CPG batch IV	1.15	120	-	**CPG batch V**	2.10	148	-
10BTEVB	0.98	103	15	**10BTEVB**	2.08	128	-
25BTEVB	0.85	44	19	**25BTEVB**	1.50	117	10
50BTEVB	0.61	43	32	**50BTEVB**	1.07	107	21
75BTEVB	0.24	40	70	**75BTEVB**	0.70	109	41

The pore volume decreases with increasing organosilica content in both batches and the filling degree increases. Whereas the filling degrees of 25BTEVB and 50BTEVB from batch IV are comparable to those of the other CPG batches, the impregnation degree of 70 % in the case of 75BTEVB is especially high. This samples has been shown a high *apparent* specific BET surface area before as well. The pore volume changed marginally in the case of 10BTEVB from batch V in comparison to the initial CPG so that the filling degree was incalculable. However, the pore size shifted significantly by 20 nm towards smaller pores. This has been observed and discussed before in the context of batch I for the samples 10BTEVB and 25BTEVB, thus this is independent from the pore volume or pore size since batch I and V differ in both aspects significantly.

In order to give an overview of the impregnation of the different CPG batches and the results from MIP, Figure 4-79 a) summarizes the remaining pore volumes after impregnation with BTEVB-containing solutions and c) with BTEVA-containing solution. The pore volumes of the multiple BTEVB-impregnated samples are also shown, although the filling degree was not calculated. In general, in the case of large initial pore volumes, the pore volume decreases monotonous with increasing organosilica content in the impregnation solutions, and this is less distinct for small initial pore volumes. Exceptions to this trend have already been previously discussed in detail. The plots b) and d) shows the relation between the filling degree, which was calculated from the pore volume after impregnation, and the content of BTEVB (respectively BTEVA) in the impregnation solution. The evaluation of the filling degree is difficult as no distinct trend can be identified. Overall, in the BTEVB impregnated samples, the samples from batch IV have the highest filling degree. In this CPG batch the pore size is large (120 nm), but the pore volume is medium at 1.15 $cm^3 \cdot g^{-1}$. This indicates that large pores improve the penetration of the impregnation solution and the formation of nanoporous organosilica layer inside the initial pore system. On the other hand also batch I with a low pore volume (0.9 $cm^3 \cdot g^{-1}$) and small pores (42 nm) shows high values for the filling degree, although pore blocking is assumed for this sample series. Due to the inconsistences in the filling degree in batch II and III with the same initial pore volume and different initial pore diameter is not clear to what extent the volume of the organosilica phase fluctuates with the available space.

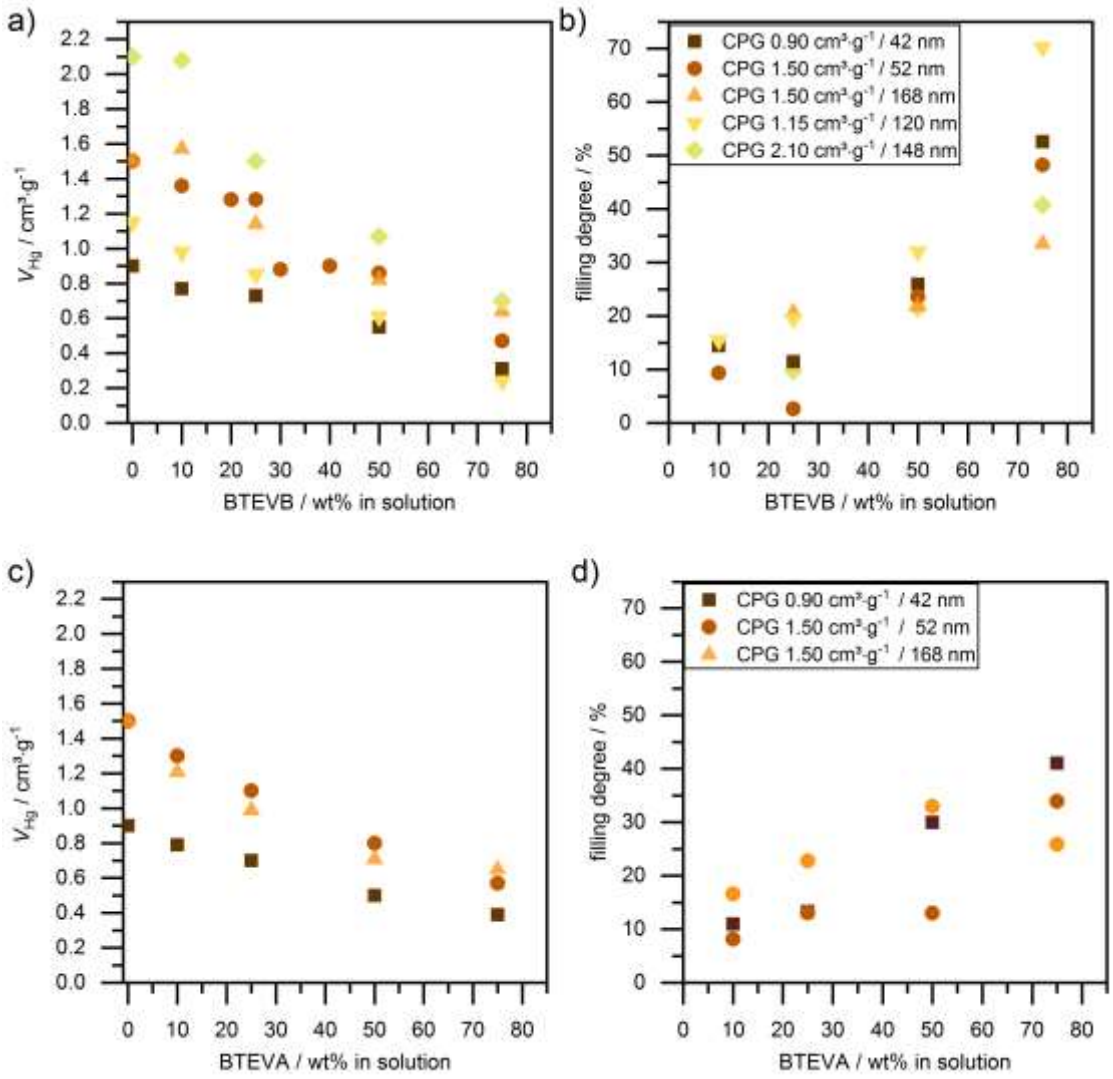

Figure 4-79: Graphic plot of the mercury intruded pore volume vs. a) BTEVB content in the impregnation solution of the CPG batches I–V and c) BTEVA content in the impregnation solution of the CPG batches III. Plot of the resulting filling degree values that were calculated from this for BTEVB b) and BTEVA d).

However, the results show that a filling degree of 100 % is impossible, even with pure organosilica. With the intention of forming a hierarchical hybrid material with an accessible organosilica phase, the supply of large pores and high pore volumes is a promising approach.

Calculation of the organosilica content by thermal analysis

In addition to the characterization of the porosity and the filling degree, the organosilica content is crucial for the characterization of the organosilica/silica hybrid material. In a first-order approximation, the molar content can be calculated from the mass loss in TG measurements. For simplification the composition of CPG was assumed to be 100 % silica. Surface-adsorbed water evaporates in the temperature range of 25–150 °C. The main mass loss occurs in the temperature range of 300–800 °C. It is assumed that only the organic bridging unit, which is highlighted in Figure 4-80 for BTEVB and BTEVA, decomposes between 300–800 °C. A further assumption is that the full condensation of the organosilica precursor occurs is given 300 °C. With this assumptions mass loss of 55 % for BTEVB and 58 % for BTEVA is calculated for the pure organosilicas.

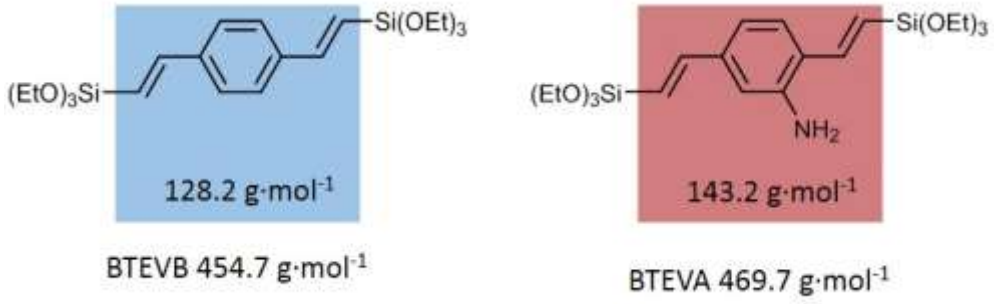

Figure 4-80: Molecular structure of BTEVB on the left and BTEVA on the right. The organic bridges which decompose in the temperature range of 300–800 °C are highlighted in blue and red, respectively. The molar mass of the whole precursors and bridge is given underneath.

Figure 4-81 shows as an example, TG measurements of CPG batch I which was impregnated with 10–75BTEVB on the left and 10–75BTEVA on the right.

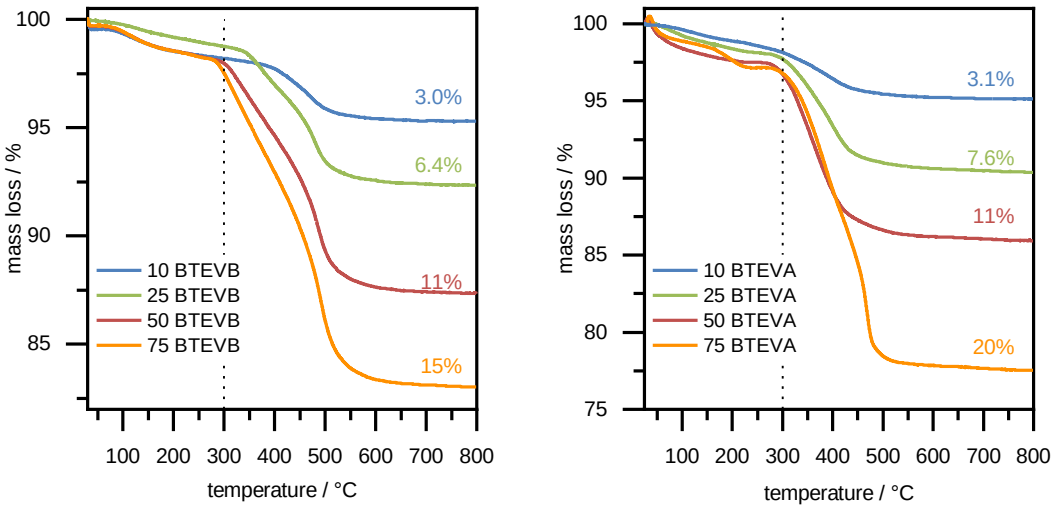

Figure 4-81: TG measurements (Ar/O_2 80/20) of impregnated CPG batch I with different percentages of BTEVB (left) and BTEVA (right).

Further TG plots are given in the Appendix, samples 10–75BTEVB and 10–75BTEVA from batch II in Figure 9-24, 10–75BTEVB and 10–75BTEVA from batch III in Figure 9-25, 10–75BTEVB from batch IV and V in Figure 9-26.

The mass loss increased with increasing organosilica content in the impregnation solutions of BTEVB and BTEVA for all batches without exception. In the example of batch I, the mass loss of BTEVA- and BTEVB-impregnated samples in the temperature range of 300–800 °C is comparable for impregnations with 10, 25 and 50BTEVB or BTEVA, but is significantly higher for 75BTEVA than for 75BTEVB. This behavior was also found for batch II and III and is interpreted as a higher organosilica content in the 75BTEVA samples. This is in contrast to the observation of higher filling degrees in 75BTEVB samples in comparison to 75BTEVA samples and hints at a less successful impregnation with BTEVA but a higher organosilica content on the outer surface of the CPGs, or a significantly higher density of the BTEVA phase due to lower porosity of this phase. Beyond, slightly higher mass loss is expected for BTEVA than for BTEVB.

The theoretically expected mass loss could be calculated for the impregnated samples 10–75BTEVB and 10–75BTEVA from batch I–III or I–V as well. Therefore, further assumptions need to be made. All samples were impregnated with a solution that contains a specific weight ratio of the precursor, but the amount of the impregnation solution was varied with the pore volume of the respectively used CPG batch. The densities of the solutions is not specified and might vary with the respective organosilica content. Since the density of toluene is 0.89 $g \cdot cm^{-3}$ and for both precursors a density of 1.0 $g \cdot cm^{-3}$ is assumed, a density of approximately 1.0 $g \cdot cm^{-3}$ could be assumed for the calculation of the theoretically expected mass loss in a first approximation. The mass loss of the impregnated samples needs to be observed in the context of the different CPG batches. The respectively calculated theoretical values are given in Table 4-30 together with the experimental values of the mass loss from TG measurements (300–800 °C) and the thereof calculated initial weight ratio of BTEVB to CPG as well as the molar percentage of the precursor in 10–75BTEVB for the different batches I–V, and the respective values for 10–75BTEVA from batch I-III. In most cases, the experimental mass loss and therewith the weight ratio BTEVB/CPG and BTEVA/CPG is higher than the theoretical value, e.g. in case of 75 BTEVB from batch II with 1.5 $cm^3 \cdot g^{-1}$ of pore volume, a mass loss of 15 % is expected but 23 % are obtained. This results in a weight ratio of BTEVB/CPG of 1.5, whereas the theoretical value is only 1.13. In 75BTEVB from batch III the theoretical values are the same as in batch II, but the mass loss is only 19 %, the weight ratio is 1.07. Hence, no conclusive trend can be found. In case of 75BTEVA from batch III the mass loss is even 30 %, which is a weight ratio BTEVA/CPG of 2.2, also likewise 1.13 was expected. Unexpectedly higher mass loss could indicate erroneous assumptions for the TGA which could include, for e.g., incomplete hydrolysis at 300 °C. Hence, the respectively calculated

molar percentage of DVA- or DVB-phases in the hybrid material is not exact, but a first-order approximation.

Table 4-30: Overview of the mass loss from TG measurements (300–800 °C), the respectively calculated weight ratio of precursor to CPG and the molar percentage of the precursor in 10–75BTEVB for the different batches I–V ad 10–75BTEVA for the batches I–III. Additionally theoretical values, which are calculated with assuming the named approximations are given in italicized letters.

Batch	I	II	III	IV	V		I	II	III
mass loss from TG 300–800 °C / %									
10BTEVB	3.0	4.5	4.6	5.2	6.5	**10BTEVA**	3.1	5.2	4.3
theoretical	*2.3*	*3.7*	*3.7*	*2.9*	*4.9*	***theoretical***	*2.5*	*4.0*	*4.0*
25BTEVB	6.4	9.3	9.4	7.5	12	**25BTEVA**	7.6	10	9.1
theoretical	5.2	7.7	7.7	6	9.7	***theoretical***	5.6	8.3	8.3
50BTEVB	11	16	16	15	20	**50BTEVA**	11	17	17
theoretical	*8.7*	*12*	*12*	*10*	*14*	***theoretical***	*9.5*	*13*	*13*
75BTEVB	14	23	19	15	24	**75BTEVA**	20	23	30
theoretical	*11*	*15*	*15*	*13*	*17*	***theoretical***	*12*	*16*	*16*
weight ratio BTEVB/CPG or BTEVA/CPG									
10BTEVB	0.11	0.18	0.18	0.19	0.26	**10BTEVA**	0.11	0.11	0.15
theoretical	*0.09*	*0.15*	*0.15*	*0.12*	*0.21*	***theoretical***	*0.09*	*0.15*	*0.15*
25BTEVB	0.26	0.40	0.41	0.31	0.56	**25BTEVA**	0.29	0.40	0.36
theoretical	*0.23*	*0.38*	*0.38*	*0.29*	*0.53*	***theoretical***	*0.23*	*0.38*	*0.38*
50BTEVB	0.49	0.82	0.82	0.75	1.16	**50BTEVA**	0.45	0.81	0.81
theoretical	*0.45*	*0.75*	*0.75*	*0.58*	*1.05*	***theoretical***	*0.45*	*0.75*	*0.75*
75BTEVB	0.74	1.50	1.07	0.75	1.59	**75BTEVA**	1.04	1.3	2.20
theoretical	*0.68*	*1.13*	*1.13*	*0.86*	*1.58*	***theoretical***	*0.68*	*1.13*	*1.13*
molar percentage precursor /%									
10BTEVB	1	2	2	2	3	**10BTEVA**	1	1	2
theoretical	*1*	*2*	*2*	*2*	*3*	***theoretical***	*1*	*2*	*2*
25BTEVB	3	5	5	4	7	**25BTEVA**	4	5	5
theoretical	*3*	*5*	*5*	*4*	*7*	***theoretical***	*3*	*5*	*5*
50BTEVB	6	11	11	10	15	**50BTEVA**	6	10	10
theoretical	*6*	*10*	*10*	*8*	*14*	***theoretical***	*6*	*10*	*10*
75BTEVB	10	19	14	10	21	**75BTEVA**	13	17	28
theoretical	*9*	*15*	*15*	*11*	*21*	***theoretical***	*9*	*14*	*14*

In the TG plot of 75BTEVB from batch II (Appendix, Figure 9-24), significant mass loss starts at temperatures of 240 °C, whereas in all other samples with BTEVA and with BTEVB no mass loss occurs at temperatures below 300 °C. This special behavior could probably be due to a lower condensation degree in the organosilica phase of this sample. It has already been mentioned, that this sample showed a comparably low *apparent* specific BET surface areas and hindered pore formation was assumed. This could cause a low condensation degree. The condensation degree could be proven by quantitative solid-state NMR spectroscopy, but the temporal effort for such measurements was evaluated as disproportional for this sample.

In the case of 25BTEVB from batch I and batch II the obtained filling degrees calculated from MIP were lower than in the respective 10BTEVB samples. The mass loss of these samples fits well with the trend in the other samples, so that the contrary trend of the pore volumes cannot be explained at this point.

The values for mass loss and respectively calculated molar percentage of BTEVB samples are plotted against the organosilica content in the impregnation solution in Figure 4-82 a) and b), those of BTEVA samples in c) and d), respectively. The molar percentage of the precursor in the DVB/CPG and DVA/CPG hybrids is calculated from the mass loss so that the general trend is the same for both values. Generally speaking, the mass loss and the molar percentage of the organic bridge increases with higher organosilica content in the impregnation solution within one batch and in comparison of the different batches it increases with larger pore volume of the respective initial CPG batch. This is reasonable since the volume of the impregnation solution was chosen to be equivalent to the pore volume and hence, the absolute organosilica amount was higher in these impregnations. Most interesting is the observation of the results from samples with the same pore volume and different pore sizes, namely from batches II and III.These samples show congruent values for the BTEVB and the BTEVA samples. It was shown previously that the filling degree of these samples is also similar, despite some inconsistencies. Hence, in this size regime, the pore size seem to have no impact on the impregnation process or on potential leaching of the precursor.

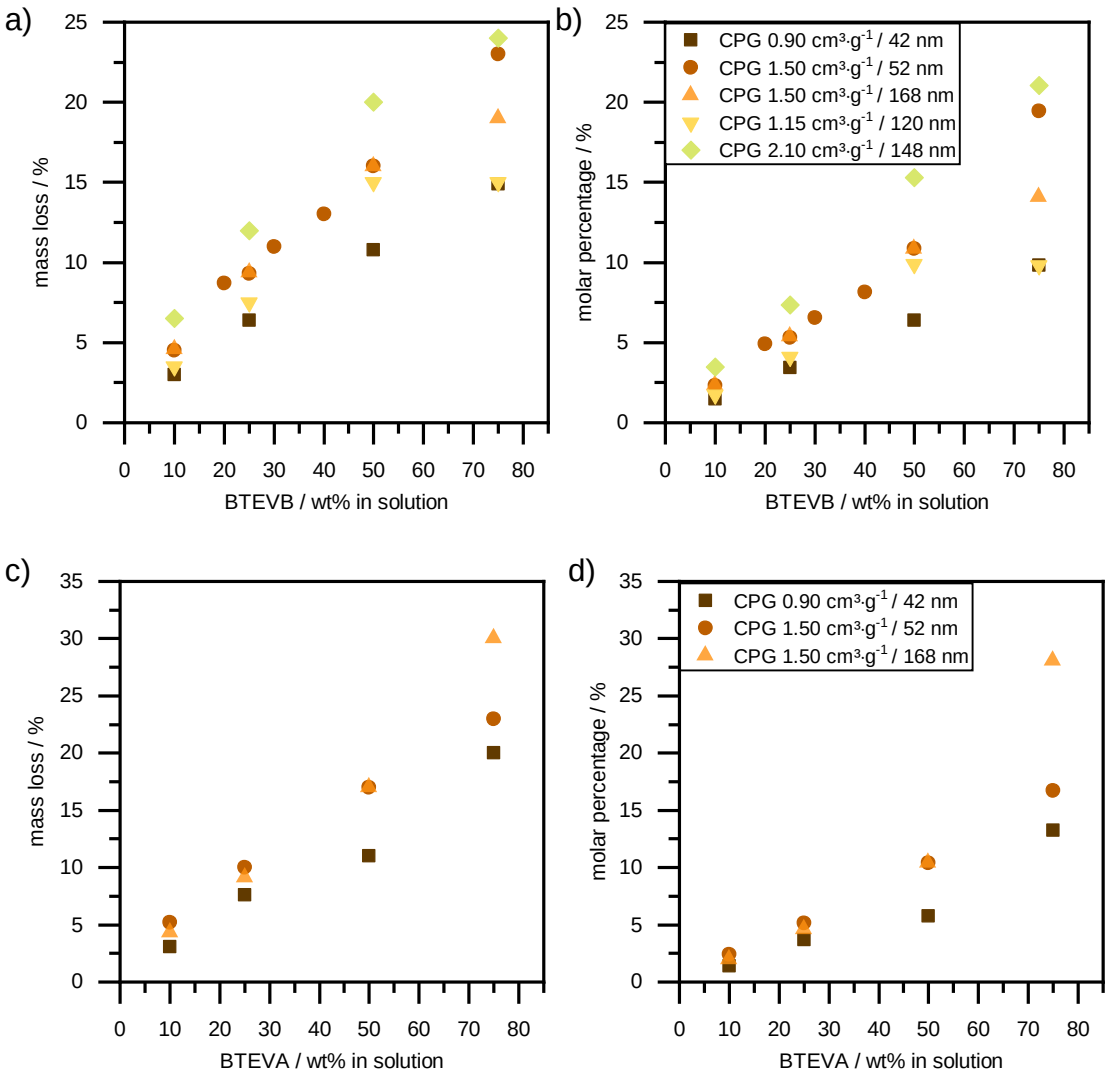

Figure 4-82: Plot of the mass loss from TG measurements for CPG batches I–V which were impregnated with impregnation solutions containing different percentages of BTEVB a) or BTEVA c). The molar percentage was calculated for each sample and is plotted for BTEVB b) and BTEVA d).

It is well demonstrated that the molar ratio of organosilica in the hybrid material can be adjusted on the one hand by the BTEVA or BTEVB content in the impregnation solution, or, on the other hand by the pore volume. Comparing 25BTEVB and 75BTEVB from batch I and V, respectively, the absolute difference of the mass loss is 5.6 % points in 25BTEVB and 9 % points in 75BTEVB. In contrast to this, the relative difference of the mass loss is higher for 25BTEVB, it is 88 % higher for 25BTEVB from batch V than in the sample from batch I, but only 71 % higher for 75BTEVB from batch V.

The summarized results show that the initial pore volume of the CPG, and not the content of organosilica in the impregnation solution is the key parameter for the reliable adjustment of the molar organosilica content in the hybrid material. It was additionally of interest, whether the *apparent* BET surface area depends on the provided pore volume, as it was assumed from the previous results or if it depends only on the molar content of the organosilica phase. In Figure

4-83 the specific (*apparent*) BET surface areas of the impregnated materials are plotted versus the molar content of the organosilica phase.

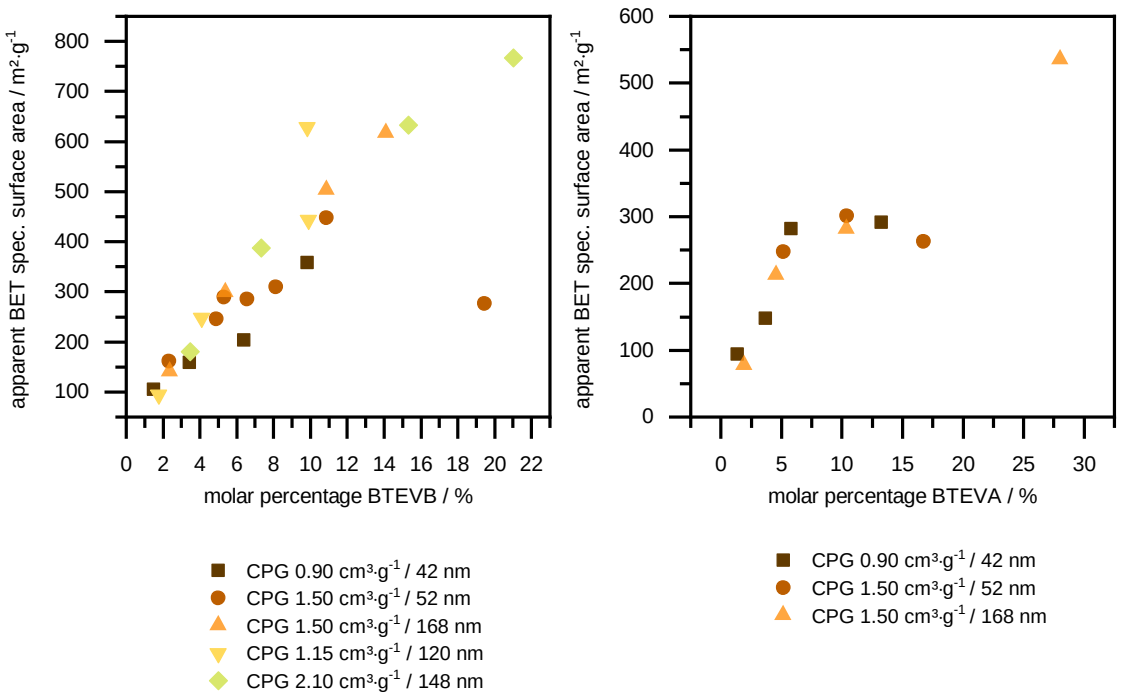

Figure 4-83: Plot of the apparent BET surface areas versus the molar percentage calculated from the TG measurements for CPG batch I–V which were impregnated with BTEVB (left) and for CPG batch I–III impregnated with BTEVA (right).

In the case of BTEVB-impregnated samples, the correlation is linear for all CPG batches, besides some expectations. This means that the specific BET surface area is proportional to the organosilica content in the hybrid material and is not significantly influenced by the pore volume. In the case of BTEVA-impregnated samples the correlation is less distinct. The molar percentage of BTEVA does change in the samples 50BTEVA and 75BTEVA from batch I and II, but the specific BET surface area even decreases in case of batch II with increasing organosilica content. This inconsistency in the BTEVA-impregnated samples has already been discussed before and might be a hint for inhibited formation of the microporous DVA-bridged organosilica, although the impregnation seem to be successful. Also very prominent is the sample 75BTEVA from batch III which combines a high specific BET surface area as well as a high molar percentage of BTEVA, whereas the molar percentages and specific BET surface areas of the 75BTEVA samples from batch I and II are significantly lower.

Characterization of the impregnated samples 50BTEVB and 50BTEVA from batch III by CP-MAS NMR spectroscopy

The sample 50BTEVB from batch III was chosen as an example for the characterization with CP-MAS NMR spectroscopy. The ^{29}Si-CP-MAS NMR spectra of pure CPG and 50BTEVB are compared in Figure 4-84.

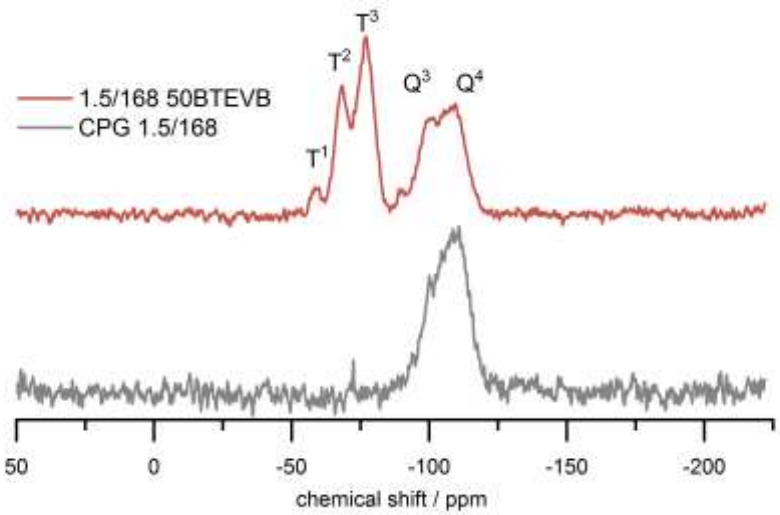

Figure 4-84: ^{29}Si CP-MAS NMR (spinning speed = 5 kHz) of CPG batch III (gray) and the sample 50BTEVB (red).

For CPG, broad overlapping signals in the range of -128 to -84 ppm are observed which can be assigned to Q^3 and Q^4 Si species, respectively. The breadth of these Q signals imply that the CPG materials contain broad distribution of local environments. After impregnation, additional T species appear. The signal at a chemical shift of -77 ppm is assigned to T^3, the signal at -67 ppm is assigned to T^2 and the signal at -59 ppm is assigned to T^1 silica species. The presence of T^1 silica species indicates that some Si atoms contain two siloxane linkage which are not condensed (i.e., Si-OH). Since Q signals from pure silica are always observed in the spectra of organosilica/silica hybrid materials, no information concerning the integrity of the Si-C bond is obtained. Since CP-MAS NMR spectra give only semi-quantitative information, direct excitation ^{29}Si MAS NMR measurements were performed to obtain relative quantity of the respective T and Q species. The exact ratio of T and Q signals can be determined by the deconvolution of Gaussian fits of the different signals. Q^4 was used as reference signal, and the relative intensities of the different T^n and Q^n species are measured in an experiment without CP and the relative ratios of T and Q are calculated. The plots are given in the Appendix (Figure 9-35) and the results are summarized in Table 4-31.

Table 4-31: Results from quantitative direct excitation solid state ^{29}Si-MAS NMR. The percentages of the different T and Q species relative to Q^4 are given separately, and the relative ratio of Q to T is calculated in the result column. Therewith the resulting molar BTEVB content in the hybrid material can be caluclated

Sample	T^1	T^2	T^3	Q^2	Q^3	Q^4	**T**	**Q**	**BTEVB**
CPG 1.5/168 50BTEVB	2.8 %	17.5 %	24.9 %	0.77 %	24.7 %	100 %	**27 %**	**73 %**	**16 mol%**

50BTEVB has a T to Q ratio of 27 % to 73 %. Considering that the organosilica precursor is bis-silylated, this is 16 mol% of BTEVB in the hybrid material. Looking back to the results from the TG analysis 11 mol% (Table 4-30) was calculated. Hence, the calculation of the molar percentage of the precursor from the TG and the measurements of quantitative solid state ^{29}Si-MAS NMR show a gap. In the TG measurements only the temperature range of 300–800 °C was considered, so that incomplete decomposition of the organic bridge under the conditions of the measurement or significant amounts of salt residues, e.g. sodium hydroxide, after impregnation and condensation might cause erroneous results. Beyond, the CPG composition was assumed to be 100 % silica. On the other hand, the results from solid state NMR are based on the integrals from deconvolution of overlapping signals which is also accompanied by an observational error. Hence, the difference between the two measurements cannot be evaluated at this point.

The integrity of the organic bridging unit can be affirmed by a ^{13}C-CP-MAS NMR spectrum that is shown in Figure 4-85, plotted together with the liquid-state NMR spectrum of the precursor (measured in $CDCl_3$) for comparison. In presentations of the solid-state NMR together with a liquid state NMR spectrum, solvent effects on the chemical shift have to be considered. However, good agreement of the signals of the two different vinyl carbons (C1’ and C2’), the quaternary carbons (C1) and the aromatic carbons (C2) of the benzene ring of the bridging unit is observed.

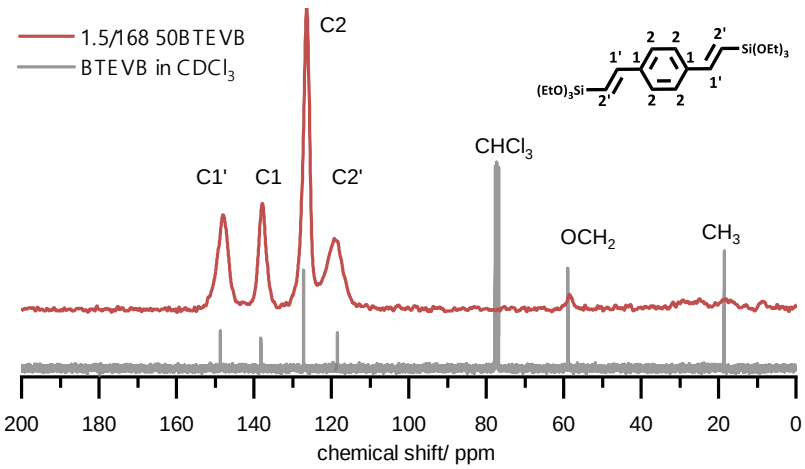

Figure 4-85: ^{13}C-CP-MAS NMR (spinning speed = 13 kHz) of 50BTEVB (red) from CPG batch III and liquid state NMR spectrum of the precursor BTEVB measured in $CDCl_3$ (gray) both plotted with normalized intensity.

Also the sample 50BTEVA from batch III was characterized with CP-MAS NMR spectroscopy. In Figure 4-86 the ^{29}Si-CP-MAS NMR spectra of 50BTEVA is compared to the pure CPG and 50BTEVB. The assignment of Q and T signals is the same as described for 50BTEVB before.

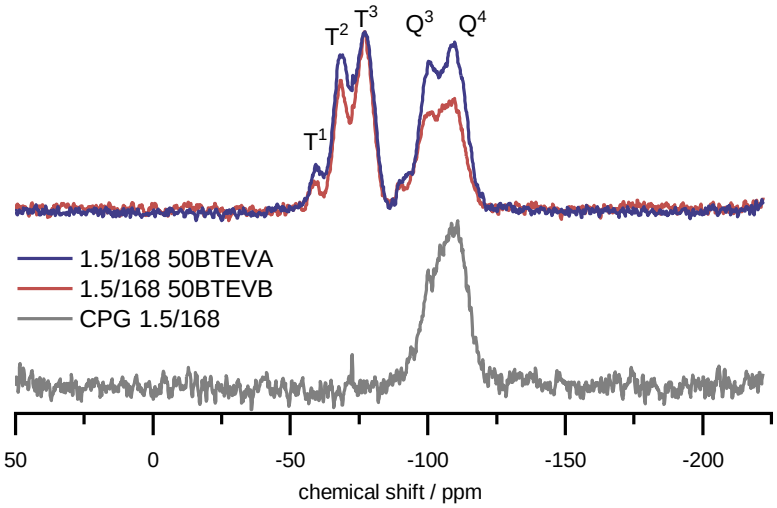

Figure 4-86: ^{29}Si CP-MAS NMR (spinning speed = 5 kHz) of CPG batch III (gray), 50BTEVB (red) and 50BTEVA (purple).

Also for 50BTEVA additional T signals appear in comparison to the pure CPG. The ratio of T^1 and T^2 species to T^3 silica species is comparable to 50BTEVB. The time consuming characterization with direct excitation ^{29}Si MAS NMR measurements were not performed for 50BTEVA. Despite the fact that the CP-MAS NMR data are not quantitative, the semi-quantitative comparison of two spectra is possible. Hence, the ratio of T to Q signals in 50BTEVA was compared to the ratio in the respective measurement from 50BTEVB. The direct overlay in the upper part of Figure 4-86 shows that ratio of T to Q signals is higher in 50BTEVA than in 50BTEVB which means that the organosilica content in 50BTEVA is significant lower than in 50BTEVB. By contrast, the theoretical values and the results from TG measurements were very similar for both samples with 16 % mass loss (11 mol% BTEVB) for 50BTEVB and 17 % mass loss (10 mol% BTEVA) in

50BTEVA. Also previously given approaches of explanation for the gap between values form TG measurements and CP-MAS NMR are valid in this case. Additionally, it has to be considered, that the BTEVA precursor cannot be purified by distillation as the BTEVB precursor which might be an explanation for the lower organosilica content in this case.

The integrity of the divinyl-aniline bridge was investigated by ^{13}C CP MAS NMR spectroscopy. Figure 4-87 shows the spectrum together with the liquid-state NMR spectrum of the precursor (measured in $CDCl_3$) for comparison. Solvent effects on the chemical shift have to be considered in this presentation as well. Since the bridging unit is not symmetrically and contains more difference ^{13}C species, the assignment of the signals is a more complex than for BTEVB. Despite overlapping of different signals in the broad spectra from solid state, good agreement of the signals from liquid state and solid state is visible. Hence, the integrity of the organic bridging unit ca be affirmed. The presence of additional broad signals in the ^{13}C-CP-MAS NMR spectrum with a chemical shift of 20-30 ppm and about 50 ppm should not be concealed. These signals cannot be assigned distinctly but could be solvents e.g. from the precursor synthesis. These potential impurities might cause higher mass loss in the TG measurement of 50BTEVA despite lower organosilica content in comparison to 50BTEVB.

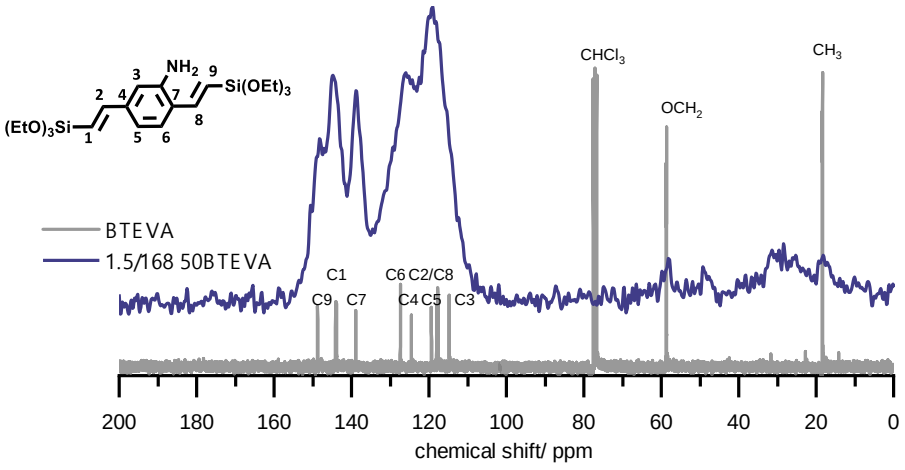

Figure 4-87: ^{13}C-CP-MAS NMR (spinning speed = 13 kHz) of 50BTEVA from CPG batch III (purple) and liquid state NMR spectrum of the precursor BTEVA measured in $CDCl_3$ (gray) both plotted with normalized intensity.

Within this chapter, the successful impregnation of different CPG batches with two different organosilica precursors BTEVA and BTEVB was shown. The thickness of the organosilica layer was adjusted by the organosilica content in the impregnation solution and also by the initial pore volume of the chosen CPG batch. During the condensation process that was initiated with a solution of ethanol and sodium hydroxide, a nanoporous organosilica phase with a high specific surface area was formed. The resulting specific BET surface area was mainly influenced by the organosilica content in the impregnation solution, but also by the initial pore system. The highest filling degree of 70 % was obtained using a CPG batch IV with comparably low pore volume but

large macropores. High molar percentages of organosilica are obtained in hybrid materials from CPG with high initial pore volumes. In future works, also the use of other precursors that have previously played a role in this thesis, for e.g. BTEB, BTEVFB, BTEV2FB or BTEVClB, might be possible. This flexibility concerning the precursor extends the applicability of the resulting organosilica/silica hybrid materials.

The diagram in Figure 4-88 shows the most important aspects of the results from the impregnation approach.

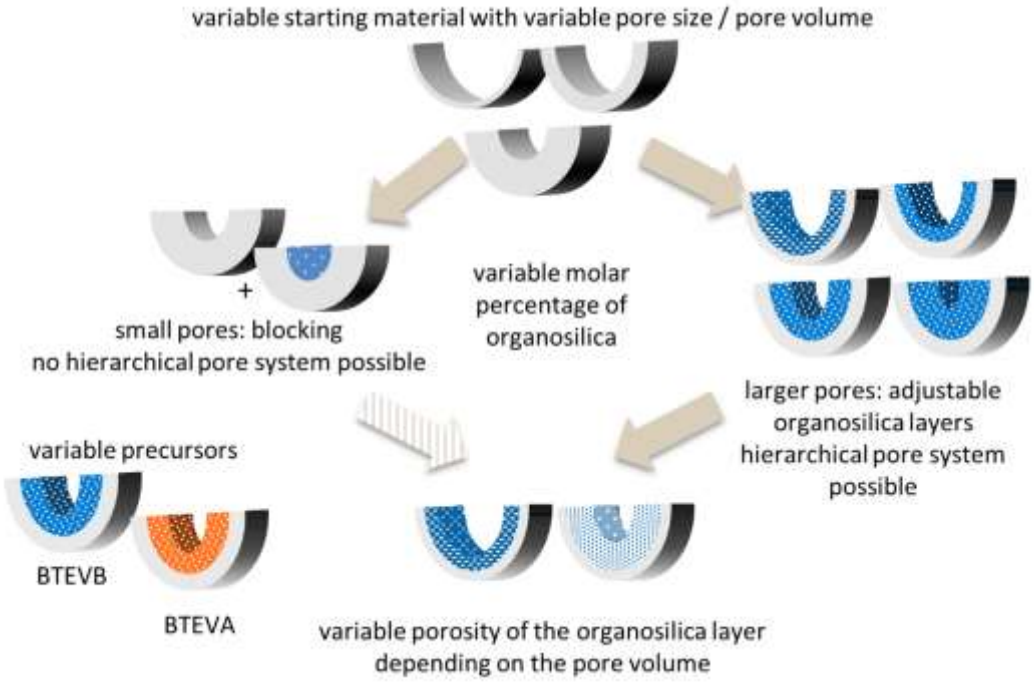

Figure 4-88: Diagram of the impregnation of different CPG pore systems (pores indicated as gray half pipes) with solutions that contain different ratios of organosilica, resulting in different nanoporous DVA- (symbolized in orange) and DVB- (symbolized in blue) organosilica layers. In small pores the impregnation is not homogeneous and some pores are blocked while some remain unaffected. Thus, no hierarchical porosity is possible. In larger pores, the layer thickness depends on the organosilica content and on the porosity of the organosilica layer. Here, in general, the formation of hierarchical pore systems is possible. High apparent specific BET surface areas occur in CPG with high pore volumes. The molar percentage of organosilica varies in the hybrid materials.

The initial motivation was the formation of a hierarchically porous organosilica/silica hybrid material with an accessible organosilica phase. This is reached at this point with the help of CPG as a morphology-providing template, although the second pore system is unordered and micro- to mesoporous.

In the following chapter, the intention was to generate an ordered mesopore system. For this reason, some of the presented hybrid materials were treated with an alkaline surfactant solution analogously to the pseudomorphic transformation of pure CPG as discussed in Section 4.2.

4.3.3 Pseudomorphic transformation of organosilica/silica hybrid materials

A hybrid material of CPG with a layer of nanoporous organosilica on the pore walls was formed by the previously discussed impregnation process. A further aim was to transform the organosilica layer into a PMO with a uniform and ordered mesopore structure. Therefore, the organosilica/silica hybrid materials from the previous chapter were treated with an alkaline surfactant solution for pseudomorphic transformation. Figure 4-89 shows a diagram of a CPG macropore (indicated as a half-pipe) that is impregnated with an organosilica layer (indicated in blue). A second mesopore system (indicated as cylinders) is generated in both layers after full pseudomorphic transformation. For improved accessibility of the organosilica phase a hierarchical pore system is required so that the initial pore system of the CPG should be preserved after pseudomorphic transformation.

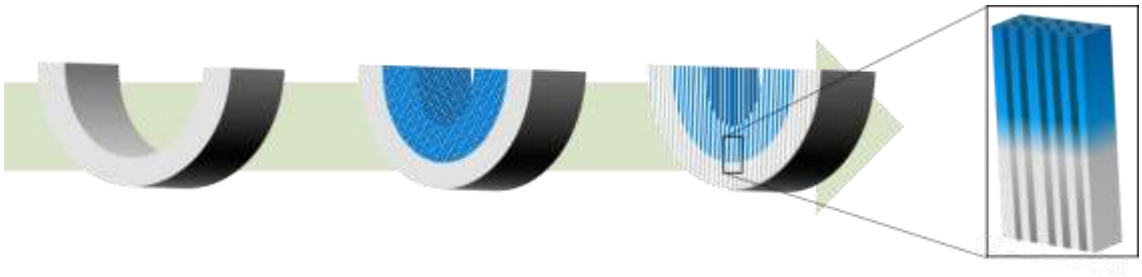

Figure 4-89: Diagram of a CPG macropore (illustrated as a gray half-pipe) in an organosilica/silica hybrid material that was obtained from impregnation of the pore volume with an organosilica precursor e.g. BTEVB (symbolized in blue). After condensation it forms a nanoporous layer (pores are indicted by a dotted pattern) on the pore wall. After the transformation a uniform mesopore system is obtained (indicated by cylinders).

Whereas the pseudomorphic transformation of CPG under different conditions has already been discussed in section 4.2, the post-synthetical micelle templating of organosilica has not yet been studied. Hence, the conditions for the transformation of nanoporous DVB-organosilicas are studied first. In the following chapter, the results of the pseudomorphic transformation of a selection of organosilica/silica hybrid materials from the impregnation process in the preceding chapter are presented. The influence of different initial pore volumes as well as pore sizes on the transformation process are discussed. The transformation process is investigated in detail below.

Transformation of nanoporous organosilica

In preparation for the pseudomorphic transformation of the organosilica/silica hybrid materials, the dissolution and recondensation behavior of nanoporous DVB-organosilica in alkaline solutions was investigated under different conditions in two synthesis series. The starting materials for this series were obtained from the treatment of BTEVB with ethanol and aqueous sodium hydroxide solution, from which micro- and mesoporous materials with high apparent specific BET surface areas are obtained, as shown in section 4.1.4. The respective materials are powders that do not show any specific morphology so that the success of the treatment was evaluated only under consideration of the specific BET surface area, the pore volume of pores smaller 20 nm and the pore diameter distribution. Hence, the term of pseudomorphic transformation is inapplicable.

In the first synthesis series the nanoporous DVB-organosilica (DVB-micro) was treated with C_{16}TAOH solution (pH 12.7) which was also used for the pseudomorphic transformation of CPG in section 4.2 for 24 hours. Subsequently, the transformation protocol for organosilicas from Simon *et al.* was adapted.[111] In these syntheses the pH value is lower (pH 12.4) and the solvent volume is significantly higher. The synthesis mixture includes ethanol as is the case in different literature examples for the pseudomorphic transformation of silica.[238] The surfactant concentration was varied between 12–21 mmol·L^{-1} in the presence of ethanol, and 24 mmol·L^{-1} without ethanol. This is significantly lower than in case of C_{16}TAOH solution with a concentration of 80 mmol·L^{-1}. All samples were treated at 100 °C.

In the second synthesis series, synthesis conditions were chosen which are closer to common DVB-PMO syntheses at a significantly higher pH value of pH 13.75 with C_{16}TAB, likewise at 100 °C. The time of treatment was decreased from 24 hours to six hours, one hour, and ten minutes. The shortest treatment was repeated with ethanol as co-solvent. The starting material DVB-micro-II shows a lower apparent BET surface area than the starting material of the first synthesis series (DVB-micro –I), so that the values of both series are not comparable, but the trend of the pore size is the same for DVB-micro I and DVB-micro-II.

For all transformation approaches, the pore diameter could be shifted into the mesopore range, whereby the pore diameter distribution was more or less broad. The apparent BET surface area decreases after the transformation, most likely due to the absence of micropores in these samples. The values of the *apparent* specific BET surface areas and pore diameter maxima of both series for the transformation of nanoporous DVB-organosilicas are summarized in Table 4-32. The pore diameter distribution was calculated from the adsorption branch using NLDFT kernel for silica with cylindrical pores, in the table the respective maxima from the Gaussian fit

are given, although it does not represent the broad pore diameter distributions. The pore volume was determined using the same NLDFT kernel, in order to leave interparticle voids aside, only pores smaller 20 nm were considered.

Table 4-32: Summary of the *apparent* specific BET surface areas, the pore volume and pore diameter maxima from the pore diameter distribution of post-synthetically treated nanoporous DVB-micro-I and DVB micro-II. All samples from DVB-micro-I were treated for 24 hours. All samples from DVB-micro-II were treated at pH 13.75 with 82 mmol·L^{-1} C_{16}TAB. Highlighted samples will be discussed in detail below. Entries marked with an asterisk (*) signify micro- and mesoporous materials without dominant pore diameter

sample	***apparent*** S_{BET} **/ m²·g^{-1}**	$V_{<20\ nm,\ NLDFT}$ **/ m³·g^{-1}**	d_{NLDFT} **/ nm**
DVB-micro-I	1299	0.91	*
pH 12.7, 80 mmol·L^{-1} C_{16}TAOH, 24 h	833	0.83	4.8
pH 12.4, 12 mmol·L^{-1} C_{16}TAB, ethanol, 24 h	766	0.66	4.5
pH 12.4, 21 mmol·L^{-1} C_{16}TAB, ethanol, 24 h	697	0.79	4.5
pH 12.4, 21 mmol·L^{-1} C_{16}TAB, no ethanol, 24 h	772	0.65	5.4
DVB-micro-II	888	0.54	*
pH 13.75, 82 mmol·L^{-1} C_{16}TAB, 24 h	620	0.8	6.4
pH 13.75, 82 mmol·L^{-1} C_{16}TAB, 6 h	747	0.77	5.4
pH 13.75, 82 mmol·L^{-1} C_{16}TAB, 1 h	774	0.70	4.7
pH 13.75, 82 mmol·L^{-1} C_{16}TAB, 1 h, ethanol	899	0.51	4.4
pH 13.75, 82 mmol·L^{-1} C_{16}TAB, 10 min	930	0.58	*
pH 13.75, 82 mmol·L^{-1} C_{16}TAB, 10 min, ethanol	873	0.70	*

Figure 4-90 shows the isotherms and the pore diameter distributions of a selection from both synthesis series. These samples are highlighted in Table 4-32. Isotherms of all samples are given in the Appendix, Figure 9-27 and Figure 9-28.

Figure 4-91 shows the P-XRD patterns of the selected samples. For P-XRD patterns of the other samples see Figure 9-29 and Figure 9-30 in the Appendix. As expected for the microporous sample no reflections are observed in the low-angle scattering region whereas broad reflections appear after the treatments. Thus, it can be assumed that micelle templating occurs, but the mesophase is poorly ordered in all transformation approaches. Additional reflections appear for all samples in the wide-angle scattering range which indicates crystal-like ordering of the organic bridging units in accordance with the literature values: 2θ = 7.37° (d = 11.9 Å), 14.8° (5.97 Å), 21.0° (4.23 Å), 22.2° (3.99 Å), 29.9° (2.98 Å), 37.8° (2.38 Å).[103]

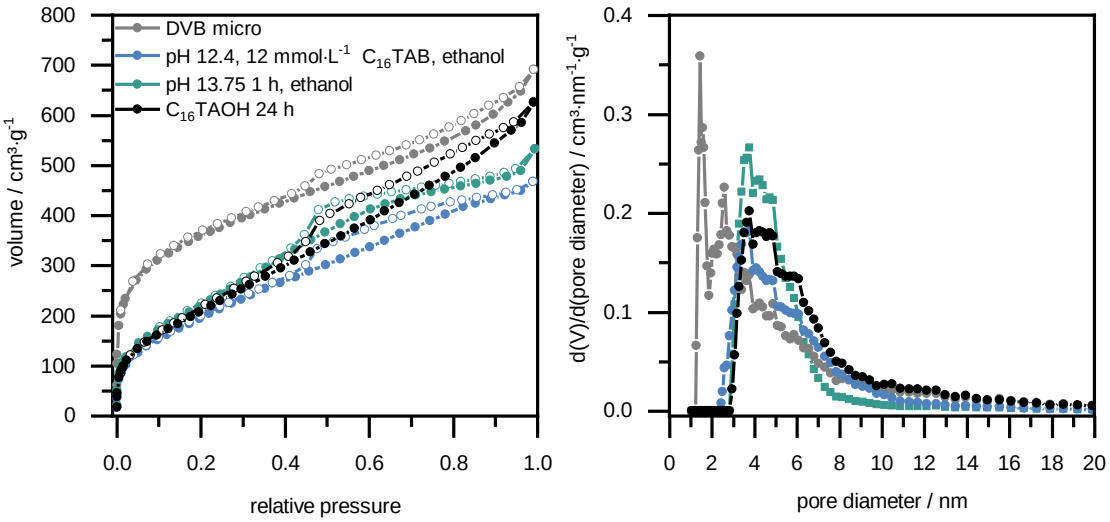

Figure 4-90: Physisorption isotherms (N_2, 77 K) and pore diameter distribution (right, calculated with NLDFT kernel for silica with cylindrical pores from the adsorption branch) of nanoporous DVB-organosilica before (gray) and after (black) treatment with C_{16}TAOH solution at pH 12.7, with C_{16}TAB at pH 12.4 with ethanol (blue) and with C_{16}TAB at pH 13.75 with ethanol for one hour (green) on the left.

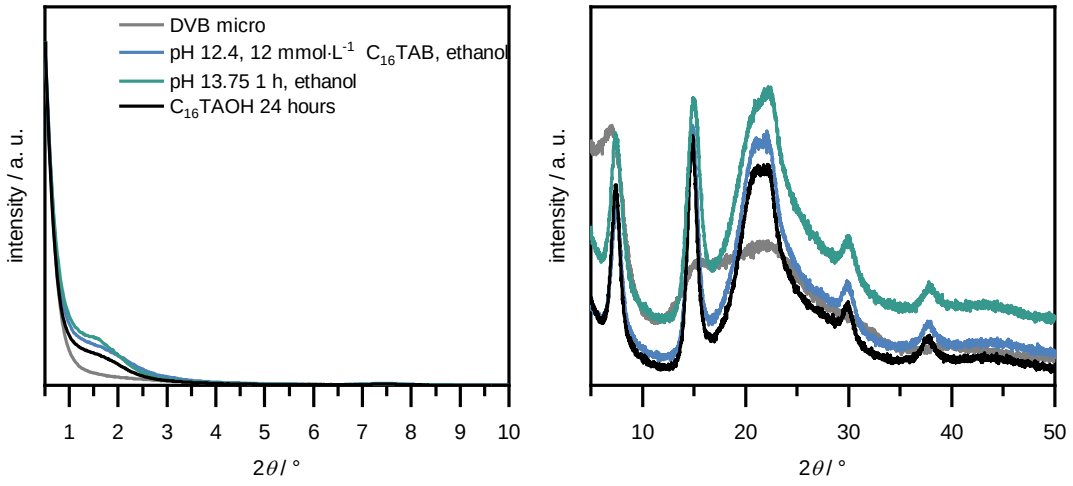

Figure 4-91: P-XRD patterns of DVB-organosilica before and after treatment with C_{16}TAOH solution at pH 12.7, at pH 12.4 with ethanol and at pH 13.75 with ethanol for one hour.

In summary, the postsynthetic micelle templating of nanoporous DVB-organosilica was studied at different pH values both in the presence and in absence of ethanol. No conditions were identified that significantly improved the pore diameter distribution or the quality of the mesophase ordering. Hence, it was decided to keep the synthesis condition of the pseudomorphic transformation of CPG with C_{16}TAOH at pH 12.7 for the pseudomorphic transformation of the organosilica/silica hybrid materials from section 4.3.2.

Pseudomorphic transformation of impregnated samples from mesoporous CPG

The concept of pseudomorphic transformation is shown below using the mesoporous samples 25BTEVB and 50BTEVB of batch II (1.5 $cm^3 \cdot g^{-1}$ pore volume, 52 nm pore size) as examples. The samples were treated with C_{16}TAOH solution with a concentration of 0.08 $mol \cdot L^{-1}$ for four days at 100 °C. These are the same conditions of the pseudomorphic transformation of pure CPG (see section 4.2). The samples are denoted with the suffix 4d_C_{16}TAOH. The products provide two pore systems: the first pore system remains from the initial porous glass, while the second system is generated by micelle-templating during the transformation process. These samples were chosen, as it is possible to characterize both pore systems with nitrogen physisorption and no mercury porosimetry is needed. However, the results of the pseudomorphic transformation of the pure CPG in Section 4.2 indicate that a hierarchical pore system, which is only given when the two pore systems are interconnected, cannot be generated in the samples since the pristine pore system collapses partially due to the formation of the second pore system, according to Figure 1-12. SEM images in Figure 4-92 and Figure 4-93 confirm the prevention of the bead morphology and the absence of a second phase after the transformation process.

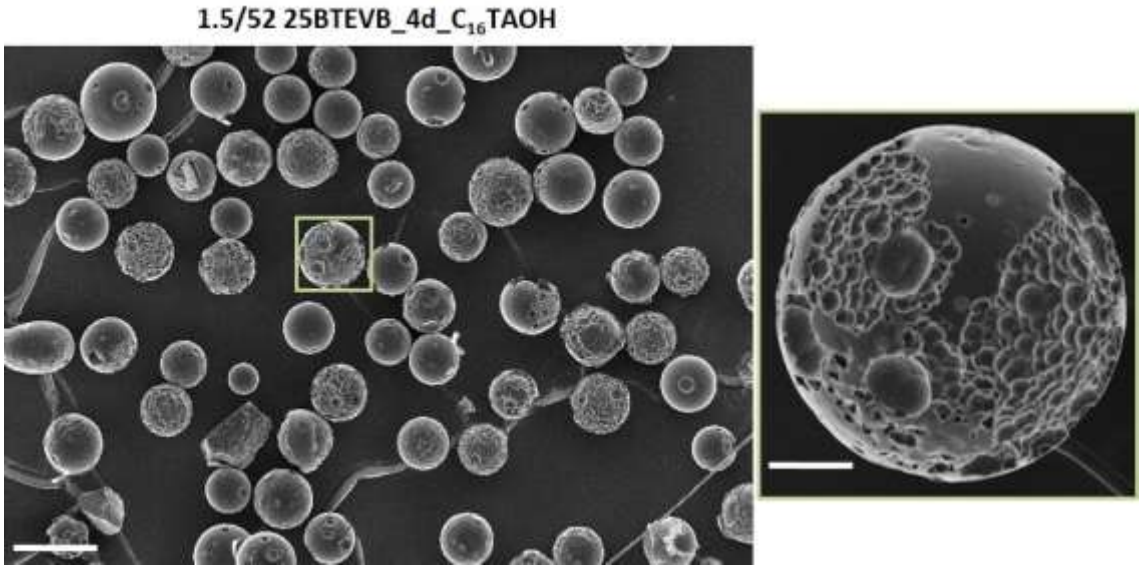

Figure 4-92: SEM images of the 25BTEVB_4d_C_{16}TAOH (CPG batch II).Left: magnification x500, scale bar of 100 µm, right: magnification x1000, scale bar 20 µm.

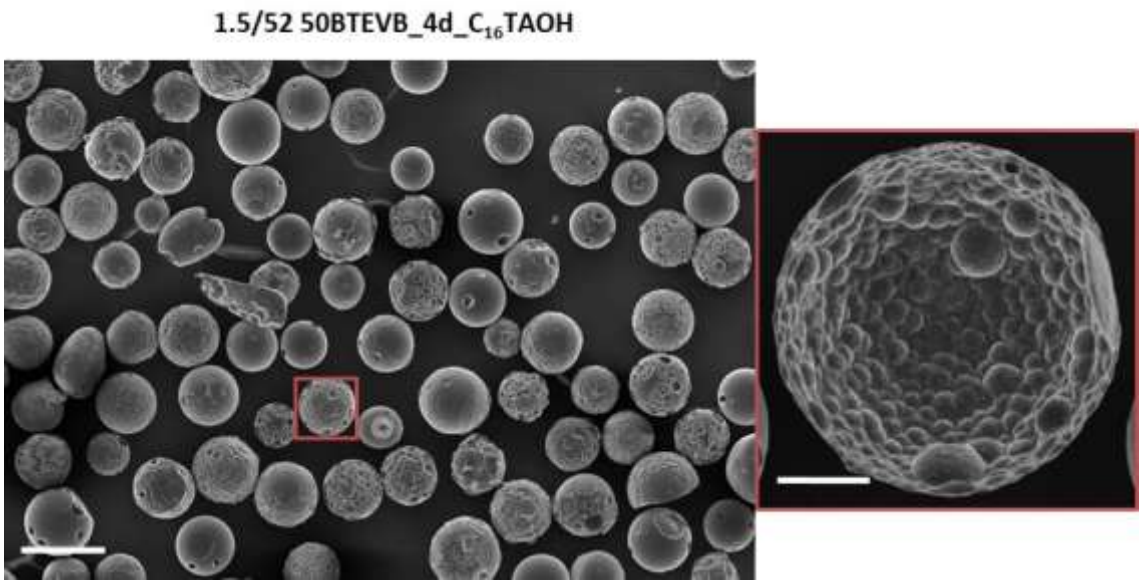

Figure 4-93: SEM images of the 50BTEVB_4d_C_{16}TAOH (CPG batch II left: magnification x500, scale bar of 100 µm right: magnification x1000, scale bar 20 µm.

P-XRD patterns in Figure 4-94 confirm the formation of an ordered mesophase during the transformation process. Similar to the results for pure silica materials, only one reflection at 2θ = 1.9°, which corresponds to a *d*-spacing of 4.5 nm is observed, whereas further reflections are very weak and broad. While an undoubted assignment of the mesophase is not possible, an MCM-41-type 2D hexagonal structure could be assumed as it is the dominating structure after pseudomorphic transformation of pure CPG. Measurements at higher scattering angles did not show further reflections so that the formation of crystal-like pore walls in the organosilica phase is not detected.

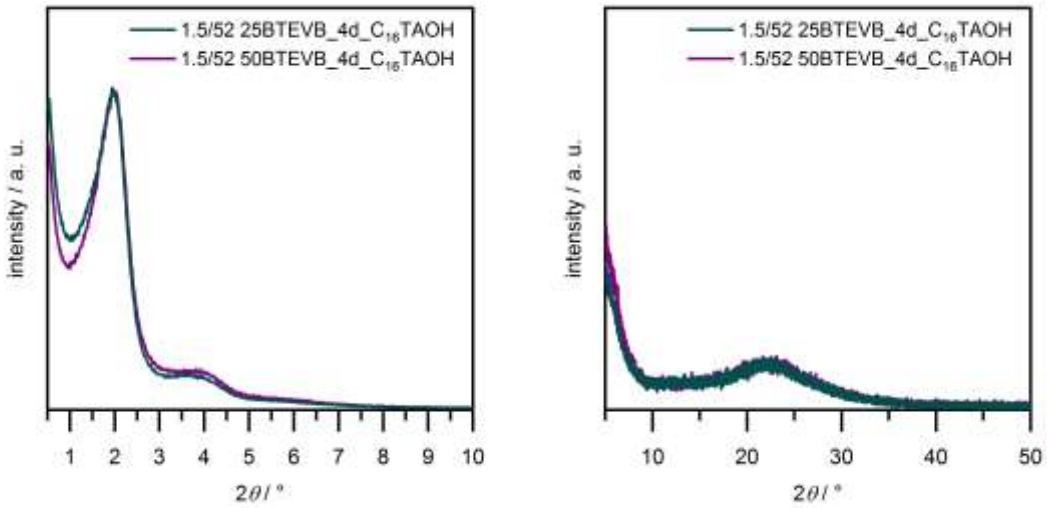

Figure 4-94: P-XRD pattern of 25BTEVB and 50BTEVB from CPG batch II after pseudomorphic transformation with C_{16}TAOH for 4 days.

Figure 4-95 shows the respective adsorption branches of nitrogen physisorption as well as the pore diameter before and after pseudomorphic transformation for four days.

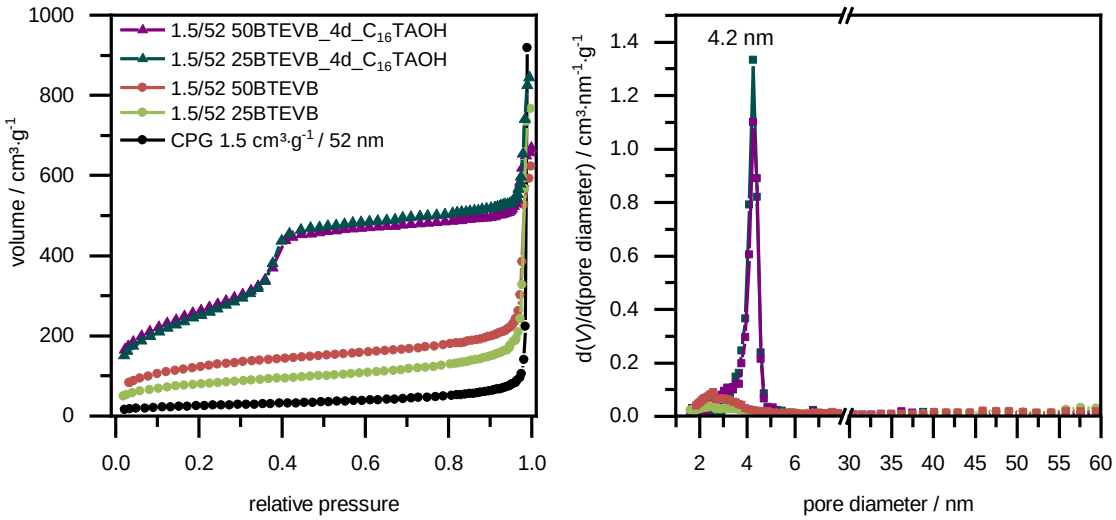

Figure 4-95: Adsorption branches of physisorption isotherms (N_2, 77 K) of 25BTEVB and 50BTEVB from CPG batch II before and after pseudomorphic transformation and the respective pore diameter distributions (calculated from the adsorption branch using NLDFT kernel for silica with cylindrical pores).

After transformation, type IV isotherms are obtained which show capillary condensation that indicates a successful micelle templating process. The mesopore size maximum is 4.2 nm with a very narrow distribution for both samples. Since the pore diameter of ordered mesoporous silicas and PMOs that were synthesized with the same surfactant can differ,[110] it needs to be discussed whether two pore diameter maxima are expected after pseudomorphic transformation of an organosilica/silica hybrid material, and whether the absence of a second mesopore diameter maximum hints at unsuccessful micelle templating of the organosilica phase. According to Mietner, the pore diameters differ less than 0.5 nm in the case of DVB-PMO and MCM-41, synthesized with C_{16}TAB and cannot be differentiated in the pore diameter distribution.[110] Thus, the observance of only one maximum in pore diameter distribution does not necessarily deny the successful transformation of the hybrid material. However, this problem will be investigated in detail in the following sections.

An additional steep step at high relative pressure (over 0.90) occurs as in the type II isotherms of the initially impregnated samples. Unfortunately, the initial pore system is not represented in the pore size distribution in Figure 4-95. As is explained in section 1.4 (see Figure 1-12), CPG pores smaller than 50 nm tend to collapse during the transformation process rather than become narrow. This is in accordance with the results for the pseudomorphic transformation of CPG of the same batch (compare with the isotherms in Figure 4-34 in section 4.2). Hence, the height of the step decreases during the transformation, but it does not shift towards lower relative pressures here neighter. Due to the low remaining pore volume, the amount of the samples was not sufficient for reliable characterization by MIP. Thus, no pore diameter distribution can be given for these samples.

To characterize the two pore systems, the cumulative pore volume calculated with the NLDFT kernel for silica with cylindrical pores for pores smaller 20 nm ($V_{<20\ nm,\ NLDFT}$) caused by the second pore volume from micelle templating, was distinguished from the respective pore volume of larger pores ($V_{>20\ nm,\ NLDFT}$) from the initial pore system of the CPG. The pore volumes $V_{>20\ nm,\ NLDFT}$ are 0.62 $cm^3 \cdot g^{-1}$ for 25BTEVB and 0.57 $cm^3 \cdot g^{-1}$ for 50BTEVB and decrease significantly to 0.41 $cm^3 \cdot g^{-1}$ for 25BTEVB_4d_ C_{16}TAOH and 0.31 $cm^3 \cdot g^{-1}$ for 50BTEVB_4d_C_{16}TAOH. $V_{<20\ nm,NLDFT}$ increases due to the formation of micelle templated mesopores to 0.74 $cm^3 \cdot g^{-1}$ and 0.81 $cm^3 \cdot g^{-1}$, respectively. Although the specific BET surface areas of 25BTEVB and 50BTEVB differ, the values are very similar for 4d_C_{16}TAOH samples with 922 $m^2 \cdot g^{-1}$ and 943 $m^2 \cdot g^{-1}$, respectively.
A comparison of the pore volumes $V_{<20\ nm,\ NLDFT}$ and $V_{>20\ nm,\ NLDFT}$ as well as the specific BET surface areas before and after pseudomorphic transformation is summarized in Table 4-33.

Table 4-33: specific BET surface area and pore volumes $V_{<20\ nm,\ NLDFT}$ and $V_{>20\ nm,\ NLDFT}$ of 25BTEVB and 50BTEVB before and after pseudomorphic transformation.

Sample	S_{BET} / $m^2 \cdot g^{-1}$	$V_{<20\ nm,\ NLDFT\ ads.}$ / $cm^3 \cdot g^{-1}$	$V_{>20\ nm,\ NLDFT\ ads.}$ / $cm^3 \cdot g^{-1}$
CPG batch II	87	0.08	0.25
25BTEVB	289	0.13	0.62
25BTEVB_4d_C_{16}TAOH	922	0.74	0.41
50BTEVB	419	0.26	0.57
50BTEVB_4d_C_{16}TAOH	943	0.81	0.31

The preservation of the organosilica phase in the hybrid material was also investigated after pseudomorphic transformation with TG/MS analysis shown in Figure 4-96. The mass loss in different temperature intervals are summarized in Table 4-34 .

Table 4-34: Mass loss in given temperature intervals of TG analysis (Ar/O_2 80/20) of 25BTEVB and 50BTEVB before and after pseudomorphic transformation. Entries marked with an asterisk (*) denote corrected values.

temperature interval	**25–150 °C**	**150–300 °C**	**300–800 °C**	**25-800 °C**
25BTEVB	0.6 %	0.6 %	9.3 %*	11 %
25BTEVB_4d_C_{16}TAOH	5.4 %	1.3 %	11 %*	18 %
50BTEVB	0.7 %	0.8 %	16 %*	17 %
50BTEVB_4d_C_{16}TAOH	5.4 %	1.7 %	17 %*	23 %

The mass loss in the temperature ranges 150–300 °C as well as 300–800 °C is slightly higher after transformation than in the samples before the transformation. This could be due to leaching of the silica phase during the transformation, as it was also observed in the pseudomorphic transformation of pure CPGs with a mass loss of up to 10 %. Another aspect could be residues of the surfactant inside the samples, although no release of the main ionization product of the

surfactant (m/z = 58) was detected. In the context of 50BTEVB from batch III a molar ratio of 16 mol% BTEVB was found by solid state NMR, but only 11 mol% by TG analysis. Hence, it is reasonable that the differences of the mass loss before and after the transformation are within the measurement error. However, the noticeable gap in the mass losses occurred for all samples and will be discussed in detail in the context of the mechanism of the transformation in the following sections.

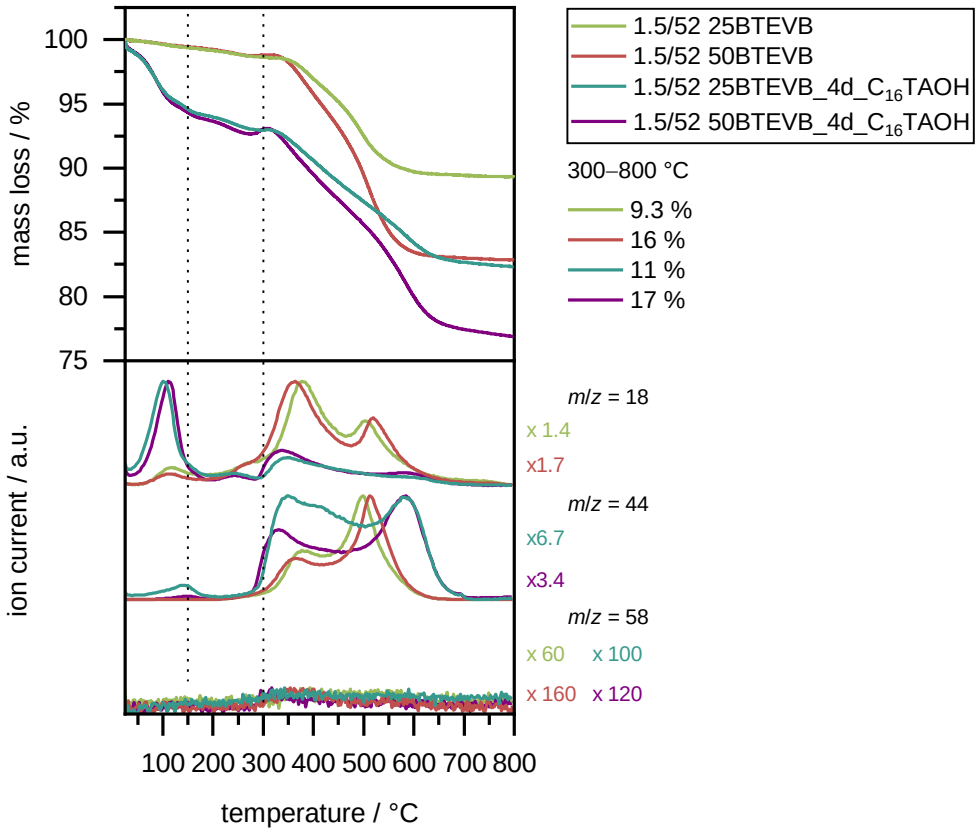

Figure 4-96: TG/MS analysis in Ar/O_2 80/20 of 25BTEVB and 50BTEVB batch II before and after pseudomorphic transformation for four days. In the upper plots: mass losses plotted against the temperature. The corrected mass loss for the temperature interval 300–800 °C is given on the right. Lower plot: selected ion currents with normalization factor given on the side.

It was shown that the pseudomorphic transformation of organosilica/silica hybrid materials was successful and two pore systems are generated in the products. It became clear that the initial pore system collapses after pseudomorphic transformation and no narrowing of the pores was observed by physisorption measurements. Hence, the formation of a hierarchical pore system that can be characterized solely by nitrogen physisorption was not successful. Therefore, the pseudomorphic transformation of organosilica/silica hybrid materials with larger initial pore diameter and a larger pore volume was attempted. The most reliable method to quantify the organosilica content is quantitative ^{29}Si-MAS NMR spectroscopy. ^{13}C-CP-MAS NMR gives further information concerning the surfactant residues in the sample. These methods are very time

consuming and are discussed for the pseudomorphic transformation of 50BTEVB from batch III below.

Pseudomorphic transformation of impregnated CPG from batch III with 1.5 $cm^3 \cdot g^{-1}$ pore volume and 168 nm pore size

The process of pseudomorphic transformation was intensively studied using the samples 25/50BTEVB and 25/50BTEVA from CPG batch III with an initial pore volume of 1.5 $cm^3 \cdot g^{-1}$ and 168 nm initial pore diameter.

Figure 4-97 shows the nitrogen physisorption isotherms (left) as well as the pore diameter distributions (right) of 25/50BTEVB and 25/50BTEVA which were further treated with C_{16}TAOH for four days for pseudomorphic transformation.

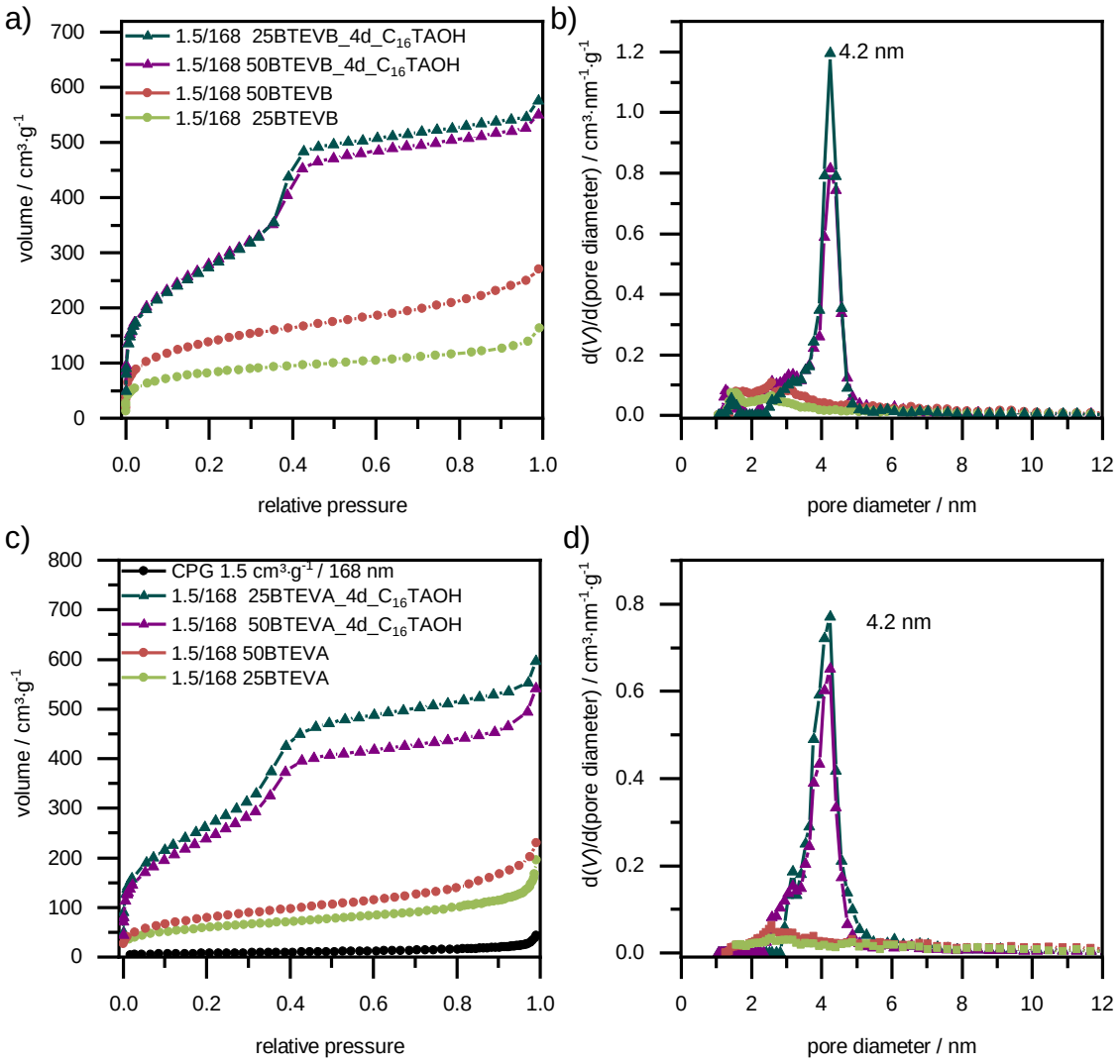

Figure 4-97: Adsorption branches of physisorption isotherms (N_2, 77 K) of a)25/50BTEVB and b) 25/50BTEVA from CPG batch III before and after pseudomorphic transformation for four day and the respective pore diameter distributions, calculated using NLDFT kernel for silica, cylindrical pores from the adsorption branch, c) 25/50BTEVB, d) 25/50BTEVA.

The isotherms are type IV after the transformation. The specific BET surface area increases up to 1000 $m^2 \cdot g^{-1}$ and the pore size is 4.2 nm after pseudomorphic transformation in both cases. The formation of a mesophase can further be proven by P-XRD showing a reflection at 2θ = 1.9°, which corresponds to a *d*-spacing of 4.5 nm, whereas further reflections between 3–5 °2θ are very weak and broad, as for the other pseudomorphic transformed materials (see Appendix Figure 9-31). Measurements at higher scattering angles did not show further reflections so that the formation of crystal-like pore walls in the organosilica phase is not detected.

The mercury intrusion curves and the respectively obtained macropore diameter distributions for the samples before and after pseudomorphic transformation, are shown in Figure 4-98. After the pseudomorphic transformation a less steep step occurs in the intrusion curves and the pore size distributions of the macropores are very broad. Additionally, intrusion occurs over a broad pressure range, which indicates the presence of smaller pores as can also be seen in the pore diameter distribution curves. Nevertheless, a shift towards smaller pores and significantly reduced pore volumes are observed after pseudomorphic transformation for all samples.

Pore volumes and specific BET surface areas are summarized for all samples in Table 4-35. After the transformation of 25BTEVA and 25BTEVB, the pore size is reduced to 110 nm and 102 nm, and for 50BTEVA and 50BTEVB it is 100 nm in both cases. The pore volume decreases to 0.69 $cm^3 \cdot g^{-1}$ in the case of 25BTEVA and 0.82 $cm^3 \cdot g^{-1}$ in case of 25BTEVA. A further decrease occurs for 50BTEVB (0.43 $cm^3 \cdot g^{-1}$) and 50BTEVA (0.57 $cm^3 \cdot g^{-1}$). After pseudomorphic transformation the mesopore volume of all samples is around 0.8 $cm^3 \cdot g^{-1}$.

Table 4-35: specific BET surface area, the pore volume calculated with NLDFT for silica with cylindrical pores from the adsorption branch of the isotherm, and the mercury intruded pore volume of 25/50BTEVA and 25/50BTEVB from CPG batch III before and after pseudomorphic transformation.

Sample	S_{BET} / $m^2 \cdot g^{-1}$	$V_{N_2, NLDFT}$ / $cm^3 \cdot g^{-1}$	V_{Hg} / $cm^3 \cdot g^{-1}$	d_{Hg} / nm
CPG batch III	26		1.50	168
25 BTEVA	203	0.17	0.99	153
25 BTEVA_4d_C_{16}TAOH	636	0.86	0.69	110
50BTEVA	279	0.26	0.71	147
50BTEVA_4d_C_{16}TAOH	998	0.80	0.54	99
25BTEVB	299	0.19	1.14	144
25BTEVB_4d_C_{16}TAOH	1006	0.84	0.82	102
50BTEVB	476	0.35	0.69	132
50BTEVB_4d_C_{16}TAOH	1007	0.80	0.43	100

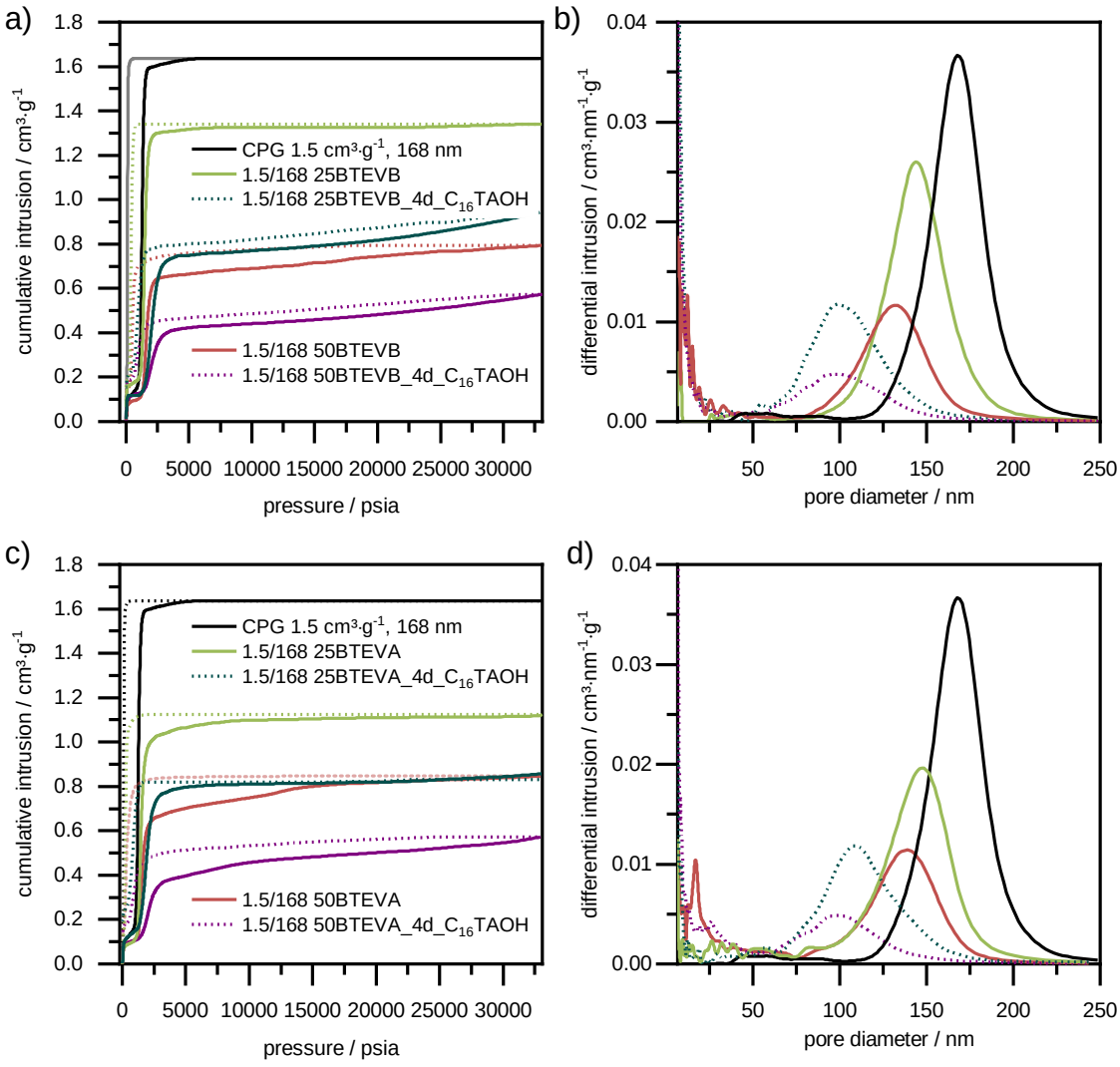

Figure 4-98: Mercury intrusion curves from a) 25/50BTEVB and c) 25/50BTEVA before and after pseudomorphic transformation, as well as the respective pore diameter distributions of c) 25/50BTEVB and d) 25/50BTEVA before and after pseudomorphic transformation (indicated by dotted lines).

SEM images show the swelling of the pore walls during transformation and together with the shrinking of the pore size and volume for both materials, 25BTEVB and 50BTEVB while comparing before and after pseudomorphic transformation (see Figure 4-99). For SEM images of the respective samples with BTEVA, see Figure 9-32 in the Appendix.

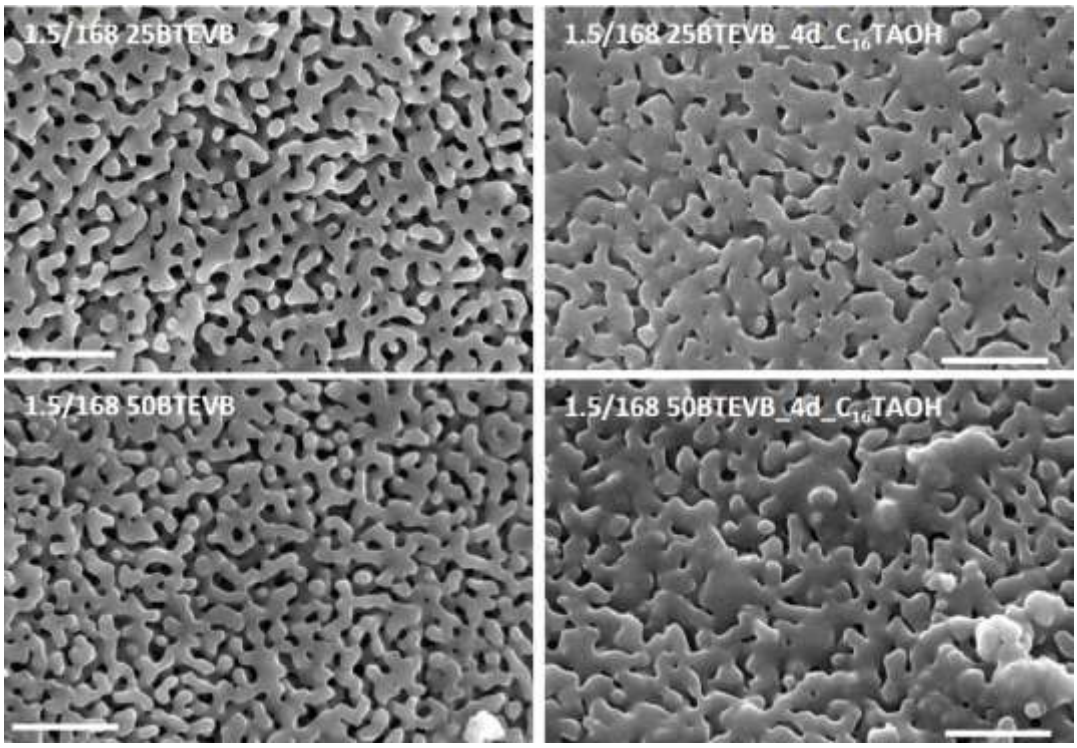

Figure 4-99: SEM images after transformation of 25BTEVB and 50BTEVB from CPG batch III, before (left) and after (right) pseudomorphic transformation with C_{16}TAOH for four days (magnification of x50000, scale bar of 1.0 µm).

TG/MS plots for 25BTEVB and 50BTEVB from CPG batch III before and after the transformation are given in Figure 4-100, for 25/50BTEVA see Figure 9-33 in the Appendix. Table 4-36 summarizes the mass loss in the different temperature intervals.

In the first temperature interval (25–150 °C), surface-adsorbed water evaporates from the samples. In the second interval (150–300 °C), no decomposition of the organosilica bridging unit is expected, hence the mass losses are very low before the transformation. After transformation the values are significantly higher, especially in case of 25/50BTEVB_4dC_{16}TAOH. Mass losses around 4.4 % are assumed to be due to residues of the surfactant. The mass loss in the temperature interval 300–800 °C is nearly the same before and after transformation for 25/50BTEVA but it is significantly higher for 25/50BTEVB_4d_C_{16}TAOH Hence, it is possible that the extraction of the surfactant was not successful or that leaching of the silica phase occurs during the transformation process. This will be discussed in details for 50BTEVB in the following sections with the help of solid state NMR spectra.

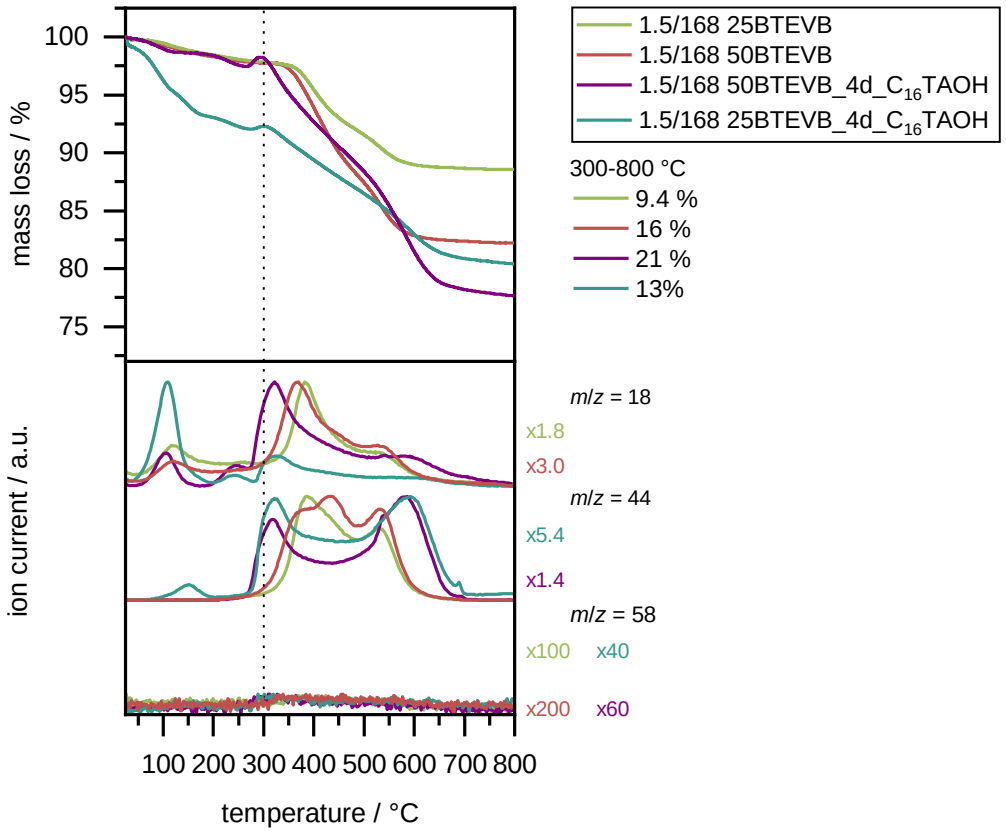

Figure 4-100: TG/MS analysis in Ar/O_2 80/20 of 25BTEVB and 50BTEVB from CPG batch III before and after pseudomorphic transformation for four days. The upper part: mass losses against the temperature. The corrected mass loss for the temperature interval 300–800 °C is given on the left. The lower plot shows selected ion currents with normalization factor given on the side.

Table 4-36: Mass loss in given temperature intervals of TG analysis (Ar/O_2 80/20) of 25 BTEVA and 50BTEVA before and after pseudomorphic transformation. Entries marked with an asterisk (*) denote corrected values.

temperature interval	**25–150 °C**	**150–300 °C**	**300–800 °C**	**25–800 °C**
25BTEVA	2.5 %	1.1 %	9.1 %*	12 %
25BTEVA _4d_C_{16}TAOH	2.9%	1.8 %	10 %*	15 %
50BTEVA	1.2 %	0.5 %	17 %*	18 %
50BTEVA_4d_C_{16}TAOH	8.4 %	1.5 %	17 %*	25 %
25BTEVB	1.2 %	1.0 %	9.4 %*	11 %
25BTEVB_4d_ C_{16}TAOH	5.4%	4.4 %	13 %*	19 %
50BTEVB	1.2 %	0.9 %	16 %*	18 %
50BTEVB_4d_C_{16}TAOH	1.4 %	0.4 %	21 %*	23 %

The adjustability of the mesopore system as well as the macropore system of organosilica/silica hybrid materials should be demonstrated in the following.

Adjustment of the mesopore diameter

In order to demonstrate the adjustability of the pore size, the pseudomorphic transformation was repeated with C_{10}TAB, a surfactant with a shorter alkyl chain that is expected to generate smaller mesopores. The pH value was adjusted to pH 13.0 since the transformation was shown to yield a narrower pore diameter at this pH value.

10 BTEVA, 25BTEVA and 50BTEVA from CPG batch III where treated that way, the products are denoted with the suffix 4d_C_{10}TAB. The nitrogen physisorption isotherms of these samples are shown in Figure 4-101. All samples show pore diameters around 2.8 nm. An *apparent* BET surface area of 776 $m^2 \cdot g^{-1}$ was obtained for 10BTEVA_4d_C_{10}TAB, 665 $m^2 \cdot g^{-1}$ for 25BTEVA_4d_C_{10}TAB, and 896 $m^2 \cdot g^{-1}$ for 50BTEVA_4d_C_{10}TAB.

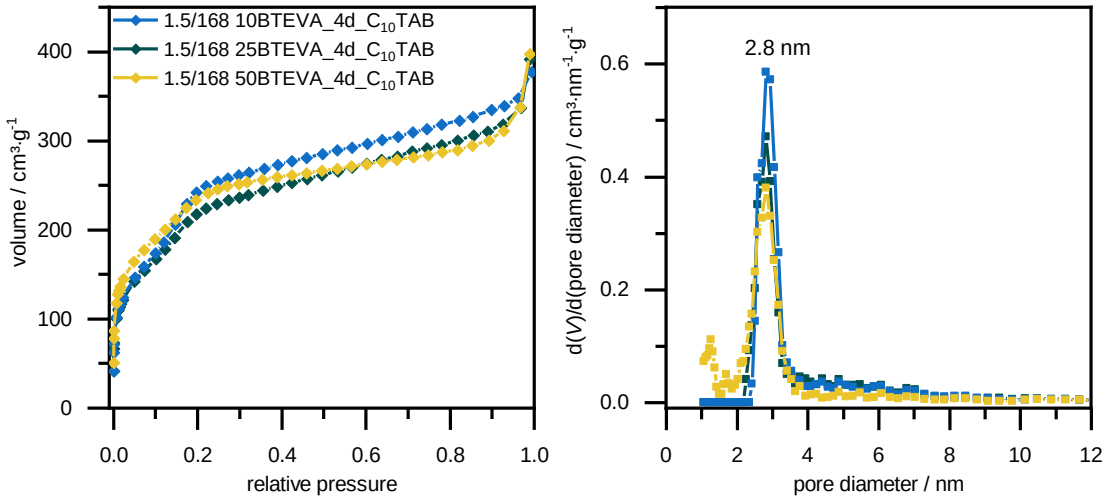

Figure 4-101: Adsorption branches of physisorption isotherms (N_2, 77 K) of 10, 25 and 50 BTEVA from CPG batch III after treatment with C_{10}TAB at pH 13.0 for four days (left) and the respective pore diameters, calculated from the adsorption branch using NLDFT for silica with cylindrical pores (right).

Figure 4-102 shows the P-XRD pattern of the samples, therein one reflection at 2θ = 2.7°, which corresponds to a *d*-spacing of 3.3 nm is visible for 10BTEVA_4d_C_{10}TAB and 25BTEVA_4d_C_{10}TAB, whereas this reflection is less dominant in 50BTEVA_4d_C_{10}TAB. Measurements at higher scattering angles did not show further reflections so that the formation of crystal-like pore walls in the organosilica phase is not detected.

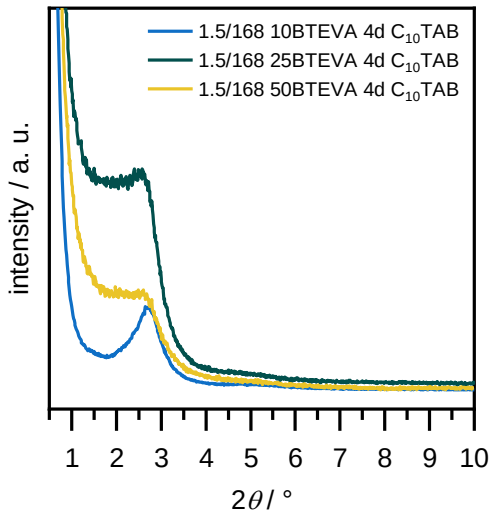

Figure 4-102: P-XRD pattern of 10/25/50BTEVA_4d_C_{10}TAB.

As the high pH value is accompanied by high losses in mas due to dissolution of the silica phase, the yield of the samples 10BTEVA_4d_C_{10}TAB and 25BTEVA_4d_C_{10}TAB were not sufficient for MIP measurements. The mercury intrusion curve and the pore size distributions of 50BTEVA before and after transformation with C_{10}TAB or C_{16}TAOH are shown in Figure 4-103. The pore size shifts to 130 nm after treatment with C_{10}TAB, which is significantly higher than for 50BTEVA_4d_C_{16}TAOH (99 nm). Hence, the templating with C_{10}TAB causes less swelling of the hybrid material.

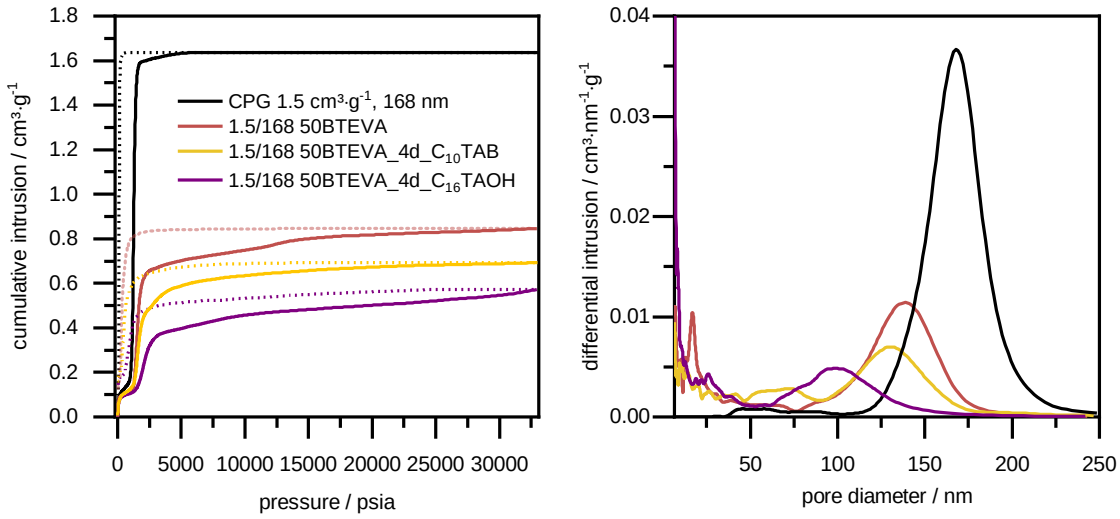

Figure 4-103: Mercury intrusion curves (left) and pore diameter distributions from MIP (right) of CPG batch III, 50BTEVA from CPG batch III before and after pseudomorphic transformation with C_{10}TAB at pH 13.0 for 4 days.

The swelling of the pore wall in 50BTEVA_4d_C_{10}TAB can also be seen in SEM images in Figure 4-104.

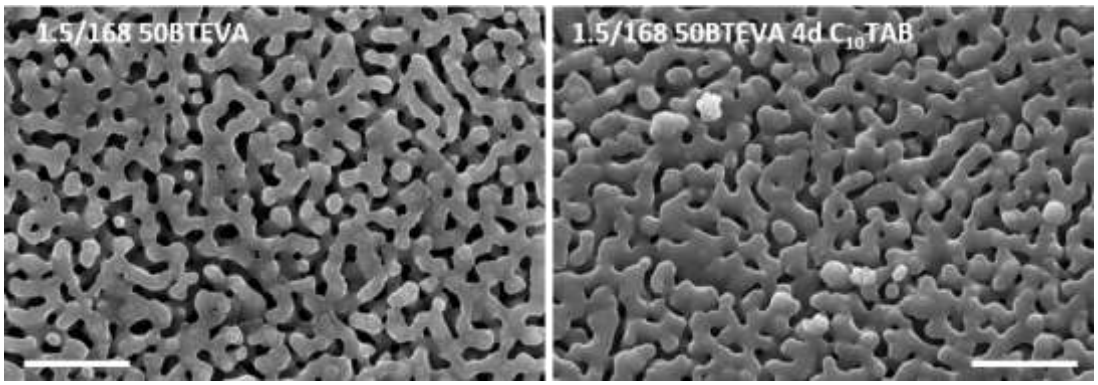

Figure 4-104: SEM images (magnification x50000, scale bar of 1 µm) of 50BTEVA from CPG batch III (left) and after pseudomorphic transformation (right) with C_{10}TAB for four days.

The high pH value is accompanied by high losses in mass due to dissolution of the silica phase, in order to reduce the mass losses by dissolution of silica, the transformation time was shortened to 24 hours for the transformation of 50BTEVB. The respective nitrogen physisorption isotherm and pore diameter distribution are given in Figure 4-105. Pores around 2.9 nm are mainly generated, but the formation of micropores also occurs. The formation of micropores in the presence of C_{10}TAB was described for common organosilica synthesis in Section 4.1.4. It might be caused by insufficiently formed micelles, probably due to low surfactant concentration. Here, the determination of the specific *apparent* BET surface area is also challenging. Due to the overlap of BET range and the pore condensation step, the surface area is overestimated to 943 $m^2 \cdot g^{-1}$ in the pressure range p/p^0 = 0.074–0.22. At lower relative pressures, micropore filling occurs which distorts the result. Considering this pressure range (0.025–0.072), an *apparent* specific BET surface area of 846 $m^2 g^{-1}$ is derived.

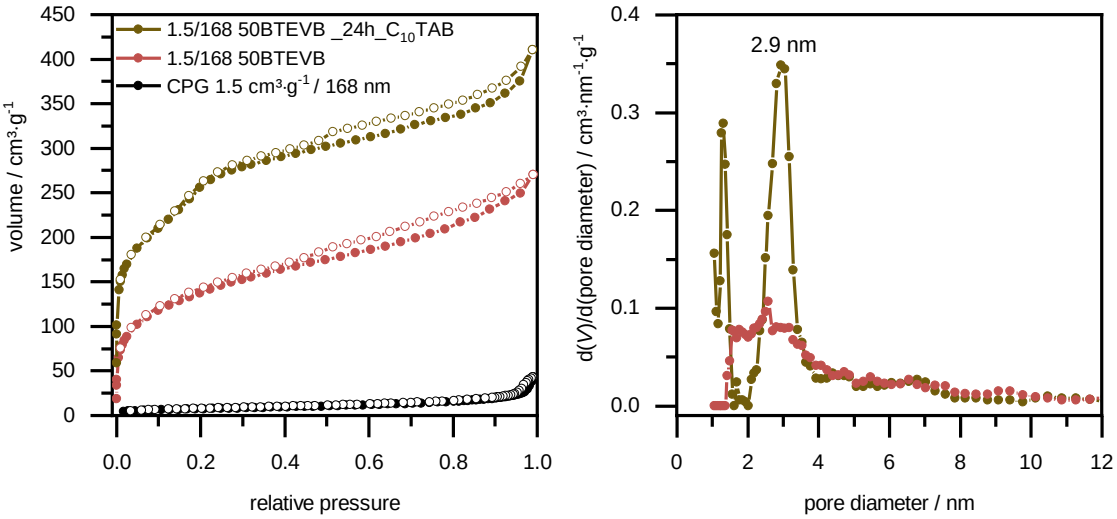

Figure 4-105: Physisorption isotherms (N_2, 77 K) of 50BTEVB from CPG batch III before and after pseudomorphic transformation with C_{10}TAB/NaOH for 24 hours (left), and pore diameter distributions (right, calculated using the NLDFT kernel for silica with cylindrical pores, from the adsorption branch).

Argon physisorption measurements were carried out for better characterization of the micropore system. The respective isotherm as well as the pore diameter distribution are shown in Figure 4-106.

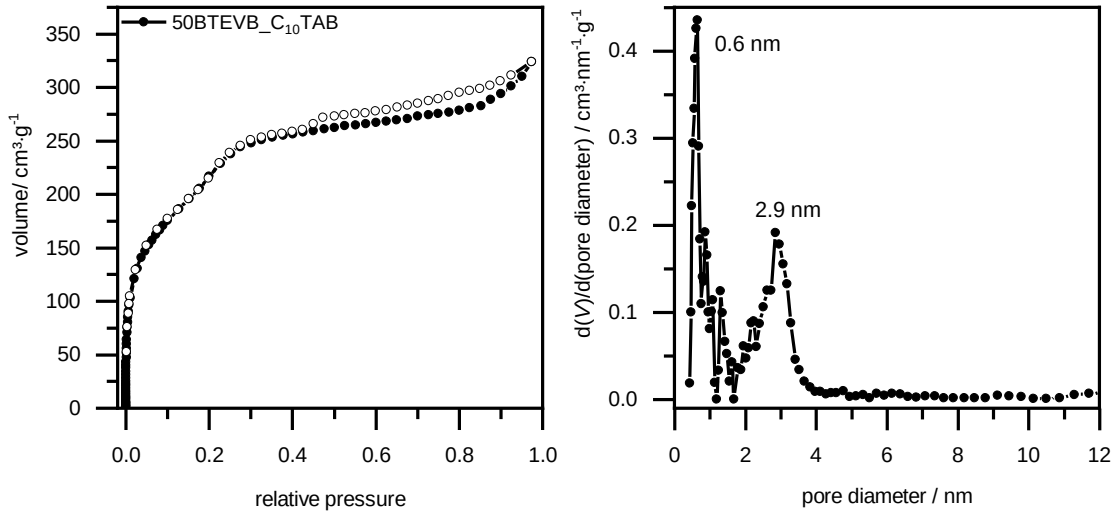

Figure 4-106: Physisorption isotherm (Ar, 87 K) of 50BTEVB from CPG batch III after pseudomorphic transformation with C_{10}TAB/NaOH for 24 hours on the left. The pore diameter distribution is shown on the right.

The specific BET surface area determination from argon physisorption measurements underlies similar restrictions as described for the nitrogen measurements. Here, the most reasonable result of S_{BET} = 668 m²·g^{-1} is obtained considering the relative pressure range of p/p^0 = 0.045–0.099. Two pore diameter maxima of 0.6 nm and 2.9 nm were found, but only 2.9 nm pores origin from a mesophase templating with C_{10}TAB.

The respective mesophase results in reflection at 2θ = 2.4°, which corresponds to a *d*-spacing of 3.6 nm in the P-XRD shown in Figure 4-107. Measurements at higher scattering angles did not show further reflections so that the formation of crystal-like pore walls in the organosilica phase is not detected.

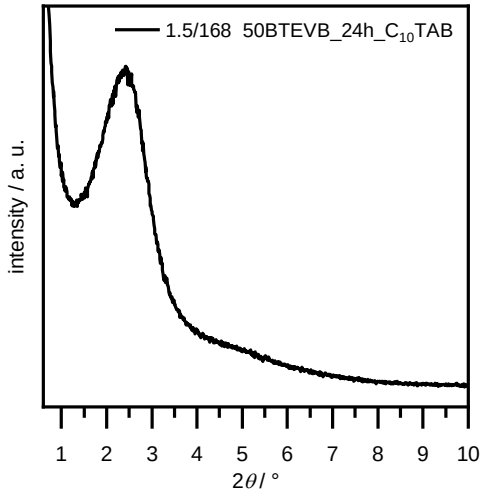

Figure 4-107: P-XRD pattern of 50BTEVB from CPG batch III templated with C_{10}TAB.

The pore diameter distribution determined by MIP before and after pseudomorphic transformation with C_{10}TAB and C_{16}TAOH is compared in Figure 4-108. It is worth noting that pseudomorphic transformation with C_{10}TAB does not influence the macropore size as much as C_{16}TOH does. This suggests less swelling of the material during the templating with the smaller surfactant, as it has already been observed for the treatment of 50BTEVA. Besides, the intrusion volume is constant after the treatment (0.69 $cm^3 \cdot g^{-1}$). The data are summarized in Table 4-37.

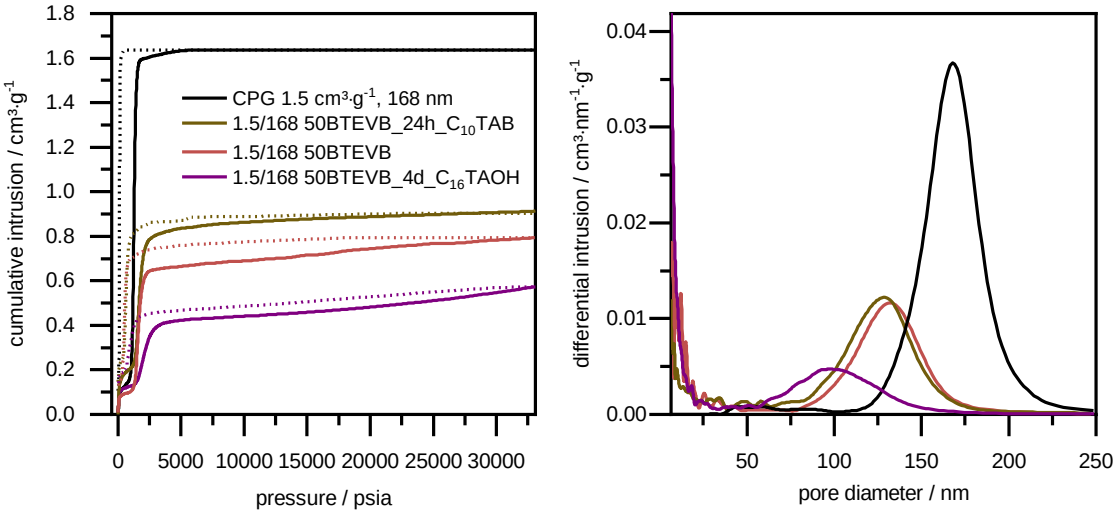

Figure 4-108: Mercury intrusion curves and pore diameter distributions from MIP of 50BTEVB (red) from CPG batch III (black) after transformation with C_{10}TAB (olive) or C_{16}TAOH (purple).

Nevertheless, swelling of the pore walls is recognizable by comparing the SEM images before and after transformation in Figure 4-109, also it is less significant as in the sample 50BTEVA_C_{10}TAB which was transformed for four days.

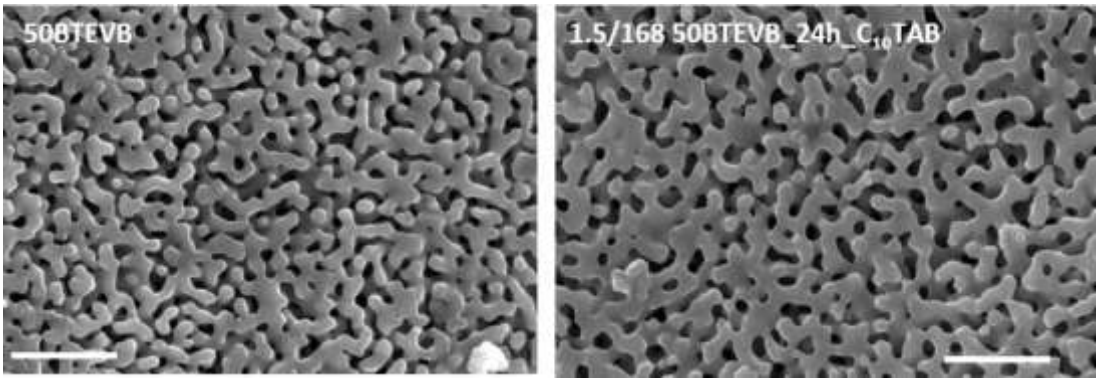

Figure 4-109: SEM images (magnification x50000, scale bar of 1 µm) of 50BTEVB from CPG batch III (left) and after pseudomorphic transformation (right) with C_{10}TAB.

Table 4-37: specific BET surface area and intruded pore volume of 50BTEVB from CPG batch III before and after pseudomorphic transformation with C_{10}TAB or C_{16}TAOH.

Sample	S_{BET}/ $m^2 \cdot g^{-1}$	V_{Hg} / $cm^3 \cdot g^{-1}$	d_{Hg} / nm
50BTEVB	476	0.69	132
50BTEVB_4d_C_{16}TAOH	1007	0.43	100
50BTEVB_24h_C_{10}TAB	668 (Ar)	0.69	127

In this case, it could be shown that the mesopore size of DVA- and DVB-organosilica/silica hybrid materials is adjustable by pseudomorphic transformation using cationic surfactants of different alkyl chain lengths. Further, in the case of smaller mesopore size, the macropore size can be also adjusted because less swelling of the material occurs.

Adjustment of the macropore size by reduction of the transformation degree

Another approach to reduce the swelling of the pore walls during transformation is the reduction of the transformation degree. Different approaches have already been presented in the previous chapter 4.2, where the variation of the transformation time turned out to be the best method to control the transformation degree. The results in that section show that after six hours of transformation the CPG should be half-transformed, so this time was chosen here for the partial transformation of 50BTEVB from batch III.

SEM images in Figure 4-110 show the pore system of the respective partially transformed sample compared with the sample that was treated for four days. It is obvious that the swelling effect is less distinct after the shorter treatment. However, the pore walls are thicker compared to the impregnated samples, and the impression of a swollen material is intensified by rounded edges.

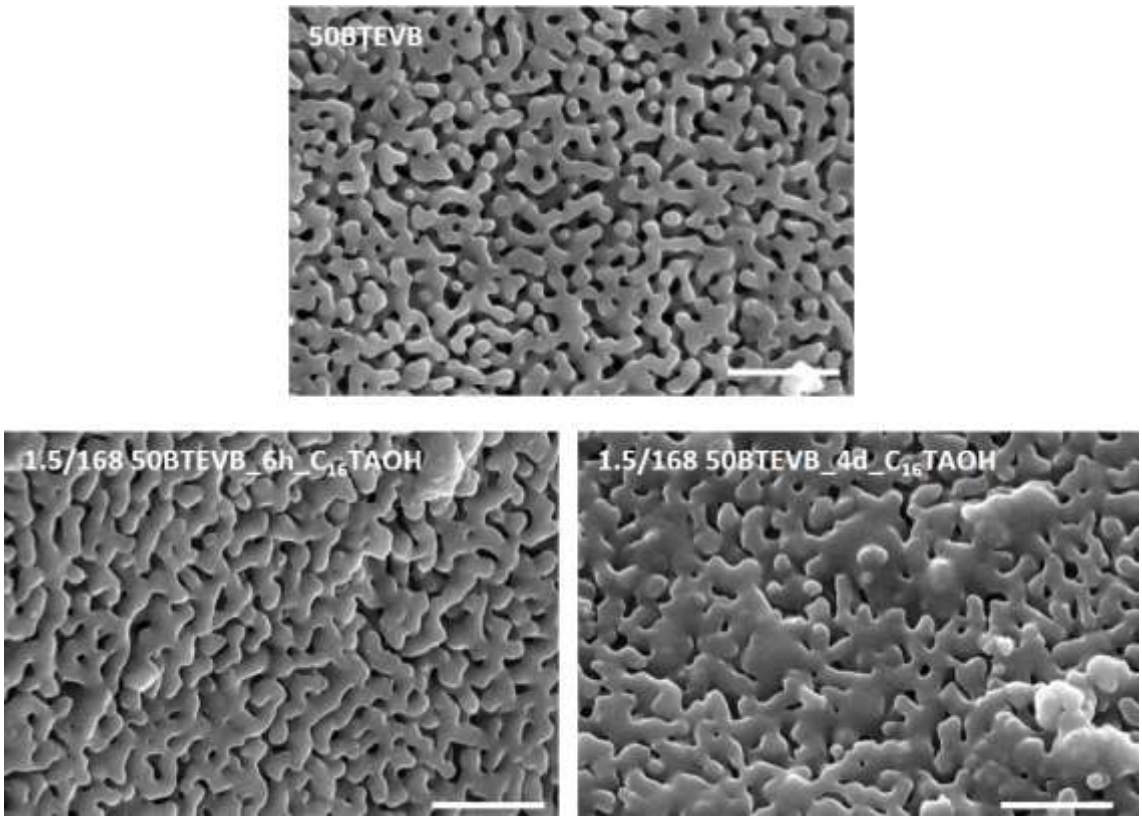

Figure 4-110: SEM images of 50BTEVB (upper part) from CPG batch III after treatment with C_{16}TAOH for six hours (left) and four days (right), magnification x50000, scale bar of 1 µm.

The porosity of the materials was further characterized by nitrogen physisorption measurements. Figure 4-111 shows the isotherms of 50BTEVB, after transformation for six hours, and after four days for comparison. The *apparent* specific BET surface areas increase from 476 $m^2 \cdot g^{-1}$ before the treatment to 835 $m^2 \cdot g^{-1}$ for 50BTEVB_6h_C_{16}TAOH and 1007 $m^2 \cdot g^{-1}$ for 50BTEVB_4d_C_{16}TAOH. Therefore, a partial transformation of the hybrid material can be assumed, but the specific BET surface area is already significantly increased. Calculation of a transformation degree based on the specific BET surface area is not suitable here since the organosilica layer was already porous before the transformation. The cumulative pore volume (NLDFT, kernel for silica with cylindrical pores, adsorption branch form N_2 physisorption isotherm) increased from 0.39 $cm^3 \cdot g^{-1}$ (50BTEVB) to 0.64 $cm^3 \cdot g^{-1}$ (50BTEVB_6h_C_{16}TAOH) in comparison to 0.81 $cm^3 \cdot g^{-1}$ (50BTEVB_4d_C_{16}TAOH). The pore diameter maximum is at 4.2 nm according to the pore diameter distribution. The P-XRD pattern shows the typical reflection at 2θ = 1.9°, which corresponds to a *d*-spacing of 4.5 nm (see Figure 9-34 in the Appendix) so that a successful micelle templating process can be assumed here. Measurements at higher scattering angles did not show further reflections so that the formation of crystal-like pore walls in the organosilica phases are not detected.

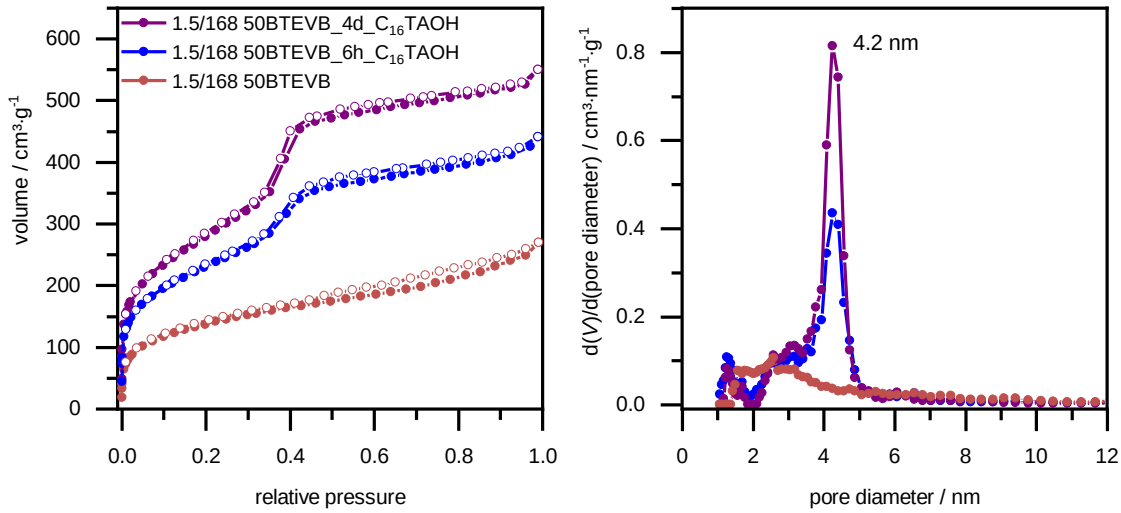

Figure 4-111: Physisorption isotherms (N_2, 77 K) of 50BTEVB from CPG batch III before and after treatment with C_{16}TAOH for six hours and four days (left) together with the respective pore diameter distributions (calculated from the adsorption branch, NLDFT kernel for silica with cylindrical pores, right).

The macropore system was characterized by MIP, and the pore size distribution can be seen in Figure 4-112.

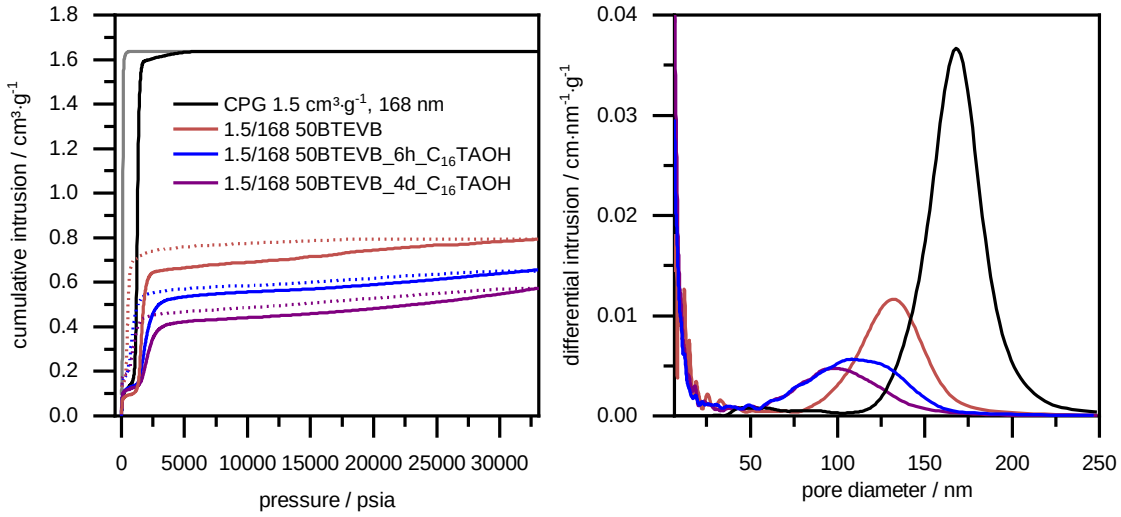

Figure 4-112: Mercury intrusion curves (left) and pore diameter distributions from MIP (right) of 50BTEVB (red) from CPG batch III (black) after transformation with C_{16}TAB for four days (magenta) and six hours (light purple).

For the partially transformed sample 50BTEVB_6h_C_{16}TAOH a maximum is found at 110 nm which is 10 nm larger than for 50BTEVB_4d_C_{16}TAOH. The intrusion volume is accordingly higher with 0.52 $cm^3 \cdot g^{-1}$ for 50BTEVB_6h_C_{16}TAOH and 0.43 $cm^3 \cdot g^{-1}$ for 50BTEVB_4d_C_{16}TAOH. Therefore, it could be shown that the macropore size and the macropore volume can be controlled by the transformation degree of the organosilica/silica hybrid materials as well, as was the case for the pure CPG (compare pore size distribution from MIP in Figure 4-29 in section 4.2). Table 4-38 summarizes the data from physisorption and MIP of the pseudomorphic transformed samples from 50BTEVB after transformation for six hours and four days with C_{16}TAOH.

Table 4-38: specific BET surface area, mesopore volume from NLDFT kernel for silica with cylindrical pores, and intruded pore volume of 50BTEVB from CPG batch III before and after pseudomorphic transformation with C_{16}TAB for four days and six hours, 50BTEVB_24h_C_{10}TAB (data calculated from argon physisorption) .

Sample	S_{BET}/ m²·g^{-1}	$V_{N_2,\ NLDFT}$/ cm³·g^{-1}	V_{Hg} / cm³·g^{-1}	d_{Hg} / nm
50BTEVB	476	0.39	0.69	132
50BTEVB_6h_C_{16}TAOH	835	0.64	0.52	110
50BTEVB_4d_C_{16}TAOH	1007	0.81	0.43	100
50BTEVB_24h_C_{10}TAB	668 (Ar)	0.42 (Ar)	0.69	127

The transformation is already well advanced after six hours, so that it was desirable to reduce the transformation degree further, thus enabling the measurement of the micelle templating mechanism. The intention was also to form a PMO inside the CPG pore system so that higher organosilica content was favored, and alternative samples were investigated. 75BTEVB from batch III was treated for one hour with C_{16}TAOH, for isotherms and the pore diameter distributions see Figure 4-113. The impregnated sample has already shown a high *apparent* specific BET surface area of 617 m²·g^{-1} which increases only slightly to 659 m²·g^{-1} after the transformation. Also, no significant change of the pore size distribution is detectable. Further, the sample proved to be X-ray amorphous. Hence, after a short transformation of one hour, micelle templating cannot be distinguished in the sample meaning it is an unsuitable starting material for the investigation of the pseudomorphic transformation mechanism.

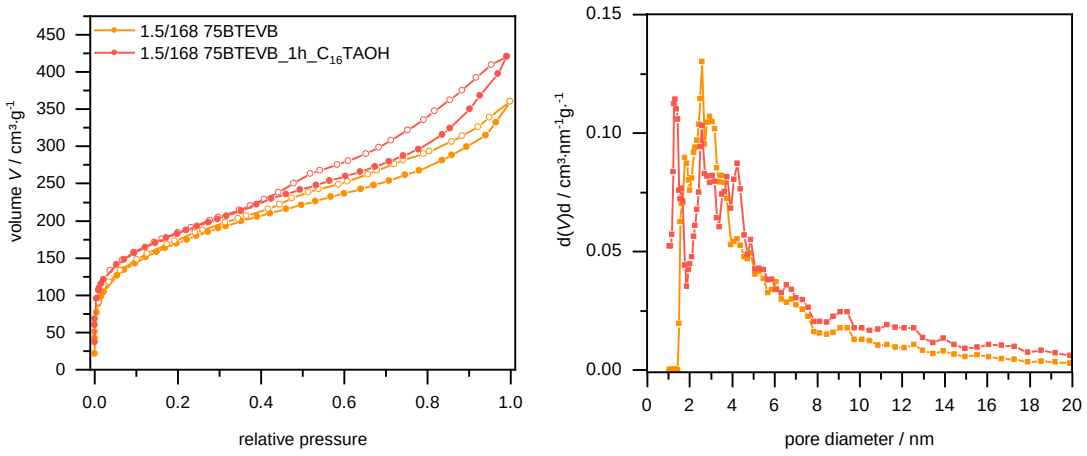

Figure 4-113: Physisorption isotherms (N_2, 77 K) of 75BTEVB from CPG batch III before and after treatment with C_{16}TAOH for one hours (left) together with the respective pore diameter distributions (NLDFT kernel for silica, cylindrical pores, calculated from the adsorption branch.

To test further alternatives, 25BTEVB from CPG batch V was treated with C_{16}TAOH for one hour (denoted as 25BTEVB_1h) and for 24 hours (denoted as 25BTEVB_24h), respectively. The high initial pore volume was assumed to have a positive impact on the micelle templating due to low spatial restrictions. Figure 4-114 shows the nitrogen physisorption isotherms for these samples

as well as the pore diameter distributions. After one hour of treatment, the pore diameter distribution is still rather broad, but in contrast to the 75BTEVB sample from CPG batch III, a dominant pore size shift towards mesopores between 2–6 nm is visible. Also the specific BET surface area increases significantly from 388 $m^2 \cdot g^{-1}$ for 25BTEVB to 538 $m^2 \cdot g^{-1}$ for 25BTEVB_1h_C_{16}TAOH and further to 962 $m^2 \cdot g^{-1}$ for 25BTEVB_24h_C_{16}TAOH, where a monomial pore diameter distribution of 4.2 nm occurs.

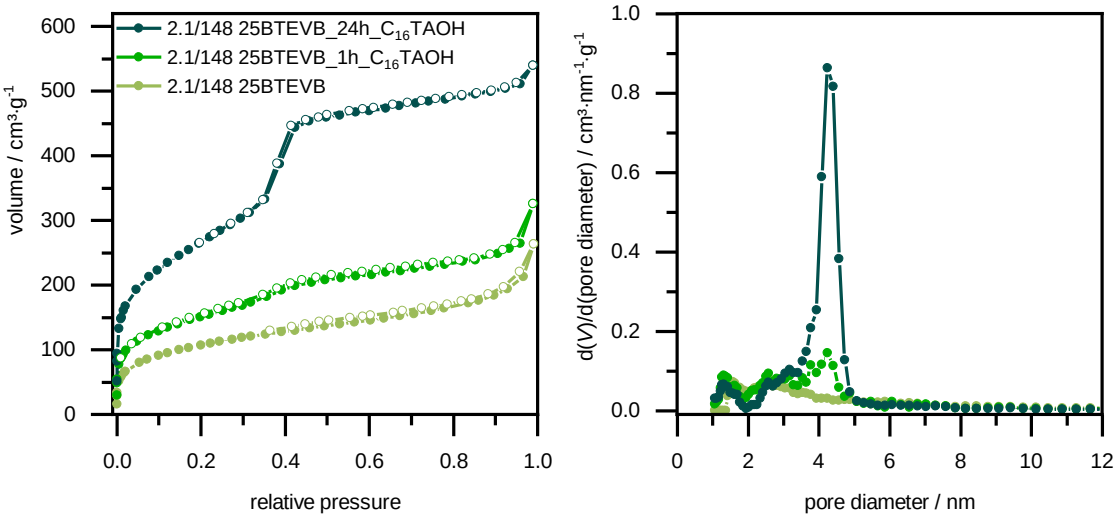

Figure 4-114: Physisorption isotherms (N_2, 77 K) of 25BTEVB from CPG batch V after treatment with C_{16}TAOH for one hour and 24 hours (left) and the respective pore diameter distributions (calculated from the adsorption branch, using NLDFT, kernel for silica with cylindrical pores), shown on the right.

The P-XRD pattern of 25BTEVB_24h_C_{16}TAOH shows one reflection at $2\theta = 2.0°$, in the case of 25BTEVB_1h_C_{16}TAOH the reflection is barely visible, see Figure 4-115. Measurements at higher scattering angles did not show further reflections so that the formation of crystal-like pore walls in the organosilica phases are not detected.

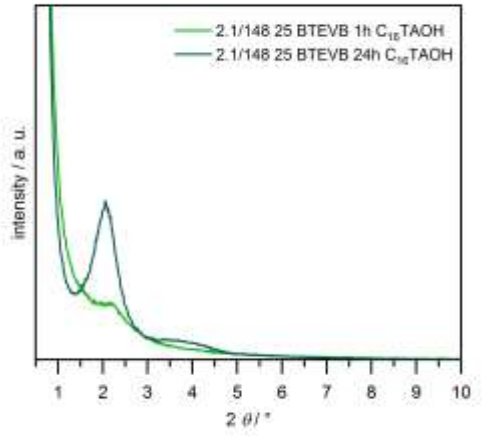

Figure 4-115: P-XRD pattern of 25BTEVB CPG batch V after treatment with C_{16}TAOH for one and 24 hours.

Mercury intrusion curves and the pore diameter distribution from MIP are shown in Figure 4-116. CPGs from batch V show two maxima, which are still identified for 25BTEVB and 25BTEVB_1h_C_{16}TAOH, but become indistinct for 25BTEVB_24h_C_{16}TAOH. Regarding only the higher maximum, the pore size decreases stepwise from 117 nm for 25BTEVB to 107 nm for 25BTEVB_1h_C_{16}TAOH and 97 nm for 25BTEVB_24h_C_{16}TAOH, respectively.

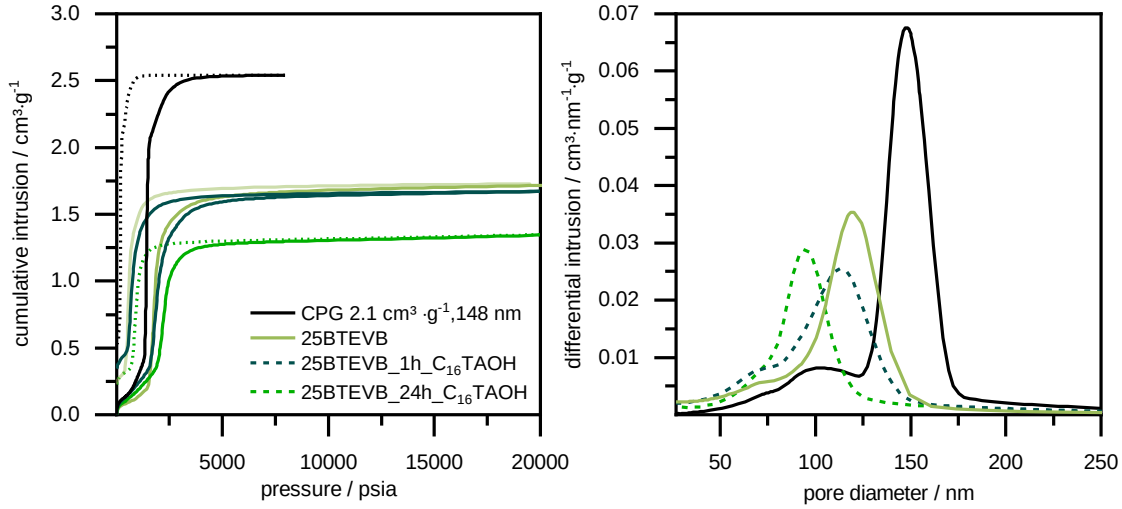

Figure 4-116: Pore diameter distributions from MIP of 25BTEVB, 25BTEVB_1h_C_{16}TAOH and 25BTEVB_24h_C_{16}TAOH from CPG batch V.

Table 4-39 summarizes the results from partial transformation of 25BTEVB from batch V.

Table 4-39: Summary of the specific BET surface area, mesopore volume from NLDFT kernel for silica with cylindrical pores, and intruded pore volume of 25BTEVB from CPG batch V before and after pseudomorphic transformation with C_{16}TAB for 24 hours and one hour, 50BTEVB_24h_C_{10}TAB (data calculated from argon physisorption) .

Sample	S_{BET}/ m²·g⁻¹	$V_{N_2,\ NLDFT}$/ cm³·g⁻¹	V_{Hg} / cm³·g⁻¹	d_{Hg} / nm
25BTEVB	388	0.37	1.50	117
25BTEVB_1h_C_{16}TAOH	538	0.47	1.44	107
50BTEVB_24h_C_{16}TAOH	962	0.80	1.16	97

SEM images of the materials before and after the transformation are shown in Figure 4-117. As expected, no obvious differences between the pure CPG and the impregnated sample after one hour of transformation is shown, whereas swelling of the material and the formation of precipitate on the outer surface of the pore system is obvious in the sample that was treated for 24 hours.

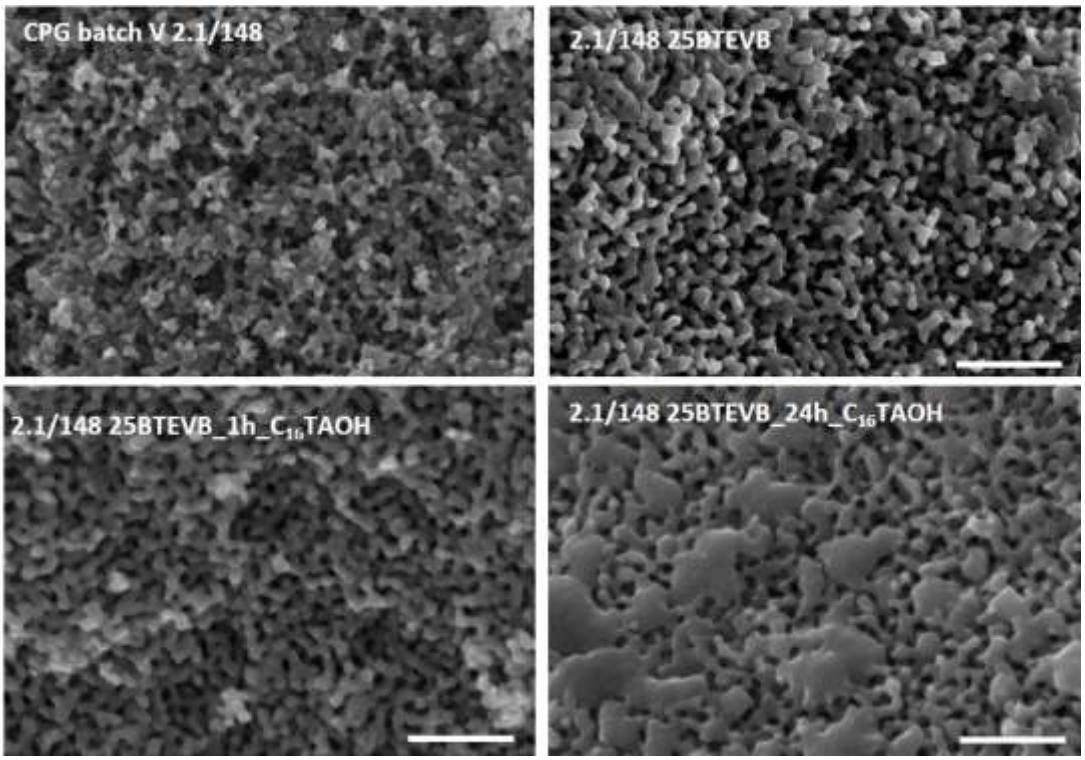

Figure 4-117: SEM images of CPG batch V, and 25BTEVB before the transformation in the upper part, and after transformation for one hour and 24 hours in the lower part (magnification x50000, scale bar of 1.0 µm).

TG/MS data of the samples follows the trend of previously mentioned samples: the mass loss in the temperature interval of 300–800 °C increases slightly after pseudomorphic transformation, so that the presence of residues of the surfactant, or leaching of the silica phase during the transformation process are assumed. Beyond, the amount of surface-adsorbed water increases significantly, see Figure 4-118 for TG/MS plots. The mass loss in different temperature intervals are given in Table 4-40.

Table 4-40: Mass loss in given temperature intervals of TG analysis (Ar/O_2 80/20) of 25 BTEVB from batch V before and after pseudomorphic transformation for 1 hour or 24 hours. Entries marked with an asterisk (*) denote corrected values.

temperature interval	25–150 °C	150–300 °C	300–800 °C	25-800 °C
25BTEVB	1.7 %	1.8 %	12 %*	15 %
25BTEVB_1h_C_{16}TAOH	3.1 %	0.5 %	14%*	17 %
25BTEVB_24h_C_{16}TAOH	4.2 %	1.5 %	15 %*	20 %

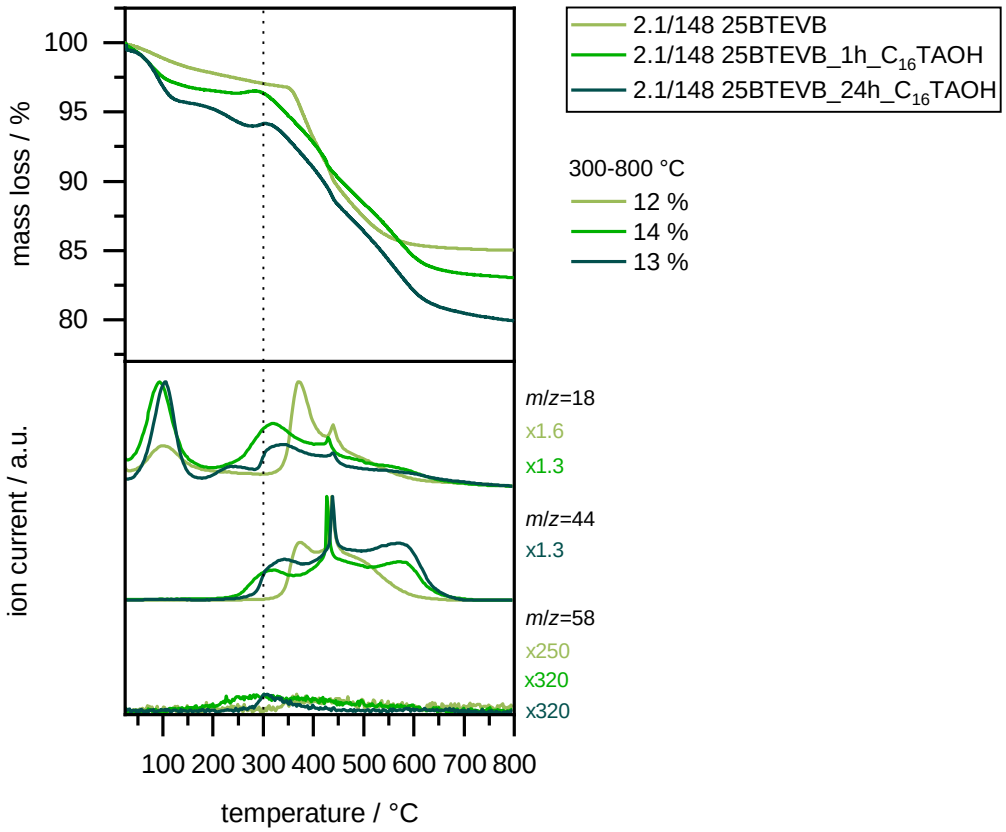

Figure 4-118: TG/MS analysis in Ar/O_2 80/20 of 25BTEVB batch V before and after pseudomorphic transformation for one hour and 24 hours. In the upper plots: mass losses plotted against the temperature. The corrected mass loss for the temperature interval 300–800 °C is given on the left. Lower plot: selected ion currents with normalization factor given on the side.

Hence, in this example the macropore diameter clearly decreases stepwise with increasing transformation degree, which means that adjustment of the macropore size is possible by partial pseudomorphic transformation. Since only a small amount of material from batch V was available, it could only be used for proof of the principle. Thus, 50 BTEVB_6h_C_{16}TAOH was used for the following investigation of the transformation mechanism.

4.3.4 Investigation of the transformation mechanism

The results of the previous chapter show the formation of an additional mesopore system and the change of the initial macro- or large mesopore system in organosilica/silica hybrid materials by treatment with an alkaline surfactant solution under unchanged morphology.

Up to now, only the pore systems of the organosilica/silica hybrid have been discussed. However, the way in which the structure of the hybrid materials changes during this pseudomorphic transformation is also of interest. In Figure 4-89 at the beginning of previous section, it was assumed that pseudomorphic transformation of CPG with a layer of organosilica would lead to

a layer of PMO on a mesoporous silica backbone. If this is the case, partial pseudomorphic transformation of the hybrid material could lead to a PMO layer on a nonporous silica backbone. Figure 4-119 shows the hypothetical progress of the pseudomorphic transformation with increasing transformation degree.

Different approaches are discussed below to answer the questions concerning the transformation mechanism. On the one hand, the organosilica content after the transformation needs to be quantified. On the other hand, homogeneous distribution of organosilica in the mesoporous silica needs to be distinguished from the formation of a PMO layer after transformation. Parts of the results were submitted for publication titled *"Pseudomorphic Transformation of Organosilica@ Controlled Pore Glass – A New Approach Forming Hierarchically Porous Organosilica/Silica Hybrid Materials"* by Malina Bilo, Maximillian Münzner, Christian Küster, Dirk Enke, Young Joo Lee and Michael Fröba.

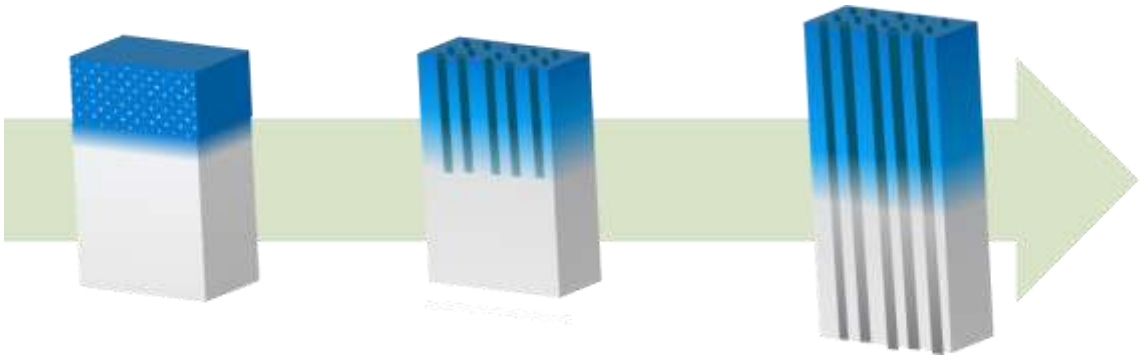

Figure 4-119: Diagram to visualizing the progress of the pseudomorphic transformation of a hybrid material from a layer of nanoporous organosilica (blue) on the CPG pore surface. It is nanoporous (shown as pattern) before ordered mesopores are generated by templating in the organosilica layer and subsequently in both layers.

Quantification of the organosilica content in the organosilica/silica hybrid material

In order to get a first insight into the organosilica content after pseudomorphic transformation, TG-MS measurements were conducted. In Figure 4-120, plots of the mass loss from 50BTEVB_6h_C_{16}TAOH are shown together with 50BTEVB before transformation on the one hand, and 50BTEVB_4d_C_{16}TAOH, as well as 50BTEVB_24h_C_{10}TAB on the other hand. Selected normalized ion currents from MS are shown in the plot below.

The mass loss in the temperature range of 300–800 °C of 50BTEVB is 16 % and after transformation, in the case of 4d_C_{16}TAOH and 6h_C_{16}TAOH it is 20 %. 50BTEVB_24h_C_{10}TAB loses 21 % in this temperature range. The gap of 4–5 % indicates the presence of surfactant residues or loss of silica due to the treatment at high pH value. It is noteworthy that the mass loss is the same for all samples after transformation. Hence, the surfactant amount, or the silica loss in all three samples seems to be coincidently the same.

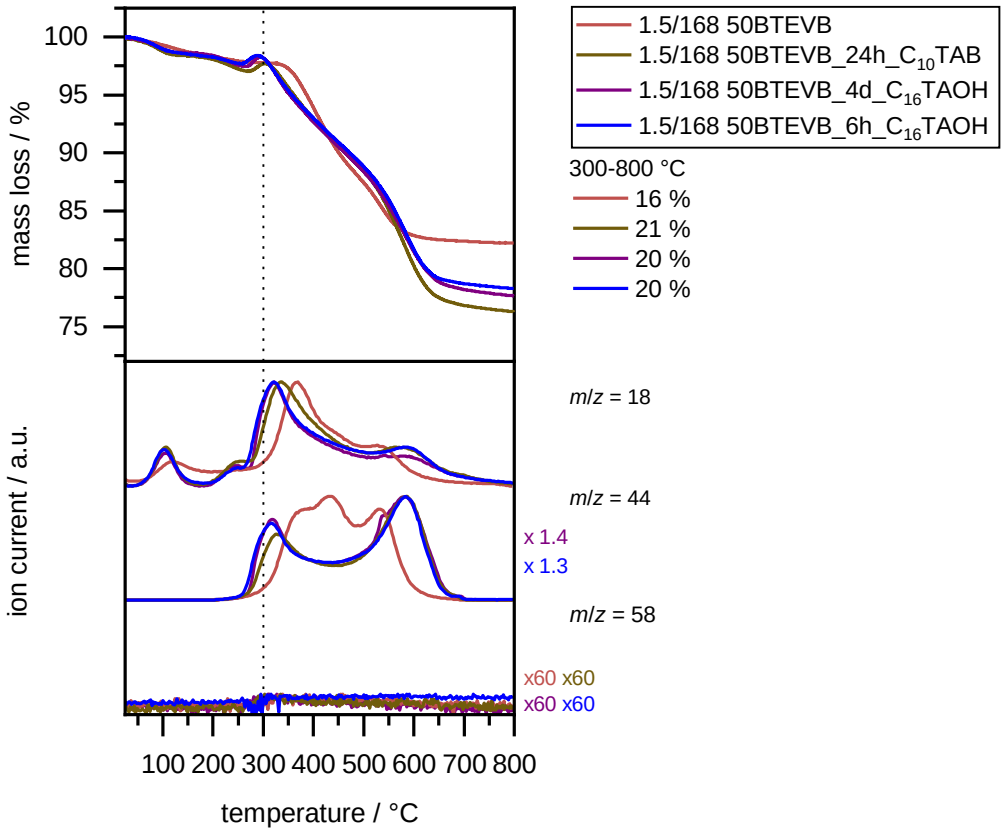

Figure 4-120: TG/MS analysis in Ar/O_2 80/20 of 50BTEVB from CPG batch III as well as the pseudomorphically transformed samples with C_{10}TAB and C_{16}TAOH for 4 days and 6 hours. In the upper plot: mass losses plotted against temperature are shown, and in the lower plot selected ion currents with normalization factor on the side are shown.

For comparison 50BTEVB_6h_C_{16}TAOH before the extraction of the surfactant was also analyzed and is shown in Figure 4-121. The overall mass loss is 45 % in three steps, and the decomposition starts significantly earlier than in the extracted samples. The mass loss below 300 °C is 19 %. In this temperature range, 80 % of the surfactant decomposes and the ion current m/z = 58 (C_3H_8N) appears most prominently (for TG/MS of C_{16}TAB see Figure 9-39 in the Appendix). In the temperature range of 300–800 °C the mass loss is 26 %.

To evaluate the extraction method, pure CPG was treated for four days with C_{16}TAOH and was subsequently extracted in ethanol and hydrochloric acid (37 %) (97/3) under reflux (CPG_4d_C_{16}TAOH extracted), which is the same treatment as was used for the impregnated samples. The respective mass loss and ion current is given in Figure 4-121. It shows a mass loss of 5.4 % in the temperature range of 300–800 °C and the ion current of m/z = 58 (C_3H_8N) cannot be detected in this case. It is possible that the intensity of the ion current is too low since most of the surfactant is extracted. Thus, this ion current does not seem to be a reliable detector. It is also noticeable that the main mass loss occurs in the temperature range of 300–800 °C, although this is not the temperature range where the surfactant mainly decomposes. This indicates a changed decomposition behavior of the surfactant under these conditions inside the CPG.

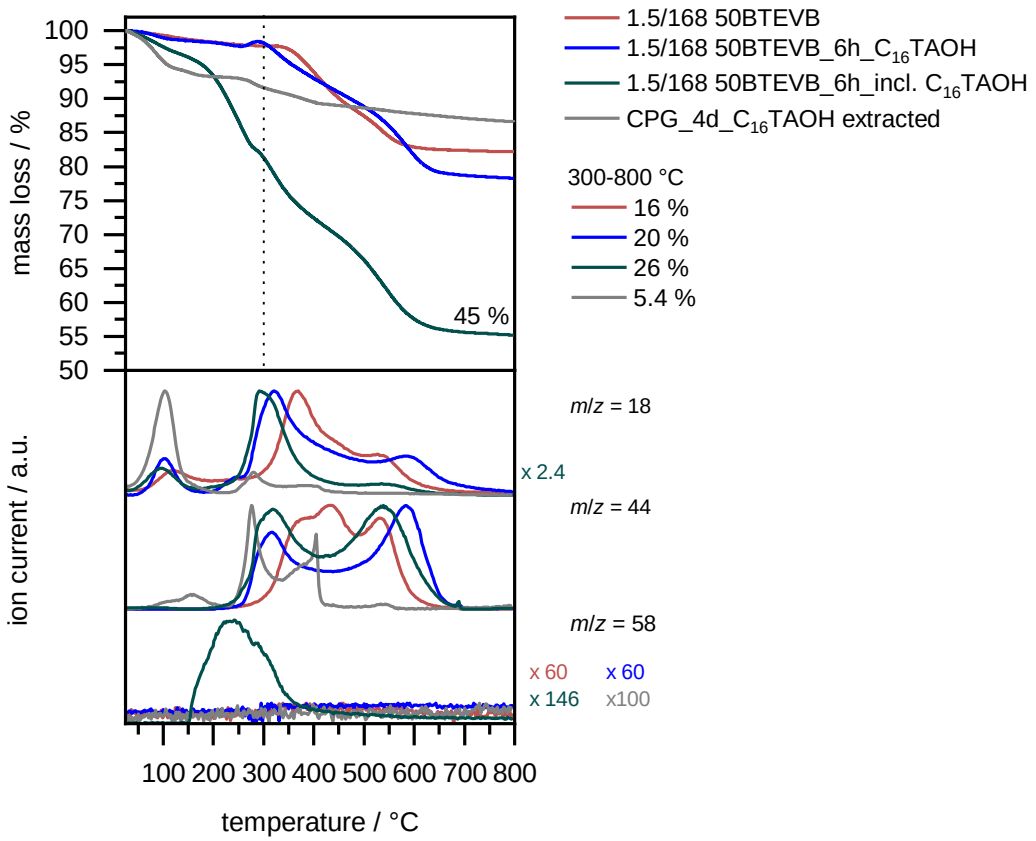

Figure 4-121: TG/MS analysis in Ar/O_2 80/20 of 50BTEVB and 50BTEVB_6h_C_{16}TAOH before and after extraction of the surfactant, and a pure CPG_4d_C_{16}TAOH after extraction. In the upper plot mass losses are plotted against temperature, while selected ion currents are in the lower plot with the normalization factors given on the side.

Table 4-41 summarizes the mass loss of the samples which were discussed here in the different temperature intervals.

Table 4-41: Mass loss in given temperature intervals of TG analysis (Ar/O_2 80/20) of 50 BTEVB from batch III before and after pseudomorphic transformation for six hours, extracted or non-extracted, the surfactant and an extracted CPG after treatment with the surfactant. Entries marked with an asterisk (*) denote corrected values.

temperature interval	25–150 °C	150–300 °C	300–800 °C	25-800 °C
50BTEVB			16 %*	
50BTEVB_24h_C_{10}TAB	1.6 %	0.7 %	21 %*	24 %
50BTEVB_6h_C_{16}TAOH	1.4 %	0.4 %	20 %*	22 %
50BTEVB_6h_C_{16}TAOH_incl. C_{16}TAOH	3.9 %	15 %	26%*	45 %
C_{16}TAB	–	78 %	28%	100 %
50BTEVB_4d_C_{16}TAOH	0.5 %	1.3 %	20 %*	22 %
CPG_4d_C16TAOH_extracted	6.0 %	2.3 %	5.4 %*	13 %

The differences in the TG plots before and after extraction of 50BTEVB_6h_C_{16}TAOH indicate that the majority amount of surfactant is extracted. Nevertheless, the extracted pure CPG shows that the complete removal of the surfactant by extraction from pseudomorphically transformed

samples is not possible – neither with a Soxhlet apparatus, nor under reflux conditions for several days. This might be caused by enclosures of the surfactant inside the material during the restructuring process.

Another characteristic of the TG plots from DVB-organosilica/silica hybrid materials after transformation is the slight mass increase at 275 °C. It was suspected, that this is due to oxidation of the organic bridge under the chosen conditions in Ar/O_2 80/20 which might cause overall higher mass loss. It is worth noting that TG analysis of pure DVB-PMO shows the same curve characteristics but the overall mass loss fits with the theoretical value.[218] To investigate this, 50BTEVB_4d_C_{10}TAB was treated for one hour at 275 °C after extraction. An additional mode at a wave number of 1707 cm^{-1} in the IR spectrum (see Figure 4-122) was assigned to a C=O stretching vibration. This confirms the oxidation of the samples during the TG/MS measurement. However, the results show that TG/MS is not reliable for the quantification of the organosilica content in organosilica/silica hybrid materials.

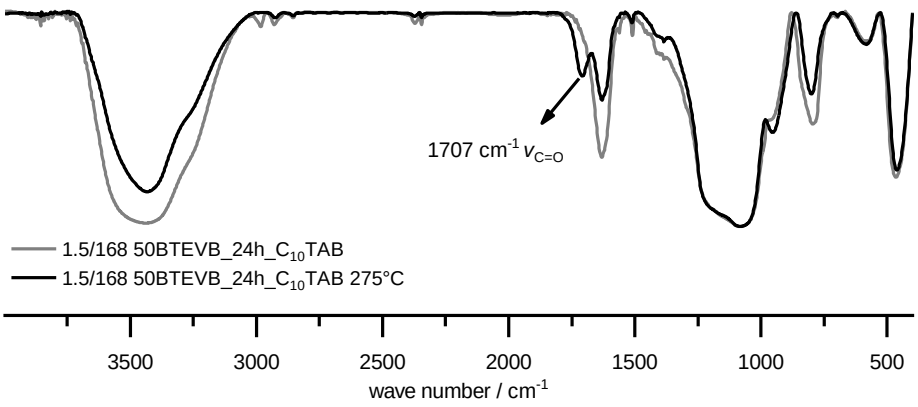

Figure 4-122: FT-IR spectra (KBr-disc) of 50BTEVB_24h_ C_{10}TAB before (gray) and after (black) treatment for one hour at 275 °C.

50BTEVB, 50BTEVB_4d_C_{16}TAOH and 50BTEVB_6h_C_{16}TAOH were further characterized by solid state MAS-NMR. This method is more time consuming than FT-IR spectroscopy or TG/MS measurements, but it is a suitable tool to check the presence of the surfactant.

Figure 4-123 shows the ^{13}C-CP-MAS NMR spectra of 50BTEVB together 50BTEVB_6h_C_{16}TAOH before and after extraction of the surfactant. Liquid state ^{13}C-NMR of C_{16}TAB in $CDCl_3$ ($CHCl_3$ at 77.16 ppm) is given as a comparison. The spectrum of the sample after four days and six hours of transformation are congruent (see the spectrum in the Appendix Figure 9-36) so it was left out here for better clarity. Before and after the transformation, the carbon signals of the bridging unit are unchanged and easily visible. The assignment of the signals to the precursor is given in the Experimental Section and has already been shown in Figure 4-85 in context of the characterization of 50BTEVB. Before extraction, additional signals that correspond to the aliphatic chain of the surfactant, can be assigned and are in good agreement with the respective

liquid-state NMR of the surfactant. The most prominent signal appears at 30.8 ppm (CH_2 groups of the aliphatic chain). After extraction these signals are not significant, which indicates that the extraction of the surfactant was almost successful. Signals at a chemical shift of 59.8 ppm and of 15.4 ppm can be assigned to ethanol or ethoxy groups, resulting from incomplete condensation, occur before and after the transformation. Another additional signal at 63.2 ppm appears only after the transformation and cannot be assigned clearly either to ethanol or to the surfactant. It might be an ethoxy species with a different chemical environment which significantly affects the chemical shift. Hence, no other organic molecule is present in the material after extraction. However, in the case of cleavage of the Si-C bond, the chemical shift of the vinyl carbons might not change, so that this option has not yet been ruled out.

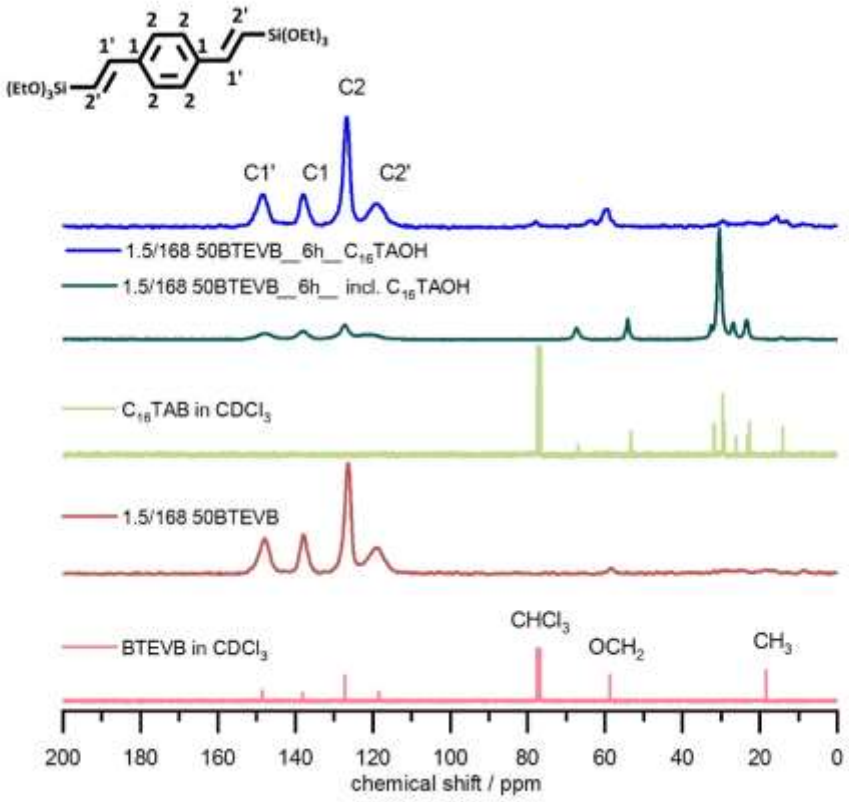

Figure 4-123: ^{13}C-C-MAS NMR spectra (ss = 13 kHz) of 50BTEVB from CPG batch III (red), 50BTEVB_6h_C_{16}TAOH after extraction (blue), and the sample including the surfactant (green). Liquid state ^{13}CNMR of C_{16}TAB (pale green) and BTEVB (pale red) in $CDCl_3$ are given for comparison. All spectra are plotted with normalized intensity.

^{29}Si-CP MAS NMR gives semi-quantitative information concerning the ratio of Q and T silica species – which is the ratio of organosilica to silica. In addition, it gives information concerning the condensation degree of the materials before and after transformation. Figure 4-124 shows the ^{29}Si-CP-MAS NMR of the above samples in one plot.

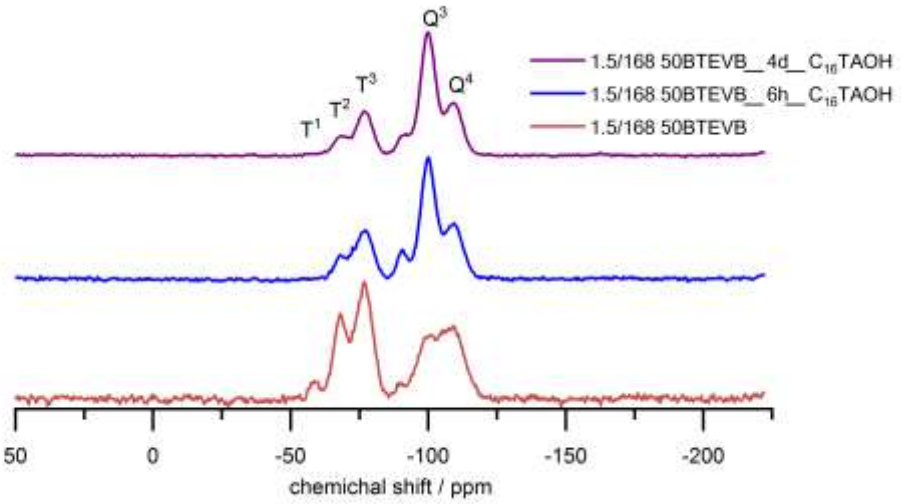

Figure 4-124: ^{29}Si-CP MAS NMR spectra (ss = 5 kHz) of 50BTEVB (red) from CPG batch III, 50BTEVB_6h_C_{16}TAOH (blue) and 50BTEVB_4d_ C_{16}TAOH (purple). All plots are given with normalized intensity.

There are some differences in the spectra before and after the transformation, but the spectra of 6h_C_{16}TAOH and 4d_C_{16}TAOH are nearly congruent. First, the Q signals become more defined after transformation. Since the Si–O–Si bond angle strongly affects the chemical shift of the silica species, narrower signals indicate harmonization of the bond angles. [198] Beyond, the ratio of Q^3 to Q^4 signals, which was nearly equal before transformation, changes to a very intense signal for Q^3 and a less intense signal for Q^4 after transformation. This behavior can also be observed for pure CPG after pseudomorphic transformation, see ^{29}Si CP-MAS NMR of CPG before and after pseudomorphic transformation in Figure 4-125.

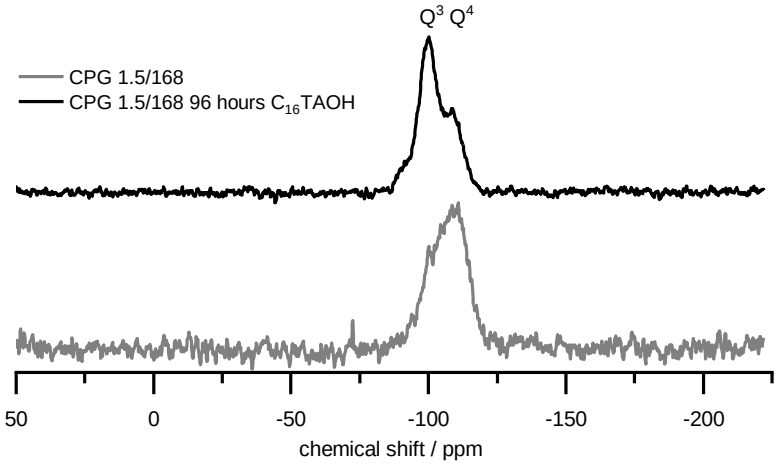

Figure 4-125: ^{29}Si-CP-MAS NMR (spinning speed = 5 kHz) of CPG batch III before and after pseudomorphic transformation for four days with C_{16}TAOH

The presence of T^1 signals after impregnation has already been discussed. After transformation, the signals disappear which is an indication of either progressed condensation or leaching of the respective precursor molecules. Further, the general ratio of Q to T signals changes after

transformation. The exact ratio of T and Q signals can be determined by deconvolution of Gaussian fits of the different signals in solid state NMR measurements of direct excitation ^{29}Si-MAS NMR. Q^4 was used as reference signal, and the relative intensities of the different T^n and Q^n species are measured in an experiment without CP and the relative ratios of T and Q are calculated. Since these measurements are especially time consuming, only 50BTEVB and 50BTEVB_6h_C_{16}TAOH were measured. 50BTEVB has already been discussed in section 4.3.2. The plots are given in the Appendix (Figure 9-35). The results are summarized in Table 4-42.

Table 4-42: Results from quantitative solid state ^{29}Si-MAS NMR of 50BTEVB and 50BTEVB_6h_C_{16}TAOH from CPG batch III. The percentages of the different T and Q species relative to Q^4 are given separately, and the relative ratio of Q to T is calculated in the result column. Additionally, the resulting molar percentage of DVB-organosilica in the hybrid materials can be calculated

Sample	T^1	T^2	T^3	Q^2	Q^3	Q^4	**T**	**Q**	**DVB**
50BTEVB	2.8 %	17.5 %	24.9 %	0.77 %	24.7 %	100 %	**27 %**	**73 %**	**16 mol%**
50BTEVB _6h_C_{16}TAOH	-	6.1 %	21.3 %	6.1 %	53.9 %	100 %	**15 %**	**85 %**	**8.1 mol%**

After the transformation, the ratio of T signals decreases from 27 % to 15 % and this corresponds to 8.1 mol% of the precursor. This could be due to two different reasons: either the organosilica content is leached out during transformation, or it decomposes during the harsh treatment of pseudomorphic transformation. In the case of cleavage of the Si-C bond, more Q signals occur whereas the ratio of T signals decreases. Cleavage of the organic bridge would explain the decreased ratio of T to Q Si species, but does not answer for the increased TG mass loss. Summarizing the results from TG/MS and from solid-state NMR, it can be concluded that the extraction of the surfactant was mostly successful, but high mass loss in TG indicate an unexplainable high organic content. Hence, leaching of the organosilica content is rather unlikely. Assuming that the Si-C bond was cleaved at one and not on two sites per unit, it was reasonable that no leaching occurs during the transformation. Beyond, the increased mass loss in TG measurement could be explained by loss of the silica phase due to treatment at high pH value, which is reasonable since mass loss was observed after pseudomorphic transformation of pure CPGs. If this is the case, the ratio of cleaved Si-C was even higher. As discussed before, both methods, the TG analysis and quantification of different silica species by deconvolution of signals from solid state NMR may have observational errors or are based on simplifying assumptions. Different factors might be combined here that does not allow the quantification of the cleavage

of the Si-C bond. However, it also occurred in the pseudomorphic transformation of organosilica from BTEVB with notable extend.[111] In follow-on research this aspect needs further systematical investigation of pure organosilica treated under the conditions of the pseudomorphic transformation with TG measurements and quantitative solid state NMR spectroscopy. Based on the respective results, milder conditions for the transformation process might be required. Maybe the results on pseudomorphic transformation of CPG at lower temperatures and under microwave radiations give beneficial input for this process.

Distinction between a PMO layer at CPG and a DVB-organosilica/silica mixed phase

This section began with the hypothesis that partial pseudomorphic transformation of the hybrid material could lead to a PMO layer on a nonporous silica backbone. This implies that the silica species are not involved in the pseudomorphic transformation process. Keeping the change in the ratio of the Q^4 to Q^3 species in the ^{29}Si-CP-MAS NMR spectra (Figure 4-124) in mind, an initial indication is given that the CPG backbone is affected, despite the fact that the transformation time was shortened to six hours. However, it is of interest to know whether a pure PMO layer is formed on a pure silica layer, since the formation of a mixed phase of both is also possible.
The sketches in Figure 4-126 show six different possible structures of the organosilica/silica hybrid material after pseudomorphic transformation. After impregnation of the CPG with organosilica solutions, two layers are formed. In (a)–(c) and (f) these two layers remain intact. The pseudomorphic transformation causes micelle templating either in the CPG whereas the microporous system in organosilica layer is unaffected, see (a), or in the organosilica layer, see (b), or in both layers, see (c). In (f) the two layers stay intact, but the organosilica phase is mixed with pure silica species which are generated by decomposition of the organosilica phase. It is also possible that the transformation causes complete restructuring of the hybrid material. The formation of a mixed phase where the organosilica species is homogeneously distributed as depicted in (d) is possible. The formation of organosilica domains inside the silica domain, where pores are formed in both or only in the silica domain is shown in (e).

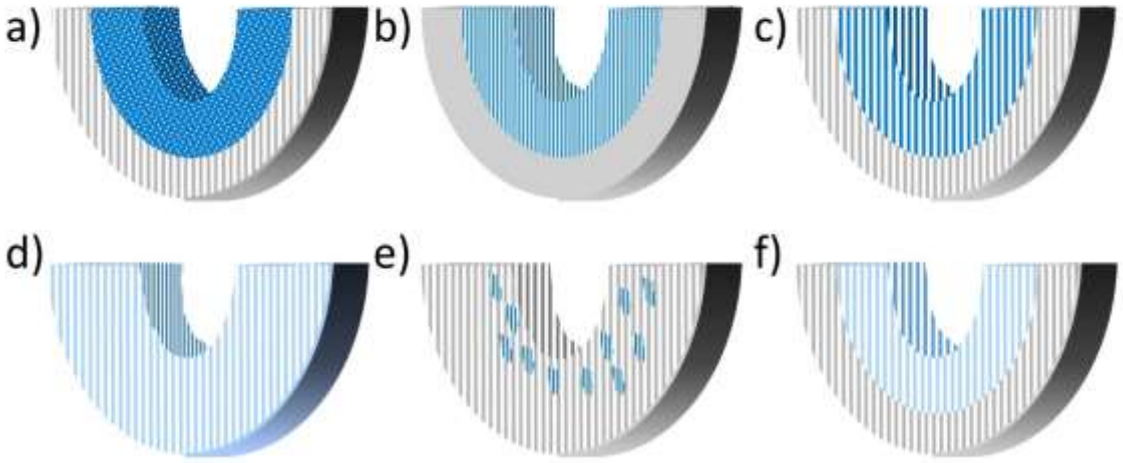

Figure 4-126: Overview of the different possible structures of the organosilica (blue)/silica (gray) hybrid materials, where pseudomorphic transformation causes micelle templating in one or both layers, (a)-(c), or mixed phases of organosilica/silica (light blue) can be formed as in (d) or (f). Also the formation of organosilica domains, surrounded by silica (d) is possible.

With the intention of determining the transformation degree of the CPG phase in the DVB organosilica/CPG hybrid material, it was calcined at 550 °C for five hours and the physisorption isotherms before and after calcination were compared. This approach was based on the assumption that the organosilica phase would become nonporous after calcination and that remaining porosity in the pseudomorphic transformed hybrid material could only correlate with the transformation of the CPG phase. Figure 4-127 shows the physisorption isotherms and the pore size distributions of 50BTEVB and 50BTEVB_6h_C_{16}TAOH before and after calcination. The *apparent* specific BET surface area of 50BTEVB changed significantly from 476 $m^2 \cdot g^{-1}$ to 250 $m^2 \cdot g^{-1}$, and mesopores below 4 nm disappear in the plot of the pore size distribution. For 50BTEVB_6h_C_{16}TAOH the *apparent* specific BET surface area changed less significant from 835 $m^2 \cdot g^{-1}$ to 799 $m^2 \cdot g^{-1}$ and the pore size shrank only slightly.

To verify the assumption that the organosilica phase would become nonporous after calcination, a sample of pure DVB-PMO was also calcined. The pore diameter distribution was distinctly affected by the treatment, but the specific BET surface area changed only from 769 $m^2 \cdot g^{-1}$ to 676 $m^2 \cdot g^{-1}$ (for isotherms see the Appendix Figure 9-37). Therefore, this method does not provide a very informative answer to the question, but it does show that the silica phase is definitively affected by the micelle templating since the change of the pore diameter distribution does not change significant in the calcined hybrid material.

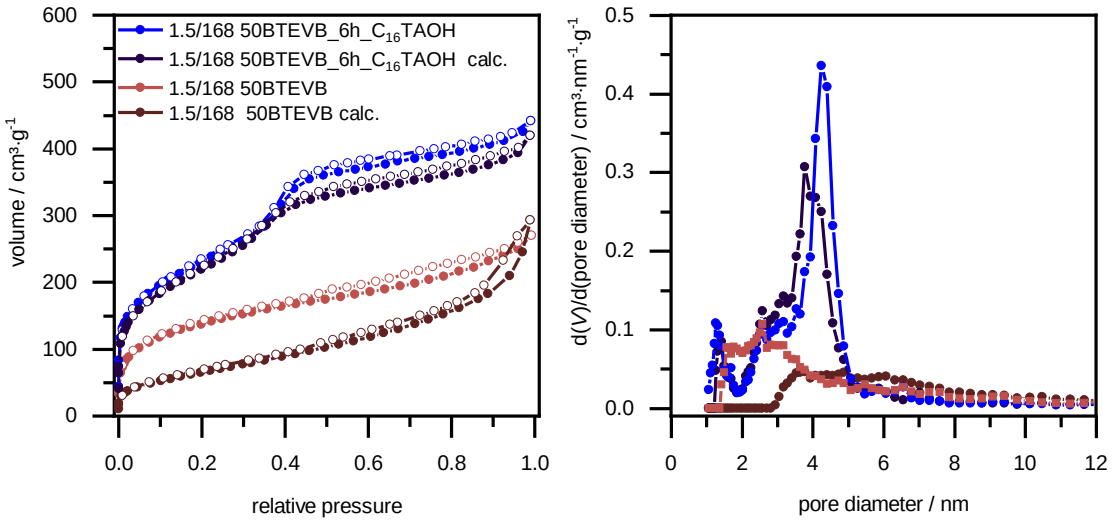

Figure 4-127: Physisorption isotherms (N_2, 77 K) of 50BTEVB from CPG batch III and 50BTEVB_6hC_{16}TAOH. Both samples were calcined, and the respective isotherms are plotted here. The pore diameter distribution is given on the right (calculated from the adsorption branch, NLDFT kernel for silica with cylindrical pores).

For further characterization of the materials, water vapor sorption measurements were carried out with 50BTEVB_24h_C_{10}TAB and 50BTEVB_4d_C_{16}TAOH. Two near-congruent cycles were measured, so that only the second cycles are shown (denoted as _C2) in Figure 4-128. From both materials type V isotherms are obtained. For comparison also the isotherms and pore diameter distributions from nitrogen and argon physisorption measurements are shown here again. 50BTEVB_24h_C_{10}TAB was characterized with argon physisorption due to the presence of small mesopores (2.9 nm) and micropores (0.6 nm). 50BTEVB_4d_C_{16}TAOH shows only mesopores of 4.2 nm in diameter. Next to the pore size, the specific BET surface area of 50BTEVB_4d_C_{16}TAOH is significantly higher (1007 $m^2 \cdot g^{-1}$) than the *apparent* specific BET surface area of 50BTEVB_24h_C_{10}TAB (668 $m^2 \cdot g^{-1}$ according to argon measurements). This causes significant differences in the water uptake capacity. The maximum water uptake is 34.6 $mmol \cdot g^{-1}$ for 50BTEVB_4d_C_{16}TAOH, but it is only 19.4 $mmol \cdot g^{-1}$ for 50BTEVB_24h_C_{10}TAB. It was assumed that the formation of two independent pore systems in a PMO and a pure silica phase would cause two separate condensation steps in the water vapor sorption. On the first sight, no two separate condensation steps are found, although this does not necessarily mean that the materials show homogeneous surface chemistry since diverse parameters influence the water uptake. The onset of capillary condensation of 0.52 for 50BTEVB_4dC_{16}TAOH and 0.30 for 50BTEVB_24h_C_{10}TAB differs significantly for both of the type V isotherms. The point of inflection for 50BTEVB_4dC_{16}TAOH is 0.61 and for 50BTEVB_24h_C_{10}TAB it is 0.41.

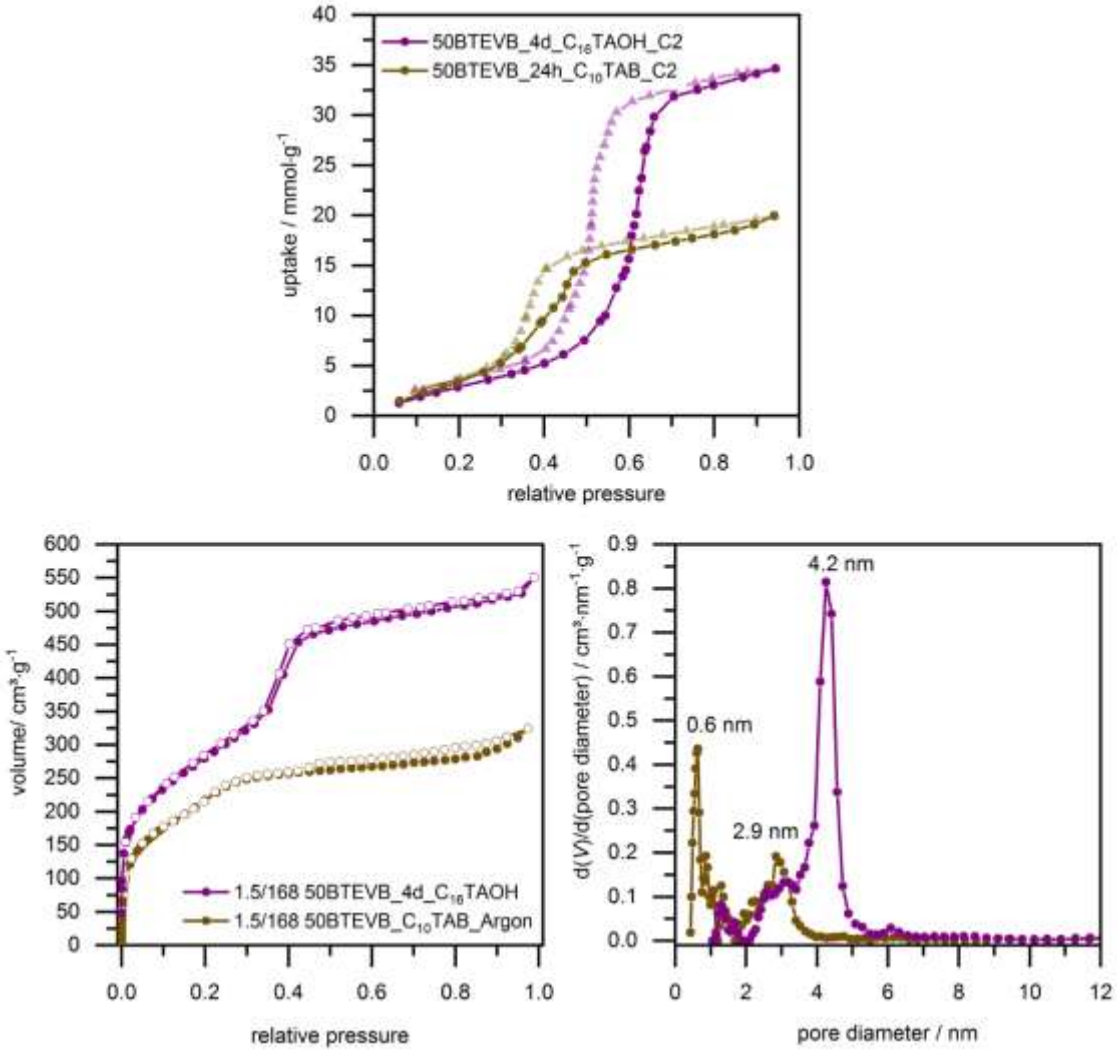

Figure 4-128: Upper part: water vapor sorption isotherms (H_2O, 298 K) of 50BTEVB_24h_C_{10}TAB and 50BTEVB_4d_C_{16}TAOH (second cycles). Lower part on the left: physisorption isotherms of 50BTEVB_24h_C_{10}TAB (Ar, 87 K) and 50BTEVB_4d_C_{16}TAOH (N_2, 77 K) and on the right: pore diameter distributions calculated from the adsorption branch, NLDFT kernel for silica or silica/zeolites with cylindrical pores.

As described in context of fluorine-containing PMOs (Section 4.1.2), the hydrophilicity indices of the materials could be estimated according to Thommes *et al*. by comparing the respectively filled pore volume with water and argon or nitrogen according to the Gurvich rule, or according to Fried *et al.* by comparing the monolayer capacity n_m from water to the maximal theoretical monolayer capacity, calculated from the argon or nitrogen physisorption measurement using the BET equation. All parameter calculated from the water vapor sorption measurements are given in Table 4-43. Since 50BTEVB_4d_C_{16}TAOH is only mesoporous, only nitrogen physisorption was measured.

Table 4-43: Summary of the onset, the point of inflection (p.o.i.) and hydrophilicity indices χ_{vol} and χ_{n_m} together with the parameters which are needed for the calculation, respectively.

sample	S_{BET} / $m^2 \cdot g^{-1}$	S_{BET} (H_2O)/ $m^2 \cdot g^{-1}$	χ_{n_m}	$V_{(N_2, Ar)}$ / $cm^3 \cdot g^{-1}$		$V_{(H_2O)}$/ $cm^3 \cdot g^{-1}$	$\chi_{vol.}$	*onset*	*p.o.i*
50BTEVB _4d_C_{16}TAOH	1007 (N_2)	246	0.22	p/p_0 = 0.95 p/p_0 = 0.80	0.81 0.79	0.62	0.74 0.78	0.52	0.61
50BTEVB _24h_C_{10}TAB	668 (Ar)	445	0.37	p/p_0 = 0.8	0.35	0.32	0.91	0.30	0.41

The pore volume of 50BTEVB_24h_C_{10}TAB was determined at a relative pressure of 0.80 because at higher relative pressure filling of interparticle voids occurs in the argon physisorption. For better comparison the respective pore volume from 50BTEVB_4d_C_{16}TAOH was also determined at a relative pressure of 0.80 in addition to the value at a relative pressure of 0.95. The obtained pore volume from these two relative pressure points is similar so that this does not change significantly the hydrophilicity index $\chi_{vol.}$. The pore volume filled from 50BTEVB_24h_C_{10}TAB is only half of the pore volume from 50BTEVB_4d_C_{16}TAOH but the hydrophilicity index χ_{vol} is significantly higher. For the determination of the hydrophilicity index χ_{n_m} the specific BET surface area was determined. It is worth mention, that the specific BET surface area determined with water is significantly higher for 50BTEVB_24h_C_{10}TAB than for 50BTEVB_4d_C_{16}TAOH, although it was the other way around with argon and nitrogen measurements before. Therewith the hydrophilicity index χ_{n_m} is also higher for 50BTEVB_24h_C_{10}TAB in this case. Hence, the two hydrophilicity indices show the same trend. The compared samples show very different pore system and the presence of micropores in 50BTEVB_24h_C_{10}TAB is expected to have particular impact on the water vapor sorption measurement. From these results it is hard to say which parameter has the main impact on the results or to extract information on the surface chemistry or the structure of the micelle templated materials. However, the results forms a basis for follow-on works in which the hydrophilicity of the materials could be investigated in direct comparison to pure organosilica and pure CPG with the same pore diameter. Therewith, an insight on the surface chemistry could be obtained.

Further information about structure and phase segregation can be obtained from 2D HETCOR-NMR spectroscopy. HETCOR-NMR spectroscopy can detect correlation nuclear spin pairs which reside in close proximity in space, thus providing information about the molecular packing structure and geometrical arrangements as well as chemical structure.

First, it was intended to use this method to determine whether the initial two phases of silica and organosilica species remained after the transformation. Therefore, it was investigated

whether the two species are in contact or not by comparing the 2D ^{29}Si {^{1}H}-FSLG HETCOR MAS NMR spectra of 50BTEVB and 50BTEVB_6h_C_{16}TAOH. Figure 4-129 shows the 2D ^{29}Si {^{1}H}-FSLG HETCOR MAS NMR spectrum of 50BTEVB. Correlation between the T^2 and T^3 silica species and divinylbenzene bridging group are observed at ^{29}Si chemical shifts of -68 ppm and -77 ppm and at ^{1}H chemical shifts of 6 ppm and 7 ppm, indicated in red and orange lines in the figure, respectively. The chemical shift of the protons of the vinyl group in the ^{1}H-NMR spectrum of the BTEVB in $CDCl_3$ is $\delta(^{1}H)$ = 6.18 ppm and 7.19 ppm, the chemical shift of the aromatic protons is 7.45 ppm. Thus, it is hard to distinguish between the aromatic protons and the second proton of the vinyl group at this point. The signal at 1.8 ppm in ^{1}H-NMR dimension which shows correlation with T^2 silica can be assigned to isolated silanol groups. In contrast, very low correlation occurs between the Q silica species and the protons of the organic bridge. Hence, the Q silica species and the organosilica molecules are not mixed, but it indicates that small amounts of the two species are in contact with each other, probably at the phase boundary, which is in accordance with the expectations for two independent layers.

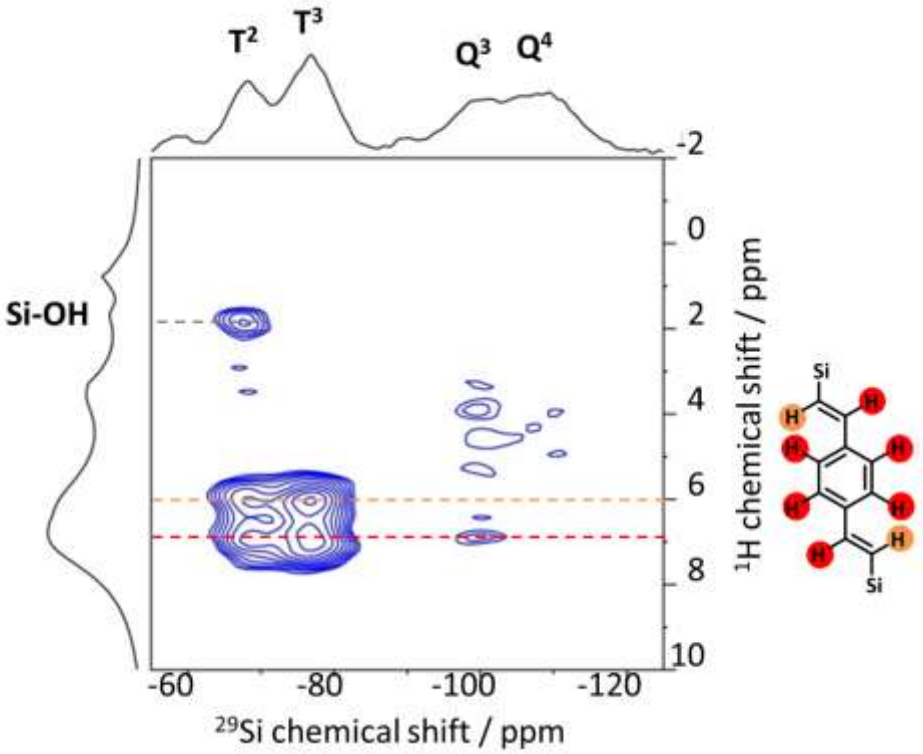

Figure 4-129: ^{29}Si{^{1}H}-FSLG HETCOR MAS NMR of 50BTEVB. The assignment of the proton signals to the organic precursor is visualized with a color code. Correlation between the T^2 and the silanol groups is indicated in gray.

The ^{29}Si{^{1}H}-FSLG HETCOR MAS NMR of the transformed sample 50BTEVB_6h_C_{16}TAOH is shown in Figure 4-130.

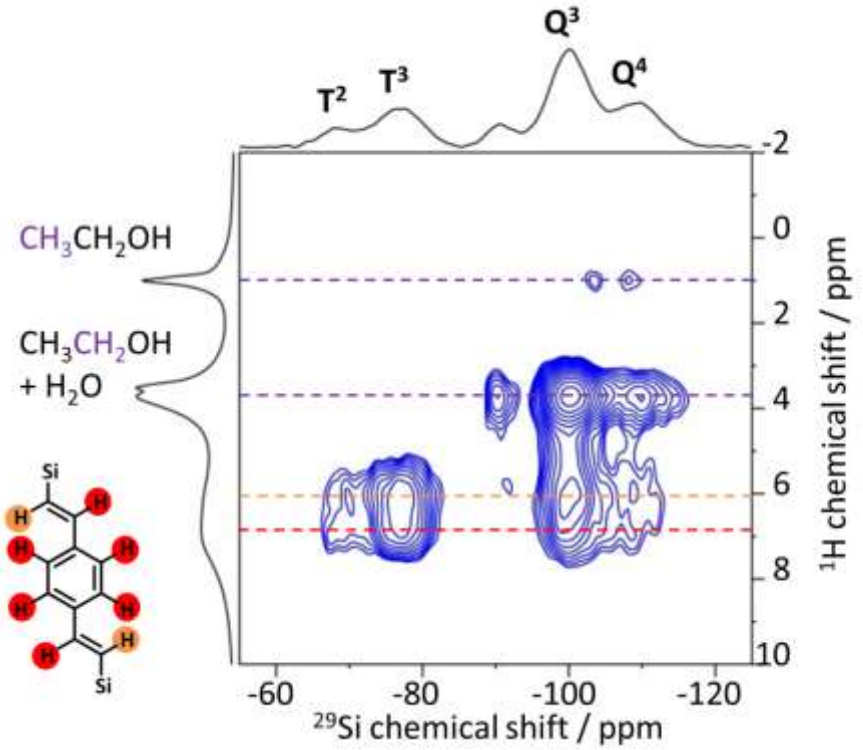

Figure 4-130: $^{29}Si\{^{1}H\}$-HETCOR MAS NMR of 50BTEVB_6h_C_{16}TAOH after extraction of the surfactant. The assignment of the proton signals to the organic precursor is visualized with a color code. Correlation between the Q species and ethanol or water are indicated in purple.

Correlation of T^3 and T^2 with the organic bridge occurs here as well. Interestingly, correlation between Q^3 and Q^4 silica species, (^{29}Si at -110 ppm and -100 ppm) and the vinyl protons (^{1}H at 6 ppm) is additionally observed, suggesting that the organic bridge is now closer to the pure silica species than it was before the transformation. This indicates that the material does not form two separate layers, but these two species are more mixed. Dominant correlation signal of the first vinyl proton with the T species is consistent with the mixed phase structure where Si atoms of Q species reside further apart from bridging group through Si(Q)–O–Si(T)–CH=CH–C_6H_4 bonds than T species. Additional cross peaks at 3.8 ppm and 0.9 ppm are caused by correlation of the Q silica species with ethanol and water as indicated in the above figure.

In order to find out whether micelle-templating occurs in the organosilica phase, in the silica phase or in both, 2D $^{29}Si\{^{1}H\}$-FSLG HETCOR MAS NMR of 50BTEVB_6h_C_{16}TAOH was also measured before the extraction of the surfactant. The spectrum is shown in Figure 4-131. ^{1}H NMR of C_{16}TAB in $CDCl_3$ is given in Figure 9-38 in the Appendix.

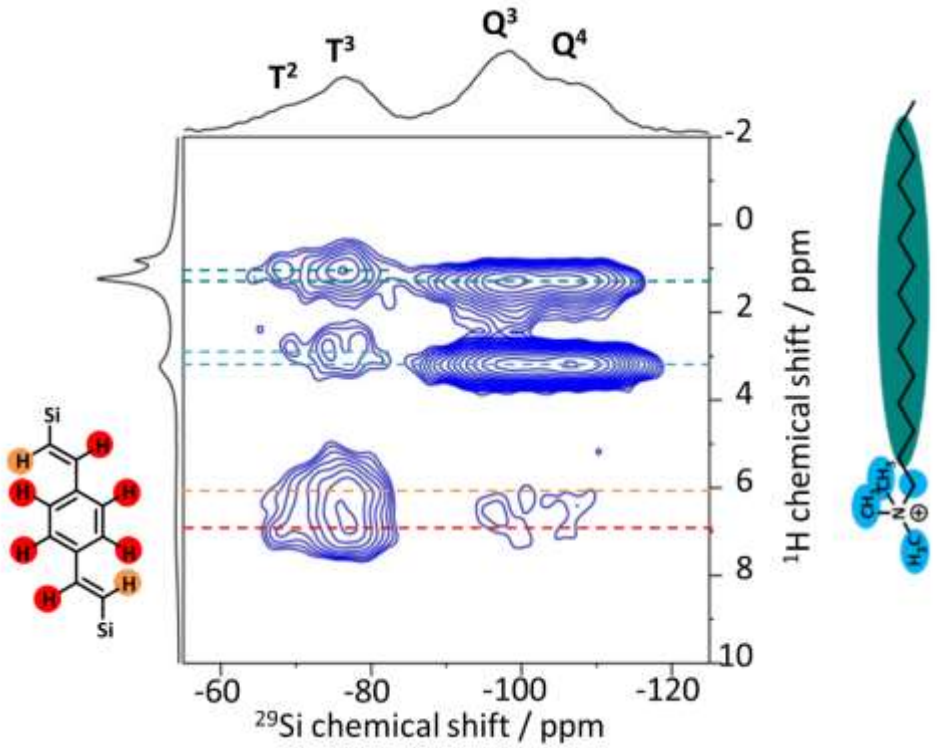

Figure 4-131: $^{29}Si\{^{1}H\}$-FSLG HETCOR MAS NMR of 50BTEVB_6h_C_{16}TAOH before extraction of the surfactant. The assignment of the proton signals to the organic precursor and the surfactant are visualized with a color code.

The color code denotes the assignment of the different signals to the surfactant and the organic bridging unit. The correlation between the different protons of the surfactant and the Q^4 and Q^3 species is very strong, indicating that the surfactants are in close contact with Q groups. In particular, stronger correlation of methyl groups than $(CH_2)_n$ suggests that the surfactant head groups are directly interacting with Q species, following the micelle structure. By contrast, correlation signals between the surfactant and T groups, mainly T^3, are weaker and appear at slightly different chemical shift position from those of the correlation with Q species, indicating that the surfactants nearby T groups exhibit relatively weak dipole-dipole couplings and are in different local environments. These correlation peaks with T^3 species cannot be attributed to Si–OH, Si–OCH_2CH_3 and residual water, since silanol and water exhibit correlation mainly with T^2 and T^1 species. This was seen in Figure 4-129 in context of the sample 50BTEVB before transformation. In addition to the correlation between T^n species and divinyl-bridging group, a correlation signal between Q species and divinyl-bridging group is seen at -98 ppm for ^{29}Si and 6.5 ppm for ^{1}H, which agree well with the results after surfactant extraction as shown in Figure 4-130. The intensity of the signal is significantly lower, since the correlation between the protons of the surfactant and the Q^3 and Q^4 is of very high intensity. The dominance of the correlation signal for Q^3 species than that of Q^4 group suggests that the formation of Q-T bonds occurs predominantly at the surface of the CPG pores, since Q^4 signals occur predominantly in the inner part, whereas the ratio of Q^3 is higher at the outer surface due to contact with e.g. humidity.

$^{13}C\{^{1}H\}$-FSLG-HETCOR MAS NMR of 50BTEVB_6hC_{16}TAOH before extraction is shown in Figure 4-132. Cross peaks of the aromatic carbon species with protons of the surfactant prove the correlation between the organosilica species and the surfactant. Hence, the organosilica phase undergoes micelle-templating during the pseudomorphic transformation process.

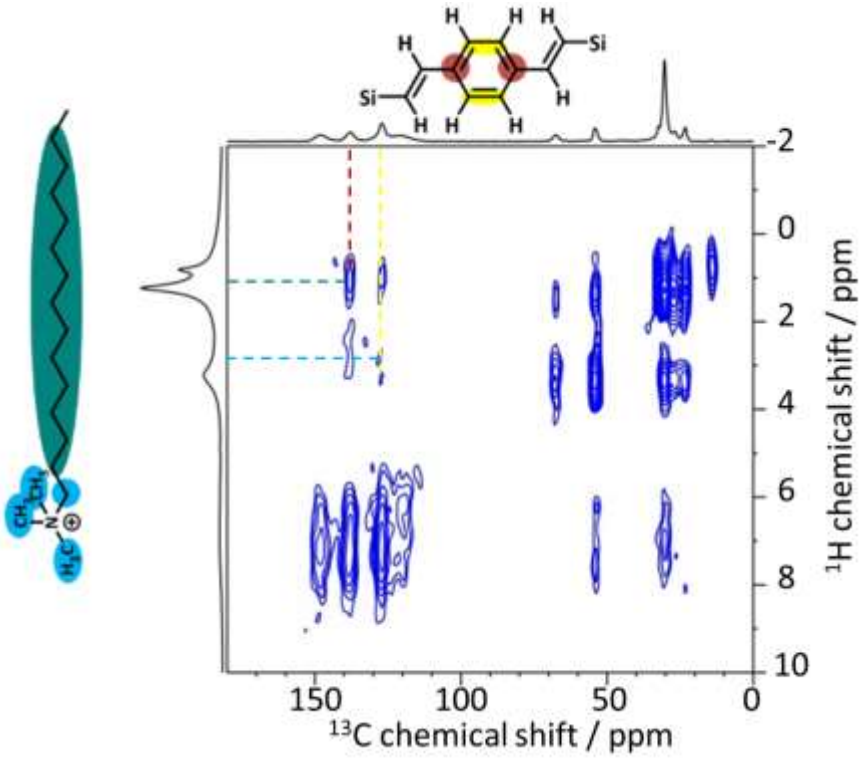

Figure 4-132: $^{13}C\{^{1}H\}$-FSLG HETCOR MAS NMR of 50BTEVB_6h_C_{16}TAOH before extraction of the surfactant. The assignment of the carbon signals of the organic bridge that correlates with protons of the surfactant, are visualized with a color code.

Since T and Q species are mixed after pseudomorphic transformation, and both species (organosilica and silica) undergo micelle templating, the above results from 2D-FSLG-HETCOR NMR narrow the possible structures of the organosilica/silica hybrid materials to two options of mixed phase models, which are repeatedly shown in Figure 4-133.

Figure 4-133: Two different structures of the organosilica (blue)/silica (gray) hybrid materials are in accordance with the results from different characterization methods. It is either one pore system of mixed organosilica/silica species or it consists of two phase, a mixed phase (light blue) and a pure silica phase.

In the model on the right, one pore system composed of mixed T and Q species via formation of Si(Q)–O–Si(T) bonds is present. In the model on the left, two phases are present which causes two types of pore structures, one consisting of mixed T/Q species and the other with Q only

species, are expected. The previously discussed results from TG analysis and quantitative ^{29}Si solid state NMR showed, that cleavage of Si-C bond is likely. Hence, the possibility of silica species inside the originally organosilica layer, and homogeneous distribution of T and Q species, as on the left, cannot be ruled out. However, it is hard to distinguish between these two models. Further it is possible that the two layer system of mixed phase is an intermediate that changes to a single mixed-phase with increasing transformation degree.

In summary, the pseudomorphic transformation of organosilica/silica hybrid materials in C_{16}TAOH solution was successful. As for pure CPG, swelling of the pore walls occurs during the transformation process, but in general the morphology of the CPG could be preserved. Mesopores of 4.2 nm are formed due to micelle templating. Unfortunately, the initial two layers of organosilica in the pores of CPG were not sustainable. Mesoporous structures composed of random mixture of T and Q species via formation of Si(Q)–O–Si(T) bonds are formed. One possible cause for this is that the organosilica species decomposes under the harsh conditions of the pseudomorphic transformation and the extraction of the surfactant under reflux.

4.4 CPG membranes

4.4.1 Pseudomorphic transformation of CPG membranes

Next to CPG granules and spherical beads, CPG membranes were provided by the research group of Professor Enke in Leipzig. . The general synthesis path for these membranes is shown in the literature.[239] As starting material for pseudomorphic transformation CPG membranes of 2.5 x 2.5 cm were used. The membrane thickness is 0.5 mm, and it shows a macropore volume of 0.16 $cm \cdot g^{-1}$ and macropores of 99 nm, the MIP measurement and the respective pore diameter distribution is shown in Figure 4-136, compared to the previously mentioned CPG granules and beads, the pore volume is comparably low. Figure 4-135 shows SEM images of 50000x and 30000x magnification.

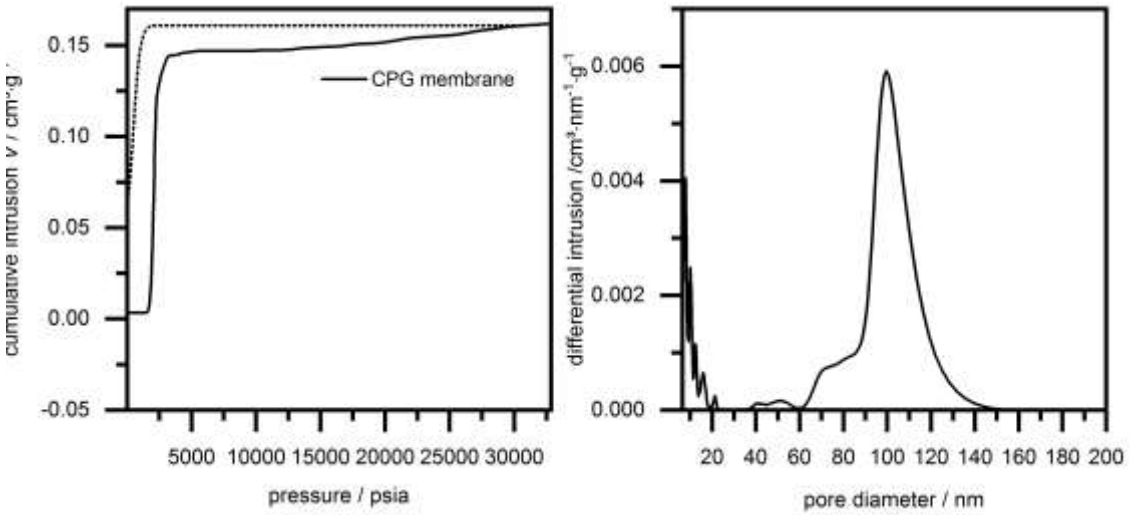

Figure 4-134: Mercury intrusion curve (left) and pore diameter distribution of the initial CPG membrane.

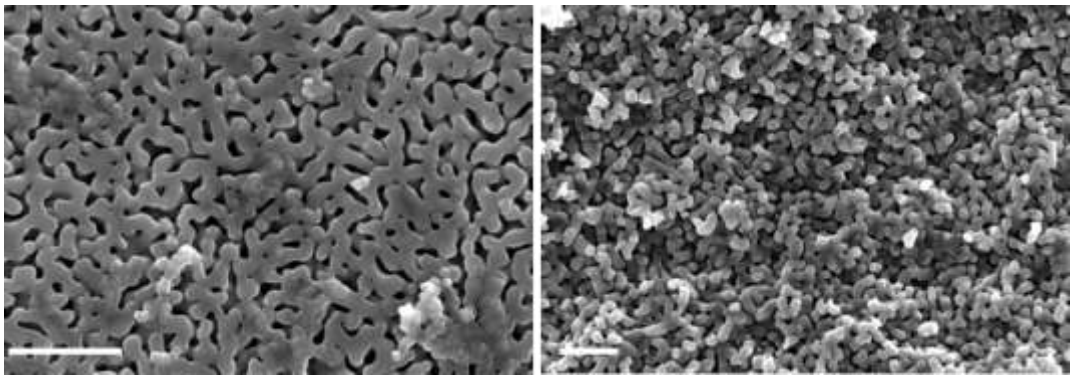

Figure 4-135: SEM images of the CPG membrane with 99 nm pore size and of 0.16 $cm \cdot g^{-1}$ pore volume with 50000x (left) and 30000x (right) magnification. Scale bar of 1.0 µm in both images.

The membranes were transformed in C_{16}TAOH solution at 100 °C, as for the previously mentioned CPG. In the first series the transformation time was varied between six hours, 24 hours and four days with a constant C_{16}TAOH solution volume of 4 mL per 100 mg CPG. Figure

4-136 shows SEM images of the pore system. After six hours of transformation the initial pore system is still identifiable to some extent, but after 24 hours and 4 days the whole pore system seems to be overgrown by the swollen pore walls. This might be due to the low initial pore volume.

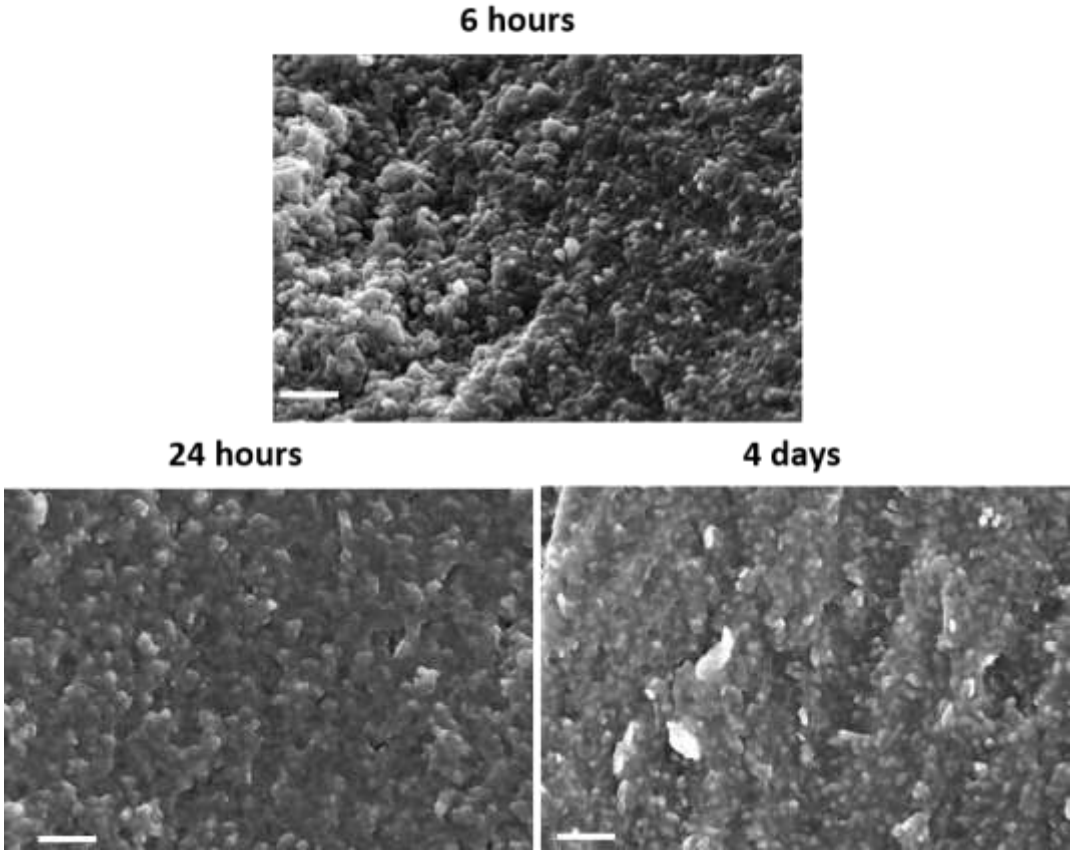

Figure 4-136: SEM images of the CPG membrane after transformation with 100 vol% C_{16}TAOH for six hours, 24 hours and four days at 100 °C. Scale bars of 1.0 µm.

the In the second series the volume was decreased to 2 mL per 100 mg (denoted as 50 % vol. below) and the transformation time was varied between 24 hours and four days. The respective SEM images are given in Figure 4-137. Also in these samples the initial pore system is barely recognizable due to the pore wall swelling during the transformation.

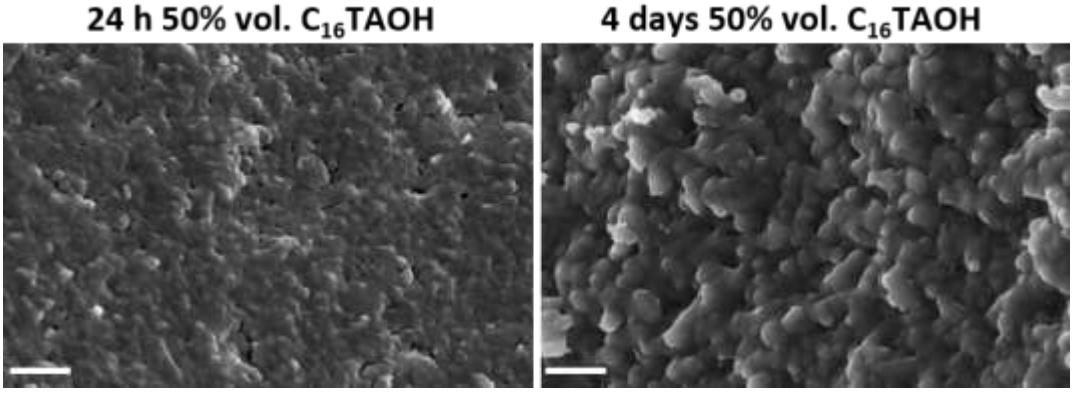

Figure 4-137: SEM images of the CPG membrane after transformation with 50 vol% C_{16}TAOH for 24 hours and four days at 100 °C. Scale bars of 1.0 µm.

Since the macropore volume decreases with the transformation, the samples were not accessible for MIP measurements due to the low initial macropore volume. Figure 4-138 shows the physisorption isotherms and pore diameter distribution of all transformed membranes together.[4]

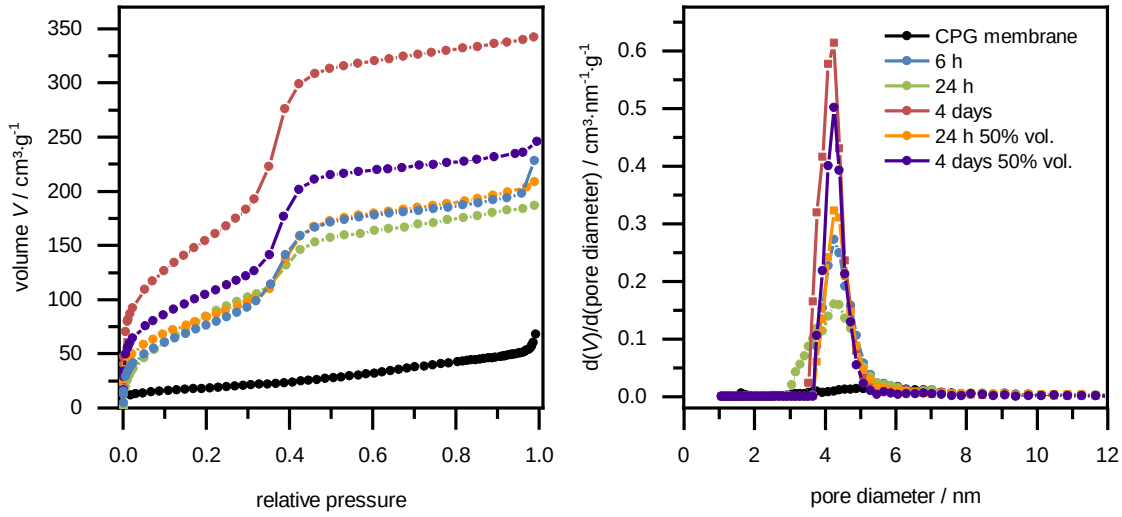

Figure 4-138: Physisorption isotherm (N_2, 77 K) of CPG membranes after pseudomorph transformation under variation of the time with 100 % or 50 % volume of C_{16}TAOH solution. The respective pore diameter distributions (calculated from the adsorption branch, using NLDFT kernel for silica with cylindrical pores) are shown on the right.

Table 4-44 summarizes the textural data of the samples. The specific BET surface areas of the sample that was transformed for six hours is close to the value of the sample that was transformed for 24 hours with halved C_{16}TAOH volume around 310 $m^2 \cdot g^{-1}$. A similar trend is given for the material that was transformed for 24 hours with a higher solution volume (349 $m^2 \cdot g^{-1}$) and four days with a halved volume (387 $m^2 \cdot g^{-1}$). The pore volume for pores smaller 20 nm (determined using the NLDFT kernel for silica with cylindrical pores) does not change that much in these four samples between 0.220.34 $cm^3 \cdot g^{-1}$. After four days with the higher C_{16}TAOH solution volume, full transformation was expected which would be accompanied by a specific BET surface area of around 800–1000 $m^2 \cdot g^{-1}$ as in common MCM-41 materials. However, the specific BET surface area was significantly lower at 589 $m^2 \cdot g^{-1}$, the pore volume of mesopores smaller 20 nm, is increased to 0.50 $cm^3 \cdot g^{-1}$, whereas it was about 1.0 $cm^3 \cdot g^{-1}$ in the pseudomorphically transformed CPG granules. This might be caused by the low pore volume of the starting material that does not allow swelling of the material and thus limits the transformation process. However, the relative transformation degree was calculated for the membranes based on this value, although no full transformation is assumed.

[4] For the determination of the pore diameter distribution for the sample which was transformed for six hours, only the measurement points in the relative pressure range up to 0.9 were considered as the abrupt volume uptake in the last measurement points significantly distort the DFT data fit. This was discussed in detail in section 4.2, Figure 4-42.

Table 4-44: Summary of the specific BET surface areas, pore volume and pore diameter (both calculated from the adsorption branch using NLDFT kernel for silica with cylindrical pores) of CPG membranes transformation for different times and solution volume

sample	S_{BET} / $m^2 \cdot g^{-1}$	$d_{N_2, NLDFT}$ / nm	$V_{<20\ nm, NLDFT}$ / $cm^3 \cdot g^{-1}$	transformation degree
CPG membrane 0.17$cm^3 \cdot g^{-1}$ 99 nm	60	-	0.07	-
6 hours, 100 % vol.	307	4.4	0.22	0.51
24 hours, 100 % vol.	349	4.4	0.27	0.58
4 days, 100 % vol.	589	4.2	0.50	1.0
24 hours, 50 % vol.	310	4.3	0.29	0.52
4 days, 50 % vol.	387	4.3	0.34	0.65

XRD patterns of the samples (Figure 4-139) show increasing intensity over time of one reflection at 2θ = 2.2° (*d*-spacing = 40.2 Å). After four days' treatment further distinctive reflections at 2θ = 3.8° and 4.4° (*d*-spacing = 23.0 Å, 20.1 Å) can be assigned to the hk0 reflections (110) and (200) which proves the formation of a 2D hexagonal pore network.

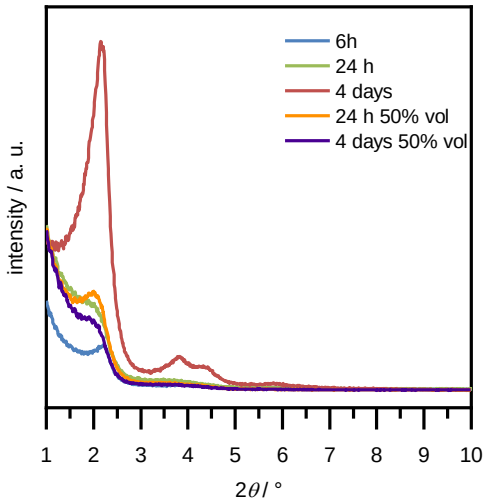

Figure 4-139: P-XRD pattern of the CPG membranes after pseudomorphic transformation for different times and with reduced C_{16}TAOH solution volume.

After 96 hours of transformation, the morphology of the membrane was conserved as the photographs in Figure 4-140 prove, although it became more fragile and semi-translucent in some places. After calcination, a slight curvature of the membrane was observed.

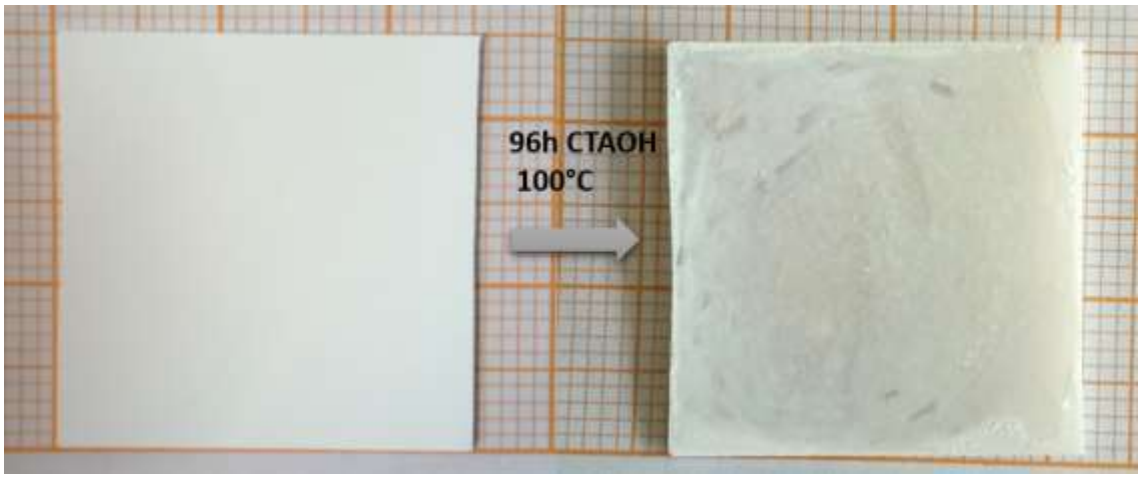

Figure 4-140: Photographs of CPG membranes before (left) and after (right) pseudomorphic transformation for 4 days in C_{16}TAOH solution. Slight damages and semi-translucence can be observed after the transformation.

4.4.2 Impregnation of CPG membranes

The CPG membranes were also impregnated with an organosilica precursor. Here, no reduced pressure was applied, but the membranes were impregnated with a solution via capillary forces. The setup of the impregnation can be seen in Figure 8-1 in the Experimental Section. For impregnation the pure BTEVB precursor as well as toluene-based solutions with 25 wt% or 50 wt% of this precursor were used. Analogous to the samples in 4.3.2, the samples are named 25BTEVB, 50BTEVB and 100BTEVB, respectively. Similarly to the samples in this section, multiple impregnations were also investigated here. The membrane was impregnated three times with a toluene-based solution with 10 wt% BTEVB, called as 3x10BTEVB.

After the impregnation condensation was initiated in a separate step similar to the synthesis protocol for the CPG granules and beads. In the case of the membranes, alkaline conditions with a mixture of ethanol and sodium hydroxide solution were found to be unsuitable for the condensation, since an opaque condensation product was visible in the excess solution and on the surface of the membrane due to leaching of the precursor from the membranes. This might be caused by the higher outer volume of the membranes compared to the micrometer-sized granules and beads. In contrast to the previously mentioned CPG, condensation inside the membranes was initiated by drying at room temperature and incubation in a bath of hydrochloric acid solution (1 mol·L^{-1}). SEM images of the impregnated samples after condensation are shown in Figure 4-141.

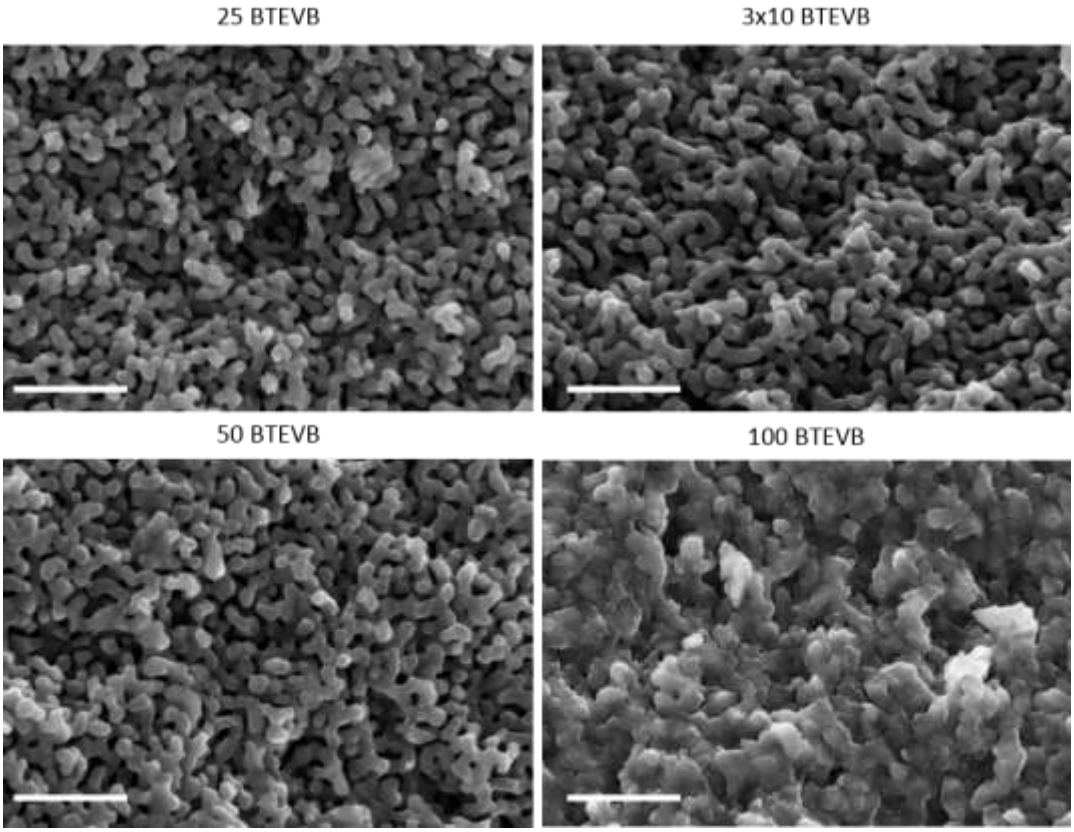

Figure 4-141: SEM images of the CPG membranes after impregnation with toluene-based solutions that contain the labeled ratio of the organosilica precursor BTEVB, and condensation. 50000x magnification, scale bar of 1 µm.

Thickening of the pore wall is observed with increasing organosilica content in the impregnation solution. However, while the initial macropore system is still intact in the sample 50BTEVB, it is unrecognizable in 100 BTEVB.

The temperature-dependent mass loss during thermogravimetric (TG) analysis is shown in Figure 4-142. It was taken as an indicator for the organosilica content in the hybrid material membranes.

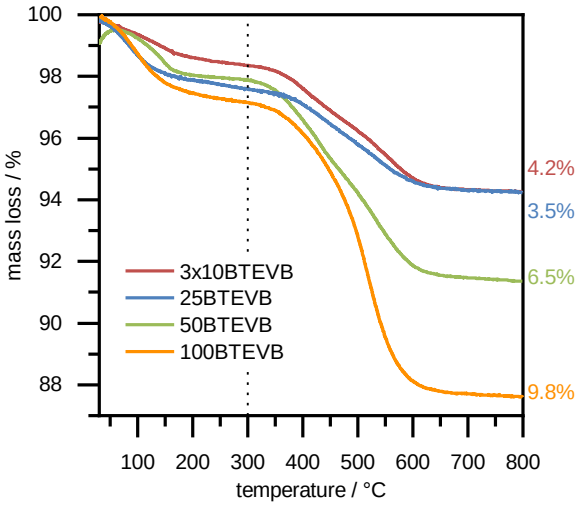

Figure 4-142: TG analysis in Ar/O_2 80/20 of CPG membranes after impregnation with different volumes of BTEVB, mass losses in the temperature range 300–800 °C.

Just as in the previously discussed samples, only mass loss between 300–800 °C, where the organic bridge of the precursor decomposes, was taken into account here. The values of the mass loss are corrected, since the mass loss due to surface-adsorbed water, in the temperature range 25–150 °C differ. As expected from the previous results of impregnated CPGs, the mass loss increases with the increasing amount of organosilica.

After impregnation with 100BTEVB, a mass loss of 9.8 % was recorded in the defined temperature range. For 50BTEVB the mass loss was 6.5 %, and for 25BTEVB it was 3.5 %. The mass loss in TG analysis from 3x10BTEVB is only slightly increased to 4.2 %. Inferring from this, the repetitive impregnation does not improve the organosilica uptake in the CPG membranes, which is in accordance with the results from the multiple impregnation of CPG beads in section 4.3.2.

The amount of precursor per gram CPG membrane (chemical composition of 100 % SiO_2 is assumed in a first approximation) can be calculated from the TG analysis data. This is summarized in Table 4-45. As previously mentioned, the macropore system cannot be characterized by MIP due to the low macropore volume so that determination of the residual macropore volume after impregnation is not possible. As the density of the precursor is not known and as it can further be assumed that the density of the condensed organosilica species is higher than the density of the precursor, no calculation of the theoretical maximum filling of the macropore volume is possible. Hence, evaluation of the impregnation process is difficult.

Table 4-45: TG mass loss in the temperature range 300–800 °C of CPG membranes that were impregnated with BTEVB and the calculated mass ratio of BTEVB and molar ratio BTEVB/CPG

Sample	TG mass loss	mass BTEVB	mol. percentage BTEVB/CPG
100% BTEVB	9.8 %	19 %	5.1 %
50% BTEVB	6.5 %	13 %	3.4 %
25% BTEVB	3.5 %	7 %	1.7 %
3 x 10% BTEVB	4.2 %	8 %	2.1 %

Pseudomorphic transformation of impregnated CPG

Two different hybrid materials of CPG membranes impregnated with organosilica in the macropore system were treated with C_{16}TAOH solution for pseudomorphic transformation. The sample 3x10BTEVB was treated with C_{16}TAOH for four days. Photographs in Figure 4-143 show the preservation of the morphology in this case. For the characterization, the membranes of 25 x 25 mm had to be broken into pieces. Even where the surface of the membranes was slightly damaged after the transformation, the membranes were still sturdy.

Figure 4-143: Photographs of the CPG membrane impregnated with 3x10BTEVB and the respective sample after pseudomorphic transformation in C_{16}TAOH for four days. The background is plotting paper with 2 x 2 mm squares.

In the second case, the membrane that was impregnated with pure BTEVB was treated for only 24 hours, as there is less space for swelling available in the pore system and only partial transformation is expected. Photographs that prove the conservation of the morphology of this sample can be seen in Figure 4-144. In this case, the samples are slightly yellow, which might be due to marginal impurities in the precursor.

Figure 4-144: Photos of the CPG membrane impregnated with 100 % BTEVB and the respective sample after pseudomorphic transformation in C_{16}TAOH for 24 hours The background is plotting paper with 10x10 mm bold squares.

Since the low macropore volume does not allow characterization with MIP, swelling of the pore walls cannot be investigated. The SEM images are given in Figure 4-145 and Figure 4-146. Due to sputtering with carbon, this method cannot be used for the estimation of pore wall thickness. As previously discussed, the pore system of 100 BTEVB was not recognized and this did not

change during the pseudomorphic transformation. Also, for 3x10BTEVB the differences are barely distinguishable in the SEM images.

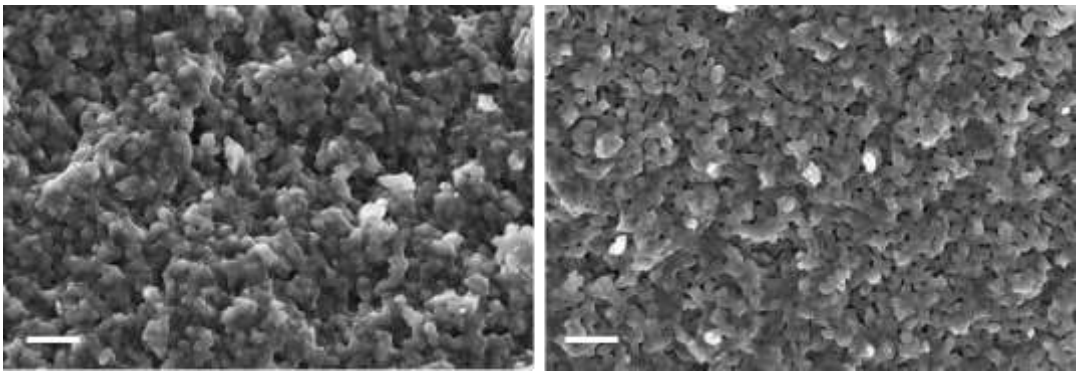

Figure 4-145: SEM images (30000x margination) of the CPG membrane impregnated with 100 % BTEVB (left) and after 24 hours of C_{16}TAOH treatment for pseudomorphic transformation (right).

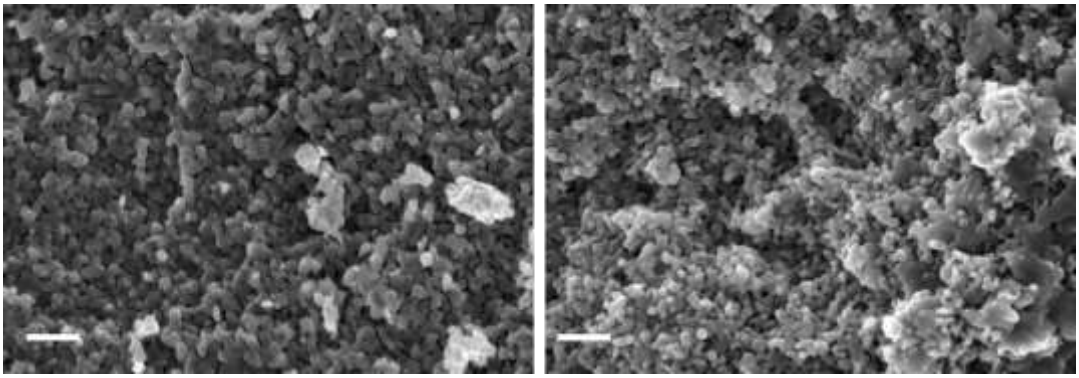

Figure 4-146: SEM images (30000x margination) of the CPG membrane 3x10BTEVB (left) and after 24 hours of C_{16}TAOH treatment for pseudomorphic transformation (right).

Successful transformation can be investigated by physisorption that proves the presence of a mesopore system. The physisorption isotherms of both samples that are discussed here are given in Figure 4-147 next to the respective pore diameter distributions. It is obvious that the pseudomorphic transformation of the sample 100 BTEVB was not successful. The specific BET surface area even decreased marginally from 99 $m^2 \cdot g^{-1}$ to 80 $m^2 \cdot g^{-1}$ after pseudomorphic transformation. As the material is completely dense after impregnation, it is not responsive to pseudomorphic transformation. According to the proposed mechanism which is explained in the Introduction, interparticle space that allows the incorporation of micelles of the surfactant is needed for a pseudomorphic transformation. On the contrary, the specific surface area of the sample 3x10BTEVB increases to 470 $m^2 \cdot g^{-1}$ by treatment with C_{16}TAOH solution for four days. The mesopores generated have a diameter of 4.3 nm.

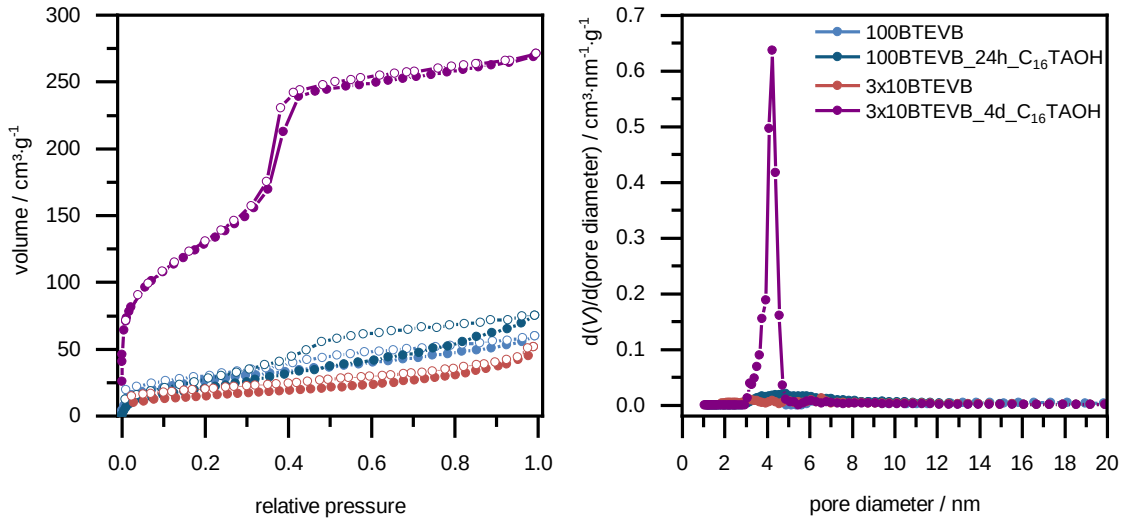

Figure 4-147: Physisorption isotherm (N_2, 77 K) of CPG membranes after impregnation and pseudomorphic transformation with C_{16}TAOH for 24 hours. On the right are the pore diameter distributions (calculated from the adsorption branch using NLDFT kernel for silica with cylindrical pores).

The P-XRD pattern of the sample in Figure 4-148 shows one reflection at $2\theta = 2.2°$ (d-spacing = 40.2 Å) as it has already been shown for pseudomorphically transformed samples.

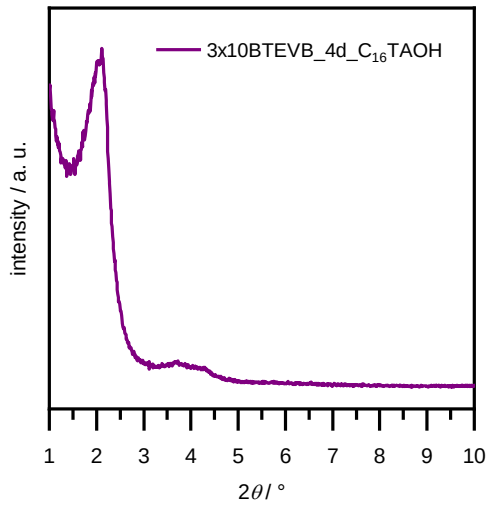

Figure 4-148: XRD patterns after pseudomorphic transformation of the CPG membrane 3x10BTEVB.

It should be discussed, whether leaching of the organosilica phase occurs during the successful pseudomorphic transformation in the sample 3x10BTEVB. The plots of TG-MS in Figure 4-149 show mass loss data and selected ion currents plotted against the temperature of the sample before and after the transformation process. The selection of the ion currents has been described before ($m/z = 18$, (H_2O); $m/z = 44$ (CO_2); $m/z = 58$ (C_3H_8N)). Table 4-46 gives an overview on the mass loss at different temperature intervals. The samples differ as was previously observed for other CPG samples which were impregnated. In the temperature range up to 120 °C mostly surface adsorbed water is released and the value doubles after hydrothermal treatment as was observed in previous examples. Between 120–300 °C, the mass is reduced by

nearly the same percentage of 0.8 % (0.9 %). However, in the temperature interval between 300–800 °C, the impregnated sample (3x10BTEVB) loses 4.2 %, whereas the hydrothermally treated sample (3x10 % BTEVB 4 days C_{16}TAOH) loses 6.6 % (values are respectively corrected). This difference is most likely due to residues of the surfactant in the sample after the hydrothermal templating process. Hence, also in this case, either the surfactant is partially entrapped in the pseudomorphically transformed matrix and is released together with the organosilica at higher temperatures or parts of the silica phase was dissolved and did not re-precipitate during the transformation process which causes higher amount of organosilica after all.

Table 4-46: Mass loss from TG analysis (Ar/O_2 80/20) of the impregnated CPG membrane (3x10BTEVB) and the respective pseudomorphic transformed sample (3x10BTEVB_4d_C_{16}TAOH). Entries marked with an asterisk (*) denote corrected values.

Temperature interval	3x10BTEVB	3x10BTEVB_4d_C_{16}TAOH
25–120 °C	0.8 %	1.9 %
120–300 °C	0.8 %	0.9 %
300–800 °C	4.2 % *	6.4 % *
25–800 °C	5.7 %	9.2 %

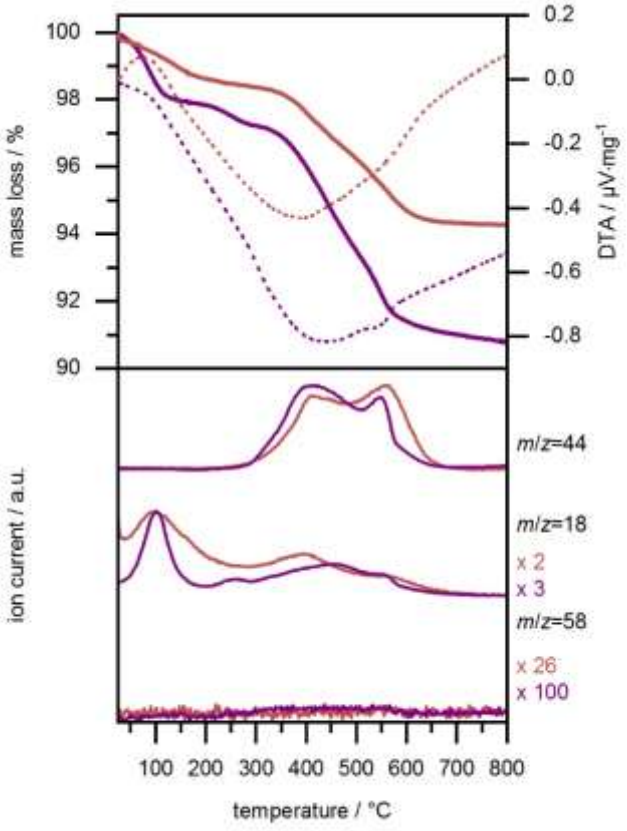

Figure 4-149: TG/MS analysis in Ar/O_2 80/20 of 3x10BTEVB (red) and 3x10BTEVB_4d_C_{16}TAOH (purple) from CPG membranes. Selected ion currents are shown in the lower plot.

Further characterization of the CPG membranes, e.g. by solid state NMR spectroscopy is not possible under retention of the morphology since grinding would be necessary due to the geometrical requirements of the sample holder. Further investigations on the pseudomorphic transformation of organosilica/silica hybrid materials were carried out with CPG granules in section 4.3.4.

In summary, the impregnation of CPG membranes with BTEVB was successful and the organosilica species could be condensed inside the macropore system. Further, a second mesopore system was generated by pseudomorphic transformation in an impregnated membrane with enough remaining macropore volume. In contrast, it could be shown that pseudomorphic transformation is not possible in a completely non-porous material.

4.5 Alginate hydrogel as form-giving matrix for nanoporous organo(silica) beads

The third part of this work is the synthesis of spherical mesoporous silica and organosilica particles in the micrometer scale which are not dusty and therefore of interest for industrial applications or as adsorbents, e.g. in breathing masks.

Spherical millimeter-sized beads were formed by dropping an alginate solution into a Ca^{2+}-containing solution. This concept was explained in the Introduction 1.6. During this process, silica was incorporated into the alginate matrix and should form an independent and stable network so that the alginate can be removed afterwards. The concept of pseudomorphic transformation was chosen to postsynthetically generate an additional mesoporous structure in the silica beads. Furthermore, this approach should also be applicable for the formation of mesoporous organosilica beads. Parts of the results of this chapter were published titled *"Millimeter-sized micellar-templated silica beads and phenylene-bridged mesoporous organosilica beads"* by Malina Bilo, Young Joo Lee and Michael Fröba. [240]

The incorporation of silica[180] and organosilica into alginate hydrogels has already been presented in the literature. Organosilica/alginate composites were obtained by dispersion of organosilica powder inside the alginate hydrogel matrix, which in turn does not form a stable network so that the hydrogel template cannot be removed.[181,241] In contrast, stable silica beads were achieved by pouring wet calcium alginate beads into an excess of TEOS which was hydrolyzed with the help of nitric acid (0.15 $mol \cdot L^{-1}$) at room temperature and subsequent removal of the alginate.[188] Here, the alginate matrix was removed from the beads with citric acid, a mild method that could also be used for organosilicas.

The bead-formation process is less suitable for organosilica materials as the use of the large excess of the bis-silylated organosilica precursor compounds is atom-inefficient and highly undesired as the structurally, more ambitious precursor molecules are typically synthesized in a multistep synthesis. Besides, within the scope of this work, it was found that the hydrolyzed organosilica species tend to condense on the outer surface of the alginate beads so that this approach could not be reproduced successfully.

In another approach, the authors show the hydrolysis of TEOS in diluted hydrochloric acid and mixed it with an alginate solution, which in turn was dropped into a calcium chloride solution so that the silica phase was homogeneously distributed inside the alginate matrix.[180]

Here, the two preceding approaches were combined to synthesize pure (organo)silica beads. Figure 4-150 shows the synthetical pathway that includes several steps that require careful optimization.

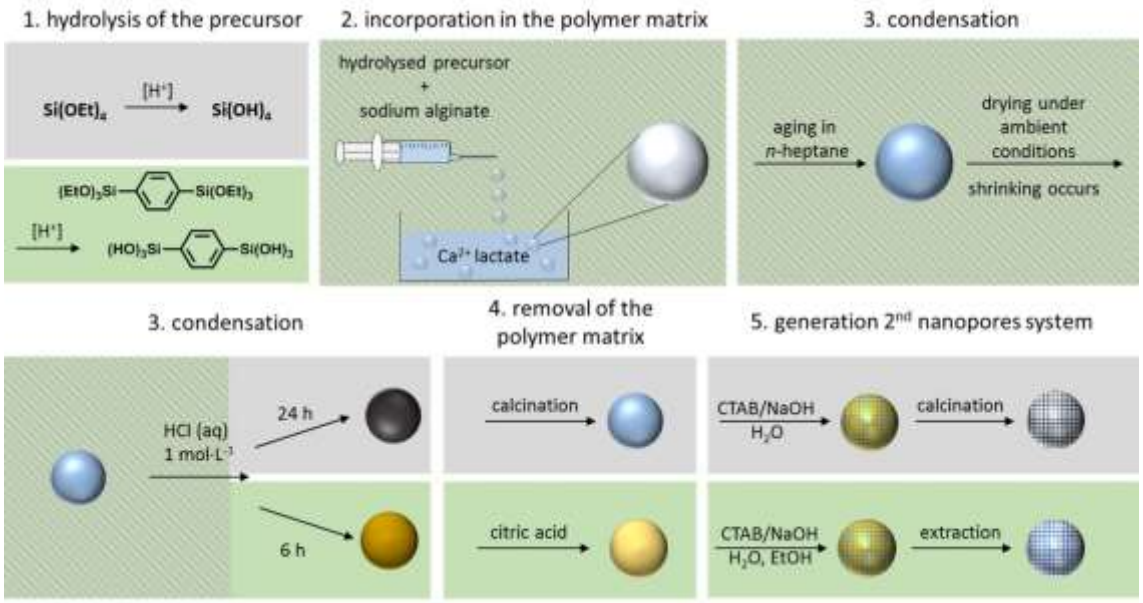

Figure 4-150: Overview of the multistep synthetical pathway for the synthesis of millimeter-sized (organo)silica beads in a calcium alginate hydrogel matrix. The precursor, TEOS for silica beads, BTEB for organosilica beads, are hydrolyzed before they are incorporated into the alginate matrix respectively. The condensation of the (organo)silica network is promoted in three synthesis steps until there is sufficient interconnection for a stable network, so that the alginate matrix can be removed. The hydrolysis conditions differ for TEOS and BTEB, but the incorporation in the polymer matrix as well as the first condensation steps are the same. The treatment time with HCl differs and so does the strategy for the removal of the polymer matrix. In a last steps, a nanopores system is generated by pseudomorphic transformation, under different conditions for organosilica and silica, and subsequent extraction or calcination of the surfactant.

In the previously mentioned reference,[180] TEOS was hydrolyzed in hydrochloric acid (0.02 mol·L^{-1}) using a volume ratio of 1:9.

Reproducing this approach, it was found that the respective silica beads were not stable after removal of the alginate template, so that the TEOS content was increased here. A gravimetric ratio of TEOS to hydrochloric acid (0.02 mol·L^{-1}) of 3:7 was found to be ideal for the formation of stable silica beads. Under acidic conditions, alginate also forms a hydrogel,[173] but unfortunately the gel of the alginic acid is unstable so that these two steps cannot be combined. Instead, the pH value of the solution had to be increased to 5–6 with a few drops of sodium hydroxide solution (0.4 mol·L^{-1}). Here, a careful observation of the pH value was crucial in order to avoid premature condensation of the silica source, as a solid silica phase is not expected to undergo homogeneous dispersion with alginate.

The optimization of the synthesis conditions results in a gravimetric ratio of alginate/TEOS of 1/6. Assuming full consumption of TEOS, this causes a gravimetric ratio of alginate/SiO_2 of 1/1.7 in the product.[5]

[5] As alginate is a biopolymer, no exact molar mass is known, hence no molar ratio was calculated.

The mixture was dropped into different Ca^{2+}-containing solutions. Calcium chloride is used as a Ca^{2+}-source in most examples known in the literature as it is inexpensive. However, calcium chloride was observed to give a rather rough bead surface, so calcium D-gluconate and calcium lactate were tested. Both of them yielded beads with smooth surfaces. Due to economic reasons, further syntheses were done using calcium lactate.

After formation and ageing in a Ca^{2+}-solution, the beads were poured into *n*-heptane, where polycondensation of the silica network takes place and the beads were observed to turn opaque. It was found that this step is essential for the bead's stability.

Finally, the beads were dried at ambient conditions spread flat on filter paper, during which shrinking of the beads occurs. When the beads were treated in hydrochloric acid (1.0 $mol \cdot L^{-1}$) at 100 °C, further improvement of the silica phase's condensation degree was observed. Under these harsh conditions, the beads turned completely black. This is attributed to decomposition of the biopolymer alginate and lactate residues in the matrix. The organic compounds were subsequently removed by calcination. Pearl white and sturdy silica beads of about 0.2 cm in diameter were finally obtained, which can be seen in the photograph in Figure 4-151.

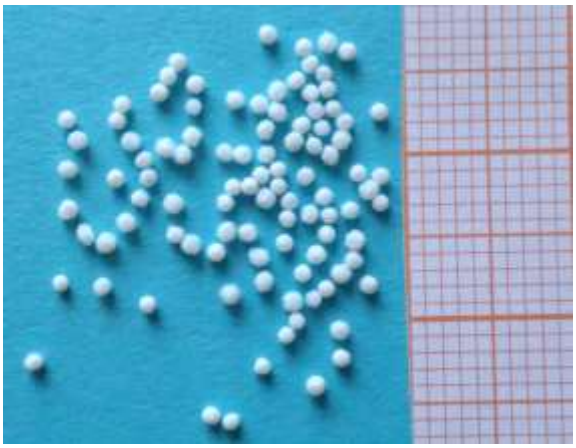

Figure 4-151: Photograph of the SiO_2 beads that were obtained by templating with alginate hydrogels. Plotting paper with 2 x 2 mm squares on the side is the scale bar.

The pseudomorphic transformation of these beads is achieved by treatment with a sodium hydroxide solution (0.05 $mol \cdot L^{-1}$, pH value of 12.7) of C_{16}TAB. The beads were treated for four hours and for four days at 100 °C. In the following paragraph, the samples will be designated as 4d-pT-SiO_2 beads and 4h-pT-SiO_2 beads (pT for pseudomorphic transformation). Preservation of the millimeter-sized bead can be demonstrated in the photograph in Figure 4-152. In order to optimize the pH value and the concentration of the surfactant solution separately, the use of C_{16}TAOH solution, which was used for pseudomorphic transformation of CPG in the preceding sections 4.2 and 4.3.3, was abandoned.

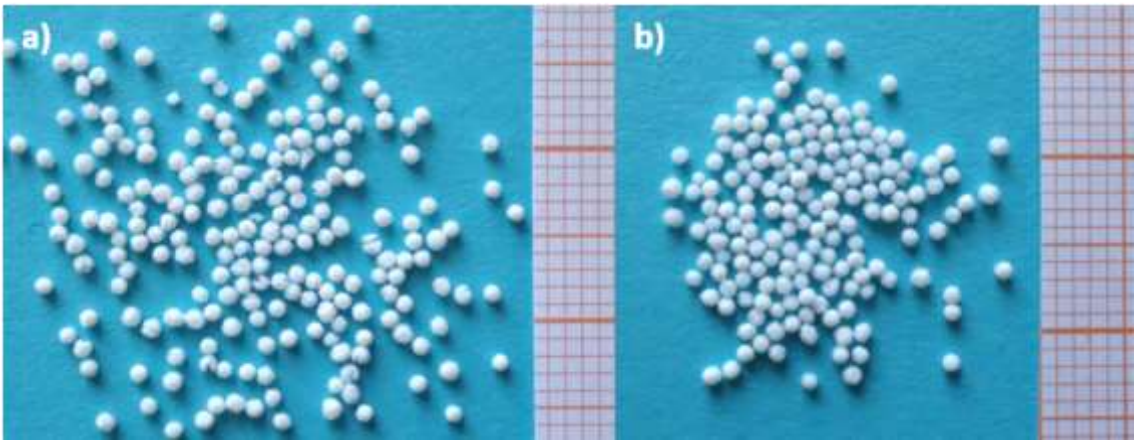

Figure 4-152: Photographs of (a) 4h-pT-SiO_2 beads and (b) 4d-pT-SiO_2 beads. Plotting paper with 2 x 2 mm squares on the side is the scale bar.

The formation of an ordered mesophase can be investigated by the P-XRD patterns in Figure 4-153. For 4d-pT-SiO_2 beads, distinct reflections at 2θ = 2.2° and further broad reflections around 2θ = 3°–5° are given. For 4h- pT-SiO_2 beads, only slight ordering of the material is possible, as indicated by a broad shoulder of reflection in this range.

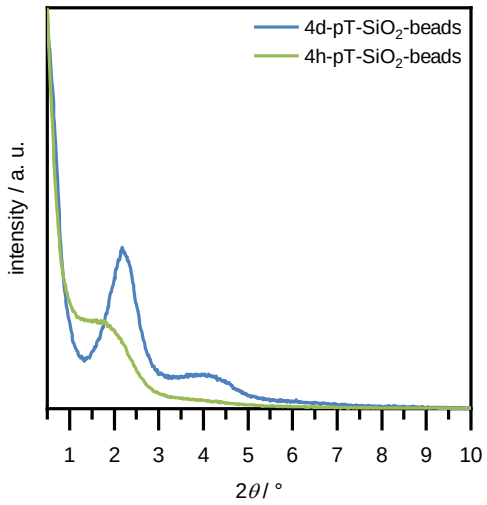

Figure 4-153: P-XRD patterns of 4h- pT-SiO_2 beads (green) and 4d- pT-SiO_2 beads (blue), respectively.

The isotherm of the calcined silica beads, which corresponds to step 4 in Figure 4-150, left photograph in Figure 4-154, shows continuous gas uptake over the whole relative pressure range, which is in accordance with the very broad pore diameter distribution (see Figure 4-154, right). The calcined silica beads provide a high specific BET surface area of 716 $m^2 \cdot g^{-1}$ even before the pseudomorphic transformation. The specific BET surface area of silica beads that were obtained from alginate templating in the literature ranges from 670 $m^2 \cdot g^{-1}$ to 755 $m^2 \cdot g^{-1}$.[188] An even higher specific BET surface area of 905 $m^2 \cdot g^{-1}$ and pores around 12 nm in diameter are obtained in silica aerogels that were synthesized in the presence of calcium salts.[184] The high specific BET surface area might be due to interparticle voids in the gel or voids that remain after removal of alginate.

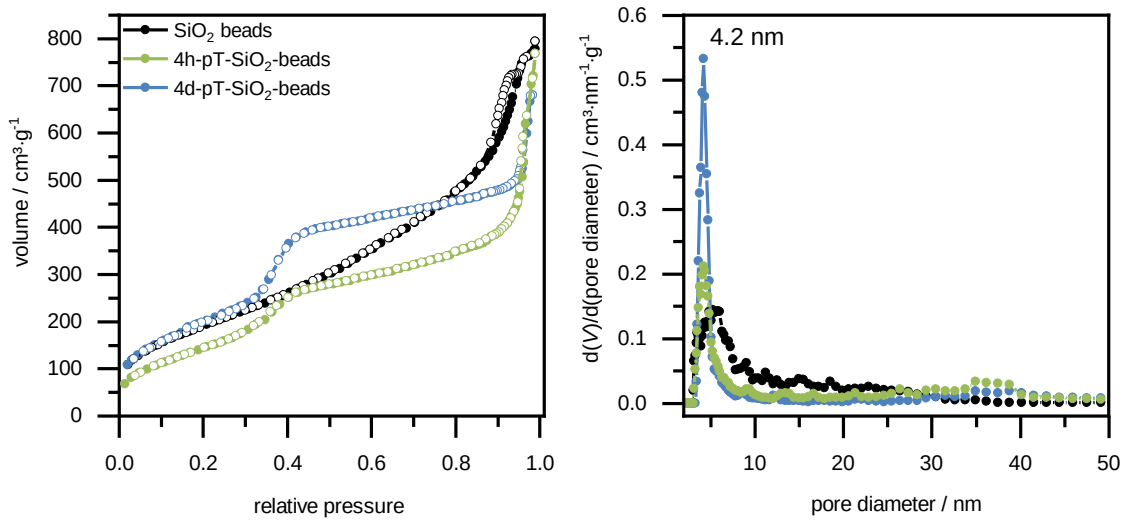

Figure 4-154: Physisorption isotherms (N_2, 77 K) of silica beads (black), and the respective samples after pseudomorphic transformation for four hours (green) and four days (blue). Right: pore diameter distributions (calculated using NLDFT kernel for silica, cylindrical pores, from the adsorption branch).

The physisorption isotherms of beads after pseudomorphic transformation can be seen in Figure 4-154, with 4d-pT-SiO_2 beads in blue and the 4h-pT-SiO_2 beads in green. The characteristic step due to pore condensation without hysteresis is typical for a type IVb isotherm and can be recognized in both isotherms as mesopores of 4.2 nm diameter are generated. The pore size distribution is more distinctive after four days, however a significant change of the pore size distribution is already given after four hours of pseudomorphic transformation. -pT-SiO_2 beads shows a slightly increased specific BET surface area of 767 $m^2 \cdot g^{-1}$, whereas this shrinks after four hours of treatment with the surfactant solution to 582 $m^2 \cdot g^{-1}$. The phenomenon of reduced specific surface area after partial pseudomorphic transformation has already been mentioned by Einicke *et al.*[37] It was explained by a collapse of the initial pore system as was explained in detail in section 1.4 (see Figure 1-12).

A steep step in the relative pressure range from 0.85 to 0.96 in the case of the silica beads and over 0.95 in the case of the beads after pseudomorphic transformation, indicates the presence of larger mesopores or macropores in all isotherms, although this is not well reflected in the pore diameter distribution from NLDFT. The macropore systems of the presented samples were investigated by MIP. The intrusion curves and the respective pore diameter distribution are given in Figure 4-155.

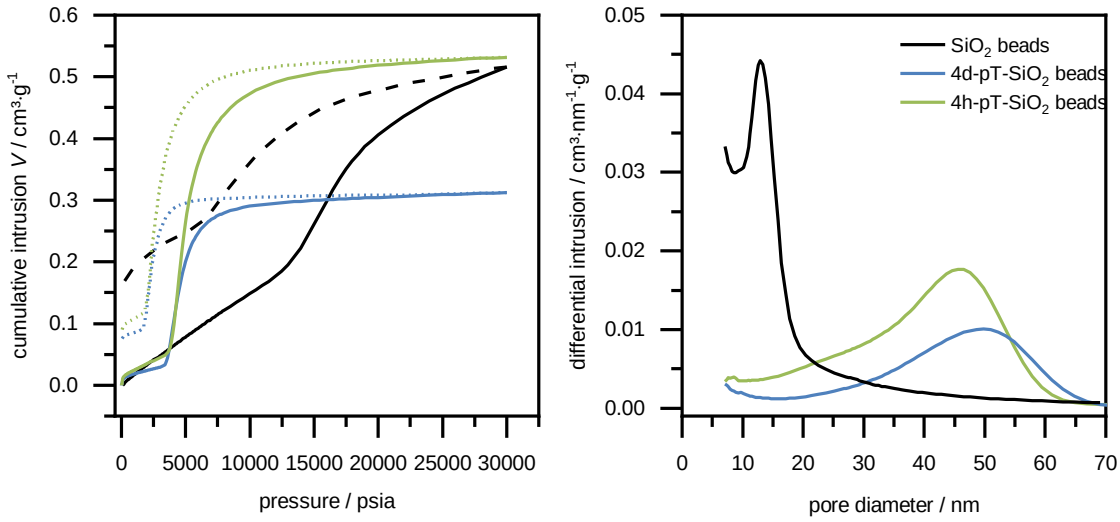

Figure 4-155: Left: mercury intrusion curves of silica beads before pseudomorphic transformation (black) and after four hours (green) and four days (blue). Right: pore size distributions of the respective material with the same color codes.

Before the pseudomorphic transformation, the silica beads have pores around 13 nm and a pore volume of 0.52 $cm^3 \cdot g^{-1}$. Pores in this size range are barely represented in the pore diameter distribution from NLDFT, where smaller pores are more prominent, which in turn are not accessible for mercury, but the isotherm of the sample does increase in the high relative pressure range, which indicates that pores in this size range might be present. The pore size distribution changes significantly after pseudomorphic transformation. As expected, the initial pores of 13 nm in the gel collapse already completely during the transformation for 4h-pT-SiO_2beads. The appearance of larger pores in the macropore range is rather unexpected, the origin of these pores cannot be explained at this point. In the 4h-pT-SiO_2 beads, the macropore volume of 0.5 $cm^3 \cdot g^{-1}$ remains constant, whereas it decreases significantly to 0.3 $cm^3 \cdot g^{-1}$ for 4h-pT-SiO_2 beads after four days. Thus, the pore volume increases during the transformation and large mesopores to macropores are generated, whereas the mesopores of 13 nm that are generated during the sol-gel process disappear soon. The textural data of all silica beads is summarized in Table 4-47, also the pore volume according to the NLDFT kernel for silica with cylindrical pores is given.

Table 4-47: Textural data of the silica beads that were synthesized within a calcium alginate hydrogel matrix before and after pseudomorphic transformation

samples	S_{BET} / $m^2 \cdot g^{-1}$	$d_{N_2, NLDFT)}$ / nm	V_{NLDFT} / $cm^3 \cdot g^{-1}$	V_{Hg} / $cm^3 \cdot g^{-1}$	d_{Hg} / nm
SiO_2 beads	716	–	1.16	0.52	13
4h- pT-SiO_2 beads	582	3.7	1.10	0.52	46
4d- pT-SiO_2 beads	767	3.7	1.00	0.30	49

The structure of the large mesopores is sponge-like, which resembles the materials that were obtained from phase separation processes as can be seen in the SEM images in Figure 4-156.

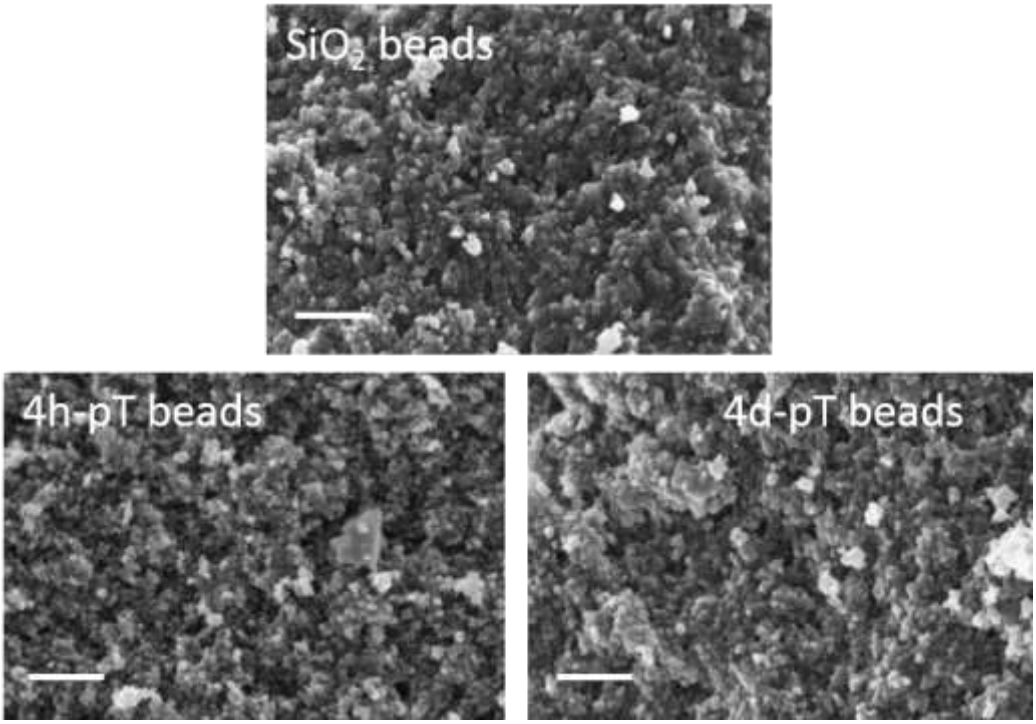

Figure 4-156: SEM images of the SiO_2 beads, before (upper image) and after pseudomorphic transformation for four hours (lower left) and four days (lower right). (Magnification x20000, scale bar 2 µm.)

Water sorption can be used as a tool to study the hydrophilic character of a material, but it is also affected by the pore size. Figure 4-157 shows adsorption branches of the silica beads before and after the pseudomorphic transformation from two subsequent measurement cycles.

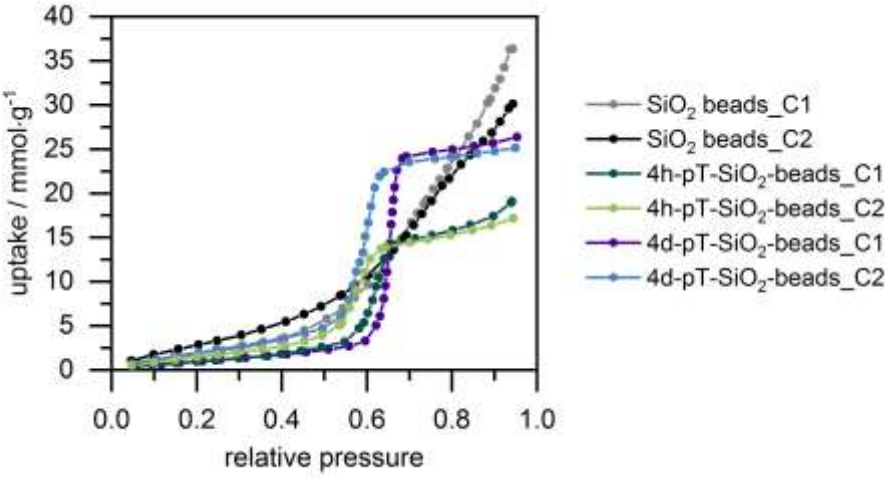

Figure 4-157: Adsorption branches of water vapor sorption isotherms (H_2O, 298 K) from silica beads before and after pseudomorphic transformation for four hours and four days, respectively. Each sample was subjected to two subsequent measurements as indicated by "_C1" or "_C2".

The isotherms of silica beads before pseudomorphic transformation show consistent water vapor uptake from a relative pressure of 0.4 in the first cycle and 0.6 in the second. In contrast, the isotherms of the materials after pseudomorphic transformation show a steep condensation step and can be assigned to isotherms of type V, which is expected for water vapor sorption isotherms of mesoporous materials. The onset of the condensation step is at similar relative pressures for 4d-pT-SiO_2-beads (0.59 in the first cycle 0.52 in the second cycle) and 4h- pT-SiO_2-beads (0.54 in the first cycle and 0.49 in the second cycle), respectively. The point of inflection is 0.58 in both curves. For the curve of the SiO_2 beads before transformation, the determination of these parameters is not possible due to the shape of the curve. The uptake of 4h- pT-SiO_2-beads is 19.1 mmol·g^{-1} which is significantly lower, compared to the uptake of 4d- pT-SiO_2-beads of 26.4 mmol·g^{-1}. A shift towards lower relative pressures in the second cycle was observed for all of the materials. The calcined silicas become more hydrophilic as silanol groups are generated on the surface of the material due to interactions with water in the first cycle.[242] From the second curve, the water filled pore volume can be determined and be compared to the pore volume from nitrogen physisorption measurement according to the Gurvich rule at a relative pressure of 0.95, the values are is given in Table 4-48. With these values the hydrophilicity index according to Thommes *et al.*, χ_{vol}, can be determined. SiO_2-beads and 4h- pT-SiO_2 beads show similar values of 0.56 and 0.46, whereas it is significantly lower, 0.31, for 4d- pT-SiO_2 beads. Also the specific BET surface area can be determined from the water vapor adsorption. It is surprising, that SiO_2 beads show the highest value of 252 $cm^2 \cdot g^{-1}$, whereas it is only 134 $m^2 \cdot g^{-1}$ in case of 4d-pT-SiO_2 beads, although the trend of the specific BET surface area from nitrogen measurements is the other way around. Just as the specific BET surface area the hydrophilicity index χ_{n_m} is also significantly lower for 4d- pT-SiO_2 beads than for 4h- pT-SiO_2 beads, whereas the latter shows a similar value as the SiO_2 beads before transformation. Therewith the two hydrophilicity indices show the same trend, although the different values are rather caused by the different porosity features of the samples as the surface chemistry is expected to be constant in all three samples. Figure 4-158 shows the complete isotherms of the second cycles of the materials discussed above. It is confirmed that the isotherms are of type V with significant hysteresis in the condensation step, as expected for water vapor sorption. Next to the plot of the uptake as measured, the isotherms are shown in a normalized plot. The normalized plot shows that the different treatment time does not change the condensation behavior of water in the two pseudomorphically transformed materials. The differences in absolute uptake are thus only caused by the different specific BET surface areas.

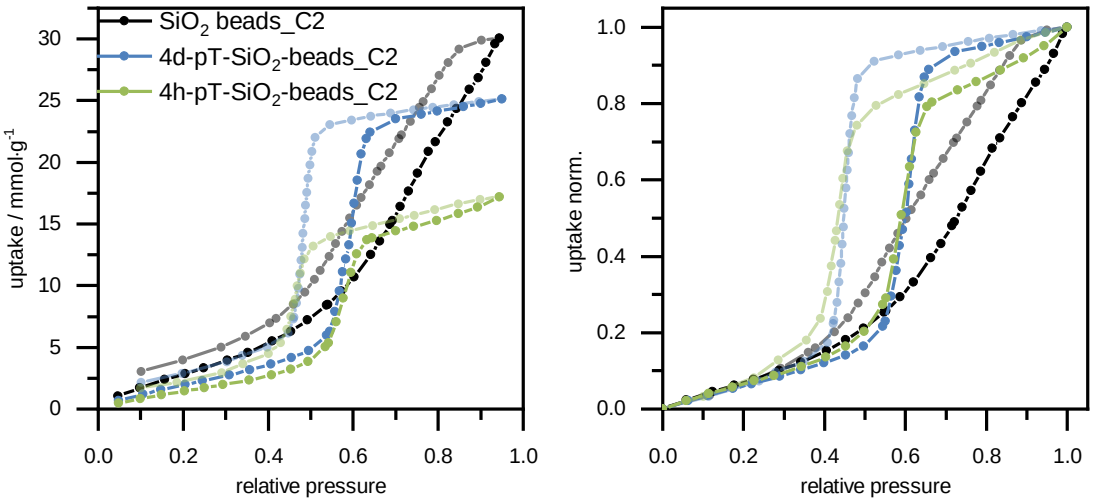

Figure 4-158: Second cycles from water vapor sorption (H_2O, 298 K) of silica beads before and after pseudomorphic transformation by treatment with C_{16}TAB and NaOH for four days and four hours. As-measured plot on the left, normalized uptake on the right.

Table 4-48: Summary of the onset, the point of inflection (p.o.i.), the pore volumes filled with water or nitrogen and the BET surface areas determined with nitrogen and water vapor adsorption measurements, respectively.

sample	$S_{BET\ (N_2)}$ / $m^2 \cdot g^{-1}$	$S_{BET\ (H_2O)}$ / $m^2 \cdot g^{-1}$	χ_{n_m}	$V_{(N_2)}$ ($p/p^0 = 0.95$) / $cm^3 \cdot g^{-1}$	$V_{(H_2O)}$ ($p/p^0 = 0.95$) / $cm^3 \cdot g^{-1}$	$\chi_{vol.}$	*onset*	*p.o.i*
SiO_2 beads	716	252	0.33	1.15	0.56	0.49	–	–
4h- pT-SiO_2 beads	582	180	0.29	0.74	0.45	0.61	0.52	0.58
4d- pT-SiO_2 beads	767	134	0.16	0.78	0.31	0.40	0.49	0.58

Hence, water sorption could be used to prove that the pseudomorphic transformation of silica beads obtained by templating with alginate behave analogously to commonly synthesized MCM-41 type silica.

Transfer of the synthesis route from silica beads to organosilica beads

The synthesis pathway of millimeter-sized silica beads as described above, was designed in such a way that it could also be easily transferred to organosilica materials. Here, BTEB was used as an organosilica precursor compound as it is widely used and chemically modifiable as was discussed in the Introduction (see section on aromatic PMOs in 1.5.2).

As it is the first step, the hydrolysis behavior of BTEB needed to be studied. For this, BTEB was stirred in hydrochloric acid with different concentrations between 1.0 $mol \cdot L^{-1}$ and 0.01 $mmol \cdot L^{-1}$ corresponding to pH values between 0 and 5. At low pH values, condensation occurred within

the first two hours, which was indicated by the solution turning opaque. At higher pH values, the precursor did not mix with the aqueous solution and no homogeneous phase could be obtained. In order to improve the solubility of the precursor, ethanol as an organic co-solvent was added to the solution. For the next step, the total content of ethanol had to be as low as possible since alginate is not soluble in ethanol. Thus, it had to be taken into account that hydrolysis of the precursor causes further equivalents of ethanol in the solution. A volumetric ratio of 1/1 ethanol/hydrochloric acid solution (0.02 $mol \cdot L^{-1}$) was found to give the best and most reproducible results. It should be noted that the separation of the two processes of hydrolysis and condensation is very fragile and can be influenced significantly by the quality and age of the precursor.

Just as in the case of the silica bead synthesis, the pH value of the precursor solution was adjusted to 5–6 before it was mixed with the alginate solution. The organosilica/alginate composite was dropped into a calcium lactate solution, and aged over-night before further ageing in *n*-heptane before it was dried at room temperature.

The stability of the beads also had to be improved in the case of BTEB, so the beads were treated with hydrochloric acid to increase the condensation degree. After 24 hours of acidic treatment, the beads turned completely black. In contrast to the silica beads, the alginate phase could not be removed by calcination, since the organic moiety of the organosilica phase would also be affected. Instead, calcium alginate could be dissolved in an aqueous solution of citric acid which is known to coordinately bind calcium ions. However, the decomposed alginate that was indicated by the black color could not be removed completely and the beads remained brownish. When the time of treatment with hydrochloric acid was shortened to six hours, the beads were less strongly colored, which indicated less decomposition of the alginate phase. Despite the shorter treatment, the organosilica beads were stable and preserved their morphology even after removal of alginate, while the coloring could also be removed. Figure 4-159 shows microscopic images of the translucent beads after drying at room temperature, and the opaque beads after treatment with hydrochloric acid and subsequent removal of alginate with citric acid.

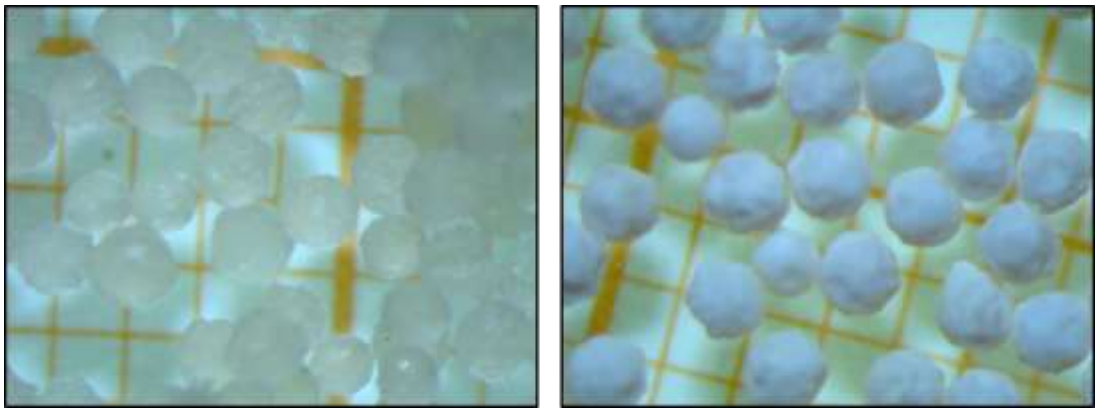

Figure 4-159: Microscopic images of BTEB organosilica beads after drying on the left, and after treatment with hydrochloric acid and removal of alginate with citric acid on the right, both with plotting paper in the background (small squares of 2 x 2 mm).

Assuming complete hydrolysis and condensation of BTEB, the resulting material has an idealized composition of $Ph(SiO_{1.5})_2$. The gravimetric ratio for alginate/$Ph(SiO_{1.5})_2$ is 1/2.1. The resulting beads are referred to as B-organosilica beads.

For further characterization, the complete removal of alginate needs to be proven. Figure 4-160 shows the IR spectra of the B-organosilica beads before and after alginate removal, as well as pure calcium (II) alginate beads. There are only few bands to distinguish between the benzene bridge and alginate. The most prominent bands of alginate are C-O stretching vibrations around 1100–1000 cm^{-1}, and these overlap with Si-O stretching vibrations. The mode at 1379 cm^{1} results from deformation vibrations of the aromatic C-H bonds. CH stretching vibrations (2924 cm^{-1} and 2856 cm^{-1}) are rather weak and close to $–CH_2$ stretching vibrations, which in turn are reasonable in B-organosilica due to ethoxy groups of the precursor. The most isolated band in alginate is at 1428 cm^{-1} ($\nu_{O\text{-}C\text{-}O}$). It disappears in the B-organosilica beads after extraction of alginate.

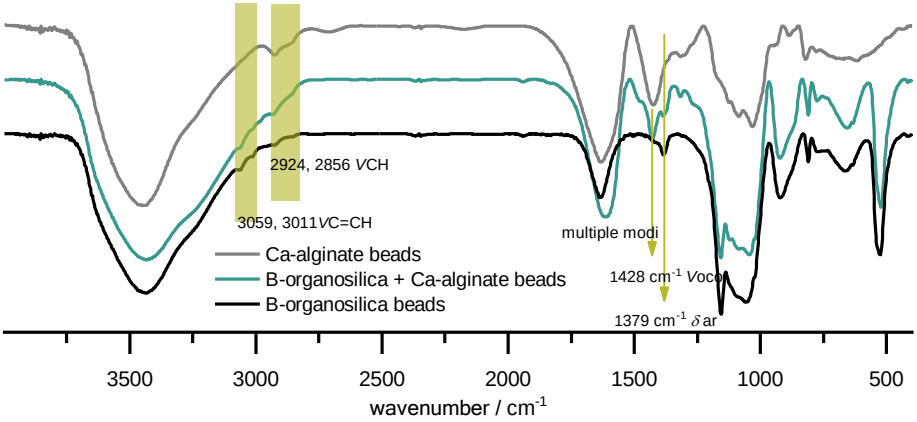

Figure 4-160: FT-IR spectra (KBr-disc) of beads of only calcium alginate (grey), beads of B-organosilica incorporated in the calcium alginate matrix (green) and the same beads after extraction of the alginate matrix with citric acid (black).

The comparison of the IR spectra gives a hint that no alginate is found in the B-organosilica, but this is not conclusive in this context.

More information can be obtained from TG data since the overall mass loss of B-organosilica is expected to be the same as it is for a commonly synthesized B-PMOs when the alginate phase is completely removed, whereas it should consequently be higher for the alginate/B-organosilica composite. Also, decomposition temperature of the benzene bridge and alginate differ.

In Figure 4-161, mass loss over temperature of the B-organosilica is compared with a pure B-PMO as a benchmark, with the composite of B-organosilica and alginate before treatment with citric acid as well as with pure calcium alginate beads.

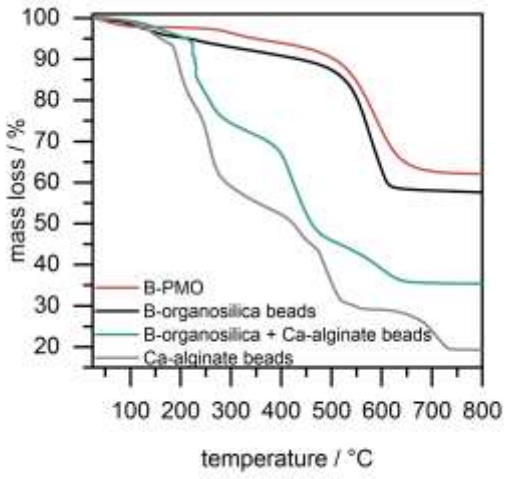

Figure 4-161: TG analysis in Ar/O_2 80/20 of B-organosilica beads (black) in comparison with the composite before alginate extraction (green), pure calcium alginate beads (gray), and standard B-PMO (red).

The benzene bridge decomposes in the temperature range between 450–800 °C. For B-PMO and B-organosilica, the mass loss in this temperature interval is nearly the same at 32 % and 31 %, respectively. Calcium alginate decomposes in three steps at 175 °C, 400 °C, and 650 °C, respectively. The absence of mass loss in the lower temperature ranges in the B-organosilica indicates complete extraction of the alginate phase, although, adsorbed surface water results in higher overall mass loss values for this sample. For comparison, the mass loss of the alginate/organosilica composite in the temperature interval 200–800 °C is 60 %, hence significantly higher than the B-organosilica beads so that a significant amount is extracted with citric acid.[6] As the decomposition of alginate overlaps with the temperature interval for B-PMO, the alginate content in the alginate/organosilica composite cannot be determined by this method.

Figure 4-162 shows the nitrogen physisorption isotherms and the respective pore diameter distribution of B-organosilica beads (black). The specific BET surface area of the material is

[6] Comparing the organosilica/alginate composite with calcium alginate, a shift of the TG curve of 50 °C in the direction of higher temperatures can be detected. This effect was reproducible and might be due to hindered accessibility of oxygen in the dense beads of the composite.

699 $m^2 \cdot g^{-1}$ which is similar to the value of the SiO_2 beads. Noteworthy volume uptake and a very steep step in the low relative pressure range indicates the presence of micropores, whereas the significantly increased uptake at higher relative pressures indicates the presence of additional macropores. As expected from the results with pore silica, the pore diameter distribution shows micro- to mesopores up to 10 nm.

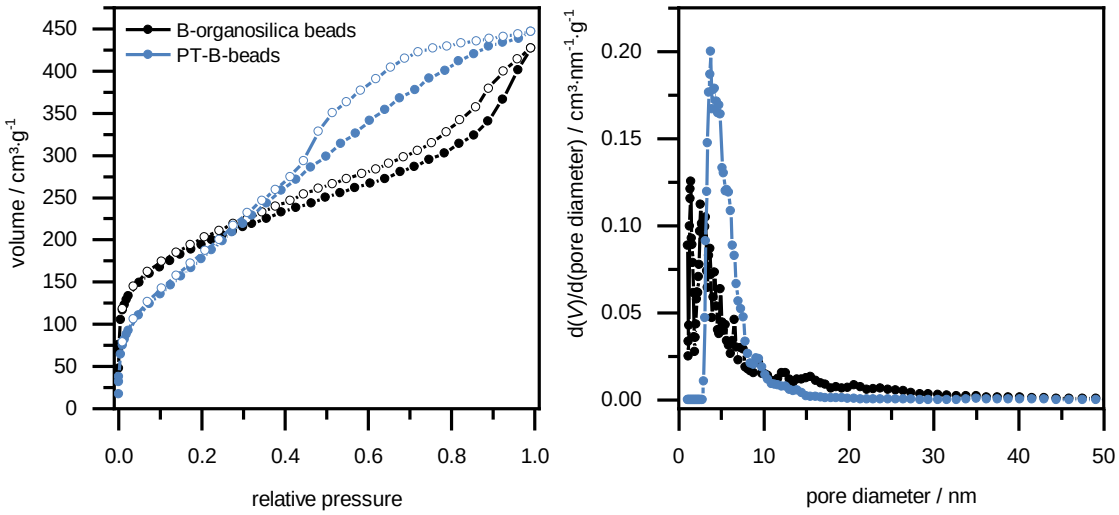

Figure 4-162: Left: Physisorption isotherms (N_2, 77 K) of B-organosilica beads that were synthesized in an alginate hydrogel template (black) and the respective PT-B-beads after pseudomorphic transformation for 24 hours (blue). Right: pore diameter distributions from NLDFT silica, cylindrical pores, adsorption branch.

As already described for SiO_2-beads, the B-organosilica beads were also treated a with C_{16}TAB/NAOH solution for pseudomorphic transformation in order to generate a mesopore system within the organosilica beads. It was determined that the addition of ethanol was essential for the preservation of the morphology as previously shown in the literature for pure silica materials.[238] The product is designated PT-B-beads.

After 24 hours of treatment and subsequent extraction of the surfactant, the specific BET surface area increased slightly from 699 $m^2 \cdot g^{-1}$ to 731 $m^2 \cdot g^{-1}$. A continuous increase in the adsorption branch indicates mesopores of broad pore size distribution (see Figure 4-162). Furthermore, a prominent hysteresis is observed, which might be attributed to pore blocking by interconnected pores with different diameters. However, comparing the pore diameter distribution of the organosilica beads before and after the pseudomorphic transformation, a significant shift to mesopores with a maximum diameter of 3.7 nm can be observed.

When the investigation of the macropore system was done by MIP and the intruded volume increased slightly from 0.26 $m^2 \cdot g^{-1}$ to 0.32 $m^2 \cdot g^{-1}$ after the pseudomorphic transformation, thus, the intrusion volumes are significantly lower than in the case of the silica materials. See intrusion curves in Figure 4-163.

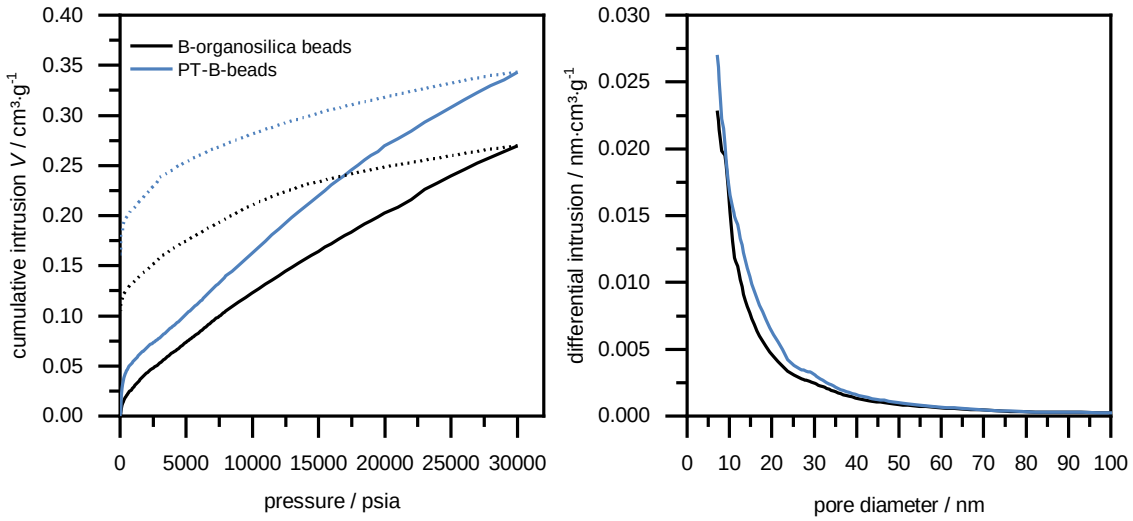

Figure 4-163: Left: mercury intrusion curves of B-organosilica beads (black) and PT-B-beads after 24 hours of pseudomorphic transformation (blue). Right: pore size distributions of the respective material with the same color code.

For SEM images of the B-organosilica and PT-B-beads are shown in Figure 4-164.

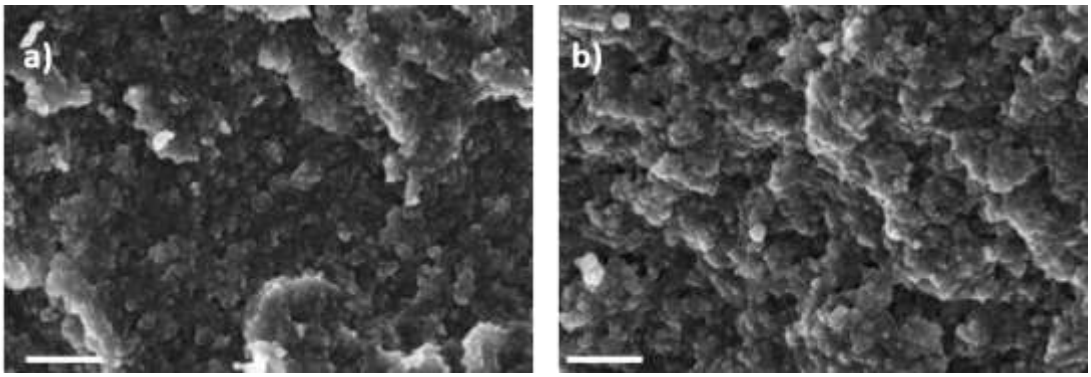

Figure 4-164: SEM images of a) B-organosilica beads and b) PT-B-beads. Magnification x2000, Scale bar is 2 µm.

Ordering of the pore system after pseudomorphic transformation is indicated by a broad reflection in the small angle region of the P-XRD pattern as can be seen in Figure 4-165. Also, the organic moieties rearrange in a crystal-like manner which causes reflections at 2θ = 12°, 20.7°, 23.5°, and 35.5°, which corresponds to d = 7.6 Å, 4.2 Å, 3.8 Å, and 2.5 Å, respectively. As explained in the literature, this is caused by the length of the benzene-bridged precursor of 7.6 Å and the respective multiples and the through-space distance of the benzene rings of 4.2 Å.[90]

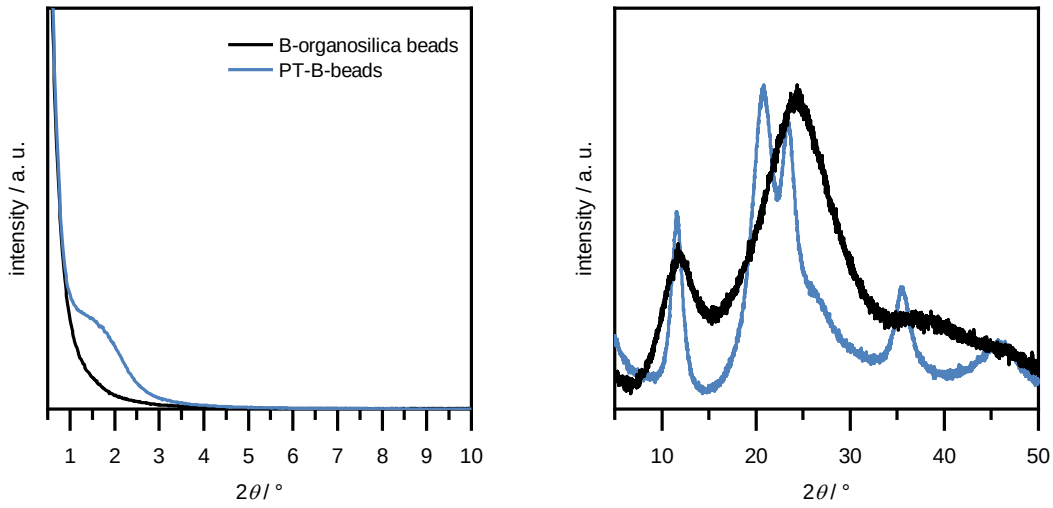

Figure 4-165: P-XRD of B-organosilica beads before (black) and after (blue) pseudomorphic transformation for 24 hours.

The morphology of the beads before and after the pseudomorphic transformation can be compared in Figure 4-166.

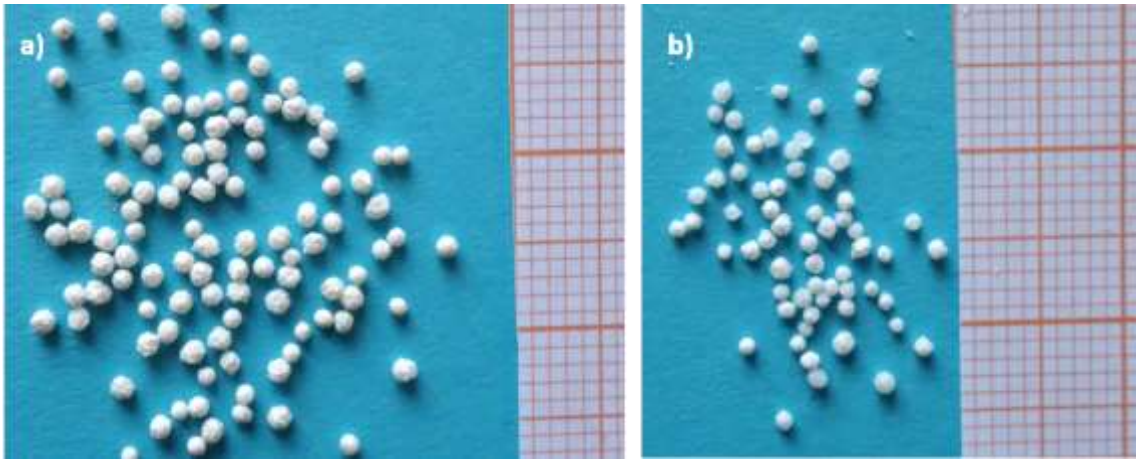

Figure 4-166: Photographs of the B-organosilica beads (a) before and (b) after pseudomorphic transformation, B-PT-beads, in C_{16}TAB/NaOH for 24 hours. Plotting paper with 2 x 2 mm squares on the side is the scale bar.

Complete removal of the surfactant can be proven by TG/MS. Again, the material was compared to a standard B-PMO and the B-organosilica before the pseudomorphic transformation, see Figure 4-167.

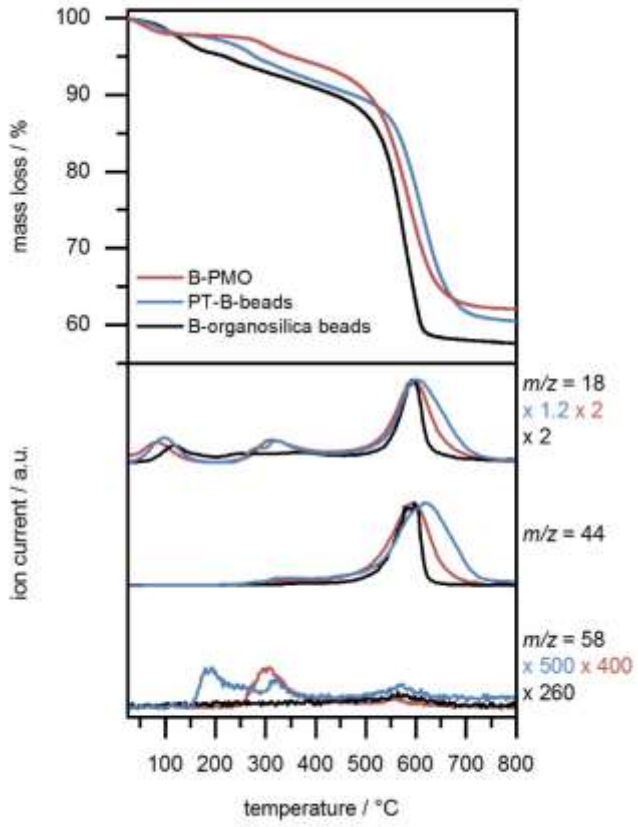

Figure 4-167: TG/MS analysis in Ar/O_2 80/20 of PT-B-beads (blue) in comparison with B-organosilica beads (black) and standard B-PMO (red). Mass loss over temperature is plotted in the upper part and selected ion currents are given in the lower plot. The ion currents are normalized and the normalization factors are given on the side in the respective colors.

The mass loss in the different temperature intervals is given in Table 4-49.

Table 4-49: Mass loss per temperature intervals of TG analysis (Ar/O_2 80/20) of the PT-B-beads in comparison with the B-organosilica beads and standard B-PMO powder.

	mass loss		
temperature interval	**B-organosilica beads**	**PT-B-beads**	**B-PMO**
25–200 °C	4.7 %	2.8 %	2.3 %
200–450 °C	5.7 %	6.7 %	5.0 %
450–800 °C	32 %	30 %	31 %
200–800 °C	40%	38 %	37 %
25–800 °C	42 %	39 %	38 %

The corrected mass loss in the temperature range of 200–800 °C is the same for B-PMO and PT-B-beads. The mass loss of the three samples in the temperature range of 200–450 °C, where the decomposition of C_{16}TAB occurs, differs only slightly and the intensity of the ion current m/z = 58

is very low. Thus, it can be concluded, that the surfactant was not completely, but sufficiently removed. For the TG/MS of C_{16}TAB see Figure 9-39 in the Appendix.

Insights into the integrity of the organic bridge are given by the IR spectra of the PT-B-beads in comparison to a benchmark B-PMO in Figure 4-168. The spectra are congruent, so that the integrity of the organic bridge can be assumed.

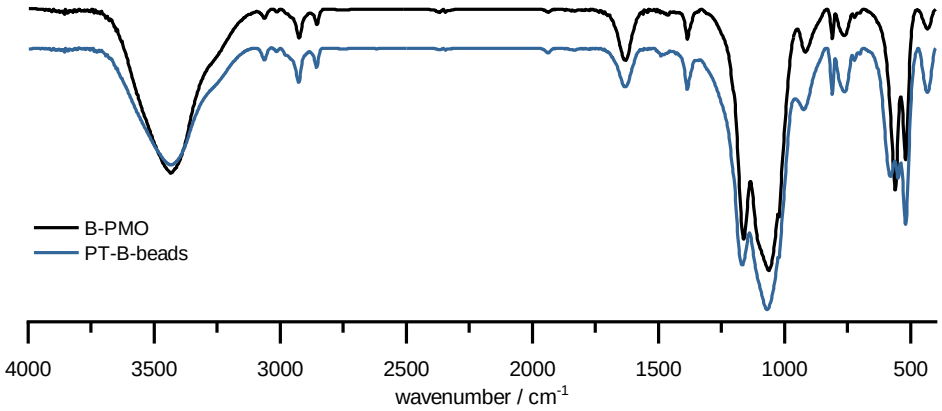

Figure 4-168: FT-IR spectra (KBr-disc) of PT-B-beads after pseudomorphic transformation (blue) and a benchmark B-PMO (black).

This is confirmed by ^{13}C-CP MAS NMR spectra in Figure 4-169. According to the literature, signals of two carbon species are expected for the benzene bridge: the quaternary carbon $C_{ar,q}$ (at 133.5 ppm for BTEB in $CDCl_3$) and the four C_{ar}-H (at 134.4 ppm for BTEB in $CDCl_3$).[68] Since chemical shift values of these two carbons are very close, ^{13}C CP-MAS NMR spectrum appears as a broad overlapping signal, which can be deconvoluted into individual signals at 133.3 and 134.4 ppm as shown in Figure 9-40 in the Appendix. There are no further signals in the spectrum before the pseudomorphic transformation, hence, complete removal of the alginate can be assumed, which confirms the results from TG/MS. After the transformation, additional signals occur which can be assigned to residues of the surfactants. The problem of incomplete extraction of the surfactant from the samples has been discussed in different contexts before in this work. It seems to be a systematic problem of the extraction protocol, although the amount of residue detected by ^{13}C-CP MAS NMR is comparably low. ^{1}H-MAS NMR spectra are shown in the Appendix, Figure 9-41, showing the presence of water and residual surfactants.

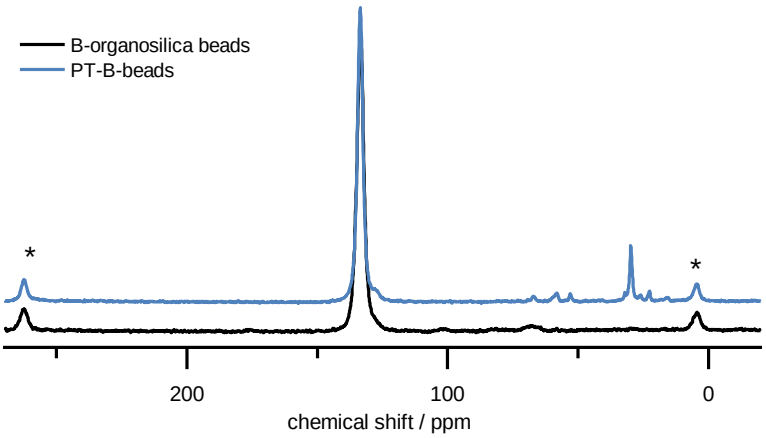

Figure 4-169: ^{13}C-CP MAS NMR spectra (spinning speed = 13 kHz, spinning side bands are indicated by *) of the B-organosilica beads (black) and the PT-B-beads (blue).

Figure 4-170 shows the ^{29}Si-CP MAS NMR of organosilica beads and PT-B-beads. In both cases Q signals are visible. Since the precursor was synthesized in a Grignard reaction from 1,4-dibromobenzene and TEOS, it is possible that residues of TEOS are still present and incorporated in the product despite purification of the precursor via distillation. On the other hand, the increase of the Q signals ratio after pseudomorphic transformation indicates decomposition of the Si-C bond during the treatment, even if only at a low percentage. Quantification of the ratio of Q to T signals from CP NMR measurements is not straightforward since signal intensity of CP experiments depends on the mobility and the number of protons attached to individual functional groups: In general, the intensity of the T signals is enhanced more than Q signals. For quantification, direct excitation ^{29}Si MAS NMR would be needed, which is extremely time consuming. From comparison between CP and direct excitation experiments of similar silica systems, a correlation factor can be obtained which can be used to estimate the relative quantitative of Q to T species. According to this method, the B-organosilica beads and the PT-B-beads contain around 10% and 20 % of Q species.

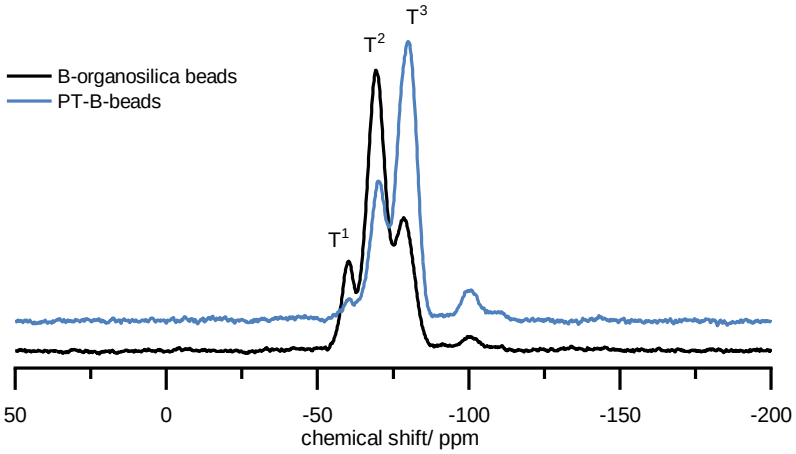

Figure 4-170: ^{29}Si-CP MAS NMR spectra (spinning speed 5 kHz) of the organosilica beads and the PT-B-beads.

During the pseudomorphic transformation process, the T signals also change. Whereas the B-organosilica beads show a significant relative amount of T^1 signals, and T^2 signals are the most prominent species, PT-B-beads contain mainly T^3 species and the T^1 species is significantly reduced. This indicates an improved condensation degree by pseudomorphic transformation, as expected, the results are in accordance with the observations from other systems after pseudomorphic transformation.

After the synthesis pathway described above, another approach was also evaluated. In this approach, PMO powder was mixed into the alginate solution together with the hydrolyzed precursor in order to optimize the mesopore size distribution and morphology separately. As the precursor blocked the mesopores of the PMO synthesized previously, this approach did not improve the results and is not be discussed here.

Here, the pseudomorphic transformation process was initially successfully adapted to a monolithic organosilica bead. Moreover, stable millimeter-sized PT-B-beads were successfully synthesized. It should be noted that, despite careful adjustment of the synthesis conditions, the quality of the material, in terms of mesophase ordering and pore diameter distribution of the mesopores, has to be further improved compared to commonly synthesized PMOs. However, the material obtained is a good basis that proves the general feasibility of this approach. In general, the synthesis procedure could be carried out with other precursors as well, although the successful separation of hydrolysis and condensation is a key challenge in this synthesis procedure. Improved hydrolysis behavior is promised by ethylene-glycol modified precursors as was described in the Introduction.[157–159]

5 Summary and Outlook

This work is subdivided into three projects, where nanoporous organosilica-based materials of different porosity and different morphologies were synthesized. In the scope of a DFG project, these different materials were intended to be used as adsorbents for the adsorption of inhalations anesthetics and toxic traces in the gas flow. The adsorption measurements were not part of this work but carried out by cooperation partners, the research group of Professor Bathen from the University Duisburg-Essen.

Organosilica powders

In the first project organosilica powders were synthesized focusing not on the morphology, but rather on the functionality and on the porosity of the materials. Materials from the precursors 1,4-Bis(triethoxysilyl)benzene (BTEB), 1,4-((*E*)-2'-Bis(triethoxysilyl)vinyl)benzene (BTEVB), 2,5-((*E*)-2'-bis(triethoxysilyl)vinyl)aniline (BTEVA), 1,4-((*E*)-2'-bis(triethoxysilyl)vinyl)-2,5-difluoro-benzene (BTEV2FB) and 2-chlor-1,4-((*E*)-2'-bis(triethoxysilyl)vinyl)benzene (BTEVClB) were synthesized. The two latter were synthesized here for the first time.
In the syntheses of F-PMO (from BTEVFB as precursor) and 2F-PMO (from BTEV2FB as precursor), the homogeneity of the product was improved by stirring under reflux conditions instead of commonly used hydrothermal treatment. The PMOs have an *apparent* specific BET surface area of 800–850 $m^2 \cdot g^{-1}$ with about 4 nm pore diameter and show crystal-like ordering on molecular scale in the pore walls next to ordered pores. The materials were characterized with argon physisorption and by water vapor sorption in order to evaluate the hydrophobic character, but the interpretation of the results was difficult in default of comparative measurements. The integrity of the organic bridges was affirmed by ^{13}C-CP-MAS NMR spectroscopy, ^{29}Si-CP-MAS NMR spectra provided information about the condensation degree of the organosilica phase and the absence of signals from Q silica species proves the stability of the Si-C bond.
The optimal conditions for PMO synthesis were found to be similar for all divinylbenzene-based precursors. However, no ordering of the pore system occurred in the case of BTEVClB, but a nanoporous material with pore diameters in the range of 2–8 nm and a specific BET surface area of 595 $m^2 \cdot g^{-1}$ was obtained. Hence, the synthesis conditions will need further optimization to obtain a Cl-PMO.

BTEB was used as representative precursor for the synthesis of high specific surface area PMOs. Under acidic conditions, a B-PMO with cubic pore symmetry in the space group $Pm\bar{3}n$ was obtained using C_{16}TAB as surfactant. In has an *apparent* specific BET surface area of 1626 $m^2 \cdot g^{-1}$

and pores of 3.5 nm in diameter (nitrogen physisorption). The synthesis was additionally carried out with C_{10}TAB, whereby a less ordered micro- and mesoporous material (0.6–4 nm pore diameter) with 1342 $m^2 \cdot g^{-1}$ of *apparent* specific BET surface area (argon physisorption) was obtained. The intention was to transfer the synthesis concept to BTEVB, BTEVFB and BTEV2FB, but no conditions were found for the synthesis of cubic mesostructures. This might be due to the lengths and rigidity of the precursors. However, nanoporous materials with specific BET surface areas between 760-900 $m^2 \cdot g^{-1}$, which are X-ray amorphous, were synthesized with these three precursors under acidic conditions.

Microporous organosilica materials were synthesized following two different synthesis routes. In syntheses at pH 12, which is a significantly lower pH value than usual for PMO synthesis, microporous materials were generated with the help of C_{10}TAB, although no micelle templating occurs. This behavior was previously noted in the literature. For B-micro an *apparent* specific BET surface area of 620 $m^2 \cdot g^{-1}$ was obtained from argon physisorption (nitrogen: 822 $m^2 \cdot g^{-1}$). The synthesis of divinylaniline-bridged and divinylbenzene-bridged microporous materials was possible following the same synthesis path. However, the *apparent* specific BET surface areas were significantly lower, with 524 $m^2 \cdot g^{-1}$ in the case of BTEVB and 397 $m^2 \cdot g^{-1}$ in the case of BTEVA. All materials prominently show the same pore diameter of 0.6 nm.
In a second approach, microporous organosilicas were obtained by treatment of the respective precursor with a solution of ethanol and sodium hydroxide solution. One of the most interesting aspects about this synthesis is the low volume of the solution, since most organosilicas are synthesized in excess aqueous solutions. A divinylbenzene-bridged material with an *apparent* specific BET surface area of 1158 $m^2 \cdot g^{-1}$ and a predominant pore diameter of 0.6 nm (according to argon physisorption) is generated. Additionally, micro- to mesoporous materials (pores below 4 nm) from BTEVFB and BTEV2FB with over 1000 $m^2 \cdot g^{-1}$ were synthesized. Syntheses with (BTEVA) as a precursor were less successful, as the micro-and mesoporous material shows an *apparent* specific BET surface area of only 553 $m^2 \cdot g^{-1}$.

Organosilica/silica hybrid materials

The second project was the synthesis of nanoporous organosilica/silica hybrid materials. In contrast to the organosilica powders in the previous project, the scale bar of the materials in this project changed to the micrometer scale. Various controlled pore glasses (CPG) granules and beads in the size rage of 40–100 µm, provided by the research group of Professor Enke from the University of Leipzig, were chosen as the silica component. It was intended to introduce uniform mesopores into the CPG by pseudomorphic transformation, a concept that is already well

established in the literature as it allows the independent optimization of the morphology and the porosity.

Since the initial pore volume and pore size both have impact on the transformation behavior, the pseudomorphic transformation was investigated comparing the results from two CPG batches with 1.5 $cm^3 \cdot g^{-1}$ of pore volume and different pore size, 52 nm or 168 nm. Partial pseudomorphic transformation was made possible either by varying the C_{16}TAOH solution (0.08 $mol \cdot L^{-1}$) volume, the transformation temperature (variation between 60–120 °C), or the transformation time (variation between one hour and four days). The variation of the transformation time was found to be the most reliable parameter to adjust the transformation degree for macroporous and mesoporous CPG batches. Stepwise decrease of the pore size was observed after pseudomorphic transformation of the macroporous CPG with initially 168 nm of pore diameter. By contrast, using a batch with pores of 52 nm in diameter, the pore diameter stayed constant and only the pore volume changed gradually. As it was also found in the literature in the meantime of this thesis, parts of the initial pore system of mesoporous samples collapses with increasing transformation degree, because of volume expansion in context of the pore generation. Hence, parts of the materials were not accessible in the transformation process. Additionally, pseudomorphic transformation under microwave radiation was tested within this thesis for the first time. It decreases the transformation time significantly: the specific BET surface area of the pseudomorphic transformed CPG after 30 minutes under microwave radiation was comparable to the product after four days under classical conditions around 850 $m^2 \cdot g^{-1}$. A key finding was that a maximum transformation degree exists for every system, e.g. after a longer transformation time, the quality of the product again decreases. There is no reliable explanation for this behavior up to now, but it could be that the equilibrium of silica dissolution and recondensation as a composite with surfactants might be disturbed as soon as the surfactant is completely used.

For the introduction of organosilica into the CPG, two different approaches were taken.

First, the behavior of the two components under alkaline conditions was intensively investigated. This includes studies of the hydrolysis and condensation behavior of BTEB in different alcoholic solutions with and without surfactant, and the etching of CPG was surveyed at different pH values and temperatures. Although conditions were found, under which B-PMO formation occurs and CPG is dissolved, it was not possible to exchange the one silica species for the other. In a competitive situation between hydrolyzed silica and organosilica, the interaction of the surfactant with silica is favored due to the higher charge density in that species. Hence, the intended exchange is improbable.

In a second approach, the organosilica species was introduced by impregnation of the CPG pore system. For this, a protocol for incipient wetness impregnation under reduced pressure was developed. Toluene-based solutions with different weight percentages between 10 wt% and 75 wt% of BTEVB or BTEVA, respectively, were used for impregnation. Afterwards, condensation of the organosilica species was initiated to immobilize it inside the CPG pore walls. After the impregnation, the formation of a nanoporous xerogel could be observed which is reasonable since the condensation solution is the same solution of ethanol and sodium hydroxide which was used for the synthesis of microporous organosilicas in the previous sections. Five CPG batches that differ in pore diameter (42–168 nm) and pore volumes (0.9–2.1 $cm^3 \cdot g^{-1}$) were systematically impregnated with BTEVB. The impregnation with BTEVA was carried out with three of these batches. The samples are denoted as 10–75BTEVB and 10-75BTEVA. The effect of the impregnation with the different organosilica-containing solutions was discussed focusing on the trend of the molar percentage of organosilica in the resulting hybrid material (calculated from mass loss in TG analysis), the *apparent* specific BET surface area, the mercury intrusion volume, the pore diameter of the initial pore system and the filling degree. In general, the molar percentage of organosilica increases with the organosilica content in the impregnation solution and with the initial pore volume of the CPG batch. Both trends are in accordance with the expectations since the volume of the impregnation solution increases with the initial pore volume of the CPG batch. It was found that the initial pore volume is an even more important aspect than the organosilica content in the impregnation solution for the resulting molar percentage of organosilica in the hybrid material. The highest molar percentage of DVB-organosilica of 21 % is given for 75BTEB from a macroporous (148 nm) CPG batch with the highest pore volume (2.10 $cm^3 \cdot g^{-1}$), whereas it is only 9 mol% in the case of 75BTEVB from a CPG batch with 0.9 $cm^3 \cdot g^{-1}$ and 42 nm pore size.

Due to the formation of nanoporous Xerogels, the *apparent* specific BET surface area increases in a linear way with increasing molar percentage of organosilica up to 767 $m^2 \cdot g^{-1}$ in the sample with 21 mol% of organosilica as the highest value for all samples. It was of particular interest whether the *apparent* specific BET surface area is also affected by the initial pore size or the pore volume of the respective CPG batch. It was assumed that the formation of meso- and macropores during the condensation process is associated with spatial extension of the organosilica phase which might be limited in smaller pore volumes, but no evidence was found for such a correlation. This can be shown by comparison of the samples with the same pore volume of 1.5 $cm^3 \cdot g^{-1}$ and different pore diameter of 52 nm and 168 nm. Only slightly higher values were found for samples 10–50 BTEVB from the batch with larger pores, e.g. 447 $m^2 \cdot g^{-1}$

and 476 $m^2 \cdot g^{-1}$ in the case of 50 BTEVB, respectively. Hence, in the discussed samples the *apparent* specific BET surface area is mainly affected by the DVB-organosilica content.

It was further found that the pore diameter of macroporous samples decreases stepwise within the series of increasing organosilica content, but this trend was limited dependent on the initial pore diameter and the initial pore volume. CPG batch which combines a large pore diameter (120 nm) with comparable low pore volume (1.15 $cm^3 \cdot g^{-1}$) showed the highest filling degrees up to 70 % for 75BTEVB. In this case the initial pore size was stepwise decreased to 40 nm. By contrast, in small pores combined with low pore volume (e.g. 0.9 $cm^3 \cdot g^{-1}$, 42 nm) the pore diameter distribution (according to MIP) does not change significantly, but the pore volume decreases stepwise in an impregnation series, e.g. from 0.9 $cm^3 \cdot g^{-1}$ to 0.3 $cm^3 \cdot g^{-1}$ in 75BTEVB. Apparently, the organosilica does not form a homogeneous layer inside the pores but rather blocks some of the pores completely. Generally spoken, large pores seem to improve the penetration of the impregnation solution and the formation of nanoporous organosilica layer inside the initial pore system. In the case of the CPG batch with 1.5 $cm^3 \cdot g^{-1}$ pore volume and 52 nm pore diameter, multiple impregnation with a solution of lower organosilica content, e.g. 2x10BTEVB or 3x10BTEVB was compared to the impregnation with high content of organosilica, e.g. 25BTEVB in the impregnation solution. The pore diameter was similar for all three samples between 44–41 nm (according to MIP) which indicates that the multiple impregnation approach does not improve the impregnation process.

Comparing the samples with BTEVB and BTEVA from the three CPG batches that were impregnated with both precursors, the BTEVA samples show in general lower specific BET surface areas than the respective BTEVB samples. To give an example, the *apparent* BET surface area of 50BTEVB was 447 $m^2 \cdot g^{-1}$, but only 301 $m^2 \cdot g^{-1}$ in the case of 50BTEVA, both from the CPG batch with 52 nm pore diameter 1.5 $cm^3 \cdot g^{-1}$. Additionally, the formation of organosilica phases on the outside of the CPGs is observed as a side effect in some samples, probably due to premature condensation of the organosilica phase. Hence, it is assumed that the given conditions are less-than-ideal for the formation of a nanoporous DVA-organosilica phase.

50BTEVB from CPG batch with 1.5 $cm^3 \cdot g^{-1}$ and 168 nm pore diameter was characterized more intensively. TEM images show a rough surface of the pore walls which indicates that an organosilica layer is formed within the CPG pores. ^{13}C-CP MAS NMR confirmed the integrity of the bridging unit in BTEVB, ^{29}Si-CP MAS NMR provides semi-quantitative information about the ratio of Q and T silica species and the condensation degree in the sample. Direct excitation ^{29}Si-MAS NMR was used to precisely evaluate the molar percentage of organosilica, which is 16 mol%. The results differ from the results which were obtained by TG analysis. This gap between the values from TG analysis and quantitative ^{29}Si-MAS NMR might be due to

erroneousness presumption or caused by the margin of errors of the two methods. However, TG analysis was found to be a reliable method to quantify the organosilica content in the hybrid materials.

Overall, the incipient wetness impregnation of the pore system in CPGs was found as a suitable approach for the synthesis of hierarchically porous organosilica/silica hybrid materials with an accessible organosilica phase and with adjustable organosilica content.

Pseudomorphic transformation of organosilica/silica hybrid materials based on CPGs

Subsequent to the impregnation, pseudomorphic transformation of the organosilica/silica hybrid materials was intended for the introduction of a second pore system of homogeneous mesopores.

In preparation, the behavior of the microporous material from BTEVB, which was synthesized in the presents of ethanol and sodium hydroxide solution, in an alkaline surfactant-containing solutions was investigated. Since the morphology of the microporous material was undefined, the transformation process was evaluated only with respect to the porosity features and the formation of mesopores was taken as successful transformation. Transformations under different conditions were compared, but no significant differences were found. Hence, the transformation of the organosilica/silica hybrid materials were carried out in C_{16}TAOH solution for as in the pseudomorphic transformation of pure CPG.

The pseudomorphic transformation was investigated with a selection of BTEVA and BTEVB organosilica/silica hybrid materials with different pore diameters. In the case of CPG starting materials with comparably small initial pores (1.5 $cm^3 \cdot g^{-1}$ of initial pore volume, 52 nm initial pore size), the transformation results in two pore systems which can both be characterized by nitrogen physisorption, a non-destructive method in contrast to mercury intrusion porosimetry. By pseudomorphic transformation with C_{16}TAOH of all organosilica/silica hybrid materials, pores around 4 nm and specific BET surface areas up to 940 $m^2 \cdot g^{-1}$ were obtained. However, it was shown before for the pseudomorphic transformation of the pure CPG that small initial pores collapse during the transformation process, so that no hierarchical pore system can be formed. Hence, the accessibility of the organosilica phase might even be hindered after the transformation.

By contrast, in the case of large initial pores (e.g. 168 nm, 1.5 $cm^3 \cdot g^{-1}$ intrusion volume) the formation of a hierarchically pore system was assumed. It could be shown that stepwise reduction of the pore diameter to 110 nm and 100 nm and the pore volume (0.52 $m^3 \cdot g^{-1}$ and 0.43 $m^3 \cdot g^{-1}$) is possible with changed transformation time from four days and six hours in the example of 50BTEVB, obtaining materials with S_{BET} up to 1000 $m^2 \cdot g^{-1}$. Hence, the resulting size of

the macropores in organosilica/silica hybrid materials can be adjusted by the organosilica content and by the transformation degree. Further, it was shown that the diameter of the newly formed mesopores can be adjusted by the alkyl-chain length of the surfactant. As a side effect, less swelling of the material occurs using C_{10}TAB than it is the case for C_{16}TAOH, with a pore diameter of 127 nm for 50BTEVB. This could be reproduced with the transformation of 50BTEVA with the different surfactants as well.

The transformation process was investigated in detail with the sample 50BTEVB (CPG batch 1.5 $cm^3 \cdot g^{-1}$ and 168 nm pore diameter). Two main questions were discussed: The first involves the quantification of organosilica in the DVB-organosilica/silica hybrid material after pseudomorphic transformation. For the quantification of the organosilica content by TG measurements, the extraction of the surfactant was a general problem in the hybrid materials after transformation. Extraction in ethanol under reflux appears to be more efficient than the commonly used extraction with a Soxhlet apparatus. However, TG/MS measurements show higher mass loss after the transformation than before, which could be due to incomplete extraction of the surfactant or loss of the silica phase during the transformation process. However, quantification of organosilica in the hybrid material was impossible with this method. ^{13}C-CP-MAS NMR experiments of 50BTEVB confirmed the complete removal of the surfactant after transformation. In addition, quantitative ^{29}Si-MAS NMR was used the quantification of the organosilica/silica ratio. According to the amount of T silica species, the molar ratio decreases from 16 mol% to 8.1 mol% after pseudomorphic transformation of the hybrid material. The combination of TG/MS and different solid-state NMR measurements suggests the assumption that cleavage of the Si-C bond occurs. Since a hybrid material is discussed, no information are provided to quantify the cleavage. Hence, this needs further investigations in follow-on works.

The second question was whether the pseudomorphic transformation affects the pore system of the organosilica or the silica species or both. Further, it was to investigate whether a PMO layer is formed on a mesoporous CPG layer or if the product is a randomly mixed material.

In 2D-FSLG-HETCOR ^{29}Si{^{1}H} and ^{13}C{^{1}H}-NMR measurements, interactions of the surfactant with the silica and the organosilica species were observed which suggest the micelle templating of both phases. After the pseudomorphic transformation, mesoporous structures composed of random mixture of T and Q species via formation of Si(Q)–O–Si(T) bonds are assumed. The measurements do not provide information weather this is caused by the formation of Q silica species in the originally organosilica species, due to Si-C bond breaking, or by migration of the organosilica species insight the silica phase during the transformation process.

This work set the course for the impregnation as potential path for the synthesis of hierarchically porous organosilica/silica hybrid materials by impregnation and for the pseudomorphic

transformation of these materials. The focus in follow-on works needs to be on the investigation of completely non-destructive pseudomorphic transformation of different organosilica species. Maybe the results on pseudomorphic transformation of CPG at lower temperatures and under microwave radiations give beneficial input for this process.

Organosilica/silica hybrid materials based on CPG membranes

After CPG beads and granules, CPG membranes of 2.5x2.5 cm with 0.16 $cm^3 \cdot g^{-1}$ mercury intrusion volume and macropores of 99 nm were used as a starting material for the pseudomorphic transformation. A maximal specific BET surface area of 589 $m^2 \cdot g^{-1}$ was obtained after four days of treatment with C_{16}TAOH. After transformation the membranes show only slight curvature and are mechanically less stable. Due to the low initial pore volume the macropore system was not investigated with MIP. The CPG membranes were impregnated as well, but unlike for the CPG beads and granules, with BTEVB and toluene-based BTEVB solution via capillary forces instead of incipient wetness impregnation. In contrast to the condensation in the impregnated CPG beads, the condensation of the precursor in the pores of the membrane process took place in acidic media, because the presence of ethanol led to leaching of the organosilica phase. The differences in the behavior of CPG beads and membranes might be caused by the different ratio of inner to outer specific surface area. The pseudomorphic transformation of the impregnated CPG membranes was successful for low organosilica content in the hybrid membrane. In contrast, no spatial extension is possible in the case of high organosilica content due to the low pore volume in the impregnated samples. This limits the transformation process. Hence, this approach shows that the established concept allows the synthesis of organosilica/silica hybrid materials which are flexible tunable for different applications in terms of the morphology, just as the pure CPGs.

Alginate hydrogel as form-giving matrix for millimeter-sized (organo)silica beads

In the last project, silica and organosilica beads of 2 mm in diameter were synthesized in a multistep synthesis path. The synthesis of these beads was possible with the help of alginate, a biopolymer that forms a hydrogel in contact with calcium ions.

In the case of the silica beads (from TEOS as precursor), a specific surface area of 716 $m^2 \cdot g^{-1}$ and pores with broadly distributed diameter were obtained after the removal of alginate by calcination. By pseudomorphic transformation of the beads, narrower pores around 4 nm were generated, leading to a specific BET surface area of up to 767 $m^2 \cdot g^{-1}$. The mercury intrusion volume shrunk from 0.5 $cm \cdot g^{-1}$ to 0.3 $cm \cdot g^{-1}$ during the pseudomorphic transformation process

for four days, but pores at the boundary between meso- and macropores of 49 nm were also generated. The morphology of the beads remained intact.

In the case of B-organosilica beads (from BTEB as precursor), the hydrogel was removed by complexation of the Ca^{2+} ions with citric acid. The respective B-organosilica beads show a specific BET surface area of 699 $m^2 \cdot g^{-1}$ with micro– to mesopores. The intrusion volume is rather low, at 0.26 $cm^3 \cdot g^{-1}$. Again from pseudomorphic transformation, a mesoporous system with maximum diameter at 3.7 nm and 731 $m^2 \cdot g^{-1}$ of specific BET surface area, was obtained. Crystal-like ordering of the benzene bridge was detectable by P-XRD, and the material shows one broad reflection in the small angle region, which indicates a slight ordering of the pore system. Due to this the product was not designated a PMO. ^{13}C-CP-MAS NMR assigned the integrity of the bridging unit. Further, ^{29}Si-CP-MAS NMR measurements show almost only signals of T silica species. A low percentage of Q signals, which increases after the pseudomorphic transformation, was also found, which indicates cleavage of a small percentage of the Si-C bond during the transformation process.

For follow-on research in this field, the synthesis path could be performed using other bis-silylated precursors. In addition, the form-giving feature of alginate hydrogel also allows the synthesis of different monoliths using a template, e.g. a vessel.

6 Zusammenfassung der Ergebnisse und Ausblick

In drei unterschiedlichen Projekten wurden poröse Organosilicas hergestellt, die sich in ihrer Porosität und ihrer Morphologie unterscheiden. Im Rahmen einer DFG-geförderten Kooperation wurden diese als potentielle Adsorbentien für die Adsorption von Inhalationsanästhetika und toxischen Spurengasen behandelte. Die dafür von der Arbeitsgruppe um Professor Bathen von der Universität Duisburg-Essen durchgeführten Messungen sind nicht Teil dieser Arbeit.

Organosilica-Pulver

Im ersten Projekt wurden Organosilicas mit unterschiedlichen chemischen Funktionalitäten und Porositätseigenschaften dargestellt, wobei die Morphologie zunächst keine Rolle spielte. Als Vorläuferverbindungen wurden 1,4-Bis(triethoxysilyl)benzol (BTEB), 1,4-((*E*)-2'-Bis(triethoxysilyl)vinyl)benzol (BTEVB), 2,5-((*E*)-2'-Bis(triethoxysilyl)vinyl)anilin (BTEVA), 1,4-((*E*)-2'-bis(triethoxysilyl)vinyl)-2,5-difluorobenzol (BTEV2FB) und 2-chlor-1,4-((*E*)-2'-bis(triethoxysilyl)vinyl)-benzol (BTEVClB) verwendet, wobei die beiden letztgenannten Verbindungen hier erstmalig dargestellt wurden.

Obwohl PMOs in den meisten Fällen in statischen Hydrothermalsynthesen dargestellt werden, konnten im Rahmen dieser Arbeit F-PMOs (ausgehend von BTEVFB) und 2F-PMO (ausgehend von BTEV2FB) bei Synthesebedingungen unter Rückfluss erhalten werden, wobei ständiges Rühren der Reaktionslösung die Homogenität der Lösung verbesserte. Die PMOs wiesen eine spezifische BET-Oberfläche von 800–850 $m^2 \cdot g^{-1}$ und Poren mit einem Durchmesser um 4 nm auf. Sie zeigten neben geordneten Poren auch pseudokristalline Ordnung auf molekularer Ebene in den Porenwänden. Um den hydrophoben Charakter der Materialien zu untersuchen, wurden Wasserdampfsorptionsmessungen durchgeführt, wobei sich die Interpretation der Ergebnisse in Ermangelung an geeigneten Vergleichsmaterialien als schwierig erwies. Die Integrität der organischen Brücke ließ sich für beide Materialien mithilfe von ^{13}C-CP-MAS NMR bestätigen. ^{29}Si-CP-MAS-NMR Spektren gaben nicht nur Auskunft über den Kondensationsgrad der Materialien, sondern konnten auch die Stabilität der Si-C Bindung durch die Abwesenheit von Signalen der Q-Siliziumspezien bestätigen.

Ein Vergleich der Synthesen von PMOs mit Divinylbenzolderivaten zeigt, dass sie alle unter ähnlichen Bedingungen hergestellt werden konnten. Für die Umsetzung von BTEVClB konnten allerdings keine geeigneten Bedingungen gefunden werden, unter denen sich ein geordnetes Porensystem erhalten ließ. Es wurde lediglich ein nanoporöses Material mit Porendurchmessern im Bereich von 2–8 nm und einer spezifischen BET-Oberfläche von 595 $m^2 \cdot g^{-1}$ erhalten. Eine

Optimierung der Synthese ist für die Darstellung eines Cl-PMOs also in anschließenden Arbeiten noch notwendig.

Mit dem Ziel PMOs mit besonders hoher spezifischer Oberfläche zu erhalten, wurde BTEB im sauren Milieu mit dem Tensid C_{16}TAB umgesetzt. Dabei wurde ein B-PMO mit kubischer Porensymmetrie der Raumgruppe $Pm\bar{3}n$ hergestellt, welcher eine spezifische BET-Oberfläche von 1626 $m^2 \cdot g^{-1}$ (Stickstoffphysisorption) und Porendurchmesser von 3.5 nm aufweist. Die Umsetzung mit C_{10}TAB führte hingegen zu einem mikro- und mesoporösen Material (Porendurchmesser 0.6–4 nm) mit einer spezifischen BET-analogen Oberfläche von 1342 $m^2 \cdot g^{-1}$ (Argonphysisorption). Eine analoge Umsetzung von BTEVB, BTEVFB und BTEV2FB führte zu nanoporösen Materialien mit spezifischen BET-Oberflächen von 760–900 $m^2 \cdot g^{-1}$, welche sich allerdings röntgenamorph zeigten. Die Bildung eine kubische Porensymmetriebei könnte aufgrund der Länge und Unbeweglichkeit bei diesen Vorläuferverbindungen gehindert sein.
Auf zwei unterschiedlichen Synthesewegen wurden mikroporöse Organosilicas hergestellt. Bei pH 12, was deutlich geringer ist, als für PMO-Synthesen üblich, konnten mikroporöse Materialien in Gegenwart von C_{10}TAB erhalten werden, wie es bereits in der Literatur beschrieben wurde, obwohl keine mizellare Templatisierung stattfand. Das so erhaltene B-micro zeigte eine spezifische BET-analoge Oberfläche von 620 $m^2 \cdot g^{-1}$ (Argonphysisorption). Bei der Umsetzung von BTEVB und BTEVA wurden deutlich geringere spezifische BET-Oberflächen erzielt, aber alle Materialien zeigten Poren von 0.6 nm Durchmesser. In einem neuen Ansatz, wurden die Vorläuferverbindungen mit einem Gemisch von Ethanol und einer Natriumhydroxid-Lösung behandelt, wobei das Volumen der Lösung deutlich geringer war, als in anderen Organosilica-Synthesen, welche in der Regel mit einem deutlichen Lösungsmittelüberschuss stattfinden. Ausgehend von BTEVB wurde ein Material mit einer spezifischen BET-analogen Oberfläche von 1158 $m^2 \cdot g^{-1}$ hergestellt und auch mikro-/mesoporöse F-DVB und 2F-DVB-Materialien mit Poren kleiner 4 nm und spezifischen BET-analogen Oberflächen über 1000 $m^2 \cdot g^{-1}$ konnten erhalten werden. Die Umsetzung von BTEVA war hingegen weniger erfolgreich und es konnte ein mikro-und mesoporöses Material mit nur 553 $m^2 \cdot g^{-1}$ spezifischer BET-analoger Oberfläche erreicht werden.

Organosilica/Silica-Hybridmaterialien auf Basis von CPG Granulaten

Im zweiten Projekt wurden Organosilica/Silica-Hybridmaterialien hergestellt. Als Silicakomponente wurde dazu von der Arbeitsgruppe um Professor Enke von der Universität Leipzig poröse Gläser (CPG) in Form von Granulat oder sphärischen Partikeln in der

Größenordnung von 40–100 µm zur Verfügung gestellt. Um ein geordnetes Mesoporensystem in diese Materialien einzubringen, sollte der post-synthetische Ansatz der pseudomorphen Transformation angewandt werden. Dieser Ansatz erlaubt es, die Porosität und die Morphologie des Materials unabhängig voneinander zu optimieren. Da die Porengröße und das Porenvolumen Einfluss auf das Transformationsverhalten der CPG haben, wurden zunächst zwei CPG-Chargen mit unterschiedlichem Porendurchmesser, 168 nm und 52 nm, und gleichem Porenvolumen von 1.5 $cm^3 \cdot g^{-1}$ untersucht. Partielle pseudomorphe Transformation war über die Variation des verwendeten Volumens der C_{16}TAOH-Lösung (0.08 $mol \cdot L^{-1}$), die Transformationsdauer und die Temperatur möglich. Dabei stellte sich die Transformationsdauer als der verlässlichste Parameter heraus, um die Transformationsgrad einzustellen. Im Falle der makroporösen CPGs mit 168 nm Ausgangsporengröße konnte die Porengröße und das Porenvolumen stufenweise verringert werden. Im Falle der kleineren Poren (52 nm) hingegen, sank lediglich das Porenvolumen sukzessive mit zunehmender Transformationsdauer und der Porendurchmesser blieb unverändert. Wie zwischenzeitlich auch in der Literatur beschrieben wurde, brach in diesem Fall das ursprüngliche Porensystem durch die Materialausdehnung während der Porenbildung teilweise zusammen, sodass Teile der Probe gar nicht von der mizellaren Templatisierung erreicht wurden.

Innerhalb dieser Arbeit wurde erstmalig die pseudomorphe Transformation in der Mikrowelle getestet, was die Transformationszeit signifikant verkürzte. Nach 30 Minuten wurde ein Material mit einer spezifischen BET-Oberfläche um 850 $m^2 \cdot g^{-1}$ erhalten, was vergleichbar mit dem Ergebnis nach vier Tagen unter klassischen Bedingungen ist. Es konnte herausgefunden werden, dass es einen maximalen Transformationsgrad für jedes System gibt und dass die Qualität der Produkte nach weiterer Verlängerung der Transformationszeit wieder abnimmt. Bislang ließ sich dafür keine Erklärung finden, aber es ist durchaus möglich, dass das Gleichgewicht von Lösen der Silicaquelle und seiner Rekondensation als Silica/Tensid-Komposit gestört wird, sobald sämtliches Tensid im Komposit eingebunden ist.

Um Organosilica in die CPGs einzubringen, wurden zwei Ansätze verfolgt. Im ersten Ansatz wurde versucht, während der pseudomorphen Transformation Silica gegen Organosilica auszutauschen. Dazu wurde zum einen das Hydrolyse- und Kondensationsverhalten von BTEB in unterschiedlichen alkalischen, alkoholischen Lösungen systematisch betrachtet. Zum anderen wurde die Löslichkeit der CPGs bei unterschiedlichen Temperaturen und pH-Werten untersucht. Obwohl Bedingungen gefunden werden konnten unter denen ein B-PMO hergestellt und das CPG aufgelöst werden können, war es nicht möglich diese beiden Prozesse zu verbinden und die Silicaspezies gegen Organosilica auszutauschen. Aufgrund der höheren Ladungsdichte ist die

Umsetzung eines Tensides mit einer hydrolysierten Silicaspezies gegenüber einer Organosilicaspezies bevorzugt, was einen Austausch sehr unwahrscheinlich macht.

Im zweiten Ansatz wurde die Organosilicaspezies durch Imprägnierung des CPG Porensystems eingebracht. Dazu wurde eine *incipient wetness*-Imprägnierung unter vermindertem Druck entwickelt, bei der das CPG Porensystem mit Toluol-basierte Lösungen, die zwischen 10–75 Gewichtsprozent BTEVB oder BTEVA enthielten, imprägniert wurde. Anschließend wurde die Kondensation der Organosilicaspezies ausgelöst, sodass sie an den CPG-Porenwänden immobilisiert wurden. Dabei konnte die Bildung eines mikro- und mesoporösen Xerogels beobachtet werden, was zu einem Anstieg der spezifischen BET-Oberfläche führte. Für die Kondensation wurde die gleiche Lösung aus Ethanol und Natriumhydroxid-Lösung verwendet, die bereits für die Darstellung von mikroporösen Organosilicas Verwendung fand. Fünf CPG-Chargen, die sich in Porengröße (42–168 nm) und Porenvolumen (0.9–2.1 $cm^3 \cdot g^{-1}$) voneinander unterscheiden, wurden systematisch mit unterschiedlichen BTEVB-haltigen Lösung imprägniert und ihr unterschiedliches Imprägnierungsverhalten diskutiert. Drei Chargen wurden außerdem mit BTEVA-haltigen Lösungen imprägniert. Die resultierenden Proben werden mit 10–75BTEVB beziehungsweise 10–75BTEVA benannt. Die Imprägnierungen wurden anhand des molaren Anteils an Organosilica (bestimmt über den Massenverlust der TG-Analysen), die spezifische BET-analoge Oberfläche und Parametern der Quecksilberporosimetrie, nämlich dem Porendurchmesser, dem Porenvolumen und dem Füllgrad diskutiert. Es zeigte sich, dass der molare Anteil von Organosilica und die spezifische BET(-analoge) Oberfläche innerhalb einer CPG-Charge mit steigendem Anteil von Organosilica in der Imprägnierlösung stieg. Bei Vergleich unterschiedlicher CPGs stiegen diese Parameter mit dem ursprünglichen Porenvolumen und es konnte gezeigt werden, dass das ursprüngliche Porenvolumen einen wichtigeren Einfluss auf den molaren Anteil von Organosilica im Produkt hat, als der Anteil in der Imprägnierlösung. Da das Lösungsvolumen, dass für die Imprägnierung verwendet wurde, dem ursprünglichen Porenvolumen entsprach, treffen diese Trends die Erwartungen. Der höchste Anteil von Organosilica mit 21 mol% konnte für 75BTEVB in einer CPG-Charge mit dem höchsten Porenvolumen (2.1 $m^3 \cdot g^{-1}$) und 148 nm Porendurchmesser erhalten werden. In 75BTEVB einer CPG-Charge mit 0.9 $cm^3 \cdot g^{-1}$ Porenvolumen und 42 nm Porendurchmesser konnten maximal 9 mol% Organosilica eingebracht werden. Aufgrund der genannten Xerogel-Bildung stieg die spezifische BET-analoge Oberfläche bis auf 767 $m^2 \cdot g^{-1}$ in der genannten Probe mit 21 mol% BTEVB als höchster Wert aller Proben. Da die Porenbildung im Kondensationsprozess mit einer Ausdehnung des Materials einhergeht, wurden Limitierungen im Falle eines geringeren Platzangebotes vermutet. Es war daher von besonderem Interesse, ob die resultierende spezifische BET-Oberfläche von dem ursprünglichen Porenvolumen oder der Porengröße

beeinflusst wurde. Dies war jedoch nicht der Fall und es ergab sich eine lineare Abhängigkeit der spezifischen BET-Oberfläche vom molaren Anteil an Organosilica im Hybridmaterial. Dies konnte am Bestem durch den Vergleich von zwei Chargen mit gleichem Porenvolumen von 1.5 $cm^3 \cdot g^{-1}$ und unterschiedlicher Porengröße, 52 nm und 168 nm, nachvollzogen werden. Dabei wurden nur geringfügig höhere Werte bei großen Ausgangsporen festgestellt, am Beispiel von 50BTEVB der beiden Proben wurden BET-analoge spezifische Oberflächen von 447 $m^2 \cdot g^{-1}$ und 476 $m^2 \cdot g^{-1}$ erhalten.

Im Falle der makroporösen Proben nahm die Porengröße mit zunehmendem Anteil von Organosilica in der Imprägnierlösung bis zu einem gewissen Ausgangsdurchmesser und Ausgangsporenvolumen schrittweise ab. Der mit Abstand höchste Füllgrad von 70 % konnte aber in 75BTEVB einer CPG-Charge mit großem Porendurchmesser (120 nm) und geringem Porenvolumen (1.15 $cm^3 \cdot g^{-1}$) erhalten werden, wobei der Porendurchmesser deutlich auf 40 nm abnahm. Im Gegensatz dazu ändert sich bei geringer Porengröße und –Porenvolumen, die mittel Quecksilberporosimetrie bestimmte Porengröße nicht und nur das Porenvolumen sankt deutlich, im Beispiel von 0.9 $cm^3 \cdot g^{-1}$ Ausgangsporenvolumen auf 0.3 $cm^3 \cdot g^{-1}$ für 75BTEVB. Dies zeigt, dass generell in große Poren das Eindringen der Imprägnierlösung und die Bildung einer gleichmäßigen nanoporösen Organosilicaschicht besser möglich ist. Eine verbesserte Imprägnierung sollte durch Mehrfachimprägnierung mit geringerem Anteil von Organosilica in der Imprägnierlösung am Beispiel der CPG-Charge mit 1.5 $cm^3 \cdot g^{-1}$ Porenvolumen und 52 nm Porengröße untersucht werden. Im Vergleich konnten für die Proben 2x10BTEVB und 2x10BTEVB und die Imprägnierung mit höheren Anteil von Organosilica in der Lösung, 25BTEVB, ähnliche Porendurchmesser von 44–41 nm mittels Quecksilberporosimetrie bestimmt werden, sodass hier kleine verbesserte Imprägnierung möglich war.

Im Vergleich der Imprägnierungen mit BTEVB und BTEVA ergibt sich für die Proben mit BTEVA generell eine geringere spezifische BET-Oberfläche. So ist die spezifische BET-analoge Oberfläche von 50BTEVB 447 $m^2 \cdot g^{-1}$, für 50BTEVA ist es nur 301 $m^2 \cdot g^{-1}$ ausgehend von der selben CPG-Charge (52 nm und 1.5 $m^3 \cdot g^{-1}$). Der Anteil von Organosilica im Produkt ist insgesamt aber für beide Vorläuferverbindungen ähnlich. Außerdem wurde in diesen Proben häufiger die Bildung einer Nebenphase auf der CPG Oberfläche entdeckt, die auf eine vorzeitige Kondensation er Organosilica-Phase zurückgeführt wurde. Es wird davon ausgegangen, dass die hier gewählten Synthesebedingungen für die Bildung eines nanoporösen Organosilicas ausgehend von BTEVA weniger geeignet sind.

Die Probe 50BTEVB einer CPG-Charge (1.5 $cm^3 \cdot g^{-1}$ Porenvolumen und 168 nm Porengröße) wurde exemplarisch weitergehend charakterisiert. In TEM Aufnahmen konnte nach Imprägnierung eine deutlich rauere Oberfläche der Porenwand beobachtet werden, als es für

das pure CPG der Fall war, was auf die Bildung einer Organosilicaschicht an der Porenwand hindeutet. Die ^{13}C-CP MAS NMR Spektroskopie konnte verwendet werden, um die Integrität der organischen Brücke des BTEVB im Hybridmaterial zu bestätigen. Das ^{29}Si-CP MAS NMR Spektrum zeigte erwartungsgemäß Q und T Signale und konnte zur semi-quantitativen Bewertung des Kondensationsgrads der Organosilicaphase verwendet werden. ^{29}Si-Festkörper NMR-Messungen mit direkter Anregung erlaubten die genaue Bestimmung des molaren Anteils von Organosilica im Hybridmaterial von 16 mol%. Es ergab sich eine Abweichung der Werte von Festkörper-NMR und TG-Analytik, was auf Abweichungen von getroffenen Annahmen für die Methoden, beziehungsweise den Fehlertoleranzbereich der Methoden zurückzuführen ist, so dass TG-Analysen weiterhin für die Quantifizierung des Anteils von Organosilica der imprägnierten Proben verwendet wurde. Insgesamt erlaubt die Imprägnierung von CPGs mit verschiedenen Organosilicaverbindungen die Darstellung hierarchisch poröser Organosilica/Silica-Hybridmaterialien mit variablem Anteil von Organosilica, in denen die Organosilicaphase gut zugänglich ist.

Pseudomorphe Transformation der Organosilica/Silica-Hybridmaterialien

Der Imprägnierung schloss sich eine pseudomorphe Transformation an, über die ein zweites, homogenes Mesoporensystem eingebracht werden sollte.
Vorbereitend dazu wurde zunächst das Verhalten des mikroporösen BTEVB-basierten Organosilicas, was in Gegenwart von Ethanol und Natriumhydroxid-Lösung hergestellt wurde, in alkalischer Tensidlösung untersucht. Da die Morphologie des mikroporösen Materials nicht definiert war, wurden lediglich die Porositätseigenschaften als Grundlage zur Bewertung der Transformation genommen. Da die Transformationen bei unterschiedlichen pH-Werten keine nennenswerten Unterschiede ergaben, wurde die C_{16}TAOH-Lösung der pseudomorphen Transformation von CPGs auch für die pseudomorphe Transformation der Organosilica/Silica-Hybridmaterialien verwendet.

Die pseudomorphe Transformation wurde mit einer Auswahl der über Imprägnierung hergestellten Organosilica/Silica-Hybridmaterialien durchgeführt. Im Falle der CPGs mit kleinen Ausgangsporen (52 nm, 1.5 $cm^3 \cdot g^{-1}$ Ausgangsporenvolumen) entstehen durch die Transformation zwei Porensysteme die gemeinsam mithilfe der Stickstoffphysisorption charakterisiert werden können. Dies ist von Vorteil, da die Probe bei dieser Methode, im Gegensatz zur Quecksilberporosimetrie, nicht zerstört wird. In einer klassischen pseudomorphen Transformation mit C_{16}TAOH entstand in allen Organosilica/Silica-Hybridmaterialien Mesoporen um 4 nm. Dabei wird in 50BTEVB aus dieser CPG-Charge eine

spezifische BET-Oberfläche von 943 $m^2 \cdot g^{-1}$ erzeug. Da aber, wie bereits erwähnt, das ursprüngliche Porensystem während der Transformation zusammenbricht, kann keine hierarchische Porenstruktur erzeugt werden und es kann davon ausgegangen werden, dass die Zugänglichkeit der Organosilicaphase sogar behindert wird. Ausgehend von CPG-Chargen mit größeren Makroporen, kann von der Bildung eines hierarchischen Porensystems ausgegangen werden. Am Beispiel von 50BTEVB der CPG-Charge mit 1.5 $m^3 \cdot g^{-1}$ ursprüngliches Porenvolumen und 168 nm Porendurchmesser wurden nach pseudomorpher Transformation Materialien mit bis zu 1000 $m^2 \cdot g^{-1}$ spezifischer BET-Oberfläche erhalten. Es konnte gezeigt werden, dass eine schrittweise Verkleinerung des Porendurchmessers auf 110 nm, bzw. 100 nm und des Makroporenvolumens auf 0.52 $m^3 \cdot g^{-1}$ und 0.43 $m^3 \cdot g^{-1}$ durch veränderte Transformationszeit von sechs Stunden und vier Tagen möglich ist. Damit ist die Größe der resultierenden Makropore über die Dicke der Organosilicaschicht und über den Transformationsgrad einstellbar. Außerdem konnte gezeigt werden, dass unter Verwendung eines Tensides mit kürzerer aliphatischen Kettenlänge, wie C_{10}TAB, auch die Größe der Mesoporen einstellbar ist. Unter Verwendung des kleineren Tensides resultiert ein größerer Makroporendurchmesser von 127 nm, sodass sich offenbar eine geringere Schwellung der Porenwand einstellen lässt. Dieses Verhalten ergab sich ebenfalls bei der Transformation der Probe 50BTEVA mit den unterschiedlichen Tensiden.

Der Transformationsprozess wurde am Beispiel von 50BTEVB (Ausgangsporenvolumen 1.5 $cm^3 \cdot g^{-1}$ und 168 nm Porengröße) noch detaillierter betrachtet, wobei der Fokus auf zwei Fragestellungen lag. Zunächst war der Anteil von Organosilica im Hybridmaterial nach der pseudomorphen Transformation zu quantifizieren. Reste des Tensides im Hybridmaterial konnten durch Extraktion unter Rückfluss anstelle von Soxhlet-Extrationen verringert werden, stellten aber ein generelles Problem für die Quantifizierung über TG Messungen dar und es ergaben sich nach der pseudomorphen Transformation teilweise höhere Massenverluste als vorher. Dies könnte auch auf ein Herauslösen von Silica während der Transformation zurückzuführen sein. TG Messungen waren daher für die Quantifizierung des Anteils von Organosilica nicht geeignet. Für 50BTEVB ließ sich die vollständige Extraktion des Tensides exemplarisch über ^{13}C-CP MAS NMR bestätigen, außerdem ermöglichten quantitative ^{29}Si-MAS NMR die Quantifizierung des Verhältnisses von Organosilica zu Silica im Hybridmaterial. Es stellte sich heraus, dass sich der Anteil von Organosilica nach der pseudomorphen Transformation von 16 mol% auf 8.1 mol% verringerte. Da der Massenverlust der TG-Messung aber höher war, als vor der Transformation, muss angenommen werden, dass Bindungsbrüche der Si-C Bindung zu einem erhöhten Anteil an Q-Signalen geführt haben. In einem

Hybridmaterial, welches Q- und T-Signale aufweist, ist der Anteil der Bindungsbrüche jedoch kaum quantifizierbar. In weiterführenden Arbeiten ist dieser Aspekt weiter zu untersuchen.
In der zweiten Fragestellung war zu klären, ob bei der pseudomorphen Transformation die Organosilicaphase, die Silicaphase oder beide Phasen transformiert werden und ob sich eine PMO-Schicht auf einer mesoporösen Silicaschicht bildet oder ob die beiden Phasen co-kondensiert vorliegen. In 2D FSLG HETCOR $^{29}Si\{^{1}H\}$-NMR und $^{13}C\{^{1}H\}$-NMR konnten Wechselwirkungen des Tensides mit beiden Phasen beobachtet werden, was bedeutet, dass eine mizellare Templatisierung beider Phasen erfolgte. Es ließ sich außerdem nachvollziehen, dass nach der Transformation T und Q Signale in Mischung vorliegen, wobei Si(Q)–O–Si(T) Bindungen angenommen werden. Es lässt sich allerdings nicht sagen, ob und in welchem Ausmaß dies durch Si-C Bindungsbrüche, die mit der Bildung von Q-Siliciumspezien einhergehen, oder durch Migration der (Organo)silica-Phasen während des Transformationsprozesses entsteht.
Die hier präsentierten Arbeiten bilden die Basis für die Imprägnierung als eine vielversprechende Methode zur Bildung von Organosilica/Silica-Hybridmaterialien und für ihre pseudomorphe Transformation. Der Fokus nachfolgender Arbeiten wäre auf der Entwicklung einer zerstörungsfreien pseudomorphen Transformation von Organosilicas zu legen. Dazu könnten die Ergebnisse der pseudomorphen Transformation von CPGs in der Mikrowelle und bei geringeren Temperaturen hilfreiche Anstöße liefern.

Organosilica/Silica-Hybridmaterialien auf Basis von CPG Membranen

Neben den mikrometergroßen CPG Granulaten und sphärischen Partikeln wurden außerdem Membranen von 2.5 x 2.5 cm, mit einer Porengröße von 99 nm und 0.16 $cm^3 \cdot g^{-1}$ Porenvolumen als Ausgangsmaterialien für die pseudomorphe Transformation verwendet. Dabei konnte eine maximale spezifische BET-Oberfläche von 589 $m^2 \cdot g^{-1}$ nach vier Tagen unter Behandlung mit C_{16}TAOH erreicht werden. Die Membranen zeigen lediglich eine geringe Krümmung und büßen einen Teil ihrer mechanischen Stabilität ein. Aufgrund des geringen Ausgangsporenvolumen wurde das Makroporenvolumen der CPG Membranen nicht mittels Quecksilberporosimetrie untersucht. Die Membranen wurden ebenfalls imprägniert, anders als die anderen CPG Ausgangsverbindungen aber nicht über *incipient wetness*, sondern über Kapillarkräfte. Darüber hinaus erfolgte die Kondensation des *Precursors* in salzsauer Lösung und nicht in der vorherig verwendeten Lösung aus Ethanol und Natriumhydroxid-Lösung, da Ethanol ein Ablösen der Organosilicaphase hervorrief. Die unterschiedlichen Verhältnisse von innerer zu äußerer Oberfläche könnten ein Grund dafür sein, weshalb sich die imprägnierten Membranen derart anders verhalten als die mikrometergroßen CPG Kugeln und Granulate. Eine pseudomorphe Transformation der imprägnierten Membranen war nur bei geringem Anteil von Organosilica

möglich, da ein zu hoher Anteil die Ausdehnung des Materials durch die Transformation nicht möglich macht. Diese Versuche zeigen, dass die Morphologie der über den hier etablierte Ansatz dargestellten Organosilica/Silica-Hybridmaterien so flexibel an die Anwendung anpassbar ist wie in den reinen CPG.

Millimetergröße Organo(silica) Kugeln

Im letzten Projekt wurden Silicakugeln und Organosilicakugeln von 2 mm Durchmesser hergestellt. Die Synthese der Kugeln war mithilfe von Alginat möglich, was bei Kontakt mit Calciumionen ein stabiles Hydrogel bildet.

Bei den Silica-Kugeln (hergestellt ausgehend von TEOS) ergab sich eine spezifische BET-Oberfläche von 716 $m^2 \cdot g^{-1}$ mit breiter Porengrößenverteilung. Über pseudomorphe Transformation der Kugeln konnten geordnete Poren von 4 nm und eine spezifischen BET-Oberfläche von 767 $m^2 \cdot g^{-1}$ erhalten werden. Dabei sank das Makroporenvolumen signifikant von 0.5 $cm^3 \cdot g^{-1}$ auf 0.3 $cm^3 \cdot g^{-1}$ und es ergaben sich Poren von 49 nm Durchmesser. Die Morphologie der Kugeln konnte aber erhalten werden.

Im Falle der Organosilica-Kugeln (hergestellt aus BTEB) konnte das Alginat nicht über Kalzination entfernt werden, es ließ sich aber durch koordinative Bindung der Calciumionen mit Citrat vollständig herauslösen. Die erhaltenen B-Organosilica-Kugeln zeigen eine spezifische BET-Oberfläche, von 699 $m^2 \cdot g^{-1}$, wobei sich Mikro-und Mesoporen bildeten. Das Porenvolumen ist mit 0.26 $cm^3 \cdot g^{-1}$ eher gering. Auch diese Proben wurden zur pseudomorphen Transformation mit basischer Tensidlösung behandelt, wobei ein Mesoporensystem mit 3.7 nm Porendurchmesser und 731 $m^2 \cdot g^{-1}$ spezifischer BET-Oberfläche erhalten wurde. Das Material zeigt einen breiten Reflex im Kleinwinkelbereich, was auf eine geringe Porenordnung hindeutet. Aus diesem Grund wird das Material nicht als PMO bezeichnet, obwohl eine pseudokristalline Ordnung der organischen Brücken in der Porenwand mittels Röntgenstrukturanalyse nachgewiesen werden konnte. Die Unversehrtheit der organischen Brücke konnte auch hier mittels ^{13}C-CP-MAS NMR Spektroskopie gezeigt werden. Das ^{29}Si-CP-MAS NMR Spektrum zeigte allerdings einen geringen Anteil an Q-Signalen, welcher sich nach der pseudomorphen Transformation erhöhte. Auch in diesem Fall bedeutet dies eine Spaltung der Si-C Bindung.

Folgende Forschungen konnten sich mit der Umsetzung des gezeigten Syntheseweges für andere Vorläuferverbindungen beschäftigen. Außerdem ist es mit dem Alginathydrogel möglich, auch andere Formkörper darzustellen, beispielsweise indem ein Gefäß ausgefüllt wird.

7 Bibliography

[1] P. Fratzl, R. Weinkamer, *Prog. Mater. Sci.* **2007**, *52*, 1263–1334.

[2] K. S. W. Sing, *Pure Appl. Chem.* **1985**, *57*, 603–619.

[3] M. Thommes, K. Kaneko, A. V. Neimark, J. P. Olivier, F. Rodriguez-Reinoso, J. Rouquerol, K. S. W. Sing, *Pure Appl. Chem.* **2015**, *87*, 1051–1069.

[4] C. Colella, in *Handb. Porous Solids* (Eds.: F. Schüth, S. W. Sing, J. Weitkarnp), Wiley-VCH Verlag GmbH, Weinheim, Germany, **2002**, pp. 1156–1186.

[5] C. S. Cundy, P. A. Cox, *Microporous Mesoporous Mater.* **2005**, *82*, 1–78.

[6] X. Meng, F. S. Xiao, *Chem. Rev.* **2014**, *114*, 1521–1543.

[7] K. Nakanishi, N. Soga, *J. Am. Ceram.* **1991**, *74*, 2518–2530.

[8] M.-H. Sun, S.-Z. Huang, L.-H. Chen, Y. Li, X.-Y. Yang, Z.-Y. Yuan, B.-L. Su, *Chem. Soc. Rev.* **2016**, *45*, 3479–3563.

[9] W. Schwieger, A. G. Machoke, T. Weissenberger, A. Inayat, T. Selvam, M. Klumpp, A. Inayat, *Chem. Soc. Rev.* **2016**, *45*, 3353–3376.

[10] R. Cimino, K. A. Cychosz, M. Thommes, A. V. Neimark, *Colloids Surf. A* **2013**, *437*, 76–89.

[11] C. T. Kresge, M. E. Leonowicz, W. J. Roth, J. C. Vartuli, J. S. Beck, *Nature* **1992**, *359*, 710–712.

[12] J. S. Beck, J. C. Vartuli, W. J. Roth, M. E. Leonowicz, C. T. Kresge, K. D. Schmitt, C. T. W. Chu, D. H. Olson, E. W. Sheppard, S. B. McCullen, et al., *J. Am. Chem. Soc.* **1992**, *114*, 10834–10843.

[13] U. Schubert, *Chem. Unserer Zeit* **2018**, *52*, 18–25.

[14] U. Schubert, N. Husing, *Synthesis of Inorganic Materials*, Wiley-VCH Verlag GmbH, Weinheim, Germany, **2012**.

[15] F. Hoffmann, M. Cornelius, J. Morell, M. Fröba, *Angew. Chemie* **2006**, *118*, 3290–3328.

[16] F. Hoffmann, M. Cornelius, J. Morell, M. Fröba, *Angew. Chem. Int. Ed.* **2006**, *45*, 3216–3251.

[17] Y. S. Lee, D. Surjadi, J. F. Rathman, *Langmuir* **2000**, *16*, 195–202.

[18] G. D. Stucky, D. Zhao, P. Yang, W. Lukens, N. Melosh, B. F. Chmelka, *Stud. Surf. Sci. Catal.* **1998**, *117*, 1–12.

[19] Q. Huo, D. I. Margolese, G. D. Stucky, *Chem. Mater.* **1996**, *8*, 1147–1160.

[20] N. Baccile, G. Laurent, C. Bonhomme, P. Innocenzi, F. Babonneau, *Chem. Mater.* **2007**, *19*, 1343–1354.

[21] D. Zhao, J. Feng, Q. Huo, N. Melosh, G. H. Fredrickson, B. F. Chmelka, G. D. Stucky, *Science* **1998**, *279*, 548–552.

[22] H. P. Hood, M. E. Nordberg, *Treated Borosilicate Glass*, **1938**, US222106744.

[23] M. E. Nordberg, *J. Am. Ceram. Soc.* **1944**, *27*, 299–305.

[24] A. Inayat, B. Reinhardt, H. Uhlig, W.-D. Einicke, D. Enke, *Chem. Soc. Rev.* **2013**, *42*, 3753–3764.

[25] F. Janowski, D. Enke, in *Handb. Porous Solids* (Eds.: F. Schüth, K.S.W. Sing, J. Weitkamp), Wiley-VCH Verlag GmbH, Weinheim, Germany, **2002**, pp. 1432–1542.

[26] D. Enke, F. Janowski, W. Schwieger, *Microporous Mesoporous Mater.* **2003**, *60*, 19–30.

[27] W. Haller, *J. Chem. Phys.* **1965**, *42*, 686–693.

[28] W. Haller, *Nature* **1965**, *206*, 693–696.

[29] D. Enke, R. Gläser, U. Tallarek, *Chem. Ing. Tech.* **2016**, *88*, 1561–1585.

[30] A. Inayat, B. Reinhardt, J. Herwig, C. Küster, H. Uhlig, S. Krenkel, E. Raedlein, D. Enke, *New J. Chem.* **2016**, *40*, 4095–4114.

[31] B. Reinhardt, D. Enke, G. Bienhaus, *Opt. Appl.* **2012**, *42*, 265–270.

[32] B. Reinhardt, D. Enke, F. Syrowatka, *J. Am. Ceram. Soc.* **2012**, *95*, 461–465.

[33] M. Münzner, G. Dornberg, C. Küster, D. Enke, *Chem. Ing. Tech.* **2016**, *88*, 1761–1769.

[34] H. B. Stonehouse, in *Mineralogy*, Springer US, Boston, MA, **1981**, pp. 418–419.

[35] T. Martin, A. Galarneau, F. Di Renzo, F. Fajula, D. Plee, *Angew. Chem. Int. Ed.* **2002**, *41*, 2590–2592.

[36] A. Galarneau, J. Iapichella, K. Bonhomme, F. De Renzo, P. Kooyman, O. Terasaki, F. Fajula, *Adv. Funct. Mater.* **2006**, *16*, 1657–1667.

[37] W. D. Einicke, D. Enke, M. Dvoyashkin, R. Valiullin, R. Gläser, *Materials* **2013**, *6*, 3688–3709.

[38] H. Uhlig, M. L. Gimpel, A. Inayat, R. Gläser, W. Schwieger, W. D. Einicke, D. Enke, *Microporous Mesoporous Mater.* **2013**, *182*, 136–146.

[39] M. Guillot, S. El Mourabit, J. Ravaux, A. Tokarev, F. Goettmann, A. Grandjean, *Microporous Mesoporous Mater.* **2014**, *197*, 83–91.

[40] M. Guillot, F. Goettmann, C. Delchet, S. El Mourabit, A. Grandjean, *Method for Preparing an Optionally Functionalised Glass Having Bimodal Porosity, and Said Glass*, **2014**, WO/2014/083162.

[41] S. El Mourabit, M. Guillot, G. Toquer, J. Cambedouzou, F. Goettmann, A. Grandjean, *RSC Adv.* **2012**, *2*, 10916.

[42] Z. Adem, F. Guenneau, M. A. Springuel-Huet, A. Gédéon, J. Iapichella, T. Cacciaguerra, A. Galarneau, *J. Phys. Chem. C* **2012**, *116*, 13749–13759.

[43] H. Uhlig, J. Hollenbach, M. Rogaczewski, J. Matysik, F. J. Brieler, M. Fröba, D. Enke, *Chem. Ing. Tech.* **2017**, *89*, 863–875.

[44] A. Galarneau, M. Cangiotti, F. di Renzo, F. Fajula, M. F. Ottaviani, *J. Phys. Chem. B* **2006**, *110*, 4058–4065.

[45] T. R. Pauly, V. Petkov, Y. Liu, S. J. L. Billinge, T. J. Pinnavaia, *J. Am. Chem. Soc.* **2002**, *124*, 97–103.

[46] A. Galarneau, J. Iapichella, D. Brunel, F. Fajula, Z. Bayram-Hahn, K. Unger, G. Puy, C. Demesmay, J. L. Rocca, *J. Sep. Sci.* **2006**, *29*, 844–855.

[47] C. Petitto, A. Galarneau, M. F. Driole, B. Chiche, B. Alonso, F. D. Renzo, F. Fajula, *Chem. Mater.* **2005**, *17*, 2120–2130.

[48] H. Uhlig, *Synthese von MCM-41 Und MCM-48-Formkörpern Durch Pseudomorphe Transformation von Amorphen Silikaten*, Dissertation, Universität Leipzig, **2015**.

[49] M. J. Reber, D. Brühwiler, *Dalt. Trans.* **2015**, *44*, 17960–17967.

[50] M. J. Reber, N. Zucchetto, D. Brühwiler, *Chim. Int. J. Chem.* **2018**, *72*, 158–159.

[51] N. Zucchetto, M. J. Reber, L. Pestalozzi, R. Schmid, A. Neels, D. Brühwiler, *Microporous Mesoporous Mater.* **2018**, *257*, 232–240.

[52] M. J. Reber, D. Brühwiler, *Part. Part. Syst. Charact.* **2015**, *32*, 243–250.

[53] X. Liu, H. Sun, Y. Chen, Y. Yang, A. Borgna, *Microporous Mesoporous Mater.* **2009**, *121*, 73–78.

[54] W. D. Einicke, H. Uhlig, D. Enke, R. Gläser, C. Reichenbach, S. G. Ebbinghaus, *Colloids Surf. A* **2013**, *437*, 108–112.

[55] A. Galarneau, A. Sachse, B. Said, C.-H. Pelisson, P. Boscaro, N. Brun, L. Courtheoux, N. Olivi-Tran, B. Coasne, F. Fajula, *C. R. Chim.* **2016**, *19*, 231–247.

[56] M. Mańko, J. Vittenet, J. Rodriguez, D. Cot, J. Mendret, S. Brosillon, W. Makowski, A. Galarneau, *Microporous Mesoporous Mater.* **2013**, *176*, 145–154.

[57] J. C. Lytle, H. Yan, R. T. Turgeon, A. Stein, *Chem. Mater.* **2004**, *16*, 3829–3837.

[58] R. R. Unocic, F. M. Zalar, P. M. Sarosi, Y. Cai, K. H. Sandhage, *Chem. Commun.* **2004**, *1*, 796.

[59] F. Hoffmann, M. Fröba, in *Supramol. Chem. Org. Hybrid Mater.* (Eds.: K. Rurack, R. Martínez-Máñez), John Wiley & Sons, Inc., Hoboken, NJ, USA, **2010**, pp. 37–111.

[60] R. Mouawia, A. Mehdi, C. Reyé, R. Corriu, *New J. Chem.* **2006**, *30*, 1077.

[61] H.-M. Kao, C.-H. Liao, T.-T. Hung, Y.-C. Pan, A. S. T. Chiang, *Chem. Mater.* **2008**, *20*, 2412–2422.

[62] J. Liu, J. Yang, Q. Yang, G. Wang, Y. Li, *Adv. Funct. Mater.* **2005**, *15*, 1297–1302.

[63] Y. Pan, H. Wu, C.-C. Kao, H. Kao, Y. Shieh, G. T. K. Fey, J.-H. Chang, H.-H. G. Tsai, *J. Phys. Chem. C* **2009**, *113*, 18251–18258.

[64] A. Sayari, S. Hamoudi, *Chem. Mater.* **2001**, *13*, 3151–3168.

[65] B. Boury, R. J. P. Corriu, V. Le Strat, *Chem. Mater.* **1999**, *11*, 2796–2803.

[66] B. Boury, R. Corriu, *Chem. Rec.* **2003**, *3*, 120–132.

[67] E. Besson, A. Mehdi, D. A. Lerner, C. Reyé, R. J. P. Corriu, *J. Mater. Chem.* **2005**, *15*, 803–809.

[68] K. J. Shea, D. A. Loy, O. Webster, *J. Am. Chem. Soc.* **1992**, *114*, 6700–6710.

[69] K. J. Shea, D. A. Loy, *Chem. Mater.* **2001**, *13*, 3306–3319.

[70] L. Zhao, M. Vaupel, D. A. Loy, K. J. Shea, *Chem. Mater.* **2008**, *20*, 1870–1876.

[71] L.-C. Hu, K. J. Shea, *Chem. Soc. Rev.* **2011**, *40*, 688.

[72] J. G. Croissant, X. Cattoën, J.-O. Durand, M. Wong Chi Man, N. M. Khashab, *Nanoscale* **2016**, *8*, 19945–19972.

[73] A. P. Dral, J. E. ten Elshof, *Microporous Mesoporous Mater.* **2018**, *267*, 267–273.

[74] T. Asefa, M. J. MacLachlan, H. Grondey, N. Coombs, G. A. Ozin, *Angew. Chem. Int. Ed.* **2000**, *39*, 1808–1811.

[75] L. Luo, Y. Liang, E. S. Erichsen, R. Anwander, *Chem. - Eur. J.* **2018**, *24*, 7200–7209.

[76] S. Inagaki, S. Guan, Y. Fukushima, T. Ohsuna, O. Terasaki, *J. Am. Chem. Soc.* **1999**, *121*, 9611–9614.

[77] T. Asefa, M. J. MacLachlan, N. Coombs, G. A. Ozin, *Nature* **1999**, *402*, 867–871.

[78] B. T. Holland, C. F. Blanford, T. Do, A. Stein, *Chem. Mater.* **1999**, *11*, 795–805.

[79] J. T. a Jones, C. D. Wood, C. Dickinson, Y. Z. Khimyak, *Chem. Mater.* **2008**, *20*, 3385–3397.

[80] O. Muth, C. Schellbach, M. Fröba, *Chem. Commun.* **2001**, *1*, 2032–2033.

[81] E. Choi, E.-B. Cho, M. Jaroniec, *J. Mater. Chem. A* **2017**, *5*, 21378–21388.

[82] W. Liu, N. Ma, S. Li, X. Zhang, W. Huo, J. Xu, X. Meng, J. Yang, *J. Mater. Sci.* **2017**, *52*, 2868–2878.

[83] A. Ryzhikov, T. J. Daou, H. Nouali, J. Patarin, J. Ouwehand, S. Clerick, E. De Canck, P. Van Der Voort, J. A. Martens, *Microporous Mesoporous Mater.* **2018**, *260*, 166–171.

[84] C. Sanchez, F. Jeremias, S. J. Ernst, S. K. Henninger, *Microporous Mesoporous Mater.* **2017**, *244*, 151–157.

[85] P. Van Der Voort, D. Esquivel, E. De Canck, F. Goethals, I. Van Driessche, F. J. Romero-Salguero, *Chem. Soc. Rev.* **2013**, *42*, 3913–3955.

[86] J. G. Croissant, X. Cattoën, M. Wong Chi Man, J.-O. Durand, N. M. Khashab, *Nanoscale* **2015**, *7*, 20318–20334.

[87] C. Yoshina-Ishii, T. Asefa, N. Coombs, M. J. MacLachlan, G. A. Ozin, *Chem. Commun.* **1999**, 2539–2540.

[88] J. Morell, M. Gungerich, G. Wolter, J. Jiao, M. Hunger, P. J. Klar, M. Fröba, *J. Mater. Chem.* **2006**, *16*, 2809–2818.

[89] V. Rebbin, A. Rothkirch, M. Fröba, S. S. Funari, *Chem. Mater.* **2010**, *22*, 3746–3751.

[90] S. Inagaki, S. Guan, T. Ohsuna, O. Terasaki, *Nature* **2002**, *416*, 304–307.

[91] L. Sandbrink, T. Lazaridis, M. Rose, R. Palkovits, *Microporous Mesoporous Mater.* **2018**, *267*, 198–202.

[92] M. A. O. Lourenço, J. R. B. Gomes, P. Ferreira, *RSC Adv.* **2015**, *5*, 9208–9216.

[93] M. A. O. Lourenço, P. Ferreira, M. J. G. Ferreira, M. Sardo, L. Mafra, J. R. B. Gomes, *Microporous Mesoporous Mater.* **2017**, *249*, 10–15.

[94] B. Schäfgen, O. D. Malter, E. Kaigarula, A. Schüßler, S. Ernst, W. R. Thiel, *Microporous Mesoporous Mater.* **2017**, *251*, 122–128.

[95] W. Huybrechts, J. Lauwaert, A. De Vylder, M. Mertens, G. Mali, J. W. Thybaut, P. Van Der Voort, P. Cool, *Microporous Mesoporous Mater.* **2017**, *251*, 1–8.

[96] A. Schachtschneider, M. Wessig, M. Spitzbarth, A. Donner, C. Fischer, M. Drescher, S. Polarz, *Angew. Chem. Int. Ed.* **2015**, *54*, 10465–10469.

[97] M. Abboud, A. Sayari, *Microporous Mesoporous Mater.* **2017**, *249*, 157–164.

[98] J. Morell, C. V. Teixeira, M. Cornelius, V. Rebbin, M. Tiemann, H. Amenitsch, M. Fröba, M. Lindén, *Chem. Mater.* **2004**, *16*, 5564–5566.

[99] M. P. Kapoor, Q. Yang, S. Inagaki, *J. Am. Chem. Soc.* **2002**, *124*, 15176–15177.

[100] M. P. Kapoor, Q. H. Yang, S. Inagaki, *Chem. Mater.* **2004**, *16*, 1209–1213.

[101] Y. Xia, W. Wang, R. Mokaya, *J. Am. Chem. Soc.* **2005**, *127*, 790–798.

[102] S. Fujita, S. Inagaki, *Chem. Mater.* **2008**, *20*, 891–908.

[103] M. Cornelius, F. Hoffmann, M. Fröba, *Chem. Mater.* **2005**, *17*, 6674–6678.

[104] A. Sayari, W. Wang, *J. Am. Chem. Soc.* **2005**, *127*, 12194–12195.

[105] M. Cornelius, F. Hoffmann, B. Ufer, P. Behrens, M. Fröba, *J. Mater. Chem.* **2008**, *18*, 2587–2592.

[106] C. S. Vogelsberg, S. Bracco, M. Beretta, A. Comotti, P. Sozzani, M. A. Garcia-Garibay, *J. Phys. Chem. B* **2012**, *116*, 1623–1632.

[107] M. Beretta, J. Morell, P. Sozzani, M. Fröba, *Chem. Commun.* **2010**, *46*, 2495–2497.

[108] S. Martens, R. Ortmann, F. J. Brieler, C. Pasel, Y. J. Lee, D. Bathen, M. Fröba, *Z. Anorg. Allg. Chem.* **2014**, *640*, 632–640.

[109] J. B. Mietner, F. J. Brieler, Y. J. Lee, M. Fröba, *Angew. Chem. Int. Ed.* **2017**, *56*, 12348–12351.

[110] J. B. Mietner, *Zu Gast in Nanoporen*, Dissertation, Universität Hamburg, **2018**.

[111] T. Simon, F. J. Brieler, M. Fröba, *J. Mater. Chem. C* **2017**, *5*, 5263–5268.

[112] M. Álvaro, M. Benitez, D. Das, B. Ferrer, H. García, *Chem. Mater.* **2004**, *16*, 2222–2228.

[113] D. Hérault, G. Cerveau, R. J. P. Corriu, A. Mehdi, *Dalton Trans.* **2011**, *40*, 446–451.

[114] G. Zhu, H. Zhong, Q. Yang, C. Li, *Microporous Mesoporous Mater.* **2008**, *116*, 36–43.

[115] S. MacQuarrie, M. P. Thompson, A. Blanc, N. J. Mosey, R. P. Lemieux, C. M. Crudden, *J. Am. Chem. Soc.* **2008**, *130*, 14099–14101.

[116] V. Jayalakshmi, T. Wood, R. Basu, J. Du, T. Blackburn, C. Rosenblatt, C. M. Crudden, R. P. Lemieux, *J. Mater. Chem.* **2012**, *22*, 15255.

[117] M. Bilo, M. Sartor, H. Nasser, Y. J. Lee, F. J. Brieler, M. Fröba, *J. Sol-Gel Sci. Technol.* **2018**, DOI 10.1007/s10971-018-4774-z.

[118] O. Cohen, R. Abu-Reziq, D. Gelman, *Tetrahedron Asymmetry* **2017**, *28*, 1675–1685.

[119] S. Polarz, A. Kuschel, *Adv. Mater.* **2006**, *18*, 1206–1209.

[120] A. Kuschel, H. Sievers, S. Polarz, *Angew. Chem. Int. Ed.* **2008**, *47*, 9513–9517.

[121] A. Kuschel, S. Polarz, *J. Am. Chem. Soc.* **2010**, *132*, 6558–6565.

[122] A. Ide, R. Voss, G. Scholz, G. A. Ozin, M. Antonietti, A. Thomas, *Chem. Mater.* **2007**, *19*, 2649–2657.

[123] J. Morell, S. Chatterjee, P. J. Klar, D. Mauder, I. Shenderovich, F. Hoffmann, M. Fröba, *Chem. - Eur. J.* **2008**, *14*, 5935–5940.

[124] L. M. Reid, C. M. Crudden, *Chem. Mater.* **2016**, *28*, 7605–7612.

[125] S. Inagaki, S. Guan, Q. Yang, M. P. Kapoor, T. Shimada, *Chem Commun* **2008**, 202–204.

[126] T. Y. Zhuang, J. Y. Shi, B. C. Ma, W. Wang, *J. Mater. Chem.* **2010**, *20*, 6026.

[127] S. Che, Z. Liu, T. Ohsuna, K. Sakamoto, O. Terasaki, T. Tatsumi, *Nature* **2004**, *429*, 281–284.

[128] T. Yokoi, K. Ogawa, D. Lu, J. N. Kondo, Y. Kubota, T. Tatsumi, *Chem. Mater.* **2011**, *23*, 2014–2016.

[129] S. Lacasta, V. Sebastián, C. Casado, Á. Mayoral, P. Romero, Á. Larrea, E. Vispe, P. López-Ram-De-Viu, S. Uriel, J. Coronas, *Chem. Mater.* **2011**, *23*, 1280–1287.

[130] B. Di, L. Cheng, Q. Jiang, M. Su, W. Hao, *New J. Chem.* **2013**, *37*, 1603.

[131] Y.-X. Li, S.-G. Fu, J.-H. Zhang, S.-M. Xie, L. Li, Y.-Y. He, M. Zi, L.-M. Yuan, *J. Chromatogr. A* **2018**, *1557*, 99–106.

[132] M. Kuroki, T. Asefa, W. Whitnal, M. Kruk, C. Yoshina-Ishii, M. Jaroniec, G. A. Ozin, *J. Am. Chem. Soc.* **2002**, *124*, 13886–13895.

[133] K. Landskron, B. D. Hatton, D. D. Perovic, G. A. Ozin, *Science* **2003**, *302*, 266–269.

[134] M. Ide, E. De Canck, I. Van Driessche, F. Lynen, P. Van Der Voort, *RSC Adv.* **2015**, *5*, 5546–5552.

[135] S. Clerick, E. De Canck, K. Hendrickx, V. Van Speybroeck, P. Van Der Voort, *Green Chem.* **2016**, *18*, 6035–6045.

[136] K. Landskron, *Science* **2004**, *306*, 1529–1532.

[137] W. J. Hunks, G. A. Ozin, *Adv. Funct. Mater.* **2005**, *15*, 259–266.

[138] K. Landskron, G. A. Ozin, *Angew. Chem. Int. Ed.* **2005**, *44*, 2107–2109.

[139] G. Smeulders, V. Meynen, K. Houthoofd, S. Mullens, J. A. Martens, B. U. W. Maes, P. Cool, *Microporous Mesoporous Mater.* **2012**, *164*, 49–55.

[140] W. Huybrechts, G. Mali, P. Kuśtrowski, T. Willhammar, M. Mertens, S. Bals, P. Van Der Voort, P. Cool, *Microporous Mesoporous Mater.* **2016**, *236*, 244–249.

[141] A. Kuschel, S. Polarz, *Adv. Funct. Mater.* **2008**, *18*, 1272–1280.

[142] S. Bracco, M. Beretta, A. Cattaneo, A. Comotti, A. Falqui, K. Zhao, C. Rogers, P. Sozzani, *Angew. Chem. Int. Ed.* **2015**, *54*, 4773–4777.

[143] M. Ge, H. Liu, *Chem. - Eur. J.* **2018**, *24*, 2224–2231.

[144] N. Tanaka, H. Kobayashi, K. Nakanishi, H. Minakuchi, N. Ishizuka, *Anal. Chem.* **2001**, *73*, 420 A-429 A.

[145] D. Cabooter, A. Fanigliulo, G. Bellazzi, B. Allieri, A. Rottigni, G. Desmet, *J. Chromatogr. A* **2010**, *1217*, 7074–7081.

[146] Y. Zhou, L. Gao, F. N. Gu, J. Y. Yang, J. Yang, F. Wei, Y. Wang, J. H. Zhu, *Chem. - Eur. J.* **2009**, *15*, 6748–6757.

[147] A. El Kadib, R. Chimenton, A. Sachse, F. Fajula, A. Galarneau, B. Coq, *Angew. Chem. Int. Ed.* **2009**, *48*, 4969–4972.

[148] K. Waldron, W. D. Wu, Z. Wu, W. Liu, C. Selomulya, D. Zhao, X. D. Chen, *J. Colloid Interface Sci.* **2014**, *418*, 225–233.

[149] F. N. Gu, W. G. Lin, J. Y. Yang, F. Wei, Y. Wang, J. H. Zhu, *Microporous Mesoporous Mater.* **2012**, *151*, 142–148.

[150] S. Scholz, J. A. Lercher, *Chem. Mater.* **2011**, *23*, 2091–2099.

[151] S. Scholz, S. R. Bare, S. D. Kelly, J. A. Lercher, *Microporous Mesoporous Mater.* **2011**, *146*, 18–27.

[152] M. Von Der Lehr, C. Weidmann, S. Mascotto, B. M. Smarsly, *Chem. Ing. Tech.* **2013**, *85*, 1700–1706.

[153] M. Von Der Lehr, C. F. Seidler, D. H. Taffa, M. Wark, B. M. Smarsly, R. Marschall, *ACS Appl. Mater. Interfaces* **2016**, *8*, 25476–25488.

[154] M. von der Lehr, R. Ellinghaus, B. M. Smarsly, *New J. Chem.* **2016**, *40*, 4455–4463.

[155] K. Nakanishi, Y. Kobayashi, T. Amatani, K. Hirao, T. Kodaira, *Chem. Mater.* **2004**, *16*, 3652–3658.

[156] K. Nakanishi, T. Amatani, S. Yano, T. Kodaira, *Chem. Mater.* **2008**, *20*, 1108–1115.

[157] N. Hüsing, D. Brandhuber, P. Kaiser, *J. Sol-Gel Sci. Technol.* **2006**, *40*, 131–139.

[158] D. Brandhuber, H. Peterlik, N. Huesing, *Small* **2006**, *2*, 503–506.

[159] M. Weinberger, T. Fröschl, S. Puchegger, H. Peterlik, N. Hüsing, *Silicon* **2009**, *1*, 19–28.

[160] S. Hartmann, D. Brandhuber, N. Hüsing, *Acc. Chem. Res.* **2007**, *40*, 885–894.

[161] M. Weinberger, S. Puchegger, T. Fröschl, F. Babonneau, H. Peterlik, N. Hüsing, *Chem. Mater.* **2010**, *22*, 1509–1520.

[162] G. Hasegawa, K. Kanamori, K. Nakanishi, T. Hanada, *J. Mater. Chem.* **2009**, *19*, 7716.

[163] G. Hasegawa, K. Kanamori, K. Nakanishi, T. Hanada, *Chem. Mater.* **2010**, *22*, 2541–2547.

[164] C. Wu, Y. Liang, K. Yang, Y. Min, Z. Liang, L. Zhang, Y. Zhang, *Anal. Chem.* **2016**, *88*, 1521–1525.

[165] G. L. Drisko, M. C. Kimling, N. Scales, A. Ide, E. Sizgek, R. A. Caruso, V. Luca, *Langmuir* **2010**, *26*, 17581–17588.

[166] L. Li, J. Yao, P. Xiao, J. Shang, Y. Feng, P. A. Webley, H. Wang, *Colloid Polym. Sci.* **2013**, *291*, 2711–2717.

[167] Y. Feng, Y. Wang, S. Liu, J. Qiu, J. Yao, *Polym. Compos.* **2017**, *16*, 101–113.

[168] Q. S. Huo, J. L. Feng, F. Schüth, G. D. Stucky, *Chem. Mater.* **1997**, *9*, 14–17.

[169] S. Yun, H. Luo, Y. Gao, *RSC Adv.* **2014**, *4*, 4535–4542.

[170] V. Singh, P. Srivastava, A. Singh, D. Singh, T. Malviya, *Polym. Rev.* **2016**, *56*, 113–136.

[171] J. T. Delaney, A. R. Liberski, J. Perelaer, U. S. Schubert, *Soft Matter* **2010**, *6*, 866–869.

[172] G. A. Paredes Juárez, M. Spasojevic, M. M. Faas, P. de Vos, *Front. Bioeng. Biotechnol.* **2014**, *2*, 1–15.

[173] S. N. Pawar, K. J. Edgar, *Biomaterials* **2012**, *33*, 3279–3305.

[174] H. Li, P. Yang, P. Pageni, C. Tang, *Macromol. Rapid Commun.* **2017**, *38*, 1–9.

[175] W. Liu, Y. Zhao, C. Zeng, C. Wang, C. A. Serra, L. Zhang, *Chem. Eng. J.* **2017**, *307*, 408–417.

[176] H. Zhu, Q. Zhang, S. Zhu, *ACS Appl. Mater. Interfaces* **2016**, *8*, 17395–17401.

[177] P. A. Kallenberger, K. Posern, K. Linnow, F. J. Brieler, M. Steiger, M. Fröba, *Adv. Sustain. Syst.* **2018**, *2*, 1700160.

[178] P. A. Kallenberger, M. Fröba, *Commun. Chem.* **2018**, *1*, 28.

[179] A. Pannier, U. Soltmann, B. Soltmann, R. Altenburger, M. Schmitt-Jansen, *J. Mater. Chem. B* **2014**, *2*, 7896–7909.

[180] J. Li, H. Wu, Y. Liang, Z. Jiang, Y. Jiang, L. Zhang, *J. Biomater. Sci. Polym. Ed.* **2013**, *24*, 119–134.

[181] N. S. Kehr, E. A. Prasetyanto, K. Benson, B. Ergün, A. Galstyan, H. J. Galla, *Angew. Chem. Int. Ed.* **2013**, *52*, 1156–1160.

[182] U. Schloßmacher, H. C. Schröder, X. Wang, Q. Feng, B. Diehl-Seifert, S. Neumann, A. Trautwein, W. E. G. Müller, *RSC Adv.* **2013**, *3*, 11185–11194.

[183] X. Zhang, C. Huang, Y. Zhao, X. Jin, *RSC Adv.* **2017**, *7*, 39349–39358.

[184] Z. Ulker, C. Erkey, *RSC Adv.* **2014**, *4*, 62362–62366.

[185] J. W. Liu, Y. Zhang, D. Chen, T. Yang, Z. P. Chen, S. Y. Pan, N. Gu, *Colloids Surf. A* **2009**, *341*, 33–39.

[186] M. Buaki-Sogo, M. Serra, A. Primo, M. Alvaro, H. Garcia, *ChemCatChem* **2013**, *5*, 513–518.

[187] M. Chee Kimling, N. Scales, T. L. Hanley, R. A. Caruso, *Environ. Sci. Technol.* **2012**, *46*, 7913–7920.

[188] S. Abramson, C. Meiller, P. Beaunier, V. Dupuis, L. Perrigaud, A. Bée, V. Cabuil, *J. Mater. Chem.* **2010**, *20*, 4916–4924.

[189] K. A. Cychosz, R. Guillet-Nicolas, J. García-Martínez, M. Thommes, *Chem. Soc. Rev.* **2017**, *46*, 389–414.

[190] M. Thommes, K. A. Cychosz, *Adsorption* **2014**, *20*, 233–250.

[191] L. Jelinek, E. sz Kováts, *Langmuir* **1994**, 4225–4231.

[192] S. Lowell, J. E. Shields, M. A. Thomas, M. Thommes, in *Charact. Porous Solids Powders Surf. Area, Pore Size Density*, Springer Netherlands, Dordrecht, **2004**, pp. 157–188.

[193] M. Hesse, H. Meier, B. Zeeh, *Spektroskopische Methoden in Der Organischen Chemie*, Georg Thieme Verlag, Stuttgart, Germany, **2005**.

[194] H. Friebolin, *Ein- Und Zweidimensionale NMR-Spektroskopie : Eine Einführung*, John Wiley & Sons, Incorporated, Weinheim, Germany, **2013**.

[195] J. B. Lambert, *Spektroskopie - Strukturaufklärung in Der Organischen Chemie*, Pearson Deutschland GmbH, **2012**.

[196] D. D. Laws, H.-M. L. Bitter, A. Jerschow, *Angew. Chem. Int. Ed.* **2002**, *41*, 3096–3129.

[197] H. Koller, M. Weiß, *Solid State NMR*, Springer Berlin Heidelberg, **2012**.

[198] M. Mägi, E. Lippmaa, A. Samoson, G. Engelhardt, A. R. Grimmer, *J. Phys. Chem.* **1984**, *88*, 1518–1522.

[199] M. Geppi, S. Borsacchi, G. Mollica, C. A. Veracini, *Appl. Spectrosc. Rev.* **2009**, *44*, 1–89.

[200] S. C. Christiansen, D. Zhao, M. T. Janicke, C. C. Landry, G. D. Stucky, B. F. Chmelka, *J. Am. Chem. Soc.* **2001**, *123*, 4519–4529.

[201] M. T. Janicke, C. C. Landry, S. C. Christiansen, D. Kumar, G. D. Stucky, B. F. Chmelka, *J. Am. Chem. Soc.* **1998**, *120*, 6940–6951.

[202] T. Langbein, H. Sonntag, D. Trapp, A. Hoffmann, W. Malms, E. P. Röth, V. Mörs, R. Zellner, *Br. J. Anaesth.* **1999**, *82*, 66–73.

[203] M. P. Sulbaek Andersen, S. P. Sander, O. J. Nielsen, D. S. Wagner, T. J. Sanford, T. J. Wallington, *Br. J. Anaesth.* **2010**, *105*, 760–766.

[204] M. P. S. Andersen, O. J. Nielsen, T. J. Wallington, B. Karpichev, S. P. Sander, *Anesth. Analg.* **2012**, *114*, 1081–1085.

[205] L. Molnar, *J. Anesth. Clin. Res.* **2014**, *05*, 1–7.

[206] R. Ortmann, C. Pasel, M. Luckas, R. Heimböckel, S. Kraas, J. Bentgens, M. Fröba, D. Bathen, *J. Chem. Eng. Data* **2016**, *61*, 686–692.

[207] D. Bucher, C. Pasel, M. Luckas, J. Bentgens, D. Bathen, *J. Chem. Eng. Data* **2017**, *62*, 1832–1841.

[208] H. Frost, T. Düren, R. Q. Snurr, *J. Phys. Chem. B* **2006**, *110*, 9565–9570.

[209] N. Gargiulo, A. Peluso, P. Aprea, Y. Hua, D. Filipović, D. Caputo, M. Eić, *RSC Adv.* **2014**, *4*, 49478–49484.

[210] Y. Hua, N. Gargiulo, A. Peluso, P. Aprea, M. Eić, D. Caputo, *Chem. Ing. Tech.* **2016**, *88*, 1739–1745.

[211] B. F. Abrahams, A. D. Dharma, P. S. Donnelly, T. A. Hudson, C. J. Kepert, R. Robson, P. D. Southon, K. F. White, *Chem. - Eur. J.* **2017**, *23*, 7871–7875.

[212] J. Xie, F. Sun, C. Wang, Q. Pan, *Materials* **2016**, *9*, 327.

[213] T.-H. Chen, I. Popov, O. Zenasni, O. Daugulis, O. Š. Miljanić, *Chem. Commun.* **2013**, *49*, 6846.

[214] T.-H. Chen, I. Popov, W. Kaveevivitchai, Y.-C. Chuang, Y.-S. Chen, O. Daugulis, A. J. Jacobson, O. Š. Miljanić, *Nat. Commun.* **2014**, *5*, 5131.

[215] T. Chen, W. Kaveevivitchai, A. Jacobson, O. Miljanic, *Chem. Commun.* **2015**, *51*, 14096–14098.

[216] T. H. Chen, I. Popov, W. Kaveevivitchai, Y. C. Chuang, Y. S. Chen, A. J. Jacobson, O. Miljanic, *Angew. Chem. Int. Ed.* **2015**, *54*, 13902–13906.

[217] M. A. Wahab, S. Sudhakar, E. Yeo, A. Sellinger, *Chem. Mater.* **2008**, *20*, 1855–1861.

[218] M. Cornelius, *Studien Zur Synthese Mesoporöser Organosilica- Hybridmaterialien Mit Konjugierten π -Systemen*, Dissertation, Justus-Liebig-Universität Gießen, **2007**.

[219] D. O'Hagan, *Chem. Soc. Rev.* **2008**, *37*, 308–319.

[220] K. Zhang, R. P. Lively, J. D. Noel, M. E. Dose, B. A. Mccool, R. R. Chance, W. J. Koros, **2012**, DOI 10.1021/la301122h.

[221] M. Thommes, S. Mitchell, J. Pérez-Ramírez, *J. Phys. Chem. C* **2012**, *116*, 18816–18823.

[222] D. I. Fried, D. Bednarski, M. Dreifke, F. J. Brieler, *J. Mater. Chem. B* **2015**, *3*, 2341–2349.

[223] Y. Goto, S. Inagaki, *Microporous Mesoporous Mater.* **2006**, *89*, 103–108.

[224] S. Che, H. Li, S. Lim, Y. Sakamoto, O. Terasaki, T. Tatsumi, *Chem. Mater.* **2005**, *17*, 4103–4113.

[225] M. Liu, H. Sheu, S. Cheng, *J. Am. Chem. Soc.* **2009**, *131*, 3998–4005.

[226] F. Lin, X. Meng, E. Kukueva, M. Mertens, S. Van Doorslaer, S. Bals, P. Cool, *RSC Adv.* **2015**, *5*, 5553–5562.

[227] Q. Huo, D. I. Margolese, U. Ciesla, P. Feng, T. E. Gier, P. Sieger, R. Leon, P. M. Petroff, F. Schüth, G. D. Stucky, *Nature* **1994**, *368*, 317–321.

[228] Q. Huo, D. I. Margolese, U. Ciesla, D. G. Demuth, P. Feng, T. E. Gier, P. Sieger, A. Firouzi, B. F. Chmelka, F. Schüth, et al., *Chem. Mater.* **1994**, *6*, 1176–1191.

[229] F. Lin, X. Meng, E. Kukueva, M. Kus, M. Mertens, S. Bals, S. Van Doorslaer, P. Cool, *Microporous Mesoporous Mater.* **2015**, *207*, 61–70.

[230] K. Yano, Y. Fukushima, *J. Mater. Chem.* **2003**, *13*, 2577.

[231] S. Hamoudi, Y. Yang, I. L. Moudrakovski, S. Lang, A. Sayari, *J. Phys. Chem. B* **2001**, *105*, 9118–9123.

[232] A. L. Kolesnikov, H. Uhlig, J. Möllmer, J. Adolphs, Y. A. Budkov, N. Georgi, D. Enke, R. Gläser, *Microporous Mesoporous Mater.* **2017**, *240*, 169–177.

[233] H. Uhlig, T. Muenster, G. Kloess, S. G. Ebbinghaus, W. D. Einicke, R. Gläser, D. Enke, *Microporous Mesoporous Mater.* **2018**, *257*, 185–192.

[234] E. B. Celer, M. Jaroniec, *J. Am. Chem. Soc.* **2006**, *128*, 14408–14414.

[235] G. Smeulders, V. Meynen, G. Van Baelen, M. Mertens, O. I. Lebedev, G. Van Tendeloo, B. U. W. Maes, P. Cool, *J. Mater. Chem.* **2009**, *19*, 3042.

[236] E. M. Domingues, N. Bion, F. M. Figueiredo, P. Ferreira, *Microporous Mesoporous Mater.* **2016**, *226*, 386–395.

[237] N. Bion, P. Ferreira, A. Valente, I. S. Gonçalves, J. Rocha, *J. Mater. Chem.* **2003**, *13*, 1910–1913.

[238] X. Li, D. Wu, J. Wang, W. Zhu, Y. Luo, C. Han, W. Ma, S. He, *Microporous Mesoporous Mater.* **2016**, *226*, 309–315.

[239] A. Barascu, J. Kullmann, B. Reinhardt, T. Rainer, H. Roggendorf, F. Syrowatka, D. Enke, *Glas. Phys. Chem.* **2015**, *41*, 73–80.

[240] M. Bilo, Y. J. Lee, M. Fröba, *Microporous Mesoporous Mater.* **2019**, *284*, 327–335.

[241] N. S. Kehr, *Biomacromolecules* **2016**, *17*, 1117–1122.

[242] S. Inagaki, Y. Fukushima, K. Kuroda, K. Kuroda, *J. Colloid Interface Sci.* **1996**, *180*, 623–624.

[243] G. R. Fulmer, A. J. M. Miller, N. H. Sherden, H. E. Gottlieb, A. Nudelman, B. M. Stoltz, J. E. Bercaw, K. I. Goldberg, *Organometallics* **2010**, *29*, 2176–2179.

8 Experimental Section

8.1 Characterization techniques – instrumental details

Physisorption

All samples were outgassed on a *Quantachrome Degasser Masterprep®* under vacuum for 16–24 hours at 80 °C for organosilica, 120 °C for pure silica.
Nitrogen physisorption data was recorded at 77 K with a *Quantachrome Quadrasorb®-SI-MP*/ *Quadrasorb evo™* or *Quantachrome Autosorb® 6B*. Pore diameter distributions were calculated from the adsorption branch with NLDFT kernel for silica, cylindrical pores. The pore volume of mesoporous materials was determine with the same NLDFT kernel for mesoporous materials, if present of interparticle voids, only pores smaller 20 nm were considered. Argon physisorption data were recorded at 78 K with *Quantachrome Autosorb®-iQ-MP* using a cryo-cooler-system. Pore diameter distributions were calculated from the adsorption branch with NLDFT kernel for silica / zeolites with cylindrical pores. If not stated differently, the micropore volume was determine with the same NLDFT kernel considering pores smaller 2 nm and pores between 2 nm and 20 nm as mesopore volume o. In absence of micropores, the range from 0 nm to 20 nm was considered for the mesopore volume, since larger pores are expected to be interparticle spaces. Analysis of nitrogen and argon measurements were carried out with *Quadrawin*™ 6.0.
Water vapor sorption measurements were carried out at 298 K with *Quantachrome Vstar™* vapor sorption analyzer using *VstarWin* 1.1.6 for analysis.

Mercury intrusion porosimetry (MIP)

Mercury intrusion porosimetry was measured with *Quantachrome Poremaster®*, measurements analysis with *Poremaster for Windows®* 7.01 and with *micromeritics AUTOPORE V SERIES*. For mercury a contact angle of 140 ° and surface tension of 480 dynes·cm^{-1} was considered. The pore size maxima were obtained with Gaussian fits.

Powder X-Ray Diffraction (P-XRD)

Diffraction patterns were recorded on two different instruments at room temperature applying filtered $Cu_{K\alpha1}$ radiation. For analysis the analysis software *X'Pert Highscore Plus* was used in both cases.

Theta-theta geometry was measured with *Panalytical MPD X'Pert Pro* at 45 kV, 40 mA, step width 0.013 °2θ in the range of 0-10 °2θ and 250 s per step and in the range of 5-50 °2θ with 74 s per step.
STOE Stadi P (transmission geometry) was measured in the range of 0-50 °2θ, using the measurement parameter: 40 kV, 40 mA, step width 0.010 °2θ, 20 s per step.

Thermal analysis (TG/DTA/MS):

Thermoanalysis was carried out with *Netzsch STA 449 F3 Jupiter* coupled with mass spectrometer *QMS 403C Aëolos Quadrupol* in Ar/O_2 (80/20) with a flow of 40 mL·min^{-1} and heating rate of 5 K·min^{-1}. For analysis software, *Netzsch Proteus Thermal Analyse 5.0* was used.
In plots of TG/MS measurements, mass loss over temperature is plotted together with the plot of selected ion currents that were temperature-dependently detected in the exhaust gas. Typical decomposition products of organic compounds, m/z = 44 (CO_2), and water m/z = 18 (H_2O), were tracked. For the detection of the surfactant the ion current of m/z = 58 (C_3H_8N), which is the main fragment in electron impact ionization of quaternary amines, was used.[193] Forrection of mass loss values, the mass at a temperature of 150 °C or 150 °C was set at 100 % to eliminate the effect of water on the surface for better comparability.

Scanning electron microscope (SEM) and transmission electron microscopy (TEM)

Three different instruments were used: *Zeiss Leo 1525 Gemini* with acceleration voltage of 5 kV using an *Inlense detector* after carbon sputtering of the sample. For measurements at low magnification (x100, x400 in Chapter 4.3) without carbon sputtering *HITACHI TM-1000 Tabletop microscope* was used. Measurements with high resolution for preparation of TEM samples were carried out with *Zeiss Leo 1550*. For TEM measurements *TEMs JEOL JEM-1011* (100 kV) and *JEOL JEM 2200 FS (200 kV)* were used, the samples were prepared by dispersion in Ethanol and measured on a standard carbon coated cupper grid (400 mesh).

Elementary analysis

Carbon, hydrogen and nitrogen percentages were quantified with *CHN Elementaranalysator vario ELII* by *elementar*, oxygen with *uroEA Elemental Analyzer* with *HEKAtech HT* oxygen *Analyzer.*

Mass spectrometry

For ESI mass spectrometry *Agilent 6224 ESI-TOF* with *Agilent HPLC 1200 Series* was used, for EI-MS the device *Thermo ISQ LT EI* with *Thermo Trace 1300*.

Nuclear magnetic resonance (NMR)

Liquid state ^{1}H-NMR and ^{13}C-NMR measurements were carried out with instruments by *Bruker Fourier* 300 MHz spectrometer or *Avance I* 500 MHz spectrometer, using software *MestreNova 10.0*, ^{19}F-NMR measurements were carried out with Bruker *AvanceIII HD* 600 MHz spectrometer, analyzed with software *TopSpin* 3.5. Solvents for reference were used according to the literature.[243]

Solid state NMR

Avance 400 spectrometer (Bruker), 4 mm double resonance probe. ^{13}C-CP MAS NMR: ramped polarization transfer from protons to carbons, operating frequency of 100.66 MHz. 1H 90° pulse length of 4.0 µs, contact time of 1 ms, and the repetition delay of 4 s, MAS rate of 13 kHz. Two phase modulation (TPPM) decoupling. ^{29}Si-CP MAS NMR: Operating frequency: 79.52 MHz using ^{1}H 90° pulse length of 4.2 µs, contact time: 2ms, and recycle delay: 5s. MAS rate: 5 kHz. Continuous wave decoupling was used during the acquisition.
2D FSLG-HETCOR-NMR: ramped polarization transfer from proton to either ^{13}C or ^{29}Si, CP times of 2 ms, ^{1}H rf field strength of 60 kHz, 200 increments with States-TPPI method for phase-sensitive detection in t_1 dimension.

IR spectroscopy

IR spectra were performed with a FT-IR spectrometer *Vertex 70* by *Bruker* as KBr discs.

8.2 Synthesis of the precursors

1,4-Bis(triethoxysilyl)benzene (BTEB)[68] and 2,5-((*E*)-2'-bis(triethoxysilyl)vinyl)aniline (BTEVA)[107] were synthesized according to the literature.
All further precursors were synthesized in a double Heck cross-coupling as described below. The respective starting materials were purchased from commercial suppliers: Bis(tri-tert-butylphosphine)palladium(0) (*abcr*, 98 %), 1,4-dibromobenzene (*Aldrich*, 98 %), 1,4-dibromo-2-chlorobenzene (*abcr*, 98 %), 1,4-dibromo-2-fluorobenzene (*abcr,* 98 %), 1,4-dibromo-2,5-

fluorobenzene (*abcr*, 98%), 2,5-dibromanilin (*Aldrich*, 98 %), *N*,*N*-dicyclohexylmethylamine (*Aldrich*, 97 %), triethoxyvinylsilane (97 %*Merck*).

The general synthesis path for 1,4-((*E*)-2'-bis(triethoxysilyl)vinyl)benzene, 1,4-((*E*)-2'-bis(triethoxysilyl)vinyl)-2-fluorobenzene 1,4-((*E*)-bis(triethoxysilyl)vinyl)2,5-difluorobenzene and 1,4-2-chloro-1,4-((*E*)-2'-bis(triethoxysilyl)vinyl)-benzene is given below. The respective amounts of substances of the starting materials for the different precursors are given as tables followed by information on the respective yield and characterizations.

The reaction was carried out under dry conditions and a nitrogen atmosphere.

1,4-Dioxane was degassed by the freeze-pump-thaw method three times before *N*,*N*-dicyclohexylmethylamine, triethoxyvinylsilane and the respective bromated starting material were dissolved. The catalyst $Pt[P(^tBu)_3)]_2$ was added and the suspension was heated to 80 °C for 18 hours. After quantitative consumption of the starting material the reaction mixture was cooled in an ice bath to precipitate the formed salt quantitatively. The reaction mixture was filtered and washed with *n*-hexane. The filtrate was concentrated under reduced pressure and the residue was diluted in cold *n*-hexane. The organic phase was washed with cold hydrochloric acid (2 x 30 mL, c = 1.0 mol·L^{-1}) and cold brine (30 mL) quickly, then dried over anhydrous magnesium sulfate. The solvent was removed under vacuum and the raw product was purified by distillation under vacuum.

8.2.1 1,4-((*E*)-2'-Bis(triethoxysilyl)vinyl)benzene (BTEVB)

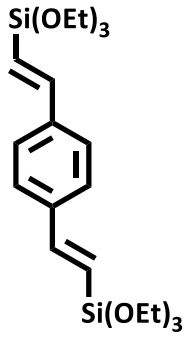

$C_{22}H_{38}O_6Si_2$
M= 454.7 g/mol

	volume / ml	mass / g	amount / mmol	equiv.
1,4-dioxane	150			
***N*,*N*-dicyclohexylmethylamine (97 %)**	29	26.4	130.9	2.1
triethoxyvinylsilane	27	24.2	130.9	2.1
$Pd[P(^tBu)_3]_2$		0.5	1.0	0.007
1,4-dibomobenzene		15.0	62.3	1

Yield: 21 g (45 mmol, 72 %), colorless liquid

b.p. = 195 °C ($1.3 \cdot 10^{-2}$ mbar)

R_f = 0.49 (*n*-heptane:ethylacetate 9:1)

HRMS(ESI^+) *m/z* [Da]: 455.230 (calc. for $[C_{22}H_{39}O_6Si_2]^+$: 455.229).; 477.212 (calc. for $[C_{22}H_{38}O_6Si_2Na]^+$: 477.210).

HRMS(EI^+) : *m/z* (%): 472.26 $[C_{22}H_{37}F_2O_6Si_2]^+$, 163.12 $[Si(OEt)_3]^+$.

Elementary analysis: C = 58.11 % (calc.: 57.91 %), H = 8.42 % (calc.: 8.45 %)

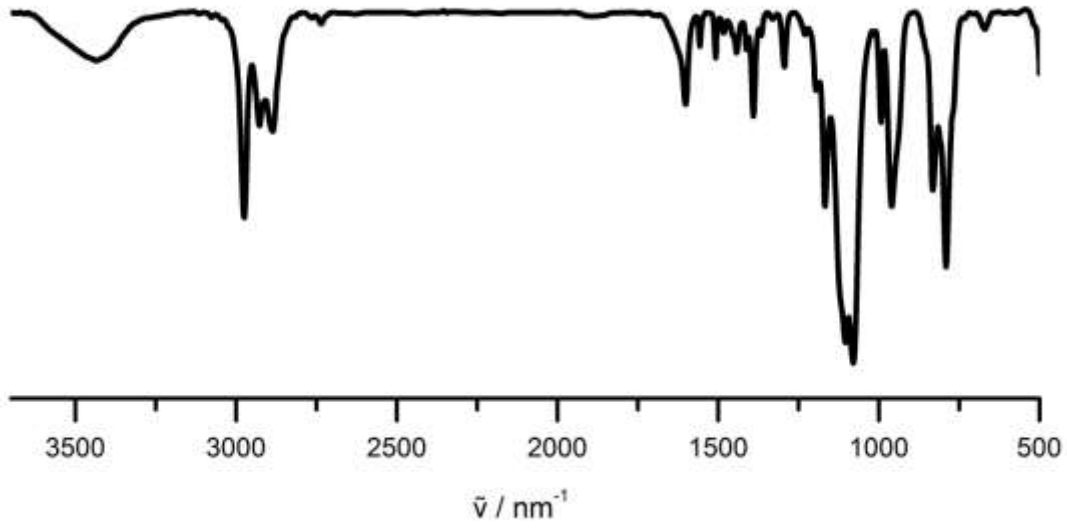

FT-IR (KBr disc): $\tilde{\nu}$ [cm^{-1}] = 3435(w), 2974 (s), 2926 (s), 2885 (s), 1601 (m), 1556 (m), 1508 (m) 1391 (m), 1167 (m), 1103 (s), 1080 (s), 993 (m), 961 (m), 831 (m).

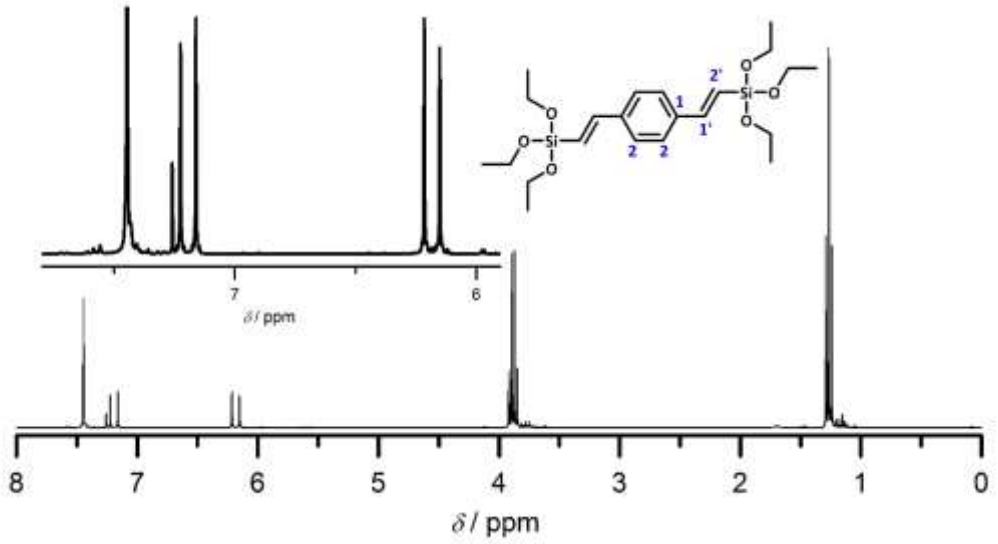

^{1}H-NMR (300 MHz, $CDCl_3$, 25 °C): δ [ppm] = 7.45 (s, 4 H, H-2); 7.19 (d, 2 H, ^3J = 19.3 Hz H1'); 6.18 (d, 2 H, ^3J = 19.3 Hz, H2'); 3.88 (q, 12 H, $^3J_{CH2\text{-}CH3}$ = 7 Hz,C**H$_2$**); 1.27 (t, 18 H, $^3J_{CH2\text{-}CH3}$ = 7 Hz, C**H$_3$**).

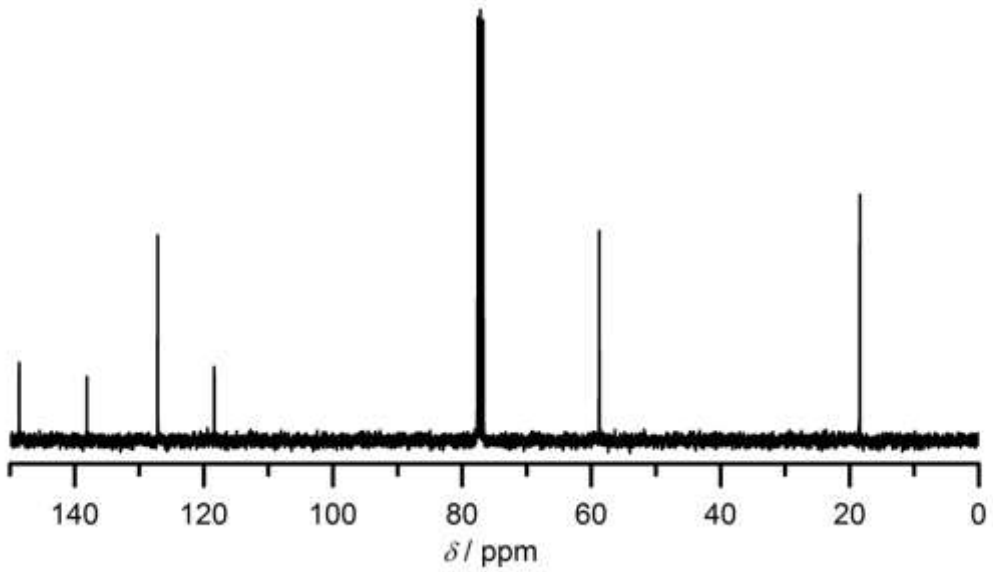

^{13}C {^{1}H}-NMR ($CDCl_3$, 100 MHz, 25 °C): δ (ppm) = 148.6 (C1'); 138.1 (C1); 127.2 (C2); 118.4 (C2'); 58.8 (CH_2); 18.4 (CH_3).

8.2.2 1,4-((*E*)-2'-Bis(triethoxysilyl)vinyl)-2-fluorobenzene (BTEVFB)

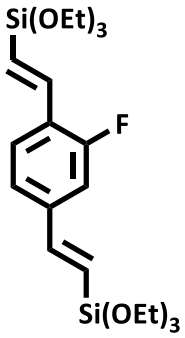

$C_{22}H_{37}FO_6Si_2$
M= 472.7 g/mol

	Volume / ml	mass / g	amount / mmol	equiv.
1,4-dioxane	150			
***N*,*N*-dicyclohexylmethylamine (97 %)**	18	16.5	81.7	2.1
triethoxyvinylsilane	17	15.1	81.7	2.1
$Pd[P(^tBu)_3]_2$		0.3	0.6	0.007
1,4-dibrom-2-fluorobenzene		10.0	38.9	1

Yield: 11.7 g (25 mmol, 72 %), colorless liquid

b.p. = 180 °C ($2.1 \cdot 10^{-2}$ mbar)

R_f = 0.57 (*n*-heptane:ethylacetate 9:1)

HRMS(ESI^+) *m/z* [Da]: 495.215 (calc. for $[C_{22}H_{37}F_2NaO_6Si_2]^+$: 495.20); 473.240 (calc. for $[C_{22}H_{37}F_2O_6Si_2]^+$: 473.219).

HRMS(EI^+) : *m/z* (%): 472.20 $[C_{22}H_{37}F_2O_6Si_2]^+$, 163.11 $[Si(OEt)_3]^+$.

Elementary analysis: C = 53.80 % (calc.: 53.85 %), H = 7.39 % (calc.: 7.39 %)

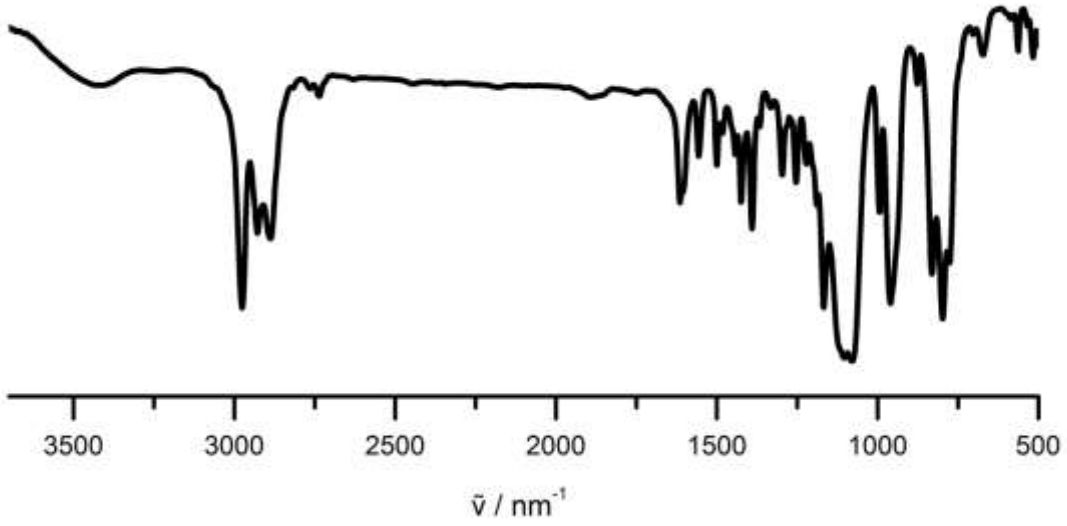

FT-IR (KBr disc): $\tilde{\nu}$ [cm^{-1}] = 3436 (w), 2977 (s), 2928 (m), 2888 (m), 2736 (w), 1603 (m), 1488 (m), 1424 (m), 1391 (m), 1168 (m), 1081 (vs), 999 (m), 962 (s), 822 (s), 781 (s).

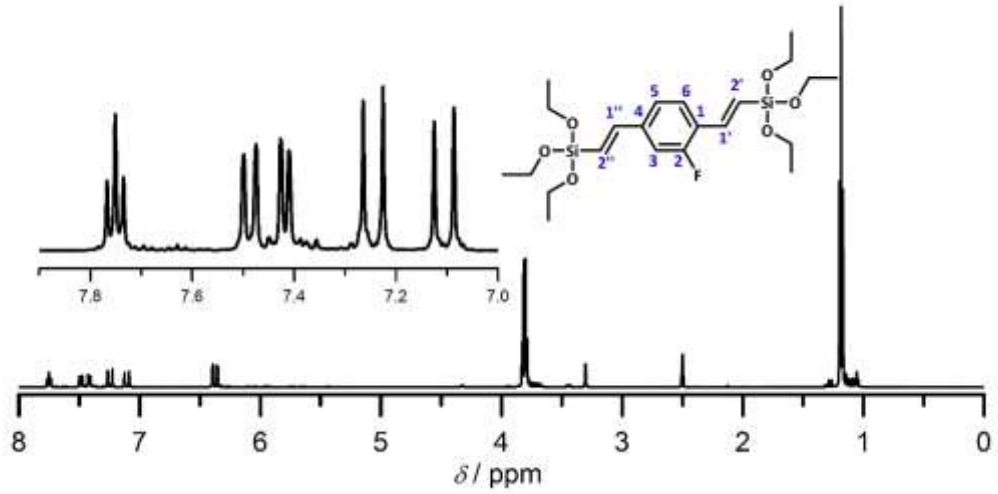

^{1}H-NMR (400 MHz, DMSO-*d*$_6$, 25 °C): δ [ppm] = 7.75 (dd, $^3J_{H5\text{-}F}$ = 8.0 Hz, 1 H, H6), 7.49 (dd, $^3J_{H2\text{-}F}$ = 12.1 Hz, $^4J_{H3\text{-}H5}$ = 1.7 Hz, 1 H, H3), 7.42 (dd,$^3J_{H5\text{-}H4}$ = 8.1 Hz, $^4J_{H5\text{-}H3}$ = 1.7 Hz, 1 H, H5), 7.25 (d,$^3J_{H1'\text{-}H2'}$ = 19.5 Hz, 1 H, H1'), 7.11 (d,$^3J_{H1''\text{-}2''}$ = 19.3 Hz, 1 H, H1''), 6.38 (d,$^3J_{H2'\text{-}H1'}$ = 19.4 Hz, 1 H, H1'), 6.38 (d,$^3J_{H2''\text{-}H1''}$= 19.4 Hz, 1 H, H2''), 3.81 (q, ^3J = 7.0 Hz, 6 H, CH'_2), 3.81 (q, ^3J = 6.9 Hz, 6 H, CH''_2), 1.18 (t,$^3J_{CH_2\text{-}CH_3}$= 7.0 Hz, 9 H, $C'H_3$), 1.18 (t, $^3J_{CH_2\text{-}CH_3}$ = 7.0 Hz, 9 H, CH''_3).

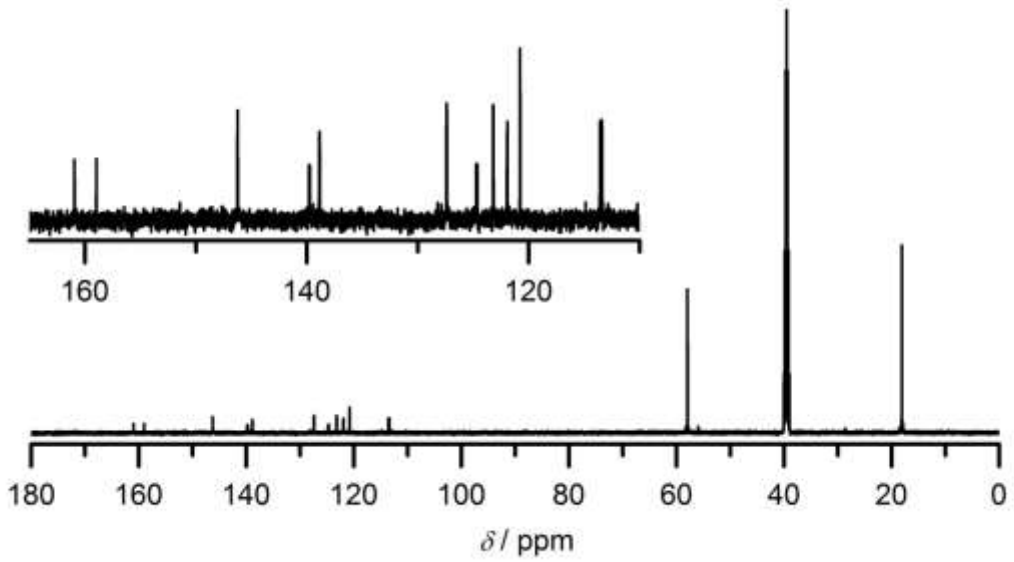

^{13}C {^{1}H}-NMR (100.6 MHz, DMSO-*d*$_6$, 25 °C): δ [ppm] = 160.0 ($^{1}J_{C2\text{-}F}$ = 248.5 Hz, C2), 146.3 ($^{4}J_{C1''\text{-}F}$ = 2.2 Hz, C1''), 139.8 ($^{3}J_{C4\text{-}F}$ = 8.7 Hz, C4), 138.8 ($^{3}J_{C1'\text{-}F}$ = 4.1 Hz, C1'), 127.4 ($^{3}J_{C6\text{-}F}$ = 3.4 Hz, C6), 124.7 ($^{2}J_{C1\text{-}F}$ = 11.9 Hz, C1), 123.2 ($^{4}J_{C5\text{-}F}$ = 2.5 Hz, C5), 121.9 ($^{4}J_{C'\text{-}F}$ = 3.3 Hz, C'), 120.8 (C''), 113.5 ($^{2}J_{C3\text{-}F}$= 22.8 Hz, C3), 58.0 (C'H_2), 57.9 (C'H_2), 18.1 (C'H_3), 18.1 (C''H).

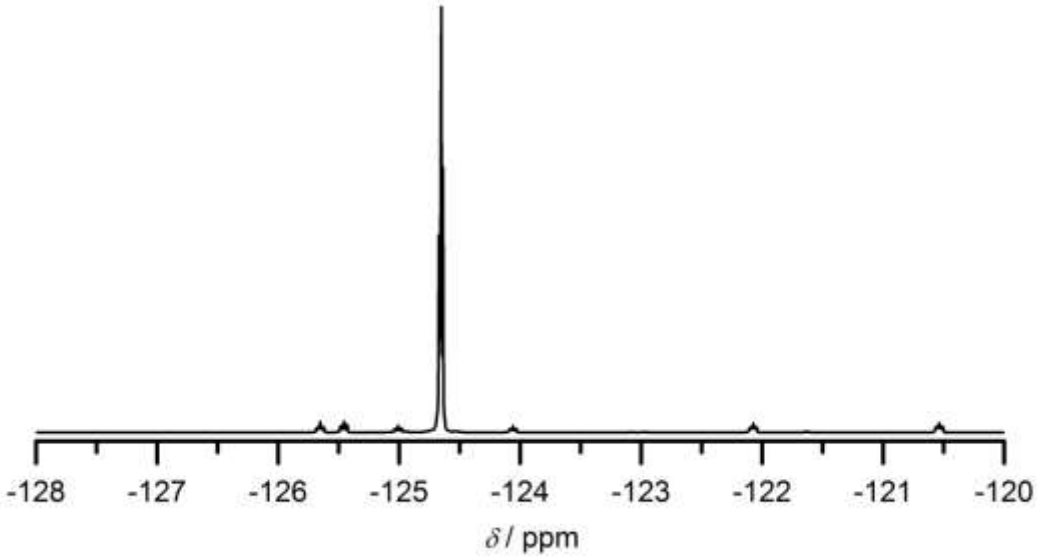

^{19}F-NMR (600 Hz, DMSO-d$_6$, 25 °C): δ [ppm] = -119.95 (dd, $^{3}J_{F\text{-}H3}$ = 12.2 Hz, 1F).

8.2.3 1,4-((*E*)-2'-Bis(triethoxysilyl)vinyl)-2,5-difluorobenzene (BTEV2FB)

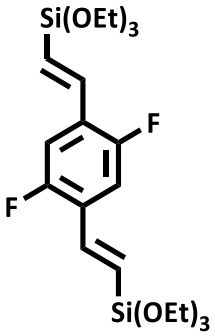

$C_{22}H_{37}ClO_6Si_2$
M= 489.2 g/mol

	Volume / ml	mass / g	substance / mmol	equiv.
1,4-dioxane	150			
***N*,*N*-dicyclohexylmethylamine (97 %)**	8	7.6	37.8	2.1
triethoxyvinylsilane	8	7.0	37.8	2.1
$Pd[P(tBu)_3]_2$		0.1	0.2	0.007
1,4-dibrom-2,5-difluorobenzene		5.0	18.0	1

Yield: 5.2 g (11 mmol, 59 %), light yellow powder

b.p.: = 162 °C ($1.9 \cdot 10^{-2}$ mbar),

R_f = 0.57 (*n*-heptane:ethylacetate 9:1),

HRMS(ESI$^+$): *m/z* [Da]: 491.288 (calc. for $[C_{22}H_{38}FO_6Si_2]^+$: 491.21).

HRMS(EI$^+$): *m/z* (%): 490.13 $[C_{22}H_{37}F_2O_6Si_2]^+$, 163.10 $[Si(OEt)_3]^+$.

Elementary analysis: C = 53.78 % (calc.: 53.85 %), H = 7.37 % (calc.: 7.39 %)

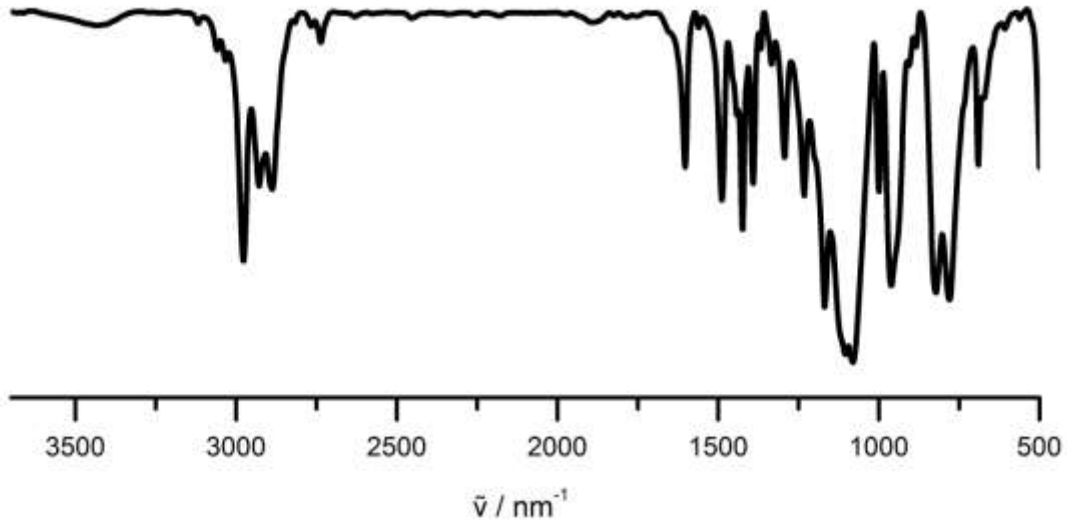

FT-IR (KBr disc): $\tilde{\nu}$ [cm^{-1}] = 3436 (w), 2977 (s), 2928 (m), 2888 (m), 2736 (w), 1603 (m), 1488 (m), 1424 (m), 1391 (m), 1168 (m), 1081 (vs), 999 (m), 962 (s), 822 (s), 781 (s).

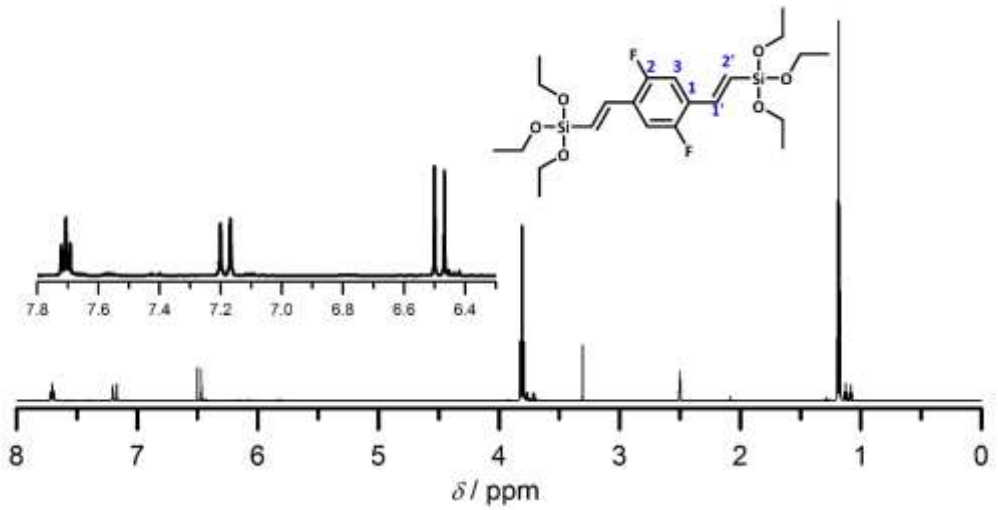

^{1}H-NMR (600 MHz, DMSO-*d*$_6$, 25 °C): δ [ppm] = 7.71 (dd, $^3J_{H3\text{-}F}$ = 8.7 Hz, 2 H, H3), 7.19 (d, $^3J_{H1'\text{-}H2'}$ = 19.3 Hz, 2 H, H1'), 6.48 (d, $^3J_{H2'\text{-}H1'}$ = 19.4 Hz, 2 H, H2'), 3.81 (q, $^3J_{CH_2\text{-}CH_3}$ = 7.0 Hz, 12 H, CH_2), 1.18 (t, $^3J_{CH_2\text{-}CH_3}$ = 7.0 Hz, 18 H, CH_3).

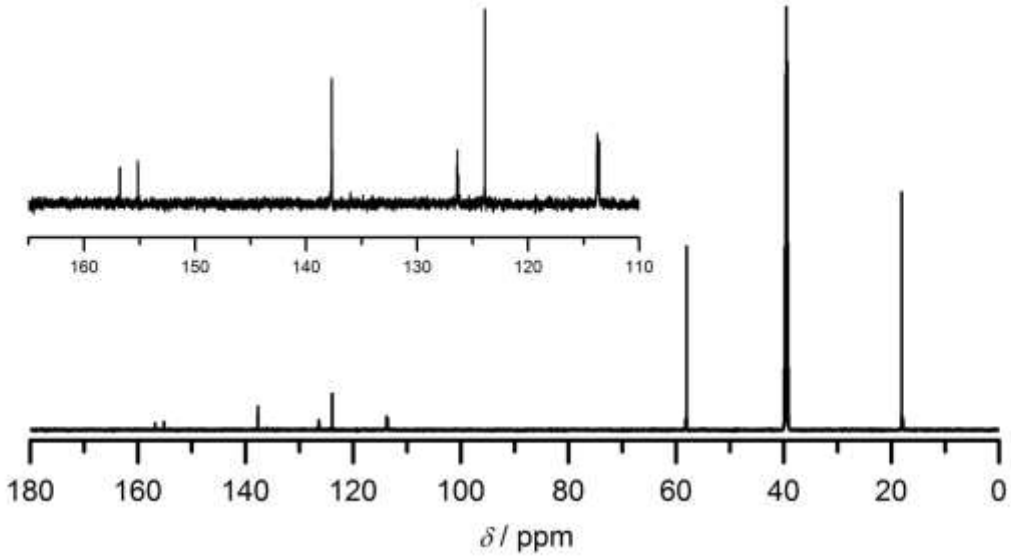

^{13}C {^{1}H}-NMR (100.6 MHz, DMSO-*d*$_6$, 25 °C): δ [ppm] = 156.0 ($^{1}J_{C2\text{-}F}$ = 246.2 Hz, C2), 137.8 (C1'), 126.4 ($^{3}J_{C1\text{-}F}$ = 12.9 Hz, C1), 123.9 (C2'), 113.8 ($^{3}J_{C1\text{-}F}$ = 19.9 Hz, C3), 58.3 (CH_2), 18.1 (CH_3).

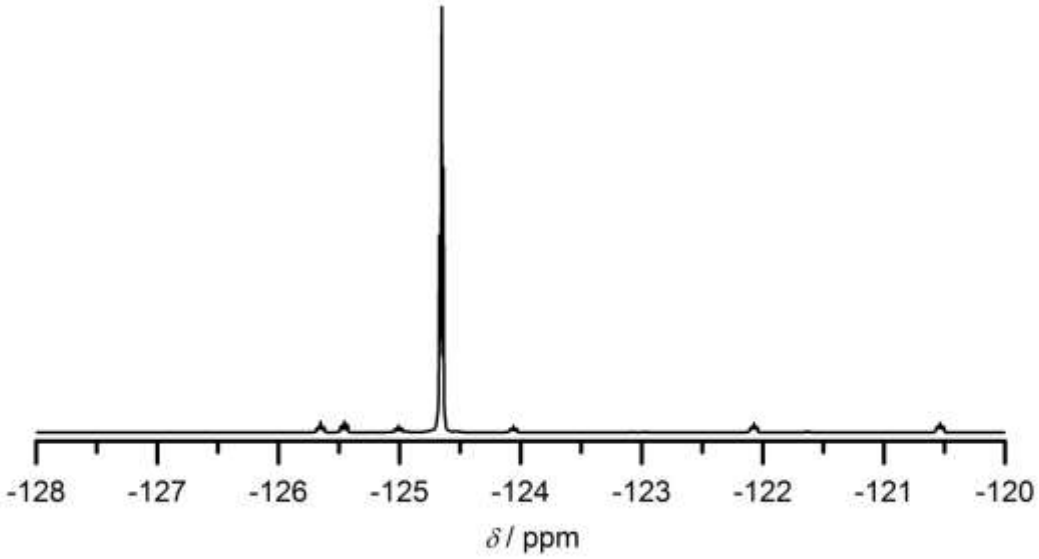

^{19}F-NMR (600 Hz, DMSO-d$_6$, 25 °C): δ [ppm] = -124.65 (t, $^{3}J_{F\text{-}H3}$ = 8.2 Hz, 2F).

8.2.4 2-Chlor-1,4-((*E*)-2'-bis(triethoxysilyl)vinyl)benzene (BTEVClB)

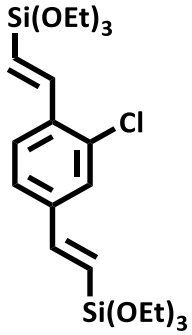

$C_{22}H_{37}ClO_6Si_2$
M= 489.2 g/mol

	Volume / ml	mass / g	substance / mmol	equiv.
1,4-dioxane	150			
***N*,*N*-dicyclohexylmethylamine (97 %)**	8	7.7	38	2.1
triethoxyvinylsilane	8	7.0	38	2.1
$Pd[P(tBu)_3]_2$		0.1	0.2	0.007
1,4-dibrom-2-chlorobenzene		5.0	18	1

Yield: 3.4 g (6.8 mmol, 37 %), light yellow liquid

b.p.: = 180 °C ($9.2 \cdot 10^{-3}$ mbar)

R_f = 0.52 (*n*-heptane:ethylacetate 9:1).

HRMS(ESI^+): *m/z* [Da]: 489.191 (100%), 491.189 (40%), 490.193 (30%) (calc for. $[C_{22}H_{38}ClO_6Si_2]^+$: 489.190 (100%), 491.187 (32%), 490.193 (24%)).

HRMS(EI^+): *m/z* [Da]: 488.210(100%), 490.217(41%), 489.225 (34%) (calc for. $[C_{22}H_{37}ClO_6Si_2]^+$: 488.182 (100%), 490.179 (32%), 489.185 (24%)), 163.188 $[Si(OEt)_3]^+$

Elementary analysis: C = 55.39 % (calc.:54.02 %), H = 7,.68 % (calc.: 7.62 %)

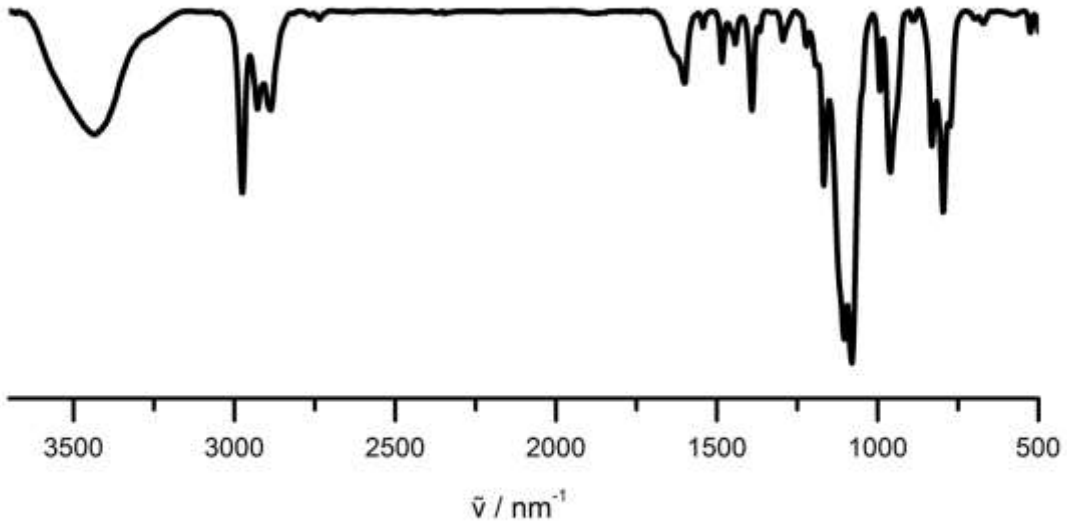

FT-IR (KBr disc): $\tilde{\nu}$ [cm^{-1}] = 3436 (w), 2975 (s), 2927 (m), 2887 (m), 2736 (w), 1600 (m), 1543 (m), 1484 (m), 1391 (m), 1366 (w), 1294 (w), 1221(w), 1167 (s), 1103 (vs), 1080(vs), 993 (m), 961 (s), 831 (s), 776 (s), 697(w), 671(w).

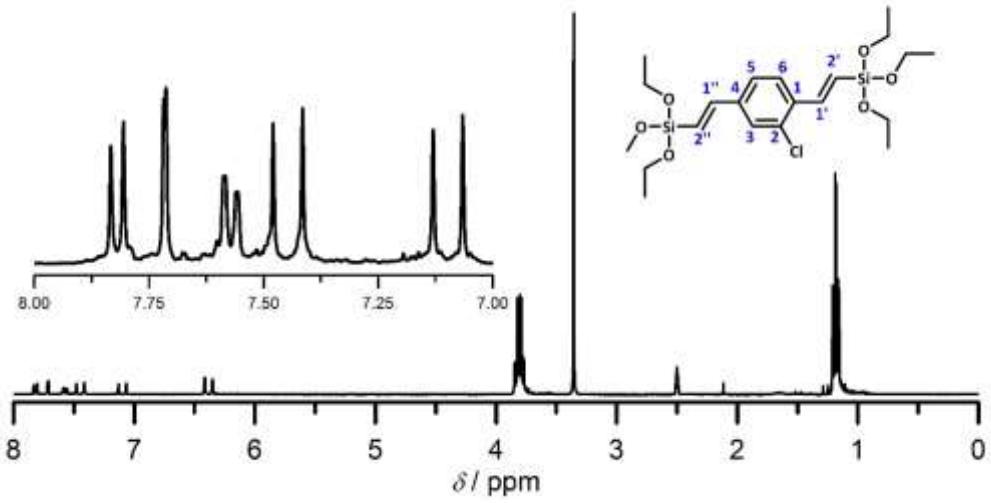

^{1}H-NMR (300 MHz, DMSO-*d*$_6$, 25 °C): δ [ppm] = 7.82 (d, $^{3}J_{H6\text{-}H5}$ = 8.2 Hz, 1 H, H6), 7.72 (d, $^{3}J_{H3\text{-}H5}$ = 19.3 Hz, 1H, H3), 7.58 (d, $^{3}J_{H5\text{-}H6}$ = 8.1 Hz, $^{3}J_{H5\text{-}H3}$ = 1.6 Hz 1H, H5), 7.45 (d, $^{3}J_{CH=CH}$= 19.3 Hz, 1H, H1‘),7.10 (d, $^{3}J_{CH=CH}$ = 19.3 Hz, 1H, H1‘‘),6.39 (d, $^{3}J_{CH=CH}$ = 19.3 Hz, 2H, H2‘, H2‘‘) 3.81 (q, $^{3}J_{CH_2\text{-}CH_3}$ = 7.0 Hz, 6 H, CH_2), 3.80 (q, $^{3}J_{CH_2\text{-}CH_3}$ = 7.0 Hz, 6 H, CH_2), 1.19 (t, $^{3}J_{CH_2\text{-}CH_3}$ = 7.0 Hz, 9 H, CH_3), 1.18 (t, $^{3}J_{CH_2\text{-}CH_3}$ = 7.0 Hz, 9 H, CH_3).

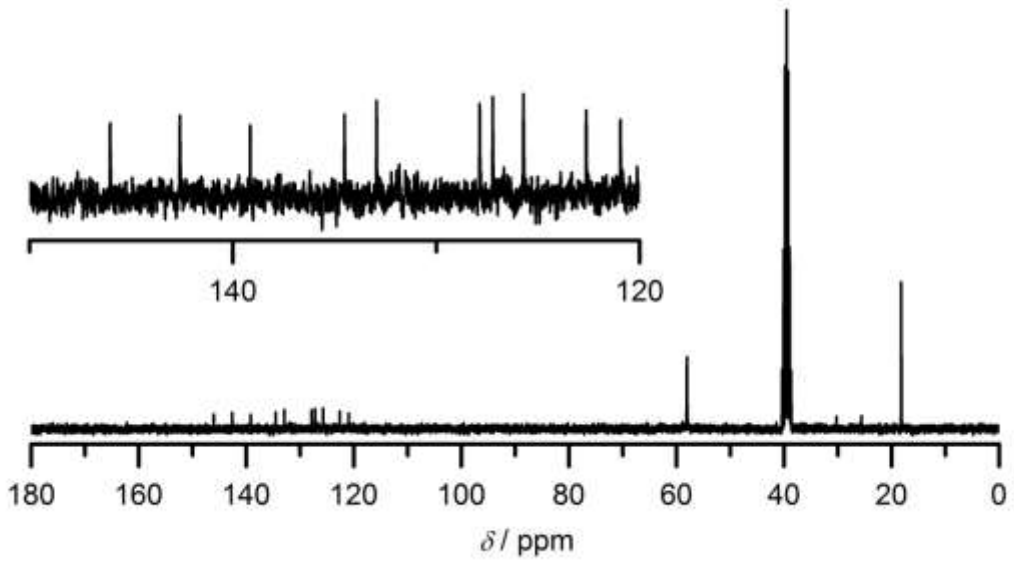

^{13}C {^{1}H}-NMR (75 MHz, DMSO-d_6, 25 °C): δ [ppm] = 146.0 (C1''), 142.6 (C1'), 139.2 (C4), 134.5 (C1), 132.9 (C2), 127.9 (C3), 127.2 (C6), 125.7 (C5), 122.6 (C2',C2'), 121.0 (C2', C2'), 58.0(CH_2), 18.2(CH_3).

8.3 General synthesis in 4.1 Syntheses of organosilicas

8.3.1 Synthesis of PMOs with halogen substituents

In a typical synthesis the surfactant C_{18}TAB (1.16 g, 3.18 mmol) was dissolved in sodium hydroxide solution (25 mL, 0.6 mol·L^{-1}) at 50 °C and stirred for another 30 minutes before the respective precursor (BTEVFB: 1.00 g, 2.11 mmol; BTEV2F, BTEVClB: 1.00 g, 2.04 mmol) was added. The solution was stirred overnight at 50 °C before the temperature was increased to 80 °C or 100 °C for 24 hours (6.5 hours F-PMO 1). For HTT synthesis glass vessels sealed with screw caps were used that were set into an oven under static conditions, whereas syntheses that were set under reflux conditions (F-PMO 4-5; 2F-PMO and Cl-PMO) were carried out in round bottom flasks with a reflux condenser at atmospheric pressure. During the synthesis a gelatinous phase was formed in all cases. For work-up of the reaction mixture the precipitate was separated from the reaction solution and ths jelly-like phase by centrifugation (10 minutes, 10000 rpm, 5 °C). For washing, it was re-suspended first in water than in ethanol. Subsequently, the surfactant was removed by Soxhlet extraction with ethanol / HCl (32 %) (97/3, v/v) for three day and the organosilica materials were dried at 80 °C.

Table 8-1: Summary of synthesis conditions for halogen-containing PMOs.

Sample		Temperature	Treatment time
F-PMO 1	HTT oven	100 °C	6.5 h
F-PMO 2	HTT oven	100 °C	24 h
F-PMO 3	HTT oven	80 °C	24 h
F-PMO 4	reflux	100 °C	24 h
F-PMO 5	reflux	80 °C	24 h
2F-PMO	reflux	100 °C	24 h
Cl-MOS	reflux	100 °C	24 h

8.3.2 General synthesis of high surface area PMOs

B-PMO synthesis

For a typical synthesis the respective volume of hydrochloric acid (32%) was dissolved in water before the surfactant was dissolved at 40 °C. The solution was cooled to room temperature and stirred for 30 minutes before the precursor was added. The opaque solution was stirred in a glass

bottle with screw cap at room temperature overnight and subsequently treated at 100 °C under static conditions for 24 hours. It was filtered and the precipitate was washed with water and ethanol before the surfactant was removed by Soxhlet extraction with ethanol/HCl (32 %) (97/3, v/v) for three days. Afterwards, the organosilica materials were dried at 80 °C.

Table 8-2: Summary of the composition of the synthesis mixtures for B-PMO 1–4.

Sample	BTEB		C_{16}TAB		HCl			H_2O
	/ µL	/ mmol	/ mg	/ mmol	conc. / mol·L^{-1}	/ ml	/ mmol	/ mol
B-PMO 1	300	0.74	300	0.82	0.1	10	0.87	0.556
B-PMO 2	300	0.74	300	0.82	1.0	10	8.7	0.537
B-PMO 3	2000	5.0	1500	4.1	1.0	50	51	2.72
			C_{10}TAB					
B-MOS	2000	5.0	3000	10.7	1.0	50	51	2.72

Further synthesis under acidic conditions

For a typical synthesis the surfactant was dissolved in the respective acidic solution at 40 °C. The solution was cooled to room temperature and stirred for 30 minutes before the precursor was added. The opaque solution was stirred in a glass bottle with screw cap at room temperature overnight and subsequently treated at 100 °C under static conditions for 24 hours For work-up of the reaction mixture the precipitate was separated from the reaction solution by centrifugation (10 minutes, 10000 rpm, 5 °C). For washing, it was re-suspended first in water than in ethanol. Subsequently, the surfactant was removed by Soxhlet extraction with ethanol/ HCl (32 %) (97/3, v/v) for three days. Afterwards, the organosilica materials were dried at 80 °C.

Table 8-3: Summary of the composition of the synthesis mixtures for materials synthesized under acidic conditions.

Sample	Precursor		C_{16}TAC		Acid 1.0 mol·L^{-1}			H_2O
	/µL	/mmol	/mg	/mmol		/mL	/mmol	/mol
DVB-MOS 1	300	0.66	660	2.1	HCl	10	100	0.56
DVB-MOS 2	300	0.66	660	2.1	H_2SO_4	20	200	1.11
DVB-MOS 3	300	0.66	660	2.1	H_3PO_4	20	200	1.11
F-MOS	300	0.63	324	0.89	HCl	8	80	0.44
2F-MOS	300	0.61	311	0.85	HCl	8	80	0.44

8.3.3 General synthesis of microporous organosilica materials

Microporous organosilica materials synthesized at pH 12.0

C_{10}TAB was dissolved in 12 mL sodium hydroxide solution (0.01 mol·L^{-1}) at 40 °C and stirred for another 30 minutes at room temperature before the precursor was added. The mixture was stirred at room temperature overnight, then treated at 100 °C in a screw cap bottle for 24 hours. The precipitate was filtered, washed with water and ethanol, the surfactant was removed in a Soxhlet apparatus using ethanol/HCl (32 vol %) 97/3 (v/v) for three days. The extracted beads were again washed with water and ethanol and dried at 80 °C.

Table 8-4: Summary of the composition of the synthesis mixtures for microporous organosilicas synthesized at pH 12.0.

Sample	**Precursor**		**C_{10}TAB**		**NaOH (0.01 mol·L^{-1})**		**H_2O**
	/µL	**/mmol**	**/mg**	**/mmol**	**/mL**	**/mmol**	**/mol**
B micro	1000	2.4	1000	3.6	35	0.35	1.9
DVB-micro	450	1.0	450	1.6	12	0.12	0.66
DVA micro	300	0.6	300	1.1	10	0.10	0.55

Microporous organosilica materials synthesized in EtOH/NaOH solution

A mixture of 7.5 mL ethanol (99.8 %) and 2.5 mL sodium hydroxide solution (0.31 mol·L^{-1}, pH 13.5) was prepared. Of this solution, 1.0 mL (resulting molar amount ethanol: 12.8 mmol, NaOH: 0.08 mmol) was mixed with 1.0 mL of the respective precursor (2.2 mmol BTEVB; 2.1 mmol BTEVA, BTVFB; 2.0 mmol BTEV2FB) and treated at 80 °C under static conditions for 24 hours. The material was filtered, washed with water and ethanol and was subsequently dried at 80 °C.

8.4 General synthesis in 4.2 Pseudomorphic transformation of CPG

Preparation of C_{16}TAOH solution

For the preparation of C_{16}TAOH solution anion exchange of a C_{16}TAB with a concentration of 0.08 mol·L^{-1} was carried out using the ion exchange resin *Ambersep®* 900 hydroxide form in a column. The resin (250 g) was prepared by soaking in demineralized water under stirring and subsequent transfer to a glass column with valve. Water was removed and the resin was activated by addition of sodium hydroxide solution (1.0 mol·L^{-1}) with a drop-wise flow. Afterwards, the resin was washed with demineralized water until it was neutral. The prepared C_{16}TAB solution was heated to 60 °C before it was added to the resin with drop-wise flow of 10 mL·min^{-1}. The pH value was determined with a pH meter.

Classical pseudomorphic transformation of CPG beads, granules and membranes

Depending on the total volume, 30 mL soda lime glass tubes with screw cap or a *Schott® Duran* pressure plus bottle 100 mL, 500 mL or 1.0 L were used as reaction vessel for pseudomorphic transformations. In a typical transformation process the CPG was placed in a glass vessel before the surfactant containing solution was added. The mixture was swiveled shortly before it was heated to the requested temperature in an oven under static conditions for the requested time. If not stated differently 8 mL of the C_{16}TAOH solution (0.08 mol·L^{-1}, 0.64 mmol, 0.2 equiv.) were added to 200 mg CPG (3.2 mmol SiO_2) and the transformation took place over 4 days at 100 °C. In labeled examples, instead of C_{16}TAOH solution, 300 mg C_{16}TAB (0.82 mmol) was dissolved in sodium hydroxide solution (0.1 mol·L^{-1} for pH 13.0 and 0.05 mol·L^{-1} for pH 12.7) at 40 °C and the solution was homogenized for 30 minutes under stirring at room temperature before CPG was added. After hydrothermal treatment the samples were cooled down to room temperature, filtered and washed with water and ethanol before drying at 80 °C. Reference samples for the microwave-assisted synthesis were not cooled down but filtered in the hot state and further treated as for all other samples. The surfactant was removed by calcination at 550 °C (heating rate of 2 K·min^{-1}, 6 hours at 550 °C).

Pseudomorphic transformation with C_{10}TAB

C_{10}TAB (0.23 g, 0.82 mmol) was dissolved in sodium hydroxide solution (0.10 mol·L^{-1}, pH 13.0) at room temperature and stirred for 30 minutes before 200 mg CPG was added and the sample was

hydrothermally treated in a screw cap bottle under static conditions at 100 °C for four days. The product was filtered, washed with water and ethanol and dried at 80 °C. The surfactant was removed by calcination at 550 °C (heating rate of 2 $K \cdot min^{-1}$, 6 hours at 550 °C).

Microwave-assisted pseudomorphic transformation of CPG

For syntheses under microwave radiation a device from *CEM Discover®* was used.
In a typical synthesis procedure C_{16}TAB (300 mg, 0.82 mmol) was dissolved in 8 mL sodium NaOH solution (0.1 $mol \cdot L^{-1}$, 0.8 mmol) at 40 °C and the solution was homogenized for 30 minutes under stirring at room temperature. 200 mg CPG were added immediate before introduction in the microwave. The solution was heated up to 100 °C with a maximum power of 15 Watt in approximately 60 seconds under stirring. The temperature was held for the requested time before cooling down to 70 °C with the help of air cooling. The samples were filtered, washed with water and ethanol and dried at 80 ° C before the surfactant was removed by calcination at 550 °C.

8.5 General synthesis of 4.3 Organosilica/silica hybrid materials

8.5.1 General synthesis in 4.3.1 Trial for the exchange of silica versus organosilica during pseudomorphic transformation

B-PMO Synthesis at different pH values

In a general synthesis, C_{16}TAB (300 mg, 0.82 mmol, 0.96 equiv.) was dissolved in 8 mL sodium hydroxide solution of given concentration under stirring for 30 minutes at 40 °C before BTEB (330 µL, 0.82 mmol, 1.0 equivalent) was added at room temperature and the mixture was stirred for 20 hours. Subsequently the mixture and treated under static conditions in a steel autoclave for 24 hours at 100 °C before it was filtered and washed with water and ethanol, extracted in a Soxhlet apparatus with ethanol/hydrochloric acid (97/3) and dried at 60 °C.
Synthesis without surfactant followed the same synthesis procedure but was not extracted.

Observation of the condensation behavior of BTEB in alcoholic solutions

The general synthesis procedure was analogous to the B-PMO synthesis in aqueous solution.
For the synthesis, alcohols were used with analytical grade: methanol (100 %), ethanol (99 8 %), isopropyl alcohol (99.7 %) and *tert*-butyl alcohol (99 %).

The respective alcohol was mixed with aqueous sodium hydroxide solution in the respective ratio for a volume of 8.0 mL. In the case of pure alcohol solution, sodium hydroxide was added as pellets. The resulting concentration of sodium hydroxide corresponds to the respective pH value in pure water. For pH 12.5 the resolution molar amount was: 0.25 mmol (30 mmol·L^{-1}), for pH 13.0 it was 0.80 mmol (0.1 mol·L^{-1}) and for pH 13.5 it was 8.0 mmol (1.0 mol·L^{-1}). The solutions were stirred at room temperature, 40 °C or 60°C for 30 minutes before BTEB (123 µL, 166 mmol) was added. Stirring continued for 24 hours at the respective temperatures. The precipitate was filtered, washed with water and ethanol and dried at 60 °C.

Etching of CPG at different pH values

For synthesis with surfactant C_{16}TAB (300 mg, 0.82 mmol, 0.5 equivalent) was dissolved in 8 mL of the respective sodium hydroxide solution before it was added to CPG (100 mg, 1.66 mmol, 1.0 equivalent) in a steel autoclave. It was treated for 24 hours or four days at 100 °C und static conditions. The product was filtered washed with water and ethanol and subsequently extracted in ethanol/hydrochloric acid (37 %) 97/3 (v/v) for four days. Finally the product was washed again and dried at 60 °C.

Pseudomorphic transformation with BTEB at pH 13.7

In 8.0 mL of sodium hydroxide solution (0.5 mol·L^{-1}, 4 mmol, 1.2 equivalent) CTAB (300 mg, 0.82 mmol, 0.25 equivalent) was dissolved before BTEB (330 µL, 0.83 mmol, 0.25 equivalent) was added and the solution was vigorously stirred for ten minutes before it was added to CPG (200 mg, 3.3 mmol, 1 equivalent) and treated at 100 °C for four days in a steel autoclave. After cooling down the product was filtered, washed with water and ethanol and was dried at 60 °C.

Pseudomorphic transformation with BTEB using a KPG® stirrer

Varying amount of C_{16}TAB (0 mg, 0 equiv.; 10 mg, 0.03 mmol, 0.17 equiv.; 40 mg, 0.12 mmol, 0.66 equiv.; 100 mg, 0.3 mmol, 1.7 equiv.) were added to a mixture of ethanol (7.0 mL, 0.12 mol) and aqueous sodium hydroxide solution (1 mL, 0.8 mol·L^{-1}) and dissolved under stirring for 30 minutes. The resulting concentration of sodium hydroxide corresponds to a pH value of 13.0 in pure water. The solution was transferred to a round bottom flask and a KPG® stirring shaft, which fits without a gap in the round bottom flask, was assembled before CPG (100 mg, 1.66 mmol, 1 equivalent) were added. After a short stirring time, BTEB (132 µL, 0.166 mmol, 0.1 equivalent) was added and the reaction was stirred for another 24 hours. The product was filtered, washed with water and ethanol and dried at 80 °C.

8.5.2 General syntheses in 4.3.2 Incipient wetness impregnation of CPG

Before impregnation CPG were heated up to 200 °C for at least 4 hours and cooled down to room temperature. For a typical impregnation 1.00 g of CPG was placed in a small round bottom flask. In a typical mixture of the impregnation solution 100 mg of the precursor was mixed with 900 mg of toluene in order to obtain a 10/90 (w/w) mixture under stirring for 10 minutes. For 25/75, 50/50 or 75/25 (w/w) mixtures the masses were respectively adjusted. From this solution the volume that corresponds to the respective pore volume of the CPG (batch I: 0.9 $cm^3 \cdot g^{-1}$, batch II and batch III: 1.5 $cm^3 \cdot g^{-1}$, batch IV: 1.15 $cm^3 \cdot g^{-1}$, batch V 2.1 $cm^3 \cdot g^{-1}$) was added to the CPG dropwise with a syringe in order to distribute it on the CPG. Impregnation was carried out with the help of a rotary evaporator *(Büchi*) using a defined pressure protocol under rotation of the flask at room temperature: for 5 minutes at 300 mbar, 25 minutes at 100 mbar, 15 minutes at full evaporation power (approx. 9 mbar) and another 15 minutes at full power where the flask was placed in a water bath at 50 °C. After impregnation, the composite of CPG and the precursor was placed in a screw cap bottle. A solution of 7.5 mL ethanol (99.8 %) and 2.5 mL sodium hydroxide solution (0.31 $mol \cdot L^{-1}$ pH 13.5) was prepared. The solution was added to the composite with a volume that corresponds to the initial pore volume of the CPG batch before it was placed in a sealed screw cap bottle in the oven at 80 °C for 20 hours. Afterwards the obtained material was filtered and washed with water and ethanol and finally dried at 80 °C.

8.5.3 General synthesis in 4.3.3 Pseudomorphic transformation of

For synthesis of nanoporous organosilica synthesized in EtOH/NaOH solution see 8.3.2.

C_{16}TAOH: Microporous DVB-organosilica was added to C_{16}TAOH (4 mL, 0.08 $mol \cdot L^{-1}$, pH 12.7).

C_{16}TAB pH 12.4/pH 12.5: Sodium hydroxide (30 mg, 0.74 mmol), was dissolved in water (23 g, 1.3 mol) before C_{16}TAB (114 mg, 0.313 mmol, or 200 mg, 0.549 mmol) was dissolved at 40°C and stirred for another 30 minutes at room temperature before DVB-organosilica (100 mg) was added. In respectively labeled samples microporous DVB-organosilica was dispersed in ethanol (2.4 g, 3.0 mL, 96 %, 52 mmol) otherwise added dry. The resulting sodium hydroxide concentration is 28 $mmol \cdot L^{-1}$ (pH 12.4) with ethanol and without ethanol is 32 $mmol \cdot g^{-1}$ (pH 12.5).

C_{16}TAB pH 13.75: C_{16}TAB (300 mg, 0.82 mmol), was dissolved in aqueous sodium hydroxide solution (8.0 mL, 0.56 mmol·L^{-1}) at 40 °C and stirred for another 30 minutes at room temperature before the dispersal of nanoporous DVB-organosilica (200 mg). If indicated ethanol (4.0 mL; 3.0 g, 96 %) was also added to the solution.

All solutions were treated at 100 °C for 24 hours (10 minutes, 1 hour, 6 hours for respectively labeled samples) under static conditions in 30 mL soda lime glass tubes with screw cap. Afterwards, it was filtered and washed with water and ethanol. The surfactant was extracted in a Soxhlet apparatus using ethanol/HCl (32 vol %) 97/3 (v/v) for three days. The extracted products were washed with water and ethanol again and dried at 80 °C.

Pseudomorphic transformation of impregnated CPG

The pseudomorphic transformation of impregnated CPG was carried out analogously to the transformation of pure CPG (see 8.4 General synthesis in 4.2 Pseudomorphic transformation of CPG.)

8.6 General synthesis in 4.4 CPG membranes

For pseudomorphic transformation of CPG membranes, see 8.4.

Impregnation of CPG membranes

For a better understanding of the setup see Figure 8-1.

Figure 8-1: Photograph of the setup for the impregnation of a CPG membrane with a BTEVB-containing toluene solution.

The organosilica precursor BTEVB or mixtures of BTEVB and toluene with different weight ratios (50% (w/w) BTEVB, 25 % (w/w) BTEVB and 10 % (w/w) BTEVB) were prepared as impregnation solutions. The conical part of a cylindrical 29 mm diameter round bottom flask was filled with

the impregnation solution before a 2.5x2.5 cm CPG membrane (ca. 330-350 mg) was placed upright in the flask where it was only just submerged to the impregnation solution. The liquid moved up the membrane due to capillary forces. Complete impregnation was ensured by leaving the membrane in the solution for an additional hour. The membrane was removed and dried at ambient conditions over night before it was submerged horizontally into a hydrochloric acid aqueous solution (45 mL, 1.0 mol·L^{-1}) for 24 hours. Finally, the membrane was washed with water and ethanol and dried at 60 °C. For multiple impregnation the whole procedure was repeated.

8.7 General synthesis in 4.5 Alginate hydrogel as form-giving matrix for nanoporous organo(silica) beads

Synthesis of the silica beads

TEOS (7.5 g, 36 mmol) was hydrolyzed in a solution of hydrochloric acid (17.5 g, 0.02 mol·L^{-1} 0.35 mol) at room temperature. As soon as a clear solution was obtained, the pH value was adjusted to 5–6 with sodium hydroxide solution (0.4 mol·L^{-1}) before it was mixed into an aqueous solution of alginate (1.25 g in 100 ml of water) under permanent stirring. The procedure was performed simultaneously in two batches. The solutions were each dropped into an aqueous solution of calcium lactate (1.0 L, 0.45 mol·L^{-1}) one after the other using a syringe pump with a dropping height of 18 cm and a flow of 250–340 mL·h^{-1}. The nascent beads were aged in the solution overnight pior to decantation and washing with water. Subsequently, the beads were aged in heptane for four days, then washed with acetone and dried spread flat on filter paper at room temperature. During this step shrinking of the beads occurs. The alginate/silica beads were treated in hydrochloric acid (80 mL, 1.0 mol·L^{-1}) at 100 °C for 24 hours and finally calcined at 550 °C for 6 hours. The whole procedure resulted in the formation of 2.1 g silica beads.

Synthesis of pT-SiO_2-beads

A solution of C_{16}TAB (900 mg, 2.5 mmol) in aqueous sodium hydroxide solution (24 mL, 0.05 mol·L^{-1}, 1.2 mmol) was prepared and stirred for 30 minutes before the silica beads (600 mg, 10 mmol) were added and treated under static conditions at 100 °C for the given hydrothermal treatment time of four days or four hours. The composite was calcined again at 550 °C for 6 hours. The molar ratio of all components: Si/C_{16}TAB/NaOH/H_2O was 1/0.25/0.1/133.

Synthesis of the organosilica beads

For hydrolysis BTEB (1 mL, 2.5 mmol) was treated in hydrochloric acid (2 mL, 0.2 mol·L^{-1} 0.4 mmol) and ethanol (99.8 %, 2 mL, 34 mmol) at room temperature. The following synthesis procedure was analogous to the already described synthesis of silica beads. The organosilica beads were treated in hydrochloric acid (80 mL, 1.0 mol·L^{-1}) at 100 °C for 6 hours before alginate was extracted with a tri-sodium citrate solution (100 mL, 1.0 mol·L^{-1}) for 24 hours, then washed with water and ethanol. After drying at 80 °C, 1.3 g organosilica beads were obtained from five batches.

Synthesis of PT-B-beads:

A solution of water (31.0 g, 1.72 mol), ethanol (99.8 %, 9.00 g, 0.195 mol), sodium hydroxide (50.0 mg, 1.25 mmol**)** and C_{16}TAB (550 mg, 1.51 mmol) was prepared and stirred for 30 minutes before the organosilica beads (500 mg) were added and treated for 24 hours at 100 °C under static conditions. After washing with water and ethanol, the surfactant was removed in a Soxhlet apparatus using ethanol/HCl (32 vol%) 97/3 (v/v) for three days. The extracted beads were again washed with water and ethanol and dried at 80 °C.

9 Appendix

9.1 Addition information to 4 Results and discussion

Additional figures to 4.1.3 High specific surface area PMOs

B-PMOs

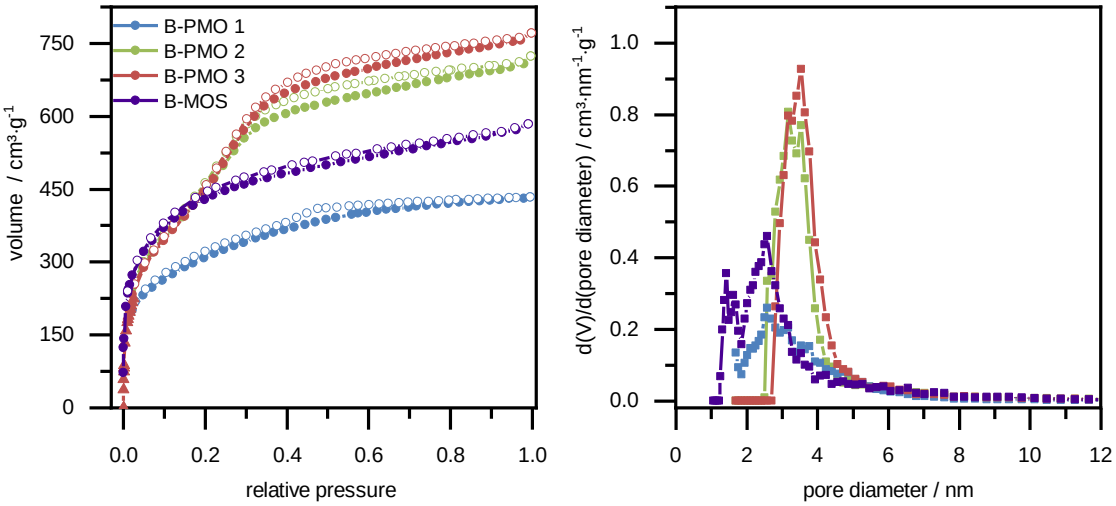

Figure 9-1: Physisorption isotherms (N_2, 77 K) of B-MOS synthesized with C_{10}TAB in comparison with the B-PMOs 1-3 synthesized with C_{16}TAB. Right pore diameter distributions of B-PMOs 1-4 NLDFT kernel for silica with cylindrical pores, calculated from the adsorption branch.

Table 9-1: Overview of the relative pressure range that was chosen to determine the apparent specific surface area for B-PMO 1-4.

Sample	p/p^0 range apparent specific surface area (N_2)	p/p^0 range apparent specific surface area (Ar)
B-PMO 1	0.048-0.197	-
B-PMO 2	0.072-0.146	-
B-PMO 3	0.069-0.122	-
B-MOS	0.048-0.170	0.048-0.189

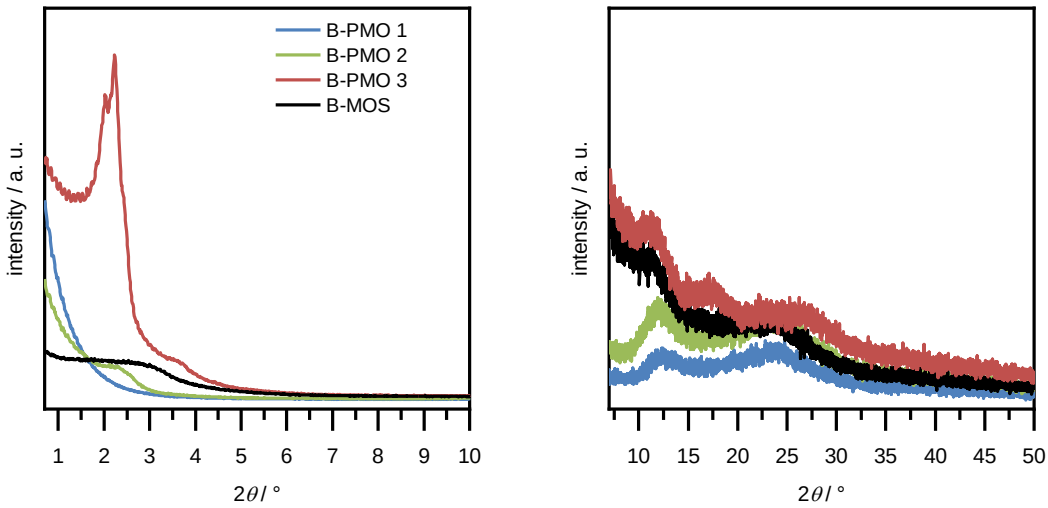

Figure 9-2: P-XRD of B-MOS synthesized with C_{10}TAB in comparison with the B-PMOs 1-3 synthesized with C_{16}TAB.

Halogen-containing PMOs

Table 9-2: Overview of the relative pressure range that was chosen to determine the apparent specific surface area F-MOS and 2F-MOS.

Sample	p/p^0 range apparent specific surface area
F-MOS-HCl	N_2: 0.02-0.18 Ar: 0.03-0.22
2F-MOS-HCl	N_2: 0.02-0.17 Ar: 0.01-0.125

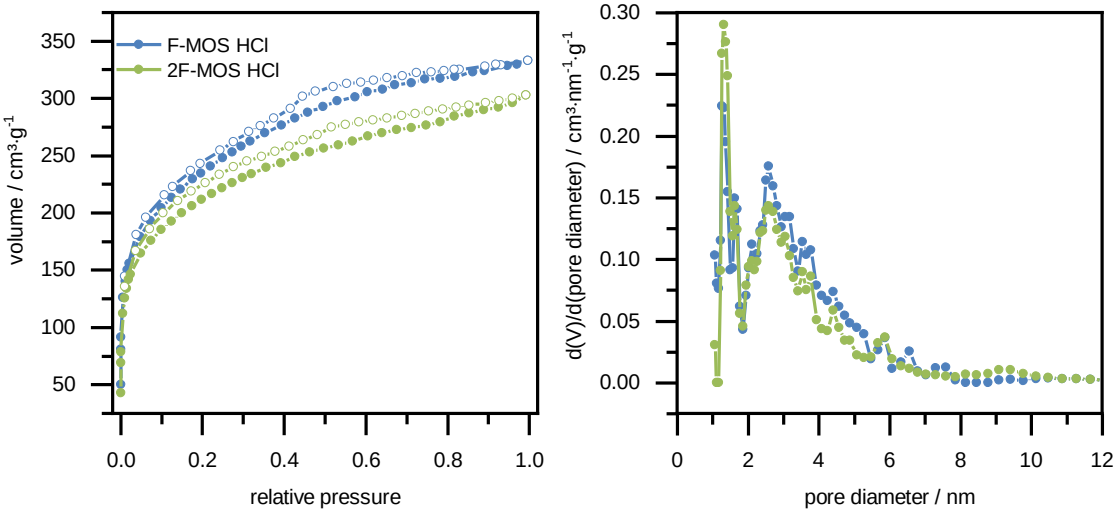

Figure 9-3: Physisorption isotherms (N_2, 77 K) of F-MOS and 2F-MOS synthesized with HCl (1.0 mol·L^{-1}). The respective pore diameter distributions are given on the right (NLDFT, silica, cylindrical pores, adsorption branch).

Additional information to 4.1.4 Microporous organosilica

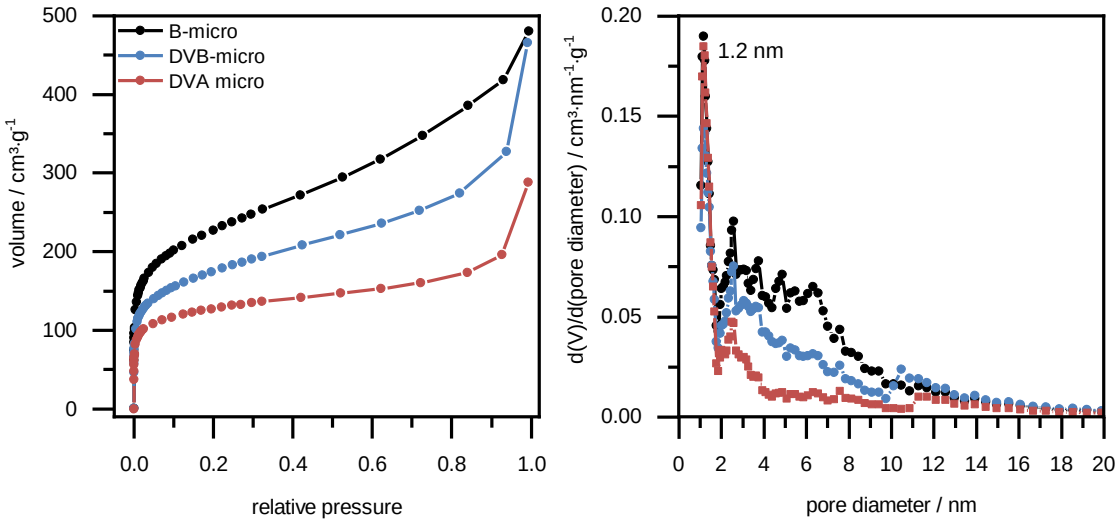

Figure 9-4: Physisorption isotherms (N_2, 77 K) of microporous organosilicas synthesized at pH 12.0. The respective pore diameter distributions are given on the right (NLDFT kernel for silica, cylindrical pores, calculated from the adsorption branch).

Table 9-3: Overview of the relative pressure range that was chosen to determine the apparent specific surface area of microporous organosilicas.

Sample	***p*/p⁰ range apparent specific surface area**	
	N_2	**Ar**
B micro	0.056-0.148	0.072-0.175
DVB-micro	0.060-0.150	0063-0.151
DVA micro	0.0158-0.0948	0.018-0.125
DVB micro (EtOH)	0.076-0.195	0.082-0.201
DVA micro (EtOH)	0.020-0.172	0.090-0.223
F-DVB micro (EtOH)	0.079-0.198	0.100-0.250

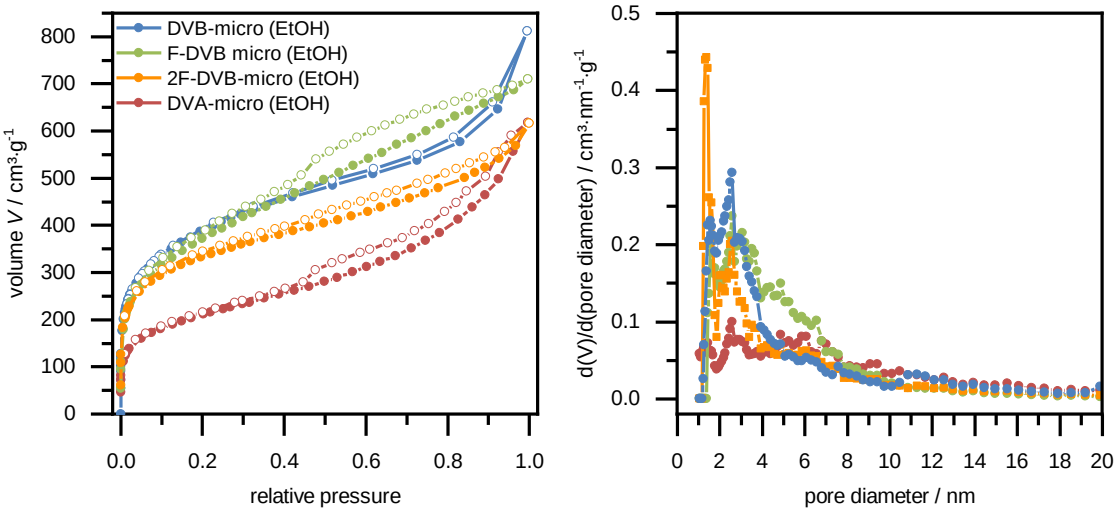

Figure 9-5: Physisorption isotherms (N_2, 77 K) of microporous organosilicas obtained from treatment with ethanol/NaOH pH 13.75. The respective pore diameter distributions are given on the right (NLDFT, silica, cylindrical pores, adsorption branch).

Additional information on 4.3.1 Trial for the exchange of silica versus organosilica during pseudomorphic transformation

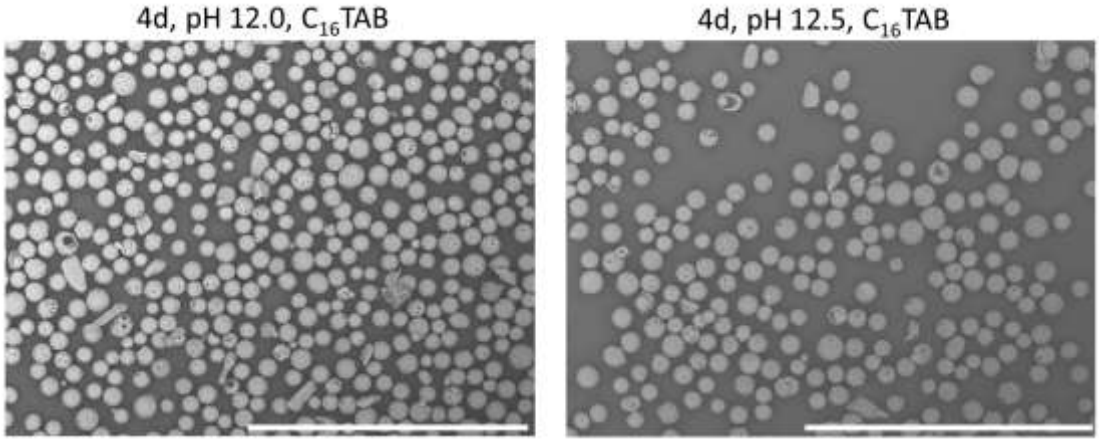

Figure 9-6: SEM images of products from CPG beads etching for four days at different pH values with C_{16}TAB (magnification x100, scale bar of 1.0 mm). Samples without carbon sputtering.

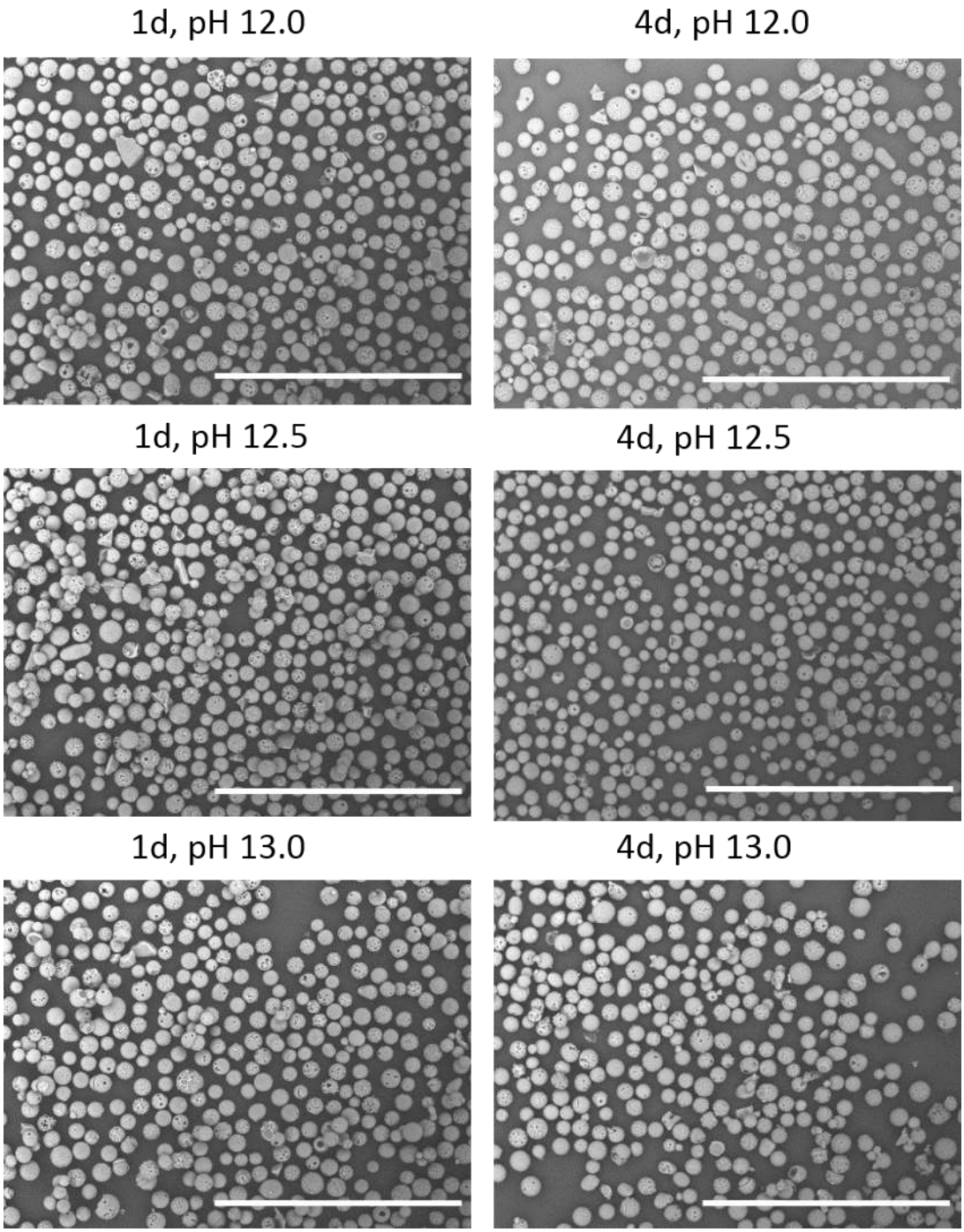

Figure 9-7: SEM images of products from CPG beads etching at different pH values without C_{16}TAB (magnification x100, scale bar of 1.0 mm). Samples without carbon sputtering.

Additional information 4.3.2 Incipient wetness impregnation of CPG

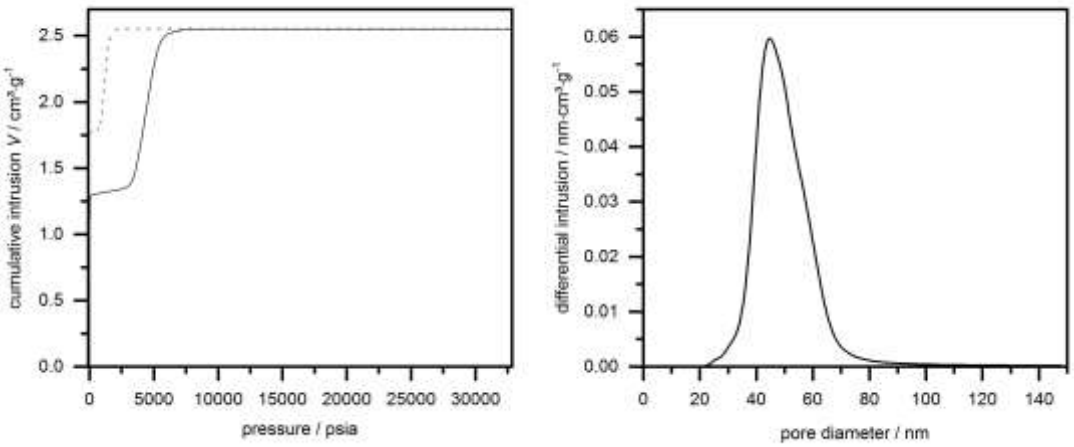

Figure 9-8: Left: mercury intrusion curve (extrusion in dotted line) of CPG that were used as starting material for impregnation with different solutions containing BTEVA and toluene. Right: pore size distribution. CPG beads of 40–100 µm in diameter, 45 nm pore diameter and 1.2 $cm^3 \cdot g^{-1}$ pore volume.

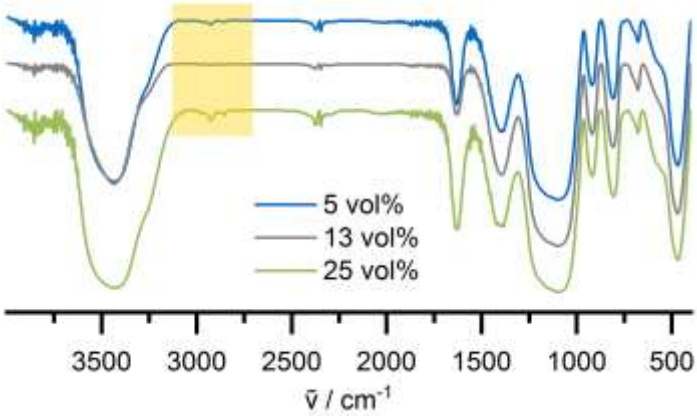

Figure 9-9: FTIR spectra (KBr plates, normalized transmittance) of CPG impregnated in an incipient wetness approach with 5 vol%. 13 vol% and 25 vol% of BTEVA. The region of =C-H and -CH_2 stretching vibration is highlighted in yellow.

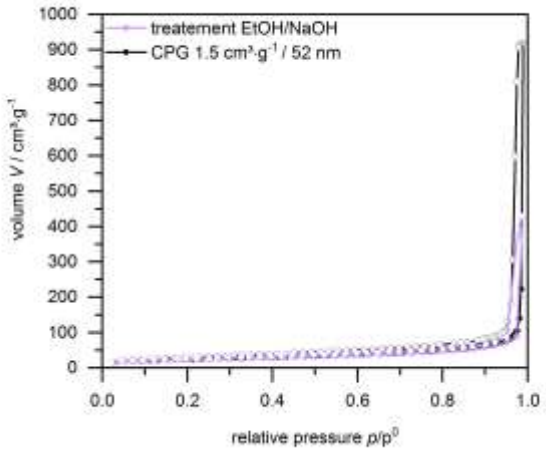

Figure 9-10: Nitrogen physisorption isotherms (77 K, N_2) of CPG batch II (black) and CPG which were impregnated with pure toluene and further treated with ethanol and sodium hydroxide solution for condensation (purple).

SEM images systematical impregnation

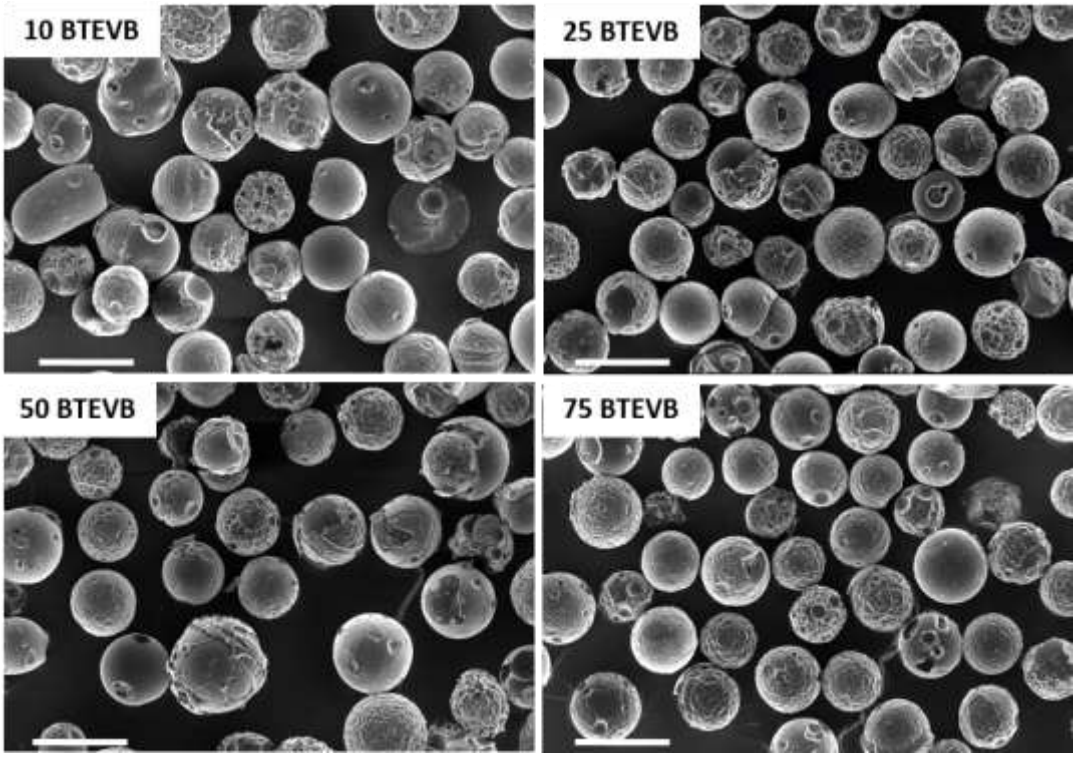

Figure 9-11: SEM images of CPG (batch I) that were impregnated with 10–75BTEVB (magnification x500, scale bar of 100 µm).

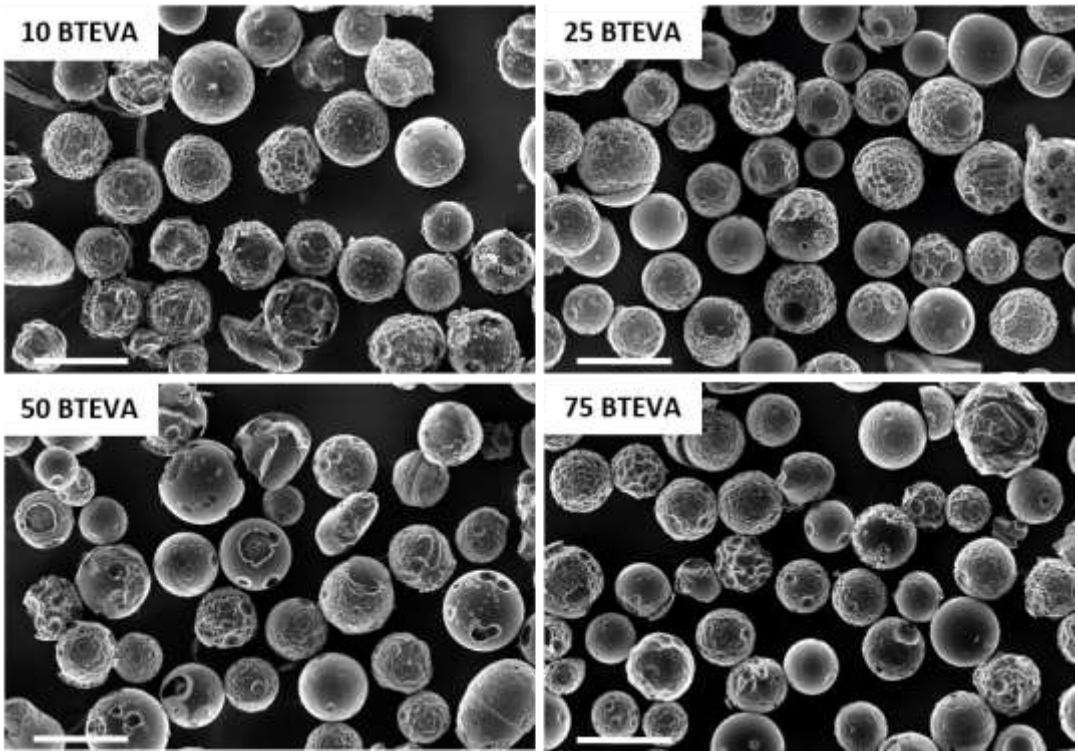

Figure 9-12: SEM images of CPG (batch I) that were impregnated with 10–75BTEVA (magnification x500, scale bar of 100 µm).

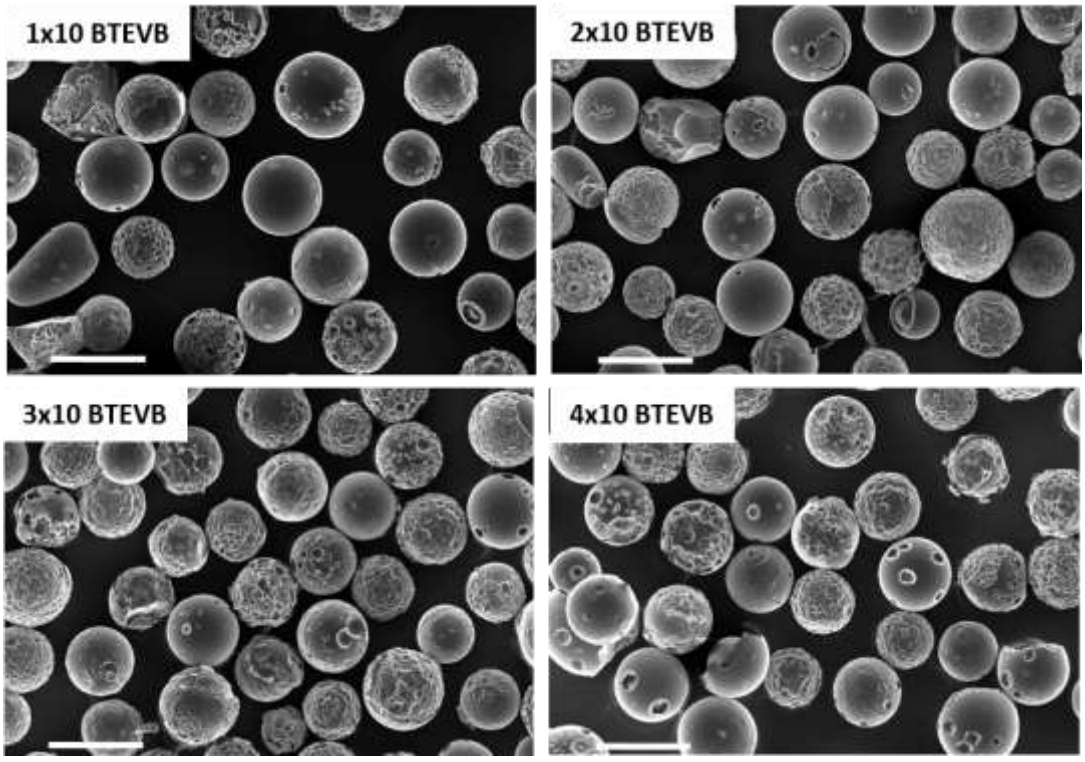

Figure 9-13: SEM images of CPG (batch II) that were impregnated one to four times with a toluene-based solution that contains 10 wt% of BTEVB. Scale bar of 100 µm, x500 magnification.

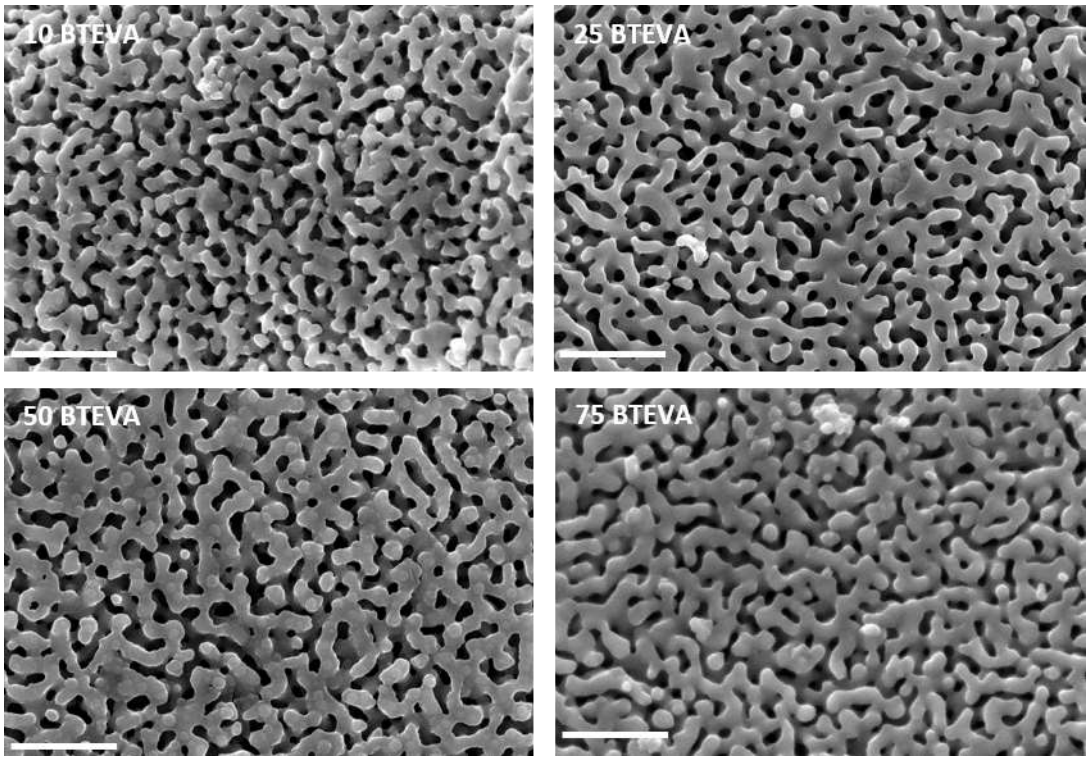

Figure 9-14: SEM images of CPG batch III impregnated with BTEVA. Scale bar of 1 µm, x50.000 magnification.

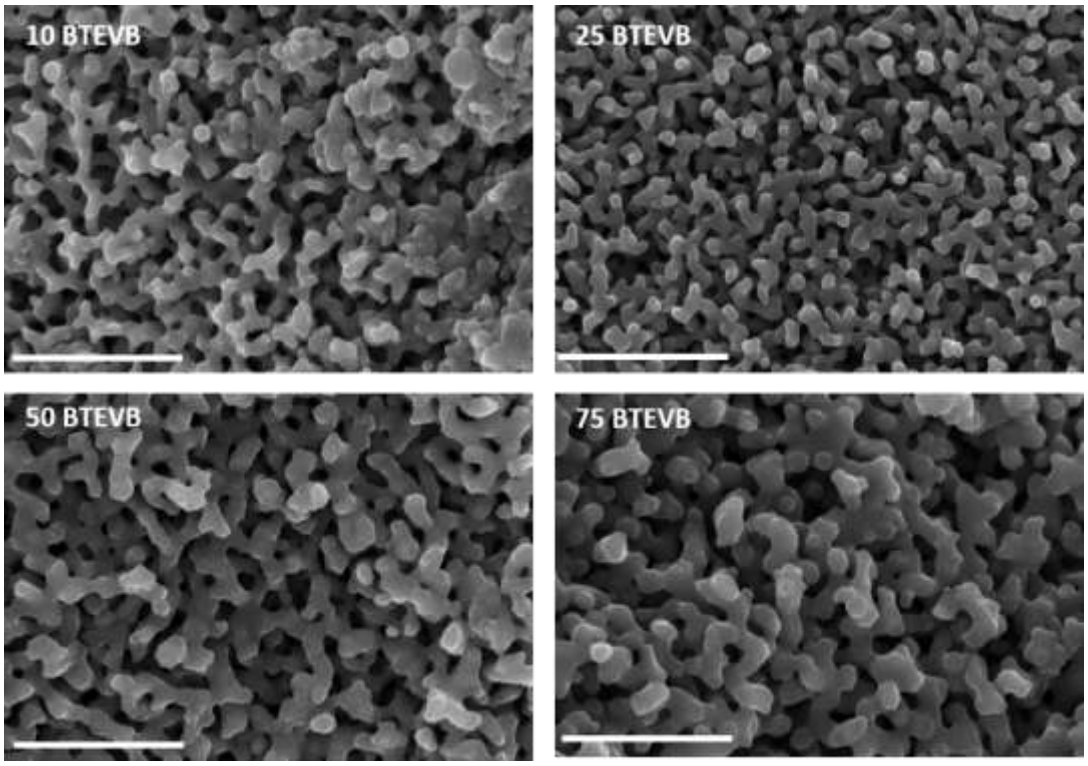

Figure 9-15: SEM images of the pore system of the CPG batch IV impregnated with BTEVB. Magnification x80000, scale bar of 1 µm.

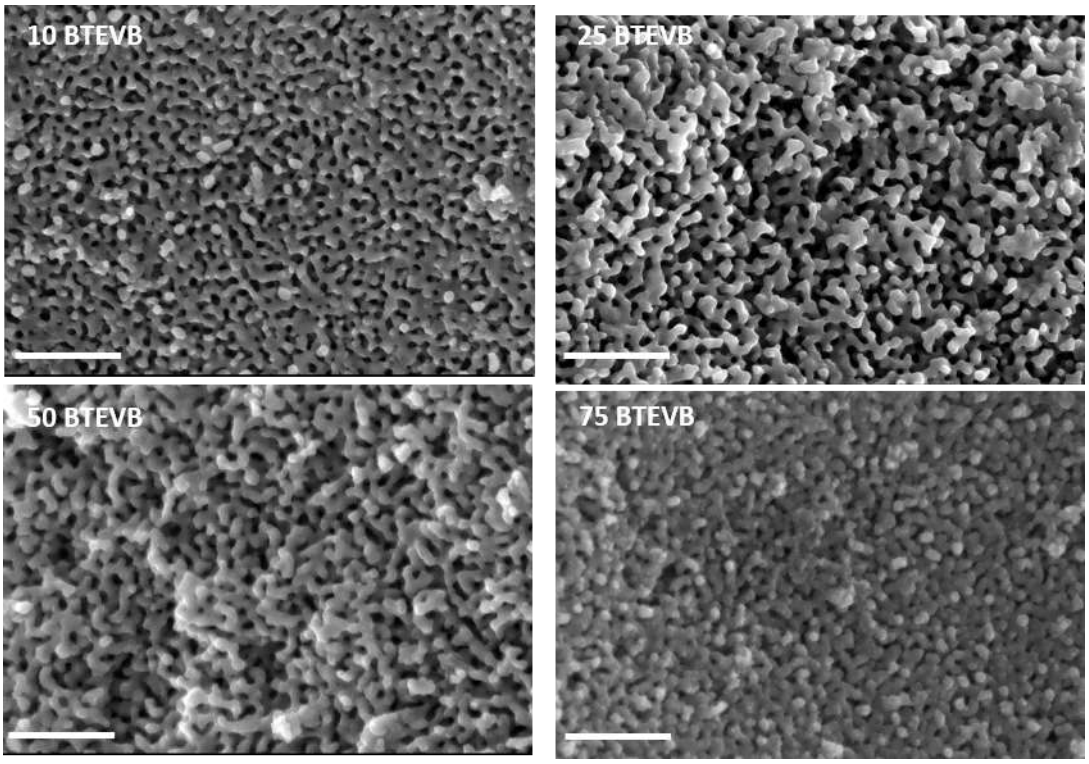

Figure 9-16: SEM images of impregnated CPG batch V 10–75BTEVB (magnifications x50000, scale bar of 1 µm).

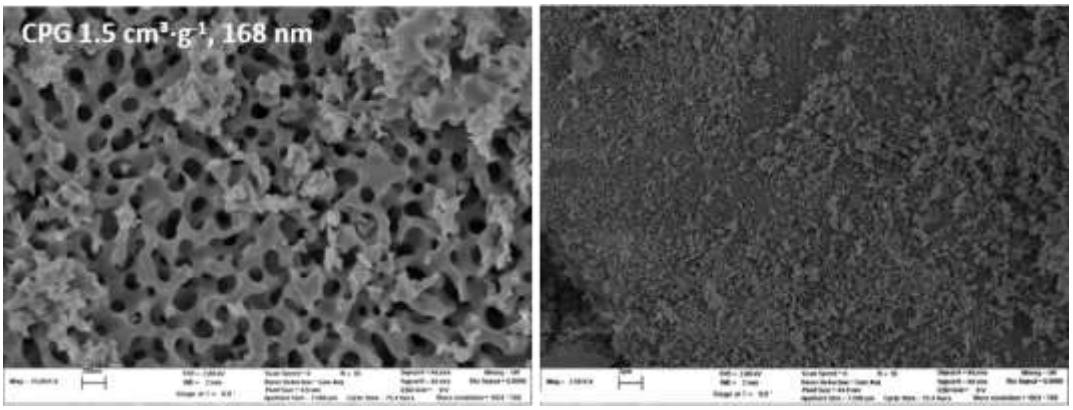

Figure 9-17: SEM images of CPG batch III without carbon sputtering. Sample was grinded before measurement.

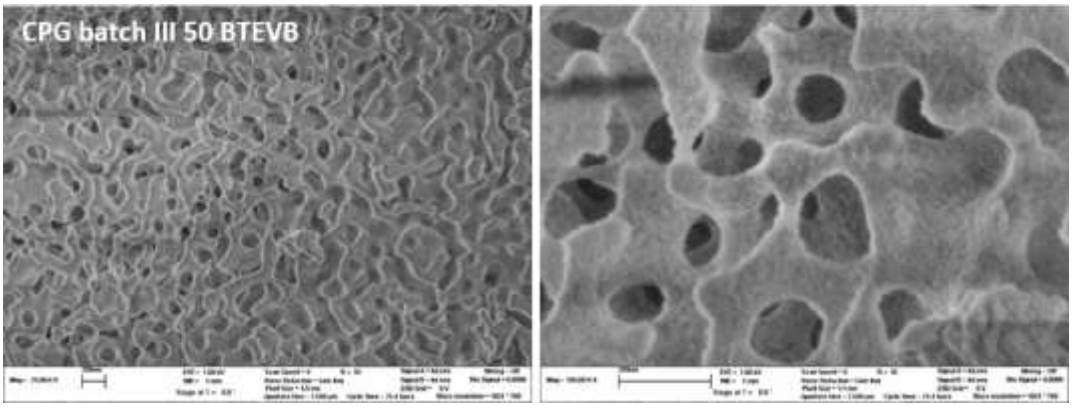

Figure 9-18: SEM images of 50BTEVB batch III without carbon sputtering. Sample was grinded before measurement.

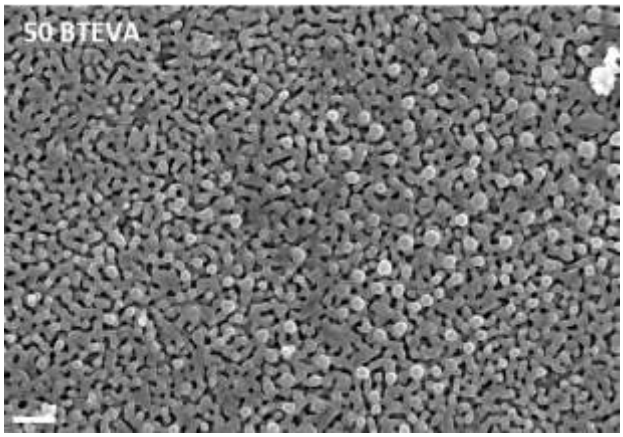

Figure 9-19: SEM image of 50BTEVA from CPG batch III as an example for the formation of a second phase of spherical spots on the CPG surface, x20000 magnification, scale bar of 1 µm.

Nitrogen physisorption isotherms of systematic impregnations

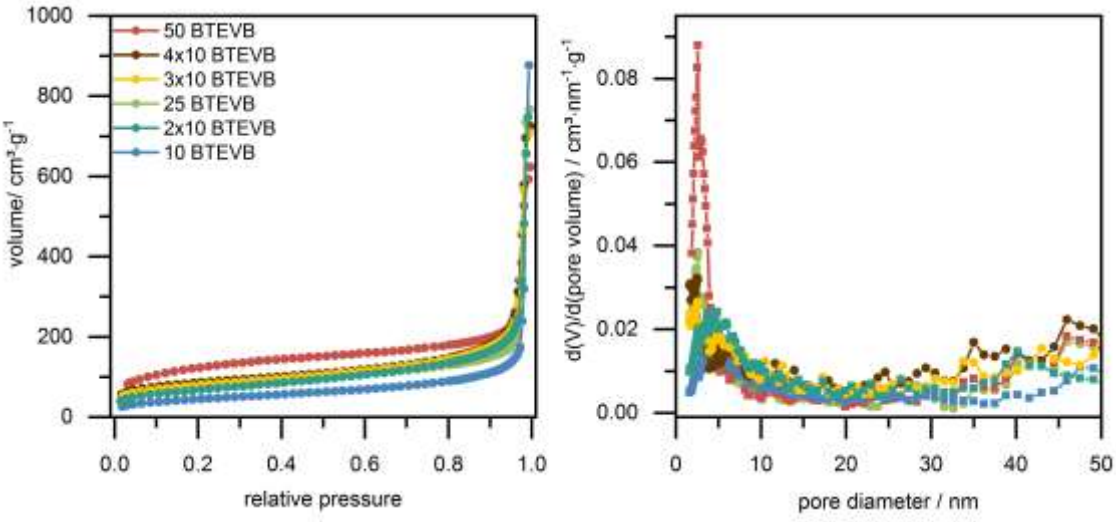

Figure 9-20: Physisorption isotherms (N_2, 77 K) of CPG batch II impregnated multiple times with 10 wt% BTEVB.1x10BTEVB; 2x10BTEVB, 3x10BTEVB and 4 10BTEVB plotted together with 25BTEVB and 50BTEVB for comparison For clarity only the adsorption branches are shown on the left. Pore diameter distributions (calculated from the adsorption branch with NLDFT kernel for silica with cylindrical pores) are shown on the right.

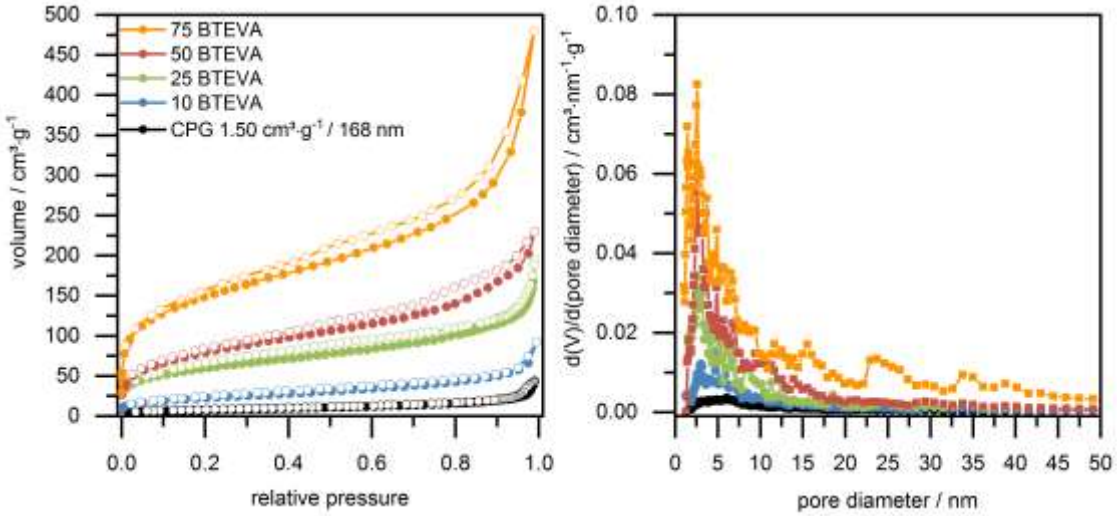

Figure 9-21: Physisorption isotherms (N_2, 77 K) of CPG batch III impregnated with 10–75BTEVA on the left. Pore diameter distributions (calculated from the adsorption branch with NLDFT kernel for silica with cylindrical pores)are shown on the right.

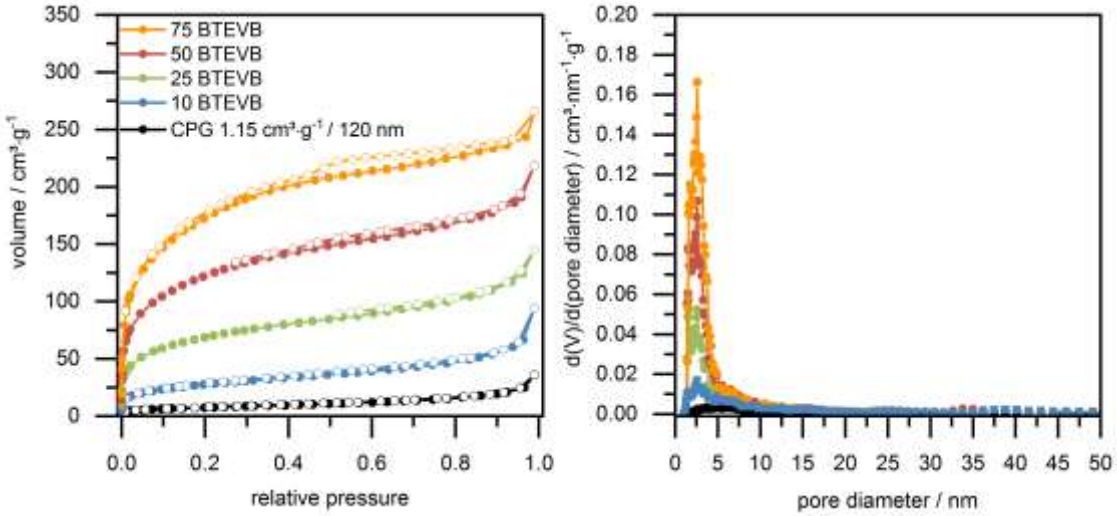

Figure 9-22: Physisorption isotherms (N_2, 77 K) of CPG batch IV impregnated with 10–75BTEVB on the left. Pore diameter distributions (NLDFT kernel for silica, cylindrical pores, calculated from the adsorption branch) are shown on the right.

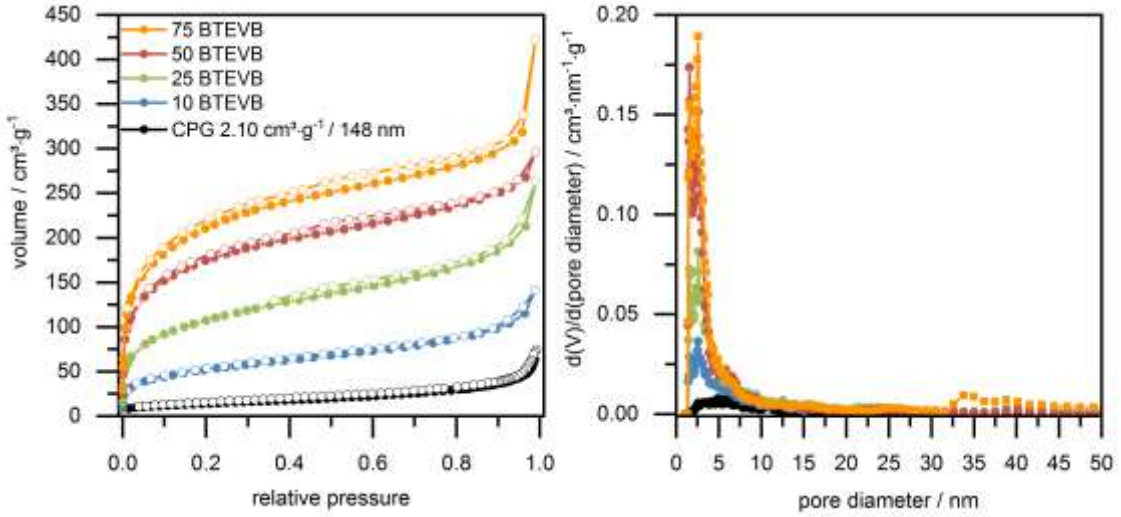

Figure 9-23: Physisorption isotherms (N_2, 77 K) of CPG batch V impregnated with 10–75BTEVB on the left. Pore diameter distributions (calculated using NLDFT kernel for silica, cylindrical pores, calculated from the adsorption branch are shown on the right.

Table 9-4: Overview of the sample mass before and after impregnation and condensation, the corrected pore volume which is based on these values and the relative pressure range that was considered for the determination of the apparent specific BET surface area.

sample	m_{CPG} / mg	$m_{CPG+Organisilica}$ / mg	V_{corr} / cm³·g⁻¹	p/p^0 range apparent S_{BET}
CPG batch I (0.9 cm³·g⁻¹, 42 nm)				
10BTEVA	1552	1530	0.80	0.067-0.309
25 BTEVA	1504	1677	0.78	0.066-0.309
50BTEVA	1545	1947	0.63	0.061-0.307
75BTEVA	1402	1907	0.53	0.066-0.304
10BTEVB	1000	970*	0.77	0.067-0.309
25BTEVB	2000	2183	0.80	0.069-0.310
50BTEVB	2000	2424	0.67	0.066-0.309
75BTEVB	1000	1377	0.43	0.082-0.206
CPG batch II (1.5 cm³·g⁻¹, 52 nm)				
10BTEVA	1000	1060	1.38	
25 BTEVA	1002	1188	1.30	0.030-0.178
50BTEVA	1052	1716	1.30	0.053-0.179
75BTEVA	1000	1756	0.99	0.049-0.203
10BTEVB	1077	984*	1.36	0.107-0.228
25BTEVB	1000	1141	1.46	0.040-0.166
50BTEVB	1010	1346	1.15	0.059-0.185
75BTEVB	1020	1685	0.78	0.103-0.226
2x10BTEVB	2330	2283	-	0.064-0.188
3x10BTEVB	1503	1441	-	0.029-0.147
4x10BTEVB	1000	1034	-	0.029-0.149
CPG batch III (1.5 cm³·g⁻¹, 168 nm)				
10BTEVA	505	522	1.25	0.052-0.304

sample	m_{CPG} / mg	$m_{CPG+Organisilica}$ / mg	V_{corr} / $cm^3 \cdot g^{-1}$	p/p^0 range apparent S_{BET}
25 BTEVA	506	592	1.16	0.066-0.189
50BTEVA	997	1412	1.01	0.054-0.277
75BTEVA	300	503	1.11	0.048-0.197
10BTEVB	1000	1053	1.65*	0.073-0.226
25BTEVB	1000	1044	1.19	0.022-0.172
50BTEVB	1995	2856	1.17	0.050-0.173
75BTEVB	1000	1559	1.00	0.072-0.222
CPG batch IV (1.15 $cm^3 \cdot g^{-1}$, 120 nm)				
10BTEVB	1000	1080	0.98	0.074-0.296
25BTEVB	2000	2179	0.93	0.040-0.175
50BTEVB	3000	3845	0.78	0.049-0.173
75BTEVB	1000	1427	0.34	0.053-0.200
CPG batch V (2.1 $cm^3 \cdot g^{-1}$, 148 nm)				
10BTEVB	2020	2288	2.36*	0.08-0.295
25BTEVB	980	1238	1.89	0.054-0.201
50BTEVB	1000	1541	1.65	0.020-0.170
75BTEVB	500	888	1.24	0.021-0.173

TG measurements of systematic impregnations

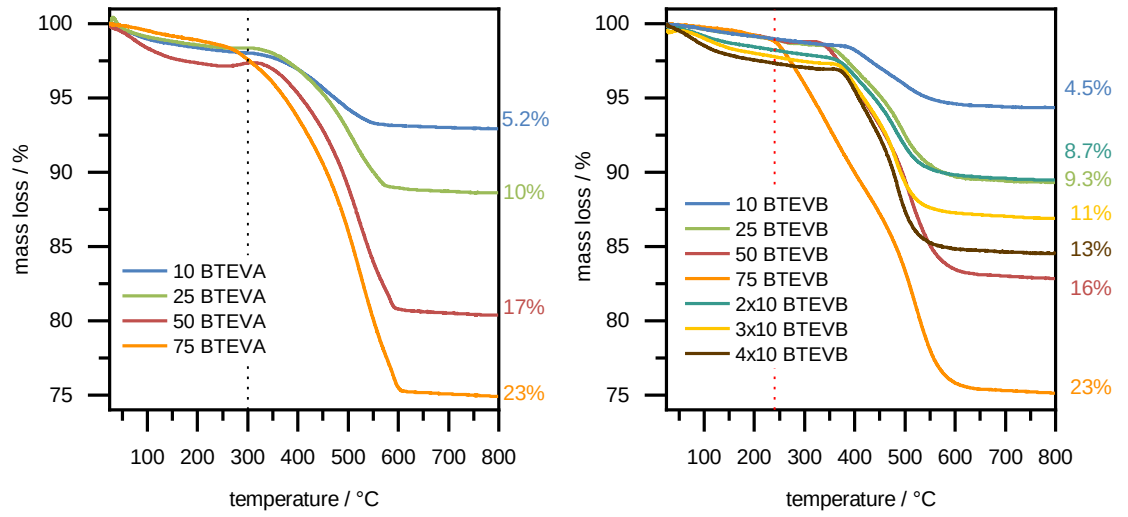

Figure 9-24: TG measurements (Ar/O_2 80/20) of impregnated CPG batch II with different percentages of BTEVA (left) and BTEVB (right).

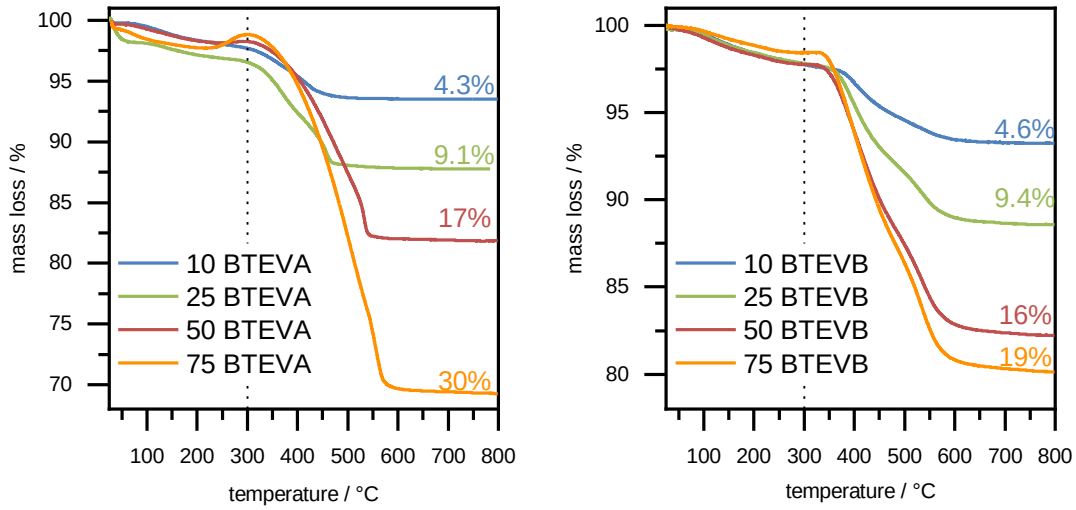

Figure 9-25: TG measurements (Ar/O_2 80/20) of impregnated CPG batch III with different percentages of BTEVA (left) and BTEVB (right).

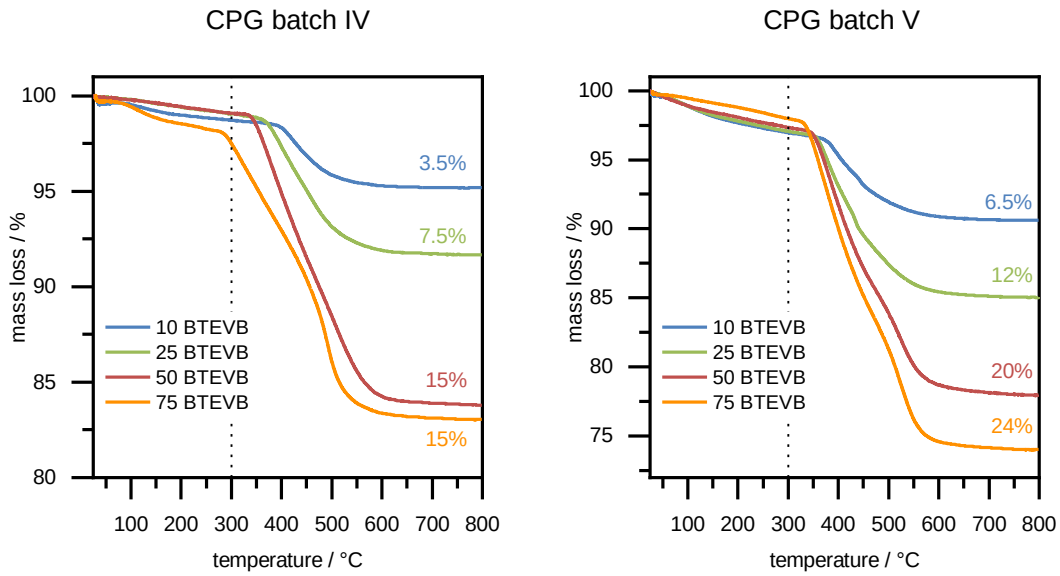

Figure 9-26: TG measurements (Ar/O_2 80/20) of impregnated CPG batch IV (left) and batch V (right) with different percentages of BTEVB.

Additional information to 4.3.3 Pseudomorphic transformation of organosilica/silica hybrid materials

Pseudomorphic transformation of nanoporous organosilica

Table 9-5: Overview of the relative pressure range that was considered for the determination of the apparent specific BET surface area.

sample	p/p^0 range apparent S_{BET}	sample	p/p^0 range apparent S_{BET}
DVB micro I	0.021-0.171	**DVB micro II**	0.0175-0.146
pH 12.7 C_{16}TAOH 24 hours	0.070-0.296	**pH 13.75, C_{16}TAB, 24 hours**	0.0749-0.294
pH 12.4 114 mg C_{16}TAB, ethanol	0.017-0.145	**pH 13.75, C_{16}TAB, 6 hours**	0.0731-0.299
pH 12.4 200 mg C_{16}TAB, ethanol	0.0731-0.299	**pH 13.75, C_{16}TAB, 1 hour**	0.0703-0.295
pH 12.4 200 mg C_{16}TAB	0.0720-0.294	**pH 13.75, C_{16}TAB, 1 hour, ethanol**	0.0188-0.149
		pH 13.75, C_{16}TAB, 10 min	0.021-0.170
		pH 13.75, C_{16}TAB, 10 min ethanol	0.074-0.294

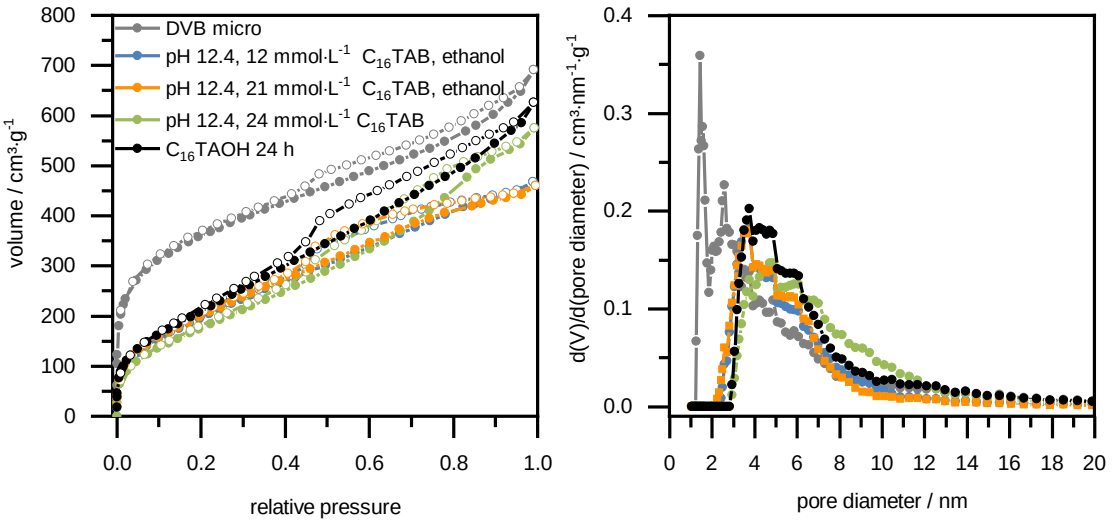

Figure 9-27: Physisorption isotherms (N_2, 77 K) and pore diameter distribution (NLDFT kernel for silica, cylindrical pores, calculated from the adsorption branch) shown on the right of nanoporous DVB-organosilica before and after treatment with C_{16}TAOH solution at pH 12.7 and at pH 12.4 with different concentrations of C_{16}TAB with and without ethanol.

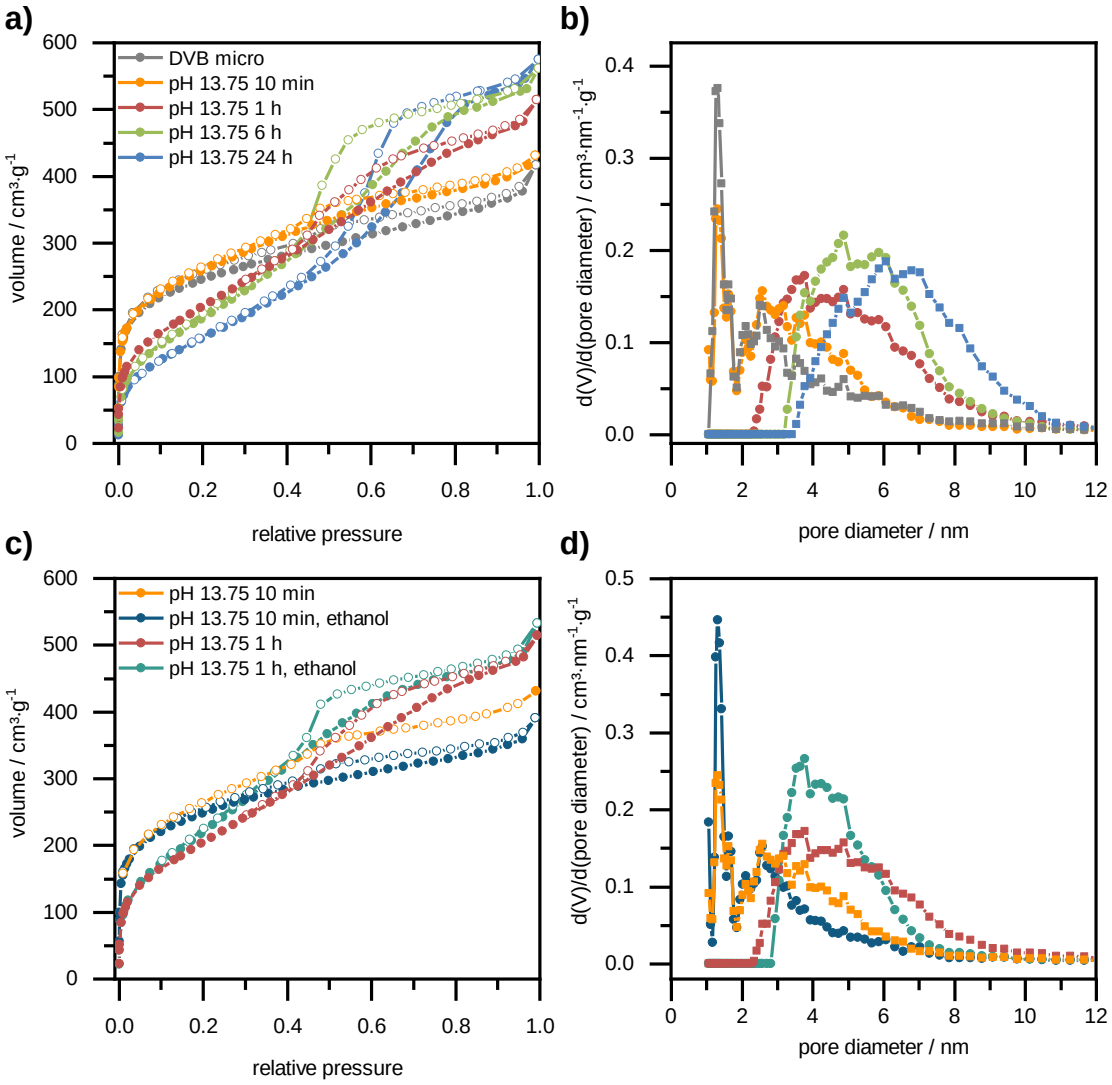

Figure 9-28: Results from nitrogen physisorption (N_2, 77 K): a) isotherms of nanoporous DVB-organosilica before and after treatment at pH 13.75 for different time periods and b) the respective pore diameter distributions(NLDFT kernel for silica, cylindrical pores, calculated from the adsorption branch. c) Isotherms of nanoporous DVB-organosilica before and after treatment at pH 13.75 for one hour and ten minutes with and without ethanol and d) the respective pore diameter distributions.

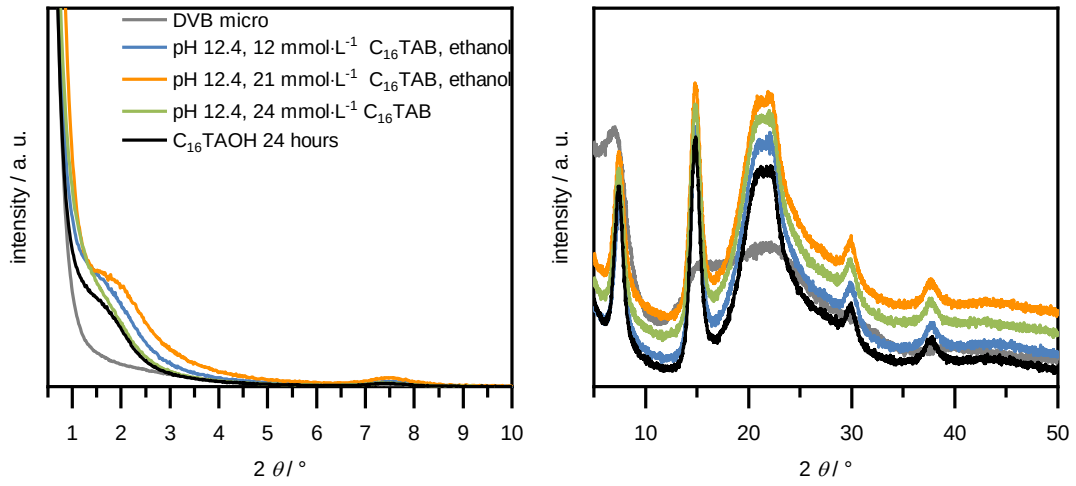

Figure 9-29: P-XRD patterns of DVB-organosilica before and after treatment with C_{16}TAOH solution at pH 12.7 or at pH 12.4 with different concentrations of C_{16}TAB with and without ethanol.

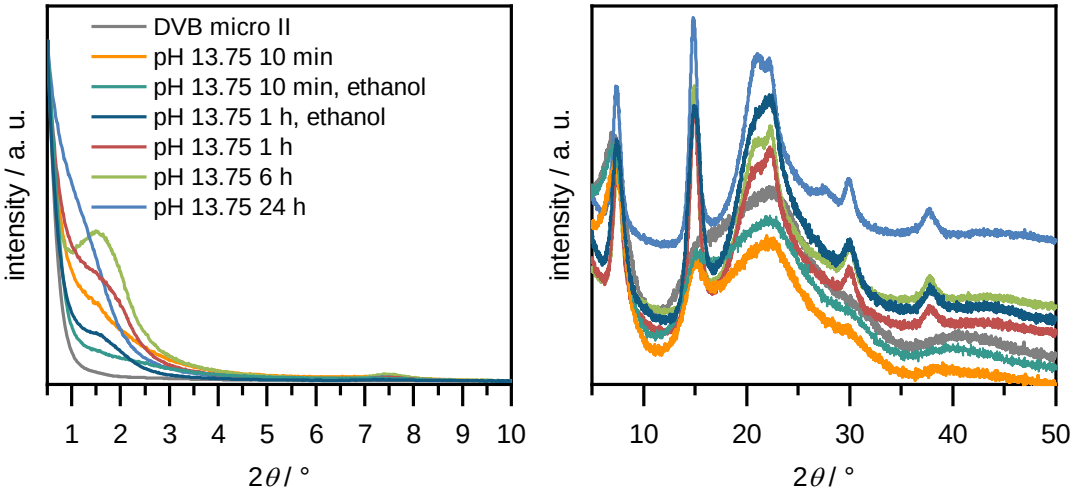

Figure 9-30: P-XRD pattern of DVB-organosilica before and after treatment with C_{16}TAB at pH 13.75 with and without ethanol.

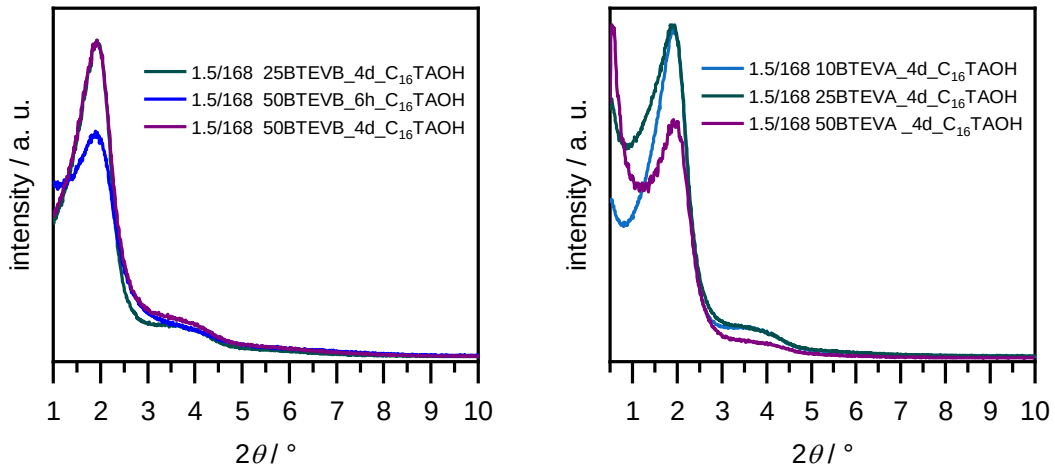

Figure 9-31: P-XRD pattern of CPG from batch III (1.5 $cm^3 \cdot g^{-1}$, 168 nm), of 25BTEVB and 50BTEVB (left) or 10–50BTEVA (right) after pseudomorphic transformation for four days with C_{16}TAOH.

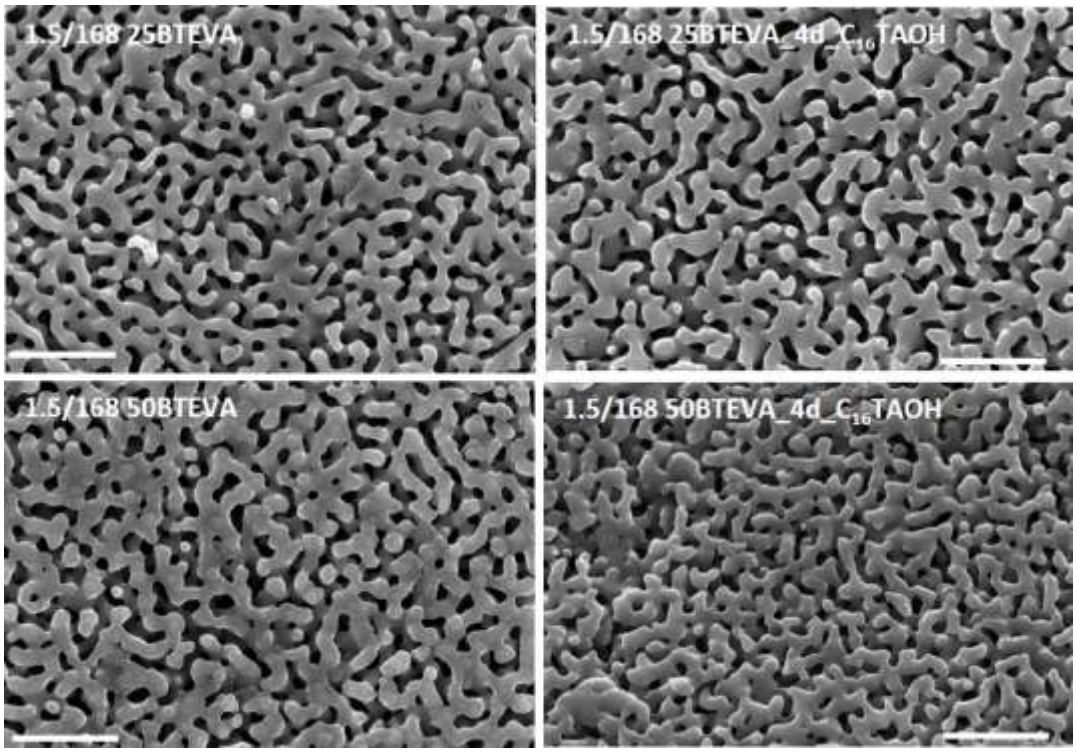

Figure 9-32: SEM images of 25 BTEVA and 50 BTEVA frim CPG batch III, respectively, before (left) and after (right) pseudomorphic transformation with C_{16}TAOH for four days (magnification of x50000, scale bar of 1.0 µm).

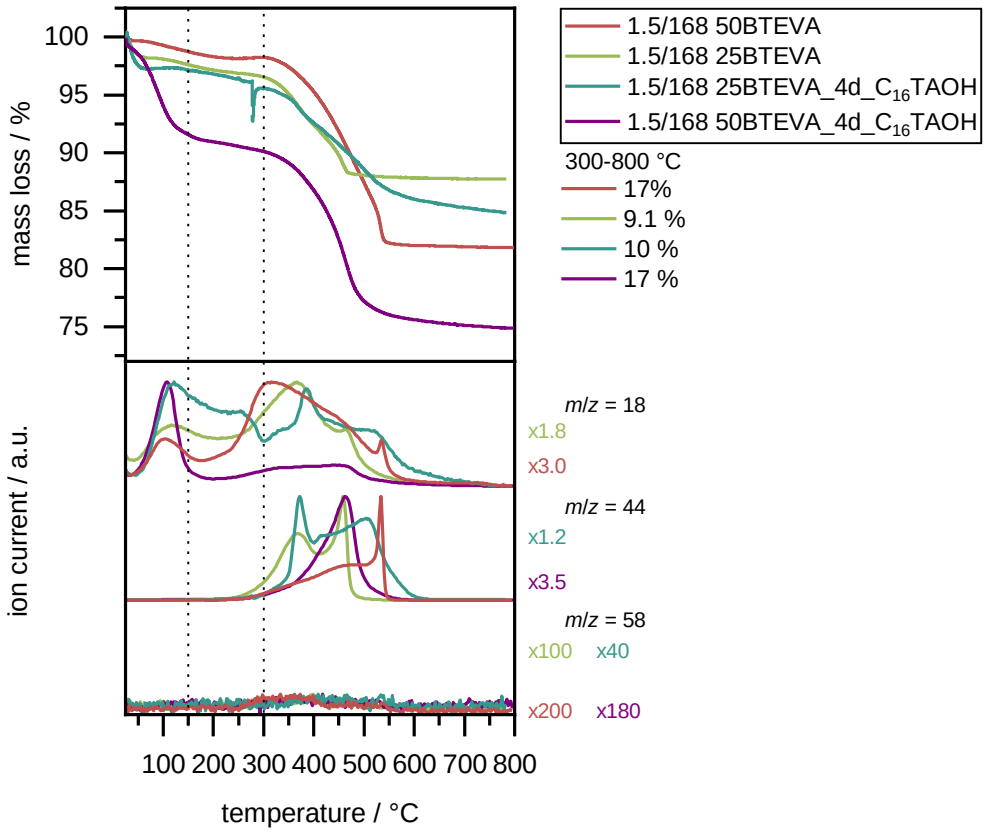

Figure 9-33: TG/MS analysis in Ar/O_2 80/20 of 25BTEVA and 50BTEVA from CPG batch III before and after pseudomorphic transformation for 4 days. In the upper plots: mass losses plotted against the temperature. The corrected mass loss for the temperature interval 300–800 °C is given on the left. Lower plot: selected ion currents with normalization factor given on the side.[7]

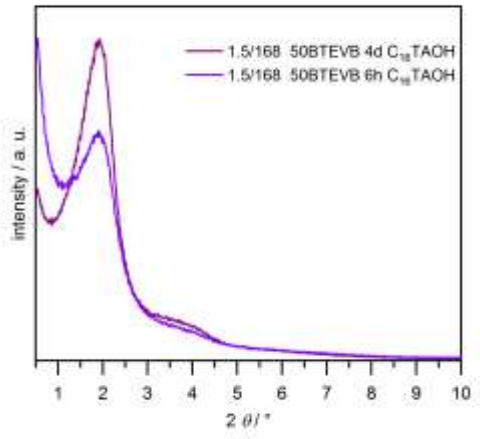

Figure 9-34: P-XRD pattern of 50BTEVB CPG batch III after treatment with C_{16}TAOH for six hours and four days.

[7] In the measurement of 25 BTEVA, ion current of m/z = 18 is detected with an unexpectedly high intensity which might be caused by a leak in the measurement apparatus. This should not reduce the valence of the rest of the measurement. Due to the low sample amount, this measurement was not reproduced.

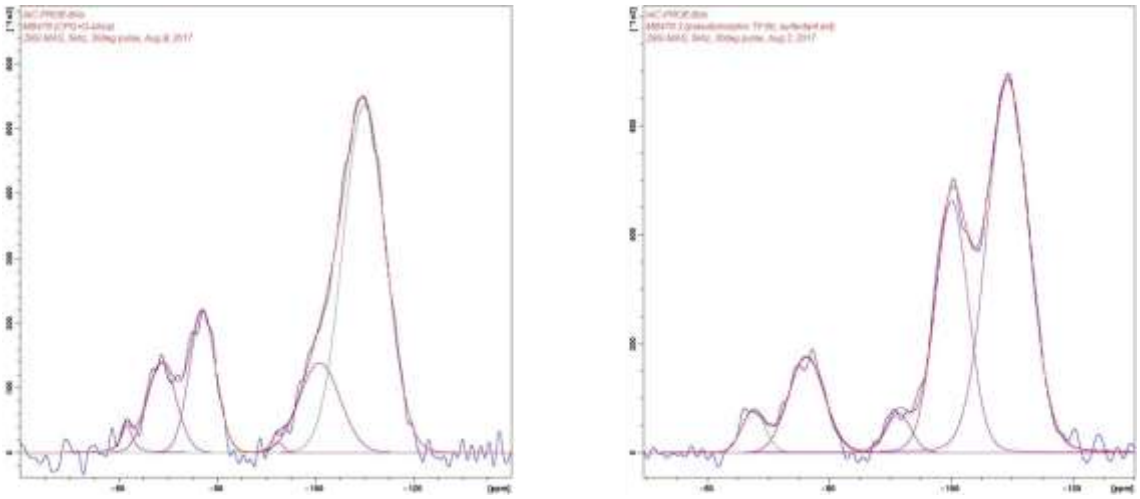

Figure 9-35: Plots of direct excitation ^{29}Si-MAS NMR signals for 50BTEVB and 50BTEVB_6h_C_{16}TAOH from CPG batch III.

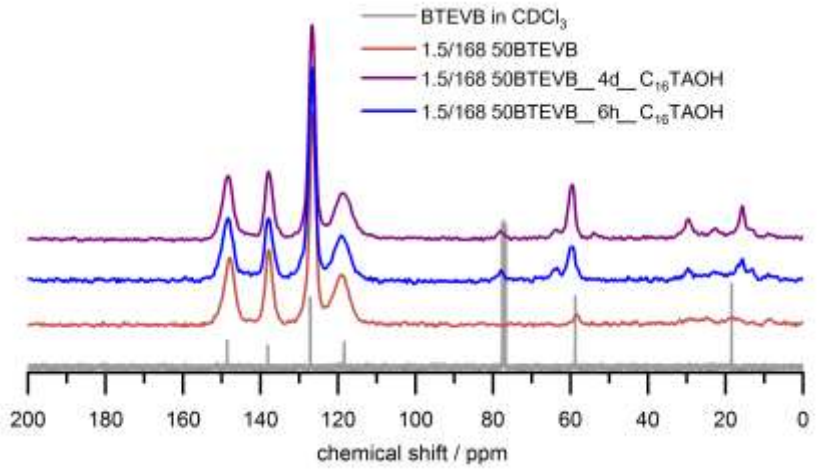

Figure 9-36: ^{13}C-CP MAS NMR (spinning speed = 13 kHz) of 50BTEVB and 50BTEVB_6hC_{16}TAOH and 4 d C_{16}TAOH. Liquid-state ^{13}C-NMR of BTEVB in $CDCl_3$ is given for comparison as well. All spectra are plotted with normalized intensity.

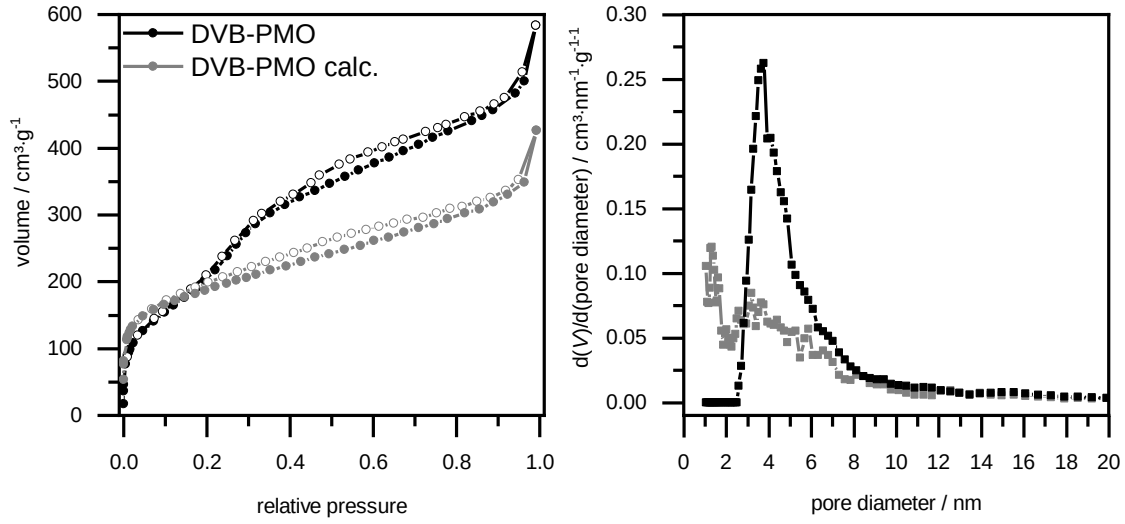

Figure 9-37: Physisorption isotherms (N_2, 77 K) and pore size distribution (NLDFT kernel for silica with cylindrical pore from the adsorption branch) of DVB-PMO that was used as benchmark to evaluate the impact of calcination on the specific BET surface area and the pore system.

Additional information on C_{16}TAB

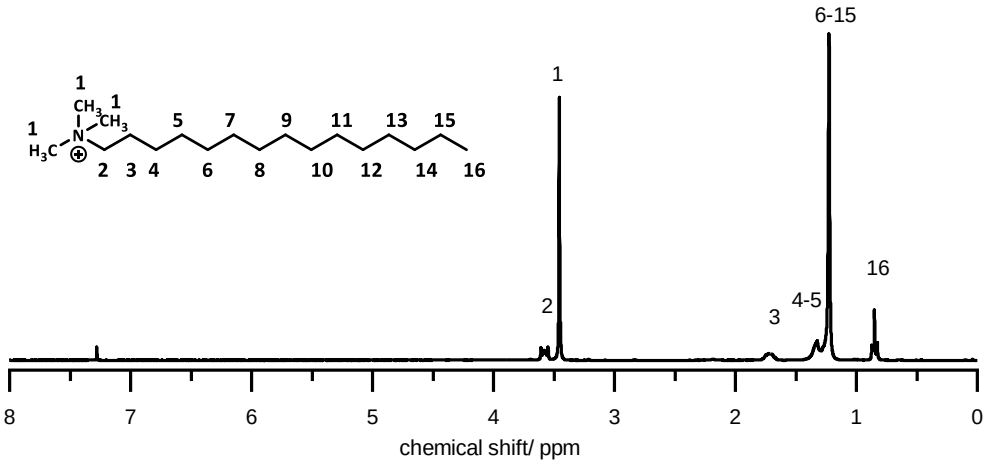

Figure 9-38: C_{16}TAB ^{1}H-NMR (300 MHz, $CDCl_3$, 25 °C): δ [ppm] = 3.55-3.61 (m, 2H, H2), 3.46 (s, 9H, H-1), 1.78-1.66(m, 2H, H-3), 1.44-1.30 (m, 4H, H-4, H-5) 1.23 (s, 22H, H-6-H-15), 0.85 (t, 3H, $^{3}J_{CH2-CH3}$ = 7.5 Hz,H16).

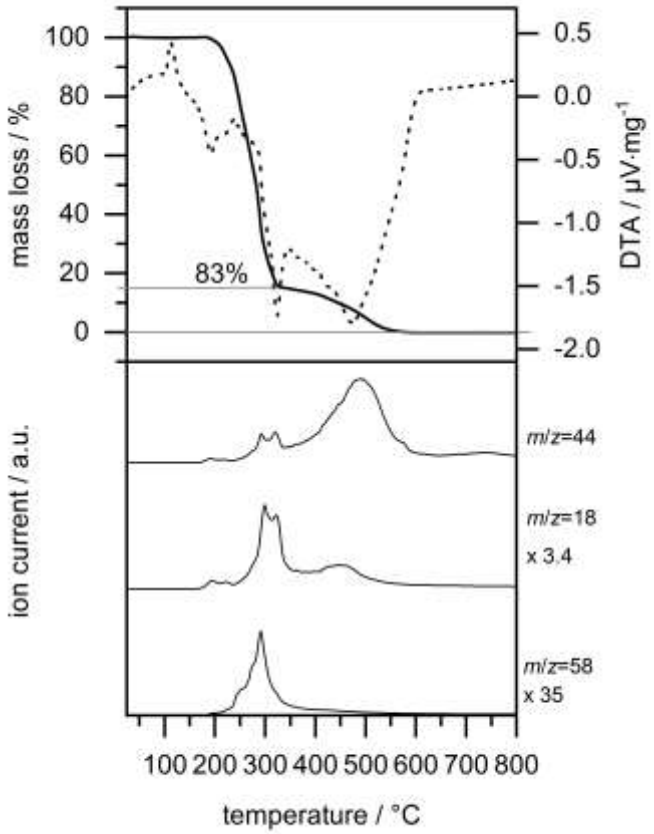

Figure 9-39: TG/DTA/MS of the surfactant C_{16}TAB.

Additional figures to 4.5 Alginate hydrogel as form-giving matrix for nanoporous organo(silica) beads

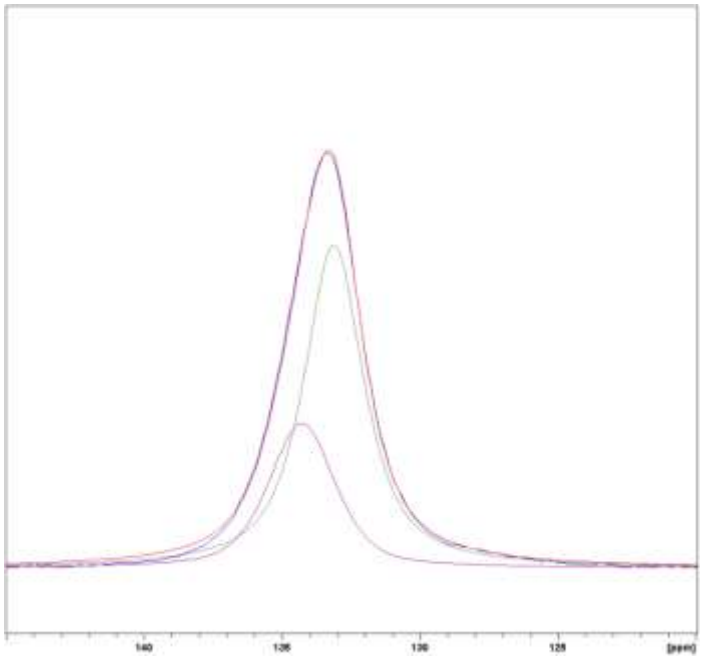

Figure 9-40: Deconvolution of ^{13}C-CP-MAS NMR spectrum of B-organosilica beads. It shows that the signal at 134 ppm is composed of two overlapping signals at 133.3 ppm and 134.4 ppm.

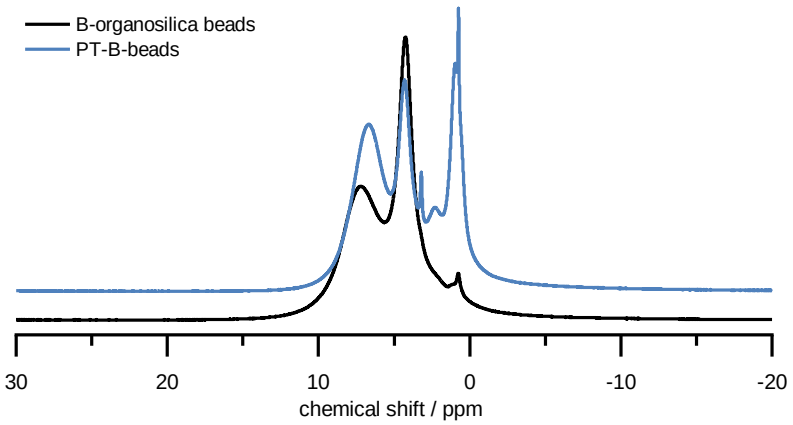

Figure 9-41:1H MAS NMR spectra (spinning speed 13 kHz) of B-organosilica beads (black) and the PT-B-beads (blue).

9.2 Hazard substances categorized according to GHS

All substances that were used in this thesis are listed in Table 9-6 together with their safety information according to the Globally Harmonized System (GHS).

Table 9-6: substances with safety information according to GHS

Substance	Pictograms	Hazard statements	Precautionary statements
1, 4-dioxane	02, 07, 08 Danger	H225-H319-H335-H351	P210-P261-P281-P305 + P351 + P338
1,4-bis(triethoxysilyl)benzene	Not a hazardous substance.		
1,4-dibromo-2,5-fluorobenzene	07 Warning	315, 319, 335	261, 305+351+338
1,4-dibromo-2-chlorobenzene	07 Warning	315, 319, 335	261, 304+340, 305+351+338, 401
1,4-dibromo-2-fluorobenzene	07 Warning	315, 319, 335	261, 305+351+338
1.4-dibrombenzene	07, 09 Danger	315, 319, 335, 400	261, 273, 305+351+338
acetone	02, 07 Danger	225, 319, 336	210, 261, 305+351+338
Bis(tri-*tert*-butylphosphin)palladium(0)	Not a hazardous substance.		
calcium lactate pentahydrate	Not a hazardous substance.		
cetyltrimethylammonium bromide (C_{16}TAB)	05, 07, 08, 09 Danger	302, 315, 318, 335, 373	280,301+312, 302+352, 305+351+338, 310, 391
chloroform-d	06, 08 Danger	302, 315, 319, 331, 351, 361d, 372	260, 280, 301+312+304+340+312, 305+351+338, 403+233
DMSO-d_6	- Warning	227	210, 280, 370+378, 403+235+501

Substance	Pictograms	Hazard statements	Precautionary statements
dodecyltrimethylammonium bromide (C_{10}TAB)	07, 09 Warning	302, 315, 319, 335, 410	261, 273, 305+351+338, 501
ethanol	02 Warning	225	210, 233, 305+351+338
ethyl acetate	02, 05 Danger	225, 319, 336	210, 261, 305+351+338
hydrochloride acid (37%)	05, 07 Danger	290, 314, 335	260, 280, 303+361+353, 304+340+310, 305+351+338
isopropyl alcohol	02, 07 Danger	225, 319, 336	210, 261, 305+351+338
methanol	02, 06, 08 Danger	225, 301+311+331, 370	210, 280, 302+352+312, 304+340+312, 370+P378, P403+P235
***N*,*N*-dicyclohexylformamide**	02, 07, 08 Danger	226, 312+332, 319, 360D	201, 210, 261, 280, 308+313, 370+378
***N*,*N*-dicyclohexylmethylamine**	05, 07 Danger	302,314	280, 305+351+338, 310
octadecyltrimethylammonium bromide (C_{18}TAB)	05, 07, 09 Danger	302, 315, 317, 318, 410	280, 301+312+330, 305+351+338+310
octadecyltrimethylammonium chloride (C_{18}TAC)	07 Warning	302, 312	280
sodium alginate	Not a hazardous substance.		
sodium hydroxide	05 Danger	290-314	260, 280, 303+361+353, 304+340+310, 305+351+338
tetraethyl orthosilicate	02, 07 Warning	226, 319, 332, 335	210, 261, 280, 304+340+312, 337+313+403+235
triethoxyvinylsilane	02, 07 Warning	226, 319, 335	261, 305+351+338

10 Publications

Articles

- Malina Bilo, Maximilian Münzner, Christian Küster, Dirk Enke, Young Joo Lee, Michael Fröba,
  Pseudomorphic Transformation of Organosilica@ Controlled Pore Glass – A New Approach Forming Hierarchically Porous Organosilica/Silica Hybrid Materials, *submitted,* **2019.**
- Malina Bilo, Young Joo Lee, Michael Fröba,
  Millimeter-sized micellar-templated silica beads and phenylene-bridged mesoporous organosilica beads,
  Microporous Mesoporous Mater. **2019**, *284*, 327-335.
  doi.org/10.1016/j.micromeso.2019.04.028.
- Malina Bilo, Michael Sartor, Hiba Nasser, Young Joo Lee, Felix J. Brieler, Michael Fröba,
  Diving into the chiral pool: enantiopure microporous polysilsesquioxane spheres from both enantiomers with an oxazolidinone motif,
  J. Sol-Gel Sci. Technol. **2018**. doi.org/10.1007/s10971-018-4774-z.

Oral Presentations

- Malina Bilo, Maximilian Münzner, Felix J. Brieler, Dirk Enke, Michael Fröba,
  PMO @ CPG – Controlling the Pore Size in Monoliths of Hierarchically Structured Nanoporous Organosilica/Silica Hybrid Materials,
  NANOPOROUS MATERIALS - VIII 2017, Ottawa**,** Kanada.
- Malina Bilo, Christina Küster, Felix J. Brieler, Dirk Enke, Michael Fröba,
  PMO@CPG – monoliths of hierarchically structured nanoporous organosilica/silica hybrid materials,
  5th Internat. Conference on Multifunctional, Hybrid and Nanomaterials, 2017, Lissabon**,** Portugal.
- Malina Bilo, Christian Küster, Felix J. Brieler, Dirk Enke, Michael Fröba,
  Synthesis of hierarchically structured nanoporous organosilica/silica composites, Jahrestreffen der ProcessNet-Fachgruppen Adsorption und Gasreinigung, 2016, Duisburg, Deutschland.

Poster

- Malina Bilo, Maximilian Münzner, Christian Küster, Felix J. Brieler, Dirk Enke, Michael Fröba, 29. Deutsche Zeolith Tagung, **2017**, Frankfurt, Deutschland.
- Malina Bilo, Christian Küster, Felix J. Brieler, Dirk Enke, Michael Fröba, 28. Deutsche Zeolith Tagung, **2016**, Gießen, Deutschland.
- Malina Bilo, Michael Sartor, Felix J. Brieler, Michael Fröba, 27. Deutsche Zeolith Tagung, **2015**, Oldenburg, Deutschland.